

**MICROWAVE AND MILLIMETER WAVE
TECHNOLOGIES: MODERN UWB
ANTENNAS AND EQUIPMENT**

**MICROWAVE AND MILLIMETER WAVE
TECHNOLOGIES: MODERN UWB
ANTENNAS AND EQUIPMENT**

Edited by
PROF. IGOR MININ

Published by In-Teh

In-Teh

Olajnica 19/2, 32000 Vukovar, Croatia

Abstracting and non-profit use of the material is permitted with credit to the source. Statements and opinions expressed in the chapters are those of the individual contributors and not necessarily those of the editors or publisher. No responsibility is accepted for the accuracy of information contained in the published articles. Publisher assumes no responsibility liability for any damage or injury to persons or property arising out of the use of any materials, instructions, methods or ideas contained inside. After this work has been published by the In-Teh, authors have the right to republish it, in whole or part, in any publication of which they are an author or editor, and the make other personal use of the work.

© 2010 In-teh

www.intechweb.org

Additional copies can be obtained from:

publication@intechweb.org

First published March 2010

Printed in India

Technical Editor: Sonja Mujacic

Cover designed by Dino Smrekar

Microwave and Millimeter Wave Technologies:

Modern UWB antennas and equipment,

Edited by Prof. Igor Minin

p. cm.

ISBN 978-953-7619-67-1

Preface

Novel generation wireless system is a packet switched wireless system with wide area coverage and high throughput. It is designed to be cost effective and to provide high spectral efficiency. The 4th wireless uses Orthogonal Frequency Division Multiplexing, Ultra Wide Radio Band and millimeter wireless and smart antenna. Highly directive, planar UWB antennas are gaining more and more attention, as required in many novel and important applications. With the release of the microwave and millimeter band, applications for short-range and high-bandwidth different new devices are primary research areas in UWB systems.

Two different techniques for Directive Ultra-Wideband Planar Antennas were presented throughout chapter 1: the operation of a novel bow-tie antenna with high front-to-back ratio and directivity and a differential planar UWB antenna characterized by higher gain (more than 11 dB around 7 GHz) with respect to conventional printed radiators has been demonstrated.

The chapter 2 is timely in reporting the aspects of the conventional and state-of-the-art antenna design in the UWB system. For example, design methods of the conventional UWB antennas such as log-periodic dipole array are overviewed and the UWB antennas which are recently researched are introduced. Also the principle and design methods to notch the particular frequency band in UWB antenna are summarized

As it well known microstrip patch antennas have problems of low bandwidths. In the chapter 3 various ways to overcome this problem by using various matching techniques for numerous patch antenna array schemes is show.

The recent progress in the development of UWB planar antenna technology has been reviewed and some types of UWB metal-plate monopole antennas, UWB printed monopole antennas and UWB printed slot antennas are described in the chapter 4.

In the chapter 5 design and implementation of a practical reconfigurable communication system including an additive ultra wide band white Gaussian noise and delay lines in X-band from 6 to 12 GHz with other necessary microwave parts as the test bed are introduced. Also design and implementation procedures of all microwave parts such as ultra wideband amplifiers, dividers, switches, drivers, gain controllers, generators, filters, delay components, bias tee, transitions and etcetera are discussed.

Slot array antennas using rectangular waveguides were widely used based on their various important capabilities in microwave telecommunications. In the chapter 6 detailed study of polarization agility achievement in Annular Waveguide Slot Antennas (AWSA) are presented. In an AWSA, the waveguide and the slots are all circularly oriented to fit the boundary.

Far-field radiation pattern control has strong potential in smart antennas, wireless communications and radar. Typical planned applications include multipath fading and interference mitigation, data rate and coverage enhancement, etc. For implementing these functionalities, either switch beam or reconfigurable Half-Power Beam-Width (HPBW) antennas are required. In the chapter 7, the authors present different antenna concepts to obtain reconfigurable radiation pattern capability in millimeter waves as follows: multibeam antennas are demonstrated based on Butler matrices at 24 and 60 GHz, and reconfigurable Half Power BeamWidth antennas are shown. Also a new technique is presented to shape the radiation pattern of an antenna to achieve directive or sectorial beams. In this case, the antenna design is based on an inhomogeneous lens fed by several sources.

In the chapter 8 author investigate the ring loop antenna for the UHF digital terrestrial broadcasting. A ring loop antenna is excited by a simple and low-cost feeder system. The broadband input impedance and the high gain are obtained in the calculation and the measurement.

During the past few decades, there has been growing interest in the use of microwave and millimeter wave radiometers for remote sensing of the earth. The chapter 9 addresses the subject of antenna array design in aperture synthesis radiometers. Also a novel antenna array is described, which is a sparse antenna array with an offset parabolic cylinder reflector at millimeter wave band.

As it well known the antenna is an important element of communication, remote sensing and radio-localization systems. The measurement of the antenna radiation pattern characteristics allows to verify the conformity of the antenna. The different antenna measurement techniques are reviewed in the chapter 10.

The interpretation of the radiated EMI measurement is a very complex problem due to many disturbing influences affecting such a measurement. The antenna brings into measurement additional errors, which increase measurement uncertainty. These errors and their effect on the entire uncertainty of the measurement are investigated in the chapter 11 in case of broadband Bilog antenna, a typical receiving antenna for radiated EMI measurement.

Over the past few years, a large number of pattern synthesis techniques of antenna arrays have been studied and developed. In the chapter 12 authors study the influence of the sensor directivity into the array beampattern, in order to test if the effects on the array pattern must be taken into consideration in design methods of pattern array synthesis, and other array design methods.

In the chapter 13, a brief introduction of mm-wave RoF system is given and the optical techniques of generating mm-wave signals are presented. Unlike the conventional discussions about mm-wave RoF systems focusing on the downlink only, the design of bidirectional mm-wave RoF systems are also considered.

Rain-induced attenuation creates one of the most damaging effects of the atmosphere on the quality of radio communication systems, especially those operating above 10 GHz. The chapter 14 presents results that have thus far been acquired from an integrated research campaign jointly carried out by researchers at Institut Teknologi Sepuluh Nopember, Indonesia and Kumamoto University, Japan. The research is aimed at devising transmission strategies suitable for broadband wireless access in microwave and millimeter-wave bands, especially in tropical regions.

High-precision and high-temporal global rainfall maps are very important for scientific studies for global water cycle and practical applications for water resources. The purpose of the chapter 15 is to briefly describe the Global Satellite Mapping of Precipitation algorithm, provide examples of rainfall maps from microwave radiometers.

Conventional metallic waveguides have several major advantages, including low propagation losses and high power transmissions in the microwave frequency range. One disadvantage of metallic waveguides is that the propagation frequency band is limited at frequencies above the cutoff frequency. The chapter 16 introduces a system that uses a dual-frequency band waveguide. Authors present the fundamental principles of this dual-frequency band waveguide in which a dual in-line dielectric array is installed. It has been shown the electromagnetic waves were propagated in a waveguide with dual in-line dielectric rods made of LaAlO₃ and without higher modes above the 2 cutoff frequencies.

In the chapter 17 authors propose a design method of a voltage-controlled oscillator using on-chip coplanar waveguide (CPW) resonator thus replacing an LC-resonator at 5 GHz band. It has been shown the advantages of employing CPW resonator is the wide frequency-tuning range, and it also saves about 30% of chip size whereas the measured other performance of the proposed oscillators are comparable to that of an oscillator using LC resonator. The design technique is applicable for higher frequencies.

The microwave and millimeter wave broadband amplifier is importance for wideband wireless communications operating within microwave frequency range. The chapter 18 provides the fundamental design concepts of broadband amplifier using the modern CMOS technology. Various design techniques are introduced for achieving high performance microwave broadband amplifiers. The main design considerations and current trends are also discussed.

The chapter 19 illustrates the interferometric concept in quadrature down-conversion for communication and radar sensor applications.

In the chapter 20 describe a new method for the analysis of passive waveguide components, composed of the cascade connection of planar junctions. This new method extracts the main computations out of the frequency loop, thus reducing the overall CPU effort for solving the frequency-domain problem.

The fundamental theory permitting the synthesis of the negative group delay cell is described in details in the chapter 21. A time domain study based on a Gaussian wave pulse response, the physical meaning of this phenomenon at microwave wavelengths is also provided and a new concept of frequency-independent active phase shifter used in recent applications are described.

In the chapter 22, the authors summarize the design procedure of broadband MMIC high power amplifiers. Some special considerations, as well as, experimental results are focused on GaN technology.

Historically magnetrons were one of the first devices used to build radar systems. In the last chapter 23 it has been shown that the utilization of recent advances in magnetron manufacturing technology, the introduction of novel approaches in radar design as well as a vast progress in digital signal processing technique result in a solid overall performance of the magnetron based millimeter wavelengths radars.

It is expected the book will attract more interest in microwave and millimeter wave technologies and simulate new ideas on this fascinating subject.

Editor:

Prof. Igor Minin

Novosibirsk State Technical University, Russia

Prof.minin@gmail.com

Contents

Preface	V
1. Directive Ultra-Wideband Planar Antennas	001
A.-D. Capobianco, F.M. Pigozzo, A. Locatelli, D. Modotto, C. De Angelis, S. Boscolo, F. Sacchetto, M. Midrio	
2. Ultra-Wideband Antenna	019
Cheolbok Kim	
3. Patch Antennas and Microstrip Lines	049
John R. Ojha and Marc Peters	
4. UWB and SWB Planar Antenna Technology	063
Shun-Shi Zhong	
5. A Complete Practical Ultra wideband Test Bed in X-Band	083
Gholamreza Askari, Khatereh Ghasemi and Hamid Mirmohammad Sadeghi	
6. Novel Polarization-Agile Annular Waveguide Slot Antennas	109
Siamak Ebadi and Keyvan Forooraghi	
7. Reconfigurable radiation pattern antennas in mm-waves	123
Olivier Lafond, M. Caillet, B. Fuchs and M. Himdi	
8. Characteristics of High-Gain Wideband Ring Loop Antenna and its Application	145
Haruo Kawakami	
9. Antenna Array Design in Aperture Synthesis Radiometers	169
Jian Dong and Qingxia Li	
10. Antenna Measurement	193
Dominique Picard	
11. The interference between ground plane and receiving antenna and its effect on the radiated EMI measurement uncertainty	215
Mikulas Bittera, Viktor Smiesko, Karol Kovac and Jozef Hallon	
12. Analysis of directive sensor influence on array beampatterns	229
Lara del Val, Alberto Izquierdo, María I. Jiménez, Juan J. Villacorta and Mariano Raboso	

13. Millimeter-wave Radio over Fiber System for Broadband Wireless Communication Haoshuo Chen, Rujian Lin and Jiajun Ye	243
14. Measurement and modeling of rain intensity and attenuation for the design and evaluation of microwave and millimeter-wave communication systems Gamantyo Hendrantoro and Akira Matsushima	271
15. High-Temporal Global Rainfall Maps from Satellite Passive Microwave Radiometers Shoichi Shige, Satoshi Kida, Tomoya Yamamoto, Takuji Kubota and Kazumasa Aonashi	301
16. A Dual-Frequency Metallic Waveguide System Yoshihiro Kokubo	313
17. Applications of On-Chip Coplanar Waveguides to Design Local Oscillators for Wireless Communications System Ramesh K. Pokharel, Haruichi Kanaya and Keiji Yoshida	329
18. Design Techniques for Microwave and Millimeter Wave CMOS Broadband Amplifiers Shawn S. H. Hsu and Jun-De Jin	345
19. MULTI-PORT TECHNOLOGY AND APPLICATIONS Moldovan Emilia, Bosisio G. Renato, Wu Ke and Tatu Serioja O.	363
20. Wideband Representation of Passive Components based on Planar Waveguide Junctions Fermín Mira, Ángel A. San Blas, Vicente E. Boria and Benito Gimeno	389
21. Study and Application of Microwave Active Circuits with Negative Group Delay Blaise Ravelo, André Pérennec and Marc Le Roy	415
22. Broadband GaN MMIC Power Amplifiers design María-Ángeles González-Garrido and Jesús Grajal	441
23. Magnetron Based Radar Systems for Millimeter Wavelength Band – Modern Approaches and Prospects Vadym Volkov	459

Directive Ultra-Wideband Planar Antennas

A.-D. Capobianco ^{#1}, F.M. Pigozzo ^{#2}, A. Locatelli ^{*3}, D. Modotto ^{*4}, C. De Angelis ^{*5}, S. Boscolo ⁺⁶, F. Sacchetto ⁺⁷, M. Midrio ⁺⁸

#DEI, Università degli Studi di Padova

**DEA, Università degli Studi di Brescia*

*+DIEGM, Università degli Studi di Udine
Italy*

1. Introduction

Since the acceptance of unlicensed use of the Ultra-Wideband (UWB) technology in the range between 3.1 and 10.6 GHz in the USA (FCC, 2002) and more recently between 3.4 and 8.5 GHz in Europe (ETSI, 2008), the realization of low-cost UWB wireless systems is considered a fundamental research goal both for military and commercial applications. The possible use and benefits of UWB technology are significant and among its potential applications, high-resolution radar and short-range ultra-high speed data transmission are very attractive. In this scenario, design, fabrication and characterization of effective antennas for UWB systems are challenging tasks with respect to the case of narrowband systems. A suitable UWB antenna should be capable of operating over an ultra-wide bandwidth. Therefore it is necessary to guarantee a good behavior of the antenna in the band of interest in terms of impedance matching with the transmitter, radiation and time-domain properties. Moreover, recent UWB antenna development tends to focus on ultra-compact planar antennas as they are more practical in terms of manufacturing, integration with the system electronics board and form factor. Typical configurations exhibit radiation patterns similar to the traditional monopole/dipole antennas, i.e. they behave as omnidirectional radiators in the plane normal to the radiating element. This feature is desirable in UWB devices which do not have a fixed or a-priori defined orientation with respect to the environment and thus when it is not necessary to favour any specific direction. On the other hand, strongly directive radiators are required for radar applications, especially when low-power, low-interference and high-resolution devices are needed. Directive UWB radiators are also interesting towards several complementary goals, e.g. to provide extra radio link gain to single antenna transceivers, to mitigate the effects of multipath in the indoor UWB channel, and, last but not least, to result in a high front-to-back ratio, which is desirable in many applications such as in wireless body-area networks (WBAN).

In the past few years, several printed broadband monopole-like configurations have been reported for UWB applications, but presently, very few efforts have been made to increase their directionality. This chapter intends to provide the reader with two different design methodologies for increasing the directivity of planar UWB antennas. In section 2, a novel antenna layout will be presented, as the result of subsequent modifications of a native

omnidirectional radiator: the bow-tie antenna. A high front-to-back ratio, low-profile design will be developed by exploiting a planar reflector and studying ad-hoc optimizations of both the antenna geometry and the feeding arrangement. The final layout could be particularly well-suited for point-to-point high data-rate UWB radio links around the 5.5 GHz center frequency.

In section 3, a different approach will be adopted: instead of backing an omnidirectional printed wideband dipole, a structured ground plane will be employed with a two-element array of disc monopoles. The resulting highly directive UWB antenna is designed to be used in combination with a single-chip radar transceiver operating between 6 and 8 GHz (Cacciatori et al., 2007).

The reader will find a detailed step-by-step design procedure, along with experimental data obtained through characterization of several prototypes in anechoic chamber.

2. An UWB Bow-Tie Antenna with High Front-to-Back Ratio

2.1 Design Principles

As previously said in the introduction of this chapter, in the UWB communication framework there are scenarios in which directivity is mandatory, for example when the antenna has to be located in the corner of a room or against a wall to provide a sectoral radio coverage from the transmitter (i.e. an access point) to the receiver (i.e. a set-top box). Moreover, small dimensions and low-profile are desirable features for an easier integration in the final device. For all these reasons the RF engineer may start the antenna design with the choice of the candidate wideband radiator along with its initial geometrical parameters. As directionality can be effectively achieved through the use of a planar reflector, the wideband, planar radiating element can be natively omnidirectional, such as the bow-tie antenna. In the following, a design methodology is presented, starting from the technical specifications summarized in Table 1.

center frequency	5.5 GHz
fractional bandwidth	$\geq 20\%$
laminar	Rogers RO4003C
laminar dimensions	30 x 50 mm ²
flat reflector dimensions	100 x 70 mm ²
laminar - reflector distance	roughly 5 mm

Table 1. Technical specifications.

The well known design guidelines for a bow-tie resonating at 5.5 GHz (Balanis, 2005) would lead to a total length of 16 mm, a small value that may cause problems when connecting the antenna to the feed-line whose dimensions are comparable with the radiator itself; this fact imposes to enlarge the antenna, and thus to force it to operate at a higher order resonance.

However, the laminar technical specifications limit the maximum size of the bow-tie. As a consequence, a good trade-off is the antenna layout shown in Fig. 1. The latter will in turn allow to save enough space to arrange the feeding/matching line on the same laminar. It is important to note that an antipodal configuration is preferable since the antenna will be fed using a 50 Ohm SMA connector.

Such an early model, mounted at a given distance above a planar reflector, can be studied and subsequently optimized through numerical simulations with CST Microwave Studio commercial software (CST, 2009).

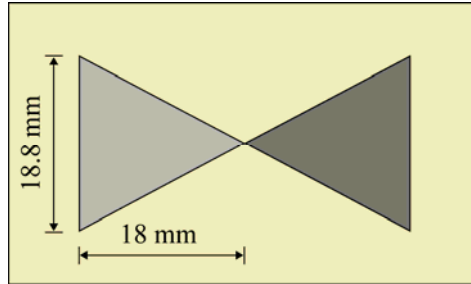


Fig. 1. The bow-tie planar wideband dipole. The reflector is omitted for sake of clarity. The dark (light) gray region is on the bottom (top) of the laminate, in antipodal configuration.

As shown in Fig. 2, the computed input impedance reveals a narrowband behavior, as the reactance is nearly zero over a small frequency range around the highest resonance; however, the real part is nearly constant between 6 and 8 GHz. This suggests to investigate a modified design to move down the highest resonance, as well as the flat resistance region, towards the 5.5 GHz center frequency.

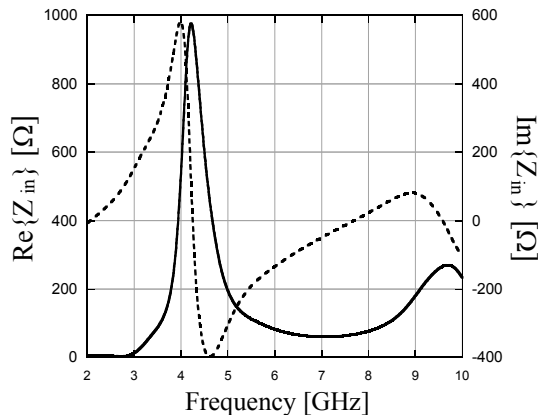


Fig. 2. Input impedance of the initial antenna of Fig. 1; real part (solid line) and imaginary part (dashed line).

Aiming to keep untouched the reference bow-tie dimensions, the effect of moving the feeding point off the vertex and along the edge of the patches can be numerically explored (see Fig. 3). In Figs. 4(a) and 4(b) the real and imaginary part of the input impedance are plotted versus frequency, for different values of the distance between the feeding point and the vertex. It is interesting to note that when this distance (“*a*” parameter in Fig. 3) ranges between 5 and 6 mm, the flat region of the real part of the input impedance falls in the band of interest, and the resonance approaches the desired center frequency of 5.5 GHz.

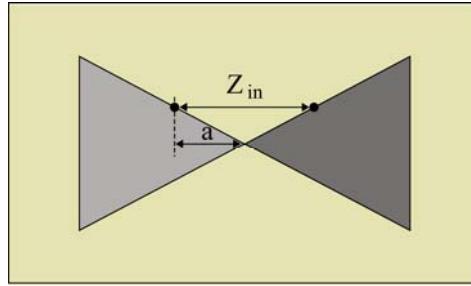


Fig. 3. Unconventional bow-tie feeding.

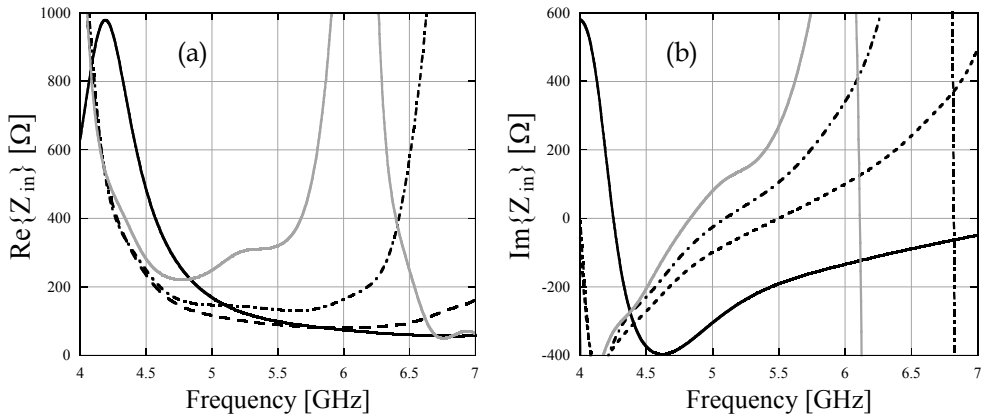


Fig. 4. (a) real part and (b) imaginary part of the input impedance versus frequency for different positions of the feeding point: $a = 0$ mm (solid line), $a = 5$ mm (dashed line), $a = 6$ mm (dashed-dotted line), $a = 7$ mm (gray line).

The next step in the design procedure is to provide a feasible microstrip transmission line to drive the signal up to the feeding points. A transmission line with 200 Ohm intrinsic impedance, a value which roughly coincides with the real part of the antenna input impedance, may be designed by suitably choosing the stripes widths and spacing (see Fig. 5(a)). Notice that, as in the case of many other planar transmission lines, the intrinsic impedance decreases for increasing strip widths. This in turn suggests that matching to a conventional 50 Ohm connector can be obtained by suitably tapering the strip widths.

Further refinements of the antenna resonance may be obtained by acting on the bow-tie tips, i.e. where the most intense currents flow. For instance, we observed that if we truncate the tip edges as shown in Fig. 5(b), a slight increase of the resonant frequency takes place (see Fig. 6, where the reflection coefficient of the antenna with and without the tips is reported).

If the antenna with truncated tips is chosen, two ways of designing the transmission line may be envisaged. Indeed, the stripes may be bent upward or downward from the feeding points. The latter option (see Fig. 7) is preferable, as a longer transmission line will in turn result in a smoother tapered transition to the 50 Ohm connector.

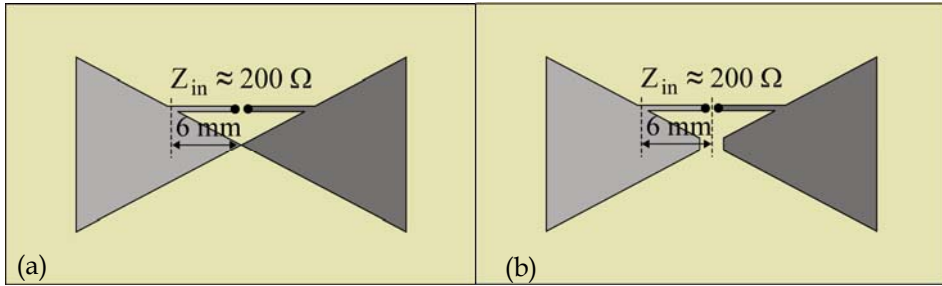


Fig. 5. Selected feeding point position and stripes arrangement: (a) with and (b) without bow-tie tips.

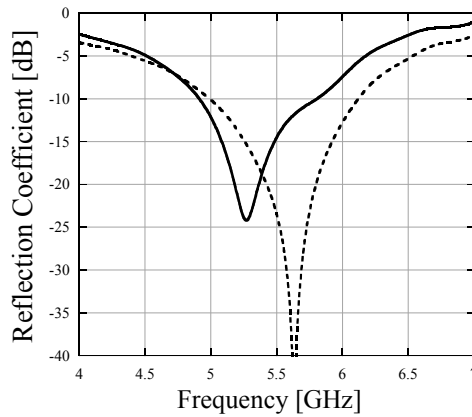


Fig. 6. Reflection coefficient of the antenna with off-vertex feeding: solid line refers to design of Fig. 5(a), dashed line refers to design of Fig. 5(b). In both cases, the reference impedance was set to 200 Ohm.

Bending the stripes downward will also cause the transmission line to run through the bow-tie truncated tips. As we will show in section 2.3, if the spacing between the line stripes and the truncated tips is small enough, two radiating *slots* (Balanis, 2005) are created. This will provide an additional resonance that may be tuned to further increase the overall antenna bandwidth.

2.2 Antenna Layout

Fig. 8 shows the final antenna layout. The laminate is a $50 \times 30 \times 1.575 \text{ mm}^3$ Rogers RO4003C mounted above a $110 \times 90 \text{ mm}^2$ rectangular metal reflector (not depicted in the figure for sake of clarity) at a distance of 6 mm.

The thickness of the copper is $35 \mu\text{m}$ everywhere. A linear tapering of the feed-line ending with 3 mm width for the top layer and 8 mm width for the bottom layer provides the transition to the 50 Ohm SMA connector.

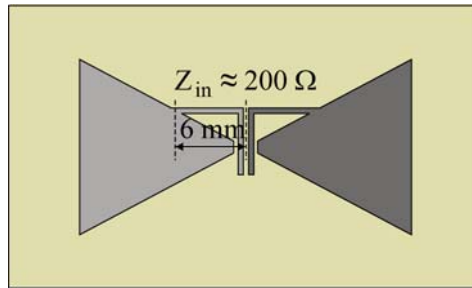


Fig. 7. Schematic of the candidate design with off-vertex feeding point, truncated bow-tie tips and bent feed-lines.

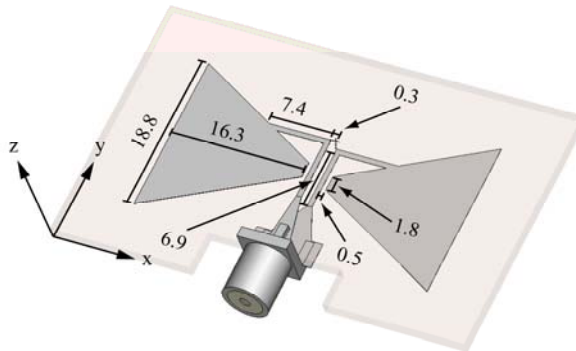


Fig. 8. Model and dimensions (in millimeters) of the proposed antenna. The left half of the planar radiator is on the top of the substrate, whereas the right half is on the bottom (antipodal configuration).

The parallel stripes which run between the bow-tie tips have a width equal to 0.6 mm. They are printed on opposite sides of the substrate and are separated by a 0.3 mm gap (with respect to the x -axis). The stripes are bent at a right angle and connect to the triangular patches via two 7.4 mm-long branches. The central vertex of each triangular patch is “cut away”, resulting in a 0.5×1.8 mm² slot between the feed-line and the patch. The entire structure has been numerically modeled with CST Microwave Studio. All the elements have been included in the simulations: the metallic patches, stripes and planar reflector, as well as the SMA connector and the ending part of a 50 Ohm coaxial cable filled with lossy Teflon. All the metal parts have been regarded as perfect electric conductors, while the dielectrics in the laminate and in the coaxial cable have been modeled as lossy materials. Values $\epsilon_r = 3.38$ and $\epsilon_r = 2.1$ have been used for the relative permittivity of RO4003C and Teflon. As for the losses, $\tan \delta = 0.0027$ and $\tan \delta = 0.001$ have been used, respectively. Simulations have been performed in the 4 to 7 GHz range in order to optimize all the geometrical parameters of the antenna, including the dimensions of the stripes, the transition and the distance between the laminate and the reflector.

With the dimensions reported in Fig. 8, a prototype (Fig. 9) was fabricated using a numerically-controlled milling machine. Reflection coefficient and radiation patterns of the antenna under test have been measured in anechoic chamber using a 2-port Agilent N5230A

PNA-L network analyzer, a Satimo SGH-820 ridged horn wideband probe antenna, and a remotely controlled turntable.

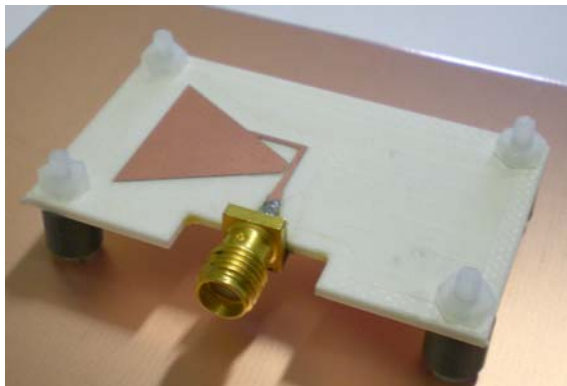


Fig. 9. Photograph of the antenna that has been fabricated and experimentally characterized.

2.3 The Radiation Mechanism

Figs. 10 and 11 show the simulated (dashed-dotted line) and measured (solid line) reflection coefficient (S_{11} parameter) and its representation on the Smith chart for the proposed antenna, as normalized to 50 Ohm. The measured band at $|S_{11}| = -10$ dB spans from 4.8 GHz to 6.1 GHz. Therefore the bandwidth equals about a fourth of the center frequency, thus making the proposed bow-tie an Ultra-Wideband antenna, according to the FCC definition (FCC, 2002).

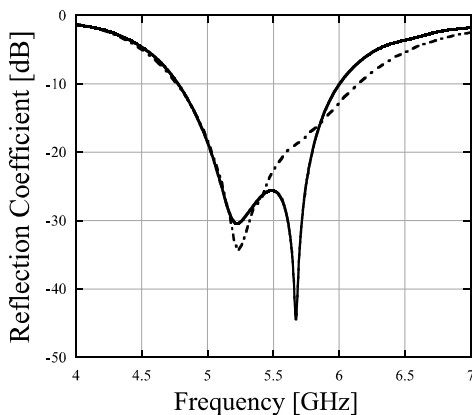


Fig. 10. Simulated (solid line) and measured (dashed-dotted line) magnitude of the reflection coefficient ($|S_{11}|$) versus frequency.

As for the radiation mechanism, we notice that the simulations clearly show two separate resonances which concur to form the antenna overall bandwidth. At the lower resonance, an

intense electric field is observed between the parallel stripes which run in the middle of the bow-tie tips. The stripes form a slot, loaded by the metallic patches which are connected at the slot far end by the T-branches. The resonant frequency scales inversely with the length of the parallel stripes.

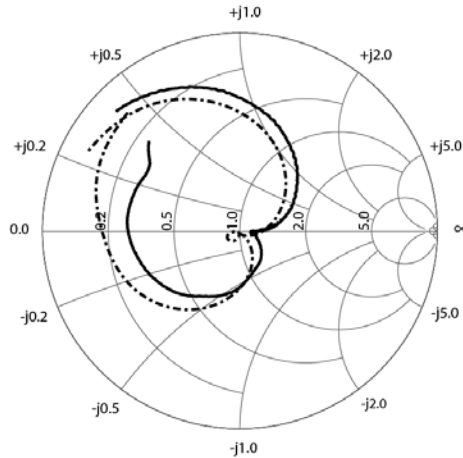


Fig. 11. Input impedance of the antenna on the Smith chart. Dashed-dotted line and solid line are used for simulated and measured data, respectively.

At the upper resonant frequency, radiation is due to the electric field which seeds in the slots etched between the parallel stripes and the bow-tie tips. The resonant frequency is influenced by the length of both the parallel stripes, and of the T-branches.

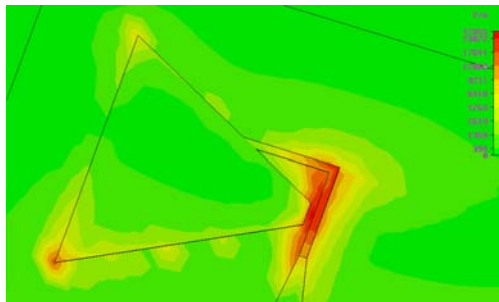


Fig. 12. Simulated surface magnetic currents intensity at the lower resonant frequency.

Figs. 12 and 13 confirm this picture by showing the numerically evaluated electric field at the two resonances. At the lower resonance (Fig. 12), a large electric field is observed all along the right-hand side of the feeding strip. Whereas, at the upper resonance (Fig. 13), it is clearly visible that the field no longer reaches the T-branch at the end of the strip. It is much more tightly confined in the region between the left-hand side of the strip and the truncated bow-tie tip, and rapidly vanishes away from the slot.

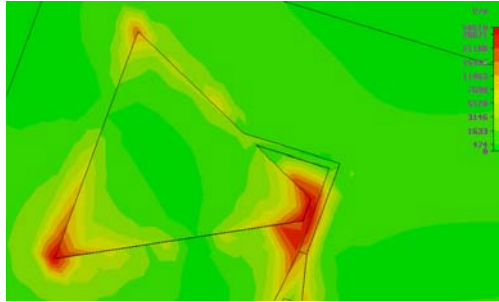


Fig. 13. Simulated surface magnetic currents intensity at the upper resonant frequency.

In the proposed antenna, therefore, the bow-tie is not used to realize a wideband radiator, as it is normally done in “conventional” bow-tie dipoles (Eldek et al., 2005), (Kiminami et al., 2004). Rather, the metallic patches are used as wideband loading or matching networks, and radiation is primarily due to magnetic currents which flow in properly designed slots.

Notice also that the two separate resonances we have observed in the simulations do not appear in the experimental results as clearly as in the simulations. We explain this discrepancy on the basis of the following considerations. When we numerically simulated the antenna, we observed that the spectral location of the upper resonant frequency is very sensitive to the electrical length of the T-branches. That is, small variations of either the physical length of these metallic stripes, or of the dielectric constant of the underlying slab may cause a noticeable shift of the upper resonant frequency. If the frequency shifts upwards, $|S_{11}|$ between the two resonances may eventually exceed the -10 dB level, finally splitting the operation bandwidth into two separate regions. Whereas, if the frequency shifts downward, the upper resonance tends to merge with the lower one, thus forming a unique dip in the $|S_{11}|$ plot. These behaviours are accompanied by easily detectable features on the Smith chart. Indeed, the two resonances form a loop near the chart center. The loop gets larger when the resonant frequencies split. Viceversa, it tends to collapse and to eventually disappear when the resonant frequencies merge. This is what happened in our experiment: the loop in the vicinity of the chart center has a very reduced extension, revealing that the two resonant frequencies have merged. The likely cause is either a misfabrication, or a slight discrepancy between the experimental and declared values of the dielectric constant.

2.4 Radiation Patterns, Front-to-Back Ratio, and Group Delay

Figs. 14, 15 and 16 show the radiation patterns in the x - z and y - z planes for the 4.8 GHz, 5.5 GHz and 6.1 GHz frequencies respectively. The -3 dB beamwidth ranges between 52 and 87 degrees and between 60 and 72 degrees in the x - z and y - z planes respectively. It may be observed that the direction of maximum radiation is slightly off the normal to the plane which contains the antenna. This is due to the antipodal layout of the antenna itself.

Fig. 17 shows the measured frequency dependence of the front-to-back ratio, which always exceeds the level of 24 dB. The measured antenna gain ranges between 8 and 10 dB.

As for the antenna performance in the time-domain, we calculated the variation in frequency of the group delay, which is related to the first-derivative of the measured phase of the S_{12} parameter. As can be seen in Fig. 18 the variation of the group delay in the band of

interest is less than 250 ps, which is appreciably low as compared to the duration of the stimulus in a pulsed transmission (about 1.5 ns for the 4.8 - 6.1 GHz band).

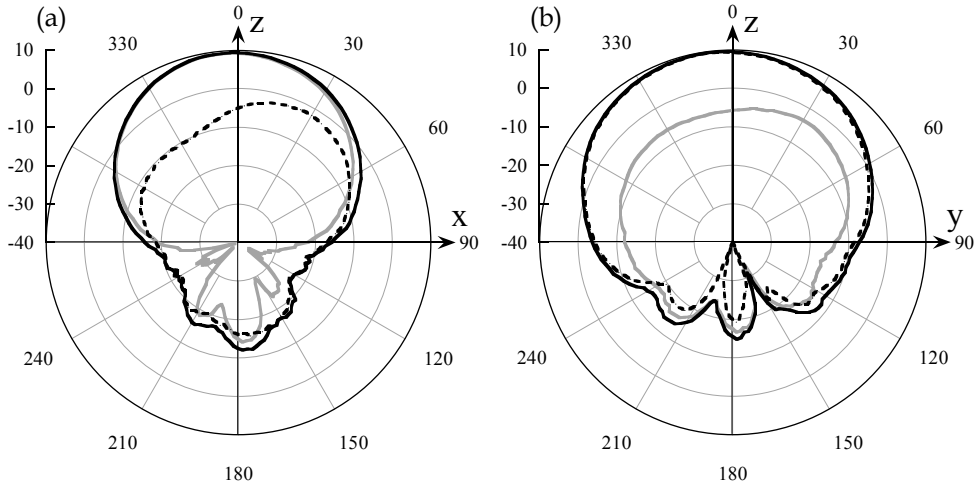


Fig. 14. Measured radiation patterns at 4.8 GHz; (a) in the x - z plane, (b) in the y - z plane. Gray line: in-plane electric field; dashed-line: electric field orthogonal to the plane; solid-line: total electric field. The results are reported in dB.

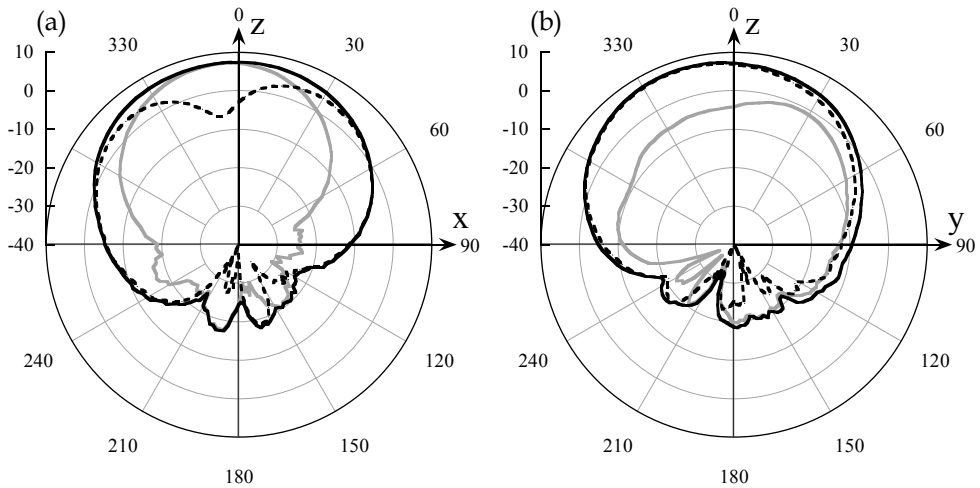


Fig. 15. Measured radiation patterns at 5.5 GHz; (a) in the x - z plane, (b) in the y - z plane. Gray line: in-plane electric field; dashed-line: electric field orthogonal to the plane; solid-line: total electric field. The results are reported in dB.

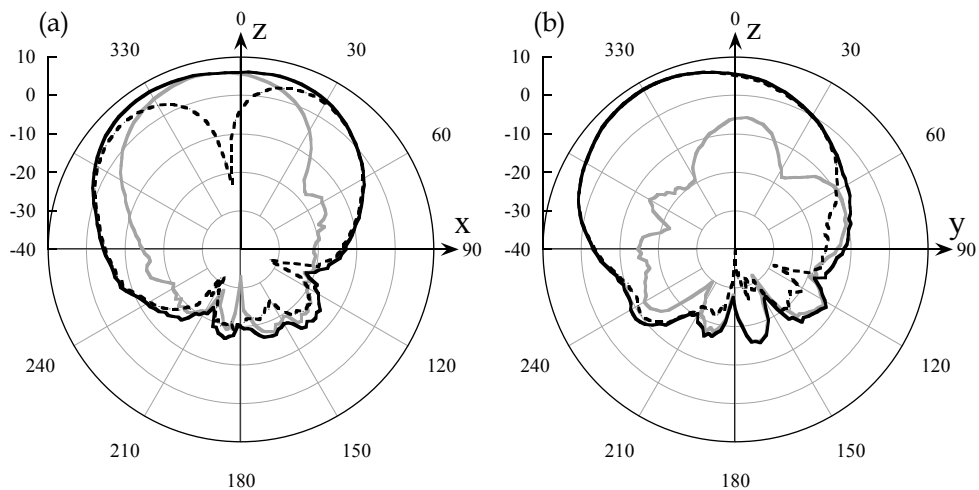


Fig. 16. Measured radiation patterns at 6.1 GHz; (a) in the x - z plane, (b) in the y - z plane. Gray line: in-plane electric field; dashed-line: electric field orthogonal to the plane; solid-line: total electric field. The results are reported in dB.

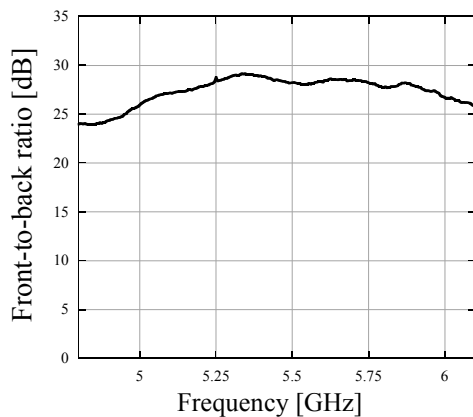


Fig. 17. Measured front-to-back ratio in the frequency range 4.8 – 6.1 GHz.

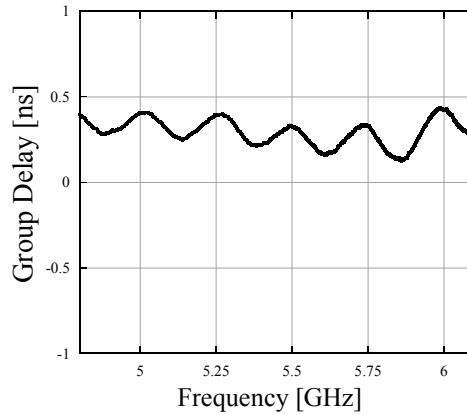


Fig. 18. Measured group delay in the frequency range 4.8 – 6.1 GHz.

3. A Planar, Differential, and Directive Ultra-Wideband Antenna

In this section a planar differential UWB antenna characterized by high directivity is described. The proposed structure is composed of two disc monopoles with L-shaped ground planes, fed by 50 Ohm microstrip lines (100 Ohm differential input). The introduction of a structured ground plane and the array effect permit to achieve a measured gain exceeding 11 dB even on a low-cost substrate, maintaining at the same time a reasonable size of the board. As reference application, the antenna has been optimized to work between 6 and 8 GHz in combination with a single-chip radar transceiver (Cacciatori et al., 2007).

3.1 Antenna Layout

A sketch of the differential UWB antenna is reported in Fig. 19. The structure is formed by two disc monopoles with L-shaped ground planes, fed by 50 Ohm microstrip lines (width equal to 3 mm), on a low-cost FR4 substrate. We assumed that the FR4 dielectric constant is 4.5, and the declared board thickness is equal to 1.6 mm. Optimization of the antenna was performed through CST Microwave Studio simulations, and the reported results correspond to the device with the geometric parameters that guarantee the best theoretical performance. In Fig. 19 we show the size of the board, and the position of the centers of the two disc monopoles, whose radius is 9 mm.

The basic element of the proposed differential antenna is the single disc monopole, with the related 50 Ohm microstrip feed-line and the L-shaped ground plane with rounded corner. The distance between the edge of each disc and the horizontal and vertical metal stripes that compose the L-shaped ground plane is 1 and 2 mm respectively. This building block (50 x 50 mm²) is then rotated by 40 degrees in the x - y plane, and it is depicted within a yellow square in Fig. 19. The second element of the array is obtained by mirroring the first one with respect to the $x = 0$ plane. The region between the two elements on the ground side is filled with metal, so that this large common ground plane can be exploited for a straightforward placement of a single-chip transceiver and its circuitry. As shown in Fig. 19, the distance

between the two disc monopoles is about 70 mm, which is larger than the maximum signal wavelength. In Fig. 20 a photograph of the fabricated antenna is reported.

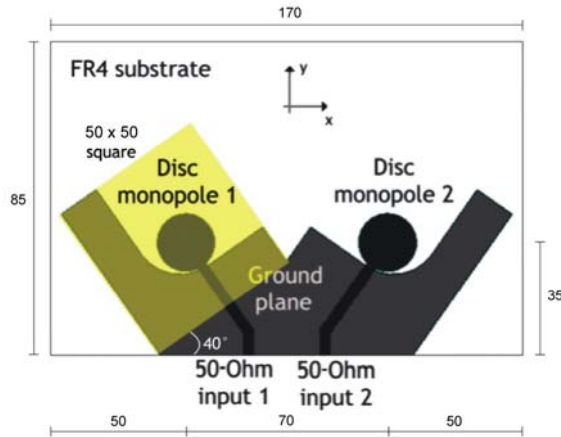


Fig. 19. Sketch of the differential UWB antenna: disc monopoles and microstrip lines (black), structured ground plane (dark gray) and the basic element of the array (yellow square) are depicted. The dimensions are in millimeters.

3.2 Reflection Coefficient, Group Delay and Radiation Patterns

Differential and common-mode reflection coefficients ($|S_{dd}|$ and $|S_{cc}|$) have been measured by using a 4-port vector network analyzer Anritsu MS4624D, whereas the single-port reflection coefficient at port 1 ($|S_{11}|$) has been measured through a 2-port Agilent N5230A PNA-L network analyzer. In Fig. 21 we report results obtained from measurements between 4 and 9 GHz; it is worth noting that the three curves are almost overlapped and this implies that, as desired, coupling between the two antenna elements is very weak. The differential reflection coefficient is below -10 dB in the frequency range between 5.3 and 9 GHz, thus the differential UWB antenna exhibits a good behavior in terms of impedance matching over a bandwidth larger than 4 GHz. Also the group delay has been measured in anechoic chamber, by using the same setup we have used for measurements of gain and radiation patterns (see below for the setup description). The results are reported in Fig. 22: it is fundamental to note that the maximum group delay variation is equal to fractions of a nanosecond, therefore the antenna is able to guarantee low pulse distortion.

The radiative properties of the differential UWB antenna have been characterized in anechoic chamber by utilizing a 2-port Agilent N5230A PNA-L network analyzer, two 180-degree hybrid couplers, a Satimo SGH-820 ridged horn wideband probe antenna, and a remotely controlled turntable. Here we report the results for co-polarization at 7 GHz; we emphasize the fact that the level of cross-polarization is quite low, and the shape of the radiation patterns is rather uniform over the entire band.

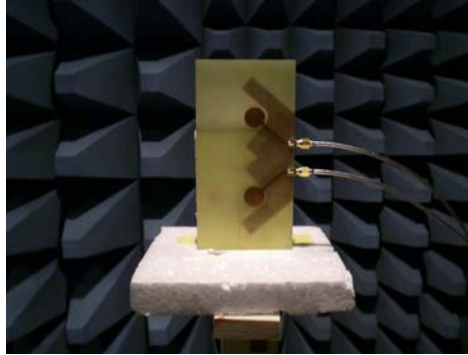


Fig. 20. Photograph of the fabricated antenna in anechoic chamber.

In Fig. 23(a) we show measured and simulated radiation pattern in the x - y plane when only port 1 is excited. The results show the typical behavior of a disc monopole with L-shaped ground plane, with a single lobe of radiation oriented along the y -axis, and the maximum gain is equal to 8.6 dB. In Figs. 23(b) and 24(a) we report measured and simulated radiation patterns in the x - y and y - z plane respectively, when the two input ports are excited with signals with opposite polarity. The increase of directionality is clearly visible even from a simple analysis of the shape of the patterns: indeed, the maximum gain is equal to 11.6 dB. In Fig. 24(b) we report, for the sake of comparison, measured and simulated radiation patterns for in-phase excitation of the two ports in the x - y plane. It is possible to note the birth of two lobes, with a maximum gain equal to 9.1 dB. In all the cases, it is worth noting the excellent agreement between numerical and experimental data. These results clearly demonstrate that the proposed differential UWB antenna is a good candidate to be used whenever a highly directive differential radiator with planar profile is required.

3.3 The Radiation Mechanism

We have numerically investigated the pattern of the surface currents on the UWB differential antenna, in order to identify the reasons for such a huge increase of directionality. The usage of a disc monopole with L-shaped ground plane guarantees the suppression of one lobe of radiation with respect to conventional monopoles, and this corresponds to an increase of gain of about 3 dB. The two disc monopoles that compose the differential antenna can be considered as an array of two elements, wherein each element radiates with only one main lobe of radiation along the y -direction. The structure should ideally behave as a broad-side array, with maximum value of the array factor in normal direction with respect to the alignment direction (i.e. x -axis) (Somedá, 1998). From the theory of antenna arrays, it is well known that we get a broad-side array when the current distribution on each antenna element is in phase.

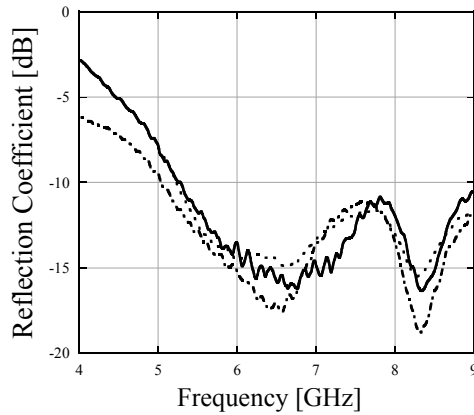


Fig. 21. Measured differential (solid line) and common-mode (dashed-dotted line) reflection coefficients $|S_{dd}|$ and $|S_{cc}|$, and measured single-port reflection coefficient $|S_{11}|$ (dotted line) between 4 and 9 GHz.

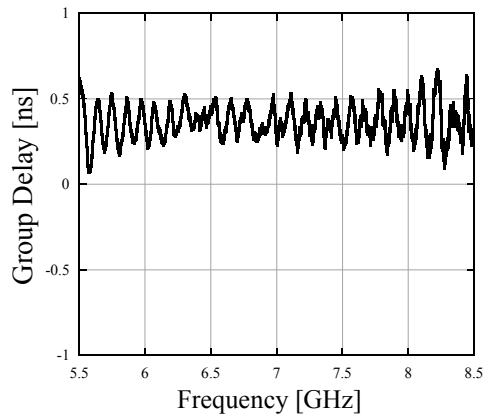


Fig. 22. Measured group delay curve between 5.5 and 8.5 GHz.

In Fig. 25 we plot the y -component of the surface currents at 7 GHz for differential input (the two ports have opposite polarity). It is straightforward to see that the currents on the microstrips have opposite polarity, whereas on the radiating elements they are predominantly distributed on the edge of the discs and are in phase due to the mirror symmetry between the two elements. As a consequence, in this case the differential antenna behaves as a broad-side array, as shown by the radiation pattern in Fig. 23(b). Viceversa, when the two input ports are fed in phase the currents on the two microstrips are obviously in phase, whereas on the radiating elements they are out of phase. Indeed, the radiation pattern in Fig. 24(b) exhibits two radiation lobes and no enhancement of directivity, as predicted by the calculation of the array factor. Notice that the increase of gain in the case of differential input with respect to excitation of a single port is about 3 dB, which is exactly the value predicted by the theory of antenna arrays for a two-element array.

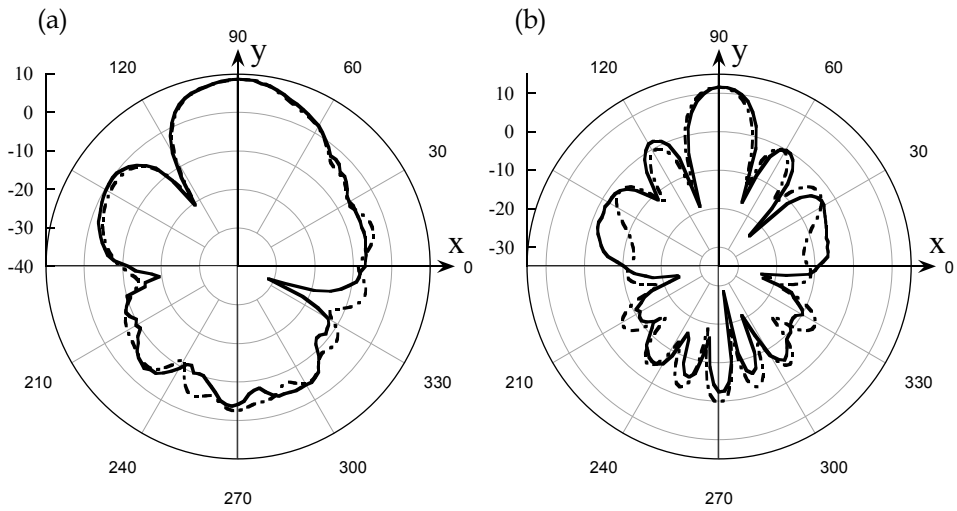


Fig. 23. Measured (solid line) and simulated (dashed-dotted line) radiation patterns in the x - y plane for in-plane polarization at 7 GHz. (a) Only port 1 was excited, maximum gain is 8.6 dB. (b) port 1 and port 2 are excited with opposite polarity (differential excitation), maximum gain is 11.6 dB. The results are reported in dB.

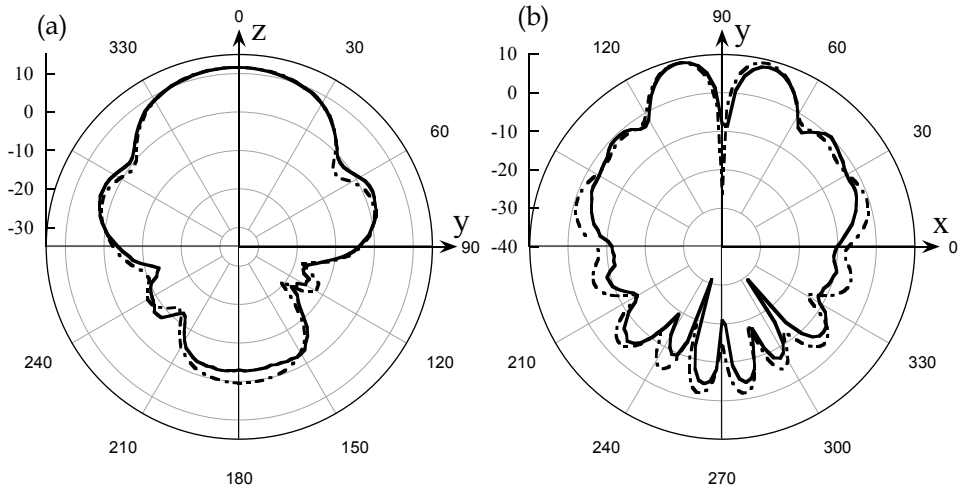


Fig. 24. Measured (solid line) and simulated (dashed-dotted line) radiation patterns for in-plane polarization at 7 GHz. (a) y - z plane, differential excitation. (b) x - y plane, port 1 and port 2 are excited with the same polarity, maximum gain is 9 dB. The results are reported in dB.

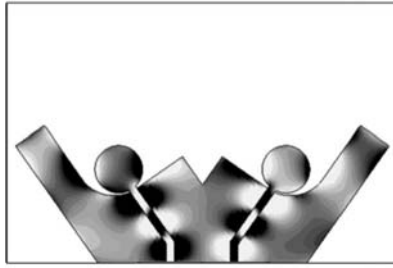


Fig. 25. Plot of the y -component of the surface currents at 7 GHz, white (black) represents positive (negative) values. The two ports are excited with opposite polarity.

3.4 Gain

In Fig. 26 we report measured and simulated gain in the band of interest for the case of differential excitation. The two curves exhibit good agreement, in spite of the high degree of uncertainty associated with the electromagnetic parameters of the FR4 substrate. In particular, in all the simulations we took a dielectric loss tangent $\tan \delta = 0.02$, which seems to be a reasonable value according to what is commonly reported in the literature. It is worth noting that the gain curves are quite flat, with values between 10 and 12 dB over the entire bandwidth. In the same figure we also report simulations that show the gain that could be achieved by fabricating the same structure on a more expensive substrate designed for RF, and thus characterized by negligible loss tangent. We have found that the maximum gain would be between 11.5 and 13.5 dB: it is worth noting that these are huge values for a structure with planar profile.

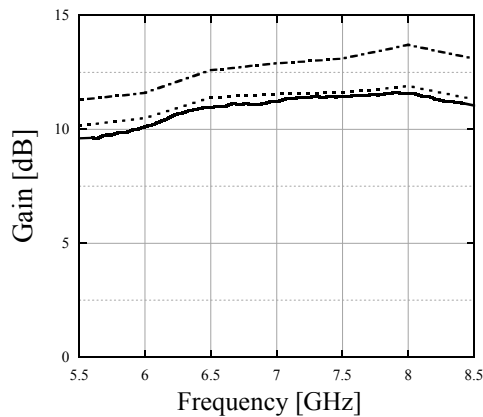


Fig. 26. Measured (solid line) and simulated (dotted line) gain of the fabricated antenna with differential excitation, and simulated gain of the same structure by considering negligible losses in the dielectric substrate (dashed-dotted line).

4. Conclusion

The logical thread of this chapter can be summarized as follows. Highly directive, planar UWB antennas are gaining more and more attention, as required in many novel and important applications. As the modern antenna design deals with low profile structures, new ways of increasing the directivity of a candidate radiator can be explored. Two different techniques were presented throughout this chapter. In Section 2, the operation of a novel bow-tie antenna with high front-to-back ratio and directivity has been demonstrated. This unconventional bow-tie antenna exploits magnetic currents excited in properly designed slots, while the two metallic patches act as a wideband loading or matching network. A prototype has been fabricated and characterized using a vector network analyzer in an anechoic chamber demonstrating the effectiveness of the proposed design in the 4.8 - 6.1 GHz band. In Section 3 we have presented a differential planar UWB antenna characterized by higher gain (more than 11 dB around 7 GHz) with respect to conventional printed radiators. The presence of a large common ground plane is a key feature in order to simplify placement of single-chip UWB transceivers, which typically have a differential input/output structure: as a consequence, direct connection between chip and antenna would be possible, without resorting to baluns. The antenna has been fabricated on a low-cost FR4 substrate and has been completely characterized: both simulations and measurements performed in anechoic chamber have demonstrated that the strong increase of directionality is mainly due to the presence of a carefully structured ground plane and to the array effect.

5. References

- Balanis, C. A. (2005). *Antenna theory, analysis and design*, John Wiley & Sons, ISBN: 0-471-66-782-X, Hoboken, New Jersey.
- Cacciatori, A.; Lorenzi, L. & Colalongo, L. (2007). A Power Efficient HBT Pulse Generator for UWB Radars. *Proceedings of ISCAS 2007*, pp. 3916-3919, ISBN: 1-4244-0920-9, New Orleans, May 2007.
- CST Microwave Studio (2009), Darmstadt, Germany.
- Eldek, A. A.; Elsherbeni, A. Z. & Smith, C. E. (2005). Wide-Band Modified Printed Bow-Tie Antenna With Single and Dual Polarization for C- and X-Band Applications. *IEEE Transactions on Antennas and Propagation*, Vol. 53, September 2005, pp. 3067-3072, ISSN: 0018-926X.
- European Telecommunications Standards Institute (ETSI), *Ultra Wideband (UWB) technologies for communication purposes*, ETSI EN 302 065 V1.1.1 (2008-02), February 2008.
- Federal Communications Commission (FCC), *Revision of Part 15 of the Commission's Rules Regarding Ultra-Wideband Transmission Systems*, First Report and Order, FCC 02-48, 2002.
- Kiminami, K.; Hirata, A. & Shiozawa, T. (2004). Double-Sided Printed Bow-Tie Antenna for UWB Communications. *IEEE Antennas and Wireless Propagation Letters*, Vol. 3, 2004, pp. 152-153, ISSN: 1536-1225.
- Someda, C. G. (1998). *Electromagnetic Waves*, Chapman & Hall, ISBN: 0-412-57870-0, London, UK.

Ultra-Wideband Antenna

Cheolbok Kim

*University at Buffalo, the State University of New York
USA*

1. Introduction

In 2002, the Federal Communications Commission (FCC) of the United State officially released the regulation for Ultra-wideband (UWB) technology. In this regulation, the spectrum from 3.1 GHz to 10.6 GHz (a fractional bandwidth of 110%) is allocated and the Equivalent Isotropically Radiated Power (EIRP) is less than -41.3 dBm/MHz for the unlicensed indoor UWB wireless communication system. According to the released regulation, UWB technology which is based on transmitting ultra short pulses with duration of only a few nanoseconds or less has recently received great attention in various fields for the short-distance (< 10 m) wireless communications. Because of the ultra-wideband property, UWB technology has many benefits, which are high data rate (> 100 Mb/s), low power consumption, compact, low cost, excellent immunity to multipath interference and reduced hardware complexity. Due to these advantages, we need to understand the principle of the UWB systems and then we should research and develop the UWB systems in context of coding, modulation, signal processing architecture and UWB antenna. This chapter is timely in reporting the aspects of the conventional and state-of-the-art antenna design in the UWB system.

This chapter consists of four sections. First, UWB technology is briefly introduced in its advantages, regulation and applications. Second, the UWB antenna plays a crucial role in UWB communication system as well as context of coding and signal processing. Design methods of the conventional UWB antennas such as log-periodic dipole array (LPDA) are overviewed and the UWB antennas which are recently researched are introduced. Third, as UWB frequency range includes existing some narrow frequency bands such as IEEE 802.11a wireless local area networks (WLANs) using the frequency band from 5.15 GHz to 5.825 GHz and new telecommunication technology based on the IEEE 802. 16, Worldwide Inter-operation for Microwave Access (WiMAX) operating on 3.3-3.6 GHz, the coexistence of UWB with other systems has been an important issue. Thus, the UWB antenna should be designed with a notch in the WLAN and WiMAX frequency band because UWB transmitters should not cause any electromagnetic interference to nearby communication systems. Therefore, the principle and design methods to notch the particular frequency band in UWB antenna are summarized and introduced in this part. Finally, we will simply forecast the development and application of the UWB communications in the future.

1.1 Advantages of UWB

UWB communication having ultra-wideband characteristic has many advantages for the short-distance wireless communication as follows:

- ✓ High data rates and large channel capacity
- ✓ Excellent immunity to multipath interference
- ✓ Low complexity and cost
- ✓ Low power consumption
- ✓ Coexistence with other wireless communication

There are three reasons causing the high data rates, which are the ultra-wideband characteristic, high signal power and low noise power. It is evident from Hartley-Shannon's capacity formula:

$$C = B \log_2 \left(1 + \frac{S}{N} \right) \quad (1)$$

where C is the maximum channel capacity, B the signal bandwidth, S the signal power, and N the noise power. Consequentially, the highest channel capacity can be obtained by increasing the signal bandwidth and low signal to noise power. The major advantage of the UWB communication is to use the large bandwidth (large B). And UWB communication is capable of working in harsh communication channels with low SNRs. Thus, these conditions offer a large channel capacity which causes high data rates according to equation (1).

Next, UWB communication has excellent immunity to multipath interference. In the narrow band communication, the fading which is caused by reflected signal from various things is the unavoidable phenomenon and it can make the received signal weak up to -40 dB. On the other hand, impulse signals have low susceptibility to multipath interference in transmitting information in UWB communication system because the transmission duration of a UWB pulse is shorter than a nanosecond in most cases. Even it gives rise to a fine resolution of reflected pulses at the receiver. Therefore, UWB communication system can resolve the fading problem and it is good in multipath diversity like MIMO system.

Furthermore, UWB system is quite simple and low cost due to the carrier-free nature of the signal transmission. In convectional communication system, a carrier frequency is necessary to send the baseband signal at the desired frequency band. It requires an additional radio-frequency (RF) mixing stage in up/down-conversion processes. However, the very wideband nature of the UWB signal means it spans frequencies commonly used as carrier frequency. Thus, the UWB signal will propagate well in the transmitters and will be received well in the receivers without RF mixing stage for the up/down-conversion. It makes the UWB system allow the whole UWB system to be integrated with single-chip CMOS implementation. It contributes to the low complexity and low cost characteristic.

Finally, very low power density (like noise level) obtained through the FCC's radio regulation emission mask of -41.3 dBm/MHz (equal to 75 nanowatts/MHz) for UWB system is the other advantage. It causes the UWB system to enable the signal to consume the low power and to coexist with already deployed narrow-band systems with minimal or no

interference. Consequently, UWB communication system is a good candidate for the short-distance wireless communication due to the above-mentioned advantages.

1.2 Regulation

In USA, the FCC approved a UWB spectral mask specified 7.5 GHz of usable spectrum bandwidth between 3.1 GHz and 10.6 GHz for communication devices and protected existing users operating within this spectrum by limiting the UWB signal's EIRP level of -41.3 dBm/MHz (known as Part 15 Limit). In this restriction, the limitation of the power spectral density (PSD) measured in a 1 MHz bandwidth at the output of an isotropic transmit antenna to a spectrum mask is shown in Figure 1 for indoor and outdoor environments, respectively.

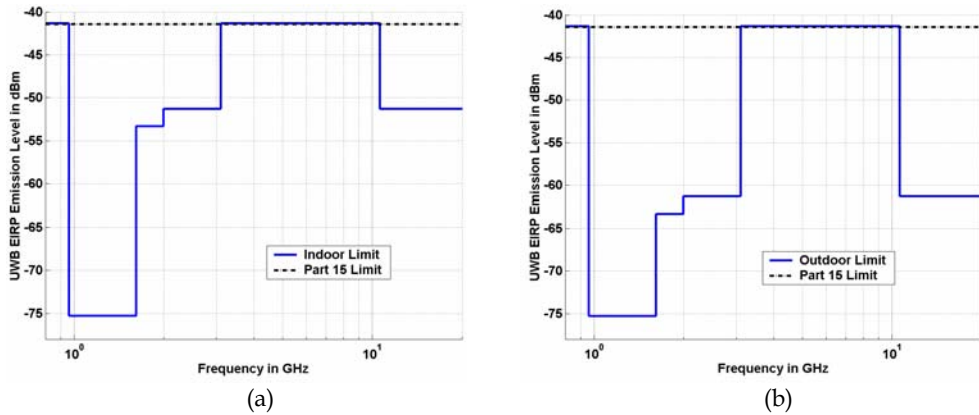


Fig. 1. Spectrum mask of UWB for (a) indoor environments and (b) outdoor environment

Although UWB currently is legal only in the United States, international regulatory bodies are considering possible rules and emission limits that would help it enable worldwide operation of UWB devices. Figure 2 shows the graph of the worldwide spectrum mask that is defined now for UWB communication devices. There is difference in EIRP levels among USA, Europe, Japan and Singapore. In some countries, there is an exclusive obligation to protect the existing communication systems. Countries that have a sole obligation to protect existing users tend to be much more conservative in international fora that are designed to achieve spectrum harmonization, such as the international Telecommunication Union (ITU). Therefore, it is extremely necessary to gain compromises and agreement among all of them for making the international UWB policy because UWB is not only a new technology but also a new regulatory paradigm. In the processes of the compromise for UWB policy, there are two useful technologies to prevent the interference with other signal. One is Detect and Avoid (DAA) and the other is Low Duty Cycle (LDC). The former is a technology to mitigate interference potential by searching for broadband wireless signals and then automatically switching the UWB devices to another frequency to prevent any conflict. The latter reduces interference with other signal by using the UWB signal with very low duty cycle.

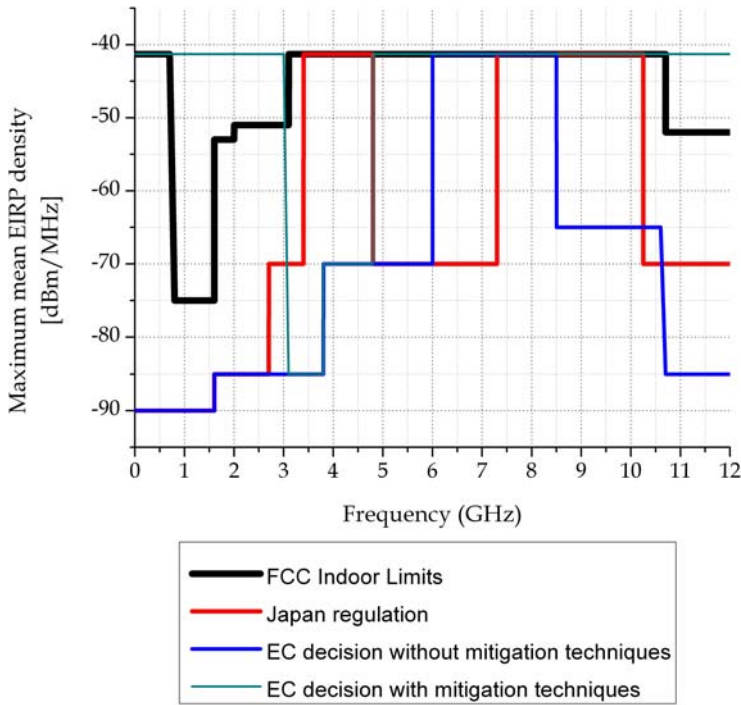


Fig. 2. The worldwide spectrum masks for UWB communication devices

1.3 Applications

UWB technology can be applied in a wide variety of applications. Based on the FCC guidelines, UWB technology is deployed in two basic communication systems.

- ✓ High data rate (IEEE 802.15.3a)
- ✓ Low data rate (IEEE 802.15.4a)

The high data rate WPANs can be defined as wireless data connectivity between the hosts (PC, high quality real time video player and so on) and the associated peripherals (keyboard, mouse, speaker, VCRs and so on). It will remove the wires and cables with high transfer data rate and rapid file sharing or download of images/graphic files. In other hand, the low data rate wireless communications will be primary focused on position location applications because of UWB's centimetre accuracy in ranges of 100m.

In the other aspect, UWB applications are classified three major categories.

- ✓ Communications and sensors
- ✓ Position location and tracking
- ✓ Radar

Applications for wireless communications and sensors are the most attractive one due to the high speed data transmission and low power consumption. UWB will be applied to the movable wireless devices such as keyboard, mouse, printer, monitor, audio speaker, mobile phone and digital camera. It will give us convenient and enrich daily life because the wires will disappear. And sensors which will be used to secure home, automobiles and other property also make our life more comfortable. Specially, it will contribute to patients in the hospital by using the monitoring of their respiration, heart beat and other medical images with wireless devices.

Position location and tracking also have a potential in UWB applications. Due to the centimetre accuracy, UWB can be used to find a lost something or people in a various situations including fire fighters in a burning building, police officers in distress, and injured skiers or climbers and children lost in the mall or amusement park. And with UWB tracking mechanisms, we can not only know item locations and their movement but also secure the high value assets.

UWB signals enable inexpensive high definition radar. This property could be applied to many applications such as automotive sensors, collision avoidance sensor in the vehicular, intelligent highway initiatives, smart airbag and through-the-wall public safety applications. These applications will prevent the accidents and damages from the occurred accidents.

2. UWB Antenna

2.1 Conventional Broadband Antennas

The term "Broadband" has been applied in the past, but has usually described antennas whose radiation and input impedance characteristics were acceptable over a frequency range of 2 or 3:1 before the 1950s. At that time, the bandwidth of the radiation pattern has been the limiting factor since antennas have been developed with an input-impedance that stays relatively constant with a change in frequency. But in the 1950s, a breakthrough in antenna evolution was made which extended the bandwidth to as great as 40:1 or more. The antennas introduced by the breakthrough were referred to as frequency independent, and they had geometries that were specified by angles. These broadband antennas are practically independent of frequency for all frequencies above a certain value as well as impedance. The general formula for their shape is

$$r = e^{a(\varphi + \varphi_0)} F(\theta) \quad (2)$$

where r , θ , φ are the usual spherical coordinates, a and φ_0 are constants and $F(\theta)$ is any function of θ . Assuming a to be positive, φ ranges from $-\infty$ to ∞ which determines the low frequency limit. For such antennas a change of frequency is equivalent to a rotation of the antenna about $\theta = 0$. It appears that the pattern converges to the characteristic pattern as the frequency is raised, if a is not ∞ , and that the impedance converges to the characteristic impedance for all ∞ (Rumsey, 1957).

Rumsey's general equation, Equation 2, will be used as the unifying concept to link the major forms of frequency independent antennas. Classical shapes of such antennas include

the equiangular geometries of planar and conical spiral structures and the logarithmically periodic structures.

Fig. 3(a) illustrates a simple example which gives a practical antenna design. Fig. 3(b) also illustrates the case where $F(\theta)$ is periodic in θ with period 2π . This gives a simple surface like a screw thread which is uniformly expanded in proportion to the distance from the origin: an increase of 2π in φ is equivalent to moving one turn along the screw.

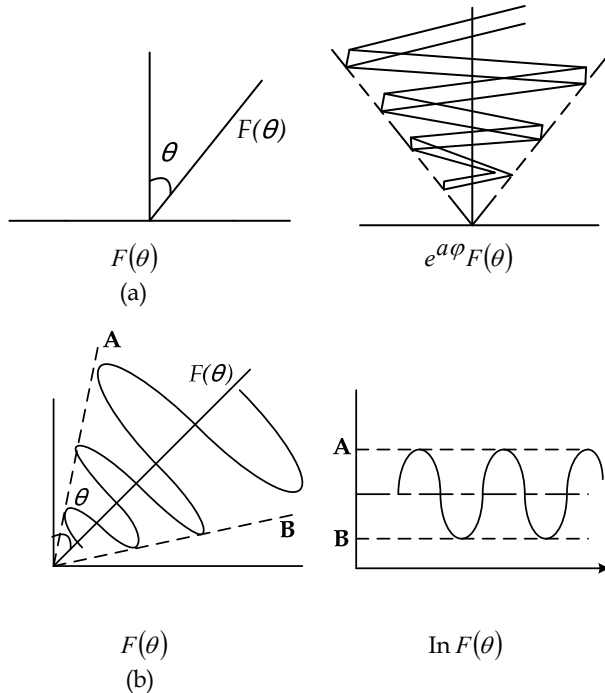


Fig. 3. The surface of the example for a practical antenna design

2.1.1 Equiangular Spiral Antennas

The design of the equiangular spiral antenna is based upon a simple fundamental principle. If all dimensions of a perfectly conducting antenna are charged in linear proportion to a change in wavelength, the performance of the antenna is unchanged except for a change of scale in all measurements of length. Thus, as Rumsey has pointed out, it follows that if the shape of the antenna was such that it could be specified entirely by angles, its performance would be independent of frequency (Balanis, 1997).

Fig. 4 shows the equiangular or logarithmic spiral curve which may be derived by letting the derivative of $F(\theta)$ is

$$\frac{dF}{d\theta} = F'(\theta) = A\delta\left(\frac{\pi}{2} - \theta\right) \tag{3}$$

where A is a constant and δ is the Dirac delta function. Using equation (3), equation (2) can be reduced as follows:

$$r_{\theta=\pi/2} = \rho = \begin{cases} Ae^{a\phi} = \rho_0 e^{a(\phi-\phi_0)} & \theta = \pi/2 \\ 0 & \text{elsewhere} \end{cases} \quad (4)$$

where

$$A = \rho_0 e^{-a(\phi_0-\theta_0)} \quad (5)$$

Another form of Equation (4) is

$$\phi = \frac{1}{a} \ln\left(\frac{\rho}{A}\right) = \tan\psi \ln\left(\frac{\rho}{A}\right) = \tan\psi (\ln\rho - \ln A) \quad (6)$$

where $1/a$ is the rate of expansion of the spiral and ψ is the angle between the radial distance ρ and the tangent to the spiral, as shown in Figure 4.

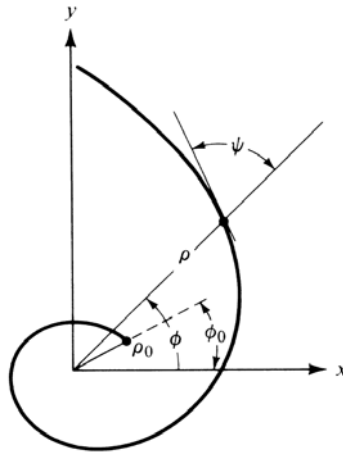


Fig. 4. The equiangular single spiral

If the angle ϕ is increased by one full turn, the radius vector is increased by the factor $e^{2\pi a}$, hence each turn of the spiral is identical with every other turn except for a constant multiplier. Therefore, we can have frequency independent antennas.

At that time, the total length L of the spiral can be calculated by

$$L = \int_{\rho_0}^{\rho_1} \left[\rho^2 \left(\frac{d\phi}{d\rho} \right)^2 + 1 \right]^{1/2} d\rho = (\rho_1 - \rho_0) \sqrt{1 + \frac{1}{a^2}} \quad (7)$$

where ρ_0 and ρ_1 represent the inner and outer radius of the spiral (Dyson, 1959).

2.1.2 Log-Periodic Antennas

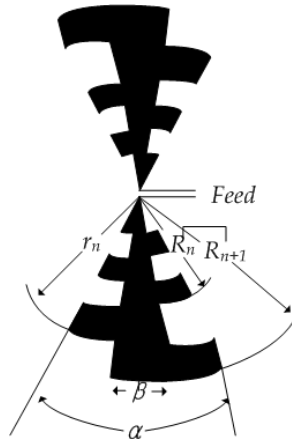


Fig. 5. The logarithmically periodic antenna structure

Next antenna configurations having the frequency independent property are the log-periodic antenna introduced by DuHamel and Isbell (DuHamel & Isbell, 1959; Isbell, 1960). A logarithmically periodic antenna which properties vary periodically with the logarithm of the frequency embody three basic design principles. The first of these is the “angle” concept which is a design approach wherein the geometry of the antenna structure is completely described by angles rather than lengths such as an infinite biconical antenna. The second principle makes use of the fact that the input impedance of an antenna identical to its complement is independent of the frequency. These two principles are presented well in reference (Rumsey, 1957) which title is Frequency independent antenna. The third principle is to design the antenna structure such that its electrical properties repeat periodically with the logarithm of the frequency.

Fig. 5 shows the logarithmically periodic antenna structure. The slots are bounded by the radius R_n , r_n and the subtended angle β . The radius R_{n-1} , R_n , R_{n+1} , ... form a geometric sequence of terms where the geometric is defined by

$$\tau = \frac{R_n}{R_{n+1}} \quad (8)$$

The radius r_{n-1} , r_n , r_{n+1} , ... form a similar sequence having the same geometric ratio. The width of the slot is defined by

$$\sigma = \frac{r_n}{R_n} \quad (9)$$

It can be seen that infinite structures of this type have the property that, when energized at the vertex, the fields at a frequency (f) will be repeated at all other frequencies given by $n\tau f$ (apart from a change of scale) where n may take on any intergral value. When plotted on a logarithmic scale, these frequencies are equally spaced with a separation or period of $\ln \tau$; hence the name logarithmically periodic structures. At that time, the geometric ratio τ of equation (8) defines the period of operation. For example, if two frequencies f_1 and f_2 ($f_1 < f_2$) are one period apart, they are related to the geometric ratio τ by

$$\tau = \frac{f_1}{f_2} \quad (10)$$

Extensive studies on the performance of the antenna of Fig. 5 as a function of α , β , τ and σ , have been performed (DuHamel & Ore, 1958). In general, these structures performed almost as well as the planar and conical structures. The only major difference is that the log-periodic configurations are linearly polarized instead of circular.

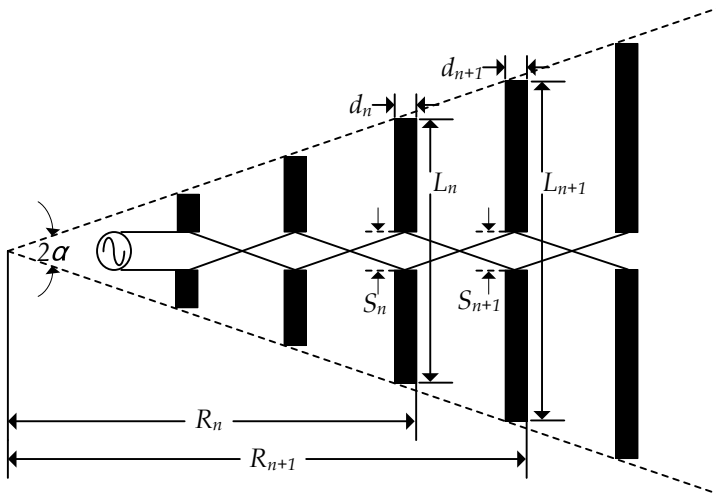


Fig. 6. The log-periodic dipole antenna geometry

The most recognized log-periodic antenna structure is the log-periodic dipole arrays (LPDA) which is introduced by Isbell (Isbell, 1960) as shown in Figure 6 and improved using techniques shown in references (Carrel, 1961; DeVito & Stracca, 1973; DeVito & Stracca, 1974; Butson & Thomson, 1976). The antenna consists of many different length dipoles. They are achievable and maintained over much wider bandwidths by adding more dipole antenna elements. The performance of a LPDA is a function of number of elements as well as element length, spacing and diameter. Antenna element lengths and spacings have proportionality factors given by a scale factor

$$\tau = \frac{L_n}{L_{n+1}} = \frac{R_n}{R_{n+1}} = \frac{s_n}{s_{n+1}} = \frac{d_n}{d_{n+1}} < 1 \quad (11)$$

and spacing factor

$$\sigma = \frac{R_{n+1} - R_n}{2L_n} = \frac{1 - \tau}{4} \cot \alpha \quad (12)$$

where the L_n is the length of n^{th} element, R_n is the spacing of elements n^{th} , d_n is the diameter of element n^{th} , and s_n is the gap between the poles of element n^{th} . The frequency limits of the operational band are roughly determined by the frequencies at which the longest and shortest dipoles are half-wave resonant, that is,

$$L_1 \cong \frac{\lambda_{\max}}{2} \quad \text{and} \quad L_N \cong \frac{\lambda_{\min}}{2} \quad (13)$$

where λ_{\max} and λ_{\min} are the wavelengths corresponding to the lower and upper frequency limits. At low frequencies, the larger antenna elements are active. As the frequency increased, the active region moves to the shorter elements. When an element is approximately one half wavelength long, it is resonant. And the number of dipoles can be obtained using

$$N = 1 + \frac{\log(L_1/L_N)}{\log(1/\tau)} \quad (14)$$

This seems to have many variables. But there are only three independent variables for a LPDA. These three parameters, which can be chosen from the directivity, length of the antenna, apex angle and the upper/lower frequency, should come with the design specifications. After extensive investigations, a summary of the optimum design data is produced in Table 1, which can be aid antenna design (Huang & Boyle, 2008).

Directivity(dBi)	Scale factor (τ)	Spacing factor (σ)	Scale factor (α)
7	0.782	0.138	21.55
7.5	0.824	0.146	16.77
8	0.865	0.157	12.13
8.5	0.892	0.165	9.29
9	0.918	0.169	6.91
9.5	0.935	0.174	5.33
10	0.943	0.179	4.55
10.5	0.957	0.182	3.38
11	0.964	0.185	2.79

Table 1. Optimum design data for log-periodic antenna

2.2 Innovative UWB Antennas

As I mentioned above, broadband antennas have been around for many decades and are used extensively. In the past, traditional broadband antennas satisfied the requirements for commercial UWB systems. However, the UWB technology has gained more and more popularity and become a good candidate for short-distance high-speed wireless communication since the approval of UWB by the FCC in 2002. The proposed commercial UWB radio concept with its frequency 3.1 GHz to 10.6 GHz differs significantly from traditional wideband, short-pulse applications, such as radar. Furthermore, UWB antennas need different requirements due to its applications such as portable electronics and mobile communications. Therefore, the conventional UWB antennas are not suitable. To satisfy different requirements such as size, gain and radiation patterns, many kinds of the new antenna are proposed.

2.2.1 Biconical, Bowtie and Monopole Antennas

Figure 7 shows the developing processes from biconical antenna to disc cone antenna and planar monopole antenna. The biconical antenna formed by placing two cones of infinite extent together as shown in Figure 7 (a) is one of the antennas having broadband characteristics (Balaris, 1996; Stusman, 1997). Since this structure is infinite, it can be analyzed as a uniformly tapered transmission line. With a time varying voltage applied across the gap, currents in turn create an encircling magnetic field. The input impedance of the transmission line is calculated with them. For a free-space medium, the characteristic impedance represented as follow:

$$Z_{in} = 120 \ln \left[\cot \left(\frac{\alpha}{4} \right) \right] \quad (15)$$

where, α is a cone angle. Input impedance is a function of the cone angle and broadband property of the antenna can be obtained when the angle, α , lies between 60° and 120° . Although biconical antennas are attractive due to its broadband characteristics, they are so massive and impractical to use. Therefore, the modified structures of the biconical antennas as shown in Figure 7 (b) and (c) are represented. Many structures of monopole type UWB antenna having a horizontal ground plane like the structure in Figure 7 (c) are introduced. Zhi Ning Chen and Y. W. M. Chia represented trapezoidal planar monopole antenna on the ground plane (Chen & Chia, 2000). Compared to the square monopole antenna, it could have a broad impedance bandwidth, typically of $>80\%$ for $VSWR=2:1$ by controlling the ratio of the lengths of top side and bottom side. M. J. Ammann introduced the pentagonal planar monopole antenna having 6.6:1 impedance bandwidth ratio (2.1~12.5 GHz) (M. J. Ammann, 2001). The wide bandwidth is achieved by varying the trim angle of the cut of the square patch. Kin-Lu Wong et al. also introduced square planar metal plate monopole antenna with a trident shaped feeding strip (Wong et al., 2005). With the use of the feeding strip, the antenna has a very wide impedance bandwidth. And it is easily fabricated using a single metal plate, thus making it easy to construct at a low cost. Qit Jinghui et al. presented a circular monopole antenna for UWB systems which is consisted of a 9×9 cm² ground plane and a metal plate with a radius of 2.5 cm and 5 cm perpendicular to the ground plane, and fed by a single coaxial cable that passed through the ground plane and connects to the

bottom metal plate (Jinghui et al., 2005). The proposed antenna's return loss is better than 10 dB from 1.25 GHz to more than 30 GHz and better than 15 dB from 3 to more than 30 GHz. Daniel Valderas et al. introduced UWB folded plate monopole antenna which is based on the rectangular plate monopole antenna (Valderas et al., 2006). Folded configurations are presented in order to reduce antenna size and improve radiation pattern maintaining the planar monopole broadband behavior.

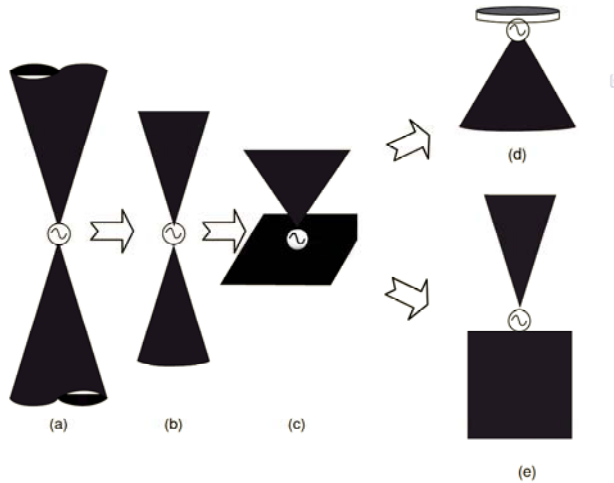


Fig. 7. Evolution processes from the conical antenna to disc cone antenna and planar monopole antenna

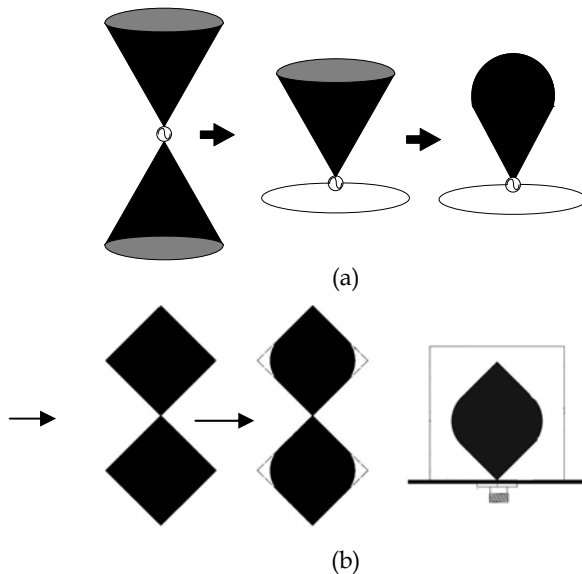


Fig. 8. The modified bowtie antenna structures

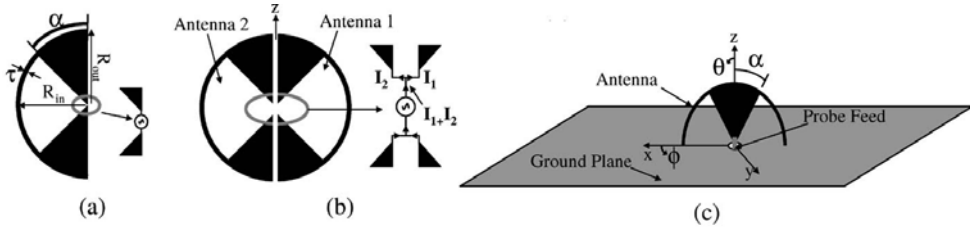


Fig. 9. The developing processes of the folded bowtie antenna

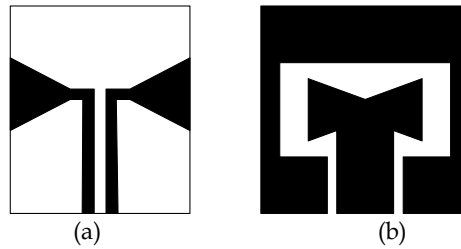


Fig. 10. The UWB bowtie antennas

The structure in Figure 7 (c) developed into the planar monopole structure by replacing an electrically large conducting plate acting as a ground plane as shown in Figure 7 (e). They have received a great deal of attention on the recent UWB literature due to its ease of fabrication, a novel small size and low cost. Many kinds of the planar monopole UWB antennas are introduced. Furthermore, Shiwei et al. (Qu & Ruan, 2005) and Tu Zhen et al. (Tu et al., 2004) are respectively introduced quadrate bowtie antenna with round corners and ultra wideband dipole antenna having a wideband property in Figure 8. The former improved its properties, better return loss in high frequency, smaller size and high gain, by inserting round corners on the rectangular bowtie antenna. The later developed the UWB dipole antenna from the cone antenna. Except that, the folded bowtie antenna in Fig. 9, also called sectorial loop antennas (SLA) is suitable for UWB antenna (Behdad & Sarabandi, 2005). Its performance is improved by adding a shorting loop to the outside of a bowtie antenna. The optimized antenna has a 8.5:1 impedance bandwidth and consistent radiation parameters over a 4.5:1 frequency range with excellent polarization purity over the entire 8.5:1 frequency range. And the antennas in Figure 10 are good examples of the UWB bowtie antenna (Kwon et al., 2005; Nakasuwan et al., 2008). Their bandwidth achieves more than the 3~10.6 GHz needed for UWB communication systems.

The planar monopole antenna for UWB systems can be sorted by feeding methods, microstrip feeding and coplanar waveguide feeding. There are four types of the patch shape in the microstrip fed UWB antennas such as rectangular, triangular, circular and elliptical. Figure 11 shows microstrip fed monopole UWB antennas with rectangular patch. At first, Seok H. Choi et al. proposed a new ultra-wideband antenna as shown in Figure 11 (a) (Choi et al., 2004). Three techniques to achieve wide bandwidth are used: the use of (i) two steps, (ii) a partial ground plane and (iii) a single slot on the patch, which can lead to a good impedance matching. And Jinhak Jung et al. introduced a small wideband microstrip monopole antenna which consists of a rectangular patch with two notches at the two lower corners of the patch and a truncated ground plane with the notch structure (Jung et al., 2005).

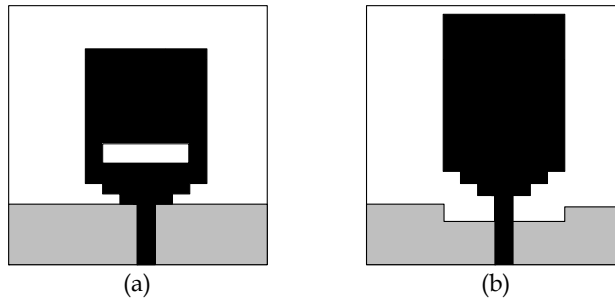


Fig. 11. The microstrip fed monopole antennas with rectangular patch

Second, the triangular patch and its modified structures of microstrip fed UWB antenna are introduced as shown in Figure 12 (Lin et al., 2005; Verbiest^b & Vandenbosch, 2006; Cho et al., 2006). The structure in Figure 12 (a) is based on the triangular monopole antenna. It consists of a tapered radiating element fed by microstrip line. The VSWR of the antenna with the optimized constructive parameters is less than 3 from 4 to 10 GHz. And it was developed by inserting a slot in the tapered radiating element and in the ground plane, which yields a wideband property with a relative good matching as shown in Figure 12 (b). In UWB antenna in Figure 12 (c), the broad bandwidth was achieved by triangular shaped patch with the staircases instead of the bowtie patch, a partial modified ground plane and two slits near the 50 Ω microstrip line fed by the SMA connector. Compared with antennas without these techniques, the proposed antennas have the widest bandwidth.

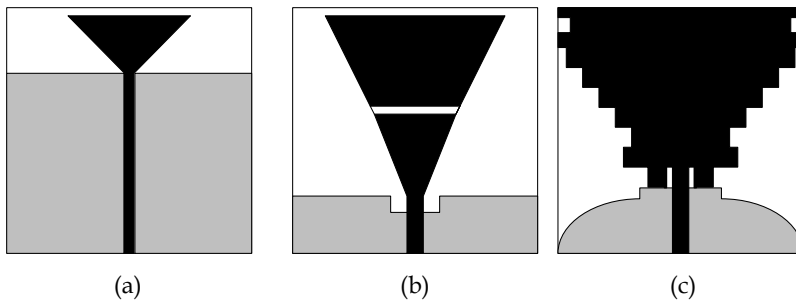


Fig. 12. The microstrip fed monopole antennas with triangular patch

Third, the circular and elliptical patch antennas fed by the microstrip line are a good candidate for the UWB antenna design. Their structures are presented in Figure 13. The UWB antenna in Figure 13 (a) based on the previous studies (Liang et al., 2004) is designed by using a circular patch, a 50 Ω microstrip feed line and a conducting ground plane (Liang^a et al., 2005). The circular disc monopole UWB antenna is miniaturized by using tapered feeding line and improved ground shape as shown in Figure 13 (b), while the performance of the antenna is maintained (Zhang^b et al., 2008). With circular disc monopole antenna, a planar elliptical patch monopole antenna structure is also a good for UWB antenna. The elliptical patch caused similar effect of bevelling the radiating element and cutting slot in the ground plane provide an ultra-wideband impedance bandwidth (Huang & Hsia, 2005).

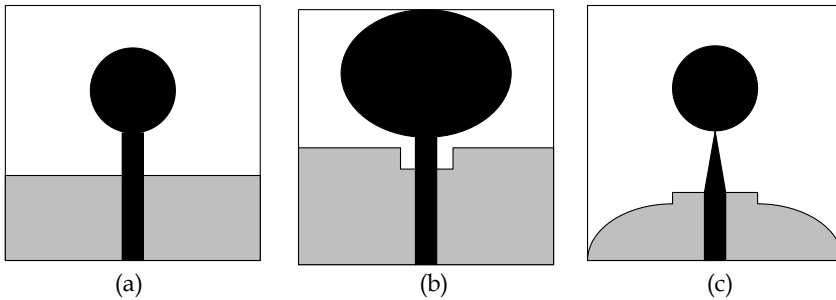


Fig. 13. The microstrip fed monopole antennas with circular and elliptical patch

Instead of microstrip fed monopole antennas, there are many patch shapes for UWB antenna fed by couplanar waveguide (CPW) feeding method as shown in Figure 14 (Gupta et al., 2005; Liang^b et al., 2005; Yang & David, 2004; Tran et al., 2007; Liang^c et al., 2005; Shrivastava & Ranga, 2008; Liang et al., 2006; Wang et al., 2004; Kim et al., 2005). The rectangular and circular patch in Figure 14 (a) are well known for UWB antenna, and Figure 14 (b) shows the modified shapes from the previous shapes. The UWB antennas in Figure 14 (c) are designed using a prapeziform ground plane which has three functions: (1) a ground plane for the monopole and CPW, (2) radiationg element and (3) component to form the distrubuted matching network with the monopole. The antenna in Figure 14 (d) is designed for UWB systems by using FDTD and genetic algorithm.

2.2.2 Slot typed UWB Antennas

Slot antennas are currently under consideration for use in ultra-wideband (UWB) systems due to the attractive advantages such as low profile, light weight, ease of fabrication and wide frequency bandwidth. This type of antenna has been realized by using microstrip line and CPW feeding structures.

Figure 15 shows various UWB antenna structures using microstrip line feeding (Qing et al., 2003; Chang et al., 2005; Lui et al., 2007; Chen et al., 2008). The antenna in Figure 15 (a) is consisted of the ground plane with wide rectangular slot and microstip feeding line with a fork-shaped tuning stub. Its measured bandwidth covers the UWB band from 2.5 GHz to 11.3 GHz that is a 127 % fractional bandwidth for $S_{11} < -10\text{dB}$. Its bandwidth is improved by using a tuning pad which is made of copper as shown Figure 15 (b). The improved antenna covers from 2.3 GHz to 12 GHz. And Figure 15 (c) uses a tapered monopole like slot instead of the rectangular slot to decrease the low resonant frequency. Wen-Fan Chen et al. are introduced new shape UWB antenna, keyhole shaped slot antenna, which is consisted of an indented circular-pie slot, a rectangular stub slot and a microstip feed line as shown in Figure 15 (d). It also have a required bandwidth for UWB communication systems.

Figure 16 shows CPW-fed slot antennas for UWB systems (Pell et al., 2008; Archevapanich et al., 2008; Chen et al., 2006; Gopikrishna et al., 2009). The designed antenna in Figure 16 (a) is based on a simple CPW fed slot antenna which is consisted of two rectangular slots seperated by center strip and the CPW feeding line. In the simple CPW-fed slot antenna, the wide bandwidth can be obtained by inserting L-strip tuning stubs which is etched at the bottom of conner edge in the rectangular slots.

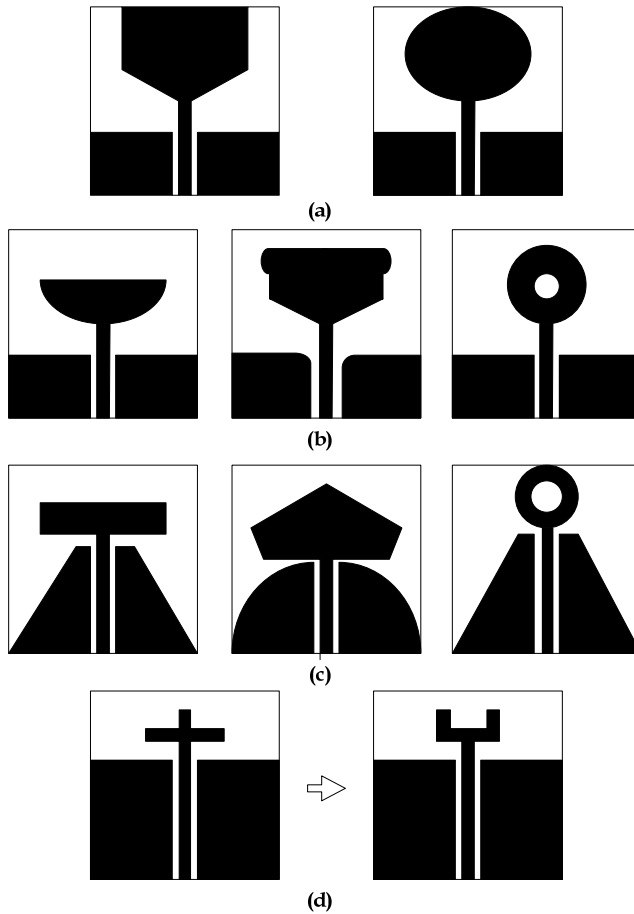


Fig. 14. The CPW-fed monopole UWB antennas

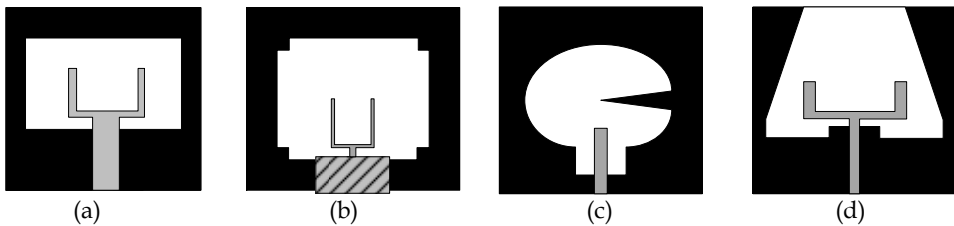


Fig. 15. The UWB slot antennas using microstrip feeding line

The optimized antenna has wide bandwidth, from 1.8 GHz to 11.2 GHz. In Figure 16 (b), Brendan Pell et al. are presented the CPW fed planar inverted cone antenna (PICA) which is composition of a semicircle and an equilateral triangle. Shih-Yuan Chen et al. proposed a CPW-fed log-periodic slot antenna as shown in Figure 16 (c). In this antenna, wide

bandwidth can be obtained from log-periodic antenna's properties. And Figure 16 (d) presents a compact semi-elliptic monopole slot antenna. It is consisted of a modified ground plane heaped as a semi-ellipse near the patch and semi-elliptic patch. Its bandwidth is from 2.85 GHz to 20 GHz with omni directional radiation. And then, for the comparison between microstrip line feeding and CPW feeding, Pengcheng Li et al. and Evangelos S. Angelopoulos et al. studied elliptical/circular microstrip-fed/CPW-fed slot antennas as shown in Figure 17 (Li et al., 2006; Angelopoulos et al., 2006).

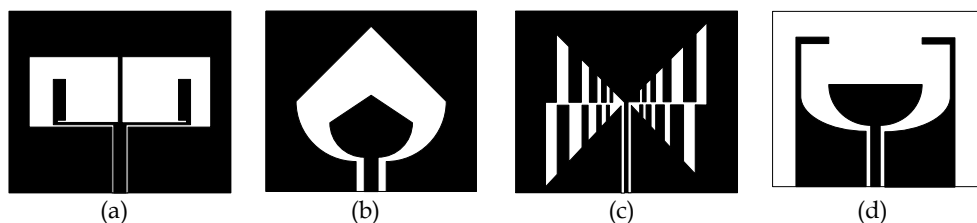


Fig. 16. The UWB slot antennas using CPW feeding line

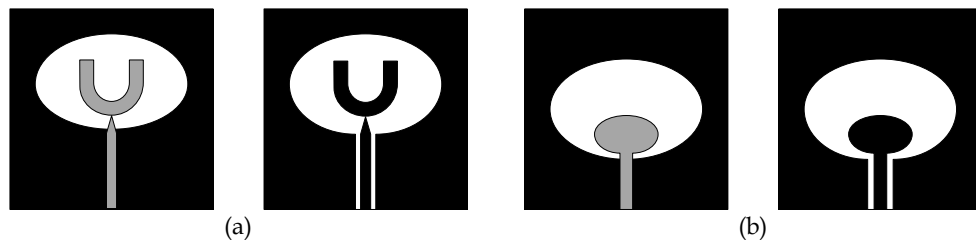


Fig. 17. The Microstrip-fed / CPW-fed UWB slot antennas

2.2.3 Tapered Slot UWB Antennas

Tapered slot antennas (TSA) belonging to the general class of endfire traveling-wave antennas (TWA) has many advantages such as low profile, low weight, easy fabrication, suitability for conformal installation and compatibility with microwave integrated circuits (MICs). In addition, TSA have multioctave bandwidth moderately high gain and symmetrical E- and H- plane beam patterns (Lee & Chen, 1997). Thus, many people studied it for the UWB applications. Figure 18 shows the presented TSA for UWB systems (Verbiest^a & Vandenbosch, 2006; Gopikrishna^a et al., 2008; Ma & Jeng, 2005; Nikolaou et al., 2006). Antennas in Figure 18 (a) and (b) are the tapered slot antenna consisted of similar structure, tapered slot in the ground plane and microstrip feeding line. But the latter could have a wide bandwidth by inserting rectangular slot on the feeding line. And Figure 18 (c) shows a planar miniature tapered slot fed annular slot antenna. The radiating annular slot and its tapered slot feeding structure are on the top layer of the substrate whereas the microstrip line and its open stub are printed on the bottom layer of it. It possesses ultrawide bandwidth, uniform radiation patterns and low profile. Tzyh-Ghuang Ma introduced an ultrawideband CPW fed tapered ring slot antenna in Figure 18 (d) which is formed by a 50Ω couplanar waveguide, a CPW to slotline transition and a pair of curved radiating slots. In this antenna, the very wide bandwidth can be obtained by gradually changing the width of the radiating slots. Symeon Nikolaos et al. proposed a double exponentially tapered slot antenna

(DE TSA) on flexible liquid crystal polymer (LCP) organic material suitable for packaging and integration with other components, as shown in Figure 18 (e). The antenna is characterized not only in the traditional planar form, but also in the case that is flexed in a conformal shape that mimics the shape of an automobile hood or bumper or the leading edge of an aircraft wing.

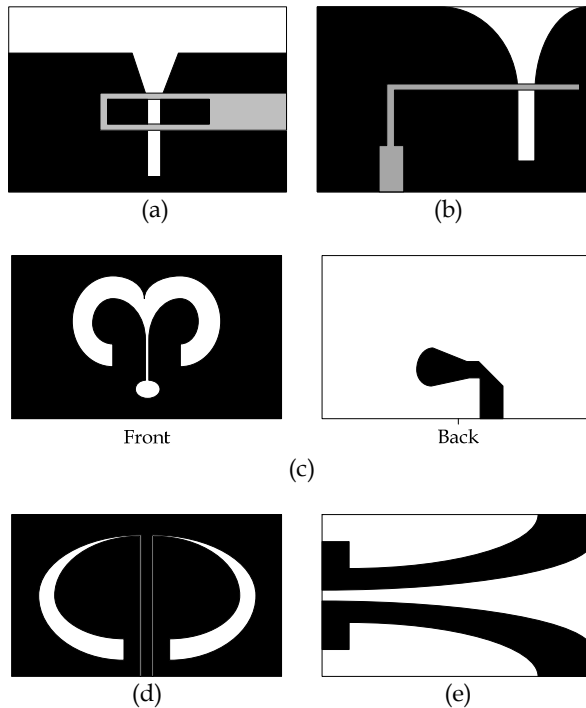


Fig. 18. The tapered slot antennas for UWB systems

2.2.4 Fractal UWB Antennas

Many studies are specially concentrated on fractal antennas because they possess not only small size, light weight and thin shape for portable devices that have a rigorous limitation of space, but also wide bandwidth and good radiation patterns. Thus, the fractal technology is applied to realize the UWB characteristic with its self-similarity and space filling properties. Figure 19 shows two fractal antennas for UWB applications (Naghshvarian-Jahromi & Falahati, 2008; Ding et al., 2006). The former used a circular patch with triangular slot, which is called a crown circular microstrip fractal antenna. The latter selected a pentagonal patch for initial design and then repeated Penta-Gasket Khock (PGK) iteration. These antennas have a required properties for UWB communication systems.

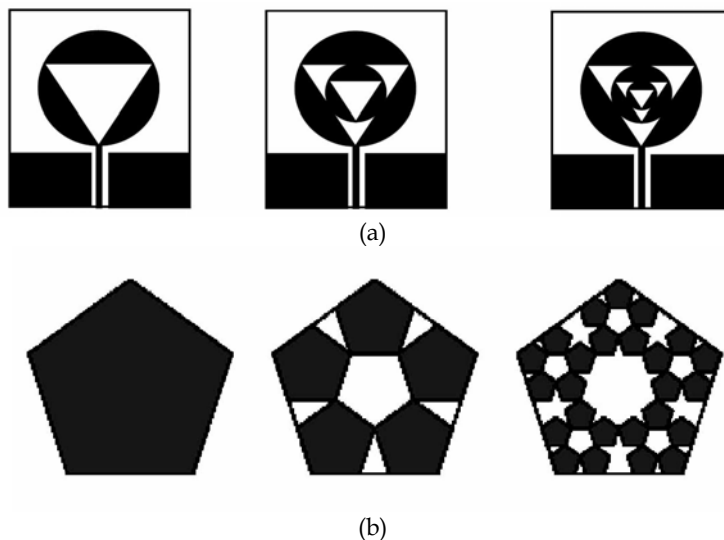


Fig. 19. The fractal UWB antennas

3. Frequency Notched Function in UWB Antenna

UWB systems must share their frequency bands with existing systems such as WLAN, WiMAX and so on due to its wideband characteristic. So it is necessary to avoid interfering with nearby communication systems. While it was accomplished by a conventional filter in the radio frequency receiver front end, it is possible to design UWB antennas with a band notch characteristic to aid in narrowband signal rejection. In this section, many methods to notch some frequency bands such as inserting slots, removing narrowband resonant structure, using fractal structure, using optimization algorithm and using metamaterial structures are introduced. In addition, the techniques to control the notched band and to notch multiple bands are introduced.

3.1 Inserting the slots

To obtain the frequency band notched function in UWB antenna, it is the most known method to insert the slots. Various frequency notched UWB antennas studied by many researchers can be classified according to slot's locations such as radiating element, ground plane, feeding line and vicinity of the radiating element as shown in Figure 20 to 23.

UWB antennas in Figure 20 have a slot on the various radiating elements (Dissanayake & Esselle, 2007; Yau et al., 2007; Kim^a et al., 2008; Yoon et al., 2005). In this case, the notched frequency is determined by the total length of the slot which is equal to nearly half wavelength. Figure 21 shows the UWB antenna having L-shaped and U-shaped slots on the ground plane (Pancera et al., 2007; Lu et al., 2008; Dong et al., 2009). In this case, the lengths of the slots are a half or a quarter of the wavelength. It is also a good method to insert a slot on the feeding line. UWB antenna in Figure 22 obtained the frequency band notched function by inserting slot on the CPW feeding line (Qu et al., 2006). Beside these locations, it

is possible to insert slots in the vicinity of the radiating element as shown in Figure 23 (Kim & Kwon, 2004; Gopikrishna^b et al., 2008; Zhang^a et al., 2008).

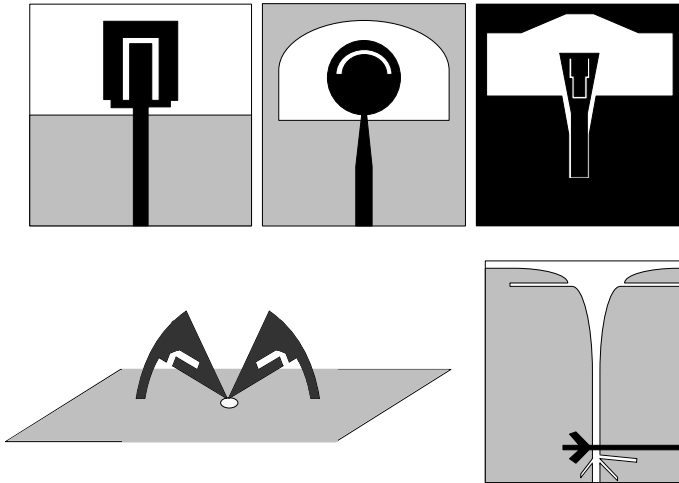


Fig. 20. The frequency notched UWB antennas using the slots on the radiating element

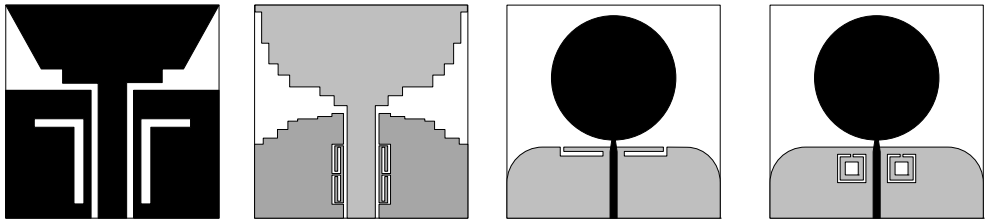


Fig. 21. The frequency notched UWB antennas using the slots on the ground plane

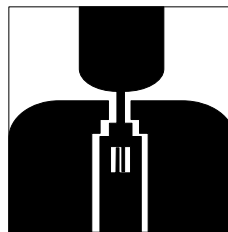


Fig. 22. The frequency notched UWB antenna using the slots on the feeding line

3.2 Remove narrowband resonant structure

Similar with inserting slots, it is also good method to remove narrowband resonant structure. Hans Gregory Schantz et al. introduced this technique as shown in Figure 24. They insert narrowband resonant structure on the UWB antenna element to notch the specific frequency bands. By doing so, they can achieve to realize the frequency notched UWB antenna. And

Shih-Tuan Chen inserted the two vertical slots in the uniplanar log-periodic slot antenna to remove narrowband resonant structure as shown in Figure 25.

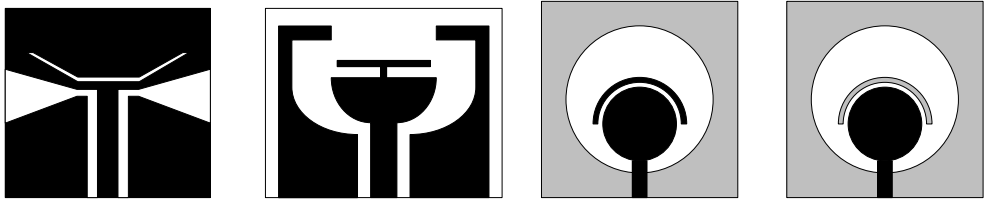


Fig. 23. The frequency notched UWB antennas using the slots near the radiating element

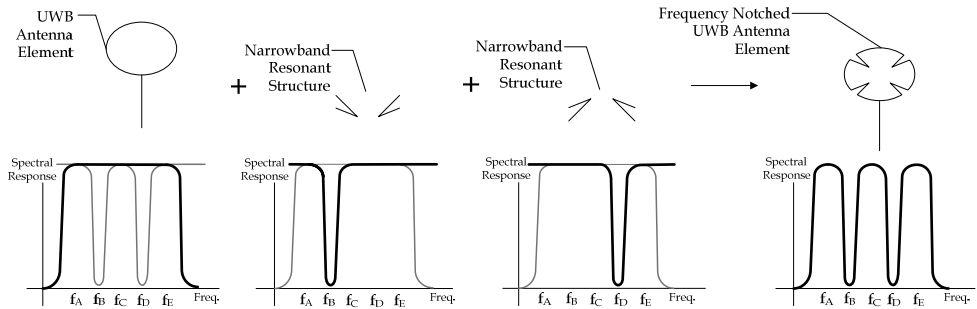


Fig. 24. Combining a UWB antenna element with narrowband resonant structures to notch frequency bands

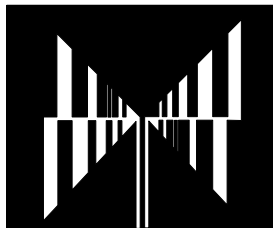


Fig. 25. The frequency notched log-periodic slot antenna

3.3 Using fractal structure

W. J. Lui used the fractal structure to achieve both size reduction and frequency notched characteristic in UWB antenna. Figure 26 shows two types of the frequency notched UWB fractal slot antenna (Lui et al., 2006; Lui et al., 2005).

3.4 Using the optimization algorithm

Current methods used for band notched UWB antenna design need to foresee the structure of the designed UWB antenna so that the design greatly depends on the designer’s experience. But we can design the frequency notched UWB antenna by using the optimization algorithm. M. Ding et al. achieved it by using genetic algorithm (GA) as shown

in Figure 27 (Ding et al., 2008). As you can see, the antenna structure doesn't have specific structure. But it satisfies the good required performance in UWB communication systems.

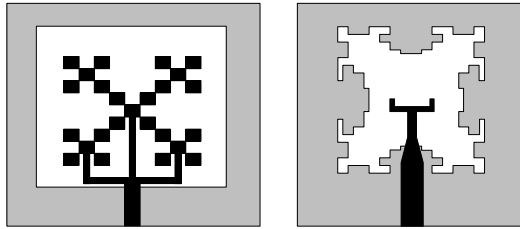


Fig. 26. The frequency notched UWB fractal slot antennas

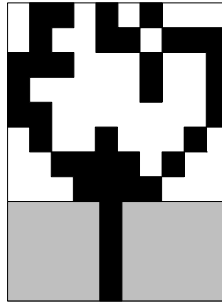


Fig. 27. The frequency notched UWB antenna using genetic algorithm

3.5 Metamaterial Structures

Using metamaterial structures, split ring resonator (SRR), is also possible to notch some frequency band due to its unordinary properties. When electromagnetic waves propagate the SRR structures along x direction, the electric field polarization is kept long y -axis a magnetic field polarization is kept along z -axis. Due to this property, these structures perfectly reflect the EM waves. Cheolbok Kim et al. and J. Kim et al. inserted the SRR structure on the CPW feeding line and radiating element to obtain the notched function in UWB antenna. It is presented in Figure 28 (Kim^b et al., 2008; Kim et al., 2006).

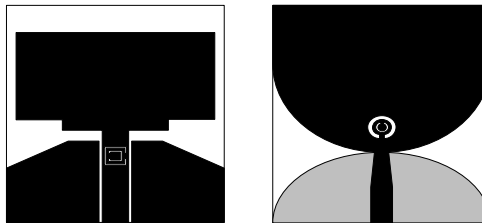


Fig. 28. The frequency notched UWB antennas using SRR structure

3.6 Switchable UWB antenna

Based on above techniques to notch frequency band, active UWB antenna with switchable or tuneable band notched behaviour are designed by using a biased PIN diodes or varactor

diode as shown in Figure 29 (Kim et al., 2007; Antonino-Daviu et al., 2007). Figure 29 (a) is switchable notched band by setting the diode on or off. And Figure 29 (b) can control the notched frequency by changing the capacitance value of the varactor diode.

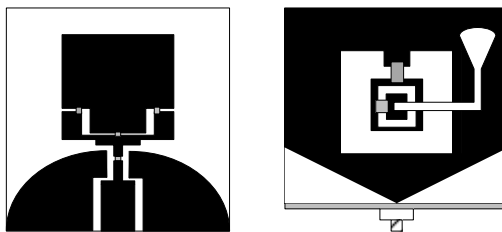


Fig. 29. Active UWB antennas

3.7 Multiband notched UWB Antenna

There are so many wireless services, WLAN (2.4 /5.8GHz), WiMAX (3.3-3.7 GHz), C-band (3.7-4.2 GHz), HIPERLAN (5.1-5.3 GHz). Therefore, UWB antennas also need to notch wide bandwidth or multiple bands to avoid interfering with them. Figure 30 (Lee^a et al., 2006) and 31 (Lee^b et al., 2006; Zhou et al., 2008; Yin et al., 2008; Zhang^c et al., 2008; Deng et al., 2009) show multiple band notched UWB antenna structures. Wang-Sang Lee et al. introduced dual band notched UWB antennas with inserting several slots on the radiating patch in several methods as shown in Figure 30. Figure 31 (a) had a wideband notched characteristic with dual band notched function by inserting slots on the patch and feeding line. Figure 31 (b) obtained a dual-band notch characteristic with inserting a slot on the radiating element and a slot near the radiating element. Like them, others UWB antennas in Figure 31 had multiband notched function by using several techniques such as using a metamaterial structure in Figure 31 (c), (d) and (e), a stepped impedance resonator (SIR) in Figure 31 (d), U-shaped aperture in Figure 31 (b), L-type bandstop filter in Figure 31 (c), L branches on the radiating disk in Figure 31 (c).

4. Future of the UWB

After new FCC regulation authorizing the use of a wide bandwidth to transmit signals in an unlicensed frequency band from 3.1 GHz to 10.6 GHz, UWB technology attracted many engineers' attention due to its advantages, high transmitting data rate and low power consumption. But the early developments in UWB lacked performance, cost too much and were not compatible with worldwide standards which have been subject to much debate and conflict. In addition to them, the economic drawback makes UWB industry go downhill and representative companies leading to the UWB technology shut the door and run out of funding.

However, these are all common growing pains for any new technology like Bluetooth and Wi-Fi which experienced these difficulties. Compared with them, UWB is five times faster than Wi-Fi, 10 times more power efficient and superior user density. There is no better technology to transfer media content wirelessly, at high-speed and low-power. Thus, UWB communication is a potential candidate for wireless personal area network (WPAN). In the

future, UWB technology will be applied to numerous fields such as stealth, LAN, position location, security and vehicular radar system.

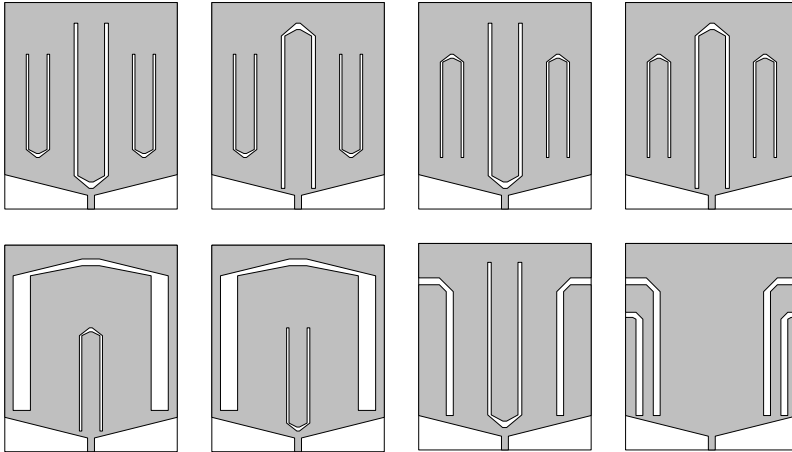


Fig. 30. The dual-band notched UWB antennas with slots

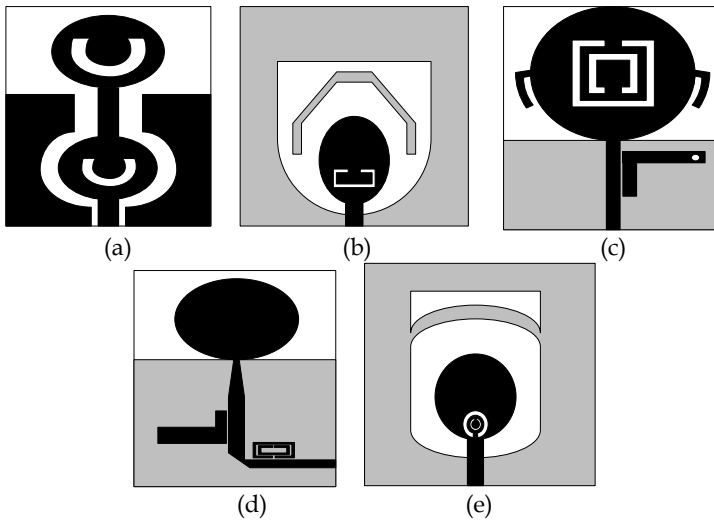


Fig. 31. Multiple band notched UWB antennas

5. Conclusion

This chapter reviewed the various designs of the UWB antennas as well as the conventional frequency independent antennas and the methods to notch some frequency bands for avoiding interfering with other existing wireless communication systems after introducing the history, advantages, disadvantages and applications of the UWB. The introduced structures satisfied the required UWB characteristics and we can realize and control the

notched frequency bands. As I mentioned in this chapter, UWB communication is a potential candidate leading the future short-distance wireless communication.

6. References

- Ammann F. R. (2001). The Pentagonal Planar Monopole for Digital Mobile Terminals; Bandwidth Considerations and Modelling, *Proceedings of 11th International Conference on Antennas and Propagation*, pp. 82-85, ISBN: 0-85296-733-0, Manchester, UK, 17-20 April 2001, Institution of Electrical Engineers, London
- Angelopoulos E. S.; Anastopoulos A. Z.; Kaklamani D. I.; Alexandridis A. A.; Lazarakis F. & Dangakis K. (2006). Circular and elliptical CPW-fed slot and microstrip-fed antennas for ultrawideband applications, *IEEE Antennas and Wireless Propagation Letters*, Vol. 5, No.1, pp. 294-297, ISSN: 1536-1225
- Antonino-Daviu E.; Cabedo-Fabre's M.; Ferrando-Bataller M. & Vila-Jimenez A. (2007). Active UWB antenna with tuneable band notched behaviour, *Electronics Letters*, Vol. 43, No. 18, pp. 257-258, ISSN: 0013-519
- Archevapanich T.; Jearapraditkul P.; Puntheeranurak S.; Anantrasirichai N. & Sangaroon O. (2008). CPW-fed slot antenna with inset L-strip tuning stub for ultra-wideband, *Proceedings of SICE Annual Conference 2008*, pp. 3396-3399, ISBN: 978-4-907764-30-2, Chofu, Tokyo, Japan, 20-22 Aug. 2008
- Balanis C. A. (1996). *Antenna Theory: Analysis and Design*, 2nd ed., John Wiley & Sons, ISBN: 978-0-471-66782-7, New York
- Behdad N. & Sarabandi K. (2005). A Compact Antenna for Ultrawide-Band Applications, *IEEE Transactions on Antennas and Propagation*, Vol. 53, No. 7, pp. 2185-2192, ISSN: 0018-926X
- Butson P. C. & Thomson G. T. (1976). A note on the calculation of the gain of log-periodic dipole antennas, *IEEE Transactions on Antennas and Propagation*, Vol. 14, No. 1, pp. 105-106, ISSN: 0018-926X
- Carrel R. L. (1961). *Analysis and design of the log-periodic dipole antenna*, Ph.D. Dissertation, Elec. Eng. Dept., University of Illinois, University microfilms, Inc, Ann Arbor, MI.
- Chang D. C.; Liu J. C. & Liu M. Y. (2005). Improved U-shaped stub rectangular slot antenna with tuning pad for UWB applications, *Electronics Letters*, Vol. 41, No. 20, pp. 1095-1097, ISSN: 0013-5194
- Chen Z. N. & Chia Y. W. M. (2000). Impedance Characteristics of Trapezoidal Planar Monopole Antennas, *Microwave and Optical Technology Letters*, Vol. 27, No. 2, pp. 120-122, ISSN: 0895-2477
- Chen S.-Y.; Wang P. H. & Hsu P. (2006). Uniplanar log-periodic slot antenna fed by a CPW for UWB applications, *IEEE Antennas and Wireless Propagation Letters*, Vol. 5, No. 1, pp. 256-259, ISSN: 1536-1225
- Chen W.-F.; Ye Z.-S.; Wu J.-M. & Huang C.-Y. (2008). Slot antennas for UWB applications, *Proceedings of Asia-Pacific Microwave Conference 2008*, pp. 1-4, ISBN: 0-7803-9433-X, Hong Kong, China, 16-20 Dec. 2008
- Cho Y. J.; Kim K. H.; Choi D. H.; Lee S. S. & Park S. O. (2006). A miniature UWB planar monopole antenna with 5 GHz band Rejection filter and the time-domain characteristics, *IEEE Transaction on Antennas and Propagation*, Vol. 54, No. 5, pp. 1453-1460, ISSN: 0018-926X

- Choi S. H.; Park J. K.; Kim S. K. & Park J. Y. (2004). A New Ultra-Wideband Antenna For UWB Applications, *Microwave and Optical Technology Letters*, Vol. 40, No. 5 pp. 399-401, ISSN: 0895-2477
- Deng J. Y.; Yin Y. Z.; Ren X. S. & Liu Q. Z. (2009). Study on a dual-band notched aperture UWB antenna using resonant strip and CSRR, *Journal of Electromagnetic Waves and Applications*, Vol. 23, No. 5-6, pp. 627-634, ISSN: 0920-5071
- DeVito G. & Stracca G. B. (1973). Comments on the design of log-periodic dipole antennas, *IEEE Transactions on Antennas and Propagation*, Vol. 21, No. 3, pp. 303-308, ISSN: 0018-926X
- DeVito G. & Stracca G. B. (1974). Further comments on the design of log-periodic dipole antennas, *IEEE Transactions on Antennas and Propagation*, Vol. 22, No. 5, pp. 714-718, ISSN: 0018-926X
- Ding M.; Jin R.; Geng J.; Wu Q. & Wang W. (2006). Design of a CPW-fed ultra wideband Crown Circular Fractal Antenna, *Proceedings of IEEE Antennas and Propagation Society International Symposium 2006*, pp.2049-2052, ISBN:1-4244-0123-2, Albuquerque, NM, USA, 9-14 July 2006, Institute of Electrical & Electronics Engineers, NY
- Ding M.; Jin R.; Geng J.; Wu Q. & Yang G. (2008). Auto-design of band-notched UWB antennas using mixed model of 2D GA and FDTD, *Electronics Letters*, Vol. 44, No. 4, pp. 257-258, ISSN: 0013-519
- Dissanayake T. & Esselle K. P. (2007). Prediction of the notch frequency of slot loaded printed UWB antennas, *IEEE Transactions on Antennas and Propagation*, Vol. 55, No. 11, pp.3320-3325, ISSN: 0018-926X
- Dong Y. D.; Hong W.; Kuai Z. Q. & Chen J. X. (2009). Analysis of planar ultrawideband antennas with on-ground slot band-notched structures, *IEEE Transactions on Antennas and Propagation*, Vol. 57, No. 7, pp.3320-3325, ISSN: 0018-926X
- DuHamel R. H. & Isbell D. E. (1957). Broadband logarithmically periodic antenna structures, *Proceedings of IRE National Convention Record*, Vol. 5, pp. 119-128, ISSN: 0096-8390, Institute of Radio Engineers, New York
- DuHamel R. H. & Ore F. R. (1958). Logarithmically periodic antenna Designs, *Proceedings of IRE National Convention Record*, pp. 139-152, ISSN: 0096-8390, Institute of Radio Engineers, New York
- Dyson J. D. (1959). The equiangular spiral antenna, *IRE Transactions on Antennas and Propagation*, Vol. 7, No. 2, pp. 181-187, ISSN: 0018-926X
- Gopikrishna^a M.; Krishna D. D.; Aanandan C. K.; Mohanan P. & Vasudevan K. (2008). Compact linear tapered slot antenna for UWB applications, *Electronics Letters*, Vol. 44, No. 20, pp.1174-1175, ISSN: 0013-5194
- Gopikrishna^b M.; Krishna D. D. & Aanandan C. K. (2008). Band notched semi-elliptic slot antenna for UWB systems, *Proceedings of Microwave Conference, 2008, EuMC 2008. 38th European*, pp.889-892, ISBN: 978-2-87487-006-4, Amsterdam, Netherlands, 27-31 Oct. 2008
- Gopikrishna M.; Krishna D. D.; Anandan C. K.; Mohanan P. & Vasudevan V. (2009). Design of a compact semi-elliptic monopole slot antenna for UWB system, *IEEE Transactions on Antennas and Propagation*, Vol. 57, No. 6, pp. 1834-1837, ISSN: 0018-926X
- Gupta S.; Ramesh M. & Kalghatgi A. T. (2005). Design of Optimized CPW fed Monopole Antenna for UWB Applications, *Proceedings of Asia-Pacific Microwave Conference 2005*, Vol. 4, ISBN: 0-7803-9433-X, Suzhou, China, 4-7 Dec. 2005

- Huang C. Y. & Hsia W. C. (2005). Planar elliptical antenna for ultra-wideband communications, *Electronics Letters*, Vol. 41, No. 6, pp. 296-297, ISSN: 0013-5194
- Huang Y. & Boyle K. (2008). *Antennas from theory to practice*, John Wiley & Sons, ISBN: 978-0-470-51028-5, United Kingdom
- Isbell D. E. (1960). Log periodic dipole arrays, *IRE Transaction Antenna and Propagations*, Vol. 8, No. 3, pp. 260-267, ISSN: 0018-926X
- Jinghui Q.; Jiaran Q. & Wei L. (2005). A Circular Monopole Ultra-Wideband Antenna, *Proceedings of 5th International Conference on Microwave Electronics: Measurement, Identification, Applications*, pp. 45-47 ISBN: 5-7782-0554-6, Novosibirsk, Russia, 13-15 December 2005
- Jung J.; Choi W. & Choi J. (2005). A Small Wideband Microstrip-fed monopole antenna, *IEEE Microwave and Wireless Components Letters*, Vol. 15, No. 19, pp. 703-705, ISSN: 1531-1309
- Kim Y. & Kwon D. H. (2004). CPW-fed planar ultra wideband antenna having a frequency band notch function, *Electronics Letters*, Vol. 40, No. 7, pp. 403-405, ISSN: 0013-5194
- Kim J.; Yoon T.; Kim J. & Choi J. (2005). Design of an ultra wide-band printed monopole antenna using FDTD and genetic algorithm, *IEEE Microwave and Wireless Components Letters*, Vol. 15, No. 6, pp. 395-397, ISSN: 1531-1309
- Kim J.; Cho C. S. & Lee J. W. (2006). 5.2 GHz notched ultra-wideband antenna using slot-type SRR, *Electronics Letters*, Vol. 42, No. 6, pp. 315-316, ISSN: 0013-5194
- Kim S.-J.; Baik J.-W. & Kim Y.-S. (2007). A CPW-fed UWB monopole antenna with switchable notch-band, *Proceedings of IEEE Antennas and Propagation Society International Symposium 2007*, pp.4641-4644, ISBN: 978-1-4244-0877-1, Honolulu, Hawaii, 9-15 June 2007, Institute of Electrical and Electronics Engineers, NY
- Kim^a C. B.; Lim J. S.; Jang J. S.; Jung Y. H.; Lee H. S. & Lee M. S. (2008). Design of the wideband notched compact UWB antenna, *International Journal of Applied Electromagnetics and Mechanics*, Vol. 28, No. 1, pp.101-110, ISSN: 1383-5416
- Kim^b C. B.; Jang J. S.; Jung Y. H.; Lee H. S.; Kim J. H.; Park S. B. & Lee M. S. (2008). Design of a frequency notched UWB antenna using a slot-type SRR, *AEU-International Journal of Electronics and Communications*, In press, ISSN: 1434-8411
- Kwon D.-H. & Kim Y. (2004). CPW-Fed Planar Ultra-Wideband Antenna with Hexagonal Radiating Elements, *Proceeding on IEEE Antennas and Propagation Society International Symposium*, pp. 2947-2950, ISBN: 0-7803-8302-8, Monterey, California, United States, Vol. 3, June 20-25, 2008, Piscataway, N.J.
- Krishna D. D.; Gopikrishna M.; Aanandan C. K.; Mohanan P. & Vasudevan K. (2009). Ultra-wideband slot antenna with band-notch characteristics for wireless UWB dongle applications, *Microwave and Optical Technology Letters*, Vol. 51, No. 6, pp. 1500-1504, ISSN: 0895-2477
- Lee K. F. & Chen W. (1997). *Advances in Microstrip and printed antennas*, John Wiley & Sons, ISBN: 978-0-471-04421-5, New York
- Lee^a W.-S.; Kim D.-Z.; Kim K.-J. & Yu J.-W. (2006). Wideband planar monopole antennas with dual band-notched characteristics, *IEEE Transactions on Microwave Theory and Techniques*, Vol. 54, No. 6, pp. 2800-2806, ISSN: 0018-9480

- Lee^b C.-M.; Yo T.-C.; Luo C.-H.; Chenh W.-S.; Tu C.-H. & Juang Y.-Z. (2006). Ultra-wideband printed disk monopole antenna with dual band notched functions, *Proceedings of IEEE Wireless and Microwave Technology Conference, 2006*, pp.1-4, ISBN: 1-4244-0849-0, Florida, USA, 4-5 Dec. 2006
- Li P.; Liang J. & Chen X. (2006). Study of printed elliptical/circular slot antennas for ultrawideband applications, *IEEE Transactions on Antennas and Propagation*, Vol. 54, No. 6, pp. 1670-1675, ISSN: 0018-926X
- Liang J.; Chiau C. C.; Chen X. & Parini C. G. (2004). Analysis and design of UWB disc monopole antennas, *Proceedings of Inst. Elect. Eng. Seminar on Ultra Wideband Communications Technologies and System Design*, pp. 103-106, ISBN: 0-86341-442-7 Queen Mary, University of London, U.K., Jul. 2004, Institution of Electrical Engineers, London
- Liang^a J.; Chiau C. C.; Chen X. & Parini C. G. (2005). Study of a Printed Circular Disc Monopole Antenna for UWB Systems, *IEEE Transactions on Antennas and Propagation*, Vol. 53, No. 11, pp. 3500-3504, ISSN: 0018-926X
- Liang^b J.; Guo L.; Chiau C. C. & Chen X. (2005). CPW-fed circular disc monopole antenna for UWB applications, *Proceedings of IEEE International Workshop on Antenna Technology*, pp. 505-508, ISBN: 0-7803-8842, Singapore, 7-9 Mar. 2005, Piscataway, NJ
- Liang^c J.; Chiau C. C.; Chen X. & Parini C. G. (2005). CPW-fed circular ring monopole antenna, *Proceedings of IEEE Antennas and Propagation Society International Symposium 2005*, Vol. 2A, pp. 500-503, ISBN: 0-7803-8883-6, Washington, USA, 3-8 July 2005, Piscataway, NJ
- Liang X. L.; Zhong S. S.; Wang W. & Yao F. W. (2006). Printed annular monopole antenna for ultra-wideband applications, *Electronics Letters*, Vol. 42, No. 2, ISSN: 0013-5194
- Lin C. C.; Kan Y. C.; Kuo L. C. & Chuang H. R. (2005). A planar triangular monopole antenna for UWB Communication, *IEEE Microwave and Wireless Components Letters*, Vol. 15, No. 10, pp. 624-626, ISSN: 1531-1309
- Lu Y.; Lam H.-J. & Bornemann J. (2008). Coplanar Printed Circuit antenna with band rejection elements for ultra wideband filtenna applications, *Proceedings of Antennas and Propagation Society International symposium 2008*, pp.1-4, ISBN: 978-1-4244-2041-4, San Diego, USA, 5-11 July 2008, Piscataway, NJ
- Lui W. J.; Cheng C. H.; Cheng Y. & Zhu H. (2005). Frequency notched ultra-wideband microstrip slot antenna with fractal tuning stub, *Electronics Letters*, Vol. 41, No. 6, pp. 294-296, ISSN: 0013-5194
- Lui W. J.; Cheng C. H. & Zhu H. B. (2007). Experimental investigation on novel tapered microstrip slot antenna for ultra-wideband applications, *IET Microwaves, Antennas & Propagation*, Vol. 1, No. 2, pp. 480-487, April 2007, ISSN: 1751-8725
- Lui W. J.; Cheng C. H. & Zhu H. B. (2008). Compact frequency notched ultra-wideband fractal printed slot antennas, *IEEE Microwave and Wireless Components Letters*, Vol. 16, No. 4, pp. 224-226, ISSN: 1531-1309
- Ma T.-G. & Jeng S.-K. (2005). Planar miniature tapered-slot-fed annular slot antennas for ultrawide-band radios, *IEEE Transactions on Antennas and Propagation*, Vol. 53, No. 3, pp.1194-1202, ISSN: 0018-926X
- Ma T.-G. & Tseng C.-H. (2006). An ultrawideband coplanar waveguide fed tapered ring slot antenna, *IEEE Transactions on Antennas and Propagation*, Vol. 54, No. 4, pp. 1105-1110, ISSN: 0018-926X

- Naghshvarian-Jahromi M. and Falahati A. (2008). Classic Miniature Fractal Monopole Antennae for UWB Applications; Modification of The Feeding Structures of Fractal Antenna for Improving Performances, *3rd International Conference on Information and Communication Technologies: From Theory to Applications, 2008*, pp.1-4, ISBN: 978-1-4244-1751-3, Damascus, Syria, 7-11 April 2008
- Nakasuwan J.; Rakhuea P. & Pirajinchai V. (2008). Printed Circuit antenna for UWB Systems, *Proceedings of IEEE Asia Pacific Conference on Circuits and Systems 2008*, pp. 1375-1378, ISBN: 978-1-4244-2341-5, Macao, China, Nov. 30-Dec 3, 2008, Institute of Electrical and Electronics Engineers, NY
- Nikolaou S.; Ponchak G. E.; Papapolymerou J. & Tentzeris M. M. (2006). Conformal double exponentially tapered slot antenna (DE TSA) on LCP for UWB applications, *IEEE Transactions on Antennas and Propagation*, Vol. 54, No. 6, pp. 1663-1669, ISSN: 0018-926X
- Pancera E.; Modotto D.; Locatelli A.; Pigozzo F. M. & De Angelis C. (2007), Novel design of UWB antenna with band-notch capability, *Proceedings of Wireless Technologies, 2007 European Conference on*, pp.48-50, ISBN: 978-2-87487-003-3, Munich, Germany, 8-10 Oct. 2007
- Pell B.; Sulic E.; Rowe W.; Ghorbani K.; John S.; Gupta R. & Zhang K. (2008). The design and realization of uniplanar CPW fed PICA slot antennas, *Proceedings of Asia-Pacific Microwave Conference 2008*, pp.1-4, ISBN: 0-7803-9433-X, Hong Kong, China, 16-20 Dec. 2008
- Qing X.; Chia M. Y. W. & Wu X. (2003). Wide-slot antenna for UWB applications, *Proceedings of IEEE Antennas and Propagation Society International Symposium*, Vol. 1, pp. 834-837, ISBN: 0-7803-8302-8, Monterey, California, USA, 22-27 June 2003, Piscataway, NJ
- Qu S. & Ruan C. (2005). Quadrate bowtie antenna with round corners, *Proceedings of IEEE International Conference on Ultra-Wideband 2005*, ISBN: 078039397X, Zurich, Switzerland, September 5 - 8, 2005, Piscataway, N.J.
- Qu S. W.; Li J.-L. & Xue Q. (2006). A band-notched ultrawideband printed monopole antenna, *IEEE Antennas and Wireless Propagation Letters*, Vol. 5, No.1, pp. 495-498, ISSN: 1536-1225
- Shrivastava V. & Ranga Y. (2008). Ultra wide band CPW-fed printed pentagonal antenna with modified ground plane for UWB applications, *Proceedings of IET International Conference on Wireless, Mobile and Multimedia Networks 2008*, pp. 1-2, ISBN:9780863418877, Mumbai, India, 11-12 Jan 2008, Institution of Engineering and Technology, London
- Schantz H. G.; Wolenc G. & Myszka E. M. III (2003). Frequency notched UWB antennas, *Proceedings of IEEE Conference on Ultra Wideband Systems and Technologies, 2003*, pp.214-218, ISBN: 0-7803-8187-4, Reston, Virginia, USA, 16-19 Nov. 2003, Piscataway, NJ
- Stuzman W. A. & Thiele G. L. (1997). *Antenna theory and Design*, 2nd ed., John Wiley & Sons, ISBN: 0-471-02590-9, New York
- Tran D.; Tanyer-Tigrek F. M.; Vorobyov A.; Lager I. E. & Ligthart L. P. (2007). A Novel CPW-fed Optimized UWB Printed Antenna, *Proceedings of 2007 European Conference on Wireless Technologies*, pp. 40-43, ISBN: 978-2-87487-003-3, Munich, Germany, 8-10 Oct. 2007, Institute of Electrical and Electronics Engineers, NY

- Tu Z.; Chen G. & Zhang G. (2004). The FDTD Analysis of two Ultra Wideband Dipole Antennas, *Proceedings of 4th International Conference on Microwave and Millimeter Wave Technology*, pp. 46-49, ISBN: 0-7803-8401-6, Beijing, China, 18-24 August 2004, Institute Of Electrical & Electronics Engineer, NY
- Valderas D.; Legarda J.; Gutierrez I. & Sancho J. I. (2006). Design of UWB Folded-Plate Monopole Antennas Based on TLM, *IEEE Transactions on Antennas and Propagation*, Vol. 54, No. 6, pp. 1676-1687, ISSN: 0018-926X
- Verbiest^a J. R. & Vandenbosch G. A. E. (2006). Low-cost small-size tapered slot antenna for lower band UWB applications, *Electronics Letters*, Vol. 42, No. 1, pp. 670-671, ISSN: 0013-5194
- Verbiest^b J. R. & Vandenbosch G. A. E. (2006). A novel small size printed tapered monopole antenna for UWB WBAN, *IEEE Antennas and Wireless Propagation Letters*, Vol. 5, pp. 377-379, ISSN: 1536-1225
- Wang W.; Zhong S. S. & Chen S.-B. (2004). A novel wideband coplanar-fed monopole antenna, *Microwave and Optical Technology Letters*, Vol. 43, No. 1, pp. 50 - 52, ISSN: 0895-2477
- Wong K.-L.; Wu C.-H. & Su S.-W. (2005). Ultrawide-Band Square Planar Metal-Plate Monopole Antenna with a Trident-Shaped Feeding Strip, *IEEE Transactions on Antennas and Propagation*, Vol. 53, No. 4 pp. 1262-1269, ISSN: 0018-926X.
- Yang T. & Davis W. A. (2004). Planar half-disk antenna structures for ultra-wideband communications, *Proceedings of IEEE Antennas and Propagation Society International Symposium 2004*, Vol. 3, pp. 2508-2511, ISBN: 0-7803-8302-8, Monterey, California, USA, 20-25 June 2004, Piscataway, NJ
- Yau Y.; Huang B. & Feng Z. (2007). A novel ultra-wideband microstrip-line fed wide-slot antenna having frequency band notch function, *Proceedings of International Conference on Microwave and Millimeter wave Technology 2007*, pp.1-4, ISBN: 1-4244-1049-5, Guilin, China, 19-22 April. 2007, Institute of Electrical and Electronics Engineers, NY
- Yin X. C.; Ruan C. L.; Ding C. Y. & Chu J. H. (2008). A compact ultra-wideband microstrip antenna with multiple notches, *Progress In Electromagnetics Research*, PIER 84, pp. 321-332, ISSN: 1070-4698
- Yoon I. J.; Kim H.; Yoon H. K.; Yoon T. J. & Kim Y. H. (2005). Ultra-wideband tapered slot antenna with band cutoff characteristic, *Electronics Letters*, Vol. 41, No.11, pp. 629 - 630, ISSN: 0013-5194
- Zhang^a G. M.; Honh J. S. & Wang S. Z. (2008). Two novel band-notched UWB slot antennas fed by microstrip line, *Progress In Electromagnetics Research*, PIER 78, pp. 209-218, ISSN: 1070-4698
- Zhang^b Y.; Nakata T. & Miyashita T. (2008). A Miniature Circular Disc Monopole UWB Antenna with a Tapered Feed Line and a Circular Ground, *Proceedings of China-Japan Joint Microwave Conference 2008*, pp. 411-414, ISBN: 978-1-4244-3821-1, Shanghai, China, Sept. 2008
- Zhang^c Y.; Hong W.; Kuai Z.-Q. & Zhou J.-Y. (2008). A compact multiple band notched UWB antenna by loading SIR and SRR on the feed line, *Proceedings of International Conference on Microwave and Millimeter Wave Technology 2008*, pp.198-201, ISBN:978-1-4244-1879-4, Nanjing, China, 21-24 April.2008
- Zhou H. J.; Sun B. H.; Liu Q. Z. & Deng J. Y. (2008). Implementation and investigation of U-shaped aperture UWB antenna with dual band-notched characteristics, *Electronics Letters*, Vol. 44, No. 24, pp. 1387-1388, ISSN: 0013-519

Patch Antennas and Microstrip Lines

John R. Ojha and Marc Peters
Germany

1. Introduction

Microstrip patch antennas have problems of low bandwidths. The aim of this chapter is to show various ways to overcome this problem by using various matching techniques for numerous patch antenna array schemes. Various approaches are used for estimating the figures of merit such as VSWR and the S11 parameter of such antennas. These patch antenna performance characteristics are addressed by simulation techniques using the full-wave method of moments (MoM). Patch antennas are also modelled as a reduced model, in an effective homogeneous dielectric space, to reduce the simulation time. Lastly a more efficient reduced model using special planar Green's functions with and without the use of non radiating networks are explained qualitatively.

2. VSWR, return loss, and bandwidth

Microstrip and coaxially fed patch antennas are commonly used in various type of smart antenna systems. In order for any given antenna to operate efficiently, the maximum transfer of power must take place between the feeding system and the antenna. Maximum power transfer can take place only when the input impedance of the antenna (Z_{in}) is matched to that of the feeding source impedance (Z_s). According to the maximum power transfer theorem, maximum power can be transferred only if the impedance of the source is a complex conjugate of the impedance of the antenna under consideration and vice-versa. If this condition for matching is not satisfied, then some of the power may be reflected back as

$$VSWR = \frac{1 + |\Gamma|}{1 - |\Gamma|}, \quad (1)$$

with

$$\Gamma = \frac{V_r}{V_i} = \frac{Z_{in} - Z_s}{Z_{in} + Z_s}, \quad (2)$$

where Γ is called the reflection coefficient, V_r is the amplitude of the reflected wave, and V_i is the amplitude of the incident wave. The VSWR is basically a measure of the impedance mismatch between the feeding system and the antenna. The higher the VSWR, the greater is the mismatch. The minimum possible value of VSWR is unity and this corresponds to a perfect match. The return losses (RL), obtained from equations (1) and (2), indicate the

amount of power that is transferred to the load or the amount of power reflected back. In the case of a microstrip-line-fed antenna, where the source and the transmission line characteristic impedance or the transmission line and the antenna edge impedance do not match, waves are reflected. The superposition of the incident and reflected waves leads to the formation of standing waves. Hence the RL is a parameter similar to the $VSWR$ to indicate how well the matching is between the feeding system, the transmission lines, and the antenna. The RL is

$$RL = -20 \log |\Gamma| \text{ (dB)}. \quad (3)$$

To obtain perfect matching between the feeding system and the antenna, $\Gamma = 0$ is required and therefore, from equation (3), $RL = \text{infinity}$. In such a case no power is reflected back. Similarly at $\Gamma = 1$, $RL = 0$ dB, implies that all incident power is reflected. For practical applications, a $VSWR$ of 2 is acceptable and this corresponds to a return loss of 9.54 dB. Usually return losses ranging from 10 dB to 12 dB are acceptable.

The most serious limitation of a microstrip antenna is its narrow bandwidth (BW). The bandwidth could be defined in terms of its Voltage Standing Wave Ratio ($VSWR$) or input impedance variation with frequency. The $VSWR$ or impedance bandwidth of a microstrip antenna is defined as the frequency range over which it is matched with that of the feed line within specified limits. Therefore, the BW of a microstrip antenna is inversely proportional to its quality factor Q and is

$$BW = \frac{VSWR - 1}{Q\sqrt{VSWR}}. \quad (4)$$

The bandwidth is usually specified as the frequency range over which the $VSWR$ is less than 2 (which corresponds to a return loss of 9.5 dB or 11 % reflected power). Sometimes for stringent applications, the $VSWR$ requirement is specified to be less than 1.5 (which corresponds to a return loss of 14 dB or 4 % reflected power). In the case of a patch antenna, the input impedance with the source impedance is used as an intermediate parameter for determining the S_{11} parameter (a measure of the reflection coefficient Γ), return loss, Voltage Standing Wave Ratio ($VSWR$), and bandwidth. The return loss is expressed in dB in terms of S_{11} as the negation of the return loss. The bandwidth can also be defined in terms of the antenna's radiation parameters such as gain, half power beam width, and side-lobe levels within specified limits.

3. Matching of Microstrip Lines

Matching of microstrip transmission lines is done by matching each line to the source, its interconnecting transmission lines, and to the edge of a patch antenna. The patch antenna edge connected to the transmission lines is given an inset to match the radiation edge impedance of the patch antenna to the characteristic impedance of the transmission line.

3.1 Matching of microstrip lines to the source

The characteristic impedance of a transmission line of a microstrip feed patch is designed with respect to the source impedance. The characteristic impedance Z_0 of the transmission line with respect to the source impedance Z_S is

$$Z_0 = n \cdot Z_S, \quad (5)$$

where the factor n is the number of twigs emanating from a node connected to a source. It follows that the characteristic impedance for a single, duplex, and quadruple antenna, illustrated in figure 1 is 50, 100, and 200 ohms respectively. The above equation can be illustrated by considering a 2×2 antenna array as shown in figure 2 where an edge feed is matched to a source impedance of 50 ohms. The transmission lines from the source therefore have an impedance of 100 ohms. Similarly the characteristic impedance of the transmission line feeding the antennas is 200 ohms.

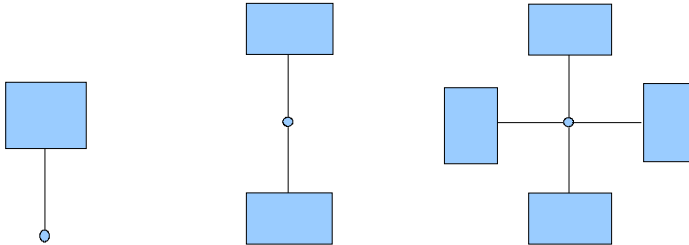


Fig. 1. Characteristic impedances with respect to a 50-ohms source impedance for a (a) single antenna, (b) duplex antenna, and (c) quadruple patch antenna.

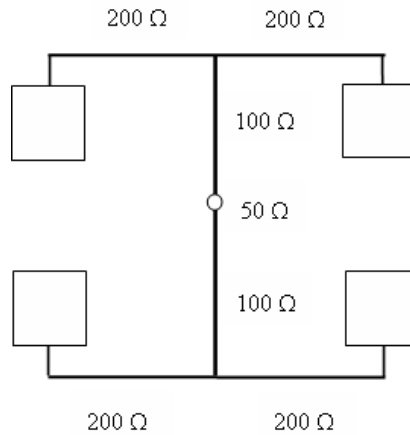


Fig. 2. Matching network of a 2×2 microstrip patch antenna array.

The characteristic impedance of a transmission line therefore depends on the source impedance as well as the number of patch antennas as shown in figure 2. The width of the transmission line w is designed from the empirical relation

$$Z_o = \frac{42.4 \Omega}{\sqrt{\epsilon_r + 1}} \ln \left[1 + C_c \left\{ (C_c \cdot C_d) + \sqrt{(C_c \cdot C_d)^2 + \frac{\pi^2}{2} \cdot \left(1 + \frac{1}{\epsilon_r}\right)} \right\} \right], \quad (6)$$

where C_c and C_d are expressed in terms of line width w , substrate thickness d , and relative permittivity ϵ_r as $C_c = \frac{14 + \frac{8}{\epsilon_r}}{11}$ and $C_d = \frac{4d}{w}$.

3.2 Matching of microstrip lines to the patch edge

In most microstrip patch antennas the feed line impedance is 50Ω whereas the radiation resistance at the edge of the patch is on the order of a few hundred ohms depending on the patch dimension and the substrate used. The performance of the antenna is affected due to this mismatch since the maximum power is not being transmitted. A matching network must therefore be implemented on the feed network, in order to minimise reflections, thereby enhancing the performance of the antenna.

A typical method used for achieving such an antenna is by providing an inset feed. The inset fed distance x_0 can be set such that the feeding edge of the antenna can be matched to the characteristic impedance of the transmission line. The input resistance for an inset fed patch (see figure 3) is given by

$$R_m(x = x_0) = \frac{1}{2(G_1 + G_{12})} \cos^2\left(\frac{\pi x_0}{L}\right), \quad (7)$$

where G_1 is expressed in terms of the antenna width W and the propagation constant k_0 in free space. The inset patch antenna is designed with respect to the characteristic impedance of the transmission line at the resonance frequency of the patch and therefore the imaginary part is zero. The mutual conductance G_{12} is negligible with respect to G_1 for microstrip patch antennas.

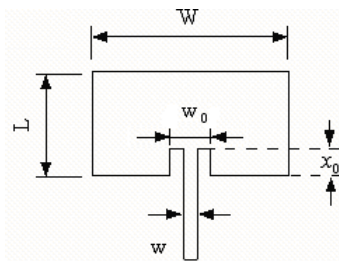


Fig. 3. Microstrip-line-fed inset patch antenna.

4. Design guidelines for patch antenna arrays

For a given center frequency and substrate relative permittivity, the substrate height should not exceed 5% of the wavelength in the medium. The following guidelines are a must for designing patch antenna arrays fed by microstrip lines.

- The length of the patches may be changed to shift the resonances of the centre fundamental frequency of the individual patch elements. The resonant input resistance of a single patch can be decreased by increasing the width of the patch. This is acceptable as long as the ratio of the patch width to patch length (W/L) does not

exceed 2 since the aperture efficiency of a single patch begins to drop, as W/L increases beyond 2.

- To increase bandwidth, increase the substrate height and/or decrease the substrate permittivity (this will also affect resonant frequency and the impedance matching).
- To increase the input impedance, decrease the width of the feed lines attached directly to the patches as well as the width of the lines attached to the port. The characteristic impedance of the quarter-wave sections should then be chosen as the geometric mean of half the impedance of the feed lines attached to the patches and the impedance of the port lines.

Antenna Magus (see figure 4) is a software tool that helps choose the appropriate antenna for a given application and estimates the S_{11} / $VSWR$ and the far field gain characteristics.

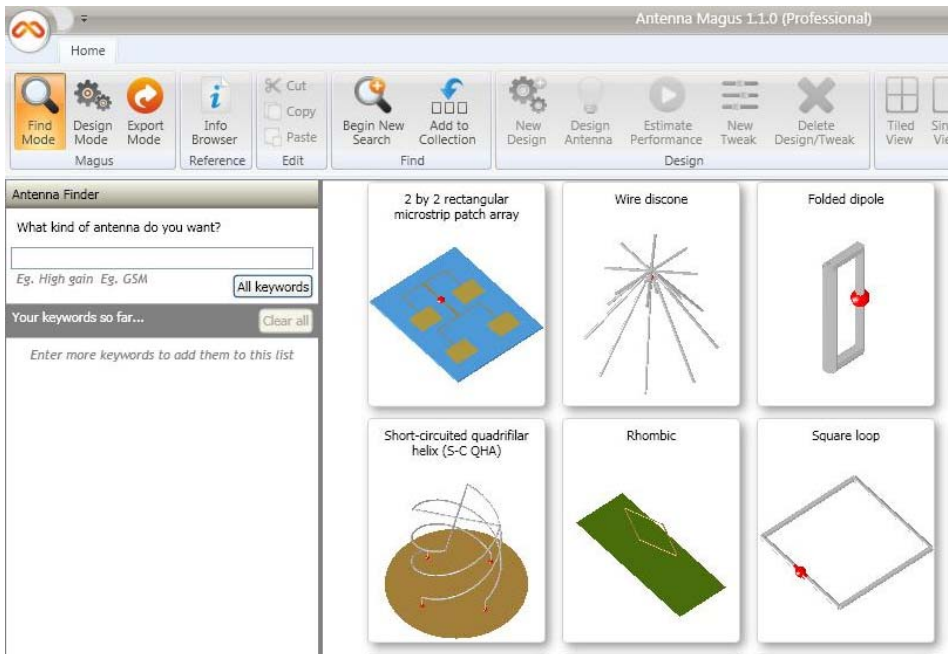


Fig. 4. Microstrip-line-fed inset patch antenna selected from Antenna Magus.

Caution: Antennas on very thin substrates have high copper-losses, while thicker and higher permittivity substrates may lead to performance degradation due to surface waves. The transmission line must be matched to the source as well as to the patch in order to improve the bandwidth and have an acceptable level of $VSWR$ at the centre frequency. The earlier subsection 3.1 explained the approach of matching the transmission line to the source. Figure 5 shows the schematic layout of a patch antenna using the transmission line model where Z_L represents the load impedance or input impedance of the patch antenna. The matching of the transmission line to the patch antenna was explained earlier in section 3.2.

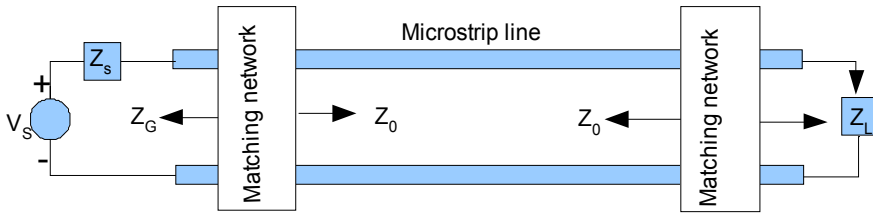


Fig. 5. Transmission line model of a matched patch antenna.

5. Matching of microstrip lines

5.1 Dual Band Antenna Array

In this section an 8×2 inset patch antenna array, shown in figure 6, is discussed, which is designed for a dual band of 1.9 GHz and 2.1 GHz used in UMTS applications. In order to achieve a dual band, the antenna array is designed such that for a 16 patch configuration, half the number of patches i.e. 8 patches are designed to radiate at 1.9 GHz and the remaining 8 patches are designed to radiate at 2.1 GHz as shown in figure 7. Table 1 shows the size of the patch antenna in terms of its dimensions and inset length, where the patch antenna lengths, $L_1 = 39.6$ mm and $L_2 = 35.9$ mm, are designed to resonate at 1.9 GHz and 2.1 GHz, respectively.

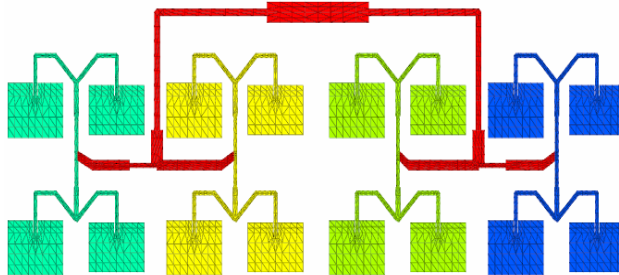


Fig. 6. A discretized structure of a dual band antenna array.

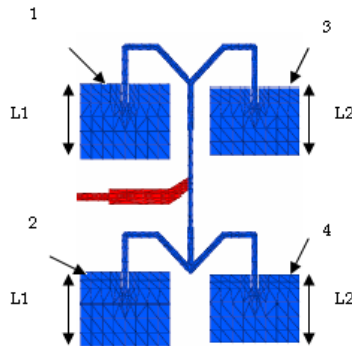


Fig. 7. Array section showing two sets of patch antenna sizes.

Patch number	x_0 (mm)	w (mm)	w_0 (mm)	L (mm)	W (mm)	f (GHz)	$R_{in}(x = x_0)$ (Ω)
1	9.3	3	3.2	39.6	52	1.9	99.2
2	9.3	3	3.2	39.6	52	2.1	90.25
3	7.7	3	3.2	35.9	52	1.9	111.25
4	7.7	3	3.2	35.9	52	2.1	100.60

Table 1. Inset depths of various patches of an 8×2 patch antenna array as a function of antenna length and frequency.

The transmission line width $w = 3$ mm (figure 3) is obtained from equation 6 for a substrate thickness and dielectric constant of 6 mm and 3 respectively. The width is designed for a characteristic impedance to match the antenna array system shown in figure 7. The antenna array system is matched at 1.9 GHz and 2.1 GHz so that the input resistance at the edges of the patch antenna, obtained from equation 7, is 100Ω (Table 1). A comparison will be made in the next subsections with respect to the reduced model and the full model, for the S11 parameter and the VSWR. The effective permittivity ϵ_{eff} used in the reduced model is 0.78 times ϵ_r used in the full-wave MoM. These approaches are explained later in this chapter.

5.2 Broadband Antenna Array

It was seen in section 5.1 that for an 8×2 patch antenna array, the use of different patch size combinations were used for a dual band antenna. In this section all antenna sizes in the array are identical. Broad band characteristics are achieved by following the basic guidelines mentioned in the earlier sections viz. that the characteristic impedance of the transmission line must match the source impedance as well as the impedance at the feeding edge of the patch. This is obviously a significant advantage of an inset patch antenna over a conventional microstrip antenna. The drawback of microstrip lines over a coaxially fed patch antenna is that for a given patch antenna array the width of the transmission lines decreases as the number of antennas increase, and therefore the fabrication of a patch antenna becomes impossible if the number of antennas illustrated in section 2 in figure 1 (a) to (c) exceeds 4. The parameter values given in table 2 for these schemes hold good for the most commonly used substrate thickness of 1.59 mm for patch antennas having a dielectric constant of 2.32.

No. of patch antennas	Z_s (ohms)	Z_0 (ohms)	w (mm)
1	50	50	4.61
2	50	100	1.30
4	50	200	0.15

Table 2. Microstrip line width with respect to antenna array size.

For a larger antenna array, the size of the microstrip lines would be much less than 0.1 mm making fabrication of such an array impossible. A quarter wave transformer is therefore included in an array of 16 antennas e.g. 4×4 microstrip fed patch antenna array, to

overcome this problem, where a 200 ohm line which feeds the patch antenna is matched to the source impedance via 100 ohms feed lines as shown in figure 8 (a). The discretised model of such a scheme is shown in figure 8 (b). The patch antenna sizes are (4 cm x 4 cm). The effective permittivity ϵ_{reff} used in the reduced model is 0.85 times ϵ_r .

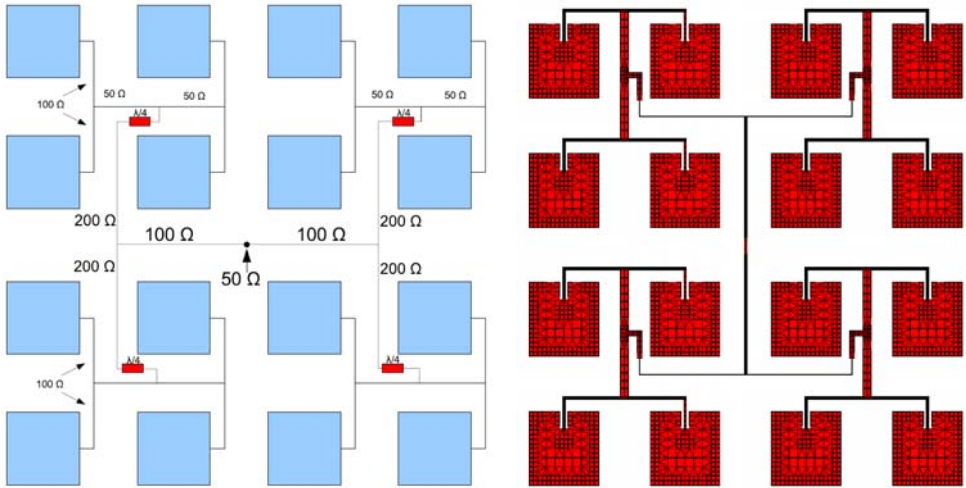


Fig. 8. 4 x 4 patch antenna array using a quarter wave transformer: (a) Schematic diagram and (b) discretised model.

5.3 Results of a Dual band and Broad band Antenna Array -

The VSWR and S11 are obtained using the full-wave MoM and the reduced model for the above designed dual band and broad band antennas. These are explained briefly in the next sections.

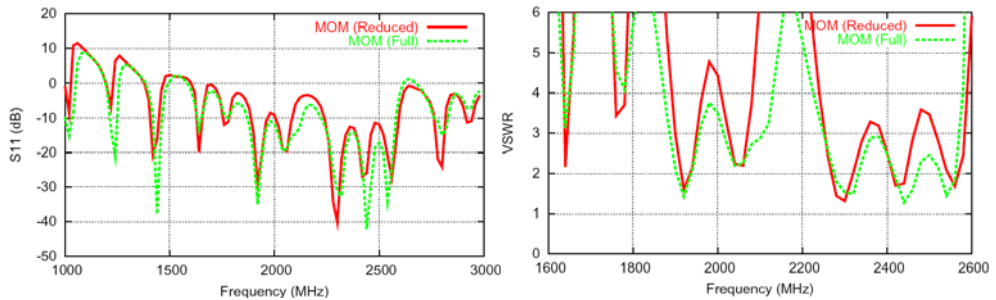


Fig. 9. (a) S11 characteristics and (b) VSWR characteristics of the full model and the reduced model of a 8x2 dual band antenna array.

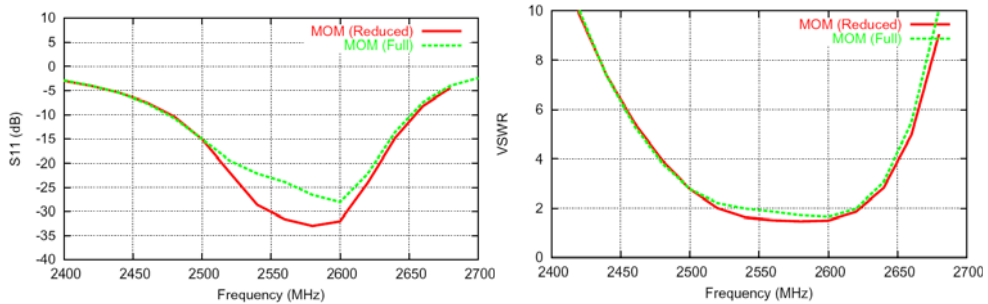


Fig. 10. VSWR characteristics of the full model and the reduced model of a 4x4 broadband antenna array using a quarter wave transformer.

In this section it can be seen that although the patch sizes in section 5.2 are identical, the bandwidth is broader than that of the array shown in section 5.1. This is due to good matching between the source and the transmission lines as well as between the transmission lines and the patch edge. Better broadband characteristics are still possible if the two-patch-size combination is adopted provided that the disparities in the patch lengths do not vary appreciably. For larger variations in patch lengths, thicker substrates are recommended. In section 5.1 the two-patch-size combination has been adopted. However, due to the large difference in patch lengths, a dual band is obtained instead of a broadband, even for a substrate thickness of 6 mm. It can be concluded that a combination of the two-patch-size approach indicated in section 5.1 and the line-to-source and line-to-patch matching approach, along with a quarter wave transformer in section 5.2 would give the best antenna characteristics. The improvement in bandwidth characteristics indicated in figure 10 with respect to figure 9 indicates the importance of providing a quarter wave transformer in terms of the return loss and bandwidth characteristics. The absence of a quarter wave transformer leads to undesirable values of return loss in the frequency spectrum of interest.

5.4 Full-wave method of moments (MoM)

The MoM analysis can be carried out either in the spectral or in the time domain. The spectral / frequency domain has an advantage in that the spectral Green's function is obtained and calculated more easily and hence the spectral approach is employed. A patch antenna comprising metallic and dielectric parts with a feeding pin or microstrip line is solved using the traditional MoM by decomposing the antenna as

- discretized surface parts
- wire parts
- attachment node of the wire to the surface element.

Metallic surfaces contain basis functions as shown in figure 11. The MoM uses surface currents to model a patch antenna. In the case of ideal conductors, the boundary condition of $E_{\text{tan}} = 0$ is applied

The most commonly used basis functions for line currents through wires are stair case functions, triangular basis functions, or sine functions. The MoM code uses triangular basis functions. In contrast to wires, two-dimensional basis functions are employed for surfaces. The current density vectors have two-directional components along the surface. Figure 11 shows the overlapping of so-called hat functions on triangular patches. An integral equation is formulated for the unknown currents on the microstrip patches, the feeding wire / feeding transmission line, and their images with respect to the ground plane. The integral equations are transformed into algebraic equations that can be easily solved using a computer. This method takes into account the fringing fields outside the physical boundary of the two-dimensional patch, thus providing a more exact solution. The coupling impedances Z_{ik} are computed in accordance with the electric field integral equation.

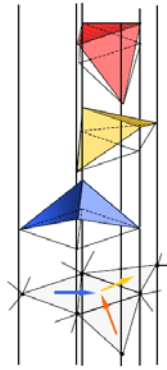


Fig. 11. Hat basis functions on discretised triangular elements on patches.

The MoM uses either surface-current layers or volume polarization to model the dielectric slab. In the case of dielectric materials we have to consider 2 boundary conditions

$$\vec{n} \times \vec{E}_1 = \vec{n} \times \vec{E}_2, \quad (8)$$

$$\vec{n} \times \vec{H}_1 = \vec{n} \times \vec{H}_2. \quad (9)$$

The traditional full-model applied in the MoM code uses a surface-current approach which is categorised as

- double electric current layer approach or
- single magnetic and electric current layer approach.

5.5 Reduced model

Unlike the full model (figure 12 a), which involves the discretisation of metallic and dielectric surfaces, the reduced model involves only the discretisation of metallic parts in a

homogeneous dielectric medium (figure 12 b), having equivalent values of dielectric constant and loss angle with respect to the dielectric slab used in the full model. The reduced model therefore provides the flexibility of the numerical approach, but keeps the modelling effort and computation at a reasonable degree with lesser simulation time.

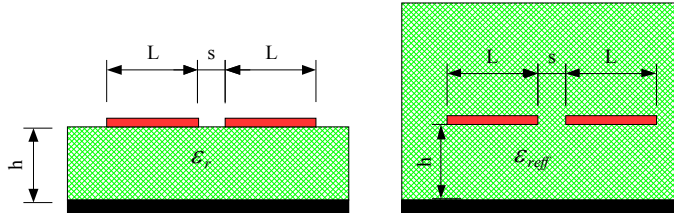


Fig. 12. Patch antenna array modelled as (a) full and (b) reduced model

As mentioned earlier, the greatest drawback of a patch antenna is its narrow bandwidth. Steps were taken to broaden the antenna bandwidth. Two methods were used to study the antenna characteristics viz. the reduced model and the full model. The reduced model shows accurate results with respect to the full-wave model. The full model used in section 5.2 for the broad band antenna comprises approximately 40,000 unknowns and consumes a large memory space of 32 GB since the microstrip lines and the surrounding dielectric surfaces surrounding it have to be finely discretised. The reduced model on the other hand occupies 7000 unknowns and requires less than 2 GB of memory space. Despite these merits viz. speed, accuracy, and storage space its greatest drawback is that of modelling the effective permittivity. The reduced model, which appears to overcome the problem of the full model, is of historical importance since it is not easy to form empirical formulae with respect to the effective permittivity for every antenna shape. This becomes even more complicated especially for inset fed patch fed antennas or patch antennas fed by microstrip lines. The next section deals with an example which makes use of special planar Green's functions which overcomes the problem of the reduced model.

6. Modelling of a circular polarized antenna using non radiating networks

A right hand circularly (RHC) polarised patch antenna at 2.4 GHz is simulated by making use of planar special Green's functions available in FEKO. This approach can in a way be also viewed as a reduced model since only the metallic parts are discretized. The dielectric parts (substrate) and ground plane are imaginary and extend to infinity as shown in figure 13. The model can be further reduced by partitioning the model so that the feed network is characterised as S-parameters which are stored in a Touchstone file. The Touchstone file is then used as a non-radiating network to feed the patch. The input impedance as well as the simulation time and memory required for the two reduced methods (section 6.2 and 6.3) are compared. We will see that subdividing the problem greatly reduces the required resources and simulation time.

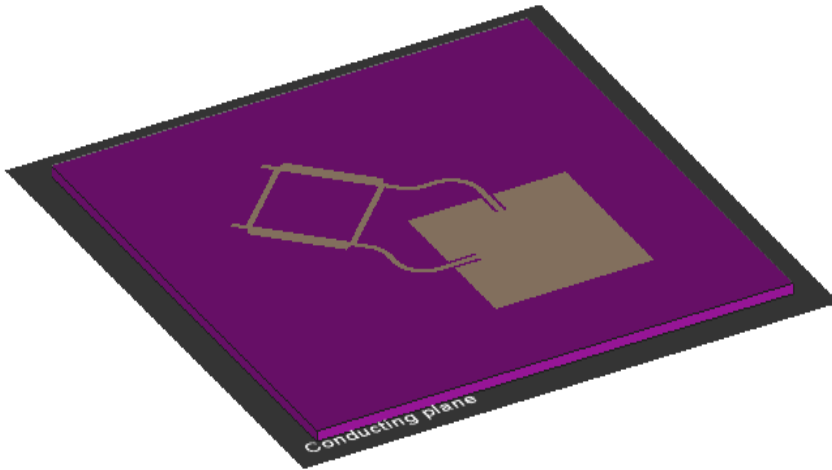


Fig. 13. The model of a RHC patch antenna with feed network.

6.1 Feed network

The feed network consists of a branch line coupler that divides the power evenly with 90 degree phase difference between the outputs. The output signals are then extended to the patch-feed interfaces using microstrip transmission lines. The entire system is designed in a 120Ω system (system or reference impedance).

6.2 Patch with non-radiating feed network

The feed network for the patch antenna is simulated and characterised and its results are saved in a Touchstone file in the form of either S parameters. The stored data which models a non-radiating network is combined with the patch antenna. Effective modelling is also possible by replacing a passive source with an active source e.g. patch antennas fed by a transistor amplifier

6.3 Patch with radiating feed network

The required memory space with the 3D simulation is more as compared to the non-radiating network. The advantage of using the radiated feed networks is that the coupling between the feeding network and the patch antenna is taken into account.

6.4 Results

The difference in solution time and memory requirements is shown in Table 3. We see that the solution time is almost halved by subdividing the problem. Since the field coupling between the feed and the patch cannot be taken into account when substituting the feed with a general non-radiating network, the results are slightly different as seen in figure 14. Although the model with non radiating networks is less accurate, simulation time is saved considerably since only the patch needs to be discretized and not the feeding network. The advantage of memory space and simulation time becomes clear in table 3.

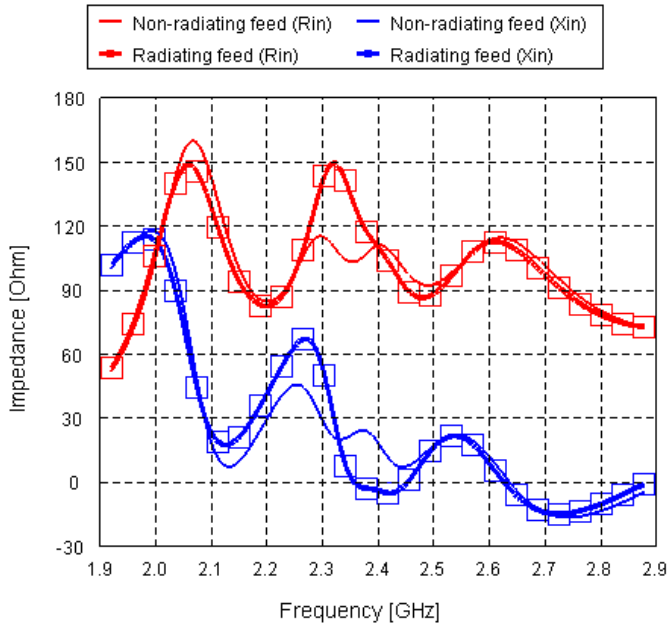


Fig. 14. Input impedance (real and imaginary) of the path with radiating and non-radiating feed.

Verification can also be done using a full 3D field solution comprising the patch, finite substrate, finite ground plane and the feed network. In the case of a full 3D field solution all the aforesaid components have to be discretized.

Model	Memory	Time	Total Time
Full model	7.6 Mb		412
Network only	3.5 Mb	202	
Patch with general network	4.3 Mb	23	225

Table 3: Comparison of resources for the simulations.

7. References

- Balanis, C. A. (2005). *Antenna Theory, Analysis and Design*, Wiley & Sons, Artech House, ISBN 978-0471603528, USA.
- Kumar, G. & Ray, K.P. (2003). *Broadband Microstrip Antennas*, Artech House, ISBN 978-1580532440, USA.
- Garg, R. (2001). *CAD for Microstrip Antennas Design Handbook*, Artech House, ISBN, Artech House
- Sainati, R. A. (1996). *CAD for Microstrip Antennas for Wireless Applications*, Artech House, Publisher, ISBN 978-0890065624, Boston.
- Bancroft, R. (1996). *Understanding Electromagnetic Scattering Using the Moment Method - A Practical Approach*, Artech House, ISBN 978-0890068595, Boston.

Refer to FEKO by using the following information: Author: EM Software & Systems - S.A. (Pty) Ltd Title: FEKO (www.feko.info) Suite: (the suite number reported by FEKO) Publisher: EM Software & Systems - S.A. (Pty) Ltd Address: PO Box 1354, Stellenbosch, 7599, South Africa

Refer to Antenna Magus by using the following information: Author: Magus (Pty) Ltd Title: Antenna Magus (www.antennamagus.com) Version: (the version number reported by Antenna Magus) Publisher: Magus (Pty) Ltd Address: PO Box 1354, Stellenbosch, 7599, South Africa

UWB and SWB Planar Antenna Technology

Shun-Shi Zhong

*School of communication and Information Engineering,
Shanghai University, Shanghai 200072
China*

1. Introduction

Various wideband antennas have been interesting subjects in antenna designs and have found important applications in military and civilian systems. For examples, the super-wideband (SWB) antenna is a key component of electronic counterwork equipment in the information warfare; while the ultra-wideband (UWB) antenna is widely used in impulse radar and communication systems. With the development of high-speed integrated circuits, and the requirement of the miniaturization and integration, the research and application of UWB/SWB planar antennas have been growing rapidly. On February 14, 2002, the Federal Communications Commission (FCC) in the United States allocated the 3.1-10.6GHz spectrum for commercial application of UWB technology, which has sparked renewed attention in the research of ultra-wideband planar antennas. Fig.1 shows its some applications.

It is worth noting that the actual frequency range of an indoor UWB communication antenna in the provision of UWB technology is from 3.1 to 10.6GHz with a ratio bandwidth of 3.4:1, while the antenna with a ratio bandwidth not less than 10:1 is generally called the super-wideband (SWB) antenna in antenna engineering. Both types are reviewed and for simplification, usually they are called the UWB antenna in this chapter. In the UWB system, the former operates just like a kind of pulse figuration filter, which requires the antenna to radiate pulses without distortion. To that end, the UWB antenna should not only possess an ultra-wide impedance bandwidth, but also have good phase linearity and a stable radiation pattern. Hence, for this sort of UWB antenna some particular considerations are entailed [1].

The earliest antenna with wideband properties is the biconical antenna executed by Oliver Lodge in 1898, as shown in Fig.2a. It can be regarded as a uniformly tapered transmission line excited by TEM mode so as to possess the ultra-wideband input impedance properties. Its bandwidth is mainly influenced by the ending reflection due to its limited dimension. Following improvements consist of Carter's improved match biconical antenna (Fig.2b) and conical monopole antenna (1939), Schelkunoff's spheroidal antenna (1941), Kandoian's disccone antenna (1945), Brillouin's omni-directional and directional coaxial horn antenna (1948), etc[2]. All these antennas are based on three-dimensional structures with bulky volume. In the late 1950s and early 1960s, a family of antennas with more than 10:1

bandwidth ratio was developed by V. Ramsey et al., which was called frequency-independent antenna^[3]. Classical shapes of such antennas basically include the equiangular spiral antenna and the planar log-periodic dipole antennas, as shown in Fig.3. These designs reduce the volume, but the transfer of effective radiating region for the different frequencies results in waveform distortion in transmitting pulse. Later on, P.J. Gibson presented in 1979 the Vivaldi antenna, or called tapered slot antenna, as shown in Fig.4, which behaves like an endfire traveling wave antenna with a moderate gain and is of a super-wide bandwidth^[4].

From 1990s, many new-style ultra-wideband planar antennas have been proposed, which can be sum up as three types^[5], namely the Ultra-wideband planar metal-plate monopole antennas, the UWB printed monopole antennas and the UWB printed slot antennas. The progress in these three types of UWB planar antennas is introduced and compared below . In addition, the UWB printed antennas with the band-notched functions are also reviewed.



Fig. 1. Some applications of UWB systems

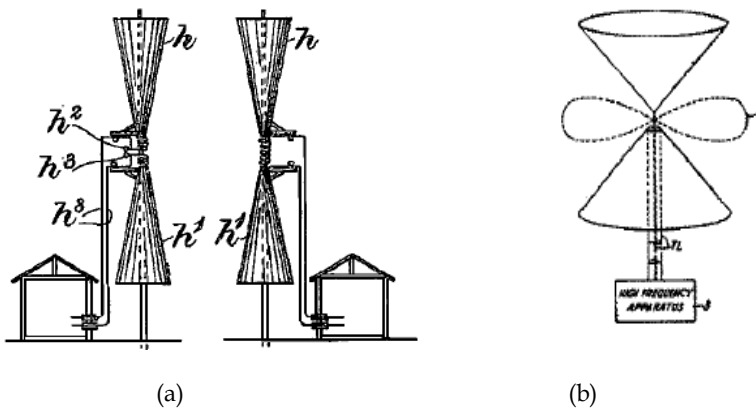


Fig. 2. Lodge's biconical antenna and Carter's improved match biconical antenna^[2]

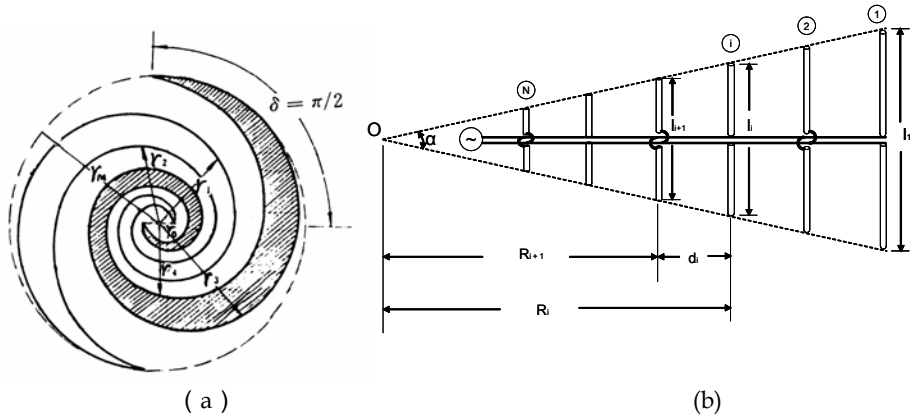


Fig. 3. Equiangular spiral antenna and log-periodic dipole antenna

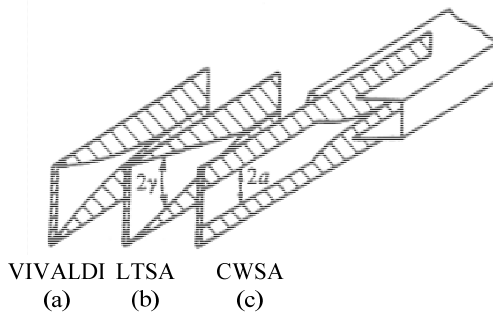


Fig. 4. Vivaldi-like antennas [4]

2. UWB metal-plate monopole antennas

The wideband metal-plate monopole antenna was first proposed by G. Dubost [6] in 1976 and continually developed. Its impedance bandwidth has been broadened by optimizing the structure of metal-plate monopole, such as discs or elliptical monopole antenna [7], trapezium monopole antenna[8], inverted cone monopole and leaf-shaped planar plate monopole antennas etc, as shown in Fig.5. The planar inverted cone antenna (PICA) designed by S.Y. Suh, as shown in Fig.5c [9], provides an impedance bandwidth ratio of more than 10:1, and a radiation pattern bandwidth of 4:1. The one with two circular holes has extended the radiation pattern bandwidth due to the effective changing of its surface current. In the author’s laboratory, another leaf-shaped plate monopole antenna with three circular holes was developed, as shown in Fig.5d [10]. It achieves the impedance bandwidth ratio better than 20:1, covering the frequency range from 1.3GHz to 29.7GHz. As is well known, the rectangular metal-plate monopole antenna is a wideband metal-plate monopole antenna with the simplest structure and a steady radiating pattern, but its impedance bandwidth is only about 2:1 in the early period. In order to realize the ultra-wideband

properties, many methods have been brought forward, such as using an offset feed, double or three feeds, shorting post with beveling technique, etc. P.V. Anob improved its impedance bandwidth to 6:1 by changing the location of the feeding [11]. M.J. Ammann widened the bandwidth to 10:1 ($VSWR \leq 3$) by combining the short post and beveling technique [12], as shown in Fig.6. Some designs, such as double or three feeds in Fig.7, not only consumedly widen the impedance bandwidth, but also improve the stability of radiation pattern [13]. The Ultra-wideband metal-plate monopole antennas always need a perpendicular metal ground plane.

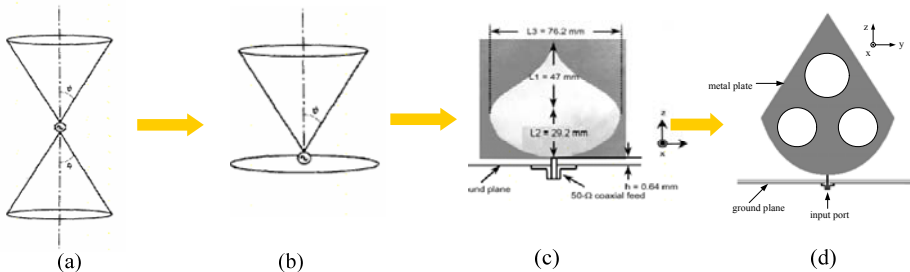


Fig. 5. Evolution from biconical antenna to metal-plate monopole antenna^[5]

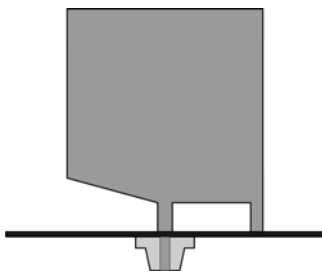


Fig. 6. Monopole antenna with short post^[12]

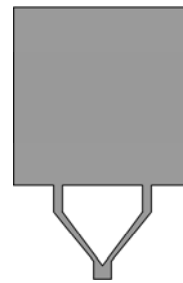


Fig. 7. Monopole antenna with double feeds^[13]

3. UWB printed monopole antennas

The UWB printed monopole antenna consists of a monopole patch and a ground plane, both printed on the same or opposite side of a substrate, while a microstrip line or CPW is located in the middle of the ground plane to feed the monopole patch. Compared with the ultra-wideband metal-plate monopole antenna, the UWB printed monopole antenna does not need a perpendicular ground plane. Therefore, it is of smaller volume and is suitable for integrating with monolithic microwave integrated circuits (MMIC). To broaden the bandwidth of this kind of antennas, a number of monopole shapes have been developed, such as heart-shape, U-shape, circular-shape and elliptical-shape ,etc. A circular printed monopole antenna designed by J. Liang and L. Guo, as shown in Fig 8a^[14], possesses a ratio bandwidth of $S_{11} \leq -10\text{dB}$ exceeding 5.3:1, with the frequency range from 2.27 to 12GHz or above. The UWB printed monopole antenna designed by J. Jung^[15], as shown in Fig. 8b, has

a trapezium transition in the monopole patch and a rectangle slot in its ground plane , equivalent to add a matching network between the patch and the ground plane , thereby to broadening the antenna bandwidth. It covers the frequency range 3.1~11GHz with a mere size of 16 mm×18mm. A printed elliptical monopole antenna designed by C.Y. Huang [16] also uses a rectangular slot in the ground plane to widen the bandwidth. The circular printed monopole antenna with an annulus, as illustrated in Fig. 9, possesses $S_{11} \leq -10\text{dB}$ from 2.127GHz to 12GHz [17]. All these designs are fed by a microstrip line. In the meantime some printed monopole antennas fed by coplanar waveguides (CPWs) have been developed too, as shown in Fig10 [18, 19]. The ratio bandwidth of aforementioned antennas mostly are about 3~7:1. Based on the idea to plate the discone antenna, our group has developed a new type of modified printed monopole antennas with super-wide bandwidth, as plotted in Fig 11, which consists of a monopole patch and a trapeziform ground plane with a tapered coplanar waveguide (CPW) feeder in the middle, achieving an impedance bandwidth ratio of exceeding 10:1[20-23]. To have wider bandwidth, we have changed the rectangular patch to elliptical patch and optimized the dimension, as shown in Fig.11 , whose parameters are: $a=120\text{mm}$, $b=30\text{mm}$, $t=2.3\text{mm}$, $D_{\min}=9\text{mm}$, $D_{\max}=140\text{mm}$, $H=75\text{mm}$, $G = 3.0\text{mm}$ $w_{\text{top}}=1.0\text{mm}$, and $w_{\text{bottom}}=2.7\text{mm}$, with a substrate of thickness $h=1.524\text{mm}$ and relatively permittivity $\epsilon_r = 3.48$ [24]. Its tapered CPW transmission line smoothly transforms the input impedance of about 100Ω at the top point A to 50Ω of an N-type connector at Point B.

This antenna achieves a measured impedance bandwidth of exceeding 21:1, covering frequency range from 0.41~8.86GHz, with a good gain and omni-directional radiation performance, as shown in Fig 12, while its area is only about $0.19\lambda_l \times 0.16\lambda_l$, where λ_l is the wavelength of the lowest operating frequency. In this figure, the simulated results are obtained by means of CST Microwave Studio software based on the finite integration technique (FIT) method.

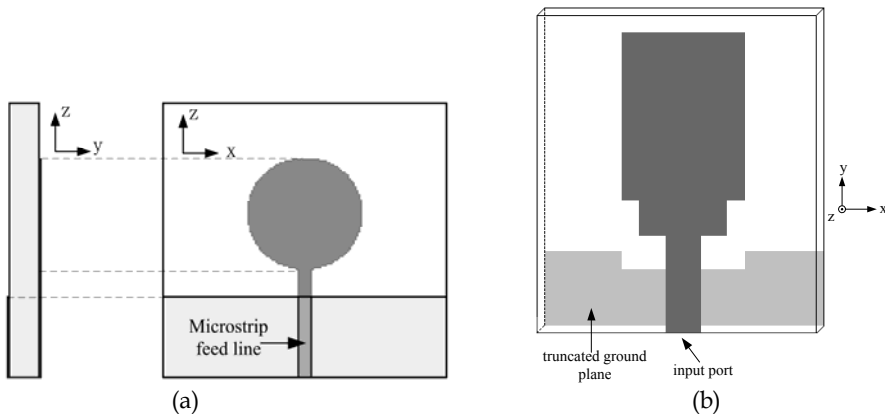


Fig. 8. Microstrip-fed printed monopole antennas[14] [15]

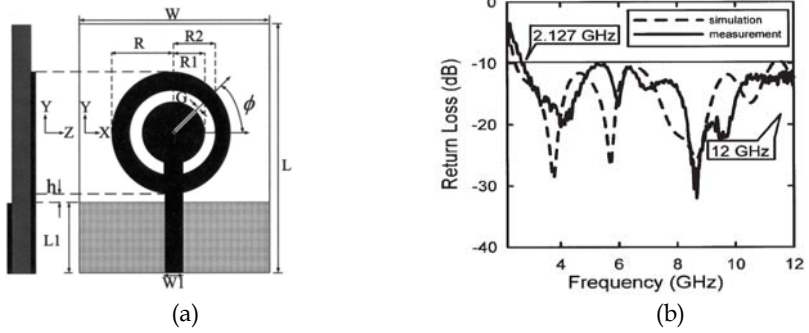


Fig. 9. Printed circular monopole antenna with an annulus^[17]



Fig. 10. Printed CPW-fed monopole antennas^[18, 19]

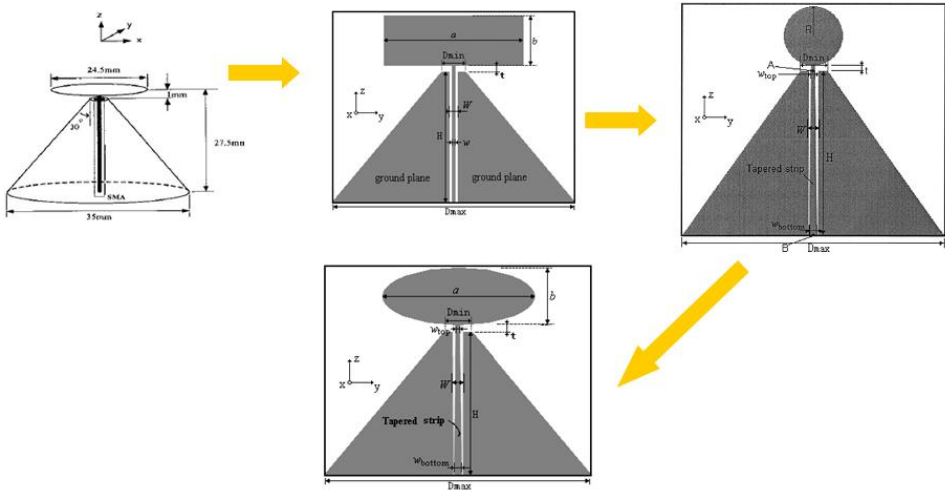
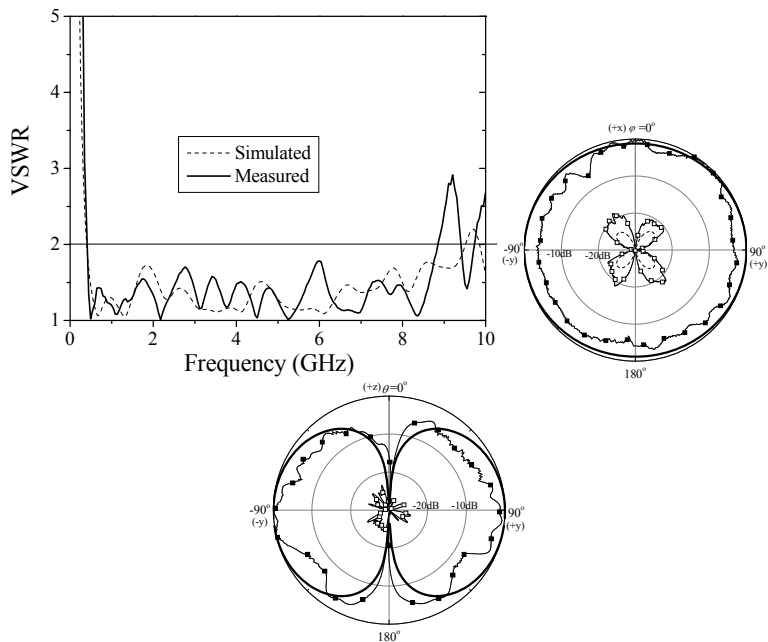
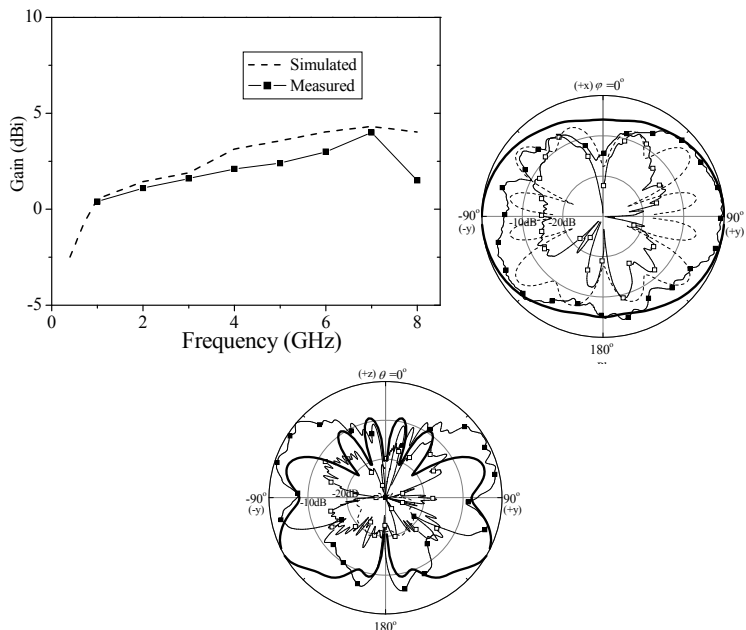


Fig. 11. UWB printed monopole antennas with trapeziform ground plane^[20-24].



(a) $f=1.0\text{GHz}$



(b) $f=6.0\text{GHz}$

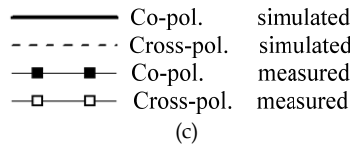


Fig. 12. VSWR , gain and radiation patterns of the Fig.11c antenna with trapeziform ground plane^[24]

In Table1, the simulated and measured $VSWR \leq 2$ bandwidths for two elliptical monopoles and other monopoles with rectangular and circular shapes^{[22] [23]} are listed. Comparing the measured bandwidths of No.1 and No.2, it is seen that by adopting the tapered CPW (No.2), the $VSWR \leq 2$ bandwidth is enhanced by $10.7/6.3=1.7$ times. Comparing the calculated bandwidths of No.3 and No.4, it is shown that using the trapeziform ground plane instead of a rectangular one may broaden the impedance bandwidth to $11.0/7.2=1.5$ times; while comparing No.4 with No.6, it is noted that by selecting the elliptical monopole with an optimum major axis a , the measured impedance bandwidth is enhanced to more than 21:1, *i.e.* almost double. Therefore, the bandwidth broadening of the Fig.11c antenna comes from three improvements: the optimum elliptical monopole shape, a trapeziform ground plane and a tapered CPW feeder.

No	Antenna Configuration	Frequency range of $VSWR \leq 2$ (GHz)		Ratio bandwidth of $VSWR \leq 2$	
		Calculated	Measured	Calculated	Measured
1	Rectangular monopole with a 50Ω CPW ^[22]	0.64 ~ 3.46	0.59 ~ 3.72	5.4:1	6.3:1
2	Rectangular monopole with a tapered CPW ^[22]	0.83 ~ 8.17	0.76 ~ 8.15	9.8:1	10.7:1
3	Circular monopole with a rectangular ground plane ^[23]	1.3 ~ 9.4	--	7.2:1	--
4	Circular monopole with a trapeziform ground plane ^[23]	0.87 ~ 9.56	0.79 ~ 9.16	11.0:1	11.6:1
5	Elliptical monopole of $a=60\text{mm}$ ^[24]	0.58 ~ 9.54	0.64 ~ 8.94	16.4:1	14.0:1
6	Elliptical monopole of $a=120\text{mm}$ ^[24]	0.4 ~ 9.51	0.41 ~ 8.86	23.8:1	21.6:1

Table 1. Comparison of impedance bandwidths

The current distribution of elliptical monopole antenna is shown in Fig.13. It is noted that, at all frequencies of its operation bandwidth, the surface currents of the monopole patch are mostly concentrated on the bottom periphery of the patch close to the feed, while those on the upper periphery and around the center of the patch are of very low current density. From this observation, a circular hollow was cut out from the elliptical patch to eliminate the region of low current density, resulting in the new design of Fig.13, whose measured $VSWR \leq 2$ bandwidth is 24.1:1, covering a frequency range from 0.44 to 10.6 GHz ^[25]. Its area is only about $0.18\lambda_l \times 0.13\lambda_l$. In order to reduce size, a semi-monopole printed antenna was developed and the $VSWR \leq 2$ ratio bandwidth of 25.9:1 (0.795-20.6 GHz) was measured ^[26]. However, its cross-polarization radiation is higher.

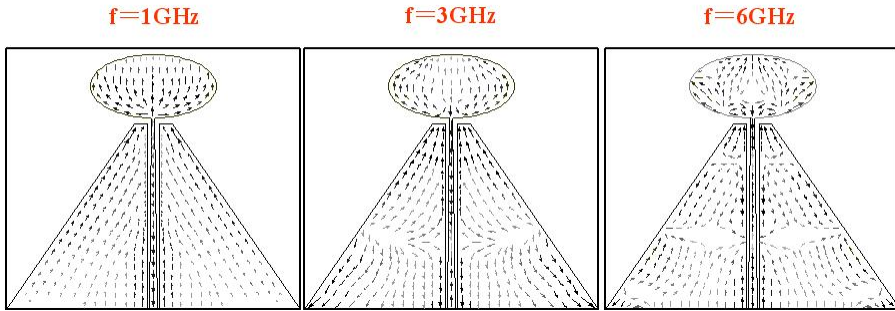


Fig. 13. Current distribution of elliptical monopole antenna

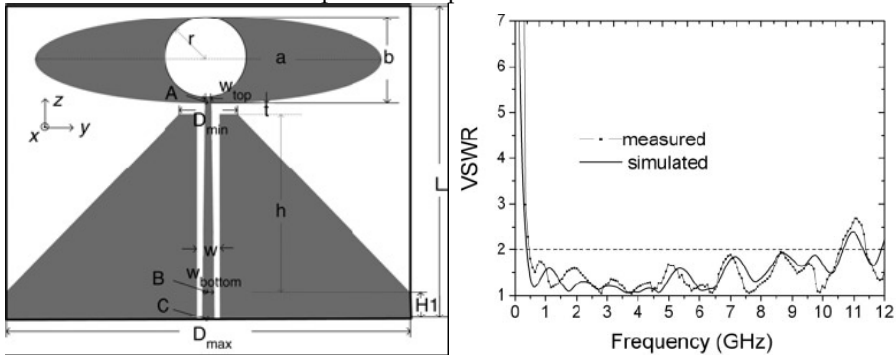
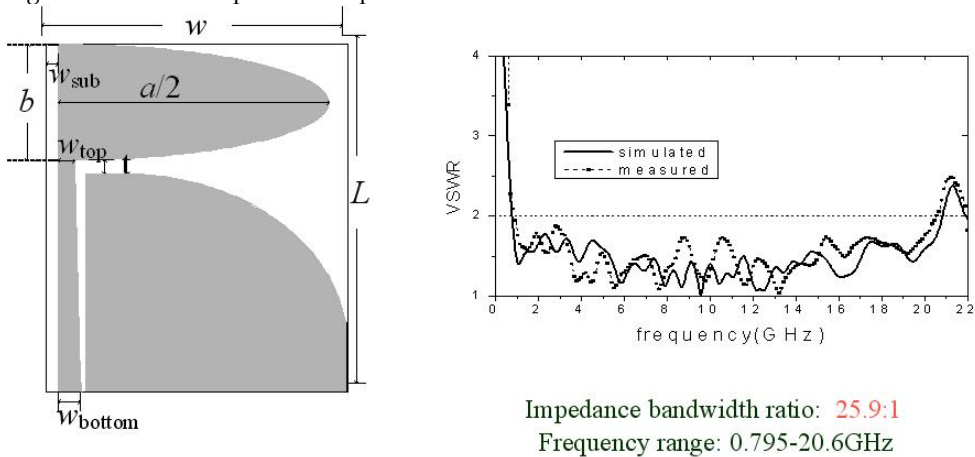


Fig. 14. Hollowed elliptical monopole antenna and its VSWR^[25]



Impedance bandwidth ratio: **25.9:1**
 Frequency range: 0.795-20.6GHz

Fig. 15. Hollowed elliptical monopole antenna and its VSWR [26]

4. UWB printed slot antennas

For the integration application of a Vivaldi-like slot antenna, its impedance bandwidth is inherently limited by the microstrip-to-slotline transition. A printed two-side-antipodal

exponential tapered slot antenna proposed by Gazit [27] has resolved the transition problem, though with a relatively higher cross-polarization level. Later, the balanced antipodal Vivaldi tapered slot antenna introduced by J.D.S. Langley[28], as shown in Fig. 16a, restrains the cross-polarization to be less than -17dB, with a ratio bandwidth of 15:1, covering frequencies from 1.3 ~ 20GHz. Fig.16b is a dual tapered UWB design using CPW feeding[29].

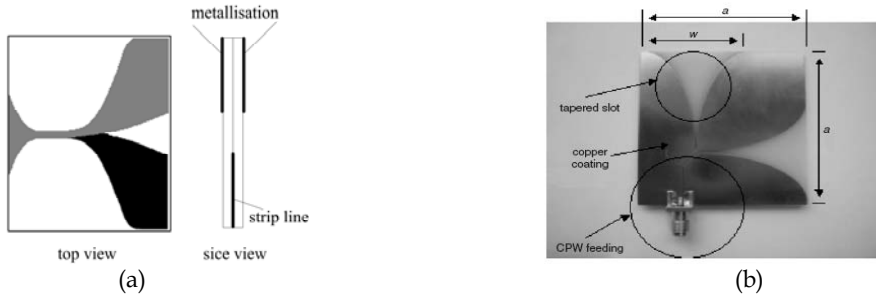


Fig. 16. Printed tapered slot antennas[28] [29]

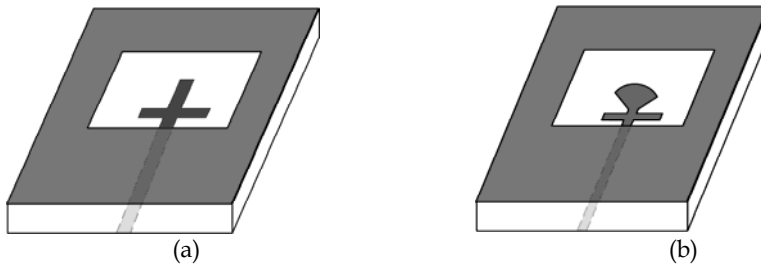


Fig. 17. Microstrip-fed rectangular slot antennas [30] [31]

In recent years, many researches have been engaged in the printed wide-slot antenna and have realized the ultra-wideband property through a combination of changing the slot shape and using different feeding structures. Fig.17 shows two kinds of printed wide-slot antennas with different feeding structures. In Fig.17a the wide-slot antenna is fed by a cross-shaped feeding with a cross-shaped stub at the end instead of the common opened microstrip feeder, which is equivalent to introducing a resonance circuit and hence resulting in an impedance bandwidth of 98% [30]. The slot antenna fed by a fan-shaped stub together with a strip line proposed by our lab, as shown in Fig 17b, has achieved a bandwidth of 114% by optimizing the length of the stub and the size of the fan-shape [31]. Fig.18 shows two printed slot antennas using U-shaped microstrip feedings. Fig. 18a adds a rectangular patch in the middle of the rectangular slot and connecting with the ground plane to achieve a measured impedance bandwidth of 111% [32]. In Fig.18b, by adding a rectangular copper sheet in one side of the microstrip to adjust the port impedance of the antenna, its impedance bandwidth extends to 135.7%, covering frequencies 2.3 ~ 12GHz[33].

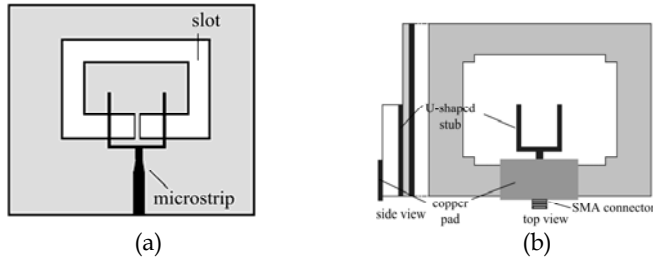


Fig. 18. U-shaped microstrip fed printed slot antennas^[32] ^[33]

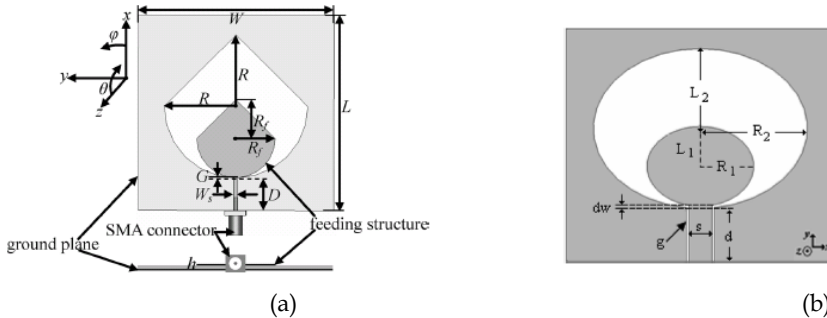


Fig. 19. Printed slot antennas with shaped-slots ^[34] ^[36]

The printed wide-slot antennas have been designed to use various slot shapes. In Fig.19a, the design of PICA(Planar Inverted Cone Antenna) achieves a $VSWR \leq 2$ ratio bandwidth of 13:1 ^[34]. The CPW-fed printed wide-slot antennas also have been designed to use various shapes of the guide strip terminal of its CPW feeder to excite the slot, and accordingly obtain the broadening of its impedance bandwidth. A design achieves an impedance bandwidth about 114%, whose CPW terminal is a rectangular patch with a concave gap^[35]. The elliptical slot antenna with an elliptical patch as its feed, as shown in Fig.19b, widens the impedance bandwidth to 175%, covering frequencies from 1.3GHz to 20GHz or above with a ratio bandwidth about 15:1 ^[36].

Another type of printed slot antenna is the printed bow-tie slot antenna, as shown in Fig.20, which has the virtue of simple configuration, wider bandwidth, lower cross-polarization level and higher gain.

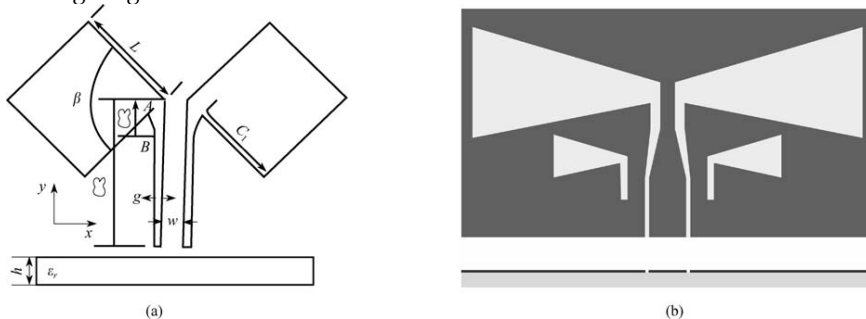


Fig. 20. CPW-fed bow-tie printed slot antennas ^[37] ^[38]

Fig.20a was designed at our lab, which widens the impedance bandwidth by using a lineally tapered slot at the joint of the coplanar waveguide and the bow-tie slot^[37]. In Fig.20b a small bow-tie slot is added under the bow-tie slot antenna, and excited by the coupling of the coplanar waveguide. In addition ,a tapered coplanar waveguide feeder is applied, so that the antenna achieves an impedance bandwidth of 123%^[38].

A comparison of the main performances of several UWB planar antennas is listed in Table 2. It is noted that the UWB printed monopole antennas have dimensions close to those of UWB plate monopole antennas, whereas without a perpendicular metal ground plane. For example, a printed elliptical monopole antenna with a trapezium ground plane has the dimension of only $0.19 \times 0.16 \lambda_l^2$, where λ_l is the wavelength of the lowest operating frequency, and an impedance bandwidth of 21.6:1. UWB printed slot antennas possess a relatively higher gain compared with the other two UWB antennas, and a relative larger size.

No.	Antenna type	Bandwidth(GHz) (VSWR \leq 2)	Ratio bandwidth (VSWR \leq 2)	gain (dBi)	size (λ_l^2)
1	Trapezoidal metal plate monopole [8]	1.07 ~ 12.2	11.4:1	0.5 ~ 4.5	0.89×0.89*
2	Planar inverted cone antenna [9]	1 ~ 10	10:1	0.3 ~ 8.6	0.25×0.25
3	Leaf-shaped plate monopole [10]	1.3 ~ 29.7	22.8:1	3 ~ 5	0.35×0.35
4	Circular monopole with a trapeziform ground plane [21]	0.79 ~ 9.16	11.6:1	0.8 ~ 4.1	0.37×0.24
5	Rectangular monopole with a trapeziform ground plane [22]	1.76 ~ 8.17	10.7:1	0.65 ~ 4.2	0.35×0.30
6	Elliptical monopole with a trapeziform ground plane [24]	0.41 ~ 8.86	21.6:1	0.4 ~ 4	0.19×0.16
7	Tapered slot antenna [29]	1.3 ~ 20	15.4:1	3.2~ 9	0.43×0.32
8	printed Elliptical slot antenna [36]	1.3 ~ 20	15.4:1	-----	0.39×0.39

* Ground plane dimension

Table 2. Comparison of UWB planar antennas

The UWB printed monopoles are more suitable for smaller portable devices where volume constraint is a significant factor. In such devices a main requirement for antennas is the capability to transmit a pulse with minimum distortion and thus preserve the shape of the pulse. Three printed monopole antennas with typical shapes and sizes have been evaluated in the radio channel in the context of frequency and time domain performances^[39]. The antenna geometries used are shown in Fig.21, where (A) is a rectangular planar monopole of area 75 mm×40 mm with FR4 substrate of 1.52 mm thick, (B) a smaller antenna with both radiator and ground plane spline-shaped of area 30 mm×40 mm on a 0.76 mm thick RO 4350 substrate, and (C) an even smaller spline antenna on 0.4 mm FR4 of area 30mm×30mm . The measured S11 for each antenna is shown in Fig.22. Ant. A exhibits a 10 dB return loss from 1.59 to 6.9 GHz, and Ant. B offers a 14 dB return loss over the bandwidth 3.1-10.6 GHz,

while Ant.C offers 6 dB from 2.31-6.7 GHz.

To quantify the distortion of each antenna, a pair of each antenna shape was set up to transmit and receive a pulse. The correlation of the received pulse with the input one was expressed by the fidelity factor, which is a measure of the capability of an antenna to preserve a pulse shape, and is written as^[40]

$$F = \max_{\tau} \int_{-\infty}^{\infty} L[\hat{f}(t)] \hat{r}(t + \tau) dt$$

Where the input $\hat{f}(t)$ and the output $\hat{r}(t)$ have been normalized to have unit energy, and $L[\hat{f}(t)]$ is the idealized system function, while the delay τ is varied to maximize the integral term.

Each pair of antennas was placed in different orientations, face-to-face, back-to-back, face-back, and so on. The pulse used was a raised cosine pulse of 0.4 GHz bandwidth centered at 4 GHz. The fidelity factor for each combination is listed in Table 3. It is seen that Ant. B generally achieves the best fidelity in any configuration. The analysis shows a general advantage for the spline based antenna geometries over the rectangular monopole shape. Fig.23 shows the input and normalized measured output pulse for Ant. B in the back-to-back configuration. It is demonstrated that the shape of the pulse is preserved very well by the antennas.

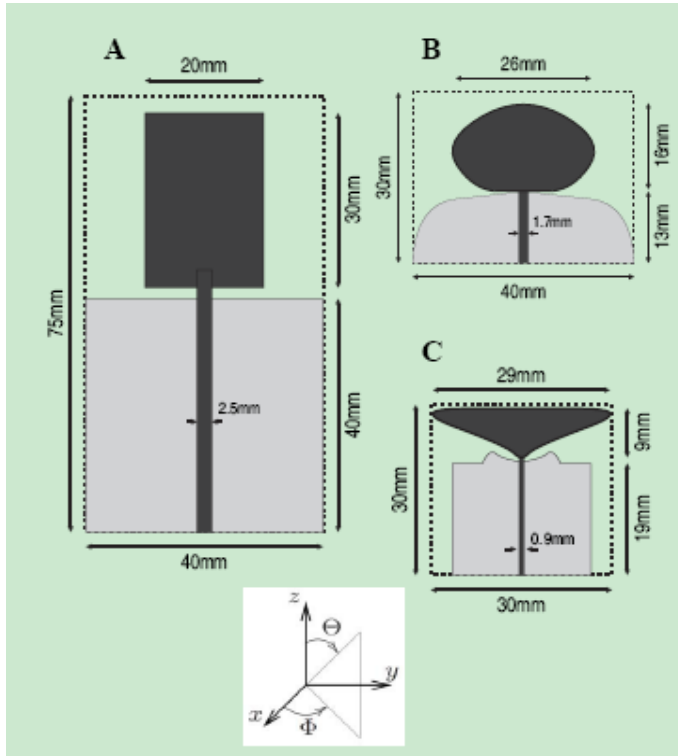


Fig. 21. Geometries and dimensions of 3 test printed monopole antennas^[39]

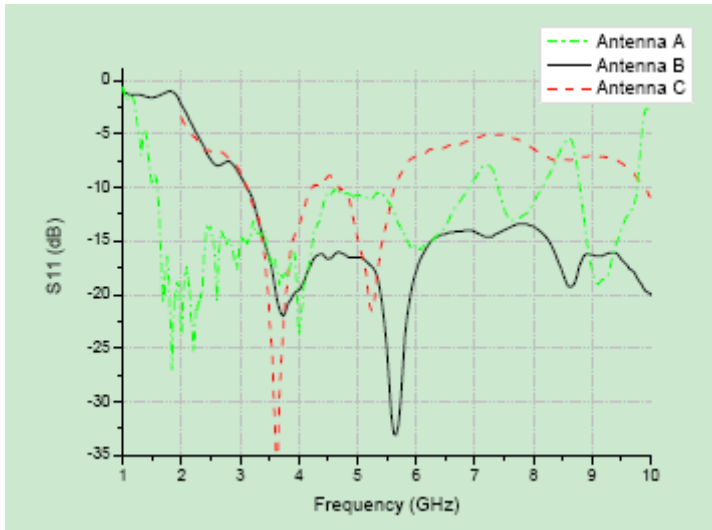


Fig. 22. Measured S11 for 3 test antennas [39]

Table 3 [39]

FIDELITY FACTOR OF THE THREE ANTENNAS IN DIFFERENT ORIENTATIONS (%)			
	A	B	C
face-to-face	94.9	96.7	93.9
back-to-back	95.2	99.4	95.4
face-to-back	95.9	98.8	96.7
face-to-side	92.9	96.3	96.2
back-to-side	94.2	99.1	95.8
side-to-side	95.3	98.1	92.0

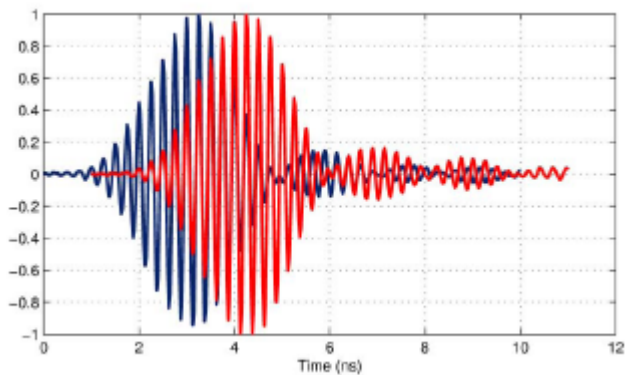


Fig. 23. Input and normalized measured output pulses for Ant. B [39]

5. UWB band-notched planar antennas

To avoid the interference between the UWB system and the wireless local area network (WLAN) 802.11a system with 5.15 to 5.825 GHz frequency band, a band-notch filter in the UWB system is needed. To avoid adding filters and possible interference with existing WLAN systems, UWB antennas with band-notched characteristics have been developed. The sail-boat antenna, as shown in Fig 24a, achieves the UWB property by using an inverse taper planar patch, and forms the band-notch function near the 5GHz frequency by cutting two slots in the patch, which possesses a bandwidth of 3~11GHz for $V_{SWR} \leq 2$ except frequencies neighboring 5.2GHz^[41]. A UWB circular disc monopole antenna designed by our lab, as shown in Fig. 24b, provides the band notched function by inserting an arched slot in the circular monopole patch^[42]. The antenna of Fig. 25 achieves the wide bandwidth property by using a step-shape taper in the pear-shape monopole patch, then forming the band-notch function by introducing two parasitic printed patches^[43]. The CPW-fed antenna of Fig. 26 obtains the UWB performance also by means of the step-shape taper in the monopole patch, while its band-notch function is realized by introducing two folded-striplines on the backside of the substrate^[44].

In Fig.27a,the configuration of a novel band-notch printed antenna is illustrated^[45], where the double-feed technique combined with the tapered impedance transformer is used to obtain a wide impedance bandwidth, and an inverted U-shaped slot embedded in the microstrip feeder is adopted to realize the band-notch characteristic, which does not worsen antenna radiation performance. As shown in Fig.27b, the measured VSWR with slot exhibits a notched-band of 5.15-6.02 GHz for $V_{SWR} > 2$,while the wideband performance from 3.05 to 10.84 GHz is maintained.Fig.27c shows the simulated omnidirectional performance in the entire operating bandwidth, where the omnidirectional fluctuation is denoted by the max-radiation level minus the min-radiation level in the H-plane. It is noted that the fluctuation is below 4.8 dB in the frequency range of 3.1-10 GHz, and that the cross-polarization is below -19dB in the whole bandwidth. The measured antenna gain is about 2.6-4.5 dBi in the operating bandwidth while a sharp decreased gain is about -5.5dBi in the notched-band of 5-6 GHz.

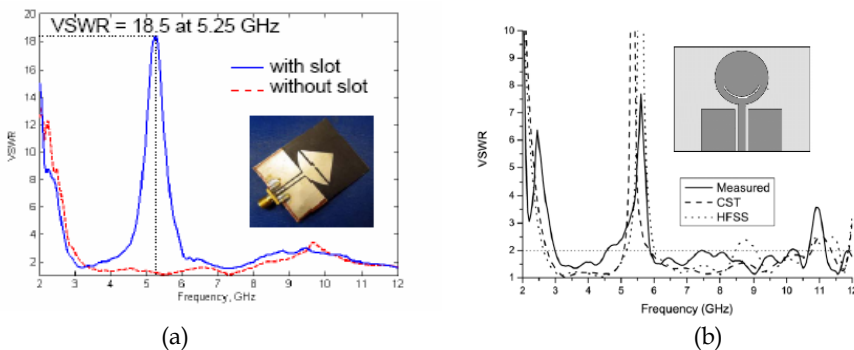


Fig. 24. UWB printed monopole antennas with band-notch function^[41] [42]

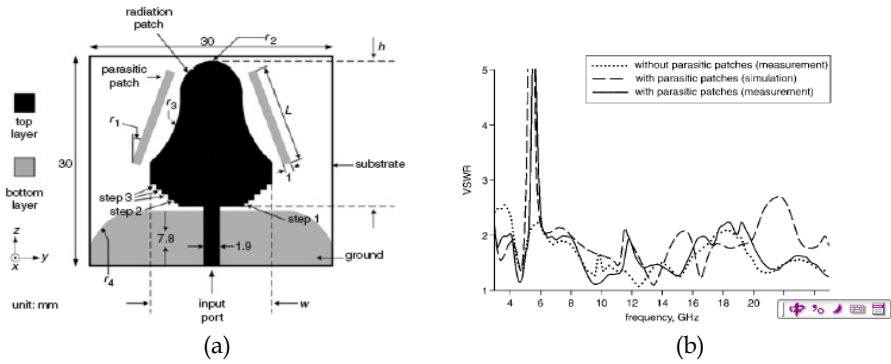


Fig. 25. UWB printed band-notch antenna with two parasitic patches^[43]

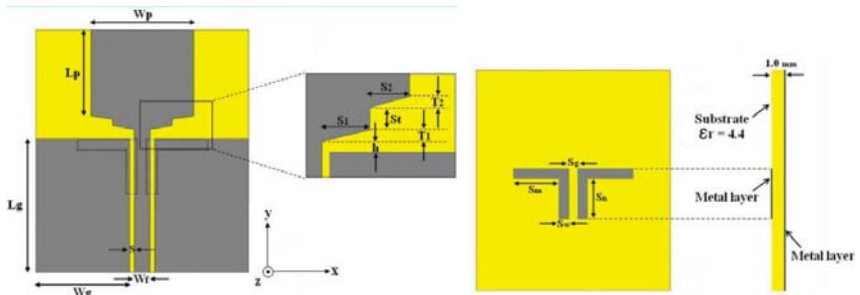
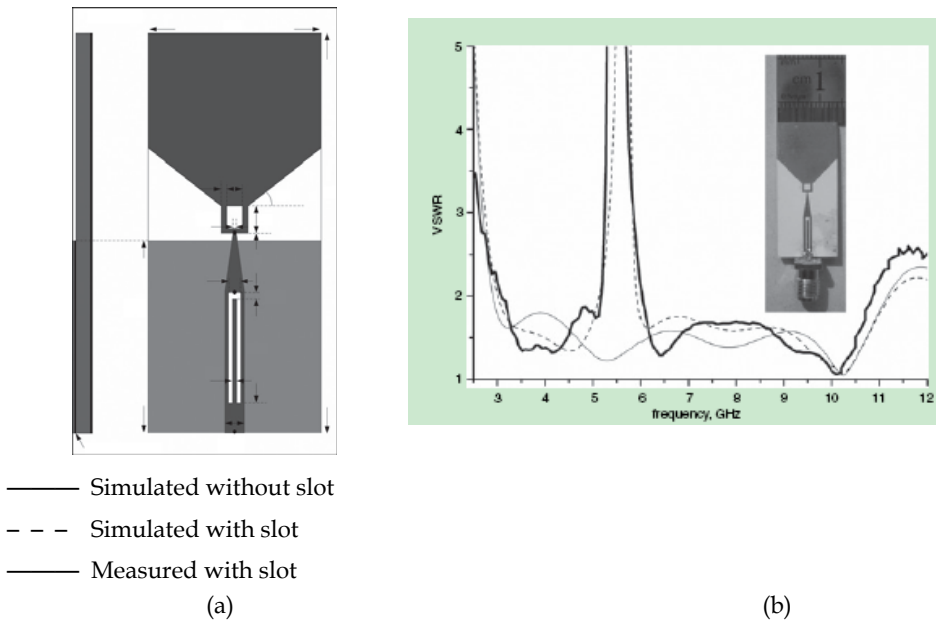
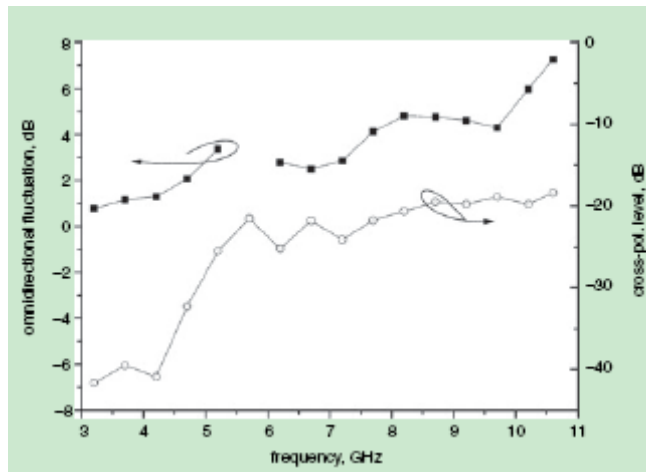


Fig. 26. UWB printed band-notch antenna with two folded-striplines^[44]



- Simulated without slot
- - - Simulated with slot
- Measured with slot



(c)

Fig. 27. UWB printed band-notch antenna with an inverted U-shaped slot in the feeder^[45]

6. Conclusion

The recent progress in the development of UWB planar antenna technology has been reviewed. Some types of UWB metal-plate monopole antennas, UWB printed monopole antennas and UWB printed slot antennas are presented. The comparison results indicate that the UWB printed monopole antennas can realize relatively smaller dimensions, and that the UWB printed slot antennas can achieve relatively higher gain. Finally, some realization manners of the band-notch function of UWB printed monopole antennas have been introduced. Along with the wide application of the UWB technology, compact UWB antennas will achieve further development.

7. Acknowledgements

This work was supported by the National Natural Science Foundation of China (Grant No. 60571053), and the Shanghai Leading Academic Discipline Project (No.S30108).

8. References

- [1]Z.N. Chen, et al. Considerations for source pulses and antennas in UWB ratio systems [J]. IEEE Trans. Antennas propag., 2004, 52(7): 1739-1748.
- [2]H. Schantz. A brief history of UWB antennas[J]. Aerospace and Electronic Systems Magazine, 2004, 19(4): 22-26.
- [3]V. Rumsey. Frequency Independent Antennas [M]. Academic Press. New York, 1966.
- [4]P.J.Gibson, The Vivaldi aerial[C]. 9th European Microwave Conference, Brighton, UK, 1979:101-105.
- [5]S. S. Zhong,X. R. Yan and X. L. Liang, UWB planar antennas technology [J] . Frontiers of Electric and Electronic Engineering in China, 2008, 3(2):136-144.

- [6]G. Dubost and S. Zisler. Antennas a Large Bande [M]. New York: Masson, 1976:128-129.
- [7]N.-P. Agrawall, G.. Kumar and K.-P. Ray. Wide-band planar monopole antennas [J]. IEEE Trans. Antennas Propag., 1998, 46(2):94-295.
- [8]J.A. Evans and M.J. Ammann. Planar trapezoidal and pentagonal monopoles with impedance bandwidths in excess of 10:1 [C]. IEEE Antennas Propagat. Symp., Orlando, FL, 1999, vol.3:1558-1561.
- [9]S.Y. Suh, W.L. Stutaman and W.A. Davis. A new ultrawideband printed monopole antenna: the Planar Inveted Cone Antenna (PICA) [J]. IEEE Trans. Antennas Propagat., 2004, 52(5):1361-1365.
- [10]X.F. Bai, S.S. Zhong and X.L. Liang. Leaf-shaped monopole antenna with extremely wide bandwidth [J]. Microwave Opt. Tech. Lett., 2006, 48(7): 1247-1250.
- [11]P. V. Anob, K. P. Ray, and G. Kumar. Wideband orthogonal square monopole antennas with semi-circular base[C]. IEEE Antennas Propagat. Symp., Boston, 2001, vol.3:294-297.
- [12]M.J. Ammann and Z.N. Chen. A wide-band shorted planar monopole with bevel [J]. IEEE Trans. Antennas Propagat., 2004, 51(4): 901-903.
- [13]E. Antonino-Daviu, M. Cabedo-Fabres, *et al.* Wideband double-fed planar monopole antennas [J]. Electron. Lett., 2003, 39(23):1635-1636.
- [14]J. Liang and L. Guo. CPW-fed circular disc monopole antenna for UWB applications [C]. IEEE International Workshop on Antenna Technology: Small Antennas and Novel Metamaterials. Singapore, 2005:505-508.
- [15]J. H. Jung, W. Y. Choi and J.H. Choi. A small wideband microstrip-fed monopole antenna [J]. IEEE Microwave and Wireless Component Letters, 2005, 15(10): 703-705.
- [16]C.Y. Huang and W.C. Hsia. Planar elliptical antenna for ultra-wideband communications [J]. Electron. ett., 2005, 41(6):296-297.
- [17]Y.C. Kang, C.N. Chiu and S.M. Deng. A new planar circular disc-and-ring monopole antenna for UMTS/UWB dual-network applications [J]. Microwave and Opt. Tech. Lett., 2006, 48(12):2396-2399.
- [18]N. Fortino, G. Kossiavas, J.Y. Dauvignac and R. Staraj. Novel antennas for ultra-wideband communications [J]. Microwave and Opt. Tech. Lett., 2004, 41(3):166-169.
- [19]W.S. Chen, S.C. Wu and K.N. Yang. A study of the printed heart monopole antenna for IEEE 802.16a/UWB applications [C]. IEEE Antennas Propagat. Symp., Albuquerque, Mew Mexico, 2006:1685-1688.
- [21]X.-L. Liang, S.-S. Zhong, W. Wang and F.-W. Yao. Printed annular monopole antenna for ultra-wideband applications [J]. Electron. Lett., 2006, 42(2):71-72
- [22]S.-S. Zhong, X.-L. Liang, F.-W. Yao, W.Wang and X.-F. Bai, Ultra-wideband printed antennas for communication applications [J]. Journal of Shanghai University (English Edition), 2006, 10(1):48-52.
- [23]X.-L. Liang, S.-S. Zhong and W. Wang, Tapered CPW-fed printed monopole antenna [J]. Microwave and Opt. Tech. Lett., 2006, 48(7):1242-1244.
- [24]X.-L. Liang, S.-S. Zhong and W. Wang, UWB printed circular monopole antenna [J]. Microwave and Opt. Tech. Lett., 2006, 48(8):1532-1534.
- [25]S.-S. Zhong, X.-L. Liang and W. Wang, Compact elliptical monopole antenna with impedance bandwidth in excess of 21:1 [J]. IEEE Trans. Antennas and Propagation 2007, 55(11) Part 1 :3082 - 3085

- [26]X.-R. Yan, S.-S. Zhong and G.-Y. Wang, Compact printed monopole antenna with 24:1 impedance bandwidth[J]. *Electron. Lett.* 2008,44(2):73-75.
- [27]S.-S. Zhong and X.-R. Yan, A semi-monopole printed antenna with extremely wide bandwidth[C].*IEEE International Symposium on Antennas and Propagation, San Diego, CA, July 2008.*
- [28]E. Gazit. Improved design of the Vivaldi antenna [J]. *Proc. Inst. Elect. Eng.*, 1988, 135(2):89-92.
- [29]J.D.S. Langley, P.S. Hall, and P. Newham. Novel ultra-wide-bandwidth Vivaldi antenna and low cross-polarisation [J]. *Electron. Lett.*, 1993, 29(23): 2004-2005.
- [30]Y. Kim and D.-H. Kwon. CPW-fed right-angled dual tapered notch antenna for ultra-wideband communication [J]. *Electron. Lett.*, 2005, 41(12):674-675.
- [31]Y.W. Jang. Broadband cross-shaped microstrip-fed slot antenna [J]. *Electron. Lett.*, 2000, 36(25):2056-2057
- [32]F.W. Yao, S.S. Zhong and X.L. Liang. Wideband slot antenna with a novel microstrip feed [J]. *Microwave Opt. Tech. Lett.*, 2005, 46(3): 275-278.
- [33]S. Sadat and M. Fardis. A compact microstrip square-ring slot antenna for UWB applications [C]. *IEEE Antennas Propagat. Symp.*, Albuquerque, New Mexico, 2006: 4629-4633.
- [34]D.C. Chang , J.C. Liu and M.Y. Liu. Improved U-shaped stub rectangular slot antenna with tuning pad for UWB applications [J]. *Electron. Lett.*, 2005, 41(20):1095-1097.
- [35]S. Cheng, P. Halbjorner and A. Rydberg, Printed slot planar inverted cone antenna for ultra-wideband applications [J]. *IEEE Antennas and Wireless Propagat. Lett.*, 2008, Vol.7:18-21.
- [36]S.H. Hsu and K. Chang. Ultra-thin CPW-fed rectangular slot antenna for UWB applications [C]. *IEEE Antennas Propagat. Symp.*, Albuquerque, New Mexico, 2006: 2587-2590.
- [37]S.A. Evangelos and A.Z. Anastopoulos, *et al.* Circular and elliptical CPW-Fed slot and microstrip-fed antennas for ultrawideband applications [J]. *IEEE Antennas and Wireless Propagat. Lett.*, 2006, vol.5: 294-297.
- [38]J.W. Niu and S.S Zhong. A CPW-fed broadband slot antenna with linear taper [J]. *Microwave and Opt. Tech. Lett.*, 2004, 41(3): 218-221.
- [39]E.S. Angelopoulos, A.Z. Anastopoulos, *et al.*, A modified bow-tie slot antenna fed by a CPW-to-CPW transition loaded with inductively coupled slots for ultra-wideband applications [C]. *IEEE International Workshop on Antenna Technology: Small Antennas and Novel Metamaterials, Singapore, 2005: 513-516*
- [40]M. J. Ammann, A. Dumoulin, M. John and P. McEvoy, Time-domain performance of printed UWB Antennas[C]. *3rd European Conference on Antennas and Propagation, Berlin Germany, March 2009:3766-3769.*
- [41]D. Lamensdorf and L. Susman, Baseband-pulse-antenna techniques[J]. *IEEE Antennas Propag. Mag.*, Feb. 1994, 36(1): 20-30.
- [42]S.Y. Suh, Stutzman, W.L. Davis, *et al.* A UWB Antenna with a Stop-band Notch in the 5-GHz WLAN band[C]. *Wireless Communications and Applied Computational Electromagnetics*, 2005:203 - 207
- [43]X.-A. Qu, S.-S. Zhong and W. Wang. Study of the band-notch function for a UWB circular disc monopole antenna[J]. *Microwave and Opt. Tech. Lett.*, 2006, 48(8):1667-1670

- [44]K.-H. Kim, Y.-J. Cho, S.-H. Hwang and S.-O. Park. Band-notched UWB planar monopole antenna with two parasitic patches [J]. *Electron. Lett.*, 2005, 41(14):783-785.
- [45]S.-H. Lee, J.-W. Baik and Y.-S. Kima, Coplanar waveguide fed monopole ultra-wideband antenna having band-notched frequency function by two folded-striplines[J]., *Microwave and optical Tech.Lett.*,Nov.2007, 49(11):2747-2750.
- [46]L.-N. Zhang, S.-S. Zhong, X.-L. Liang and C.-Z. Du, Compact omnidirectional band-notch ultra-wideband antenna[J]. *Electron. Lett.*, June 2009, 45(13)

A Complete Practical Ultra wideband Test Bed in X-Band

Gholamreza Askari, Khatereh Ghasemi
and Hamid Mirmohammad Sadeghi
Isfahan University of Technology
(Information and Communication Technology Institute)
84156, Isfahan, Iran

1. Introduction

Design of an UWB system has several challenges some of which are not shared with more traditional narrowband systems [David et al.,2005]. Also the multifunction test bed is designed and implemented to receive, change and transmit multiple simultaneous independent RF signals, including communications, Radar and Electronic Warfare (EW) [Gregory et al.,2005; Blair et al.,1998]. It is important that this test bed includes of an ultra wideband white Gaussian noise generator and delay lines circuits, so it is capable to test, evaluate and calibrate many types of systems especially with radio receivers [Askari et al.,2008(a); Askari et al.,2008(b)]. In summary this test bed will be used for evaluating communication systems performance by allowing an operator to add a controlled amount of thermal noise to a reference signal and determine the effect of noise on system performance, such as BER [Matthews,2006]. Also, a delay line is used to delay a signal by certain time while minimizing the distortion caused by crosstalk, dispersion and loss [Hohenwarter et al.,1993]. With those capabilities this test bed can be used as a Gaussian modulating signal source to mimic real conditions such as Rayleigh fading and other simulated models. In ECM applications, High power amplified noise modules can be used to produce many types of interference for RF systems such as RADARs. Also for RADAR applications, it can be useful for effects of target amplitude fluctuations, beam shape, missed detections, false alarms, target maneuvers, pulse compression, track loss, Stand Off Jammer (SOJ) broadcasting wideband noise and targets attempting range gate pull off (RGPO) [Blair et al.,1998]. In Noise application, Noise Figure measurement, Bandwidth, Linearity, Inter-modulation, Frequency Response and Impulse Response of a DUT can be measured [Gupta,1975; Upadhyaya,1998]. In Encryption application, an electrical thermal noise source is more random than anything else in nature. It can also be used for Continuous Monitoring of System Performance for Built In Test Equipment (BITE)[Robbins,2004].

In this chapter design and implementation of a practical reconfigurable communication system including an additive ultra wide band white Gaussian noise and delay lines in X-band from 6 to 12 GHz with other necessary microwave parts as the test bed are introduced. The challenges that affect the design of a custom CW/pulsed UWB

architecture is discussed, also design and implementation procedures of all microwave parts such as ultra wideband amplifiers, dividers, switches, drivers, gain controllers, generators, filters, delay components, bias tee, transitions and etcetera are presented.

2. Transceiver general descriptions

Transceiver is short for *transmitter-receiver*, a device that both receives, process and transmits signals. Fig.1 shows a general block diagram of a transceiver test bed with important sections. Important sections of a transceiver is front end, intermediate receiver, programmable delay, white gaussian noise, driver and control. The specific goals are to achieve a test bed in X-band from 6GHz to 12GHz with the following specifications.

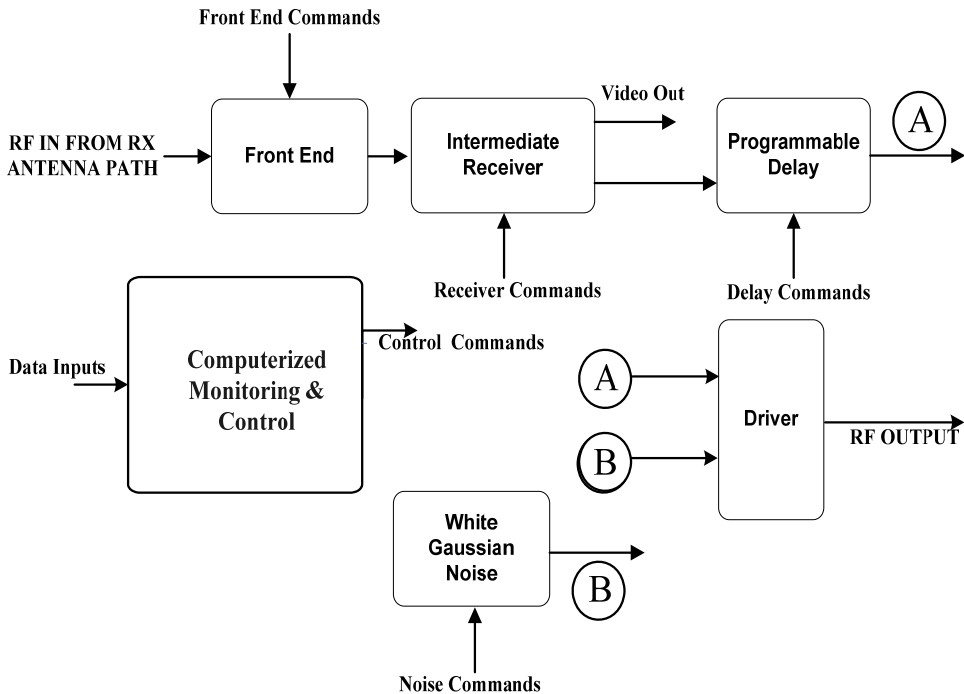


Fig. 1. General transceiver test bed with important sections

Frequency Range: 6-12 GHz

Pulse Duration: 100 nsec to CW

CW or Pulse Transmitter Output: 25 dBm

Sensitivity: -45 dBm in a 100 nsec pulse

Delay Mode & Gain Control

CW Rejection with Operator Command: 30dB

Programmable Control Commands from Control & Monitoring Section

Fault Generation

Wide Band White Gaussian Noise in 6-12GHz

Blanking switch isolation: 55dB

Narrow Band White Gaussian Noise bandwidth: 20 ~ 40 MHz

Fig. 2 shows the complete block diagram that encompasses all desired specifications.

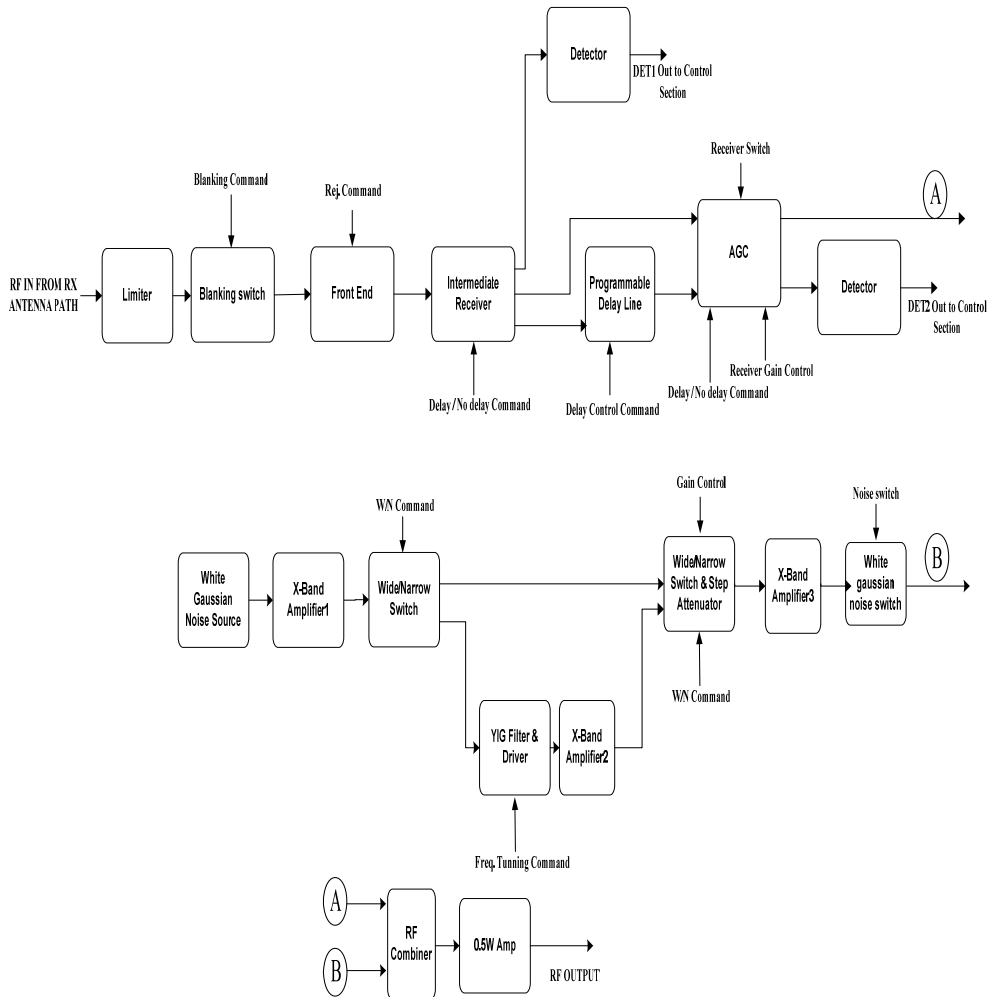


Fig 2. complete block diagram of the test bed

3. Design procedure

To achieve a transceiver test bed with desired specifications, each component of block diagram should have specific features which are discussed in the following.

3.1 The limiter

Limiter is an optional circuit that allows signals below a specified input power to pass unaffected while attenuating the peaks of stronger signals that exceed this input power and is used to protect receiver from strong signals. ACLM4616 from *Advanced Control Components* is used as a limiter. According to the datasheet and the experimental results the specifications of this component are represented in table 1.

Frequency Range (GHZ)	Part Number	Peak Input Power (Watts)	CW Input Power (Watts)	Flat Leakage (CW Power) (dBm)	Insertion Loss (dB) (Experimental)	Maximum VSWR
6-18	ACLM4616F	100	2	13	0.3 ~ 1.2	2.2:1

Table 1. Specifications of ACLM4616F according to the datasheet and the experimental results

3.2 The blanking switch

The RF signal from limiter is entered to the blanking switch. This switch is used to protect the receiver from specified signals by the suppression command. S1D2018A5 from *Herotek* is a circuit that switches the RF input by the TTL control input. According to the datasheet and the experimental results, the specifications of this component are represented in table 2.

Model	Insertion Loss(dB) (Experimental)			Min Isolation(dB) (6-12 GHz) (Experimental)	Max VSWR
	0.5-2GHz	6-12GHz (Exp.)	12-18GHz		
S1D2018A5	-	1.5-2.5	2.5	65	2:1

Table 2. Specifications of S1D2018A5 according to the datasheet and the experimental results

3.3 The front end section and circuit design

RF front end is a generic term for everything in a receiver that sits between the antenna and the intermediate receiver stage. For most architectures, this part of the receive chain consists of a matching circuit allowing all the received energy from the antenna to get to the next stage. All important specifications such as maximum gain and flatness in frequency response in all attenuation levels have been solved in this section. The final experimental result is a front end block with max 8 dB of gain, 31.5dB attenuation and 2dB of flatness in frequency bandwidth of 7-11GHz. In this section, a low noise amplifier, a band-pass filter (BPF) to reject out-of-band signals and a variable attenuator to cancel or control input signal power (if needed) are used. The block diagram of front end board is shown in fig 3.

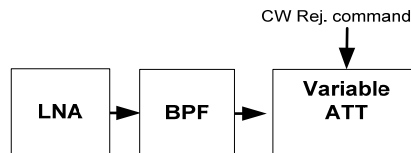


Fig. 3. Front end block diagram

The sub circuits specifications of this board are mentioned below:

- Low noise amplifier

The LNA is used to set the receive sensitivity of the receiver by offering high gain and low noise figure. Because in this design the input signals are mentioned strong enough, so the noise figure is not very important. *Agilent Technology's* 6-18GHz MMIC, AMMP5618 is used as a low noise amplifier to amplify the input signal power and improve the system MDS and compensate the filter loss.

- Band pass filter

A compensated Chebychev filter with 0.5dB ripple and 9GHz center frequency and 5GHz bandwidth is designed to maximize the MDS of system and minimize the out of band interference. To achieve maximum bandwidth and better second order response due to implementation on micro-strip technology and feasibility of micro-strip fabrication, the Edge-Coupled BPF with tapped input and output is used. This parallel arrangement gives relatively large coupling for a given spacing between resonators, and thus, this filter structure is particularly convenient for constructing filters having a wider bandwidth than other structures [Askari et al.,2008(a); Hong&Lancaster,2001].

- Variable attenuator

The variable attenuator is used to cancel CW signal (if needed) and also to control the variations of output power and gain of front end from 0.5 to 31.5 dB with 0.5dB step. *Hittite* DC-13GHz attenuator, HMC424LH5 is used as a variable attenuator to decrease the signal power by 0.5 dB LSB Steps to 31.5 dB.

After combining sub circuits together and optimizing by ADS (Advanced Design System 2005) simulation, the final structure is achieved. For feasibility of implementation, the filter section is implemented on a micro-strip laminate with lower permittivity and the other sections are implemented on a laminate with higher permittivity. The BPF is fabricated on *Rogers-5880* and other parts of block design are fabricated on *Rogers-6010* microstrip board. All footprints, lines and ground planes of final design are simulated and optimized in EM simulator of ADS.

After implementing all parts together, the final circuit was achieved and tested. Fig. 4-a shows the photograph of front end block and fig. 4-b shows the experimental results S_{21} vs. frequency with 0,2,6,14,30 dB attenuation.

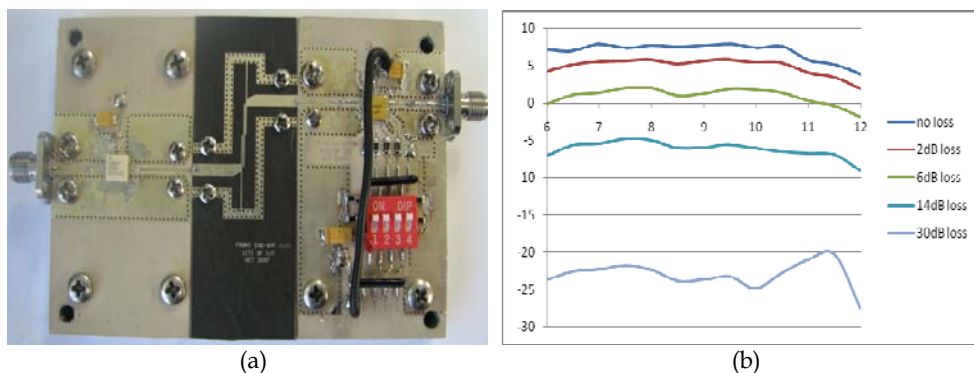


Fig. 4. (a) Photograph of front end block (b) experimental results S_{21} vs. frequency with 0,2,6,14,30 dB attenuation.

3.4 The intermediate receiver section and circuit design

The front end board output signal is entered to the intermediate receiver section. As it was shown in fig.2 this section is used to produce three RF output signals. So, a divider is necessary to divide the input signal to the detector path and delay-no delay path. The signal in the detector path is amplified and sent to a BPF and then is sent to a RF envelope detector to make the video signal. The other signal is sent to a switch after amplifying to select between two paths, delay or no delay with a command.

The main important challenge in this section is amplifying and dividing the ultra wide band RF signal to three paths with preservation of flatness in overall frequency response.

The block diagram of intermediate receiver board is shown in fig. 5. In this design, divider, amplifier (#2), BPF and switch are used.

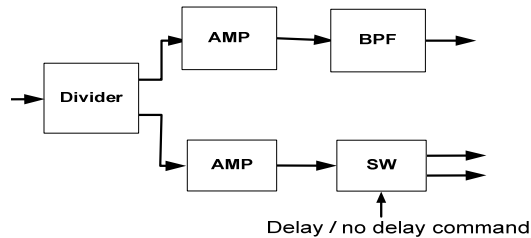


Fig. 5. Intermediate receiver block diagram

The sub circuits' specifications of this board are discussed in the following:

- Divider :

A wide band divider is necessary to divide signal to the detector path or delay-no delay path. All important specifications such as insertion loss and flatness in frequency response have been solved in this section. For this purpose, two types of compensated Wilkinson dividers are supposed and finally a double stage compensated Wilkinson divider with two isolation resistors is selected [Askari et al.,2008(b); Fooks&Zakarevicius,1990]. After simulation and optimization by ADS, the final structure for this part is obtained. Fig. 6-a shows the final layout of this divider which is designed and implemented on a Rogers-5880 microstrip board. Fig. 6-b shows the photograph of divider.

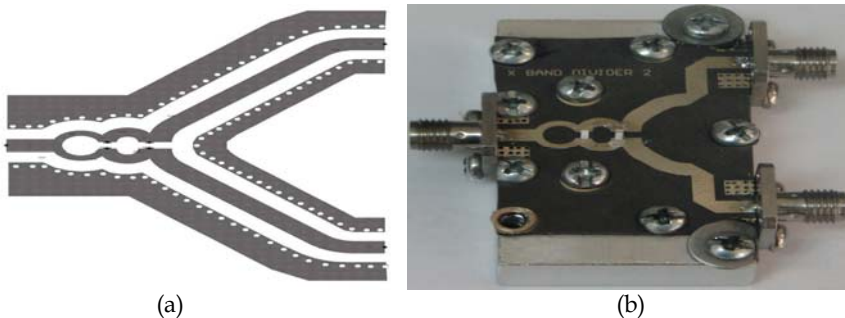


Fig. 6. (a) Divider layout (b) Divider photograph

The first and second resistors (100 ohm and 200 ohm, respectively) are mounted to improve the isolation between output ports up to 20dB. The experimental results, insertion loss and isolation of two ports are shown in fig. 7-a and 7-b. The final experimental result is a divider block with 3dB insertion loss and 1dB of flatness and minimum 20dB isolation in frequency bandwidth of 6-12GHz.

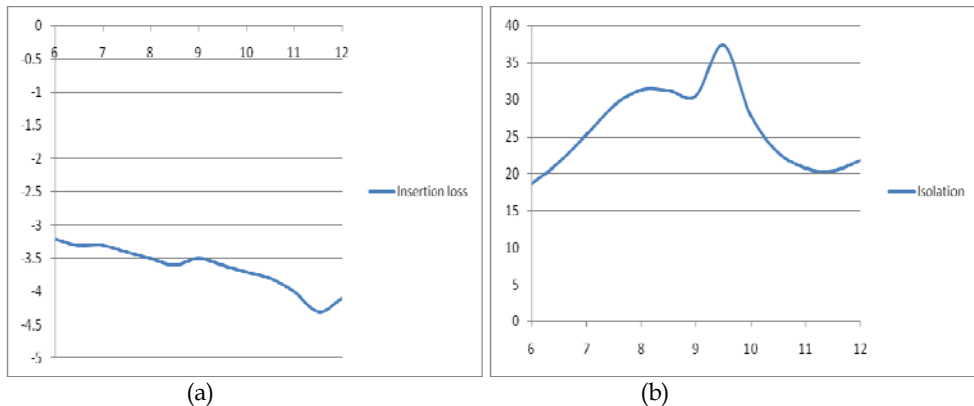


Fig. 7. (a) Insetion loss vs. Frequency (b) Isolation vs. Frequency

- amplifier :

To increase the output power signals and to achieve the output signals to the desired power level, after dividing, amplifiers are used in each path. To design a wideband amplifier with flatness in gain, the variations of $|S_{21}|$ have to be compensated. There are many methods to design wideband amplifiers such as reactive matching, lossy matching, balanced matching and matching with negative feedback [Gonzalez, 1997]. In this section, lossy matching combined with reactive matching is used to increase the bandwidth of amplifier and to flatten the gain. One MMIC amplifiers (*Avago Technologies AMMP-5618*) are used in each path. Amplifiers are simulated with Advanced Design System. Each amplifier increases the output power to approximately 13 dB. AMMP-5618 specifications are explained completely in section 3-3.

- Band pass filter :

A third order Chebychev filter with 0.5dB ripple and 9GHz center frequency and 5GHz bandwidth is designed to minimize the interference and to achieve the best detector sensitivity and dynamic range over the desired bandwidth. The BPF is the same as BPF in front end (Edge Coupled BPF), but it is not tapped input and output.

- switch :

To select RF signal to be sent to the delay or no delay path, a high speed switch should be used in the design of intermediate receiver section. *Hittite GaAs MMIC SPDT non-reflective, DC - 20.0 GHz switch*.

After combining subcircuits together and doing simulations and optimizations by considering undesired effects, the final structure is achieved. For feasibility of implementation , the filter section is implemented on a micro-strip laminate with lower permittivity and the other sections are implemented on a laminate with higher permittivity. The BPF is fabricated on *Rogers-5880* and other parts of block design are fabricated on

Rogers-6010 microstrip board. All footprints, lines and ground planes of final design are simulated in EM simulator of ADS.

After implementing all parts together, the final circuit was achieved and tested. Fig. 8-a shows the photograph of intermediate receiver block and fig. 8-b and 8-c show the experimental results. The final experimental result is an intermediate receiver block with a 10dB gain in output to detector over 6.5-11 GHz with 3 dB of flatness, and 8dB gain in output to delay or no delay paths and 3dB of flatness in frequency bandwidth of 6-12GHz.

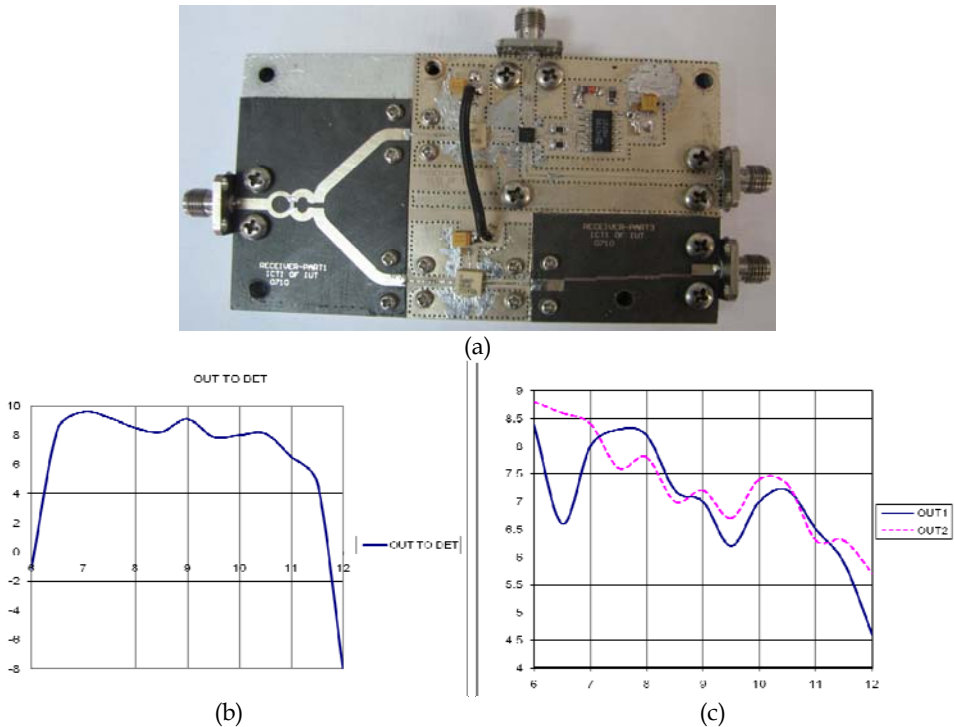


Fig. 8. (a) Photograph of intermediate receiver block, Experimental result: (b) Insertion loss of output to detector vs. frequency (c) Insertion loss of output to delay and no delay path vs. frequency

3.5 The envelope detector

The output of intermediate receiver (out to detector) is the input of the envelope detector. The detector is used to detect the envelope of RF signal to make the video signal. The detector must have a very fast pulse response and wideband frequency response. ACTP1528N from *Advanced Control Components* is used as a detector.

3.6 The Selective delay section and circuit design

The intermediate receiver board output (output to delay path) is entered to the selective delay section. The selective delay section can make delay to RF signal from 0 to 1500 nsec by

100 nsec steps (the maximum delay can be increased, independently). In this design delay control commands (4bits) are entered to the decoder to make 16 bits commands (b0-b15) and to control the delay of each 100nsec delay block. The structure of 100 nsec delay block will be explained in the following.

The main problems to construct a wide band delay block with more than 10nsec delay are insertion loss and its high variation in overall frequency bandwidth. In this block, design and implementation of a wideband delay circuit in X-band are presented. All important specifications such as insertion loss and flatness in frequency response and free of high order effects in time domain have been solved in this section [Askari et al., 2008(b)].

A delay line is used to delay a signal by certain time while minimising the distortion caused by crosstalk, dispersion and loss. There are many applications for a delay line like phase shifter in phase array radars, pulse compression radars, calibration of microwave altimeter, and loop circuits in ECM circuits [Askari et al.,2008(b); Hohenwarter et al.,1993].

There are a few ways to delay a signal. One of them is Piezoelectric Transducer which converts electromagnetic energy to acoustic energy (and also reconverts acoustic energy back into electromagnetic energy after the energy is delayed in the acoustic crystal). Another way to delay a signal is a CPW transmission line with a superconductor. This can be used as a low loss ultra wide band delay line. To achieve a larger bandwidth, it has to be smaller in size to decrease the undesired effects of resonance frequencies [Hohenwarter et al.,1993; Wang et al.,2003]. Microstrip transmission lines are another way to produce small delay [Lijun et al.,2006] which have high loss and variation of loss over frequency so they can be used for delays less than 12nsec [Hohenwarter et al.,1993]. Like microstrip, coaxial cables are high loss delay lines, but they are better than microstrip or stripline because of less loss and variation of loss [Askari et al.,2008(b)]. It is difficult for coaxial cables and/or microstrip printed circuit board (PCB) delay lines to get a long delay whilst maintaining a small size and low insertion loss over a wide frequency band [Wang et al.,2003].

Fig. 9 shows a block diagram of a 100 nsec delay line which can make delay or cancel it by a TTL command. The goal of this design is achieving a long delay (100nsec) in X-band signal from 6GHz to 12GHz with frequency response variation less than 3dB over frequency bandwidth. It should have selectable delay, VSWR better than 2 and 0dB of overall gain. To achieve desired results, each part of this block diagram should have some specifications which are explained in the following.

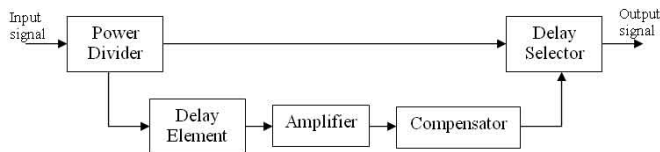


Fig.9. Block diagram of a 100 nsec delay line

- Divider

A wide band divider is necessary to select delay or not. For this purpose, a double stage compensated Wilkinson divider is designed and implemented on a *Rogers-5880* microstrip board that was explained completely in section 3-4.

- Delay Element

In this block, the final solution to make delay is a high precision 18GHz *Huber & Suhner* coaxial cable (S_04272_B). The signal delay of this cable is 4.1nsec/m; so to achieve 100nsec of delay, 24.4m length of it is required.

- Compensator

Since 24.4m of cable makes a high insertion loss and approximately 8dB linear variation of insertion loss over the frequency bandwidth, a special amplification and structure is needed to compensate these effects. There are different methods to compensate the slope of a frequency response in a circuit. First of all, a lumped network of resistor, capacitor and inductor can be used as an equalizer [Fejzuli et al.,2006; Kurzrok,2004]. The most important problem of these networks is that achieving 8dB linear slope over almost 1-octave is not possible. The next method is to use the out band positive slope of a BPF. This design contains two microstrip lines which are joined together with two different widths and a stub between them. The simulation result of this design is good but the reflection of input and output (S11, S22) makes a mismatch for amplifiers and other parts of the total circuit [Askari et al.,2008(b)]. So, the next important goal in this part is to achieve an absorptive compensator. The last design is an unbalanced Wilkinson divider that is optimized in ADS to make an 8dB positive linear slope for S21 and to have S11 less than -7dB and S22 less than -5dB. Fig. 10-a shows the layout of this compensator in ADS on a *Rogers-5880* microstrip board and Fig. 10-b shows the simulation results of S11, S22 and S21.

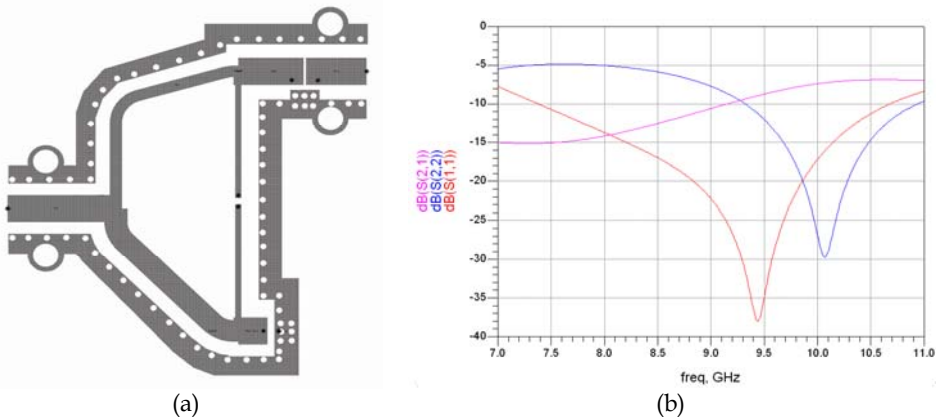


Fig. 10. (a) Compensator layout (b) Simulation results: S11, S22, S21

There are two 50ohm resistors for matching of port3 and isolation resistor consequently and a 3dB attenuator is used to improve S22 at the output.

- Amplifiers

To compensate insertion loss of 24.4m cable and compensator, 36dB gain is necessary to achieve 0dB gain for this block. In this design, two types of MMIC are used. The first one is *Agilent Technology's* 6-18GHz MMIC, AMMP5618 and the next one is *Hittite's* 6-18GHz MMIC, HMC441LC3B.

After combining sub circuits together and optimizing by ADS simulation by considering undesired effects, the final structure is achieved. In the block diagram of Fig. 9, to terminate insertion loss of divider and *Hittite* switch (HMC547LP3) in the output, a 6dB attenuator and

an AMMP Amplifier are required. Except divider and compensator, other parts of block design are on *Rogers-6010* microstrip board.

All footprints, lines and ground planes of final design were simulated in EM simulator of ADS.

After implementing all parts together, the final circuit was achieved and tested. Fig. 11 shows a photo of circuit after mounting. All connectors for this circuit are SMA (stripline) type and the material of fixture is Aluminium. The final experimental result is a delay block with a 100nsec delay, 0dB compensated insertion loss and 3dB of flatness in frequency bandwidth of 7-11GHz and a very good time response without second and third order reflection effects in time domain.

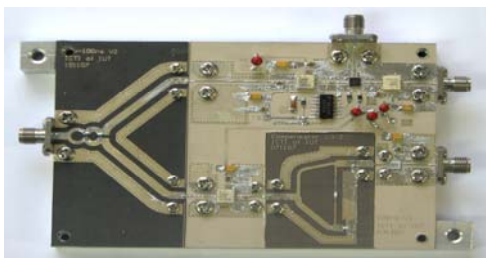


Fig. 11. Photo of 100nsec compensated delay block without cable

To measure the delay of two paths, a pulse modulated RF signal is used and at the output, a detector (ACTP1528N) is used to detect the envelope of RF. Fig.12-a shows the delay of no delay path related to reference pulse (wave form no.1) and Fig.12-b shows the delay of delay path. A 31nsec common delay for both paths is because of gate delay of input switch control circuit so the individual delay is 100nsec. As it is shown in Fig. 12, there is no effect of second and third reflections in time response and a pure response is achieved. The complete discussion of this section has been described by [Askari et al., 2008(b)].

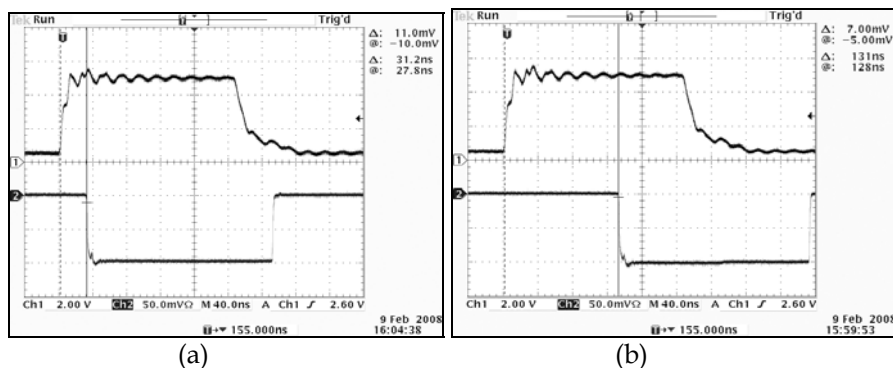


Fig. 12. Measurement of delay (a) No delay path (b) Delay path

3.7 The AGC section and circuit design

The intermediate receiver board output (output to no delay path) and the selective delay section output are entered to the AGC section and one of them is selected by the delay/no

delay TTL command. This section is used to produce two RF outputs. So, the divider is necessary to divide the selected signal to the detector path and driver path. The signal in the detector path is sent to the detector after amplifying to make the envelope of RF signal detect the probable error and/or to provide an automatic gain control feedback from the control and monitoring section. The signal to the driver path is sent to the amplifier and switch to make RF signal on/off by the TTL receiver switch command. A 6-bit receiver gain control command is used to control the output power variation from 0.5 to 31.5dB with 0.5dB step size.

All important specifications such as fault detector and AGC loop, have been solved in this section. In this design, variable attenuator, divider, amplifier (#3) and switch (#2) are used. The block diagram of AGC board is shown in fig. 13.

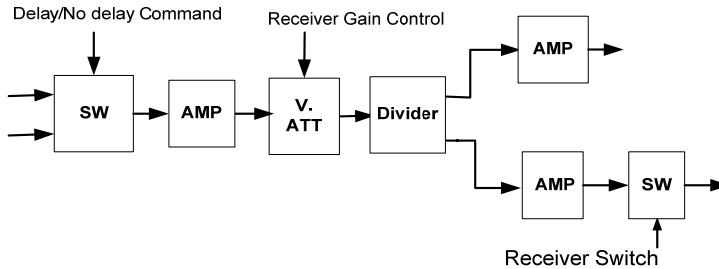


Fig. 13. AGC block diagram

The sub circuits' specifications of this block are mentioned below:

- Switch (#1,#2) :

Switch #1 selects one of the RF inputs (delay / no delay) by a TTL command and switch #2 is used to make RF output to driver on/off by a receiver switch TTL command. two high speed switches should be used in the design of AGC section. HMC547LP3 is used as a switch that was explained completely in section 3-4.

- variable attenuator :

To control and decrease input signal to 31.5 dB by 0.5 dB step the input signal is sent to the variable attenuator. HMC424LH5 is used as an attenuator that was explained completely in section 3-3.

- divider :

A wide band divider is necessary to divide signal to the detector or driver path. For this purpose, a double stage compensated Wilkinson divider is used that was explained completely in section 3-4.

- amplifier :

To increase the output signals power and to achieve the output signals to the desired power level, amplifiers are used in each path. The first one in the input path is *Hittite's* 6-18GHz MMIC, HMC441LC3B and the others in the output paths are *Agilent Technology's* 6-18GHz MMIC, AMMP5618. Amplifiers are simulated with Advanced Design System.

After combining sub circuits together and optimizing in ADS by considering undesired effects, the final structure is achieved. For feasibility of implementation, the divider section is implemented on a micro-strip laminate with lower permittivity and the other sections are implemented on a laminate with higher permittivity. The divider is on *Rogers-5880* and

other parts of block design are on *Rogers-6010* microstrip board. All footprints, lines and ground planes of final design were simulated in EM simulator of ADS.

After implementing all parts together, the final circuit was achieved and tested. Fig 14-a and 14-b show the experimental results of output to detector and output to driver, gain vs. frequency in different attenuation. The final experimental result is the AGC block with a 18dB gain in output to detector, -16 ~ +16 gain variation in output to driver and 3dB of flatness in frequency bandwidth of 6-11GHz.

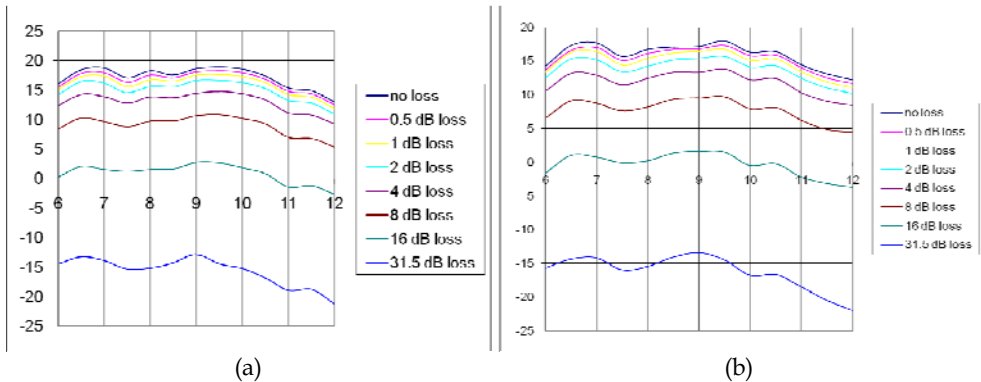


Fig 14. Experimental result: (a) out to detector, gain vs. frequency in different attenuation (b) out to driver, gain vs. frequency in different attenuation

3.8 noise source

One type of favorite source signal is a white noise signal having a Gaussian PDF. Such a signal has a relatively flat signal spectrum density. White Gaussian noise generators can serve as useful test tools in solving engineering problems. Test and calibration of communication and electronics systems, cryptography and RADAR interfering are examples of noise generator applications. A few of the measurements that can be made with these sources are: Noise Equivalent Bandwidth, Amplitude Response and Impulse Response [Carlson, 2002].

Depending upon how the noise is employed, noise applications are somewhat arbitrarily clustered into many categories which were explained in introduction [Askari et al., 2008(a)]. In this section design and implementation of an X-band noise generator used in identifying the specifications of the communication and electronics systems are described. This noise generator has 4dB bandwidth of 5.5GHz (6-11.5GHz) and 60dB of ENR or -114dBm/Hz of noise density.

Due to internal noise of measurement systems and to overcome the noise floor of these systems for testing DUT, noise generators need ENR of about 60-70dB.

The noise-generator output can be viewed as a collection of sine waves separated by, say, 1-Hz. Each separated frequency "bin" has its own Gaussian amplitude and random phase with respect to all the others. So, the DUT is simultaneously receiving a collection or "ensemble" of input signals. As the spectrum analyzer frequency sweeps, it looks simultaneously at all of the DUT frequencies that fall within the spectrum analyzer's IF

noise bandwidth [Straw,2005]. The general block diagram of the noise generator is shown in fig. 15.

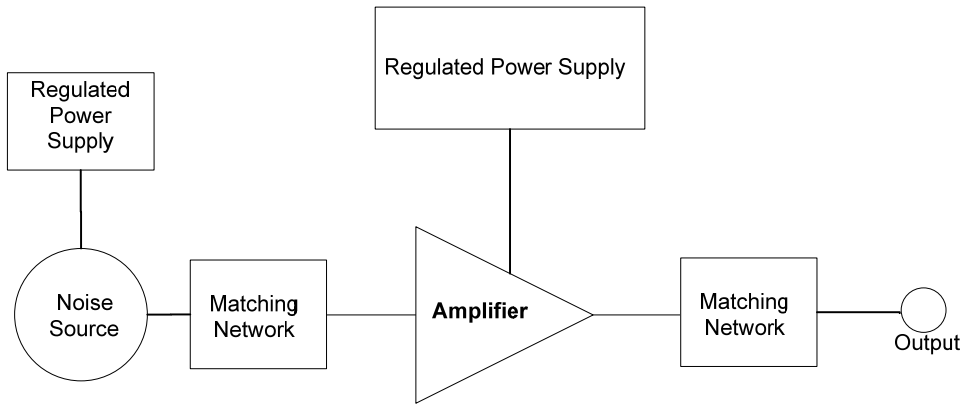


Fig. 15. Noise Generator Block Diagram

The elements of the block diagram are demonstrated in the following sections.

- Noise source

One method of generating white Gaussian noise is to amplify thermal noise in a resistor. The density of the thermal noise is -174dBm/Hz at room temperature. Amplifying the thermal noise to overcome the internal noise of measurement systems in a wide bandwidth isn't an easy problem [Carlson,2002; Motchenbacher & Connelly,1993].

The other method is to use a noise diode with ENR of about 25-35dB. Any Zener diode can be used as a source of noise. If, however, the source is to be calibrated and used for reliable measurements, avalanche diodes specially designed for this purpose are preferable by far. A good noise diode generates its noise through a carefully controlled bulk avalanche mechanism which exists throughout the PN junction, not merely at the junction surfaces where unstable and unreliable surface effects predominate due to local breakdown and impurity. A true noise diode has a very low flicker noise ($1/f$) effect and tends to create a uniform level of truly Gaussian noise over a wide band of frequencies. In order to maximize its bandwidth, the diode also has very low junction capacitance and lead capacitance [Straw, 2005]. Insensitivity of power value and frequency response of noise generator due to variation of its parameters such as dynamic resistor of diode, breakdown current of zener diode, load pulling, source pushing and matching network are very necessary in order to design a noise generator and its power supply.

There is noise diode up to 110GHz made by NOISE/COM. In this project, the NOISEWAVE NW401 diode is used. It is rated for use from 10MHz to 18GHz, if appropriate construction methods are followed.

In order to maximize the flatness of frequency response, noise source construction methods should aim for Microwave circuit lead length as close to zero as possible as well as minimum inductance in the ground path and the coupling capacitors. The power-supply voltage must be clean, well bypassed and set accurately [Straw,2005].

- amplifier

As mentioned before, noise generators need high ENR (60-70dB) to overcome the noise floor of the measurement instruments. Based on Noise Diode's ENR, up to 40-50dB amplification is needed over the wide bandwidth. Four stage amplifiers are used in this design. MMIC amplifiers (*Avago Technologies* AMMP-5618) are used in each stage. Amplifiers are simulated with Advanced Design System. Matching network and filter are optimized to flatten the gain and decrease the input and output mismatch compared to 50Ω over the desired bandwidth. Also, sensitivity of matching and filter due to dimension variation of filter and matching network are reviewed.

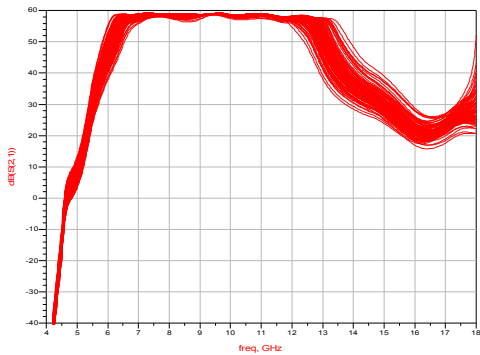
- filter

A third order Chebychev filter with 0.5dB ripple and 9GHz center frequency and 5GHz bandwidth is designed to maximize the output noise density over the desired bandwidth. The filter design is explained completely in section 3-4. For feasibility of implementation based on amplifier selection, the filter section of noise generator is implemented on a micro-strip laminate with lower permittivity and the other sections are implemented on a laminate with higher permittivity.

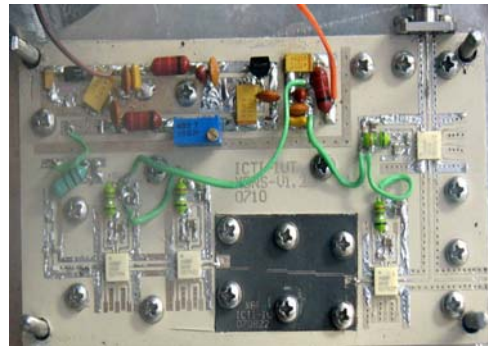
After prototype design, the total response including amplifiers matching network and filter response are optimized for flat gain and lower return loss.

In order to study the sensitivity of the overall response, variations of dimensions are considered with $\pm 25\%$ tolerances due to variation in implementation process and environmental conditions. The effect of the tolerances in simulation is shown in fig. 16-a and the photo of the implemented noise generator is shown in fig. 16-b.

Moreover, sensitivity simulation was executed for any element in filter and matching network. Although, not all sections of noise generator are optimized because exact model of noise diode doesn't exist. Wideband and narrowband Experimental results of noise generator are shown in fig. 17-a and fig. 17-b. All results are measured by Anritsu MS2665C Spectrum Analyzer.



(a)



(b)

Fig. 16. (a) Effect of implementation tolerances (b) Photo of the implemented noise generator

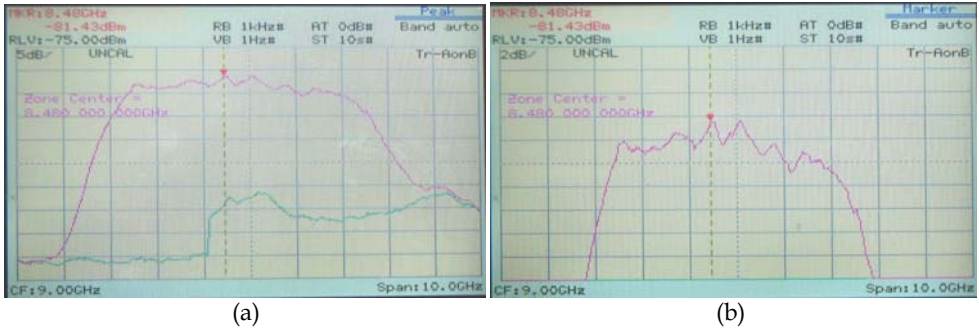


Fig. 17. (a) Experimental result in wideband comparing to spectrum noise floor (b) Experimental result with more detail

3.9 The X-band Amplifier1, 2, 3

Agilent Technology's 6-18GHz MMIC, AMMP5618 is used as an amplifier to amplify the noise signal power. 3-stage amplifier with AMMP5618 is used in x-band amplifier1 and x-band amplifier2 blocks. 1-stage amplifier with AMMP5618 is used in x-band amplifier3. After simulating and optimizing, the experimental results of 1-stage amplifier gain vs. frequency at -10dBm input power and 3-stage amplifier gain vs. frequency at -40dBm input power is shown in fig. 18.

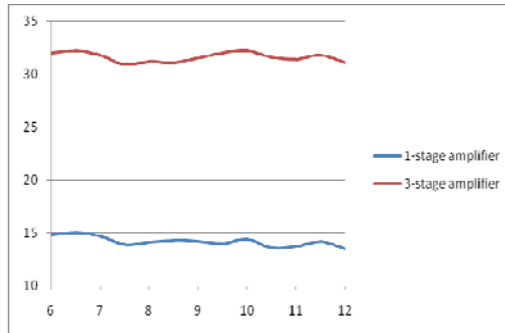


Fig. 18. Gain vs. frequency in 1-stage and 3-stage amplifier

3.10 The Wide/Narrow switch

The amplifier1 output is entered to the wide/narrow selector switch to select the direct path (wide band White Gaussian Noise) or the YIG path (narrow band White Gaussian Noise) by W/N command.

HMC547LP3 is selected as a fast switch that was explained completely in section 3-4.

3.11 YIG Filter & Driver

The output of wide/narrow switch block is entered to the YIG filter block. M979 from OMNIYIG is used as a YIG filter. According to the datasheet and experimental results, the specifications of this component are represented in table 3.

Frequency Range (GHZ)	Part Number	Insertion Loss (dB)	Bandwidth @ 3dB (MHz) (Experimental)	Passband Ripple (dB) (Experimental)	Freq. Drift 0 to 60C (MHZ)	OFF RESONANCE ISOLATION (dB) (Experimental)
2-18	M979	6.5	25-60	2.5	13	100

Table 3. Specifications of M979 according to the datasheet

The 6-bit frequency control command is converted to the analog command to control the center frequency of 6-12 GHZ. The photograph of YIG filter and its driver are shown in fig. 19.



Fig. 19. Photograph of YIG filter and driver

3.12 Wide/Narrow Switch and Step attenuator

The narrow and wide white Gaussian noise signals are entered to this block. This section is used to select one of the signals and control the output power gain variation from 0.5-31.5 dB with 0.5dB step. In this design, switch, variable attenuator, amplifier and 3 dB attenuator are used. The block diagram of Wide/Narrow Switch and Step attenuator board is shown in fig. 20.

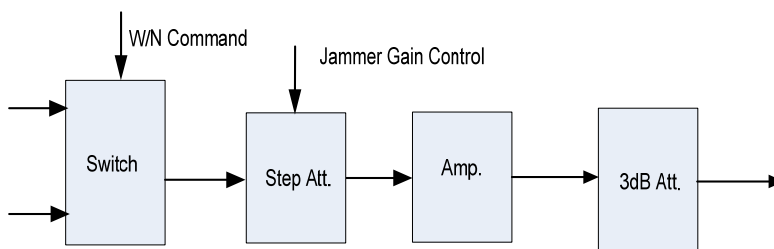


Fig. 20. Wide/Narrow selector Switch and Step attenuator block diagram

After combining sub circuits together and doing simulation and optimization by considering undesired effects, the final structure is achieved. All parts of block design are on *Rogers-6010* microstrip board. All footprints, lines and ground planes of final design were simulated in EM simulator of ADS.

After implementing all parts together, the final circuit was achieved and tested. Fig. 21-a and fig. 21-b show the experimental results gain in different attenuation and isolation vs. frequency. The final experimental result is a Wide / Narrow Switch and Step attenuator block with a 3dB gain and 3dB of flatness in frequency bandwidth of 6-11.5GHz.

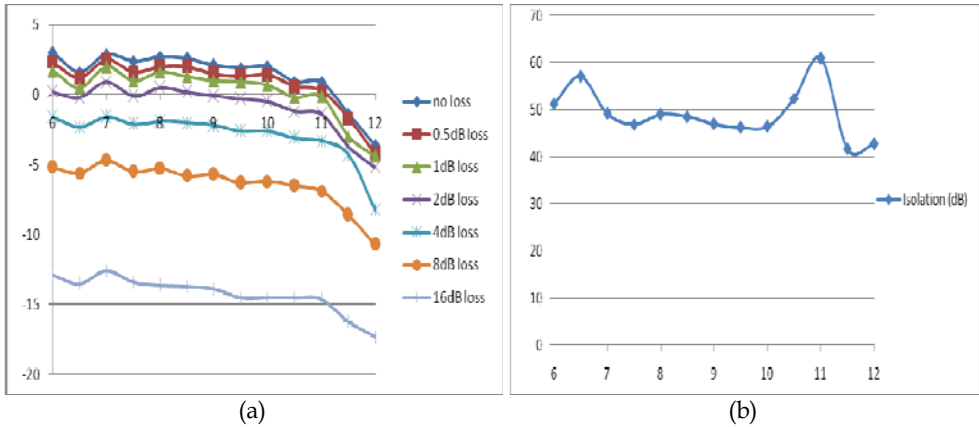


Fig. 21. (a) Gain vs. freq. in different attenuation, (b) Isolation vs freq.

3.13 White Gaussian Noise switch

To make RF output to driver with or without WGN a high speed and remarkable on/off isolation switch should be used, HMC547LP3 is used as a switch that was explained completely in section 3-10.

3.14 RF Combiner

The input RF signals from receiver section and WGN can be entered together or alone into the RF combiner section. The Combiner is a circuit that combines the input signals with minimum loss. R2SC-2.0-18.0-sf-1W-L from *Raditek* is used as a combiner. According to the datasheet, the specifications of this component are represented in table 4. The picture of combiner is shown in fig. 22.

Freq. Range (GHZ)	Part Number	Max Insertion Loss (dB)	Isolation (dB)	VSWR In	VSWR Out	Amp. Balance (dB)	Ph. Ang.	Total Power (W)
2-18	R2SC-2.0-18.0-sf 1W-L	3.9	17	1.4	1.4	<+/-0.3	<+/-3°	1

Table 4. Specifications of R2SC-2.0-18.0-sf 1W-L according to the datasheet

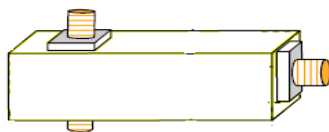


Fig. 22. Picture of the combiner

3.15 0.5W amplifier

The combiner signal output is entered to the 0.5W amplifier section. This section is used to produce about 0.5w RF output. So, the 0.5W amplifier is necessary in the final RF path and the pre amplifier must be used to produce the sufficient input power. In this design, a pre amp, a 0.5W amplifier, a bias T network and a coupler are used. The block diagram of 0.5W amplifier board is shown in fig 23.

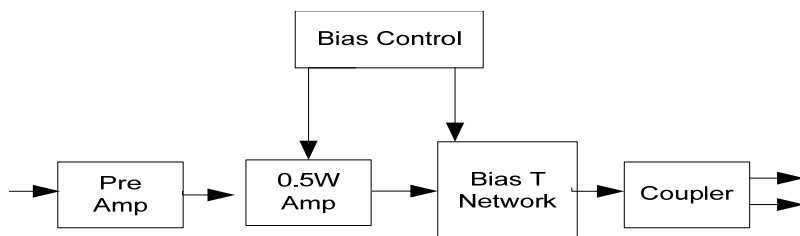


Fig. 23. 0.5W amplifier block diagram

The sub circuits' specifications of this board are mentioned below:

- Pre Amp :

To produce the sufficient input power for 0.5W amplifier the pre amplifier is used. In this design, *Hittite's* 6-18GHz MMIC, HMC441LC3B with 14dB gain and 21.5dB output at 1dB compression point is used as a pre amplifier.

- 0.5W Amp :

To have 0.5w RF output the 0.5W amplifier is used. In this design, *iterra Hittite's* 2-20GHz, iT2008K is used as a 0.5W amplifier.

- Bias Tee Network :

A single-sided butterfly combined with a double-sided ultra wide band butterfly bias tee is used to bias the amplifier that is the broadband model of bias tee [Hong&Lancaster,2001]. After optimizing in ADS by considering undesired effects, the final structure is **Coupler** :

An ultra wide band 15 dB coupler is used to produce a sample RF output to detect probable error for control section. This coupler must have flat insertion loss response and remarkable return loss and 15dB coupling factor in the frequency bandwidth 6~12GHz. After optimizing in ADS by considering undesired effects, the final structure is achieved.

Pre amp is on *Rogers-5880* and the other parts of block design are on *Rogers-6010* microstrip board. The photo of implemented 0.5W amplifier is shown in fig. 24-a and the experimental test result 1dB comp. output vs. frequency is shown in fig. 24-b. The final experimental result is a 0.5W amplifier block with a 25dB output power at 1dB comp. point and 3dB of flatness in frequency bandwidth of 6-13GHz.

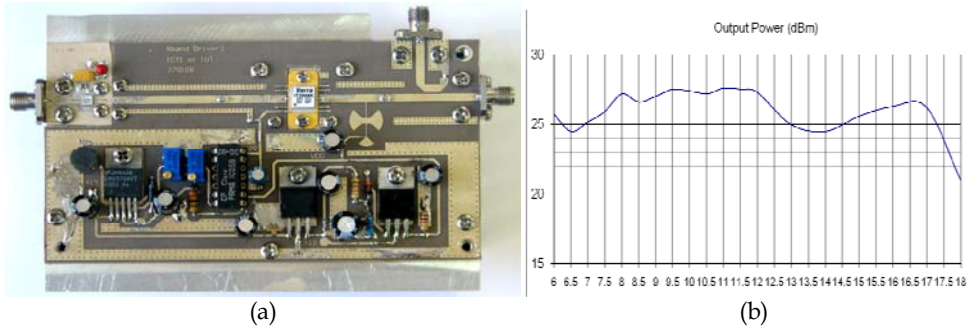


Fig. 24. (a) photograph of 0.5W amplifier (b) 1dB comp. output vs. frequency

4. Overall experimental test results

Overall system in different modes is tested and the results are given in the following:

4.1 Transceiver in CW mode

The output power levels (dBm) of different blocks in the RF path and the final output (0.5W amp output) and video output (mV) vs. frequency bandwidth are shown in fig. 25.

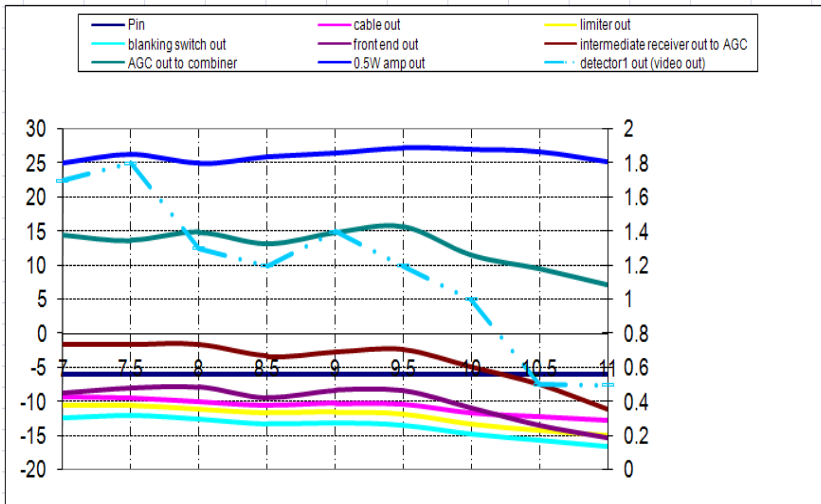


Fig. 25. Output power of different blocks in the RF path and video output vs. frequency

4.2 Transceiver in pulse mode

The video output of the receiver and driver sections together in the delay mode is shown in fig. 26. In this fig. the receiver input RF signal is modulated with an RF pulse modulator and the envelope of the driver video output after 100nsec delays is depicted.

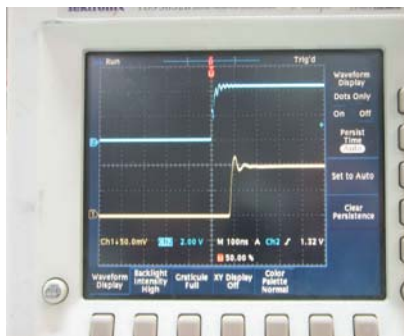


Fig. 26. Modulating pulse and video out after 100nsec delay

4.3 Wideband White Gaussian Noise mode

The output of x-band amplifier1 in the Wideband White Gaussian Noise mode path is measured by the spectrum analyzer that is shown in fig. 27. 3dB bandwidth of the noise is approximately 5GHz.



Fig. 27. The experimental results of wide band WGN in output of x-band amplifier1 on the spectrum analyser.

The outputs of noise source, x-band amplifier1, Wide/narrow switch and step attenuator and 0.5W amp are measured by the power meter and the results are given in table 6.

Noise source	-21 dBm
x-band amp1	+8 dBm
Wide/narrow switch and step att.	+4 dBm
0.5W amp	+25.8 dBm

Table 5. Power levels at different block outputs

4.4 Narrowband White Gaussian Noise mode

The output of wide/narrow switch and step att. in narrowband noise selection at two typical center frequency 7GHz and 9.5GHz is measured by the spectrum analyzer that is shown in fig. 28-a and 28-b. 3dB bandwidth of the noise is approximately 40MHz.

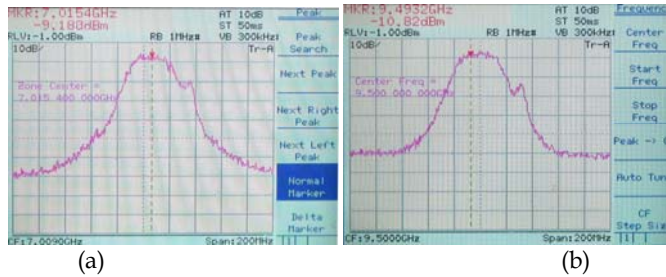


Fig. 28. The experimental results of narrowband WGN in output of wide/narrow switch and step att. (a) At 7 GHz (b) At 9.5 GHz

The outputs of YIG filter, x-band amplifier2, Wide/narrow switch and step att. and 0.5W amp are measured by the power meter and the results are given in table 6.

YIG Filter	-28dBm
x-band amp2	+5dBm
Wide/narrow switch and step att.	+4dBm
0.5W amp	+25.5dBm

Table 6. Power levels at different block outputs

5. Technical guidelines

There are lots of technical points of view for everyone who is interested in microwave research, especially practical project. In this section some of the most important technical guidelines in transitions, implementations and assembly and test points in x-band are given.

5.1 Transitions

One of the most important effects to decrease the band widths is transition. A transition is an interconnection between two different transmission lines or components that possesses low insertion loss and high return loss. These characteristics can be achieved only through careful matching of the impedances and electromagnetic fields of the two transmission lines. The designs of the signal and ground current paths through a transition are also critical. For a transition to function properly, these paths must often be continuous, in close proximity to suppress radiation, and as short and closely matched in length as possible. Additionally, a good transition should be easy to fabricate, mechanically robust, and insensitive to ambient temperature variations. In this project there are lots of transitions which some of the final results are discussed in the following.

The connection of connector to the microstrip board and a line with 0.58 mm width and 5mm length via the Aluminum box is simulated in HFSS simulator and the best result is obtained in the diameter hole of 2.4mm. The simulation results are shown in fig. 29-a and 29-b and 29-c.

- SMA connectors of Stripline type are selected to be completely tangent with the fixture.

- The connector is connected to the fixture by a 3-mm tapping screw. Through all the stages care should be taken to trim the bulge created at the edge of the hole after tapping on the fixture by a 5- or 6-mm drill bit.
- For the preparation of the connector, the edge of its nipple is broken in the beginning, but a little solder is placed on it and then the back of the connector (the same soldered side) is smoothed with soft sandpaper so that the solder knob on the nipple does not prevent the correct connection of the connector.
- To solder the connector to the line, it is recommended that a little solder be placed at the end of the line, so that after complete connection of the connector by a screw the connection is made by one touch of a 450°C hot soldering iron over nipple connection.
- with regard to the simulations made in HFSS for the connection of two transmission lines of boards, care should be taken to cover the connection of the two lines (on the two boards) with a little solder and care should also be taken to prevent the formation of any sharp point or crack in its physical shape and the two lines with two widths be connected together in a 3-D taper shape.
- Another method for the connection of the two boards is the use of a 50Ω line separated from a 10.2 board in a bridge manner, but fully stuck to the board.
- Another transition is connections between microstrip transmission lines to the IC pins, for this connection ultra wide band tapering is needed. The best transition is obtained by using microstrip laminate with greater permittivity and the minimum size of tapers from the transmission lines to the IC pins. (In this project *Rogers-6010* microstrip board is used for implementing of ICs).
- Also after simulating the best results of transitions between the capacitors pins and transmission lines are given at 1mm gap and the best result of coupling capacitor value is approximately 1.5pF (from the *Johanson Technology*, with 402 footprints) and also the best results of distance between coupling capacitors and IC pins, In/Out is approximately $\lambda / 4$.

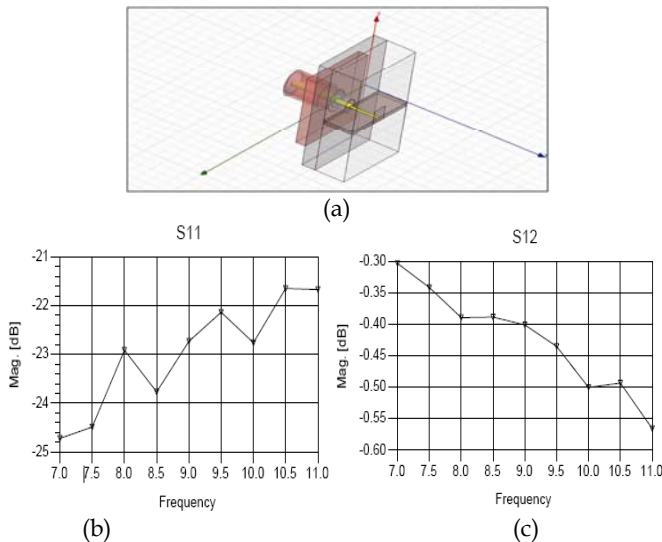


Fig. 29. (a) HFSS structure of transition between connector to the microstrip board and line via the hole with 2.4mm diameter and simulation results (b) Return loss (c) Insertion loss

5.2 Implementation

- Simulation and experimental results show that the fixture is better than the box for implementing boards in x-band frequency and the fixture in use is made from Aluminum with fully polished surfaces.
- Install the board on the fixture by 3-mm tapping screws. Through all the stages, care should be taken that after tapping on the fixture, the edge of the hole bulges a little which should be trimmed by a 5-mm or 6-mm drill bit.
- Placing two screws at the two sides of each line connected to the connector is a must. The edges of these screws from the transmission line and the edge of the board are 1.5mm and 2.5mm, respectively.
- At the connection of the two 2.2 and 10.2 boards, each is screwed to the fixture by two 2-mm tap screws. The distance of the 2-mm screws from this point to the transmission line and to the side of the board is 1.5mm.
- The size of the fixture should be exactly equal to the total of $\epsilon r=10.2$ and $\epsilon r=2.2$ boards.
- A box with the same length and width as the fixture for being placed on the fixture should be designed in a manner that its top has the least height with a view to elements and absorbent.
- using absorbent is very useful to reject unwanted reflections and radiations.
- The wall of the box at the connection of the connector nipple to the line on the board should be vacant as much as the size of a semi-circle with a diameter of 7mm.

5.3 IC assembly

- For mounting the ESD sensitive ICs on the board, care should be taken to use ESD bracelets connected to a large metal plate on which the board is placed. Pincer and needle should be insulated and a special soldering iron be used. In spite of observing all these tips avoid touching the IC pins.
- First, the ground plate and the pins under the IC are coated with a thin layer of tin in a manner that no coarseness is felt on the surface.
- Fill all the holes of the ground under the IC over the board with solder paste by a needle in a manner that the solder paste just covers inside of the holes and not the surface of the ground to produce coarseness.
- With regard to the shaking of the board (to avoid displacement of the IC), the IC should be placed on the desired points precisely then the background under the IC from the back of the board should be heated about 10~20 sec so that smoke rises from under the IC. After rechecking the accuracy of placement, the IC ground should be checked for it firm connection (by shaking the IC with a pincer). The good connection of background is very important in ultra wide band frequency response.
- Then by placing 0.3 mm of tin by a 350~ 400 soldering iron on the footprint beside the IC and pushing it under the IC with the use of a fluxpen, the rest of the pins are mounted.
- After mounting, first check all the pins from the sides of the IC by at least by a magnifying glass and then spray clean the board to avoid stray capacitances.
- Finally the board should be placed upside down on a metal plate and pressed at the two sides of IC. Then the ground behind the IC is heated for 3 to 4 seconds by a 450°C soldering iron once again. The use of fluxpen in this stage produces better results.

5.5. Other points

- All simulations in ADS2005 have been done in RF enable mode, also in all simulations in edge of the boards the single ports, and in the middle of the boards, internal ports, have the best coincidence with the experimental results.
- Gnd region around the board and RF path make better isolation and better power ripple in the frequency band. Connection to the bottom of the board in gnd region is made by the vias with 1mm distance from each other.
- Always high precision cable and connectors with good reflection should be used and if a cable or connector is employed in the test, the effect of their drop should be taken into consideration.
- As much as possible, use a connector instead of a cable for testing.

6. Conclusion

In this chapter design and implementation of a practical reconfigurable communication system including an additive ultra wide band white Gaussian noise and delay lines in X-band from 6 to 12 GHz with other necessary microwave parts as the test bed were presented. The challenges that affect the design of a custom CW/pulsed UWB architecture were discussed, also design and implementation procedures of all microwave parts such as ultra wideband amplifiers, dividers, switches, drivers, gain controllers, generators, filters, delay components, bias tee, transitions and etcetera were presented. In the feature works, extending the band width from one octave to one decade has been considered.

7. Acknowledgment

The authors would like to thank the staff of Information and Communication Technology Institute (ICTI), Isfahan University of Technology (IUT), Iran for their co-operator and supporting this work.

8. References

- Askari, Gh.; Motamedi, N.; Karimian, M. & Mir Mohammad Sadeghi, H. (2008(a)). Design and Implementation of an X-band White Gaussian Noise Generator. *CCECE/CCGEI*, May 5-7 2008, Niagara Falls, Canada
- Askari, Gh.; Miri, S. M.; Ghasemi, Kh. & M. M. Sadeghi, H. (2008(b)). Design and Implementation of an 1-Octave 100nsec Compensated Delay in X-Band. *Proceedings of the 38th European Microwave Conference*, October 2008, Amsterdam, The Netherlands
- Blair, W. D.; Watson, G. A.; Kirubarajan, T. & Bar-shalom, Y. (1998). Benchmark for Radar Allocation and Tracking in ECM. *IEEE Transactions on Aerospace and Electronic Systems*, VOL. 34, NO. 4, OCTOBER 1998
- Carlson, A.B. (2002). *An Introduction to Signals and Noise in Electrical Communication*, Communication Systems, 4th Edition, McGraw Hill, 2002
- David, D.; Wentzloff; Raúl Blázquez; Fred S., Lee; Brian, P.; Ginsburg; Johnna Powell & Anantha, P. (2005). System Design Considerations for Ultra-Wideband Communication. *IEEE Communications Magazine*, August 2005

- Fejzuli, A.; Kaarsberg, R. & Roldan, N. (2006). Broadband amplifier gain slope equalization with a single passive component. *High Frequency Electronics*, vol.5, no.6, Jun. 2006, pp. 22-26
- Fooks, E. H. & Zakarevicius, R. A. (1990). *Microwave Engineering using Microstrip Circuits*, Printice Hall, Sydney, Australia, 1990
- Gonzalez, G. (1997). *Microwave Transistor amplifiers: Analysis and Design*, Prentice Hall, 1997
- Gregory, C.; Tavik; Charles, L; Hilterbrick; James, B.; Evins; James, J.; Alter ; Joseph, G.; Crnkovich, Jr.; Jean, W.; de Graaf; William Habicht; Gregory, P.; Hrin; Steven, A.; Lessin; David, C. Wu & Stephen, M. (2005). The Advanced Multifunction RF Concept. *IEEE Transactions on Microwave Theory and Techniques*, VOL. 53, NO. 3, MARCH 2005
- Gupta, M.S. (1975). Applications of Electrical Noise. *Proceeding of the IEEE*, Vol.63, No.7, July 1975
- Hohenwarter, G. K. G.; Track, E. K.; Drake, R. E. & Patt, R. (1993). Forty five nanoseconds superconducting delay lines. *IEEE Transaction on Applied Superconductivity*, vol. 3, no.1, Mar. 1993, pp. 2804-2807,
- Hong, J.Sh.& Lancaster, M.J. (2001). Micro-strip Filters for RF/Microwave Applications. *John Wiley & Sons*, 2001
- Kurzrok, R. M. (2004). A review of key Equalizer specifications and what they mean. *High Frequency Electronics*, vol.3, no.9, Oct. 2004, pp. 22-26
- Lijun, C.; Qi, Z. & Shanjia, X. (2006). Delay lines based on left-handed transmission line structure. *Antennas and Propagation Society International Symposium*, 2006, p.1189
- Mattews, P. (2006). Properly Understanding Noise In Test Applications. *Microwaves & RF*, June 2006
- Motchenbacher, C.D. & Connelly, J.A. (1993). *Low Noise Electronic System Design* , John Wiley & Sons, 1993
- Robbins P. (2004). Using Noise for RF Receiver Built In Test Applications. *Microwave Journal*, February 2004
- Straw, R.D. (2005). *The ARRL Handbook for Radio Communications 2006*, American Radio Relay League (ARRL), 2005
- Upadhyaya, S.J. (1998). Noise Generators. *Technical Paper*, state university of New York at Buffalo, 1998
- Wang, Y.; Su, H. T.; Huang, F. & Lancaster, M. J. (2003). Design of wideband superconducting coplanar delay lines. *High Frequency Postgraduate Student Colloquium*, 2003, p. 86

Novel Polarization-Agile Annular Waveguide Slot Antennas

Siamak Ebadi and Keyvan Forooraghi
*Microwave Lab., Tarbiat Modares University
Tehran, Iran*

1. Introduction

Slot array antennas using rectangular waveguides were widely used in past decades based on their various important capabilities in microwave telecommunications. Having a low profile, ability to implement different current distributions and high power handling are among the advantages of such antennas. On the other hand, there exist some restrictions in optimum and efficient performance of rectangular slotted waveguide antennas due to the use of rectangular waveguides and slots in a circular boundary (Elliott, 2003). These limitations are mainly caused by the disharmony between the rectangular geometry of radiating elements and the circular boundary of the antenna. This has been the inspiration for exploring novel alternative structures with improved geometrical balance with the circular boundary (Fusco et al., 2003, Noghianian et al., 2001, Takahashi et al., 1995, Kelly et al., 1961).

Annular Waveguide Slot Antennas (AWSA) were introduced in (Ebadi et al., a, 2007) intending the application in circular boundary planar slot array antennas. Resonant characteristic along with linear polarization perpendicular to the slot direction were proved the single slot case and it was shown that the AWSA could be modeled as a shunt conductance in the annular line. As the first step to the study of an AWSA, the annular waveguide was compared with the rectangular waveguide (Ebadi et al., b, 2008) and the design procedure was provided in (Ebadi et al., c & d , 2008). It was shown that such waveguide bend could be considered as a transmission line along the cylindrical ϕ direction. Sinusoidal field distribution along the waveguide cross section and single mode transmission were also provided. As the second step, the Green's functions required for the analysis of an AWSA by the method of moment were derived and presented in (Ebadi et al., e, 2009). These functions will be used in analyzing the AWSA to derive exact field distribution along the slot and the variation of slot conductance in different frequencies.

In an AWSA, the waveguide and the slots are all circularly oriented to fit the boundary. Due to its similarity with the rectangular slotted waveguide case, the circuit model for the AWSA was proposed to be a shunt admittance. Fig. 1 shows a sample AWSA structure. The transmission line is supposed to be the H-plane waveguide bend which is also called azimuthal waveguide. The waveguide is fed from one end and is short-ended at the other

side operating in the resonance mode. The slot length is selected as the resonance length appropriate to its radial offset from the centerline.

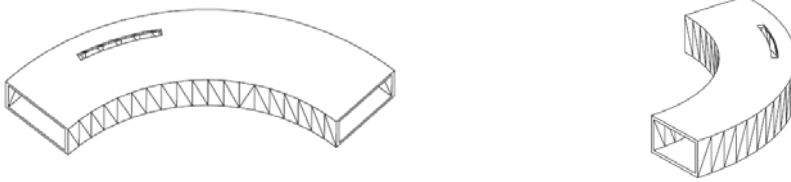


Fig. 1. Different views of an AWSA. The waveguide is an H-plane bend and the wave is annularly guided through it. (Ebadi et al., a, 2007)

Regarding the interesting applications of AWSA arrays, the main point to mention will be the polarization agility. As it was presented in (Ebadi et al., f, 2008), a four element AWSA array (four quadrants in the general form) could be used to form linear horizontal or vertical polarization. This will require four phase shifter units with two states of 0 and 180 degree (1-bit phase shifters). Such polarization agility will allow the system designer to switch between the two principal polarizations in situations where one has more advantages over the other one. This characteristic is not a common property in usual antennas and is usually difficult to achieve. It was also recently reported in (Ebadi et al., g, 2009) that this property could be extended to circular polarization using phase shifters with 4 states (2 bits). Although the change in polarization was shown in these papers, there were lack of enough reasoning and theoretical basis. Additionally, the presented radiation patterns for each polarization did not follow a predefined and predicted shape and suffered from high levels of grating lobes.

In this chapter, detailed study of polarization agility achievement in AWSA will be presented. All required phase distribution to change the polarization to any of linear horizontal/vertical or right/left hand circular will be presented and verified by various simulations. The graphical demonstration of different phase combinations over the slots leading to different polarizations will be added. It will lead to better understanding of the polarization change concept. As another important parameter, the proper array factor will be derived for the two principal orthogonal planes which could predict the shape of the radiating pattern. This is based on the equivalent inter-element spacing between the slots in orthogonal directions. The structure will be modeled as a four-element array and the pattern could be derived theoretically. The simulation results for the radiation pattern will be compared to the presented theory and good agreement will be observed. This will be the basis for the design of more complex AWSA arrays in the future with the capability to synthesize desired ϕ -symmetric patterns with low level of quantization error.

2. Analysis of a single slot AWSA (Ebadi et al., a,b,c,d,e)

In this section a short review of the procedure for analyzing an AWSA structure will be presented. At the first step, an annular waveguide will be studied as a transmission line and some brief results of this study will be provided following by the method of moment analysis results at the end. Fig. 2 shows the proposed annular waveguide and compares it with a common rectangular one. After a set of formulations which could be followed in

(Ebadi et al., b, 2008), a sample graphical solution of the deterministic equation for the X-band annular waveguide is provided in Fig. 3. It is observed that this waveguide completely supports the X-band in its single mode operation. Fig. 4 depicts the range of single mode operation for different values of waveguide inner radius. It is interestingly found that this structure will support the desired band for approximately all values of a .

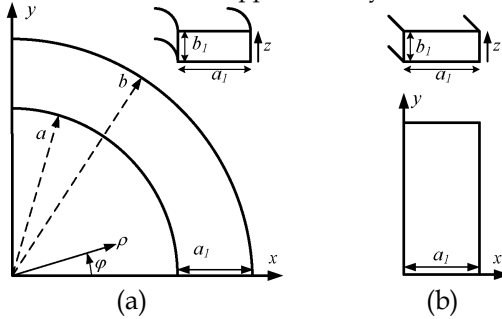


Fig. 2. Demonstration of (a) an annular waveguide and its comparison with (b) the rectangular case in the same geometry: top and 3-D views. (Ebadi et al., b, 2008)

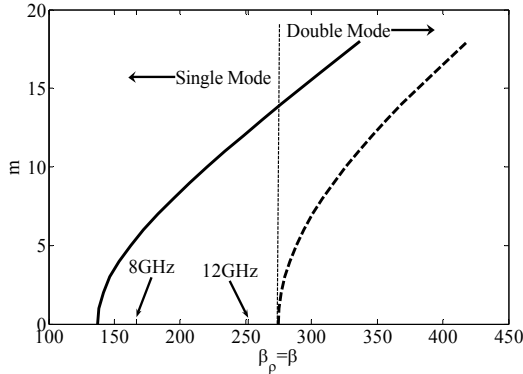


Fig. 3. Graphical solution of the deterministic equation. The region supporting the single mode transmission completely covers the X-band. (Ebadi et al., b, 2008)

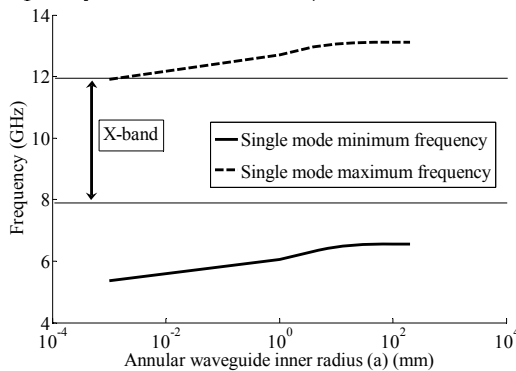


Fig. 4. Supported frequency range in the single mode operation for different values of annular waveguide inner radius ($b-a=0.9in=22.86mm$). (Ebadi et al., b, 2008)

Effect of waveguide radius on the sinusoidal field distribution across the annular waveguide (T) is depicted in Fig. 5. It is shown that for $a > 50\text{mm}$ at X-band, this variation will be sinusoidal. The same distribution could be derived from theoretical MoM analysis and the comparison is made in Fig. 6. The other important result of such analysis would be the annular resonant length of the slot which is provided in Fig. 7. Good agreement is observed between the direct simulation and theoretical analysis in the last two diagrams.

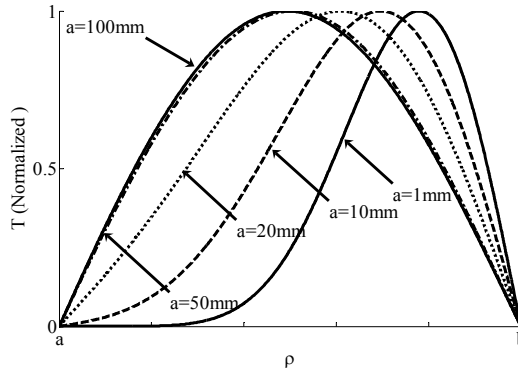


Fig. 5. Plots of T for different values of a and for $m=8$ and $b-a=22.86\text{mm}$: for $a > 30\text{mm}$, sinusoidal field distribution becomes approximately valid. (Ebadi et al., b, 2008)

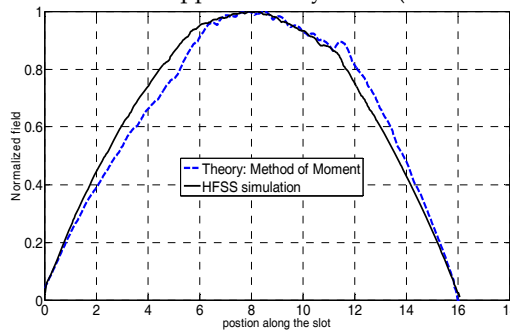


Fig. 6 Field distribution along the slot; comparison of MoM analysis and simulation

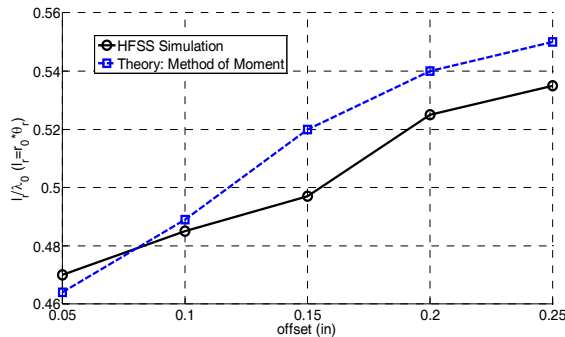


Fig. 7 Annular slot resonant length; comparison of MoM and simulation.

Using the provided theoretical basis and based on the circuit model derived from the MoM analysis and the propagating mode in the annular waveguide described in the previous sections, a single slot AWSA was designed and simulated at 9.3GHz. The designed antenna is fabricated as shown in Fig. 8. The impedance measurement results are provided in Fig. 9 and compared with the circuit model theory (which is that of a shunt conductance resonating at the design frequency) and simulation. The relative radiation pattern measurement results are also provided in Fig. 10 at two principal planes. Good agreement is observed between the design and measurement results.



Fig. 8 The implemented AWSA structure: It is implemented through exact aluminum wire-cut procedure of each face and final assembly step. (Ebadi et al., a, 2007)

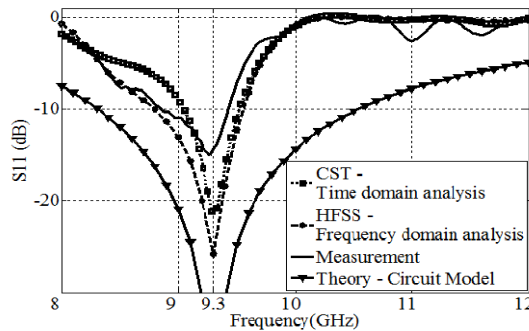


Fig. 9 S_{11} of the implemented AWSA. Circuit model, full wave simulations and measurement results are compared. (Ebadi et al., a, 2007)

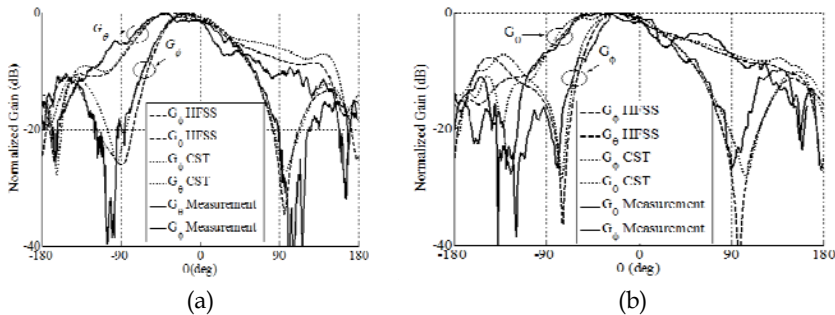


Fig. 10 Normalized pattern of the proposed AWSA: (a) $\varphi=0$ (b) $\varphi=90$ (Ebadi et al., a, 2007)

3. Application: polarization agility in AWSA (Ebadi et al., f & g)

3.1 Theoretical background

In this section, the procedure for designing an array of the proposed AWSA with the ability to change the polarization using a set of phase shifters will be introduced. The array under study is a four element (four quadrants in its general form). Each element consists of an annular waveguide with an annular slot on its top face. The waveguides are closed at both ends and are excited by some coupling slots or coaxial lines from the bottom. In this chapter we do not care about the annular waveguide excitation details and it is supposed to be done ideally. The top view of the array is depicted in Fig. 11(a). As it is shown, the total antenna is symmetric regarding both principal planes ($x=0$ and $y=0$). The four waveguides are excited in the same way and there are the same current distributions on the slots.

As known from the slot theory, the electric field in the slots will mainly have the cylindrical ρ component. It neglects the components of electric field along the slot direction (φ). Assuming narrow slot width the main electric field component over the slots could be divided to two components along x and y as follows

$$\begin{cases} \vec{E}_{r1} = \hat{x}E_x + \hat{y}E_y \\ \vec{E}_{r2} = -\hat{x}E_x + \hat{y}E_y \end{cases}, \quad \begin{cases} \vec{E}_{r3} = -\hat{x}E_x - \hat{y}E_y \\ \vec{E}_{r4} = \hat{x}E_x - \hat{y}E_y \end{cases} \quad (1)$$

The components have the same amplitude but since they are directed to different directions, the signs are different. These four tangential electric fields could be considered as secondary sources (\vec{M}) and will be responsible for the radiation of the array antenna. After insertion of the excitation coefficients (A to D) to all quarters (1 to 4), the far-field radiation pattern could be generally defined as in (2).

$$\begin{cases} \vec{E}_1^{rad} = f(A\{\hat{x}E_x + \hat{y}E_y\}) \\ \vec{E}_2^{rad} = f(B\{-\hat{x}E_x + \hat{y}E_y\}) \\ \vec{E}_3^{rad} = f(C\{-\hat{x}E_x - \hat{y}E_y\}) \\ \vec{E}_4^{rad} = f(D\{\hat{x}E_x - \hat{y}E_y\}) \end{cases} \rightarrow \begin{cases} \vec{E}_T^{rad} = \hat{x}E_{Tx}^{rad} + \hat{y}E_{Ty}^{rad} \\ E_{Tx}^{rad} = f(\{A - B - C + D\}E_x) \\ E_{Ty}^{rad} = f(\{A + B - C - D\}E_y) \end{cases} \quad (2)$$

In which \vec{E}_1^{rad} to \vec{E}_4^{rad} represent the radiated fields due to the four slots and \vec{E}_T^{rad} represents the total radiated field which is the weighted combination of the four aforementioned components. The function f will relate the far-field radiated electric field components to the four magnetic currents on the slots based on the half space Green's function. It should be mentioned that the field components under study could also be chosen as E_θ and E_φ without loss of generality.

It is clearly obvious that the total electric field components are dependent on the respective feed excitation of the annular waveguides in each quarter. This will be the motivation to form array configurations with proper quarter feed excitations to achieve desired total

polarizations. Although this proportional relation could be complicated radiating functions in general, but due to the structure symmetry and the proposed assumptions, the relation will be shown to be considerably valid through detailed simulation for different cases.

As a demonstration, Fig. 11 (b) shows the resulted electric field components for the three cases of null radiation, linear horizontal and linear vertical polarizations. It also shows the effective distance between the slots considering them as single point sources. In the top-right case, it will be found that if the waveguides are excited with the same phase distributions, the four components will cancel each other and there will be null radiation in the broadside direction. In the two bottom figures it is shown in this figure how the electric field components will rotate with simple 0° or 180° phase shifts in a way that the total radiated field vector will point to our desired horizontal or vertical directions. As mentioned before, there are four 1-bit phase shifters (two states for each) required to change the polarization to these cases in the linear form.

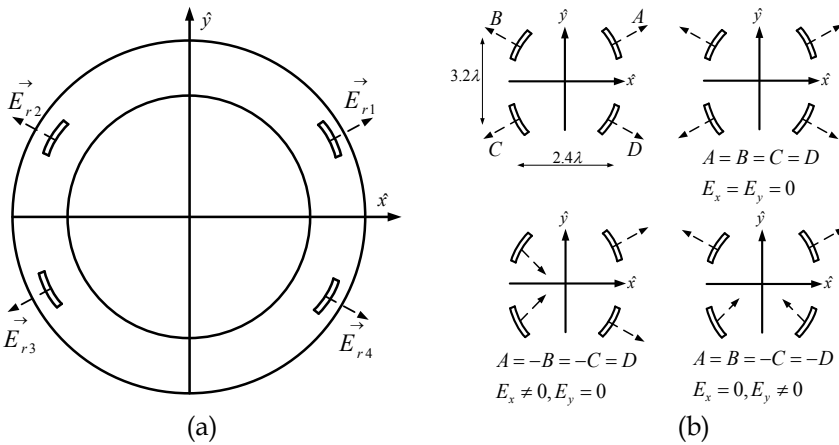


Fig 11. A 4-element AWSA array. (a) the combination of four short-ended single slot AWSAs (b) corresponding electric field components for null and linear horizontal/vertical radiations.

Table I shows the proposed values for feed excitation coefficients in order to achieve linear horizontal/vertical polarization in as well as LHCP or LHCP. In the first column the four possible radiation cases are listed along with the case of no radiation. In the second column the required phase distribution for each case are provided and the resulted field components are listed in the third column. For the circular cases, both x and y components of the total radiated electric field should be present with 90° of phase shift lead/lag based on the kind of circular polarization. It is interestingly observed that by simple 180° or 90° phase shifts at three quarters with respect to the reference one, the total electric field could have the desired polarization.

Desired Polarization	Feed Coefficients Requirements	Resulted Field Vectors
Zero Electric Field (Null radiation)	$A = B = C = D$	$E_{Tx}^{rad} = E_{Ty}^{rad} = 0$
Linear (y)	$B = A$ $C = -A$ $D = -A$	$E_{Tx}^{rad} = 0$ $E_{Ty}^{rad} = 4AE_y$
Linear (x)	$B = -A$ $C = -A$ $D = A$	$E_{Tx} = 4AE_x$ $E_{Ty} = 0$
LHCP	$B = jA$ $C = -A$ $D = -jA$ ($E_x = E_y$)	$E_{Tx}^{rad} = 2A(1-j)E_x = 2\sqrt{2}AE_x e^{-j\frac{\pi}{4}}$ $E_{Ty}^{rad} = 2A(1+j)E_x = 2\sqrt{2}AE_x e^{+j\frac{\pi}{4}}$
RHCP	$B = -jA$ $C = -A$ $D = jA$ ($E_x = E_y$)	$E_{Tx}^{rad} = 2A(1+j)E_x = 2\sqrt{2}AE_x e^{+j\frac{\pi}{4}}$ $E_{Ty}^{rad} = 2A(1-j)E_x = 2\sqrt{2}AE_x e^{-j\frac{\pi}{4}}$

Table 1. Proposed Feed coefficients for the AWSA array combination: by proper choice of the coefficients, the total structure will radiate the desired polarization

3.2 Simulation results

A full-wave simulation based on finite-element method is performed using Ansoft HFSS to verify the proposed method for achieving arbitrary polarization in AWSA arrays. The simulated structure is shown in Fig. 12. The 4-element array is constructed using four sets of single slot AWSA as designed and measured in (Ebadi et al., a, 2007) at 9.3GHz. The four waveguides are closed at both ends and are excited from the bottom and are internally separated. There will be four available ports for the simulation of this structure with their respective phases playing a critical role in our application.

Fig. 13 depicts the simulated gain components of a single slot AWSA. As its unique property, the single slot radiation patterns have both horizontal and vertical components (G_x & G_y) with approximately equal maximum values in both planes. This is different from the conventional rectangular slotted waveguides in which each slot has only one main gain component forcing the total array to have the same polarization as a result. As mentioned

before, this interesting characteristic in AWSA is the motivation to form array combinations with desired arbitrary polarization.

Fig. 14 shows the radiated gain components of the 4-element array with the feed coefficients chosen from Table I to have only horizontal polarization (G_x). It is observed that the four-element array has only the predicted G_x component with the G_y component being completely cancelled down to -300dB which is quite in agreement with our prediction. It should be mentioned that the level of such cancellation will depend on mechanical considerations and the precision of the phase shifters and in actual cases will not go below -50dB. The plots are shown for both principal planes ($\varphi=0, 90$).

The same simulation was performed for the linear vertical polarization (G_y) case and is depicted in Fig. 15. As predicted, the gain component along the y direction is conserved and the other unwanted component is completely cancelled. The same discussion is valid for the level of cancellation as in the previous case. This finishes the first part of simulation results dealing with linear polarization agility and proved the proposed method in this level.

The other interesting property of an AWSA array would be the circular polarization with the right or left hand sense of rotation changeability. This would be also performed following the coefficients introduced in Table I. In this case 90° phase shifts at the quarters would be also required. This will add a higher level of complexity to the structure. In this case there will be three 2-bit phase shifters required to set the desired phase differences between quarter A and other quarters. But this extra complexity will lead to a very interesting extra performance of the AWSA array: the designer could change the polarization of the array to circular right/left hand. This will be so useful in operating environments causing high level of rotation in the polarization of the travelling electromagnetic field.

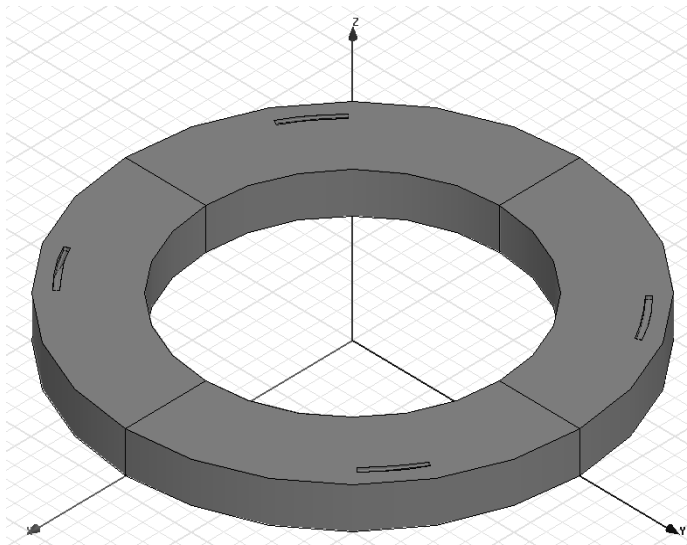


Fig 12. HFSS Simulated 4-element AWSA array. (Ebadi et al., f &g)

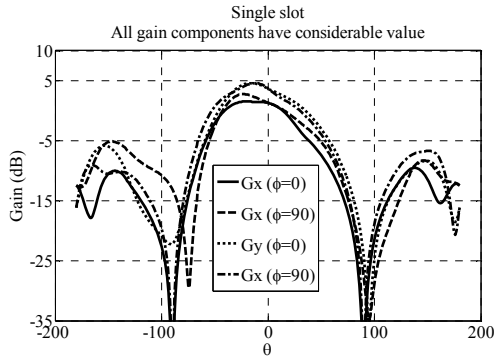


Fig. 13. Simulated pattern of a single slot (AWSA): the pattern has vertical and horizontal components as the motivation to form arrays with desired polarization. (Ebadi et al., a, 2007)

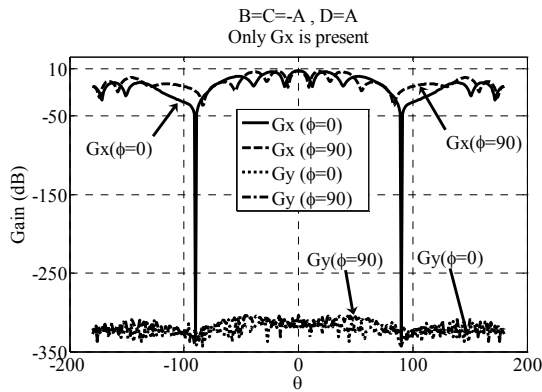


Fig. 14. Simulated radiation pattern of a 4-element AWSA array: excitation coefficients are chosen in a way to have only linear horizontal (G_x) gain component. (Ebadi et al., f & g)

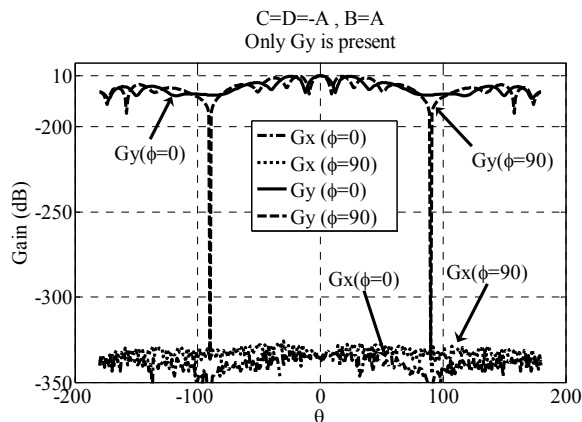


Fig. 15. Simulated radiation pattern of a 4-element AWSA array: excitation coefficients are chosen in a way to have only linear vertical (G_y) gain component. (Ebadi et al., f & g)

Fig. 16 shows the simulated axial ratio for left hand case (LHCP). It is observed that the antenna radiates a circular polarization (Axial ratio=1) in the region $-50 < \theta < 50$ which is acceptable for many practical systems. It is understood that the structure is more sensitive in circular mode and has a narrower range of operation compared to the linear case which was valid for almost all θ values. The extension of this operating region and study of different effective parameters in this behavior will be one of the future possible research interests of the authors. Fig. 17 depicts the polarization ratio for the desired LHCP case. This parameter is representative of the respective strength of left and right hand components of the circular polarization. As expected, the LHCP has a complete superiority in the aforementioned region over RHCP and the proposed method is again verified in predicting the sense of rotation in circular case. It should be mentioned however that the polarization ratio has some variations that means a small change in the level of purity of the desired polarization. Although it might be considered as another drawback of the approach, this variation is not so high and destructive.

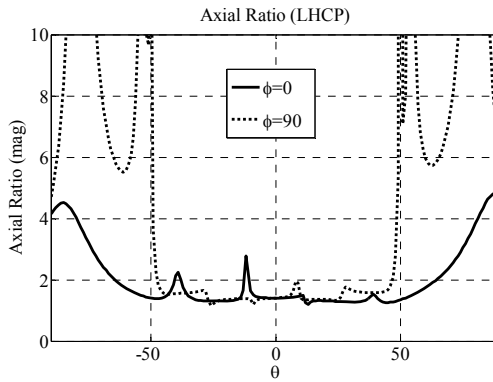


Fig. 16. Simulated axial ratio of a single slot (AWSA) in LHCP case: it is observed that the array radiates a circular polarization in a wide range of angles. (Ebadi et al., g, 2009)

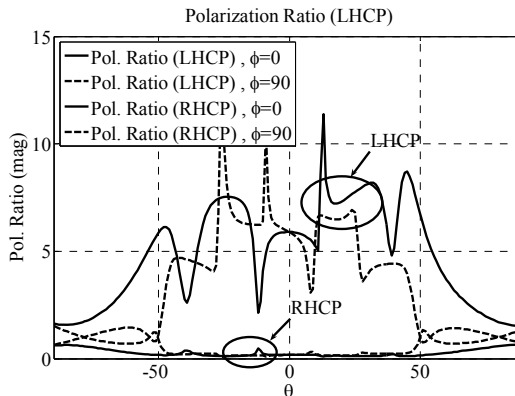


Fig. 17. Simulated polarization ratio of a 4-element AWSA array: the excitation coefficients are chosen in a way to have only LHCP and the RHCP is suppressed. (Ebadi et al., g, 2009)

The same procedure was performed for the RHCP case. Fig. 18 proves the circular polarization validity over the same region and Fig. 19 shows that the correct sense of rotation is achieved. Therefore, it was shown that by simple phase shifts at the four quarters, all possible practical polarizations could be achieved from the novel AWSA array

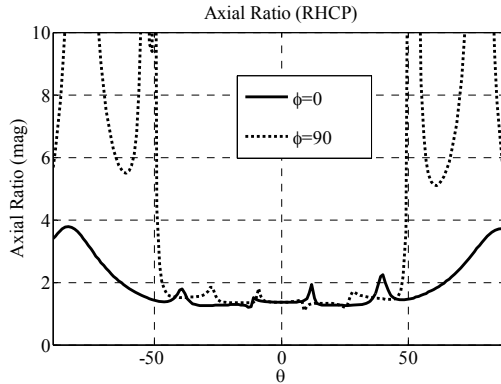


Fig. 18. . Simulated axial ratio of a single slot (AWSA) in RHCP case: it is observed that the array radiates a circular polarization in a wide range of angles. (Ebadi et al., g, 2009)

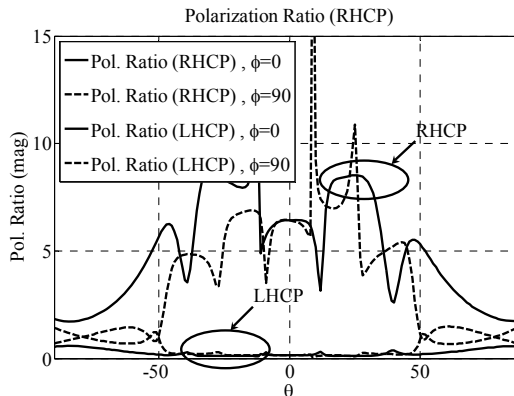


Fig. 19. Simulated polarization ratio of a 4-element AWSA array: the excitation coefficients are chosen in a way to have only RHCP and the LHCP is suppressed. (Ebadi et al., g, 2009)

3.3 Array Factor Modeling

Till now it was shown that by proper choice of quadrant excitations in a four element AWSA array the polarization of final radiated field could be changed between linear and circular form of any kind. The other important concept in the antenna design would be the shape of the radiation pattern. Although we have succeeded in forcing the radiated field to have our desired direction or polarization, the variation of the field in different angles in its far-field region should be studied and synthesized as well. In this section we will propose a simple method to study and predict the form of AWSA radiation pattern.

Referring to the radiation patterns in the linear case as an example (Fig. 14 and Fig. 15), it could be observed that the patterns suffer from high level of grating lobes with almost the same values as the main beam. The reason for such behavior could be found by considering the AWSA array as a four element array with the distances between the elements provided in Fig. 11(b) in both directions. The pattern of this array could be then predicted by using array factor theory and the element patterns derived in previous sections at both planes. The equivalent arrays at both principal planes are formed and shown in Fig. 20. Using this configuration, one could predict the radiation pattern easily.

Fig. 21 compares the patterns derived from the proposed array-factor modeling method with that of full-wave simulations. It is observed that the two results are in a very good agreement in both orthogonal planes. This opens a broader field of future research and study on the concept of pattern synthesis in AWSA arrays. The four-element array studied in this chapter was proved to be successful in altering the polarization but fails to provide a low sidelobe level pattern due to the large spacing between the elements. Using arrays with larger number of elements and performing an appropriate pattern synthesis will improve the pattern behavior.

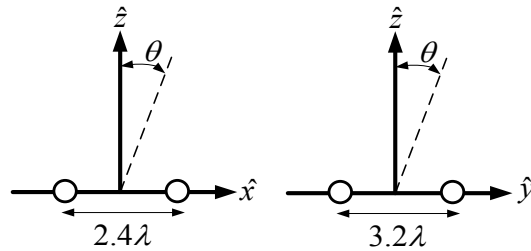


Fig. 20. Two equivalent arrays of the AWSA array in Fig. 2. The radiation patterns could be theoretically predicted using these arrays.

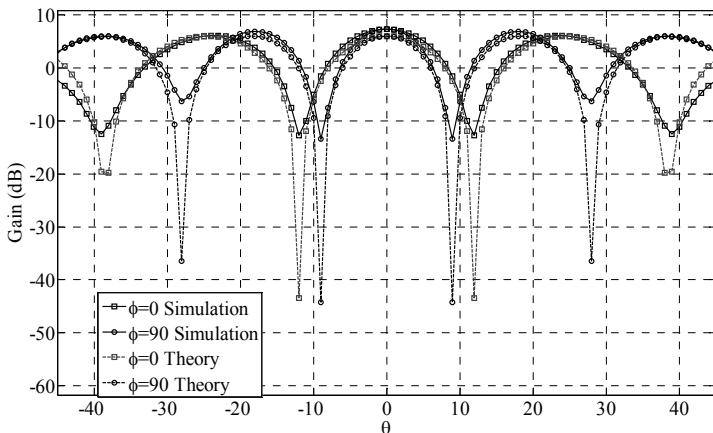


Fig. 21. Radiation pattern for linear polarization (x-direction) for two orthogonal planes: comparison of simulation and array factor theory.

4. Conclusion

Annular waveguide slot antennas were introduced to form arrays with the possibility to alter the polarization of the antenna between the four major cases of linear horizontal or vertical and right or left hand circular. This important achievement needs the array to be formed in a four-quadrant scheme with three phase shifter units to set the desired phase differences with respect to the first quarter. Different phase distributions were provided for all polarization cases. The angular range in which the polarization follows the predicted form was studied for different cases and it was shown that the linear polarization is valid in a larger angular range. The radiation pattern was also theoretically predicted by modeling the array and forming the respective array factor and good agreement was achieved. Such polarization-agile AWSA array would be of high usage in complicated applications.

5. References

- Elliott, R. S. (2003). *Antenna Theory and Design*, John Wiley & Sons, Inc., New Jersey.
- Fusco, V.F. & Subbarao, B. (2003). Probe-fed circularly polarized Monopulse radial line slot antenna, *Electronics Letters*, Volume 39, Issue 21, pp.1495 – 1496.
- Noghanian, S. & Shafai, L. (2001). Analysis of conducting ring and double layer dielectric loaded annular slot array antennas, *Microwaves, Antennas and Propagation, IEE Proceedings Volume 148, Issue 5 Page(s):327 – 333*.
- Takahashi, M.; Ando, M.; Goto, N.; Numano, Y.; Suzuki, M.; Okazaki, Y. & Yoshimoto, T. (1995). Dual circularly polarized radial line slot antennas, *Antennas and Propagation, IEEE Transactions on Volume 43, Issue 8, Page(s):874 – 876*
- Kelly, K. & Goebels, F. (1961). Arbitrary polarization from annular slot planar antennas, *Antennas and Propagation, IEEE Transactions on Volume 9, Issue 4, pp. 342 – 349*.
- (a) Ebadi, S. & Forooraghi, K. (2007). An annular waveguide slot antenna, *IEEE Antennas and Wireless Propagation Letters*, Volume 6, Issue 99, Page(s):525 – 528.
- (b) Ebadi, S. & Forooraghi, K. (2008). Comparative study of annular and rectangular waveguides for application in annular waveguide slot antennas (AWSA), *Journal of Electromagnetic Waves and Applications*, Vol. 22, 2217–2230.
- (c) Ebadi, S. & Forooraghi, K. (2008). Waveguide Design Considerations in Annular Waveguide Slot Antennas (AWSA), *Proceedings of 2008 IEEE Int'l Sym. on Antennas and Prop., 2008, San Diego, USA*.
- (d) Ebadi, S. & Forooraghi, K. (2008). Annular Waveguide Analysis for Application in Annular Waveguide Slot Antennas (AWSA), *Proceedings of 38th European MW Conf., October 2008, Netherlands*.
- (e) Ebadi, S. & Forooraghi, K. (2009). Green's function derivation of an annular waveguide for application in method of moment analysis of annular waveguide slot antennas, *Progress In Electromagnetics Research, PIER 89, 101-119*.
- (f) Ebadi, S. & Forooraghi, K. (2008). Polarization agility in annular waveguide slot antenna arrays, *Proceedings of The 20th Asia-Pacific Microwave Conf. 2008, Hong Kong, China*.
- (g) Ebadi, S. & Forooraghi, K. (2009). Linear and circular polarization agility in annular waveguide slot antennas, *Proceedings of 2009 IEEE radio and wireless symposium (RWS2009), San Diego, 2009, CA, USA*.

Reconfigurable radiation pattern antennas in mm-waves

Olivier Lafond, M. Caillet, B. Fuchs and M. Himdi
*IETR, University Of Rennes 1
France*

1. Introduction

Far-field radiation pattern control has strong potential in smart antennas, wireless communications and radar. Typical planned applications include multipath fading and interference mitigation, data rate and coverage enhancement, etc. For implementing these functionalities, either switch beam or reconfigurable Half-Power Beam-Width (HPBW) antennas are required. In particular, short range and “Stop and Go” radars are deployed by car industry (Wenger, 2005) and operate in millimeter wave frequency bands. Multi-beam antennas have been studied extensively and realized using diverse techniques. Butler (Butler & Lowe, 1961) and Blass (Blass, 1960) matrices are complex feed networks composed of couplers and phase shifters which provide phase difference between radiating elements to steer a beam in a given direction. Rotman lens (Rotman & Turner, 1963), (Schulwitz & Mortazawi, 2006) is a quasi-optical system based on a cavity limited by two arcs. Inputs and outputs are placed along the two arcs and phase difference between the output ports is achieved by microwave propagation through the cavity. Micro-Electro-Mechanical Systems (MEMS) have been employed either to mechanically orientate an array (Baek et al., 2003) or to switch between two antennas having a different beam angle (Cetiner et al., 2003). Lens array (Popovic & Popovic, 2002) and dielectric lens (Wu et al., 2001) are other interesting concepts used to design multi-beam antennas by moving the feed at the back of the lens. In this chapter, the authors present different antenna concepts to obtain reconfigurable radiation pattern capability in millimeter waves.

- First, multibeam antennas are demonstrated based on Butler matrices at 24 and 60 GHz. Passive and active designs are considered and manufactured prototypes are presented to show radiation patterns and gain results.
- Furthermore, reconfigurable Half Power BeamWidth (HPBW) antennas are shown. The objective is to modify the directivity of an array by changing the number of fed patches. Passive and active prototypes have been fabricated to prove the reconfigurability concept at 24 GHz.
- Finally, a new technique is presented to shape the radiation pattern of an antenna to achieve directive or sectorial beams. In this case, the antenna design is based on an inhomogeneous lens (Maxwell Fish-Eye lens) fed by several sources.

In addition, the authors designed element array in millimeter waves using multilayer technology to separate radiating elements and feeding lines, in order to avoid spurious radiation from lines and to keep good performances in terms of sidelobe and cross polarization levels. Details of the multilayer technology are given in the first part of this chapter.

2. Multibeam antenna based on Butler Matrix

The Butler matrix (Butler & Lowe, 1961) allows to turn an antenna array into a multibeam system. In addition, the Butler matrix and microstrip technologies are both suitable for the use of active devices to design active antenna. The Butler matrix includes hybrid couplers (3dB, 90°), passive phase shifters and cross-over elements in order to feed the different radiating elements with the appropriate phases. However, in millimeter waves, low efficiency is often obtained due to metallic and dielectric losses of the printed lines.

Moreover, printed multilayer technologies are desirable to avoid spurious radiation from the lines of the matrix (Lafond & Himdi, 2002). Based on these facts, multilayer technology has been considered in the proposed designs to achieve neat radiation patterns.

2.1 Multilayer Technology

In this part, details are provided regarding the used multilayer technology. It consists of two different substrate layers separated by a thick ground plane. The first microstrip line printed on the bottom layer couples to the second one, printed on the top substrate, via a slot engraved in the ground plane. The second line is electromagnetically coupled to the slot. In this case, this design is named microstrip line - slot - microstrip line transition (Fig. 1a). Another option is to excite a microstrip patch through an aperture slot (Fig. 1b). These different multilayer feeding techniques have been tested up to 60 GHz (Lafond et al., 1999), (Lafond et al., 2002), (Lafond et al., 2005).

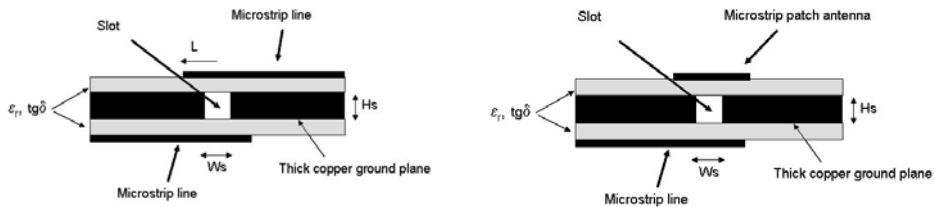


Fig. 1. (a) Microstrip line - slot - microstrip line transition, (b) Aperture coupled patch antenna

In millimeter waves, thin substrates (0.1 to 0.2mm) are usually used to avoid surface wave losses, and to achieve good efficiency when antennas are designed. Then, the manufactured prototypes are often soft or breakable. To solve this problem, a thick ground plane (0.2mm to 0.5mm) is added between the two substrate layers. Moreover, this thick ground plane is appropriate to active components (MMIC ...). The thickness of the ground plane has to be taken into account because it reduces coupling through the slot. Thus, these multilayer

technologies give the possibility to design active antennas by separating radiating elements from circuits and feeding lines.

2.2 Passive Butler matrix and printed array at 60 GHz

For indoor communication systems at 60 GHz, the link between transmitter and receiver can be cut even by human body if directive antennas are used. Thus, multibeam antennas can be a solution to avoid these failures. In this part, a passive Butler matrix with four beams is used to feed a four patch array. Each input of the matrix allows to steer one beam. Each beam is achieved by applying a phase shift between the patch antennas. This phase shift is obtained thanks to the butler matrix which is composed of hybrids and phase shifters. But, to feed the patches with appropriate phases, the microstrip lines must be crossed inside the matrix. To realize these crossings, a cross-over hybrid is used in the Butler matrix system (Fig. 2a). For this design, aperture coupled patches are optimized and are connected to the outputs of the Butler matrix via coupling slots. RT 5880 Duroid substrate ($h = 0.127\text{mm}$ and $\epsilon_r = 2.23$) is used for both layers of the prototype. The four configurations under consideration (F1 to F4) reveal tilt angles of $\pm 15^\circ$ and $\pm 45^\circ$. The element spacing is $0.5 \lambda_0$ to maintain low side lobe level, whatever the tilt angle. The actual matrix and antenna array are presented in Fig. 2b wherein the two distinct layers are shown. In addition, the return loss is measured for each configuration (F1 to F4) in order to check that all configurations are properly matched (Fig. 3). The return loss is greater than 10 dB around 60 GHz. The measured radiation patterns are presented in Fig. 4 for all configurations. Good results can be observed in terms of tilt angle and side lobe level. These results prove that achieving good performance with a multibeam antenna is possible in mm-waves. Regarding efficiency, its value is close to 40% due to metallic and dielectric losses in the cross-over and feeding network.

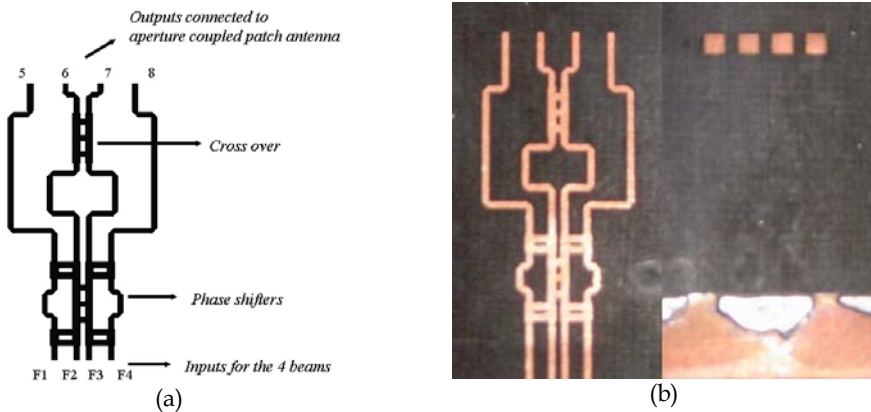


Fig. 2. (a) Butler Matrix, (b) Butler Matrix and array using multilayer technology

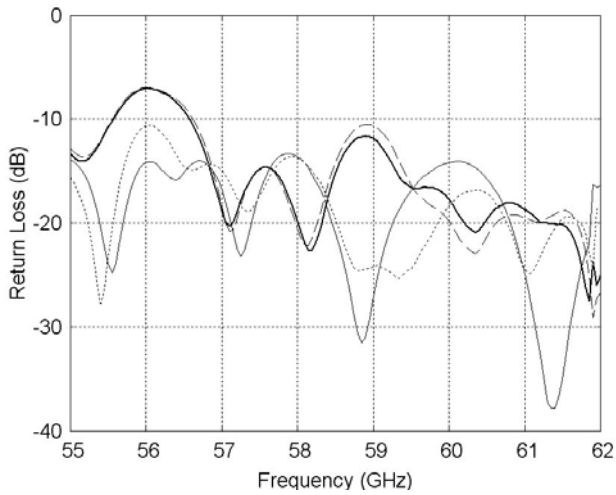


Fig. 3. 4x4 Butler-matrix: return loss (dB) of each input (F1 to F4)

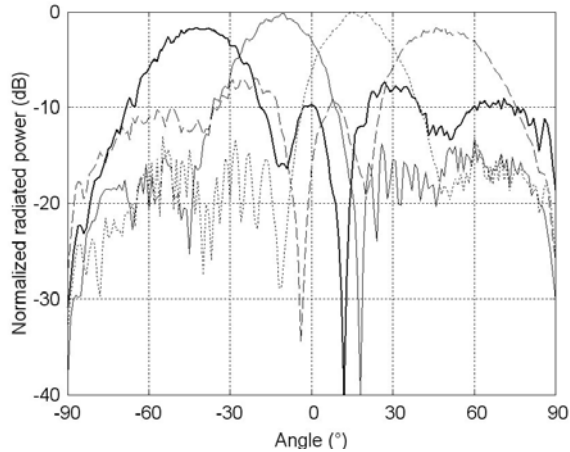


Fig. 4. 4x4 Butler-matrix: radiation patterns at 60 GHz for all configurations

This first design is a passive one, but a complete prototype must include active devices to select the beam. Then, an active feeding system has to be designed to achieve this function. An active Butler matrix is presented in Section 2.3 at 24 GHz. Details about switches, matching technique and measured radiation patterns are provided.

2.3 Active Butler matrix and printed array at 24 GHz

An active switch beam antenna based on Butler Matrix includes a switching network. The objective of the switching network associated to the Butler matrix (Fig. 5) is to select one beam among four. This means that only one switch will be ON and the other ones OFF at a given time. The main issue in the conception of this antenna is the design of the feed network in front of the matrix to maintain a good matching for all configurations. But before

to explain the technique used to match the active antenna, the switch configuration must be chosen. Many technologies exist for RF switch design. The most common is based on semiconductors (Macom), (Rebeiz, 2003) and electromechanical switches (Quinstar). The latter ones are expensive, hardly integrable and have low switching speed. For MEMS, the isolation is better than semiconductors but, again, the switching speed is low and internal parasitic radiation could affect the signal integrity. Based on these facts and considering that discrete components are available and cheaper, the semiconductor technology has been selected to design a switch. In addition, discrete components can be easily integrated with the microstrip double layer technology selected to develop the prototypes. Two types of discrete components are useful to design switches: PIN diodes and transistors. Switches based on PIN diodes have insertion losses, while switching circuits using transistors have on the opposite gain. Moreover, transistors have a better isolation than diodes, thus a FET transistor has been retained.

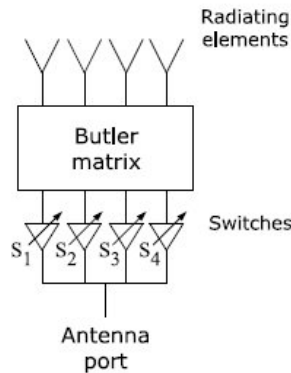


Fig. 5. Butler matrix and active feeding system to select one beam among four

A receiving antenna is considered here, thus a variable gain amplifier has been designed with control on the drain bias. The configuration of this switch amplifier has been optimized to minimize the Noise Figure (NF). Hence, when the switch is in the ON state, the gain should be positive, the input return loss equals to Γ_{OPT} to minimise the NF, and the output return loss matched to 50Ω . Besides, as explained in (Caillet, 2006), the matching concept of the antenna is based on an open circuit impedance of the "OFF" switch is in the OFF state, associated with design of path lengths in the feed network at a multiple of $\lambda_g/2$. Thus, each junction will see open circuit(s) from the "off" switch output(s).

Characterization of the transistor's S-parameters is required because both ON and OFF states' S-parameters are used to meet the constraints. A TRL calibration method has been used to obtain the scattering parameters into two planes at 1 mm from transistor's grid and drain. The S-parameters of a NEC NE3210s1 transistor have been characterized with $V_{DS} = 0V$ (OFF state) and $V_{DS} = 2V$ (ON state) and, $V_{GS} = 0V$ in both states. Parallel stubs have been placed at the input and output of the transistor and microstrip lines' impedances and lengths have been optimized to match the constraints. This switch, optimized on a RO3003 substrate ($\epsilon_r = 3$ and $h = 0.127mm$), allows to have a 3.5 dB gain and close to 20 dB in term of isolation. In the OFF state, the output impedance is not a real open circuit but higher than 260Ω . Combining this switch with the matching network, an active Butler matrix has been

designed and feed a four printed patch array at 24 GHz. A multilayer technology has been used with RO3003 substrate for the active layer (Fig. 6a) and RT 5880 substrate ($\epsilon_r = 2.2$ and $h = 0.127\text{mm}$) for the radiating elements (Fig. 6b). The patches are fed by microstrip line - slot - microstrip line transition. The slots are etched in a 0.2mm thick ground plane.

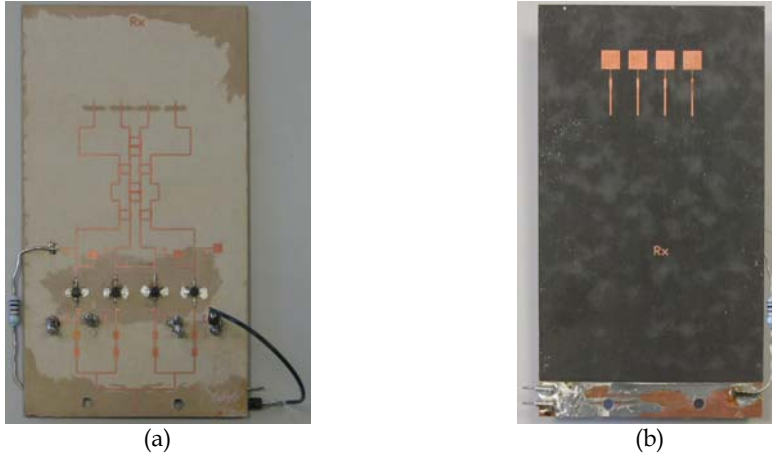


Fig. 6. (a) Active Butler matrix on RO3003 substrate, (b) Radiating element array fed by microstrip line - slot - microstrip line.

Acceptable matching results have been obtained by measurement (Fig. 7). S_{11} is close to -12 dB for all configurations at 23.9 GHz. Concerning radiation patterns (Fig. 8), the tilt angles are -14° , 40° , -45° and 13° . In Fig. 8, all the radiation patterns have been normalized but the gain is not the same for all configuration but equals to 10dB, 8dB, 8.3dB and 11.5 dB respectively. These gains correspond to 50 % efficiency for the active antenna. The gain decreases when the tilt angle increases. Cross polarization levels are in the vicinity of -17dB for all configurations. Back radiation level is close to -10dB and is most probably due to slots and stubs contributions.

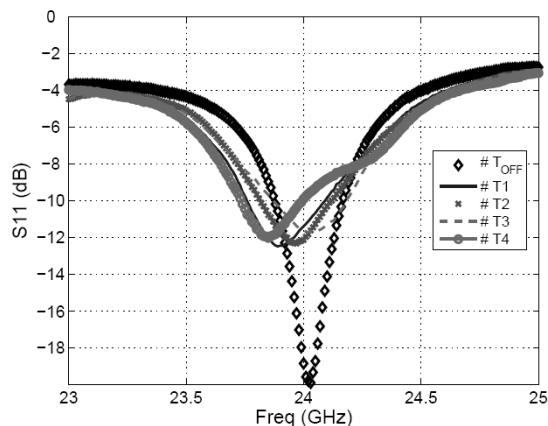


Fig. 7. Active Butler matrix and array - Measured S_{11} results for all configurations

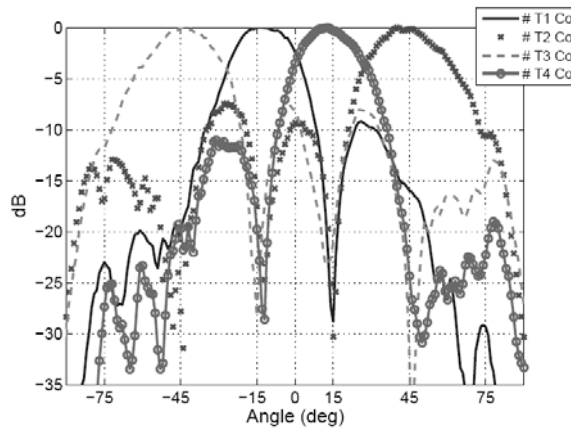


Fig. 8. Active Butler matrix and array – Measured radiation patterns for all configurations

All these results show the potential of the Butler matrix system for the design of active multibeam antennas in millimetre waves. Nevertheless, metallic and dielectric losses in the feeding network of the Butler matrix induce a quite low efficiency if printed technologies are used. Other technologies like Substrate Integrated Waveguide could be investigated to reduce the losses of such systems.

3. Half-power beam width reconfigurable antenna

Tunable half-power beam width (HPBW) antennas are of interest for automotive radars at 24 and 77 GHz. Indeed, these antenna systems allow to adjust the directivity of the antenna to have either a narrow beam for long range radar application, or a wide beam for short range radar application. This functionality can be obtained using an antenna array by changing the number of fed sources in the array. The feed network of the array is composed of switches associated to each radiating element (Fig. 9(a)). The HPBW is determined by the number of ON switch(es). In this case, the input impedance is varying with the number of switches in the ON state. Thus, the feeding line network has to be optimized to guarantee a low return loss whatever the fed sources number in the array (Fig. 9 (b)).

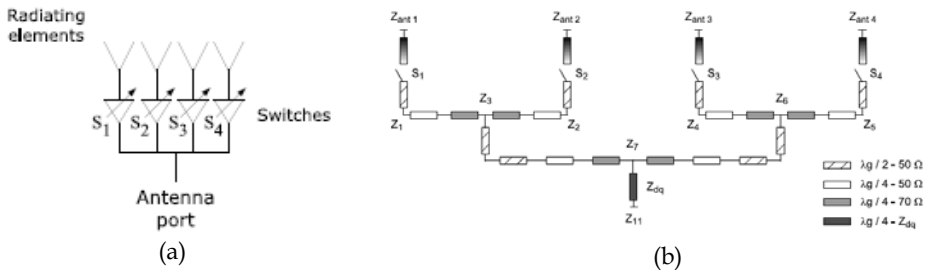


Fig. 9. (a) Active HPBW antenna concept, and (b) Unconventional feeding network

3.1 Matching technique

As the input impedance will change with the number of fed sources, an unconventional feeding network has been defined to match this reconfigurable antenna. Based on the Butler matrix antenna feed network described in Section 2.3, it is possible to change the value of some quarter wavelength transformers to translate the impedances of all configurations in a Voltage Standing Wave Ratio (VSWR) lower than 2. 70.71 Ω quarter wavelength lines are placed around each tee junction to have a 50 Ω input impedance when all radiating elements are fed. An additional quarter wavelength line Z_{dq} is disposed between the antenna port and the lower tee junction. The input impedance is computed using the following equation:

$$Z_{11} = Z_{dq}^2 \cdot \frac{Z_1 Z_2 (Z_4 + Z_5) + Z_4 Z_5 (Z_1 + Z_2)}{4 Z_1 Z_2 Z_4 Z_5} \quad (1)$$

With $Z_p = 50 \Omega$, $p = 1, 2 \dots 5$, if the switch is in the ON state

With $Z_p = \infty$, $p = 1, 2 \dots 5$, if the switch is in the OFF state.

When $Z_{dq} = 50 \Omega$, the obtained impedances are varying from 50 to 200 Ω (D4 to D1 configurations). These impedances are shown on the smith chart in Figure 10. The impedance center (Z_b) is then:

$$Z_b = \sqrt{Z_{\min} \cdot Z_{\max}} = 100 \Omega \quad (2)$$

Based on this facts, one solution to match the reconfigurable antenna whatever the fed sources number is to modify the Z_{dq} value to obtain $Z_b = 50 \Omega$. Thus, the antenna matching will be optimal for $Z_{dq} = 70.7 \Omega$. This new matching technique can be generalized for larger arrays and explained in (Caillet, 2006).

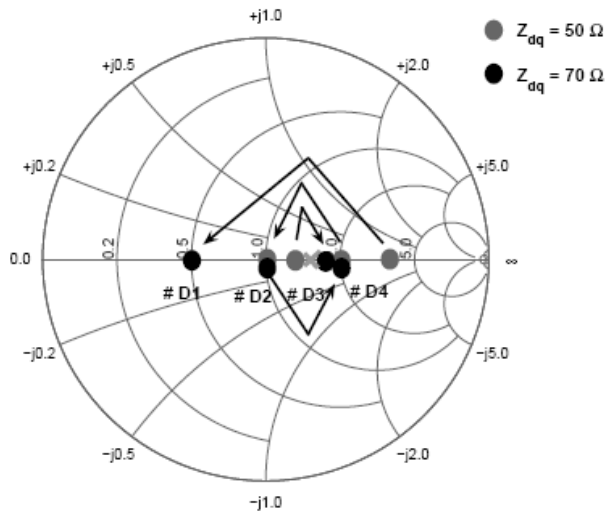


Fig. 10 . Input impedances for D1 to D4 configurations

3.2 Passive HPBW reconfigurable antenna at 24 GHz

Using the matching concept described in Section 3.1, a passive HPBW antenna has been designed and manufactured for characterization. The developed prototype is shown in Fig. 11 for the feeding network printed on RO3003 substrate ($\epsilon_r = 3$ and $h = 0.127\text{mm}$) and for the patch array printed on RT Duroid 5880 ($\epsilon_r = 2.2$ and $h = 0.127\text{mm}$). In this case, a multilayer technology is used and patches are fed by electromagnetic coupling with microstrip line - slot - microstrip line transitions.

This antenna has been designed and simulated using Ansoft Designer (feeding network) and CST Microwave Studio (global antenna). This passive prototype has been built by replacing switches by gaps. The switching process used during measurements consists in soldering gap(s) to have ON-state switch(s). The return loss (Fig. 12) is greater than 20 dB at 24.15 GHz for all configurations (D1 to D4). These results validate the new matching technique described earlier. The measured radiation patterns are shown in Fig. 13 for the four configurations. According to the results, measured half-power beam widths are 71° when one patch is fed, 36° when two patches are fed, 25° when three patches are fed, and 20° with four patches at 24.15 GHz. The measured gains are 5.4, 7.6, 10.0, and 12.4 dB, respectively. The levels of the cross-polarization component are lower than -15 dB.

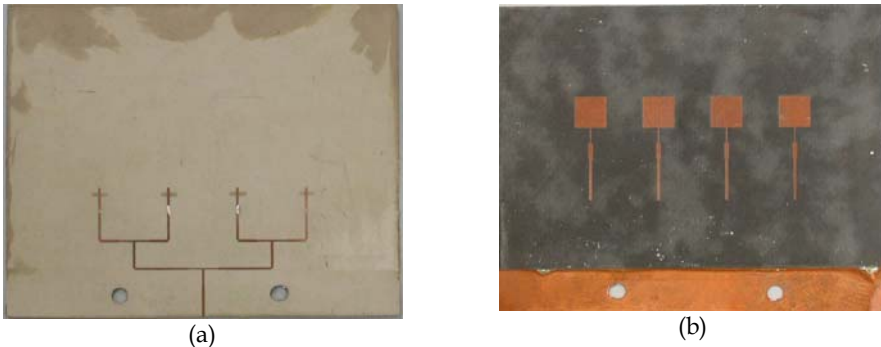


Fig. 11. Passive HPBW antenna - (a) feeding network and (b) patch array

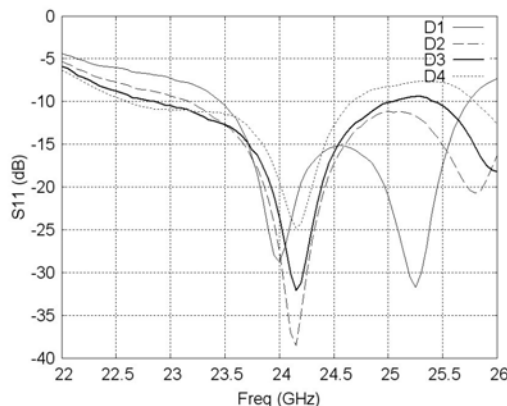


Fig. 12. Passive HPBW antenna - Measured S11 results for all configurations

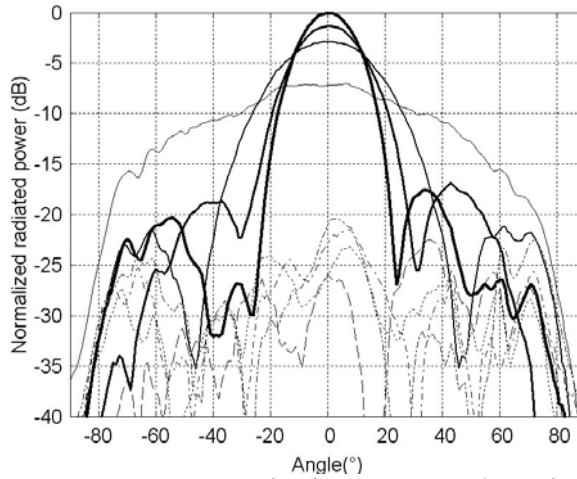


Fig. 13. Passive HPBW antenna – Measured radiation patterns (co and cross polarization) for all configurations

3.3 Active HPBW reconfigurable antenna at 24 GHz

An active HPBW reconfigurable has been designed and measured at 24 GHz. The same substrates are used (RO 3003 for active layer and Duroid 5880 for radiating layer). Thanks to the used multilayer technology (Fig. 14), the active switches are connected to the feeding line network. The active switch is the same than for Butler matrix design, based on a LNA amplifier configuration (section 2.3). The manufactured prototype is presented in Fig. 15 for both layers.

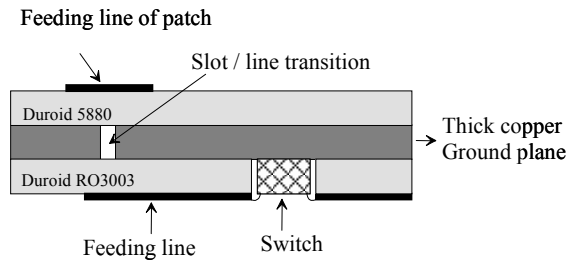


Fig. 14 . Active HPBW antenna – Multilayer technology and switches' structure

The directivity depends of the number of fed patches and is respectively equals to 7.3, 11.2, 13.6 and 15.1 dBi in simulation (D1 to D4 configurations). The measured S_{11} results are given in Fig. 16 and show a good matching at 23.9 GHz even if only -8dB is achieved for the D4 configuration. The measured radiation patterns are shown in Fig. 17 for the same configurations. The measured gains are respectively equal to 9 dB, 12.3 dB, 15.3 dB and 16.4 dB. These results are higher than the simulation predictions, but it could be explained by a higher than predicted active switch power gain.

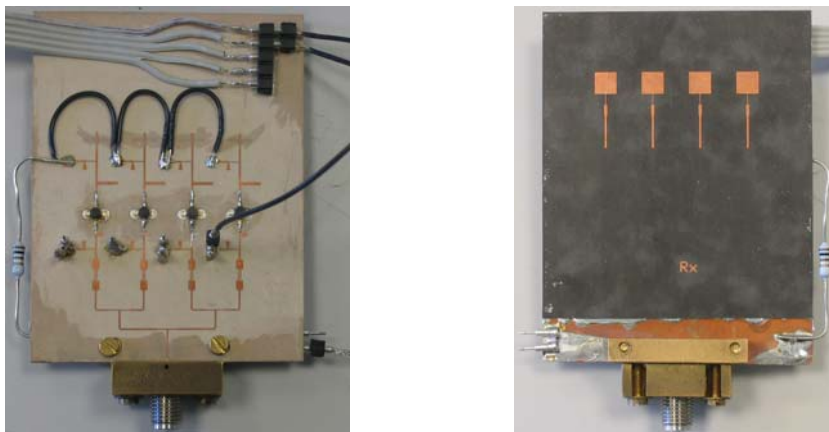


Fig. 15 . Active HPBW antenna - Photos of the manufactured prototype

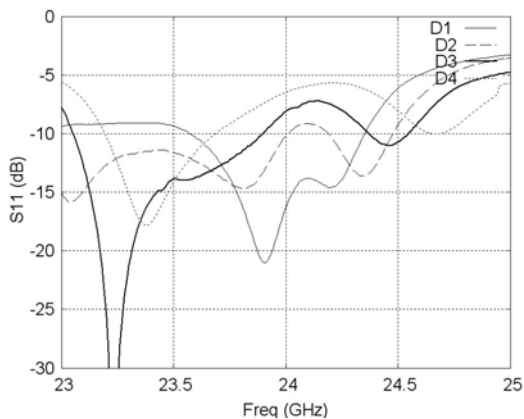


Fig. 16 . Active HPBW antenna - Measured S11 results for all configurations

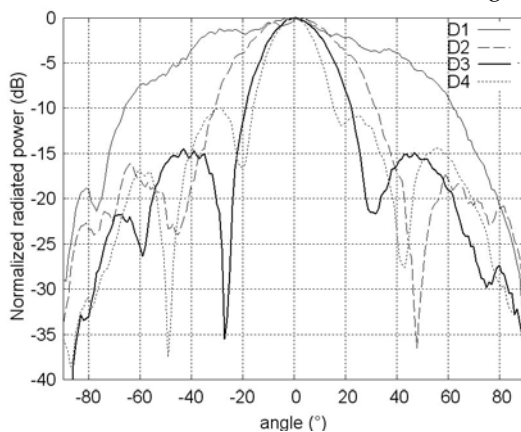


Fig. 17. Active HPBW antenna - Measured radiation patterns for all configurations

An active tunable HPBW printed antenna has been demonstrated at 24 GHz. This prototype allows to vary the half-power beam width of the antenna by changing the number of fed patches in the array. To achieve this result, the design of a switch based on a FET transistor has been proposed. The matching of this antenna is obtained whatever the number of fed patches by modifying the characteristic impedance of a quarter wavelength transformer. However, the design of the tunable HPBW does not allow beam steering. An innovative principle based on sources array and lens is presented in the following section to have radiation pattern shaping capabilities.

4. Inhomogeneous lens and sources array to shape the beam

4.1 Introduction about inhomogeneous lenses

Inhomogeneous lenses have focusing and beam forming capabilities. In such lens, the refraction index $n(r)$ inside the lens follows a radial distribution. The most known example is the 'Luneburg' lens (Luneburg, 1944), but we investigated, since a few years, another kind of inhomogeneous lens named Half Maxwell Fish Eye (HMFE) (Lafond et al., 2007). The refraction index law is given by:

$$n(r) = \frac{2}{1+r^2} \quad \text{where } r \text{ is the normalized radial position.} \quad (3)$$

With this particular law inside the lens, a plane wave is achieved at the middle of the lens and then a hemispherical lens can be used (Fig. 18). It is very interesting to reduce the lens dimension compare to a classical Luneburg lens.

The dielectric constant inside the lens ranges between 1 ($r = 1$) and 4 ($r = 0$). To approximate the continuous gradient index law, several concentric homogeneous dielectric shells are assembled and their characteristics have been optimized (Fuchs et al., 2006), (Fuchs et al., 2007, a). The radius and dielectric constant of shells are chosen to optimize the directivity when the lens is fed by only one source (Fig.19). It is known that if only one source feeds the HMFE lens, a directive pattern is achieved.

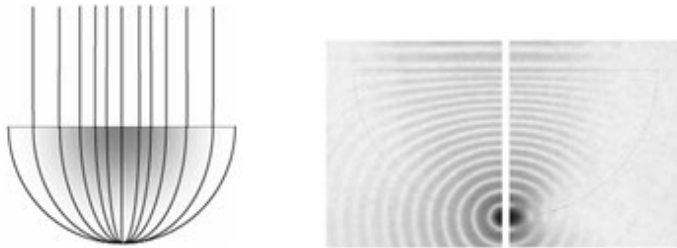


Fig. 18. Plane wave with an hemispherical HMFE lens

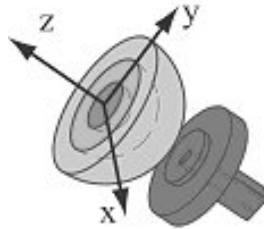


Fig. 19. HMFE lens fed by a WR10 open-ended waveguide

4.2 Focusing capability with an HMFE lens

An HMFE lens experimental prototype has been manufactured using a 9-shells 60mm diameter HMFE lens (Fig. 20) fed by a WR10 open-ended waveguide. The measured radiation pattern in both E and H planes are compared to the computed radiation pattern (mode matching technique) (Fuchs, 2007) at 77 GHz (Fig. 21). For this antenna, a 28.5dB measured gain is achieved.

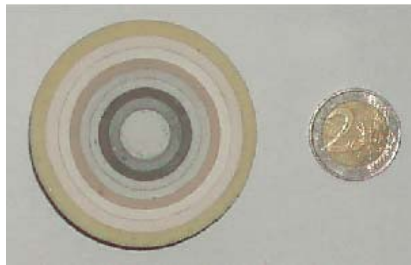


Fig. 20. A 9 - shells 60mm diameter HMFE lens

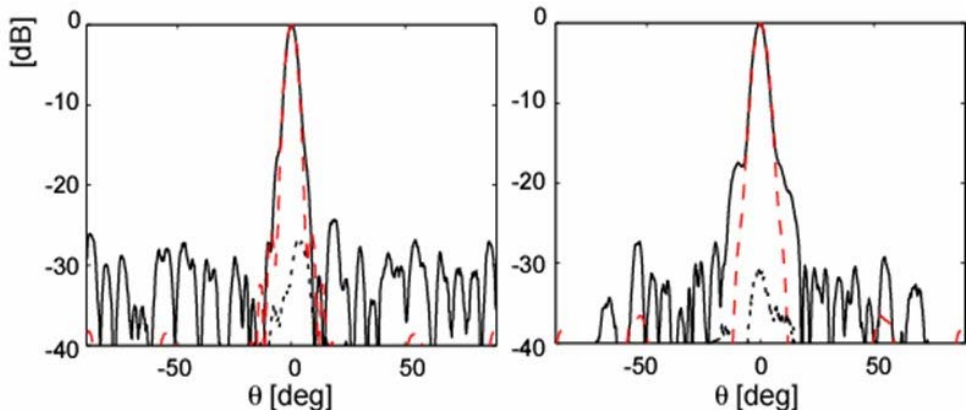


Fig. 21. A 9 - shells 60mm diameter HMFE lens H plane radiation pattern (left), E plane radiation pattern (right)

4.3 Beam scanning capability with an HMFE lens

In our case, the lens gradient index is approximated by assembling several concentric homogeneous dielectric shells. Then, the law is not perfect and a focal spot appears under the lens. Thus, if the feeder moves under the lens, it has been shown that it was possible to obtain beam scanning capability (Fuchs et al. 2007, b). To validate this principle, the 9-shells 60mm diameter has been fed by an open-ended waveguide at 77 GHz. To translate the feed, a mechanical system with a high precision has been added (Fig. 22).

Measurements have been done (Fig. 23) at 77 GHz to show this capability in the H plane of the antenna. The 9-shell 60mm diameter HMFE lens is always fed by a WR10 open-ended waveguide. It is possible to steer the beam up to 12° when the feeder offset equals 5mm. It is possible to increase this tilt angle but the side lobe level will increase and the gain will decrease. A summary of these results is given in the Fig. 24 where the gain and scan angle are shown. Up to a 5mm offset, the gain is quite stable (27.5 dB - 28.5 dB). A good agreement is achieved between simulation with CST Microwave Studio (Dot curve) and measurement (solid curve).

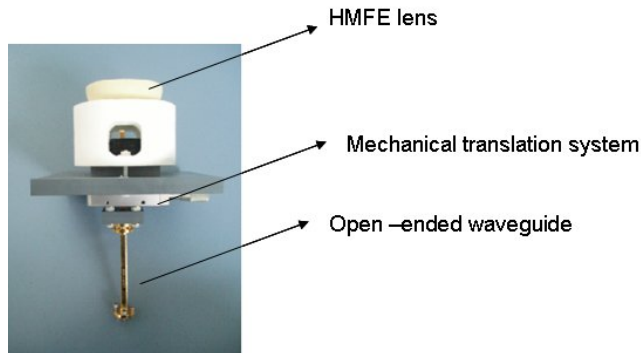


Fig. 22. A 9 - shells 60mm diameter HMFE lens associated with a off-axis source to scan the beam

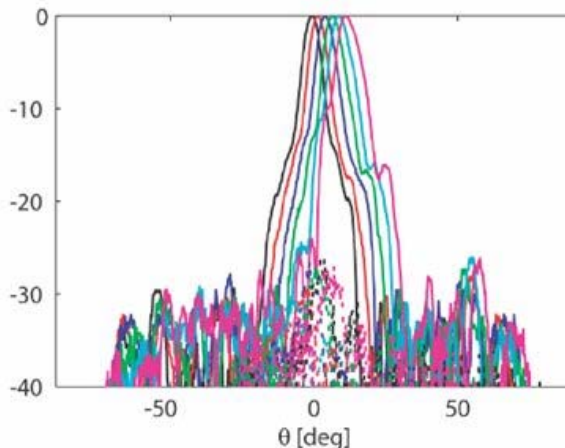


Fig. 23. A 9 - shells 60mm diameter HMFE lens associated with a off-axis source to scan the beam - Measured radiation patterns at 77 GHz for 5 source positions (1 to 5mm)

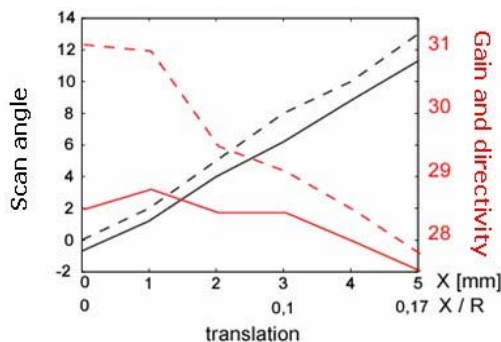


Fig. 24. A 9 - shells 60mm diameter HMFE lens associated with a off-axis source to scan the beam - Measured gain and scan angle are compared with simulation results (CST Microwave Studio)

The last results show that is possible to have high gain antenna and beam scanning capability when a HMFE lens is fed with only one feeder. We decided to look what it happens if several sources are associated with such a lens.

4.4 Beam shaping capability with an HMFE lens

HMFE lens and a sources array - principle

For the reconfigurable antenna in W band (77 GHz), the 9-shells 60mm diameter HMFE lens is fed by 9 open-ended waveguides placed along the H plane (Fig 25). All simulations have been done using CST Microwave Studio at 77 GHz. If only one waveguide feeds the lens, a directive pattern is achieved with a plane wave at the lens output (Fig. 26 right). If the lens is fed by the 9 waveguides, a sectorial beam is obtained (Fig. 26 left). So, it becomes easy to reconfigure the antenna directivity changing only the alimented source number (Fuchs et al., 2007, c), (Lafond et al., 2008), (Lafond et al., 2009). It is important to note that a sectorial radiation pattern is obtained without any phase shifter. It is a main advantage in millimeter waves, because these devices are often scarce and expensive. The electric fields of each source that feeds the lens are added to obtain the sectorial radiation pattern. Obviously, an amplitude and phase tapering can be applied between sources to obtain another kind of radiation pattern. But in this case, amplifiers and phase shifters have to be added in the feeding line network.

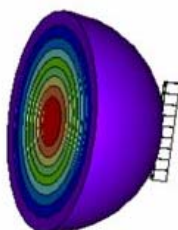


Fig. 25. A 9 - shells 60mm diameter HMFE lens associated with a 9 sources array to shape the beam

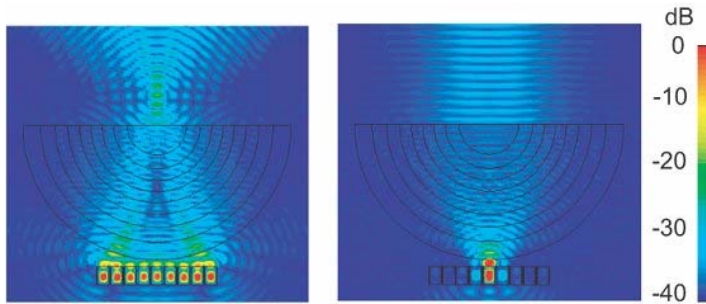


Fig. 26. A 9 - shells 60mm diameter HMFE lens associated with a sources array to shape the beam - left : A sectorial pattern is achieved if several sources feed the lens, right : A directive pattern is achieved if only one source feed the lens

HMFE lens and a sources array – Simulation results at 77 GHz

We show (Fig. 27) the achieved radiation patterns for different configurations when 1, 3, 5, 7 or 9 waveguides feed the lens. The directivity can be modified between 20 and 31 dBi. More the number of sources is high and more we obtain a wide beam (Fig. 28). With this configuration, the beam width in the H plane is comprised between 5° (1 fed source) and 70° (9 fed sources).

Furthermore, in this case, for the E plane, the beam width pattern is always narrow thanks to the focusing capability of the lens. But it could be possible to shape the radiation pattern in both H and E planes simultaneously using a 2D sources array.

Thus, an easy reconfigurable antenna can be optimized by using only switches to control the number of active sources.

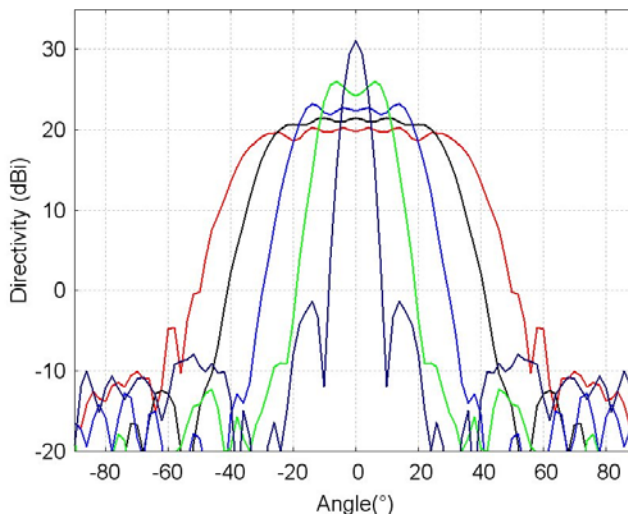


Fig. 27. A 9 - shells 60mm diameter HMFE lens associated with a sources array to shape the beam - Simulated radiation patterns when 1, 3, 5, 7 or 9 waveguides feed the lens

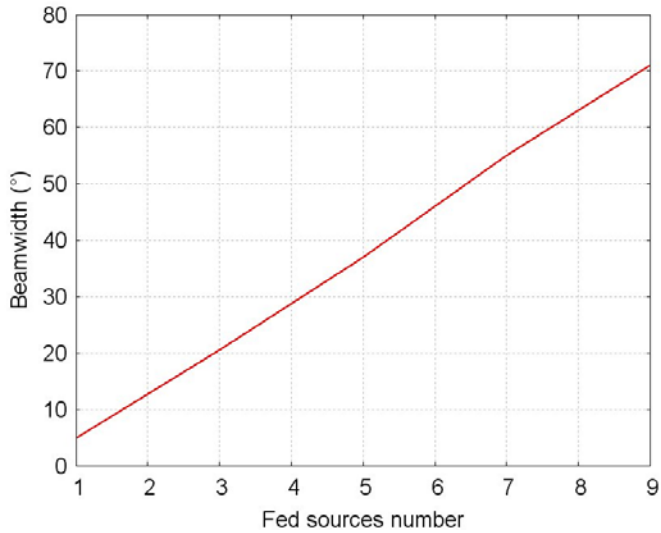


Fig. 28. A 9 - shells 60mm diameter HMFE lens associated with a sources array to shape the beam - Simulated beam width versus the fed sources number in the array

Besides, this antenna system also allows having beam scanning properties. Indeed, for example, if a 3 sources group is considered and feeds the lens, the radiation pattern can scan if one moves the fed sources group (Fig. 29). An off-axis sectorial beam is shown because many sources feed the lens simultaneously (Fig. 30).

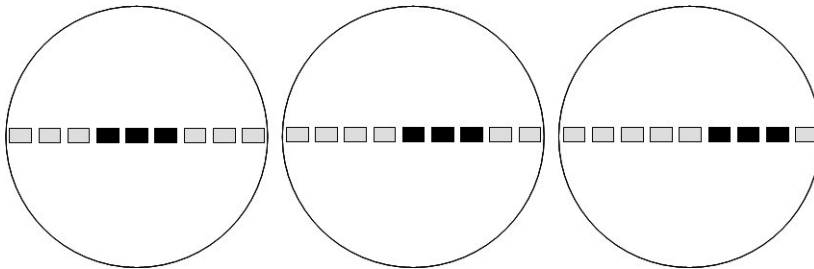


Fig. 29. A 9 - shells 60mm diameter HMFE lens associated with a fed, sources group that moves under the lens

HMFE lens and an active sources array - Measured results at 24 GHz

In this section, an active sources array is considered and feed the lens to validate the radiation pattern agility presented before. This active prototype is based on the active HPBW reconfigurable antenna shown in the section 3.3. This multilayer printed antenna array is composed of four slot coupled patches and each of them is fed via a LNA amplifier switch (Fig. 31a). First, the passive multilayer printed antenna fed the 9-shells HMFE lens to simulate the global design (Fig. 31b).

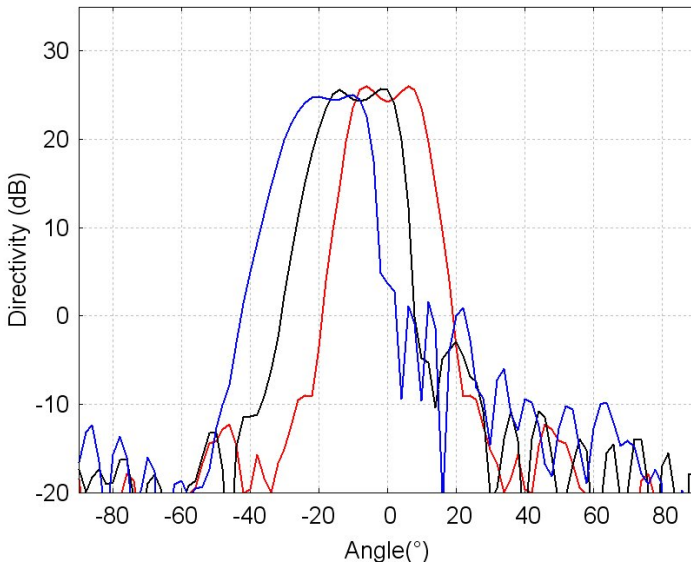


Fig. 30. A 9 - shells 60mm diameter HMFE lens associated with a fed, sources group that moves under the lens - Simulated off axis sectorial radiation patterns

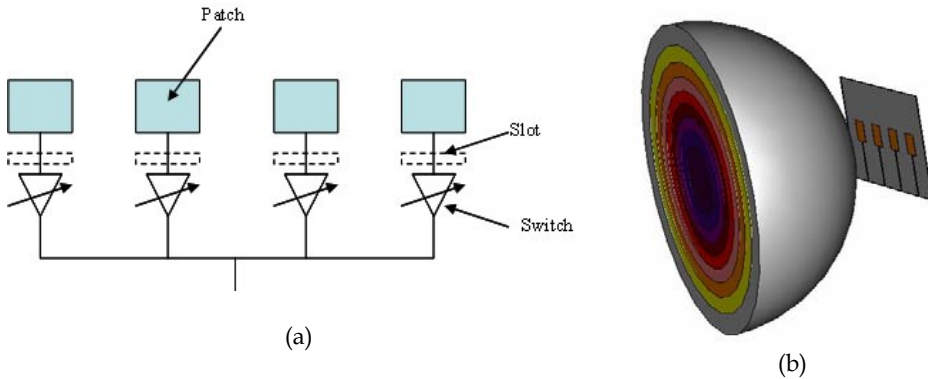


Fig. 31. (a) The active HPBW reconfigurable antenna based on multilayer printed antennas and switches, (b) Association with the HMFE lens

Two configurations are considered in simulation : two fed patches to obtain a directive pattern and four fed patches to obtain a sectorial one. The simulated radiation patterns are shown in Fig. 32 for both cases. The measured radiation patterns are shown on Fig. 33 and are in good agreement with simulation results. If the two central patches feed the lens, a directive pattern is achieved with a 25° beam width and a 22.5 dB gain. If all the patches feed the lens, a sectorial pattern is obtained with a 58° beam width and a 19dB gain. The beam in the E plane is narrow thanks to the focusing capacity of the lens.

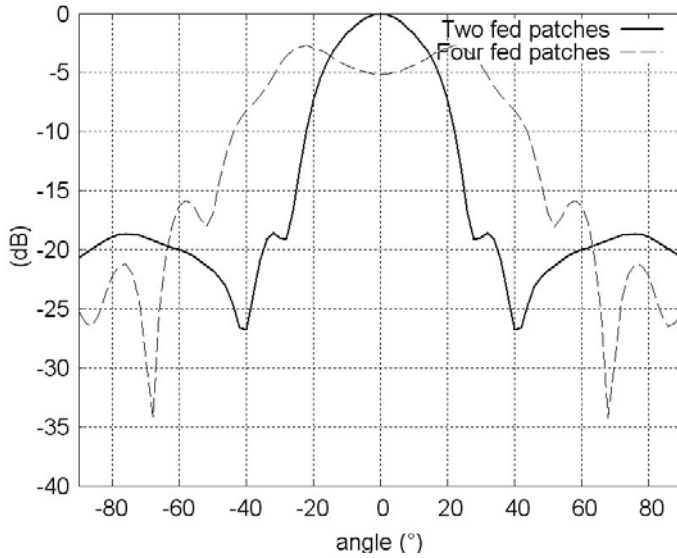


Fig. 32. A 9 - shells 60mm diameter HMFE lens fed by the multilayer printed array - Simulated radiation patterns for two configurations

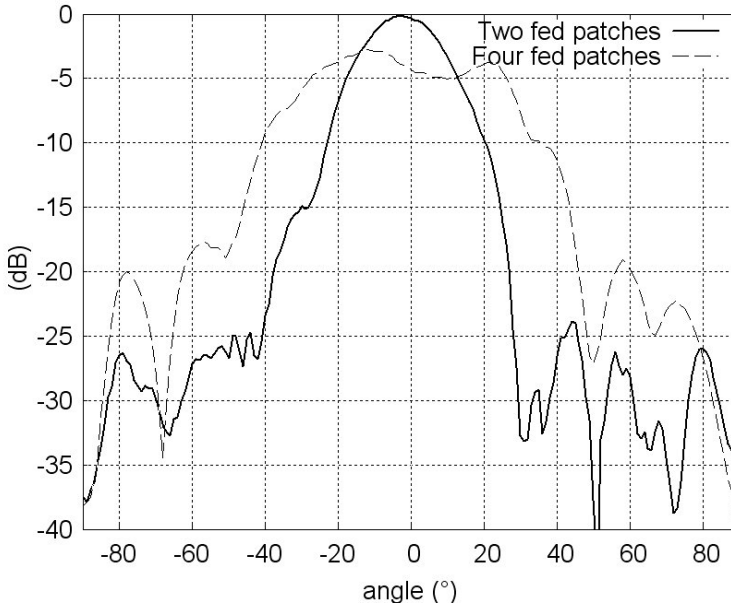


Fig. 33. A 9 - shells 60mm diameter HMFE lens fed by the multilayer printed array - Measured radiation patterns for two configurations

All these results show that it is possible to obtain a reconfigurable radiation pattern antenna based on a HMFE lens fed by an active sources array. A Sectorial radiation pattern for example can be improved without phase shifters but with only RF switches, that is an advantage because millimetre wave phase shifter are often expensive and have bad performances in term of losses.

5. Conclusions

In the section 2 of this chapter, the potential of the Butler matrix system has been demonstrated for the design of active multibeam antennas in millimetre waves. But, metallic and dielectric losses in the feeding network of the Butler matrix induce a quite low efficiency. Currently, works are investigated to design a such system using Substrate Integrated Waveguide to improve the gain and the efficiency.

In the section 3, an active tunable HPBW printed antenna has been demonstrated at 24 GHz. This prototype allows to vary the half-power beamwidth of the antenna by changing the number of fed patches in the array. To achieve this result, the design of a switch based on a FET transistor has been proposed. The matching of this antenna is obtained whatever the number of fed patches by modifying the characteristic impedance of a quarter wavelength transformer.

Finally, authors have shown an innovative antenna system based on inhomogeneous lens (half Maxwell Fish Eye lens) and fed by several sources. With this antenna concept, it is possible to obtain beam steering and beam shaping capabilities without phase shifters to improve gain and efficiency.

6. References

- Wenger, J. (2005). 'Automotive radar - Status and perspectives', in Proc. IEEE Compound Semiconductor Integrated Circuit Symposium, 2005.
- Butler, J & Lowe, R. (1961). 'Beam-forming matrix simplifies design of electrically scanned antennas', *Electronic Design*, Vol. 9, pp. 170-173, April 1961.
- Blass, J 'Multi-directional antenna : new approach top stacked beams', IRE International Convention record, Pt. 1, pp. 48-50, 1960.
- Rotman, W & Turner, R. F. (1963) 'Wide-angle microwave lens for line source applications', *IEEE Trans. Antennas Propag.*, Vol. 11, No. 6, pp. 623-632, November 1963.
- Schulwitz, L & Mortazawi, A. (2006). 'A New Low Loss Rotman Lens Design for Multibeam Phased Arrays', in Proc. IEEE MTT-S Int. Microwave Symp. Dig., pp. 445-448, June 2006.
- Baek, C-W & al. (2003). 'A V-band micromachined 2-D beam-steering antenna driven by magnetic force with polymer-based hinges', *IEEE Trans. Microw. Theory Tech.*, Vol. 51, No. 1, pp. 325-331, January 2003.
- Cetiner, B.A & al. (2003). 'Monolithic integration of RF MEMS switches with a diversity antenna on PCB substrate', *IEEE Trans. Microw. Theory Tech.*, Vol. 51, No. 1, pp. 332-335, January 2003.
- Popovic, D & Popovic, Z. (2002). 'Multibeam Antennas With Polarization and Angle Diversity', *IEEE Trans. Antennas Propag.*, pp. 651-657, Vol. 50, No. 5, May 2002.

- Wu, X; Eleftheriades, G.V. & Van Deventer-Perkins, T.E. (2001). 'Design and characterization of single- and multiple-beam mm-wave circularly polarized substrate lens antennas for wireless communications', *IEEE Trans. Microw. Theory Tech.*, Vol. 49, No. 3, pp. 431-441, March 2001.
- Lafond, O. & Himdi, M. (2002). 'Multibeam antenna in millimetre waves', in *Proc. of the 32nd European Microwave Conference (EuMC)*, Milan, September 2002.
- Lafond, O.; Himdi, M. & Daniel, J.P. (1999). 'Aperture coupled microstrip patch antenna with thick ground plane in millimeter-waves,' *Electronics Letters*, Vol. 35, no. 17, pp. 1394-1396, August 1999.
- Lafond, O.; Himdi, M.; Daniel, J.P & Haese-Rolland, N. (2002). ('microstrip / Thick-slot / microstrip transitions in millimeter-waves,' *Microwave and Optical Technology Letters*, Vol. 34, Issue 2, pp. 100-103, July 2002.
- Lafond, O.; Himdi, M; Vendier, O. & Cailloce, Y. (2005). 'Thick-slot transition and antenna arrays in the Q band,' *Microwave and Optical Technology Letters*, Vol. 44, Issue 1, pp. 24-29, January 2005.
- www.macom.com/Products/switches.htm
- Rebeiz, G. M. (2003). 'RF MEMS: Theory, Design and Technology,' Wiley- Interscience, February 2003.
- www.quinstar.com/qwz_electromechanical_waveguide_switches.html
- Caillet, M.; Lafond, O. & Himdi, M. (2006). 'A Directivity Diversity Microstrip Antenna Array in Millimeter Wave,' *Microwave Opt. Tech. Letters*, Vol. 48, No. 6, pp. 1190-1194, June 2006.
- Caillet, M. (2006). 'Etude et Conception d'un système Radar Courte Portée et d'Antennes Reconfigurables en Bande Millimétrique,' Thèse de l'Université de Rennes 1, 2006.
- Luneburg, R.K. (1944). 'Mathematical theory of optics,' Providence, Rhode Island, Brown University Press, 1944.
- Lafond, O; Himdi, M; Rondineau, S. & Fuchs, B. (2007) . 'Lentilles inhomogènes à gradient d'indice de type œil de Poisson de Maxwell, système d'antennes et applications correspondantes', French Patent n° 2888407 (2007).
- Fuchs, B; Lafond,O; Rondineau, S & Himdi, M. (2006). 'Design and characterization of half Maxwell fish-eye lens antennas in millimeter waves,' *IEEE Trans. Microwave Theory Tech.*, vol. 54, no. 6, pp. 2292-2300, June 2006.
- Fuchs, B; Le Coq, L; Lafond,O; Rondineau, S & Himdi, M. (2007), "Design Optimization of Multi-Shell Luneburg Lenses," *IEEE Transactions on Antennas and Propagation*, vol.55, n°2, pp. 283- 289, Feb 2007.
- Fuchs, B. (2007). 'Lentilles stratifiées et Sources réelles associées - Analyses théoriques et validations expérimentales en Ondes Millimétriques', Thèse de l'Université de Rennes 1, 2007.
- Fuchs, B; Lafond,O; Rondineau, S & Himdi, M & Le Coq, L. (2007). 'Off-Axis Performances of Half Maxwell Fish-Eye Lens Antennas at 77GHz,' *IEEE Transactions on Antennas and Propagation*, vol.55, n°2, pp. 479- 482, Feb 2007.
- Fuchs, B; Palud, S; Lafond,O; Rondineau, S; Himdi, M & Le Coq, L,: 'Système antennaire dont le diagramme de rayonnement est reconfigurable parmi des diagrammes de rayonnement sectoriels et directifs, et dispositif émetteur/ou récepteur correspondant', French Patent n° R13414FR (2007).

- Lafond, O; Caillet, M; Fuchs, B; Palud, S; Himdi, M ; Rondineau, S & Le Coq, L. (2008) 'Millimeter Wave Reconfigurable Antenna Based on Active Printed Array and Inhomogeneous Lens, 'EUMW 2008, Amsterdam, October 2008.
- Lafond, O; Fuchs, B; Palud, S; Caillet, M; Himdi, M ; Rondineau, S & Le Coq, L. (2009), 'Reconfigurable antenna in mm-waves based on stratified lens and sources array, 'EUCAP 2009, Berlin, March 2009.

Characteristics of High-Gain Wideband Ring Loop Antenna and its Application

Haruo Kawakami
Antenna Giken Corp.
Japan

1. Introduction

Digital terrestrial broadcasting services are in the Japanese UHF band of 470 to 770 MHz. The bandwidth of the UHF-TV channel is 6 MHz. In this paper we investigate the ring loop antenna for the UHF digital terrestrial broadcasting. The characteristics of the linear ring loop and circular ring loop antenna are calculated by NEC-WIN Pro. We evaluate the characteristics of these antennas in the Japanese UHF-TV broadcasting band (470MHz-770MHz).

A broadband antenna consisting of the ring loop antenna is presented for the digital terrestrial broadcasting. A ring loop antenna is excited by a simple and low-cost feeder system. The broadband input impedance and the high gain are obtained in the calculation and the measurement.

The input impedance became 50Ω and wideband characteristics were obtained in the simple power supply construction. Then the high-gain and wideband characteristics were obtained with the simple power supply construction. This antenna has sufficient characteristics as the transmitting antenna for digital terrestrial broadcasting stations and repeater stations in the Japanese UHF band.

The characteristics of the ring loop antenna were calculated using the moment method proposed by Harrington[1][2], who conducted experiments on this antenna.

This antenna examined the ring loop antenna with which circumference length fed in parallel in about full-wavelength of loop antenna element as an antenna for digital terrestrial broadcasting. That is, numerical analysis was performed about conditions for both the directivity of the ring loop antenna of many stages and the impedance characteristic to show the broadband characteristic. It is the ring loop antenna of the structure, which carried out parallel electric feed of all the elements in this antenna, added one reflector element, and was arranged to the vertical form. All number element of the antenna was consisted of sum total of 5-elements of director element of 3-elements, radiator element, and compound reflector element. This antenna it was the simple structure in order to solve the problem, and the diameter was small, and the miniaturization was possible, and again, it developed ring loop antenna (RLA) for the digital terrestrial broadcasting of which

good voltage standing wave ratio (VSWR) characteristics over all bands in the use frequency band was obtained. That is to say, the circumference length parallels supplied loop antenna element of the about one wavelength on the 5-element loop antenna. Both directionalities, impedance characteristic show wide-band characteristics on the loop antenna. The next high-gain ring loop antenna element for the digital terrestrial broadcasting with wide-band characteristics is described. As a feed circuit of the log-periodic structure, the condition as radiation pattern and impedance characteristic of ring loop antenna of the 12-elements together showed wide-band characteristics was analyzed numerically in respect of all component count.

It is possible that it is high-gain by arranging loop antenna element of the 12-elements, and again, that it gets the good antenna of impedance characteristic with the feeder circuit of the log-period structure.

The Log-Periodic antenna did the feeder circuit system in the log-period structure, and the constant of the antenna structure was made to be $\tau = 0.9$ and $\sigma = 0.16$. And, it was made to change at $W_0 = 50\Omega - 200\Omega$ characteristic impedance of the feeder, and it was made to be optimum value $W_0 = 70\Omega$. The antenna element number is wide-band ring loop antenna of the $N=12$ structure which lined up vertically.

The ring loop antenna to which the circumference length parallel supplied loop antenna element of the about one wavelength in the previous paper was described. This antenna described the antenna which constituted the circularly polarized wave characteristics in order to use for the experiment which verifies the digital broadcasting system using the airship which does the fixed point stay in ground station, and it described the condition necessary for generating the circularly polarized wave.

This antenna was used as an antenna of the digital terrestrial broadcasting experiment with the airship in NICT, and it got the result of the good reception experiment.

Finally, characteristics of the 16-element ring antenna are shown. This antenna was used as an antenna for the transmission, and it was used as repeater antenna, and wide band, high gain, low-cost and simple structure, miniaturization were made to be a goal.

2. Moment Method

2.1 Thin wire

This antenna discusses with the moment method proposed by Harrington and deals with the Galerkin's method where antenna current is developed using triangle function and the same weight function as the current development function is used. The Galerkin's method can save calculation time because the coefficient matrix is symmetrical, and the triangle function is widely used because it presents a better performance in calculation time and accuracy, etc. for an antenna element without sudden change in antenna current.

Scattering electric field E^s by antenna current and charge is given by

$$E^s = -j\omega A - \nabla\phi \quad (1)$$

Vector potential A and scalar potential ϕ are given by

$$A = \frac{\mu}{4\pi} \iint_S J \frac{e^{-jkr_0}}{r_0} dS \quad (2a)$$

$$\phi = \frac{1}{4\pi\epsilon} \iint_S \sigma \frac{e^{-jkr_0}}{r_0} dS \quad (2b)$$

The following relation exists between charge density σ and current J

$$\sigma = \frac{-1}{j\omega} \nabla \cdot J \quad (2c)$$

Now, assuming that the surface of each conductor is perfect conductor and letting E^i be incoming electric field, the following equation must hold true:

$$n \times E^S = -n \times E^i \quad (3)$$

The following simultaneous equation holds true from the boundary condition of the antenna surface of this antenna system:

$$\sum_{i=1}^N I_i \langle W_j, E_{\tan}^i \rangle, \quad (i=1, \dots, N, \quad j=1, \dots, M) \quad (4)$$

where L is the operator for integration and differentiation. Current is given, from (4), by

$$[I_i] = \left[\langle W_j, LF_i \rangle \right]^{-1} \left[\langle W_j, E_{\tan}^i \rangle \right] \quad (5)$$

and the matrix representation of (5) gives (6).

$$[I] = [Z]^{-1} [V] \quad (6)$$

Now, let the current at point t on each element be represented by

$$I(t) = \hat{t} \sum_{i=1}^N I_i T_i(t) \quad (7)$$

where \hat{t} is the unit vector in the direction of antenna axis, and coefficient I_i is the complex coefficient determined by boundary condition. Letting $T_i(t)$ be the triangle development function, $T_i(t)$ is given by (8),

$$T_i(t) = \begin{cases} 1 - \frac{|t-t_i|}{\Delta l_i} & t_{i-1} < t < t_{i+1} \\ 0 & \text{elsewhere} \end{cases} \quad (8)$$

where for $\Delta l_i = t_i - t_{i-1}$ and for $\Delta l_i = t_{i+1} - t_i$.

Impedance matrix Z in (6) is given by (9),

$$Z_{ji} = \int_{axis} dl \int_C dl' \left[j\omega\mu W_{jm} F_{in} + \frac{1}{j\omega\epsilon} \frac{dW_{jm}}{dl} \cdot \frac{dF_{in}}{dl'} \right] \frac{e^{-jk r_0}}{4\pi r_0} \quad (9)$$

where C represents an antenna surface l' parallel to the antenna axis l . F_{in} and W_{jm} are divided into four in the triangle development function shown in Fig.1, the triangle is configured so that the value is one at the center, and the divided antenna elements are obtained approximately by the four pulse functions. The expansion equation of (5) is used for Green function.

2.2 Thick wire

As shown in Fig.2, a monopole antenna excited by a coaxial cable line consists of a perfectly conducting body of revolution being coaxial with the z-axis. Conventionally, the integral equation is derived on the presumption that the tangential component of the scattered field cancels the corresponding impressed field component on the conductor surface.

Alternately, according to the boundary condition proposed by Dr. P. C. Waterman [3], an integral equation can be derived by utilizing the field behavior within the conductor. Also, the conventional integral equation has a singular point when the source and the observation point are the same. On the other hand, the integral equation, after Waterman, is well behaved, and so it is more convenient for numerical calculation. When applying the extended boundary condition to an antenna having an axial symmetry as shown in Fig.2, the axial component of the electric field is required to vanish along the axis of the conductor.

More explicitly, on the axis inside the conductor, the axial component of the total field is the sum of the scattered field (the field from current on the conductor) and the impressed field (the field from excitation). The corresponding integral equation is written as

$$\frac{j\eta}{4\pi k} \int_{-h}^h I_z(z') \left(k^2 + \frac{\partial^2}{\partial z^2} \right) G(z, z') dz = E_z^{inc} \quad (10)$$

$$I_z(\pm h) = 0$$

$$\text{with } G(z, z') = \frac{e^{-jk\sqrt{(z-z')^2+a^2}}}{\sqrt{(z-z')^2+a^2}} \text{ and } k = \frac{2\pi}{\lambda}, \quad \eta = 120\pi, \quad I_z = 2\pi a J_z$$

This integral equation reduces to the well-known equation (11) when the current is assumed to be zero on the antenna end faces:

$$\frac{j\eta}{4\pi k} \left\{ k^2 \int_S J_z(z') G(z, z') ds' + \frac{\partial}{\partial z} \int_S \nabla' \cdot J G(z, z') ds' \right\} = E_S^{inc} \quad (11)$$

Taking the current at the end faces into account, (11) becomes

$$\begin{aligned} \frac{j\eta}{4\pi k} \left\{ k^2 \int_{-h}^h I_z(z') G(z, z') dz' + \frac{\partial}{\partial z} \int_{-h}^h \frac{\partial I_z(z')}{\partial z'} G(z, z') dz' \right. \\ \left. + \frac{\partial}{\partial z} \int_{S'} \frac{1}{\rho'} \frac{\partial J_\rho(\rho')}{\partial \rho'} G(z, z') ds' = E_S^{inc}, \quad ds' = \rho' d\phi' d\rho' \right\} \end{aligned} \quad (12)$$

where, on the end surface S' , a in $G(z, z')$ becomes ρ .

Dr. C. D. Taylor and Dr. D. R. Wilton[4] analyzed the current distribution on the flat end by a quasi-static type approximation method; the resulting theoretical and experimental values were in good agreement. This analysis makes the same assumption that, as show in Fig.3, the current flowing axially to the center of the end surface without modification.

In applying the moment method, sinusoidal functions were used as expansion and weight functions. Accordingly, the Galerkin's method was used to generate the integral equation.

Notice that the expansion and weight functions have been changed only on the dipole end faces. This is done so that the impedance matrix becomes symmetrical for the end current and for the current flowing on the antenna surface (excluding the antenna end face).

Expanding the unknown current in terms of sine functions, we have

$$I_z(z') = \sum_{n=1}^N I_n F_n \quad (13)$$

If the expansion functions are overlapped,

$$F_n = \begin{cases} \frac{\sin k(\Delta - |z' - z_n|)}{\sin k\Delta} & z' \in (z_{n-1}, z_{n+1}) \\ 0 & z' \notin (z_{n-1}, z_{n+1}) \end{cases} \quad (14)$$

$$\Delta = |z_{n+1} - z_n|$$

where z' indicates an axial coordinate taken along the conductor surface. Equations (13) and (14) are substituted into (12) to obtain

$$\begin{aligned}
& \frac{j\eta}{4\pi k \sin k\Delta} \sum_{n=1}^N I_n \left[\int_{z_{n-1}}^{z_{n+1}} G(z, z') \left(k^2 + \frac{d}{dz'^2} \right) F_n dz' + \right. \\
& k \{ G(z, z_{n+1}) + G(z, z_{n-1}) - 2 \cos k\Delta G(z, z_n) \} \\
& \left. + \frac{j\eta}{4\pi k} \frac{\partial}{\partial z} \int_{s'} \frac{1}{\rho'} \frac{\partial J_\rho(\rho')}{\partial \rho'} G(z, z') ds' = E_z^{inc} \right] \quad (15)
\end{aligned}$$

The first term in the integral is zero because F_n consists of sine functions. Assuming that

$$E_z^{end} = \frac{j\eta}{4\pi k} \frac{\partial}{\partial z} \int_{s'} \frac{1}{\rho'} \frac{\partial J_\rho(\rho')}{\partial \rho'} G(z, z') ds' \quad (16)$$

then (15) becomes

$$\frac{j\eta}{4\pi \sin k\Delta} \sum_{n=1}^N I_n \{ G(z, z_{n+1}) + G(z, z_{n-1}) - 2 \cos k\Delta G(z, z_n) \} + E_z^{end} = E_z^{inc} \quad (17)$$

Applying a weight function of the same form as (13) and taking the inner product of both sides of (17) and the weight function, the equation becomes

$$\begin{aligned}
& \frac{j\eta}{4\pi \sin k\Delta} \sum_{n=1}^N I_n \langle G(z, z_{n+1}) + G(z, z_{n-1}) - 2 \cos k\Delta G(z, z_n), W_m \rangle \\
& + \langle E_z^{end}, W_m \rangle = \langle E_z^{inc}, W_m \rangle \quad (m = 1, 2, \dots, N) \quad (18)
\end{aligned}$$

where

$$W_m = \begin{cases} \frac{\sin k(\Delta - |z - z_m|)}{\sin k\Delta} & z \in (z_{m-1}, z_{m+1}) \\ 0 & z \notin (z_{m-1}, z_{m+1}) \end{cases} \quad (19)$$

$$\Delta = |z_{m+1} - z_m|$$

Here z indicates a coordinate taken on the axis. The above results can be expressed in matrix form as

$$[Z][I] = [V] \quad (20)$$

The impressed field E_z^{inc} of the $[V]$ matrix is considered to be excited by a frill of magnetic current[5] across the aperture of the coaxial cable line feeding a monopole as shown in Fig.2. In other words, assuming the field on the aperture of a coaxial cable line at $z = 0$ to be identical to that of a transverse electromagnetic (TEM) mode on the coaxial transmission line, the equivalent frill of magnetic current can be determined. And, by considering the image of an excitation voltage as V_0 , and the inner diameter and outer diameter of the coaxial cable line by a and b , respectively, it follows that

$$E_z^{inc} = \frac{V_0}{2l_n(b/a)} \left\{ \frac{e^{-jk\sqrt{z^2+a^2}}}{\sqrt{z^2+a^2}} - \frac{e^{-jk\sqrt{z^2+b^2}}}{\sqrt{z^2+b^2}} \right\} \quad (21)$$

2.3 Charge density and current on end faces

Now, we proceed with the study of the current over the antenna end surface. We presume that the current is zero at the center to the edge (in the case of a thin cylindrical antenna, the end current is assumed to be zero as shown by the dotted line the figure). If we express the total charge on the end surface by Q and its radius by a , then the charge density, σ , and the current density, J_ρ , are given by

$$\sigma = \frac{Q}{\pi a^2}, \quad J_\rho = \frac{-j\omega Q}{2\pi a^2} \rho \quad (22)$$

Also, by the current continuity condition on the edge, we have

$$Q = \pm \frac{I_z(z')}{j\omega} \quad (23)$$

Furthermore, the axial component of the field strength on the z -axis, produced by sources on the end surfaces, is given by

$$E_z = \pm \frac{j\eta I_z(z')}{2\pi k a^2} (z - z') \left\{ \frac{e^{-jk\sqrt{(z-z')^2+a^2}}}{\sqrt{(z-z')^2+a^2}} - \frac{e^{-jk|z-z'|}}{|z-z'|} \right\} \quad (24)$$

We impose the boundary condition that the total axial field is zero in the range of $-h < z < h$, not including $z = \pm h$. Now, if we select the end face weight functions to be the same as the expansion functions, it follows that the same weight function will also be applied to the end faces $z = \pm h$, as shown in Fig.3.

Referring to the difference between the analysis of Taylor and Wilton and that presented here, the former uses the point-matching method and is applied only to the body of revolution. On the other hand, the latter employs the Galerkin's method and is applied to antennas which are asymmetrical and which also contain discontinuities in the conductors. By using the moment method and taking the end surfaces into consideration, a relatively thick antenna can be treated.

For example, the calculated input admittance for $a = 0.0423\lambda$ and $b/a = 1.187$, is given in Fig.4, as a function of h . For comparison, the values measured by Holly[6] are also shown. In the calculation, the number of subsections, N , was chosen as 50 to 60 per wavelength. The theoretical values agree well with the measured values. Therefore, it is concluded that the analytic technique is adequate for thick cylindrical antennas.

3. Frequency Characteristics of Impedance and Radiation Pattern

Figure 5 showed the fundamental composition of the 5-RLA (Photo.1) for the wide-band digital terrestrial broadcasting. Theoretical calculation was carried out on these loop antenna by reception band (470-770MHz) for digital terrestrial broadcasting. The following are shown in Fig.5 horizontal of parallel feed loop antenna and frequency characteristics of the directionality in both vertical sides. The interval of the loop is the about 0.2λ for the center frequency. Especially, the loop interval could not see large difference on both directionalities and impedance in the $0.2-0.3\lambda$. The following were obtained: Horizontal directionality shown at Fig.7 (a) and vertical directionality shown in same Fig.7 (b).

In horizontal directionality shown at Fig.7 (a), the directionality over 8dB was obtained over 470-770MHz all UHF bands. And, it becomes almost similar characteristics in vertical directionality shown at Fig. 7(b) with the horizontal directionality.

And, 5-element composition linear polarization RLA VSWR characteristics of 470-770MHz in VSWR characteristics shown in Fig.6, about -7.5dB(VSWR=2.5) or less were obtained. Measured value and it Figure (b) of horizontal directionality of linear polarization RLA of the 5-element composition, which used the parallel feed system showed the measured value of the vertical directionality on Fig.7 (a). At Fig.7 (a), (b) and Figure have 3(a) and (b), the following are shown: Characteristics at 470MHz low frequency, characteristics at 620MHz center frequency, and directionality at 770MHz high frequency.

In horizontal directionality shown at Fig.7(a) and Fig.9 (a), the directionality over 8dBi was obtained over 470-770MHz all UHF bands. And, it becomes almost similar characteristics in vertical directionality shown at Fig.7 (b) and Fig.9 (b) with the horizontal directionality. In linear polarization RLA of the 5-element composition using the parallel feed system, good characteristics were obtained both horizontal directionalities and vertical directionalities. And, Fig.8 measured value parallel feed system 5-element composition linear polarization RLA VSWR characteristics and, characteristic impedance is 75Ω . Though the case in which it was made to constitute 5-elements the antenna, was shown, it is possible to make more and more to be the multiple-device composition. It is possible to improve the gain further by making to be the multiple-device composition. For example, it is possible to obtain the actual gain of about 10dBi, when it was made to be actual gain and 16-element composition of about 12dBi.

Next, the log-period type ring loop antenna was calculated on the basis of the theory. The dimension univocally depends on the value of τ , σ of the antenna constant on the interval of the loop. Frequency characteristics of the directionality in the horizontal plane of 12-element log-period type ring loop antenna and feed point are shown in Fig 10(a),(b). The impedance band is decided by the characteristic impedance of the antenna in this case of parallel line. The characteristic impedance of the antenna of This antenna shows frequency characteristics of VSWR voltage standing wave ratio using coaxial feed impedance $Z_0=50\ \Omega$ as $W_0=70\ \Omega$ in Fig.11. The voltage standing wave ratio characteristics shows the characteristics which are good over all bands, and it becomes under 2.0 over all bands in the UHF band almost. And, there is almost over 10dB for gains, and the before and behind ratio is also -20dB or less in Fig.12. An easy way to comply with the conference paper formatting requirements is to use this document as a template and simply type your text into it.

4. Ring Loop Antennas and its Application

4.1 Circularly polarized wave ring loop antenna

In the UHF band transmitting and receiving antenna, it is required the result to of be wide-band characteristics of linear polarization and circularly polarized wave. Until now, Yagi-Uda antenna of the linear polarization characteristics is mainly utilized in the transmitting and receiving antenna of the UHF band. However, the band property is narrow band on this Yagi-Uda antenna[7][8]. Therefore, in recent years, band property is improved using the looped antenna element, and circularly polarized wave Yagi-Uda array antenna, which enabled the circularly polarized wave, are considered.

However, the bandwidth is insufficient in superscription circularly polarized wave Yagi-Uda array antenna, because it has the very wide band in the UHF band. Then, establishing the one point reactance loading in radiating element, since circularly polarized antenna is constituted generates the circularly polarized wave. This antenna shown in Fig.13 showed the fundamental configuration example of 5-element circularly polarized wave ring loop antenna[9].

The reactance loading element was established 90° feeding point (the lower end division) feed line almost fixed position this circularly polarized wave ring loop antenna parallel feed system ring loop antenna radiating element. It becomes the right-hand circularly polarization in this case and the case in which the reactance loading element was established in right side of radiating element by viewing from the rear, as it is shown in Photo.2, and it becomes the left hand circularly polarized wave, when the reactance loading element was established at the left side of radiating element. Still, the case in which it is physically and electronically done is considered the reactance loading. The directionality of circularly polarized wave characteristics of circularly polarized wave ring loop antenna in the 5-element composition is shown in Fig.14. The good circularly polarized wave axial ratio characteristics were obtained. Figure 15 are the directionality (theory) in the basic configuration, and the value that it is the front face direction and that the axial ratio is good is shown. As a result, it was used as an antenna of the digital terrestrial broadcasting experiment with the airship in NICT(Photo.3), and the result of the good reception experiment was obtained.

The fundamental configuration example of 5-elements right-hand circularly polarization ring loop antenna :

Frequency band: 476-482MHz
 VSWR: All bands of 1.2 less than
 The gain: 8dB more than
 Right-hand circularly polarization characteristic: 3dB less than
 Characteristic impedance: 50 Ω

The VSWR characteristics: The reactance loading element is established 90° feeding point (the lower end part) feed line almost fixed position right-hand circularly polarization ring loop antenna parallel feed system ring loop antenna radiating element, and it is VSWR=1.2 less than at 476-482MHz (Fig.16).

The hand circularly polarization characteristics: The circularly polarized wave axial ratio characteristic of which the directionality (measured value) of circularly polarized wave characteristics of right-hand circularly polarization ring loop antenna in the 5-element composition was good was obtained.

The axial ratio is good in the front face direction of the directionality (theory) in basic configuration.

4.2 Circularly polarized wave ring loop antenna and its application

The following were carried out : Transmitting and receiving antenna for ground digital broadcasting and design for practical application of transmission receiving antenna of repeater station, trial manufacture. There is sufficiently a practicability on the wide-banding of this antenna and can be carried out. And, circularly polarized wave ring loop antenna can be realized without changing the composition of linear polarisation ring loop antenna by establishing the reactance loading element in the radiating element. Circularly polarized wave ring loop antenna also succeeded on the experiment which verified digital broadcasting experimental system with airship [10] for fixed point stay in air by NICT in November, 2004 Hokkaido Daiki experiment station in photo.3, and it was able to be used for the application to the urgent broadcasting in the disaster prevention, and the good reception experiment had been obtained, and it was realized for the expectation of the party.

4.3 Multi-ring loop antenna

Photo.4 supplies the loop in the symmetrical parallel feed element, and in addition, this is parallelly connected, and the guided wave element is arranged at the front, and loop antenna of the structure which arranged the reflection element rear are called the symmetrical parallel feed.

The type of the frequency band was divided into A,B,C, and the C- type made low-pass range, B- type medium range, A- type to be the high pass range in respect of each channel. Figure 17 shows horizontal of B- type by the symmetrical parallel feed of the 16-element ring loop antenna and pattern in the vertical plane. Almost similar characteristics in the vertical plane pattern with the horizontal plane pattern were obtained, as it was shown in the same figure. Figure 18 showed VSWR characteristics in the B- type. By going 530MHz-690MHz in VSWR characteristics shown in Fig.18, VSWR=2.0 or less than was obtained. The gain over 14dBi was obtained Fig. 19 over all UHF bands. Table 1 shows the specification for the 16-element ring loop antenna .

4.4 Ring loop antenna for pattern synthesis

The result of the pattern synthesis on the composition which placed the #1 and #2 antenna in the 90° direction, as it is shown in Photo.5, is described. The composition layout drawing is shown in Fig.20. It is necessary to contribute to the uniform electric field in the district limited to the range in which service area is very narrow in the service area direction. The directionality in supplying the #2 antenna with the current of $1\angle 0(\text{deg.})$ and $1\angle 90(\text{deg.})$ and $1\angle 180(\text{deg.})$ in making the #1 antenna with reference value of $1\angle 0(\text{deg.})$ in order to obtain the sectorial directionality in the horizontal plane in the reason, is shown in Fig. 21. The improvement in the poor televiewer in broadcasting area is possible by constituting like this. Table 2 shows the specification of ring loop antenna for pattern synthesis

5. Conclusions

It was possible to make the wide-band antenna using the loop antenna, which arranged circumference length about one wavelength loop antenna vertically. It was possible that the miniaturization became possible in the element composition of the simple shape, and again, that it realizes wide-band and high-gain linear polarization RLA. And, though in this RLA, UHF band receiving antenna for the general of the 470-770MHz band was explained as an example, there is sufficiently a practicability and so on this as transmission receiving antenna of the repeater station for the digital terrestrial broadcasting and can be carried out. By the element composition of the simple shape, the antenna element was united with feeder circuit, and light weight and miniaturization became possible, and it was possible to realize wide-band and high-gain linear polarization RLA which moreover, it covers the all UHF bands.

Theoretical calculation and measured value were performed about two kinds of above-mentioned ring loop antennas in the zone (470-770MHz) for digital terrestrial broadcasting. As a result, the VSWR characteristic is about 2.5 or less over all the zones of a UHF band, and a gain is about 8.0-10 dBi or more. It was possible to make the wide-band antenna using ring loop antenna, which arranged the circumference length about one wavelength ring loop antenna in the log-period structure. It was possible to make to be circularly polarized wave ring loop antenna This antenna without changing the composition of linear polarization ring loop antenna by establishing the reactance loading element in radiating element. And, UHF band receiving antenna for the general of the 470-770MHz band was explained as an example, and it can be carried out and so on as a transmitting and receiving antenna of repeater station for the digital terrestrial broadcasting for example.

6. References

- [1] R.F.Harrington, *Field Computation By Moment Method*, New York, Macmillan,1968.
- [2] R.F.Harrington, "Matrix Method for Field Problems," *Proc.IEEE*, vol.55, no.2, pp.136, Feb. 1967.
- [3] P.C.Waterman, "Matrix formulation of electromagnetic scattering" *Proc.IEEE*, vol.53, no.8, pp.785, Aug. 1965.
- [4] C.D.Taylor and D.R.Wilton, "The extended boundary condition solution of the dipole antenna of revolution" *IEEE Trans. Antennas & Propag.*, AP-20,6,pp.772,Nov.1972.

- [5] L.L.Tsai, "Numerical solution for the near and far field of an annular ring of magnetic current", IEEE Trans. Antennas & Propag., AP-20,5, pp.569, Sept.1972.
- [6] R.W.P.King, Tables of antenna characteristics, New York, IFI/Plenum, 1971.
- [7] H.Yagi and S.Uda, "Projector of the Sharpest Beam of Electric Waves," Proc. Proceedings of the Imperial Academy, vol.2, no.2, Feb. 1926.
- [8] S.Adachi and Y. Mushiake, "Directive Loop Antennas" *SCI. REP. RITU, B-(Elect. Comm.) Vol. 9 No.2 ,pp.105-112,Sept. 1957.*[9] H.Kawakami, T.Haga, S.Kon, M.Arishiro, and T.Yamashita, "Characteristics of Wideband Ring Loop Antenna for Digital Terrestrial Broadcasting," in Proc. of 2005 IEEE AP-S Conference, 2B, 544, July 2005.
- [10] M. Nagatsuka, M. Suzuki and R. Miura, "A Digital Broadcasting Experiment using an Autonomous Stationary-keeping Airship" *ITE. 61, 4, pp.533-542 (2007) (in Japanese).*

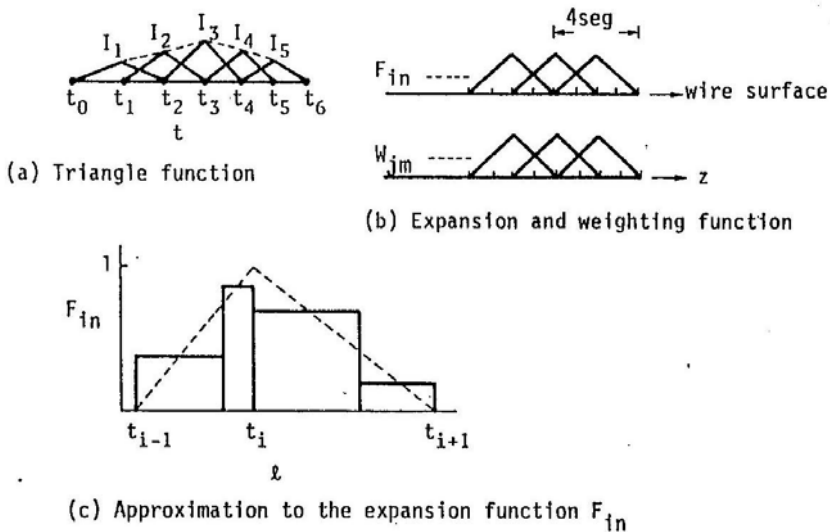


Fig. 1. Approximation to the expansion and weighting function

- (a) Triangle function
- (b) Expansion and weighting function
- (c) Approximation to the expansion function F_{in}

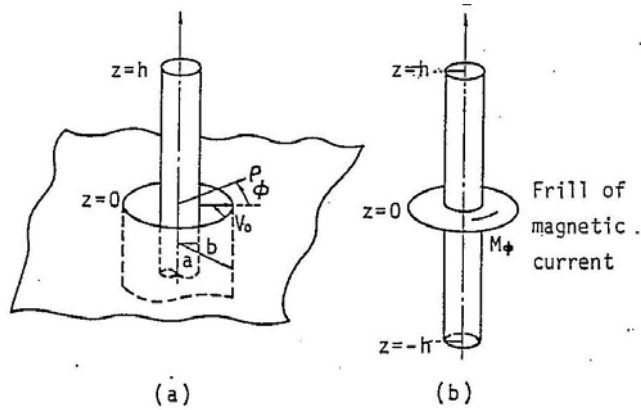


Fig. 2. Coaxial cable line feeding a monopole through a ground plane and mathematical model of the antenna

- (a) Coaxial cable line feeding a monopole through a ground plane
- (b) Mathematical model of the antenna

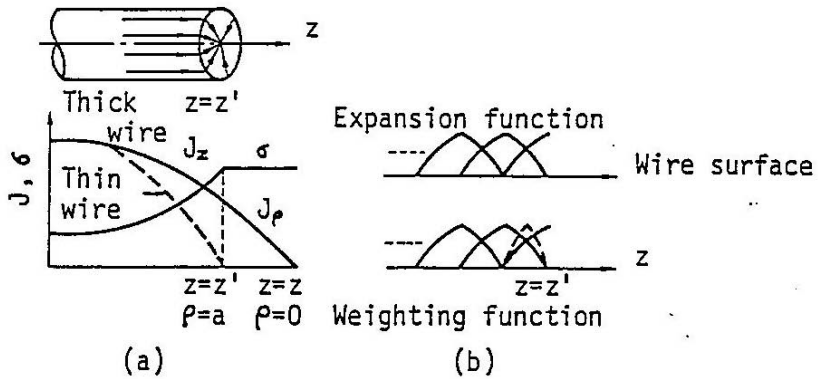


Fig. 3. Current and charge for flat end faces, expansion and weighting function

- (a) Current and charge for flat end faces
- (b) Expansion and weighting function

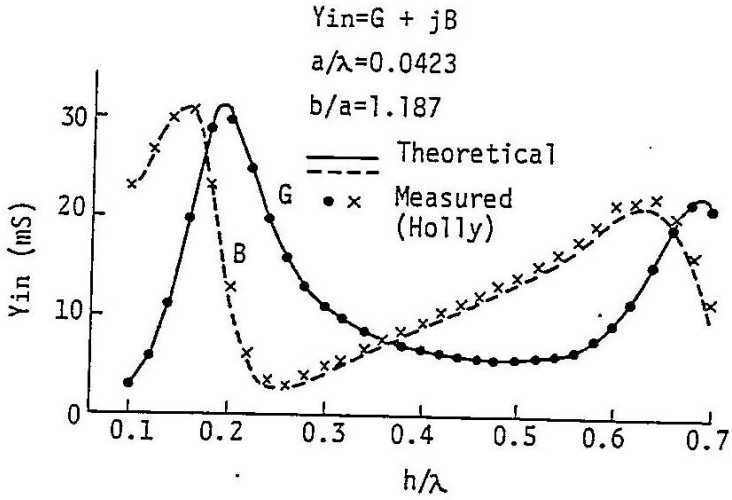


Fig. 4. Input admittance of thick-cylindrical antenna

3-Ring Reflector Element

Main Radiator Element

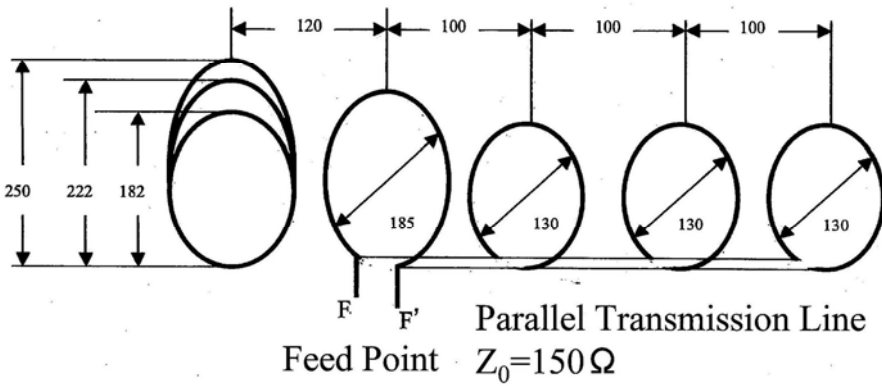


Fig. 5. Structure of RLA



Photo 1. Trial manufacture of RLA

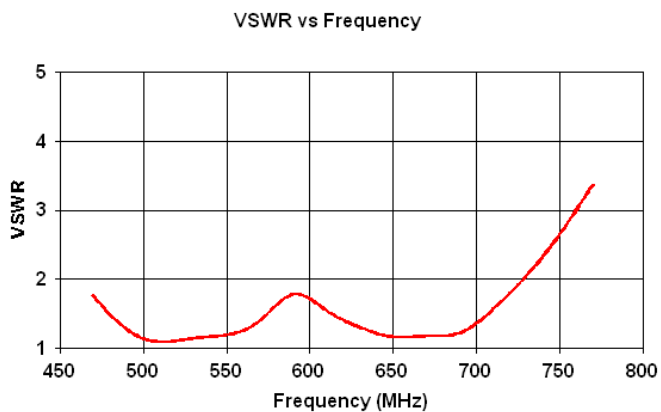


Fig. 6. VSWR characteristics of RLA (Theoretical Value)

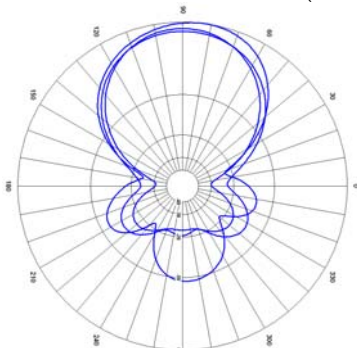


Fig. 7. (a) Horizontal Radiation Pattern

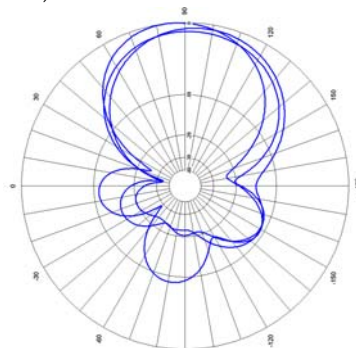


Fig.7 (b) Vertical Radiation Pattern

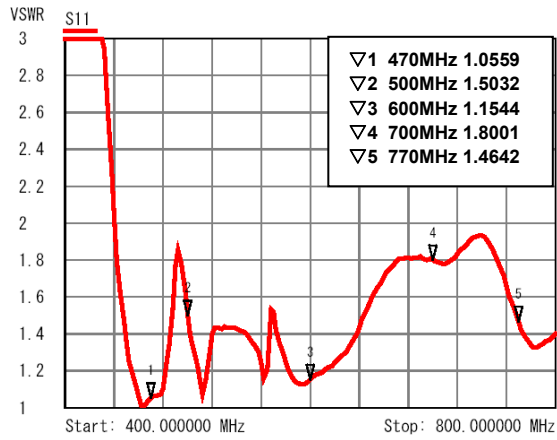
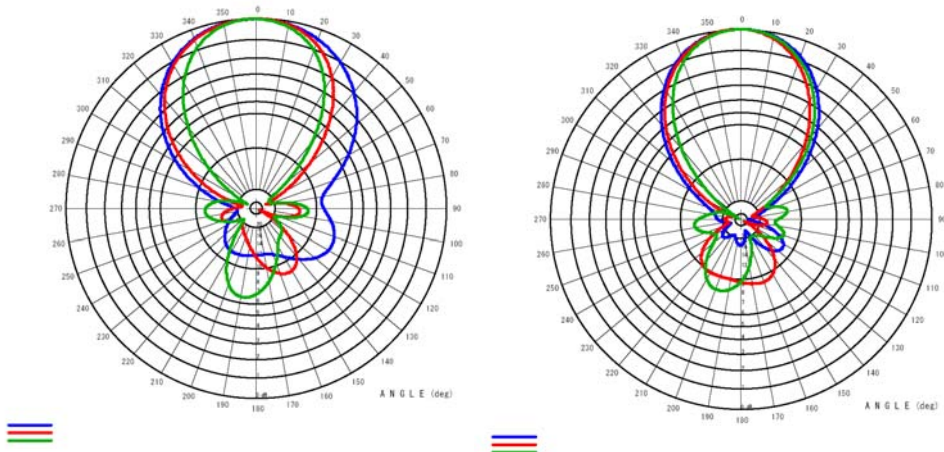


Fig. 8. VSWR characteristics of RLA (Measured Value)



Blue line 470MHz Red line 620MHz Green line 770MHz

Fig. 9. (a) Horizontal Radiation Pattern Fig.9 (b) Vertical Radiation Pattern (Measured Value)

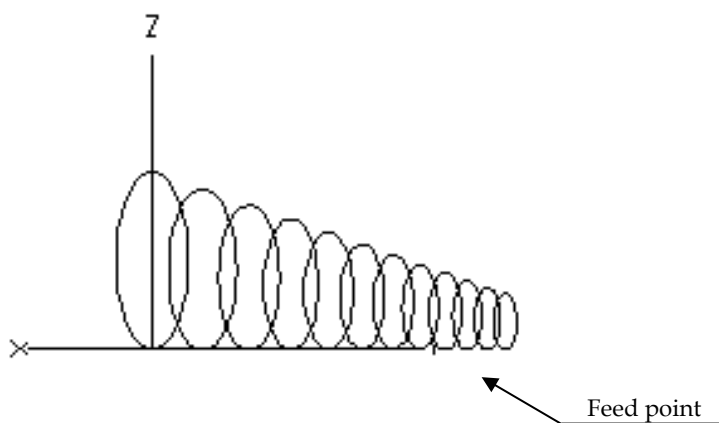


Fig. 10. (a) Structure of LPRLA

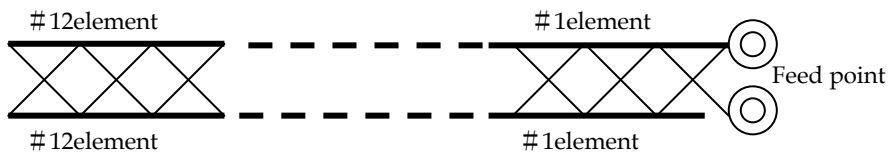


Fig. 10. (b) Feed point system

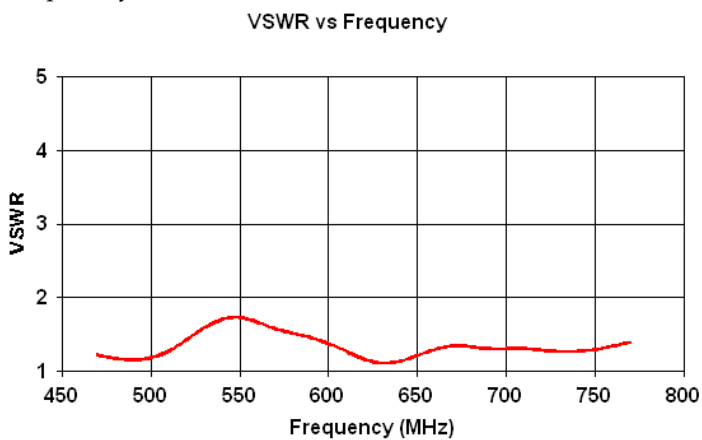


Fig. 11. VSWR characteristics of LPRLA (Theoretical Value)

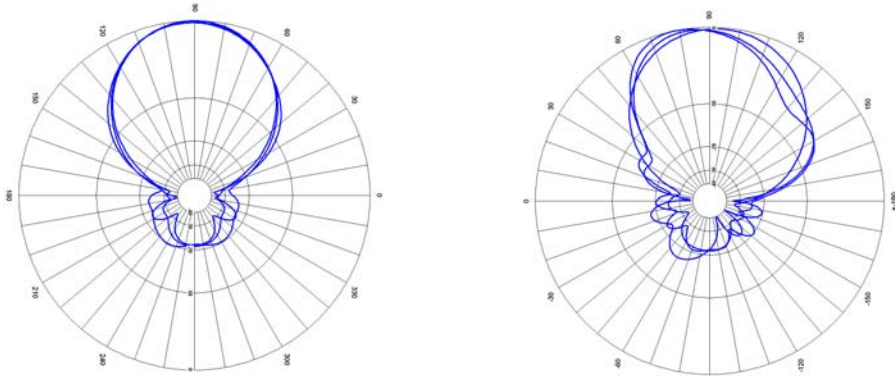


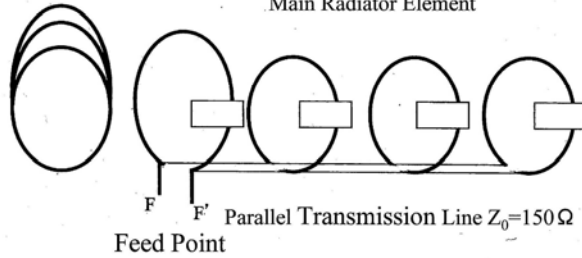
Fig. 12. (a) Horizontal Radiation Pattern

Fig. 12. (b) Vertical Radiation Pattern

(Theoretical Value)

3-Ring Reflector Element

Main Radiator Element



□ : Loaded Reactance Element

Fig. 13. Structure of Right-hand Circularly Polarized Ring Loop Antenna



Photo 2. Right-hand Circularly Polarized Ring Loop Antenna

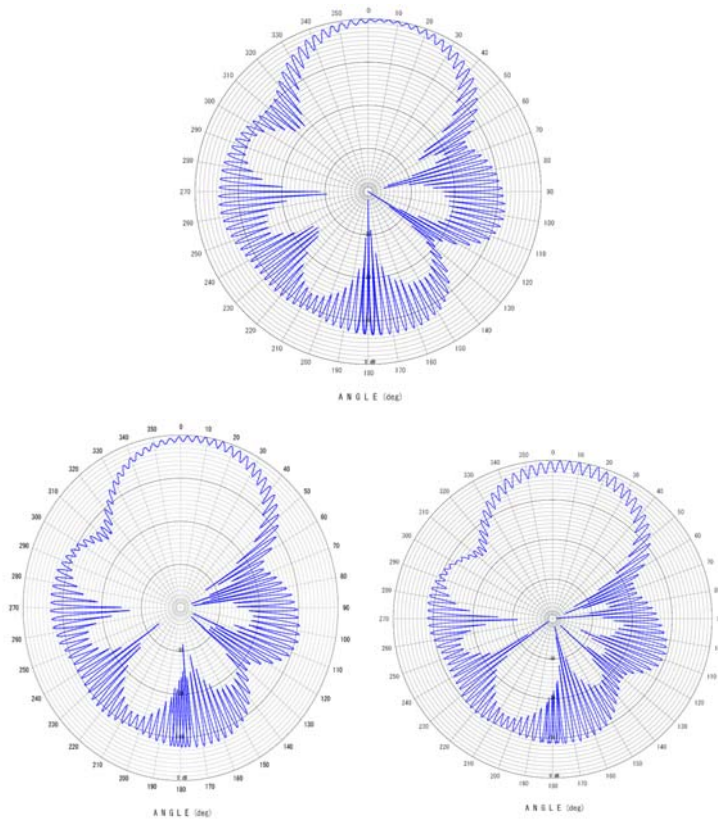


Fig. 14. Radiation Pattern of Right-hand Circularly Polarized Ring Loop Antenna (Measured value: 476MHz, 479MHz, 482MHz)

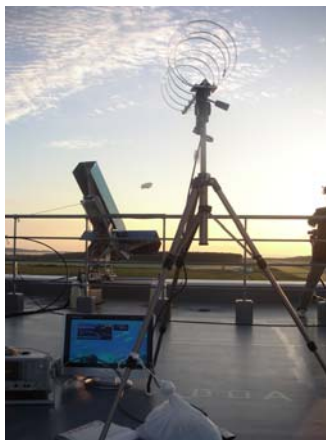


Photo 3. An antenna of the digital Right- hand Terrestrial broadcasting experiment Ring Loop with the airship in NICT

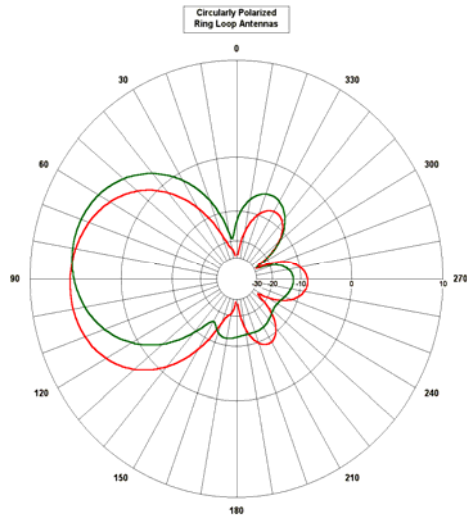


Fig. 15. Radiation Pattern of Circularly Polarized Antenna
(Theoretical value)
(red : horizontal, green : vertical) (Center frequency : 479MHz)

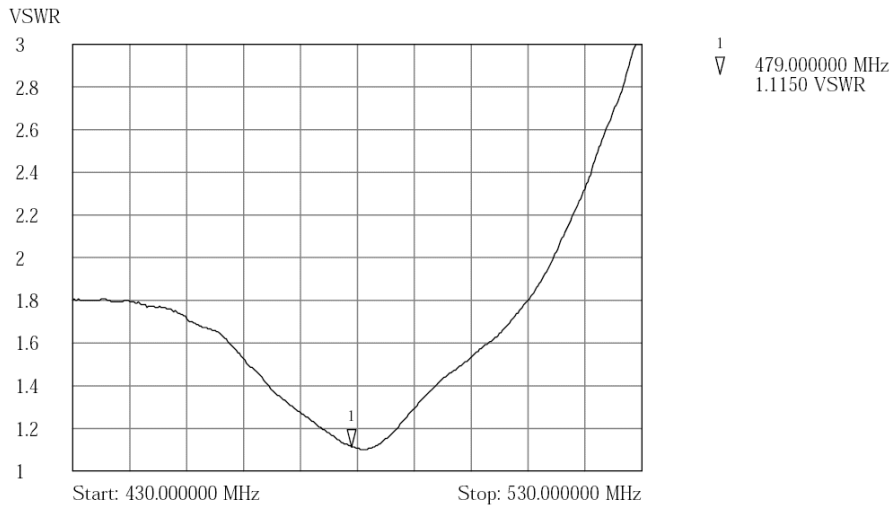


Fig. 16. Characteristics of VSWR

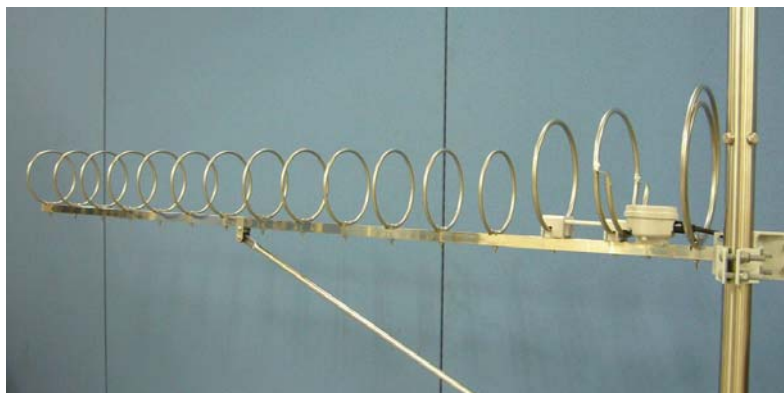
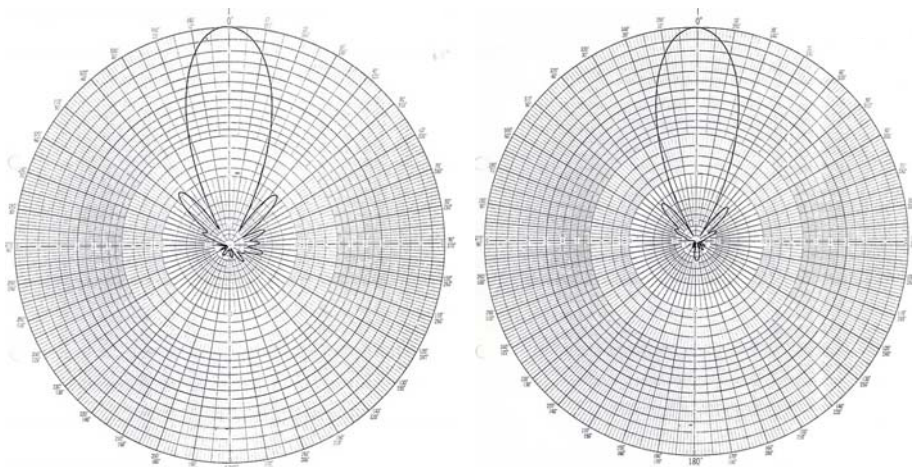


Photo 4. 16-element ring loop antenna

Frequency band	470MHz~770MHz(13ch~62ch)		
	C-Type (13ch~33ch)	B-Type (23ch~49ch)	A-Type (35ch~62ch)
Impedance	50Ω(normalized)		
VSWR	Less than 2.0		
Polarization	Horizontal		
Gain	12dBd		
Connector	N-P type		
Weight	About 3kg		

Table 1. specification for the 16-element ring loop antenna



(b) H-plane radiation patterns of B-Type antenna (641 MHz)

(a) E-plane radiation patterns of B-Type antenna (641 MHz)

Fig. 17. Radiation patterns of B-type antenna

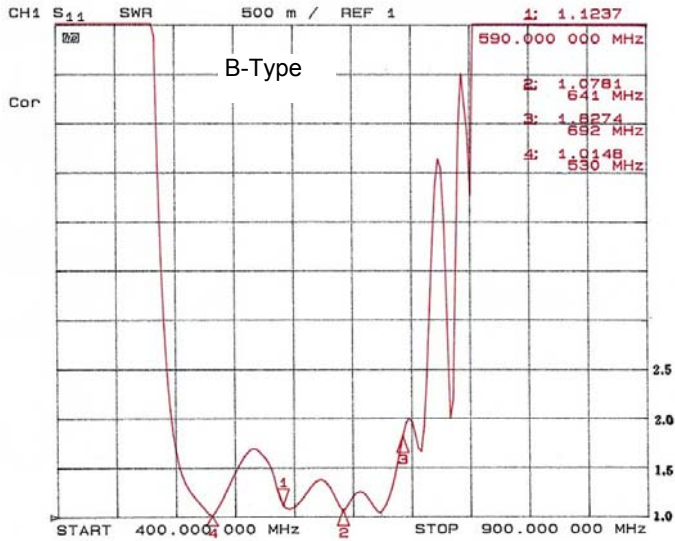


Fig. 18. Characteristics of VSWR

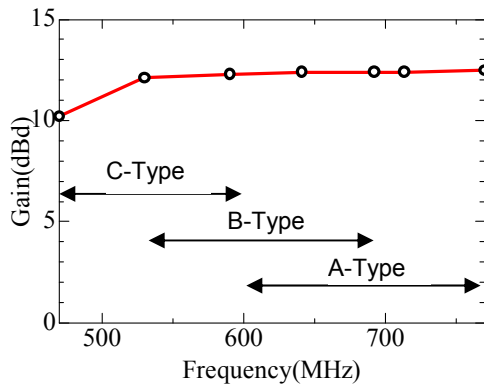


Fig. 19. Characteristics of Gain



Photo 5. pattern synthesis of ring loop antenna

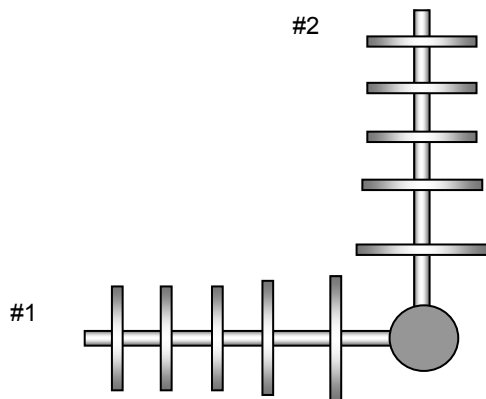


Fig. 20. Antenna arrangement

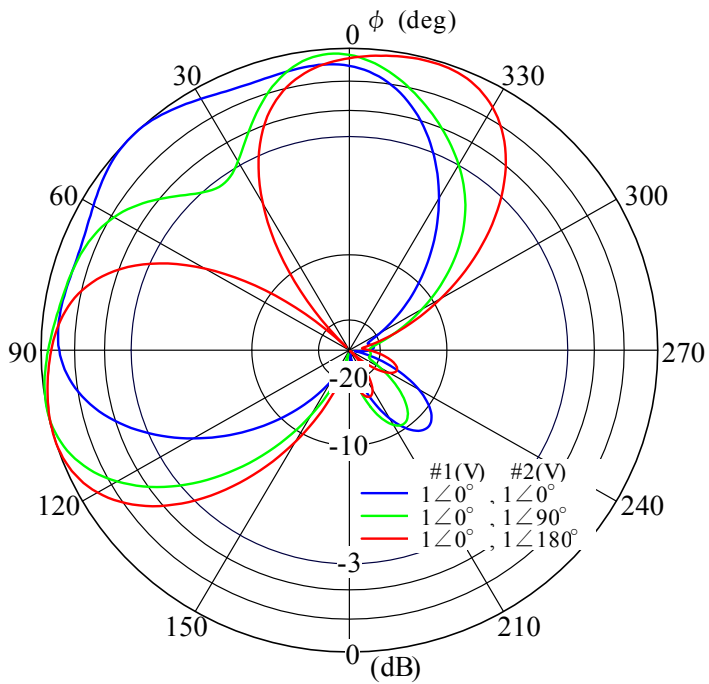


Fig. 21. Ring loop antenna for pattern synthesis of horizontal patterns

Frequency band	470MHz~770MHz(13ch~62ch)
Impedance	75 Ω (normalized)
VSWR	Less than 2.0
Polarization	Horizontal
Gain	6dBi
Connector	F-P type
Weight	About 600g(with a 1.2m feeder)

Table 2. specification for Ring loop antenna for pattern synthesis

Antenna Array Design in Aperture Synthesis Radiometers

Jian Dong and Qingxia Li

Huazhong University of Science and Technology

Wuhan, China

dongjian@smail.hust.edu.cn, qingxia_li@mail.hust.edu.cn

1. Introduction

During the past few decades, there has been growing interest in the use of microwave and millimeter wave radiometers for remote sensing of the Earth. Due to the need of large antennas and scanning mechanism, the conventional real aperture radiometer becomes infeasible for high spatial resolution application. Interferometric aperture synthesis was suggested as an alternative to real aperture radiometry for earth observation [Ruf et al., 1988]. Aperture synthesis radiometers (ASR) can synthesize a large aperture by sparsely arranging a number of small aperture antennas to achieve high spatial resolution without requiring very large and massive mechanical scanning antenna.

The fundamental theory behind aperture synthesis technique is the same as the one used for decades in radio astronomy [Thompson et al., 2001], in which the product of pairs of small antennas and signal processing is used in place of a single large aperture. In aperture synthesis, the coherent product (correlation) of the signal from pairs of antennas is measured at different antenna-pair spacings (also called baselines). The product at each baseline yields a sample point in the Fourier transform of the brightness temperature map of the scene, and the scene itself is reconstructed by inverting the sampled transform.

This chapter addresses the subject of antenna array design in ASR, which plays an important role in radiometric imaging of ASR. The chapter is organized as follows. In section 2, the basic principle of synthetic aperture radiometers is briefly formulated. In section 3, the topology optimization of the antenna array is concerned, aiming at minimum redundancy arrays (MRAs) for high spatial resolution. For one-dimensional case, different optimization methods for finding out minimum redundancy linear arrays (MRLAs) such as numerical algorithms and combinatorial methods are summarized, including their advantages and disadvantages. We also propose an effective restricted search method by exploiting the general structure of MRLAs. For two-dimensional case, different antenna array configurations as well as their spatial sampling patterns are compared, including rectangular sampling arrays, hexagonal sampling arrays, and nonuniform sampling arrays. Some original work on the design of thinned circular arrays is also described.

In section 4, a novel antenna array for our HUST-ASR prototype is presented, which is a sparse antenna array with an offset parabolic cylinder reflector at millimeter wave band.

The overall specifications, architecture design, performance evaluation, and measurement results of the antenna array are all detailed. Section 5 presents some experiment results with HUST-ASR, which indicate good capability of imaging natural scenes with high spatial resolution provided by the antenna array. Finally, section 6 concludes this chapter and suggests the further research.

2. Principle of Aperture Synthesis Radiometers

The aperture synthesis radiometer measures the correlation between the signals collected by two spatially separated antennas that have overlapping fields of view, yielding samples of visibility function V , also termed visibilities [Ruf et al., 1988], of the brightness temperature T of the scene under observation. For ideal situation, the relationship between V and T is given by

$$V(u, v) = \iint_{\xi^2 + \eta^2 \leq 1} T(\xi, \eta) e^{-j2\pi(u\xi + v\eta)} d\xi d\eta \quad (1)$$

where (u, v) is the baseline and is equal to the difference between the antenna positions over the XY plane normalized to the wavelength; $T(\xi, \eta)$ is the so-called modified brightness temperature [Camps, 1996].

$$T(\xi, \eta) = \frac{T_B(\xi, \eta)}{\sqrt{1 - \xi^2 - \eta^2}} F_{n1}(\xi, \eta) F_{n2}^*(\xi, \eta) \quad (2)$$

where $T_B(\xi, \eta)$, dimensions of Kelvin, is the actual apparent brightness temperature; (ξ, η) are the direction cosines, with respect to the (X, Y) axes, equal to $(\sin \theta \cos \varphi, \sin \theta \sin \varphi)$; $F_{n1,2}(\xi, \eta)$ are the normalized antenna voltage patterns.

In the ideal case of identical antenna patterns $F_{n1} = F_{n2} = F_n$, the modified brightness temperature can be recovered by means of an inverse Fourier transform of the visibility samples, that is

$$T(\xi, \eta) = F^{-1}[V(u, v)] \quad (3)$$

In practice, antennas can not be placed continuously; therefore, the measured visibilities are actually the discrete samples of visibility function, so

$$T(\xi, \eta) = \sum_i \sum_j V(u_i, v_j) e^{j2\pi(u_i \xi + v_j \eta)} \quad (4)$$

More generally, the relationship between V and T can be expressed as discrete matrix equation [Tanner, 1990]

$$V = GT_B \quad (5)$$

where G is a matrix, V is visibility vector, and T_B is brightness temperature vector.

G matrix is taken as a spatial impulse response of a synthetic aperture radiometer and can be exactly measured. In measurement, a noise source is placed at one end of the antenna range, and the radiometer is rotated in azimuth at the other end of the range in such a way as to scan the point source across the field of view.

When the aperture synthesis radiometer observes a scene, the brightness temperature image can be inverted by the Moore-Penrose pseudo-inverse [Tanner & Swift, 1993]

$$T_B = G^T (GG^T)^{-1} V \quad (6)$$

which is used as the basis in our inversion process.

Different from the simple Fourier transform expressed by (1) and (3), the measured G matrix contains the information of errors in the radiometer system, such as individual antenna patterns, obliquity factors, and fringe-washing functions. When G matrix is used to reconstruct images, part of errors in the system is actually corrected.

3. Topology Design of Antenna Arrays in Aperture Synthesis Radiometers

As a crucial technique for aperture synthesis radiometers (ASR), antenna array design plays an important role in radiometric imaging. Usually, antenna array design in ASR aims to find the minimum redundancy array (MRA) [Ruf et al., 1988; Ruf, 1993; Camps et al., 2001], which can provide the most uniform and complete (u, v) coverage in the Fourier plane with the given number of antenna elements and therefore achieves the highest spatial resolution of the image. In view of different manufacturing difficulties in antenna engineering and different mutual coupling, various candidates of array configurations with similar spatial resolution are also desirable in practical applications. Except for interferometric aperture synthesis radiometry, MRA is also widely used in adaptive beamforming [Jorgenson et al., 1991; Dong et al., 2008b], spatial spectrum estimation [Pillai et al., 1985], and radar imaging [Chen & Vaidyanathan, 2008; Dong et al., 2009c].

On the other hand, the radiometric sensitivity, as one of the most crucial specifications of synthetic aperture radiometers, must also be taken into account in the antenna array design. For remote sensing from space, especially from a moving platform such as low Earth orbit satellite and aircraft, too thinned arrays would much worsen the radiometric sensitivity of ASR, so a tradeoff must be made between thinning of the array (to reduce the size and weight in orbit) and obtaining the required sensitivity [Le Vine, 1990]. The sensitivity of ASR depends much on antenna array configurations because of different (u, v) spatial frequency samples and different levels of redundancy associated with array configurations [Ruf et al., 1988; Camps et al., 1998; Butora & Camps, 2003]. The problem of how to properly arrange antenna elements to achieve the optimum sensitivity of ASR is an interesting issue, on which no dedicated research has been found up to date. Detailed research on this issue is carried out by the authors and the results are presented in [Dong et al., 2009e], where the minimum degradation array (MDA) is suggested for the optimum radiometric sensitivity of ASR, and methods are proposed to search for MDA.

In this section, we only address the subject of MRA design for high spatial resolution, in which different optimization methods and different array configurations are described.

3.1 Minimum Redundancy Linear Arrays

The problem of finding out optimum MRLA has been first investigated as a purely number theoretic issue of "difference basis" [Redéi & Rényi, 1948; Leech, 1956; Wichman, 1963; Miller, 1971], in which each antenna of the array is assigned an integer representing its position, the problem then reduces to constructing a set of n integers, called a difference basis, which generate contiguous differences from 1 up to the largest possible number. Leech [1956] presented some optimum solutions for $n \leq 11$ and demonstrated that for

optimum MRLA, $1.217 \leq R \leq 1.332$ for $n \rightarrow \infty$, where the redundancy R is quantitatively defined as the number of possible pairs of antennas divided by the maximum spacing L :

$$R = \frac{C_n^2}{L} = \frac{n(n-1)}{2L} \quad (7)$$

where $C_p^q = p!/q!(p-q)!$ is the number of combinations of p items taken q at a time.

It is difficult to find the optimum MRLAs when large numbers of elements are involved because of the exponentially explosive search space, and several earlier attempts as well as our work are detailed as follows.

(a) Numerical search algorithms

For a small number of elements, it is possible to find MRLAs by a simple exhaustive search in solution space; but for a large number of elements, it is computationally prohibitive to do so. With the help of powerful modern computers, some numerical optimization algorithms were proposed to search for MRLAs.

Ishiguro [1980] proposed iterative search methods to construct MRLAs: to start with the configuration of $\{1, (L-1)\}$ (the integers in the set denote the spacing) and to examine larger spacings preferentially. A site is selected as optimum which, if occupied, gives as many missing spacings as possible. When more than one site is selected as optimum at some stage, they are registered without exception to examine all the combinations of tree structure derived from them. This process is repeated until the condition of full spacing is obtained.

Lee & Pillai [1988] proposed a "greedy" constructive algorithm for optimal placement of MRLA: like Ishiguro's algorithm, in each stage, a site is selected as optimum which, if occupied, gives as many missing spacings as possible. And the results of this stage are stored in a linked list (output linked list), which in turn becomes an input linked list for the next stage. The algorithm needs large computation time and excessive memory storage. To cope with these problems, a modified suboptimal version of this algorithm is also proposed by Lee. With the highly reduced computation time and memory storage, the resulting solution is far from optimality.

As an effective stochastic optimizer, simulated annealing (SA) algorithm was first applied to the search of MRLA by Ruf [1993] and displayed the superiority over Ishiguro's algorithm and Lee's algorithm. The most distinguished property of SA from those local search algorithms is that the algorithm can escape from local minimum wells and approach a global minimum by accepting a worse configuration with a probability dependent on annealing temperature.

Blanton & McClellan [1991] considered the problem of finding MRLA as creating a tree structure of templates, and Linebarger [1992] considered the problem as computing the coarray of MRLA from a boolean algebraic point of view. By combining Linebarger's technique with Blanton's, dramatic speedup in searching MRLA may be expected.

It is worth noting that except for simulated annealing, other global optimizers, such as genetic algorithms (GAs) [Goldberg, 1989] and ant colony optimization (ACO) [Dorigo & Stutzle, 2004], may also be used to search MRLA. Although succeeding in escaping from local minima, the global search for MRLAs with large number of antennas still requires high computational cost because of the exponentially explosive search space. Further consideration is that in order to improve the efficiency of the exploration as much as possible, we might experiment with algorithms with a different combination of randomness and gradient descent.

In summary, although various numerical algorithms were proposed, the contradiction between solution quality and computation efficiency limits practical applications of all these algorithms, i.e. reducing computation time would lead to a poor solution, like Ishiguro's algorithm and Lee's algorithm, while obtaining good solution would require large computation time, like Ruf's algorithm.

(b) Combinatorial methods

Differed from numerical search algorithms described above, the combinatorial methods usually need very little computational cost and have closed form solutions.

Ishiguro [1980] proposed a method to construct large MRLA by a recursive use of optimum small MRLA. The method are considered in two cases. In case 1, suppose that an MRLA of n antennas (MRLA1 with the maximum spacing N) are arranged in the array configuration of an MRLA of m antennas (MRLA2 with the maximum spacing M). As a result, a new nm -element MRLA is synthesized with the maximum spacing

$$L = M(2N + 1) + N = 2MN + M + N \quad (8)$$

In case 2, suppose that MRLA2 in case 1 is recursively used k times, the total number l_k of antennas and the maximum spacing L_k are, respectively,

$$l_k = m^{k-1}n \quad (k \geq 2) \quad (9)$$

$$L_k = [(2M + 1)^{k-1}(2N + 1) - 1]/2 \quad (k \geq 2) \quad (10)$$

By using a small difference basis and cyclic difference set (CDS), a combinatorial method to construct larger difference basis, i.e. MRLA, was described in [Redéi & Rényi, 1948; Leech, 1956]. The method was also reformulated by Kopilovich [1995] and used to design linear interferometers with a large number of elements. Redéi & Rényi and Leech showed that, if a sequence $\{b_i\}$ ($i=1, \dots, r$) is a basis for the $[0, P]$ segment (we call it the "initial" basis), and if $\{d_j\}$ ($j=1, \dots, k$) is a CDS [Baumert, 1971; Hall, 1986] with parameters V , k , and $\lambda=1$, then the set

$$\{d_j + b_i \cdot V\} \quad (11)$$

consisting of $K=kr$ integers, is the difference basis for the segment of length

$$L = (P + 1)V - (d_k - d_1) - 1 \quad (12)$$

Thus, using a difference basis for a small segment and a CDS, one can construct a difference basis for a much longer segment. For the same number of elements, this method outperms Ishiguro's method, i.e. having lower redundancy. Moreover, with element number increasing, the redundancy R decreases steadily (though not monotonically) and then stabilizes, while that of Ishiguro's arrays grows. In a general sense, Ishiguro's construction can also be generalized into this combinatorial method, i.e. using two difference bases for small segments, one can construct a difference basis for a much longer segment.

The two combinatorial methods described above cannot provide a solution for any given number of antennas, such as for a prime number of antennas. For any given number of antennas, Bracewell [1966] proposed a systematic arrangement method, which is summarized as follows:

For an odd number of antennas ($n=2m+1$)

$$\{1^{m+1}, (m+2), (m+1)^m\} \quad (13)$$

where i^m denotes m repetitions of the interelement spacing i , each integer in the set denotes the spacing between adjacent antennas.

For an even number of antennas ($n=2m$)

$$\{1^{m+1}, (m+2), (m+1)^m\} \quad (14)$$

The values of R for (13) and (14) approach 2 for a large value of n .

Another approach to MRLA design is based on the recognition of patterns in the known MRLA arrays that can be generalized into arrays with any number of antennas. The most successful pattern thus far is given by

$$\{1^p, (2p+2)^{p+1}, (4p+3)^l, (2p+1)^p, p+1, 1^p\} \quad (15)$$

where p and l are positive integers. This pattern was originally discovered by Wichman [1963] in the early 1960's and also found by Pearson et al. [1990] and Linebarger et al. [1993] later. Proofs that this expression yields an array with no missing spacings are found in [Miller, 1971; Pearson et al., 1990]. The pattern can be shown to produce arrays such that $n^2/L \leq 3$ ($R < 1.5$), where n and L are defined as in (7). More similar patterns satisfying $n^2/L \leq 3$ can be found in [Dong et al., 2009d]. Some patterns inferior to these patterns were also listed in [Linebarger et al., 1993], which may be of use under certain array geometry constraints.

(c) Restricted search by exploiting general structure of MRLAs

It is prohibitive to search out all the possible configurations because of the exponentially explosive search space. However, if the configurations are restricted by introducing some definite principles in placing antennas, it is not unrealistic to search out all the possibilities involved in them. Fortunately, there are apparent regular patterns in the configurations of optimum MRLAs for a large value of n , i.e. the largest spacing between successive pairs of antennas repeats many times at the central part of the array. Such MRLA patterns were presented by Ishiguro [1980] and Camps et al. [2001]. Based on previous researcher's work, we summarize a common general structure of large MRLAs and propose a restricted optimization search method by exploiting general structure of MRLAs, which can ensure obtaining low-redundancy large linear arrays while greatly reducing the size of the search space, therefore greatly reducing computation time. Details of the method can be seen in [Dong et al., 2009d].

3.2 Minimum Redundancy Planar Arrays

The main advantage of planar arrays over linear arrays in ASR is that planar arrays can provide the instantaneous spatial frequency coverage for snapshot imaging without any mechanical scanning. In two dimensions the choice of a minimum redundancy configuration of antennas is not as simple as for a linear array. By different sampling patterns in (u,v) plane, the planar arrays can be divided into:

(a) Rectangular sampling arrays

Typical configurations with rectangular sampling are Mills cross [Mills & Little, 1953], U-shape, T-shape, L-shape [Camps, 1996] arrays, where U-shape array was adopted in HUT-

2D airborne ASR for imaging of the Earth [Rautiainen et al., 2008]. Both U-shape and T-shape configurations and their spatial frequency coverage are shown in Fig. 1, assumed that the minimum spacing is half a wavelength. By ignoring the effect of the small extensions on the left and right sides of the square domain, both arrays have the same area of (u,v) coverage. An optimal T-shape (or U-shape) array (also see in Fig. 1) was proposed by Chow [1971], which has a larger area of (u,v) coverage than the regular T array but results in a unequal angular resolution in each dimension.

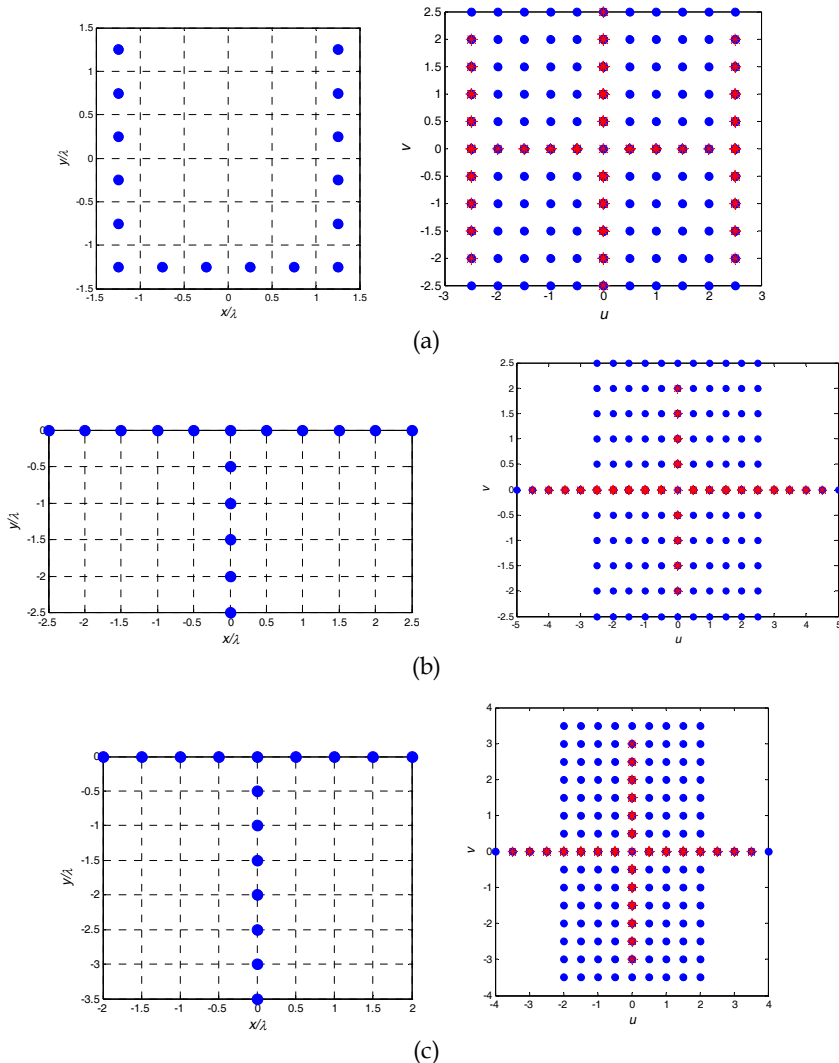


Fig. 1. Different array configurations for rectangular domain and their spatial frequency coverage. Red star points denote redundant (u, v) samples. (a) 16-element regular U-shape array; (b) 16-element regular T-shape array; (c) 16-element optimal T-shape array

A “cross product” planar array can be constructed by “multiplying” two MRLAs: Let $\{a_i\}$ denote the element location set of an MRLA arranged along x axis, and let $\{b_j\}$ denote the location set of an MRLA arranged along y axis, then the location set of the resulting “cross product” planar array is $\{a_i, b_j\}$. An example of a 5×4 “cross product” array is shown in Fig. 2. The authors show [Dong et al., 2009a] that the “cross product” array can obtain more spatial frequency samples and larger (u, v) coverage, therefore achieve higher spatial resolution, compared to U-shape or T-shape array with the same element number.

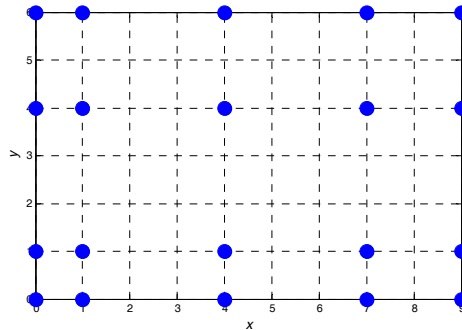


Fig. 2. An example of a 5×4 “cross product” array

A second regular structure, named as Greene-Wood (GW) array, was proposed by Greene & Wood [1978] for square arrays. The element location (i, j) of such an array of aperture L satisfies: $i=0$ or $j=0$ or $i=j=2, 3, \dots, L$. An example of a 12-element GW array with $L=4$ is shown in Fig. 3.

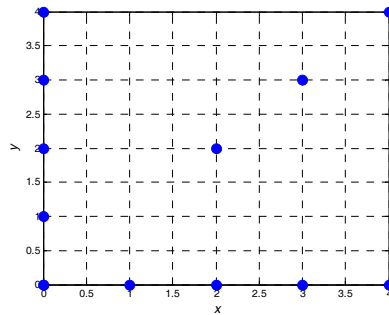


Fig. 3. An example of a 12-element Greene-Wood array with $L=4$

Two combinatorial methods to construct minimum redundancy arrays for rectangular domain were proposed in [Kopilovich, 1992; Kopilovich & Sodin, 1996]. One method is a generalization of one-dimensional Leech’s construction described in section 3.1(b), that is, by multiplying one-dimensional basis of the form in (11), one can obtain the two-dimensional basis consisting of $K = r_1 r_2 k_1 k_2$ elements for the $L_1 \times L_2$ domain,

$$\{d_j + b_i \cdot V_a, d'_s + b'_t \cdot V_b\} \quad j = 1, \dots, k_1; s = 1, \dots, k_2$$

$$i = 1, \dots, r_1; t = 1, \dots, r_2 \quad (16)$$

where $\{d_j\}$ and $\{d'_s\}$ are CDSs with the parameters $(V_a, k_1, 1)$ and $(V_b, k_2, 1)$ ($d_1=d'_1=0$ is specified), respectively, while $\{b_i\}$ and $\{b'_t\}$ are the bases for the segment $[0, P_1]$ and $[0, P_2]$; and $L_1 = (P_1 + 1)V_a - d_{k_1} - 1$; $L_2 = (P_2 + 1)V_b - d'_{k_2} - 1$.

The other method is based on the concept of two-dimensional difference sets (TDS). Similar to CDS, a TDS with the parameters (v_a, v_b, k, λ) is a set $\{a_i, b_j\}$ of k elements on a $(v_a-1) \times (v_b-1)$ grid such that pairs (v_1, v_2) of co-ordinates of any nonzero grid node have exactly λ representations of the form

$$v_1 \equiv a_i - a_j \pmod{v_a} \quad v_2 \equiv b_t - b_j \pmod{v_b} \quad (17)$$

If there exists a two-dimensional basis $\{(\gamma_j, \delta_j)\}$ with k_0 elements for a small $P_1 \times P_2$ grid and a TDS $\{a_i, b_j\}$ with the parameters (v_a, v_b, k, λ) , then the set of $K=k \times k_0$ elements

$$\{(\gamma_j v_a + a_i, \delta_j v_b + b_j)\} \quad i = 1, \dots, k \quad j = 1, \dots, k_0 \quad (18)$$

forms a basis for the $L_1 \times L_2$ grid with

$$L_1 = v_a P_1 + A_0 - 1 \quad L_2 = v_b P_2 + B_0 - 1 \quad (19)$$

where the values A_0 and B_0 depend on the parameters v_a and v_b .

Kopilovich showed that the arrays constructed by both methods outperform T-shape or U-shape array in (u, v) coverage for the same number of elements.

(b) Hexagonal sampling arrays

Hexagonal sampling is the most efficient sampling pattern for a two-dimensional circularly band-limited signal [Mersereau, 1979; Dudgeon & Mersereau, 1984], in the sense that the hexagonal grid requires the minimum density of (u, v) samples to reconstruct the original brightness temperature with a specified aliasing level (13.4% less samples than rectangular sampling pattern). Typical configurations with hexagonal sampling are Y-shape and triangular-shape arrays [Camps, 1996]. Both configurations and their spatial frequency coverage are shown in Fig. 4, assumed that the minimum spacing is $1/\sqrt{3}$ wavelengths. For the similar number of elements, Y-shape array has larger (u, v) coverage than that for a triangular-shape array, meaning better spatial resolution. On the other hand, triangular-shape arrays cover a complete hexagonal period, while Y-shape arrays have missing (u, v) samples between the star points. Hexagonal fast Fourier transforms (HFFT) algorithms [Ehrhardt, 1993; Camps et al., 1997] are developed for hexagonally sampled data that directly compute output points on a rectangular lattice and avoid the need of interpolations.

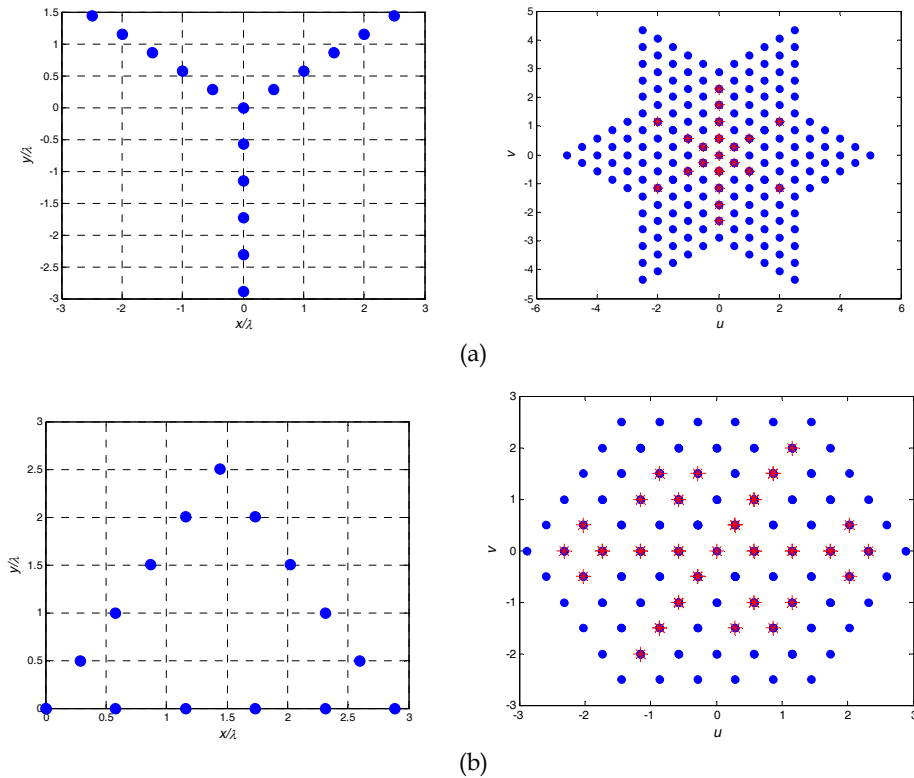


Fig. 4. Different array configurations for hexagonal domain and their spatial frequency coverage. Red star points denote redundant (u, v) samples. (a) 16-element Y-shape array; (b) 15-element triangular-shape array

Y-shape array was adopted in MIRAS [Martín-Neira & Goutoule, 1997] for two-dimensional imaging of the Earth. There are several variations for Y-shape array. Staggered-Y array was proposed for GeoSTAR [Lambrigtsen et al., 2004], which staggers the three arms counter-clockwisely and then brings them together so that the three inner most elements form an equilateral triangle. This Staggered-Y configuration eliminates the need for an odd receiver at the center. The only penalty is a slight and negligible loss of (u, v) coverage. Sub-Y configuration was suggested by Lee et al. [2005] to achieve larger (u, v) coverage at the cost of more incomplete samples than Y-shape array. Its basic unit is a subarray consisting of four elements arranged in Y-shape.

Several sparse hexagonal configurations were suggested in [Kopilovich, 2001; Sodin & Kopilovich, 2001 & 2002]. Like triangular-shape array, they cover a complete hexagonal period. One configuration is to fill up five sides of a regular hexagon of a given radius r by element which provide complete coverage of a hexagonal domain of the double radius in (u, v) plane. A second configuration is that $(3r+1)$ elements are arranged equidistantly on three non-adjacent sides of the hexagon while others are arranged inside it. A third configuration, named as three-cornered configurations (TCCs), has three-fold symmetry, i.e. invariant to

rotation by 120° around a certain centre of symmetry. Besides, based on cyclic difference sets (CDSs), Sodin & Kopilovich [2002] developed an effective method to synthesize nonredundant arrays on hexagonal grids.

(c) Non-uniform sampling arrays

Different from those open-ended configurations such as U, T, and Y, there are some closed configurations, such as a circular array and a Reuleaux triangle array [Keto, 1997; Thompson et al., 2001]. A uniform circular array (UCA) produces a sampling pattern that is too tightly packed in radius at large spacings and too tight in azimuth at small. Despite being nonredundant for odd number of elements, the (u, v) samples of a UCA are nonuniform and need to be regularized into the rectangular grids for image reconstruction. One way of obtaining a more uniform distribution within a circular (u, v) area is to randomize the spacings of the antennas around the circle. Keto [1997] discussed various algorithms for optimizing the uniformity of the spatial sensitivity. An earlier investigation of circular arrays by Cornwell [1988] also resulted in good uniformity within a circular (u, v) area. In this case, an optimizing program based on simulated annealing was used, and the spacing of the antennas around the circle shows various degrees of symmetry that result in patterns resembling crystalline structure in the (u, v) samples.

An interesting fact for a UCA is that (u, v) samples are highly redundant in baseline length. Like ULA, a large number of elements can be removed from a UCA while still preserving all baseline lengths. Thus, by several times of rotary measurement, all baseline vectors (both length and orientation) of a UCA can be obtained. Having the advantage of greatly reducing hardware cost, the thinned circular array with a time-shared sampling scheme is particularly suitable in applications where the scene is slowly time-varying. Based on the difference basis and the cyclic difference set in combinatorial theory, methods are proposed by the authors for the design of the thinned circular array. Some initial work on this issue can be found in [Dong et al., 2009b].

The uniform Reuleaux triangle array would provide slightly better uniformity in (u, v) coverage than the UCA because of the less symmetry in the configuration, and optimization algorithms can also be applied to the Reuleaux triangle array to achieve a more uniform (u, v) coverage within a circular area.

4. Antenna Array Design in HUST-ASR

The first instrument to use aperture synthesis concept was the Electronically Scanned Thinned Array Radiometer (ESTAR), an airborne L-band radiometer using real aperture for along-track direction and interferometric aperture synthesis for across-track direction [Le Vine et al., 1994; Le Vine et al., 2001]. An L-band radiometer using aperture synthesis in both directions, the Microwave Imaging Radiometer Using Aperture Synthesis (MIRAS), was proposed by ESA [Martín-Neira & Goutoule, 1997] to provide soil moisture and ocean surface salinity global coverage measurements from space. In 2004, the Geostationary Synthetic Thinned Aperture Radiometer (GeoSTAR) was proposed by NASA [Lambrigtsen et al., 2004] as a solution to GOES (the Geostationary Operational Environmental Satellite system) microwave sounder problem, which synthesizes a large aperture by two-dimensional aperture synthesis to measure the atmospheric parameters at millimeter wave frequencies with high spatial resolution from GEO.

To evaluate the performance of aperture synthesis radiometers at millimeter wave band, a one-dimensional prototype of aperture synthesis radiometer working at millimeter wave band, HUST-ASR [Li et al., 2008a; Li et al., 2008b], is developed at Huazhong University of Science and Technology, Wuhan, China.

The prototype architecture of the millimeter wave aperture synthesis radiometer is shown in Fig. 5. The HUST-ASR prototype mainly consists of antenna array, receiving channel array, ADC array, image reconstruction part. Other parts such as calibration source, calibration and gain control, local oscillator, correlating, error correction are also shown in the figure. As the most highlighted part of HUST-ASR prototype, the antenna array will be detailed in this section, including the overall specifications, architecture design, performance evaluation, and measurement results [Dong et al., 2008a].

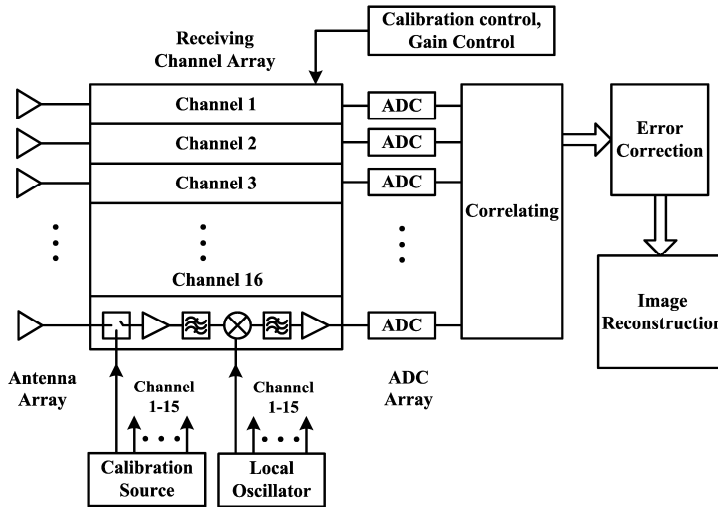


Fig. 5. Prototype architecture of HUST-ASR

4.1 Antenna Array Overall Requirements

One-dimensional synthetic aperture radiometer requires an antenna array to produce a group of fan-beams which overlap and can be interfered with each other to synthesize multiple pencil beams simultaneously [Ruf et al., 1988]. To satisfy this, each antenna element should have a very large aperture in one dimension, while a small aperture in the other dimension.

Due to the high frequency of Ka band, three candidates for the linear array elements were considered among sectoral horns, slotted waveguide arrays and a parabolic cylinder reflector fed by horns. Too narrow bandwidth and mechanical complexity make slotted waveguide arrays less attractive. Sectoral horns with large aperture dimensions would make the length of horns too long to be fabricated. The concept of a parabolic cylinder reflector fed by horns provides an attractive option for one-dimensional synthetic aperture radiometer for several good reasons including wide bandwidth, mechanical simplicity and high

reliability. The massiveness resulting from this configuration may be overcome by lightweight materials and deployable mechanism. The main design parameters of the antenna array are listed in Table 1.

Frequency Band	8mm-band
Bandwidth (GHz)	± 2
Sidelobe Level (dB)	<-20
H-plane Beamwidth (deg.)	0.7
E-plane Synthesized Beamwidth (deg.)	0.3
Gain for Each Element (dB)	30
VSWR	≤ 1.2
Polarization	Horizontal

Table 1. Main design parameters for antenna elements

4.2 Antenna Array Architecture and Design

Fig. 6 simply shows the whole architecture of the antenna array, which is a sparse antenna array with offset parabolic cylinder reflector for HUST-ASR prototype. In essence each HUST-ASR antenna element is composed of a feedhorn and the parabolic cylinder reflector. The elements are arranged in a sparse linear array and thus can share a single reflector.

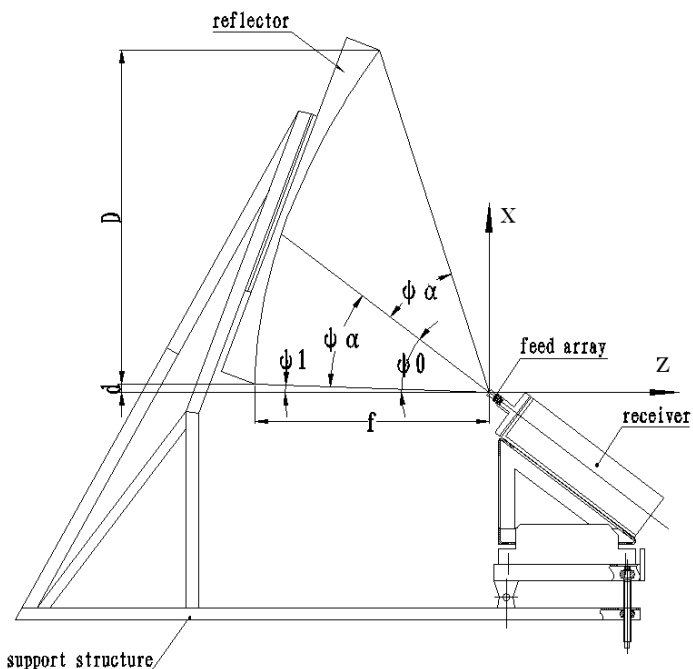


Fig. 6. Artist’s concept of the whole antenna architecture

To avoid gain loss due to feed blockage, an offset reflector configuration was adopted. This configuration would also reduce VSWR and improve sidelobe levels [Balanis, 2005; Milligan, 2002]. The ratio of focal length to diameter (f/D) for reflector was determined as 0.7 considering achieving high gain, low cross-polarization level meanwhile maintaining compact mechanical structures. A -12dB edge illumination, not a -10dB edge illumination usually for optimal gain, is designed due to the need for a low sidelobe level. Asymmetric illumination taper on reflector aperture plane due to offset configuration, causing degradation in secondary radiation pattern of the antenna, can be mitigated by adjusting the pointing angle of feed horns.

Different from a conventional uniform linear array, 16 pyramid horns are disposed in a minimum redundancy linear array (MRLA) along the focal line of the reflector to carry out cross-track aperture synthesis for high spatial resolution imaging. The position of each element in the array is shown in Fig. 7. The minimum element spacing between adjacent horns is chosen to be one wavelength ensuring an unambiguous field of view of $\pm 30^\circ$ from the normal of array axis. The maximum spacing of the feed array is 90 wavelengths. Therefore, the -3dB angular resolution in y direction by aperture synthesis of array elements is

$$\Delta\theta_y = 0.88 \frac{\lambda}{D_y} = 0.88 \frac{\lambda}{2 \cdot 90\lambda} = 0.28^\circ \quad (20)$$

where λ is the wavelength. In (20), The Hermitian of visibility samples [Ruf et al., 1988] is considered to double the maximum aperture of the array ($D_y=2 \times 90\lambda$), and therefore double the angular resolution.

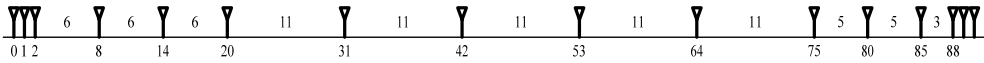


Fig. 7. Arrangement of 16-element minimum redundancy linear array

A delicate support structure connecting the parabolic cylinder reflector and the primary feed array is manufactured as shown in Fig. 6. One side of the support structure serves as back support of the reflector, while the other provides a bevel on which the primary feed array is connected to millimeter wave front-ends of receivers through straight or bent BJ-320 (WR-28) waveguides. By using three pairs of tunable bolts under the bevel, the feed array can be exactly adjusted to the focal line of the reflector.

The specific design features of each part of the whole antenna system are detailed below.

(a) Reflector Geometry

To achieve aperture synthesis in one plane, the shape of the reflector is a singly-curved offset parabolic cylinder. This type of reflector has a focal line rather than a focal point. Fig. 6 shows a vertical cross section of the parabolic cylindrical reflector.

The geometric parameters of the parabolic cylindrical reflector are designed referring to [Lin & Nie, 2002; Milligan, 2002] and listed in Table 2. The value of D_x is selected by empirical formula

$$\Delta\theta_x = 1.18 \frac{\lambda}{D_x} = 68^\circ \frac{\lambda}{D_x} \tag{21}$$

where $\Delta\theta_x$ is the -3dB angular resolution in x direction, Noticeably, the reflector length L along y direction is large enough to guarantee an E-plane edge illumination level lower than -7dB even for the element at each end of the array.

Aperture Vertical Length D_x	0.8m
Aperture Horizontal Length L	1.8m
Focal length f	0.56m
offset distance d	0.02m
Angle, lower rim ψ_1	2.05°
Angle, upper rim ψ_2	72.45°
Bisecting angle ψ_0	37.25°
Subtended half angle ψ_a	35.2°
Edge illumination (EI)	-12dB
Path loss, lower rim PL_1	0.932dB
Path loss, upper rim PL_2	-2.797dB
Path loss, average PL_{ave}	-0.933dB

Table 2. Reflector geometric parameters

(b) Feed Horn

The E-plane aperture b of each feed horn is flared as large as possible to about one wavelength in order to reduce VSWR and maximize receiving gain of each element of the antenna array, so a peculiar structure which connects three horns as a whole at each end of the array is used. The H-plane aperture size w of each feed horn is decided according to the specified edge illumination (EI=-12dB) and illumination angle ($2\psi_a=70.4^\circ$) of the parabolic cylindrical reflector. Based on the simulation results shown in Fig. 8 given by HFSS, we choose $w=14.8mm$, $R=25mm$, where R is the distance between the aperture plane center and the neck of a horn.

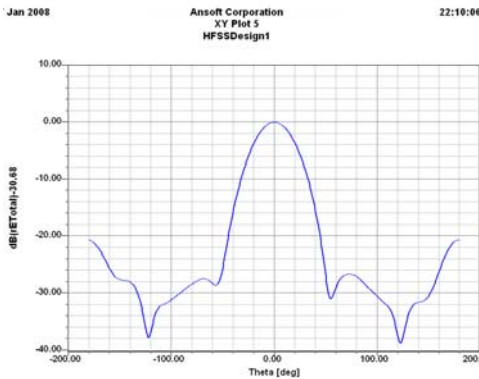


Fig. 8. H-plane radiation pattern simulated by HFSS

(c) *Antenna Tolerance Restrictions*

Antenna tolerance, having great influence on reflector antenna performance, is also considered in our design. The lateral and axial feed array element position errors are restricted to less than 0.2mm and 0.12mm separately. The RMS value of random surface error is restricted to 0.2mm, i.e. less than $\lambda/40$.

4.3 Electrical Performance Evaluation

To validate our design, the fundamental parameters of antenna such as Half-Power Beam Width (HPBW), sidelobe level and gain are evaluated below.

(a) *HPBW and Sidelobe Level*

The Aperture Integral Method [Balanis, 2005] is used to solve far field radiation pattern of our antenna array elements. The projected aperture field distribution of the reflector in the x direction can usually be approximated by the following expression [Lin & Nie, 2002; Milligan, 2002]

$$Q(x) = C + (1 - C) \left[1 - \left(\frac{x - h}{a} \right)^2 \right]^p \quad (22)$$

For our application, $C = 10^{EI/20} = 0.25$, $p=1.5$, $a=D/2=0.4m$, $h=a+d=0.42m$.

Assume that the aperture distribution has no variation in the y direction because of a flat profile in that dimension. According to scalar diffraction theory [Balanis, 2005], the far field pattern of the antenna is proportional to the Fourier transform of its aperture distribution and may be expressed as

$$E(\theta, \varphi) = \int_{\text{aperture}} Q(\vec{r}) e^{jk \cdot \vec{r}} ds \quad (23)$$

Assuming aperture field distribution is separable, from (23) we can approximately calculate the secondary pattern of the antenna in two principal planes.

In H-plane ($\varphi=0^\circ$),

$$E(\theta) = \int_d^{d+D} Q(x) e^{jkx \sin \theta} dx \quad (24)$$

In E-plane ($\varphi=90^\circ$),

$$E(\theta) = \int_{-b/2}^{b/2} e^{jky \sin \theta} dy \quad (25)$$

From (24) and (25), we can see that the HPBW of H and E plane are about 0.7° and 51° , respectively, and the first sidelobe level of H and E plane are about -23dB and -13.2dB, separately. The sidelobe level of E-plane can be further reduced by array factor of ASR [Ruf et al., 1988].

(b) *Gain*

Using (22), we can get the aperture efficiency

$$\eta_a = \frac{\left[\int_d^{d+D} Q(x) dx \right]^2}{\int_d^{d+D} Q^2(x) dx} \approx 0.88 \quad (26)$$

Due to a flat profile in the y direction, we can deem that the effective receive area A_e of each element in the array is

$$A_e = \eta_a A_p = \eta_a D b \quad (27)$$

So the gain of each element is

$$G(\text{dB}) = 4\pi \cdot \frac{A_e}{\lambda^2} \approx 30.2 \quad (28)$$

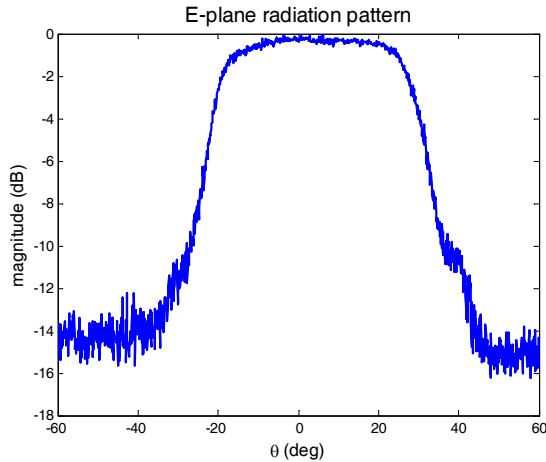
The evaluation above neglected the effect of some error sources, such as random surface errors, feed energy spillover. So the computed results would slightly deviate from the actual values.

4.4 Measurement Results

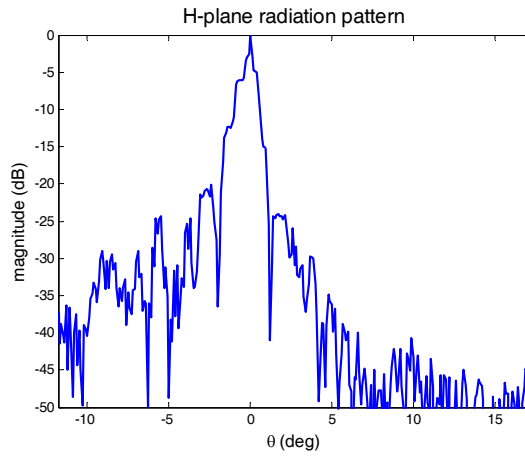
The whole antenna array system was manufactured and measured by us. The radiation patterns in two principal planes measured at the central frequency are given in Fig. 9. For brevity, here we only give the results of one element in the array. The radiation patterns for other elements are similar.

The sidelobe levels in H-plane are below the -20dB requirement, which are considered quite well, in particular, at the high frequency of Ka band. The synthetic power pattern incorporating array factor of ASR with element pattern in E-plane is given in Fig. 10 based on G-matrix method.

Table 3 shows the measured VSWR value of each element in the array at the central frequency.



(a)



(b)

Fig. 9. Measured far field radiation pattern of antenna element; (a) E-plane, (b) H-plane

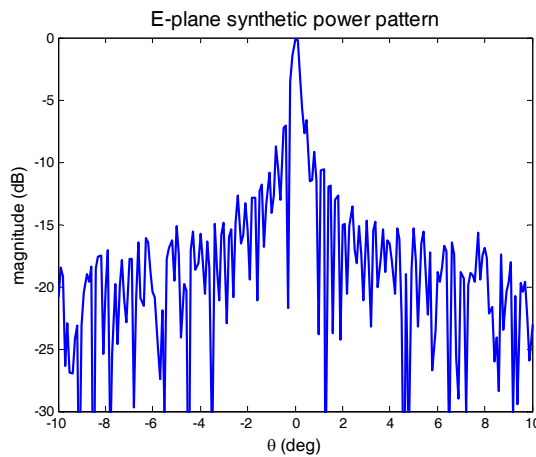


Fig. 10. E-plane synthetic power pattern by aperture synthesis

Element No.	VSWR	Element No.	VSWR
1	1.18	9	1.12
2	1.2	10	1.13
3	1.18	11	1.11
4	1.15	12	1.13
5	1.13	13	1.14
6	1.11	14	1.2
7	1.12	15	1.17
8	1.11	16	1.17

Table 3. Measured VSWR of each element in the array

All measured results indicate that the antenna array performs well with narrow main beamwidth, low peak sidelobe level and small VSWR, which are all desired for passive imaging radiometer.

5. Experiment Results with HUST-ASR

A series of experiments were conducted with HUST-ASR and brightness temperature images of natural scenes are shown in Fig. 11 and Fig. 12. In Fig. 11, natural scenes within a wide field of view are mapped. The outline of the chimney and the building nearby can be clearly distinguished. In Fig. 12, the outline and windows of the building and even the outline of the tree nearby can be seen in the image. Two air-conditioners on the wall of the building can also be seen in the image. All experimental results indicate that the HUST-ASR can generate good images of natural scenes with high spatial resolution provided by the antenna array.

Some “streaks” running along the vertical direction can be seen in the images due to the effect of slightly high sidelobes in H-plane pattern. Besides, our recent experimental work has shown that mutual effects of close antennas, as well as their individual matching, become important to fully understand the measurements. Thus, further research will be concentrated on error analysis and calibration of the antenna array in HUST-ASR.

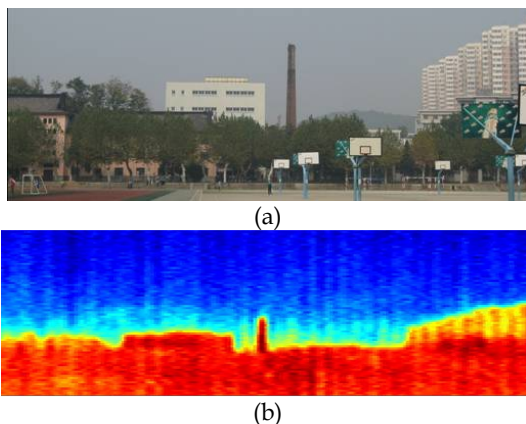
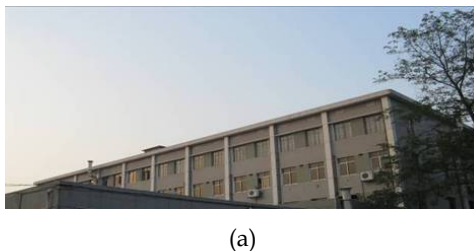
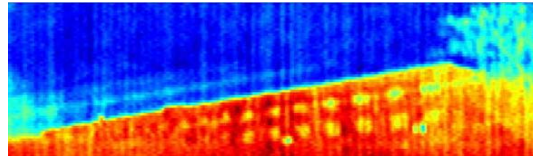


Fig. 11. Image of natural scenes within a wide FOV; (a) optic image; (b) brightness temperature image





(b)

Fig. 12. (a) Optic image of a building; (b) brightness temperature image of a building

6. Conclusion

Antenna array design is an important issue for aperture synthesis radiometers (ASR). In this chapter, two subjects are mainly addressed: one is to optimize antenna array configurations, which determines the spatial sampling performance of ASR; the other is to design the antenna array in the practical ASR system as the performance of the antenna array has much influence on the radiometric imaging performance.

The topology optimization of the antenna array in ASR aims to find the minimum redundancy array (MRA), which can provide the most uniform and complete (u, v) coverage in the Fourier plane with the least number of antenna elements and therefore achieves the highest spatial resolution of the image. In this part, different optimization methods and different array configurations for both linear and planar arrays are summarized. And some original work by the authors, including the restricted search method by exploiting general structure of MRLAs and combinatorial methods for constructing thinned circular arrays, is also briefly presented.

As a second part of the chapter, a sparse antenna array with parabolic cylinder reflector at millimeter wave band for HUST-ASR prototype is presented. The overall specifications, architecture design, performance evaluation, and measurement results of the antenna array are all detailed. Measured results indicate that the antenna array performs well with narrow main beamwidth, low peak sidelobe level and small VSWR, which are all desired for passive imaging radiometers. Experimental results indicate that the HUST-ASR can generate good images of natural scenes with high spatial resolution provided by the antenna array. Further research will be concentrated on error analysis and calibration of the antenna array in HUST-ASR.

7. Acknowledgment

This work was supported in part by the National Science Foundation of China (NSF60705018) and in part by the National High Technology Research and Development Program of China (No. 2006AA09Z143). The authors would like to thank Prof. Wei Guo, Quanliang Huang, and Liangqi Gui for their enthusiastic encouragements, and thank my colleagues Ke Chen, Liang Lang, Fangmin He, Liangbin Chen, Zubiao Xiong, and Wei Ni for their helpful suggestion. The authors also thank Handong Wu, Yingying Wang in Xi'an Hengda Microwave Technology Corp. for their contributions to the work.

8. References

- Balanis, C. A. (2005). *Antenna Theory-Analysis and Design*, 3rd ed., John Wiley & Sons Inc., New York
- Baumert, L. D. (1971). *Cyclic Difference Sets*, Springer-Verlag, New York
- Blanton, K. A.; McClellan, J. H. (1991). New search algorithm for minimum redundancy linear arrays. *Proceedings of IEEE ICASSP 1991*, Vol. 2, pp. 1361-1364
- Bracewell, R. N. (1966). Optimum spacings for radio telescopes with unfilled apertures. *Natl. Acad. Sci. Natl. Res. Council. Publ.*, Vol. 1408, pp. 243-244
- Butora, R.; Camps, A. (2003). Noise maps in aperture synthesis radiometric images due to cross-correlation of visibility noise. *Radio Sci.*, Vol.38, pp. 1067-1074
- Camps, A. (1996). Application of interferometric radiometry fro earth observation. Ph. D. Eng. thesis, Univ. of Catalonian, Catalonian, Spain, Nov. 1996
- Camps, A.; Bara, J.; Corbella, I.; Torres, F. A. (1997). The processing of hexagonally sampled signals with standard rectangular techniques: application to 2-D large aperture synthesis interferometric radiometers. *IEEE Trans. Geosci. Remote Sensing*, Vol. 35, No. 1, pp. 183-190
- Camps, A.; Corbella, I.; Bara, J.; Torres, F. A. (1998). Radiometric sensitivity computation in aperture synthesis interferometric radiometry. *IEEE Trans. Geosci. Remote Sensing*, Vol. 36, No. 2, pp. 680-685
- Camps, A.; Cardama, A.; Infantes, D. (2001). Synthesis of large low-redundancy linear arrays. *IEEE Trans. Antennas Propagat.*, Vol. 49, No. 12, pp. 1881-1883
- Chen, C. Y.; Vaidyanathan, P. P. (2008). Minimum redundancy MIMO radars. *Proceedings of IEEE ISCAS 2008*, pp. 45-48
- Chow, Y. L. (1970). Comparison of some correlation array configurations for radio astronomy. *IEEE Trans. Antennas Propagat.*, Vol. 18, pp. 567-569
- Dong, J.; Li, Q. X.; Guo W.; Zhu Y. T. (2008a). A Sparse Antenna Array with Offset Parabolic Cylinder Reflector at Millimeter Wave Band, *Proceedings of IEEE ICMMT 2008*, pp. 1667-1670, Nanjin, China
- Dong, J.; Li, Q. X.; He F. M.; Ni, W.; Zhu Y. T. (2008b). Co-array Properties of Minimum Redundancy Linear Arrays with Minimum Sidelobe Level, *Proceedings of IEEE ISAPE 2008*, pp. 74-77, Kunming, China
- Dong, J.; Li, Q. X.; Guo W.; Zhu Y. T. (2009a). An Approach to Topology Design of Two Dimensional Sparse Arrays for Synthetic Aperture Interferometric Radiometer. *J. Microwave*, Vol.25, No. 2, pp. 83-86
- Dong, J.; Li, Q. X.; Jin, R.; Huang, Q. L.; Gui, L. Q.; Zhu Y. T. (2009b). Difference Set Based Methods for Optimal Thinned Circular Arrays in Aperture Synthesis Radiometers. to be published in *J. Microwave*
- Dong, J.; Li, Q. X.; Guo, W. (2009c). A Combinatorial Method for Antenna Array Design in Minimum Redundancy MIMO Radars. *IEEE Antennas Wireless Propagat. Lett.*, vol. 8, pp. 1150-1153, 2009.
- Dong, J.; Li, Q. X.; Jin, R.; Zhu, Y. T.; Huang, Q. L.; Gui, L. Q. (2009d). A Method for Seeking Low-Redundancy Large Linear Arrays for Aperture Synthesis Microwave Radiometers. *IEEE Trans. Antennas Propagat.*, in press.
- Dong, J.; Li, Q. X.; Gui, L. Q.; Guo, W. (2009e). The Placement of Antenna Elements in Aperture Synthesis Radiometers for Optimum Radiometric Sensitivity. *IEEE Trans. Antennas Propagat.*

- Dorigo, M.; Stutzle, T. (2004). *Ant Colony Optimization*, MIT Press, Cambridge, MA
- Dudgeon, D. E.; Mersereau R. M. (1984). *Multidimensional Digital Signal Processing*, Prentice-Hall Inc., New York
- Ehrhardt, J. C. (1993). Hexagonal fast Fourier transform with rectangular output. *IEEE Trans. Signal Process.*, Vol.41, No. 3, pp. 1469-1472
- Greene, C. R.; Wood, R. C. (1978). Sparse array performance. *J. Acoust. Soc. Amer.*, Vol.63, pp. 1866-1872
- Goldberg, D. E. (1989). *Genetic Algorithms in Search, Optimization, and Machine Learning*, Addison-Wesley, Reading, MA
- Hall, M. Jr. (1986). *Combinatorial Theory*, 2nd ed., John Wiley & Sons Inc., New York
- Ishiguro, M. (1980). Minimum redundancy linear arrays for a large number of antennas. *Radio Sci.*, Vol.15, pp. 1163-1170
- Jorgenson, M. B.; Fattouche, M.; Nichols, S. T. (1991). Applications of minimum redundancy arrays in adaptive beamforming. *Microwaves, Antennas and Propagation, IEE Proceedings H*, Vol. 138, pp. 441-447
- Keto, E. (1997). The Shapes of Cross-correlation Interferometers. *The Astrophysical Journal*, Vol.475, pp. 843-852
- Kopilovich, L. E. (1992). New approach to constructing two-dimensional aperture synthesis systems. *Radar and Signal Processing, IEE Proceedings F*, Vol.139, pp. 365-368
- Kopilovich, L. E. (1995). Minimization of the number of elements in large radio interferometers. *R. Astron. Soc.*, Vol.274, pp. 544-546
- Kopilovich, L. E.; Sodin, L. G. (1996). Aperture optimization of telescopes and interferometers: A combinatorial approach. *Astron. Astrophys. Suppl. Ser.*, Vol.116, pp. 177-185
- Kopilovich, L. E. (2001). Configuration of a multielement interferometer covering hexagonal domains in the spatial-frequency plane. *Astron. & Astrophys.*, Vol.380, pp. 758-760
- Lambrigtsen, B.; Wilson, W.; Tanner, A. B.; Gaier, T.; Ruf, C. S.; Piepmeier, J. (2004). GeoSTAR - a microwave sounder for geostationary satellites. *Proceedings of IEEE IGARSS 2004*, Vol. 2, pp. 777-780
- Lee, Y.; Pillai, S. U. (1988). An algorithm for optimal placement of sensor elements. *Proceedings of IEEE ICASSP 1988*, Vol. 5, pp. 2674-2677
- Lee, H. J.; Park, H.; Kim, S. H.; Kim, Y. H.; Kang, G. S. (2005). Evaluation of angular resolution in near field using two point targets for Ka-band interferometric synthetic aperture radiometer with sub-Y-type array configuration. *Proceedings of IEEE IGARSS 2005*, pp. 4921-4924
- Leech, J. (1956). On the representation of $1, 2, \dots, n$ by differences. *J. London Math. Soc.*, Vol.31, pp. 160-169
- Le Vine, D. M. (1990). The sensitivity of synthetic aperture radiometers for remote sensing applications from space. *Radio Sci.*, Vol.25, pp. 441-453
- Le Vine, D. M.; Griffs, A. J.; Swift, C. T.; Jackson, T. J. (1994). ESTAR: a synthetic aperture microwave radiometer for remote sensing applications. *Proceedings of The IEEE*, Vol. 82, No. 12, pp. 1787-1801
- Le Vine, D. M.; Swift, C. T.; Haken, M. (2001). Development of the synthetic aperture microwave radiometer, ESTAR. *IEEE Trans. Geosci. Remote Sensing*, Vol. 39, No. 1, pp. 199-202

- Li, Q. X.; Chen K.; Guo, W.; Lang L.; He F. M.; Chen L. B.; Xiong Z. B. (2008a). An Aperture Synthesis Radiometer at Millimeter Wave Band, *Proceedings of IEEE ICMMT 2008*, pp. 1699-1701, Nanjin, China
- Li, Q. X.; Hu, F.; Guo, W.; Chen, K.; Lang, L.; Zhang, J.; Zhu, Y. T.; Zhang, Z. Y. (2008b). A General Platform for Millimeter Wave Synthetic Aperture Radiometers, *Proceedings of IEEE IGARSS 2008*, pp. 1156-1159, Boston, U.S.A.
- Lin, C. L.; Nie, Z. P. (2002). *Antenna Engineering Handbook*, Electronic Industry House, Beijing
- Linebarger, D. A. (1992). A fast method for computing the coarray of sparse linear arrays. *IEEE Trans. Antennas Propagat.*, Vol. 40, No. 9, pp. 1109-1112
- Linebarger, D. A.; Sudborough, I. H.; Tollis, I. G. (1993). Difference bases and sparse sensor arrays. *IEEE Trans. Inform. Theory*, Vol. 39, No. 2, pp. 716-721
- Mersereau, D. A. (1979). The processing of hexagonally sampled two-dimensional signals. *Proceedings of the IEEE*, Vol. 67, pp. 930-949
- Miller, J. (1971). Difference bases, three problems in additive number theory. in *Computers in Number Theory*, London: Academic Press, pp. 229-322
- Milligan, T. A. (2002). *Modern Antenna Design*, 2nd ed., John Wiley & Sons Inc., New Jersey
- Mills, B. Y.; Little, A. G. (1953). A high resolution aerial system of a new type. *Aust. J. Phys.*, Vol.6, pp. 272
- Martín-Neira, M.; Goutoule, J. M. (1997). A two-dimensional aperture-synthesis radiometer for soil moisture and ocean salinity observations. *ESA Bull.*, No. 92, pp. 95-104
- Pearson, D.; Pillai, S. U.; Lee, Y. (1990). An algorithm for near-optimal placement of sensor elements. *IEEE Trans. Inform. Theory*, Vol. 36, No. 6, pp. 1280-1284
- Pillai, S. U.; Bar-Ness, Y.; Haber, F. (1985). A new approach to array geometry for improved spatial spectrum estimation. *Proceedings of the IEEE*, Vol. 73, pp. 1522-1524
- Rautiainen, K.; Kainulainen, J.; Auer, T.; Pihlflyckt, J.; Kettunen, J.; Hallikainen, M. T. (2008). Helsinki University of Technology L-Band Airborne Synthetic Aperture Radiometer. *IEEE Trans. Geosci. Remote Sensing*, Vol. 46, No. 3, pp. 717-726
- Redéi, L.; Rényi, A. (1949). On the representation of $1, 2, \dots, n$ by means of differences (in Russian). *Mat. Sbornik (Recueil Math.)*, Vol.66(NS 24), pp. 385-389
- Ruf, C. S.; Swift, C. T.; Tanner A. B.; Le Vine, D. M. (1988). Interferometric synthetic aperture radiometry for the remote sensing of the Earth. *IEEE Trans. Geosci. Remote Sensing*, Vol. 26, No. 5, pp. 597-611
- Ruf, C. S. (1993). Numerical annealing of low-redundancy linear arrays. *IEEE Trans. Antennas Propagat.*, Vol. 41, No. 1, pp. 85-90
- Sodin, L. G.; Kopilovich, L. E. (2001). Hexagonal configuration of cross-correlation interferometers. *Astron. & Astrophys.*, Vol.368, pp. 747-748
- Sodin, L. G.; Kopilovich, L. E. (2002). Hexagonal arrays for radio interferometers. *Astron. & Astrophys.*, Vol.392, pp. 1149-1152
- Tanner, A. B. (1990). Aperture synthesis for passive microwave remote sensing: The electronically steered thinned array radiometer. Ph. D. Eng. thesis, Univ. of Mass., Amherst, American, Feb. 1990
- Tanner, A. B.; Swift, C. T. (1993). Calibration of a synthetic aperture radiometer. *IEEE Trans. Geosci. Remote Sensing*, Vol. 31, No. 1, pp. 257-267
- Thompson, A. R.; Moran, J. M.; Swenson, G. W. Jr. (2001). *Interferometry and Synthesis in Radio Astronomy*, 2nd ed., John Wiley & Sons Inc., New York

Wichmann, B. (1963). A note on restricted difference bases. *J. London Math. Soc.*, Vol.38, pp. 465-466

Antenna Measurement

Dominique Picard

*Supélec Plateau de Moulon 91192 Gif sur Yvette Cedex
France*

1. Introduction

The antenna is an important element of radiocommunication, remote sensing and radiolocalisation systems. The measurement of the antenna radiation pattern characteristics allows one to verify the conformity of the antenna. The simplest measurement method consists in the direct far-field measurement. For large antennas, the necessary measurement distance raises a problem which was resolved by the introduction of compact ranges and near-field techniques. Compact range consists in a focusing system, as a reflector, which can create a plane wave at short distance. The principle of near-field techniques is to measure the field radiated by an antenna at a short distance on a given surface surrounding the antenna, then to calculate the far-field starting from the measured near-field. These last techniques also make it possible to have an excellent precision as required by the satellite antennas for example. The near-field techniques also make it possible to carry out the diagnosis of the antennas, i.e. to find defects on the antenna. The duration of the measurement of the large antennas, which claims a large number of measurement points, was reduced considerably by the use of rapid near-field assessment system, for which the mechanical displacement of the probe was replaced by the electronic scanning of a probes array.

2. Direct far-field measurement

2.1 Antenna pattern measurement

There are four different regions for the electromagnetic field radiated by an antenna: three near-field regions and one far-field region. The nearest region is the reactive field region which extends until a distance of one wavelength λ from the antenna surface. The second near-field region is the Rayleigh region which extends from the reactive region until a distance $D^2/(2\lambda)$ from the antenna surface, a relation in which D is the tested antenna diameter. The third near-field region is the Fresnel region which extends from $D^2/(2\lambda)$ until $2D^2/\lambda$ from the antenna surface. The last region is the far-field Fraunhofer region which starts at a distance of $2D^2/\lambda$. The space variations of the electromagnetic field differ in these four regions. It is thus necessary to be at a distance sufficient ($>2D^2/\lambda$) to carry out direct far-field measurements.

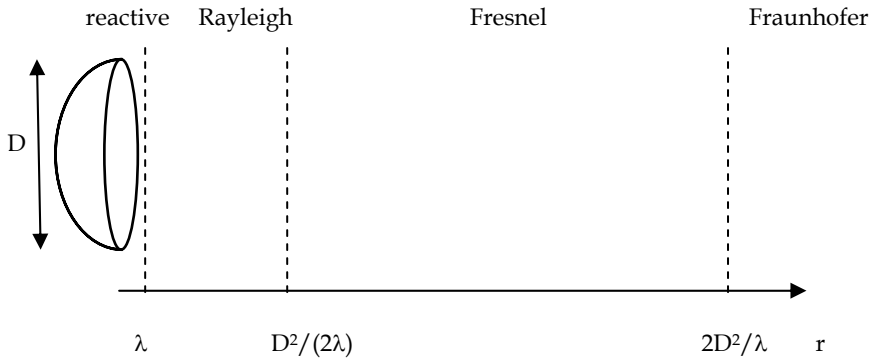


Fig. 1. Different field regions for a large antenna

Direct far-field measurement can be realized either in indoor or outdoor range (Kummer & Gillepsie, 1978). Indoor range consists in an anechoic chamber with one source antenna and the tested antenna placed on a positioner. This positioner allows one to vary the tested antenna attitude with respect to the direction of the wave incidence of the wave for far-field pattern measurement. Outdoor range consists in a tower bearing a source antenna and the tested antenna placed on a positioner. The distance between the two antennas can be larger for outdoor range, i.e. the capacity of outdoor range in terms of tested antenna dimensions is higher. On the other hand the outdoor range is sensitive to parasitic signals and ground reflections.

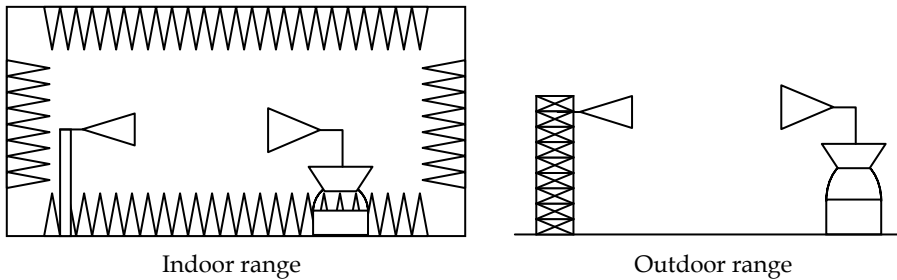


Fig. 2. Different range geometries

2.2 Measurement of the characteristics of the pattern

Gain measurement

Absolute gain measurements use power budget between antennas. The Friis transmission formula gives a relation between the gains G_A and G_B of two antennas A and B:

$$P_r = P_i G_A G_B (\lambda/4\pi r)^2 \tag{1}$$

P_r is the power received at a matched load connected to the receiving antenna, P_i the power accepted by the transmitting antenna, λ is the wavelength and r the distance between the two antennas. The use of this formula requires that the two antennas A and B are

polarization matched and that the separation distance between the antennas corresponds to far-field conditions.

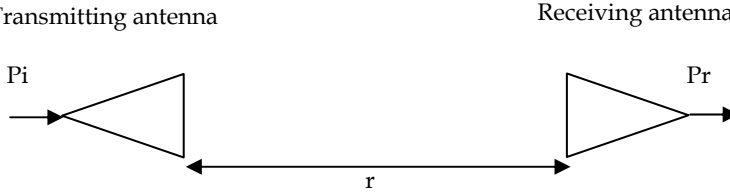


Fig. 3. The two antennas system corresponding to the Friis formula

The first method uses the tested antenna and a reference antenna with a known gain. The measurements of P_r , P_i , r , and the knowledge of λ give the value of the tested antenna gain by means of the Friis formula. The second method used two identical tested antennas with the same gain. The Friis formula gives the value of the tested gain antenna starting from the same measurements as the preceding method. The third method used three antennas A, B and C, generally the tested antenna and two other antennas. Three different power budgets are carried out, with the three possible antennas pairs leading to the three following equations:

$$G_A G_B = (P_r/P_i)_{AB} (4\pi r/\lambda)^2 \tag{2}$$

$$G_B G_C = (P_r/P_i)_{BC} (4\pi r/\lambda)^2 \tag{3}$$

$$G_C G_A = (P_r/P_i)_{CA} (4\pi r/\lambda)^2 \tag{4}$$

These three formulas provide the determination of the three different gains G_A , G_B and G_C .

Directivity measurement

There are two methods which make it possible to measure the directivity Dir of an antenna. The first method is based on the definition of the directivity. The knowledge of the relative far-field radiated by the antenna in all the directions is sufficient to know the directivity of this antenna. This method is called the pattern integration method because it uses the integration of the radiated power density (dP_e/dS) on all the directions to calculate the total power radiated by the antenna P_e . The power density is related to the electric field E at a distance r by the relation:

$$(dP_e/dS) = E^2/Z_0 \tag{5}$$

$Z_0 = 120\pi \Omega$ is the free space impedance of wave.

$$P_e = \int_{\varphi=0}^{2\pi} \int_{\theta=0}^{\pi} (dP_e/dS) r \sin\theta d\phi d\theta \tag{6}$$

$$Dir = (dP_e/dS) / [P_e/(4\pi r^2)] \tag{7}$$

The second method uses the relation between the directivity Dir and the gain G of a given antenna:

$$Dir = G/\eta \quad (8)$$

in which η is the efficiency of the antenna. The measurements of the gain and the efficiency of the antenna result in the knowledge of the directivity.

The first method is used more for directive antennas while the second is rather used more for omnidirectional antennas.

Efficiency

There are essentially three different methods to measure the efficiency of an antenna. The first method consists in the measurement of the gain G and the directivity D of the antenna, and then the relation between gain, directivity and efficiency η results in to obtain the efficiency:

$$\eta = G/Dir \quad (9)$$

The second method uses the measurement of the antenna input impedance and is called the Wheeler Cap Method. For certain antennas, microstrip patches for example, the losses can be modeled by a series resistance or a parallel resistance R_l with the antenna input resistance R_r . Two different antenna input impedance measurements are performed. The first measurement is done with the antenna in free space and the second measurement with the antenna inside a metallic hemisphere, and the input resistance of the antenna takes the values R_1 and R_2 respectively for these two measurements. If the loss resistance occurs in series, then it is short-circuited by the cap, and if the loss resistance occurs in parallel, then it is open-circuited by the cap. It is possible to have the relation between the efficiency, the radiated power and the losses power. This relation allows one to obtain the efficiency in function of R_r and R_l and then in function of the measured input resistance R_1 and R_2 . For the series modelling the efficiency is:

$$\eta = R_r / (R_r + R_l) = (R_1 - R_2) / R_1 \quad (10)$$

And for the parallel modelling:

$$\eta = R_l / (R_r + R_l) = (R_2 - R_1) / R_2 \quad (11)$$

The third method is called radiometric method. It consists in the measurement of the available noise power at the output of the antenna by means of a radiometer (Ashkenazy et al, 1985). This power U is related to the effective temperature T_e of the antenna and the equivalent temperature T_n of the radiometer by:

$$U = C(T_e + T_n) \quad (12)$$

in which C is a constant. The equivalent temperature T_n is derived from the noise figure of the radiometer. The effective temperature T_e of the antenna, at physical temperature T_a , is related to the efficiency η of the antenna by:

$$T_e = T_a (1-\eta) + T_t \eta \tag{13}$$

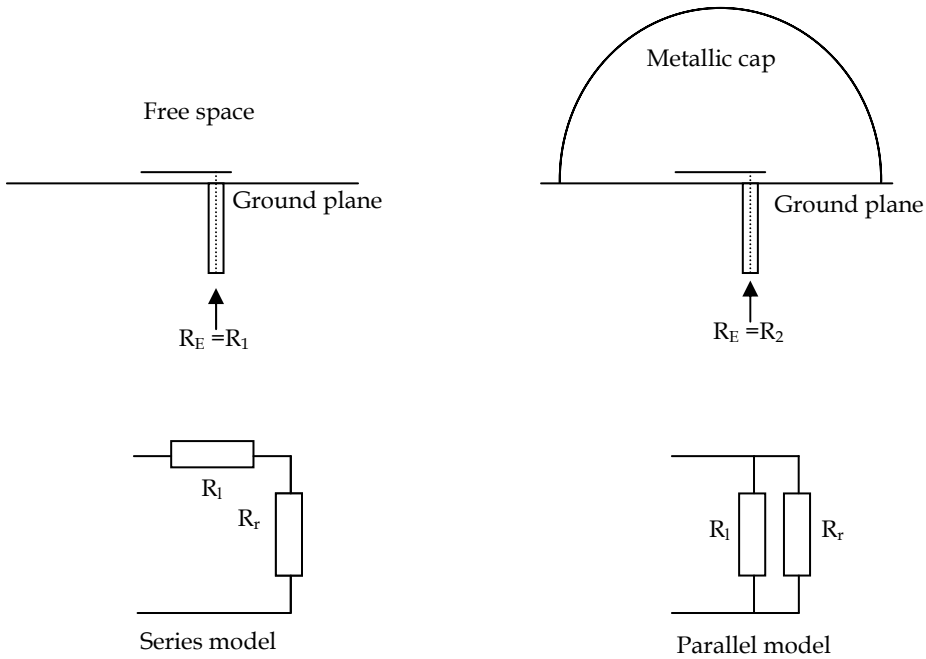


Fig. 4. The Wheeler Cap Method

T_t is the temperature target aimed by the antenna. The measurement of the noise power U for two different target temperatures, respectively the cold temperature T_c and the warm temperature T_w , allows the determination of the efficiency η . The cold target temperature is a clear sky and the warm one is an extended absorber at room temperature T_a .

$$\eta = [(T_n + T_a)(1 - \epsilon)] / [\epsilon (T_c + T_a)] \tag{14}$$

$$\epsilon = U_c / U_w \tag{15}$$

In fact it is also better to measure another antenna with high efficiency, such as a horn, for which the efficiency is equal to 1, with the same cold and warm temperatures as the first antenna. For this second antenna:

$$U_c / U_w = \delta = (T_n + T_a) / (T_n + T_c) \tag{16}$$

The efficiency η of the first antenna is:

$$\eta = [\delta (\varepsilon - 1)] / [\varepsilon (\delta - 1)] \quad (17)$$

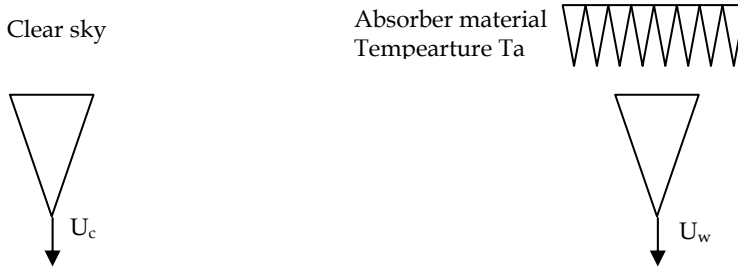


Fig. 5. The radiometric method

To achieve high sensitivity measurements the radiometer should have a low internal noise temperature and the temperature difference between the two targets should be as high as possible. The gain and directivity method and the radiometric method are well suited for directive antennas and the Wheeler Cap method for small antennas. A comparison study of these three methods for microstrip antennas has an accuracy of about 2% for the Wheeler Cap method, 10% for the radiometric method and 20% for the gain and directivity method (Pozar & Kaufman, 1988).

Polarization measurement

For harmonic mode, the electromagnetic field radiated by an antenna is polarized. Generally speaking, in one time period, the electric and magnetic fields, observed at a given point, describe a plane curve which is an ellipse. In the case of linear polarization the ellipse is reduced to its major axis. For circular polarization the modulus of the field remains constant. The knowledge of the polarization is equivalent to the knowledge of the ellipse: its axial ratio, the slope of its major axis relative to a reference direction and the sense of the displacement along the ellipse.

The experimental determination of the characteristics of the polarization ellipse can be carried out in several ways. It is possible to use amplitude-only measurements, or two amplitude and phase measurements with two different antennas with independent polarizations. The simplest method consists in using two antennas with linear polarization orthogonal one with the other. The same antenna can be used with two different orientations with orthogonal linear polarizations. Measurements provide the amplitude and the phase of the two field orthogonal components from which it is possible to calculate the characteristics of the polarization ellipse.

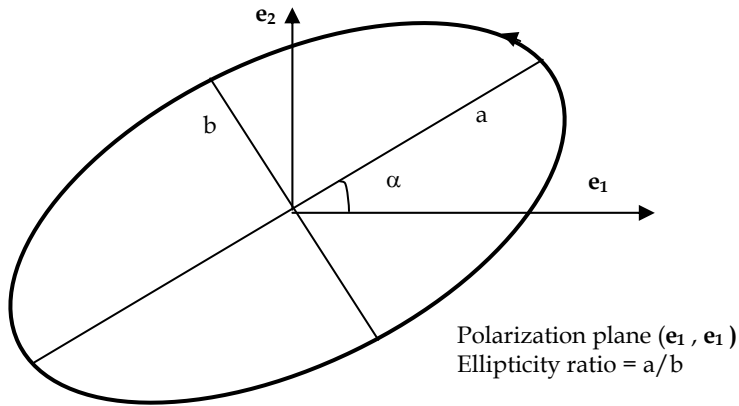


Fig. 6. Characteristics of the polarization ellipse

3. Compact antenna test ranges

3.1 Classical compact antenna test ranges

The compact ranges allow the direct far-field pattern measurement of antennas at near-field distance. It is then possible to carry out indoor antenna far field pattern measurements. The principle of compact range is to produce a plane wave at short distance, by means of a focusing system, like a reflector or a lens, illuminated by a primary feed (Johnson et al, 1969). There are two principal kinds of compact ranges. The first kind uses an offset parabolic reflector, with a possible Cassegrain geometry. The second kind uses two orthogonal cylindrical parabolic reflectors. This second geometry is equivalent to the first one with a significantly reduced cost due to the simpler reflectors geometry. The choice of an offset feed prevents aperture blockage and reduces the diffracted energy from the feed structure in the test region.

The main causes of errors on the field in the quiet zone are direct radiation from the primary feed, diffraction from the feed support, diffraction from the edges of the reflector, reflector surface deviations from the theoretical surface and room reflections. For surface deviations two parameters have to be taken into account: the value of the deviation and its extent over the surface. Calculations (Johnson et al, 1973) show that a 0.5dB error on the field corresponds to a 0.007 wavelength surface deviation. The use of serrations or rolled edges reduces the effect of the diffraction from the reflector edges. The positions and the length of the serrations are empirically adjusted so that the energy is diffracted in directions away from the test region for a broad band of frequencies. Room reflections and diffraction from the feed support are minimized by the use of absorbing material. The wise choice of the primary feed position compared to the tested antenna reduces the coupling due to the direct radiation of the feed. Time-gating of the measurement signal improve the performances of the compact range in relation to these last three errors causes.

The dimensions of the quiet zone are about the third of the reflector dimensions. Broadband compact ranges are available: 0.7GHz-100GHz with 3.6m cubic quiet zone. For such ranges,

several feed antennas are used, each antenna covering a half octave frequency band. The different feed antennas are automatically positioned at the reflector focus point and connected to the instrumentation, according to the required frequency. Typical amplitude variations of 1dB and phase variations of 10° , in the quiet zone, can be achieved. The cross polarization is better than 30dB.

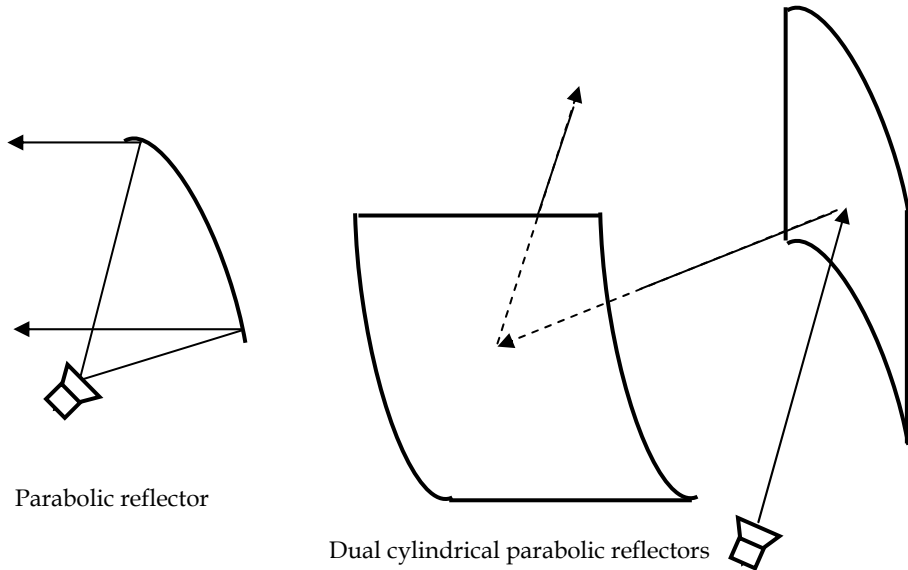


Fig. 7. Different kinds of compact ranges

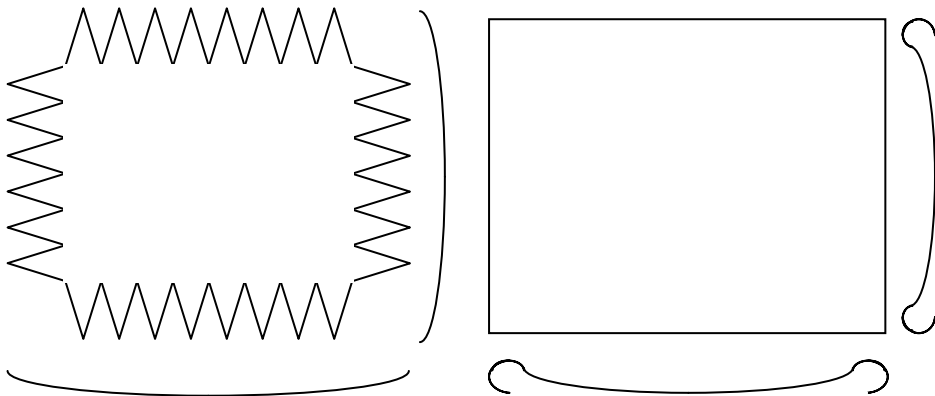


Fig. 8. Compact range reflector with serrations or rolled edges

3.2 Hologram compact antenna test range

It is difficult to test large antennas at frequencies above 100GHz. The use of near-field antenna measurements requires deformable coaxial cables or rotary joints with high performances, which is impossible at frequencies that are too high. Conventional reflector-

type compact antenna test ranges require one or more reflectors for which the surface accuracy needs to be better than about 0.01 wavelength, that is to say, for example, 15 μ m at 200GHz.

The use of a planar hologram constitutes another solution (Hirvonen et al, 1997). The surface accuracy requirements for an amplitude hologram are less stringent than those for a reflector, and its planar geometry simplifies its realization. The hologram compact antenna test range is a low-cost and easy-to-fabricate structure.

The principle of the hologram is to change the spherical wave front radiated by a source antenna (a horn for example) in a plane wave by means of the transmission through the hologram. It is possible to numerically calculate the structure required to change the known input field into the desired output field. The fabrication of the hologram is simplified by binary amplitude quantization: the local transmittance of the hologram is either 1 or 0. This is obtained by the use of a copper-plated Kapton film using an etching procedure. A hologram of 3 meters diameter has been used for the test of a 1.5 meter diameter reflector antenna at 322GHz. The envelopes of the measured and simulated far-field patterns are similar, but there are relatively important differences between the two far-field patterns.

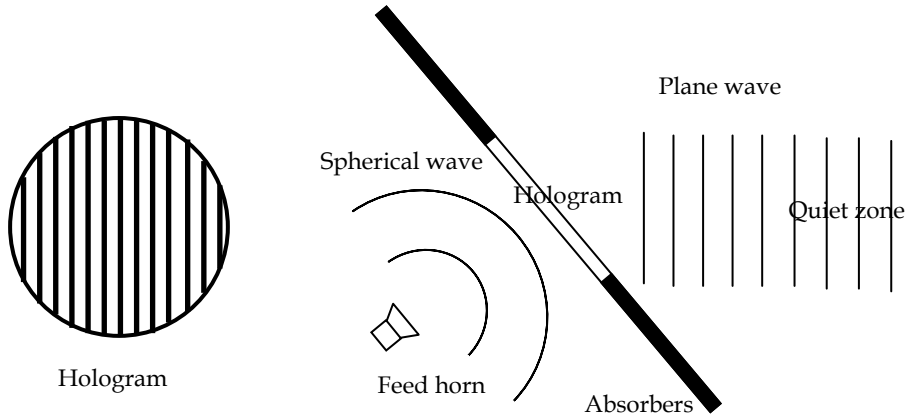


Fig. 9. Hologram and hologram compact antenna test range

4. Near-field techniques and applications

4.1 Near-field techniques

The principle of near-field techniques is to measure the field radiated by an antenna at a short distance on a given surface surrounding the antenna, then to calculate the far-field starting from the measured near-field (Yaghjian, 1986). Of the several formulations for these techniques, the two principal formulations are the Huygens principle and the modal expansion of the field.

Huygens principle

The tangential components of the electric and magnetic fields E_t and H_t are measured on an arbitrary surface S enclosing the tested antenna. These components allow one to calculate the equivalent electric and magnetic currents J_s and M_s . Then the electric and magnetic

fields can be evaluated everywhere out of the surface S starting from the equivalent currents. This method uses simple calculations, but for large antenna of diameter D the computer time varies like $(D/\lambda)^3$ and can become very long. Moreover the method requires calibrated and ideal probes and generally the measurement of the four field components. The electric and magnetic far-field \mathbf{E} and \mathbf{H} are given by the relations:

$$\mathbf{J}_s = \mathbf{n} \times \mathbf{H}_t \quad \mathbf{M}_s = -\mathbf{n} \times \mathbf{E}_t \quad (18)$$

$$\mathbf{E} = -j k / (4\pi) \iint_S [\mathbf{Z}_0 (\mathbf{J}_s \times \mathbf{u}) \times \mathbf{u} - \mathbf{M}_s \times \mathbf{u}] e^{-jkr} / r \, dS \quad (19)$$

$$\mathbf{H} = -j k / (4\pi) \iint_S [\mathbf{J}_s \times \mathbf{u} + 1/\mathbf{Z}_0 (\mathbf{M}_s \times \mathbf{u}) \times \mathbf{u}] e^{-jkr} / r \, dS \quad (20)$$

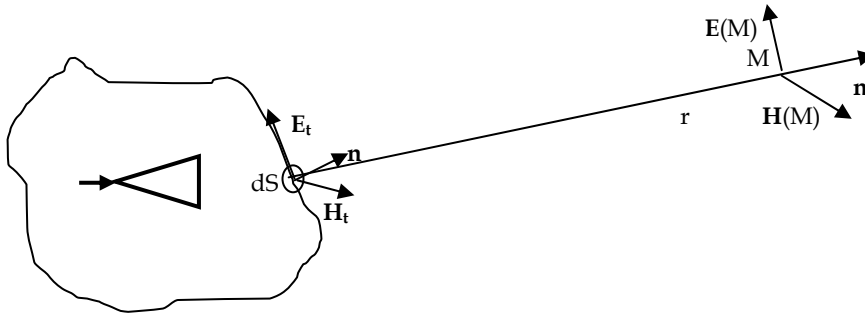


Fig. 10. The Huygens principle

Modal expansion of the field

In free space the electric and magnetic fields verify the propagation equation. This equation has elementary solutions or modes and a given field is a linear combination of these modes. The knowledge of the field of an antenna is equivalent to the knowledge of the coefficients of the linear combination. The expression of the modes is known for the different systems of orthogonal coordinates: cartesian, cylindrical and spherical. The coefficients of the linear combination are obtained by means of the two tangential field components measurement on a reference surface of the used coordinates system, then using an orthogonality integration. The case of the planar scanning is simple (Slater, 1991). The measurement of the two tangential components of the field, the electric field $\mathbf{E}_t(x,y,z)$ for example, is realized on a plane $z=0$ following a two dimensional regular grid (axis x and y). The antenna is located at $z < 0$. The tangential components of the plane wave spectrum are obtained from the measured field of the orthogonality integration:

$$\mathbf{A}_t(k_x, k_y, z) = 1/(2\pi) \int_{-\infty}^{+\infty} \int_{-\infty}^{+\infty} \mathbf{E}_t(x,y,z) e^{j(k_x x + k_y y)} \, dx \, dy \quad (21)$$

It is then possible to calculate the electric field in any point thanks to:

$$E(x,y,z) = 1/(2\pi) \int_{-\infty}^{+\infty} \int_{-\infty}^{+\infty} A(k_x,k_y) e^{-j(k_x x+k_y y+k_z z)} dk_x dk_y \quad (22)$$

$$k^2 = \omega^2 \epsilon_0 \mu_0 \quad k^2 = k_x^2+k_y^2+k_z^2 \quad (23)$$

The normal component $A_z(k_x,k_y)$ of vector $A(k_x,k_y)$ is obtained from the local Gauss equation:

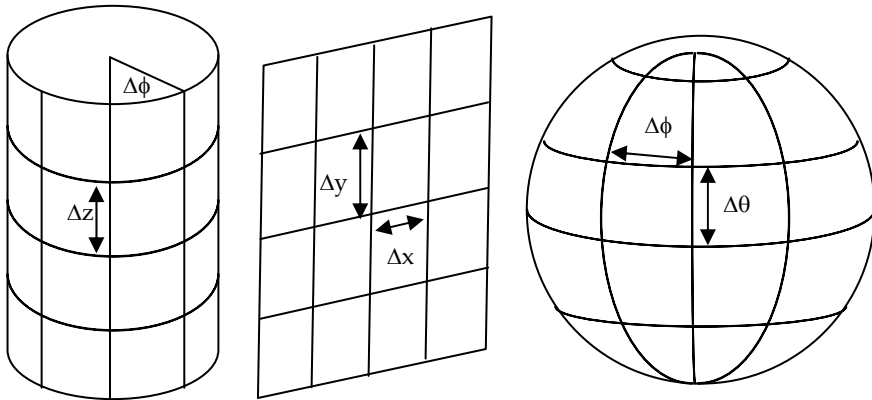
$$\mathbf{k} A(k_x,k_y) = 0 \quad \mathbf{k} = k_x \mathbf{e}_x + k_y \mathbf{e}_y + k_z \mathbf{e}_z \quad (24)$$

It is then possible to obtain the near-field of the antenna everywhere from the measurement of the near-field on a given plane. The electric far-field in the direction θ,ϕ and at a distance r is given by the relation:

$$E(r,\theta,\phi) = j k \cos\theta e^{-jkr}/r A(k\sin\theta\cos\phi,k\sin\theta\sin\phi) \quad k^2 = \omega^2 \epsilon_0 \mu_0 \quad (25)$$

It would be possible to obtain the magnetic field from the Maxwell-Faraday equation with the knowledge of the electric field.

The sampling spacing on the measurement surface is $\lambda/2$ following rectilinear axis (planar and cylindrical scanning) and $\lambda/2(R+\lambda)$ for angular variable (cylindrical and spherical scanning), R is the radius of the minimal sphere, i.e. the sphere whose centre is on the rotation axis, which contains the whole of the antenna and whose radius is minimal.



Cylindrical scanning

Planar scanning

Spherical scanning

Fig. 11. Sampling spacing for the different scanning geometries: $\Delta x = \Delta y = \Delta z = \lambda/2$, $\Delta\phi = \Delta\theta = \lambda/2(R+\lambda)$

Probe correction

In practice, the probe is not an ideal electric or magnetic dipole which measures the near-field in a point. The far-field pattern of the probe differs appreciably from the far-field of an elementary electric and magnetic dipole. For the accurate determination of electric and magnetic fields from near-field measurements, it is necessary to correct the nonideal receiving response of the probe. The probe remains oriented in the same direction with planar scanning, and the sidelobe field is sampled at an angle off the boresight direction of

the probe. Thus it is necessary to apply probe correction to planar near-field measurements. The problem is the same with cylindrical scanning for the rectilinear axis, and probe correction is also necessary in this case. For spherical scanning, the probe always points toward the test antenna and probe correction is not necessary if the measurement radius is large enough.

The formulation of probe correction is simple for planar scanning. The plane wave spectrum of the measurement A_m , as definite previously, is the scalar product of the plane wave spectra of the tested antenna A_a and the probe A_p :

$$A_m = A_a A_p = A_{ax} A_{px} + A_{ay} A_{py} \quad (26)$$

The measurement is repeated twice, for two orthogonal orientations between them, of the probe. This results in two equations on A_{ax} and A_{ay} and it is enough to invert this linear system of equations to obtain A_{ax} and A_{ay} .

Different coordinates systems comparison

In the case of planar cartesian and cylindrical coordinates systems, the measurement surface is truncated because the length of a rectilinear axis is limited. In practice, the measurement surface is a rectangle for planar exploration and a cylinder with a finite height for cylindrical exploration. Thus to minimize the effect of the measurement surface truncation, planar near-field systems are devoted to two-dimensional directive antennas and the cylindrical system requires antennas with directive pattern in at least one plane. Spherical near-field systems are convenient for omni-directional and directive antennas.

Phaseless method

The use of near-field techniques at frequencies above 100GHz is very difficult. This is due to the phase errors induced by coaxial cables or rotary joints whose performances are degraded at these frequencies. In counterpart, it is possible to measure the amplitude of the near-field until very high frequencies. This is why the phaseless methods appeared. These methods consist in the measurement of the near-field on two different surfaces, two parallel planes in front of the antenna for example, and to try to find the phase using an iterative process (Isernia & Leone, 1994). This iterative process consists in passing alternatively from one surface to the other by a near-field to near-field transformation. At the beginning, the distribution of the near-field phase on a surface is arbitrarily selected, a constant phase for example. Then when the near-field is calculated on the other surface, the calculated phase is preserved, and one associates it with the measured near-field amplitude. Then the near-field is calculated on the first surface and one starts again the process again. The process is stopped when the difference between the amplitudes of the computed and measured fields is lower than a given value.

To obtain an accurate reconstructed phase, it is necessary that the near-fields on the two planes are sufficiently different, i.e. the two planes are separated by a sufficient distance. A study shows good results for a low sidelobe shaped reflector antenna with an elliptical aperture with axes 155cm x 52cm at 9GHz (Isernia & Leone, 1995). The two planes are at a distance respectively of 4.2cm and 17.7cm from the antenna. The far-field pattern obtained

from the near to far-field transformation with phaseless method shows agreement with the reference far-field pattern, up to a -25dB level approximately.

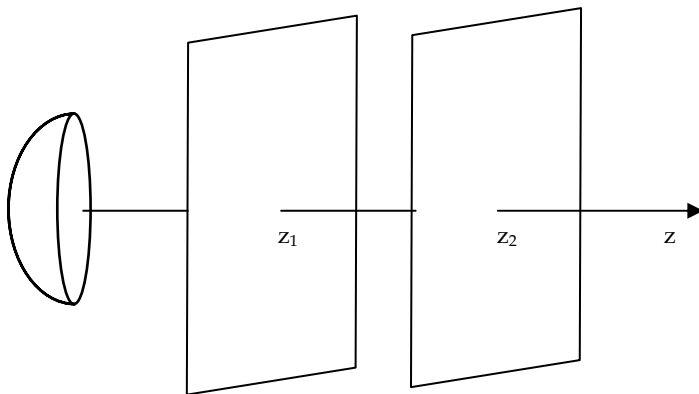


Fig. 16. Phaseless method with two parallel planes configuration

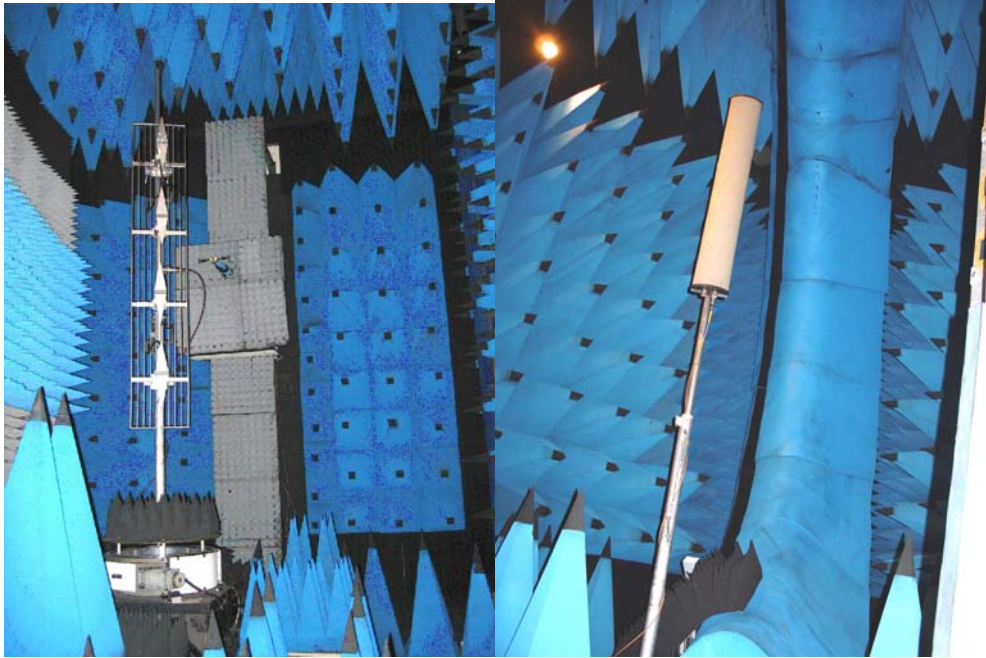
Near-field measurement errors analysis

One of the difficulties related to the use of the near-field techniques is the evaluation of the effect on the far field, of the measurement errors intervening on the near-field. A study allows the identification of the error sources, an evaluation of their level and the value of the induced uncertainties on the far-field, in the case of planar near-field measurements (Newell, 1988). About twenty different error sources are identified as probe relative pattern, gain, polarization, or multiple reflections between probe and tested antenna, measurement area truncation, temperature drift... The main error sources on the maximum gains are the multiple reflections between probe and tested antenna, and the power measurement, for a global induced error of 0.23dB. For sidelobe measurement, the main error sources are the multiple reflections between probe and tested antenna, the phase errors, the probe position errors and the probe alignment for a global induced error of 0.53dB on a -30dB sidelobe level. A comparison of the results obtained with four different near-field European ranges shows agreement on the copolar far-field pattern and directivity of a contoured beam antenna (Lemanczyk, 1988).

4.2 Near field applications

Electromagnetic antenna diagnosis

Antenna diagnosis consists in the detection of defects on an antenna. There are essentially two different electromagnetic diagnosis: reflector antenna diagnosis and array antenna diagnosis.



Cylindrical near-field range

Spherical near-field range

Fig. 12. Near-field ranges at Supélec.

Reflector antenna diagnosis

For reflector antennas, the diagnosis consists mainly in checking the reflector surface. It is possible to use an optical method to measure the reflector surface. This is a photogrammetric triangulation method (Kenefick, 1971). This method utilizes two or more long-focal length cameras that take overlapping photographs of the surface. This surface is uniformly covered with self-adhesive photographic targets whose images appear on the photographic record. The two-dimensional measurements of the image of the targets are processed with a least squares triangulation to provide the three-dimensional coordinates of each target. The accuracy of this method is of the order of one part in 100000 of the reflector diameter.

It is also possible to perform electromagnetic diagnosis of reflector antenna (Rahmat Samii, 1985). For this method, the knowledge of the amplitude and phase far-field pattern is required. This far-field can be obtained by means of near-field, compact range or direct far-field measurement. The relation between the two-dimensional amplitude and phase far-field and the electric current on the reflector surface is known. This relation can take the form of a two-dimensional Fourier transform at the cost of some approximations, and can then be inverted easily. Finally, the phase of the currents can be interpreted like a deformation starting from the theoretical geometry of the reflector. A study of this method using spherical near-field measurements on a large reflector antenna give good results: small deformations of about one λ diameter and a $\lambda/10$ thickness are detected (Rahmat Samii, 1988).

Array antenna diagnosis

The electromagnetic diagnosis of array antennas consists in detecting defective or badly fed elements on the antenna. To obtain this detection, it is sufficient to rebuild the feeding law of the antenna elements. There are two methods of array antenna diagnosis that primarily exist. The first method uses backward transform from the measurement plane to the antenna surface and is called the spectral method (Lee et al, 1988). The measurement of the radiated near field is performed on a plane parallel to the antenna surface. Then the measured near field is processed to obtain the near field at the location of each element of the array. This processing contains element and probe patterns correction. The feeding of each element is then considered as being proportional to the near field at the location of the element. The second method uses the linear relation between the feeding of each element and the measured near field and is called the matrix method (Wegrowicz & Pokuls, 1991), (Picard et al, 1996), (Picard et al, 1998). The near field is also measured on a plane parallel to the antenna surface. The number of space points is higher than or equal to the number of elements in the array. The linear equation system is numerically inverted. The advantage of the matrix method, compared to the spectral method, is that it uses a number of measurement points significantly weaker. The accuracy of these methods on the reconstructed feeding law is of the order of a few degrees and a few tenth of dB.

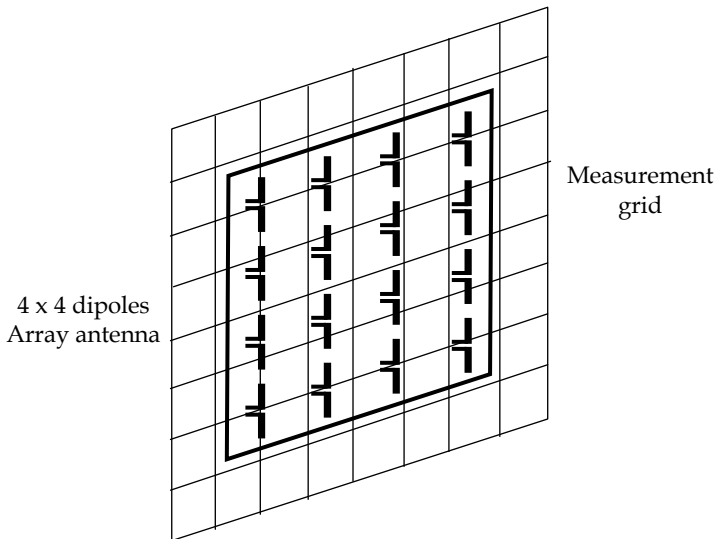


Fig. 13. Array antenna diagnosis: measurement configuration

Antennas coupling

The coupling coefficient between two antennas can be obtained by using the fields radiated by these two antennas separately (Yaghjan, 1982). The reciprocity theorem makes it possible to show that the voltage V_{BA} induced by the radiation of an antenna A at the output of an antenna B is

$$V_{BA} = - \iint_S [\mathbf{E}_a \times \mathbf{H}_b + \mathbf{H}_a \times \mathbf{E}_b] \cdot \mathbf{n} \, dS \quad (27)$$

S is a close surface surrounding the antenna B,

\mathbf{n} is the normal vector to S with the outside orientation,

$\mathbf{E}_a, \mathbf{H}_a$ electric and magnetic fields radiated by the antenna A,

$\mathbf{E}_b, \mathbf{H}_b$ electric and magnetic fields radiated by the antenna A for the emission mode with unit input current,

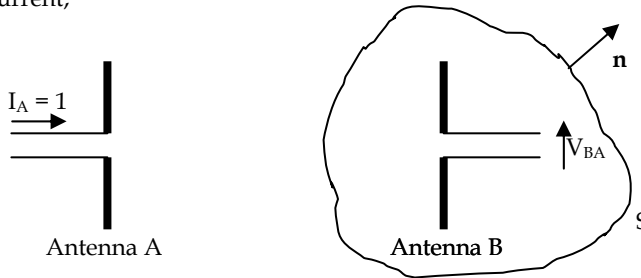


Fig. 14. The two antennas system for coupling evaluation

The advantage of this method is that it can predict, by calculation, the coupling between the two antennas for any relative position, only by means of their separate radiated near-fields measurements.

Determination of the safety perimeter of base station antennas

An application of the cylindrical near-field to near-field transformations is the determination of the base station antennas safety perimeter. The electric and magnetic near-fields level can be evaluated from the near-field measurements and from the power accepted by the antenna. The comparison of this level with the ICNIRP reference level allows the determination of the safety perimeter (Ziyyat et al, 2001), (ICNIRP, 1998). The accuracy obtained by this method is within a few percent on the calculated near-field.

Rapid near-field assessment system

The near-field measurement of a large antenna requires a considerable number of measurement points. Computers' computing power has increased regularly and was multiplied by approximately 100000 between 1981 and 2006. The result is from it that the duration of the far-field calculation decreases regularly and is no longer a problem. On the other hand the duration of measurement can be very important. This is due to the slowness of mechanical displacements. The replacement of the mechanical displacement of the probe by the electronic scanning of a probes array makes it possible to accelerate considerably the measurement rate and to reduce the measurement duration (Picard et al., 1992), (Picard et al, 1998).

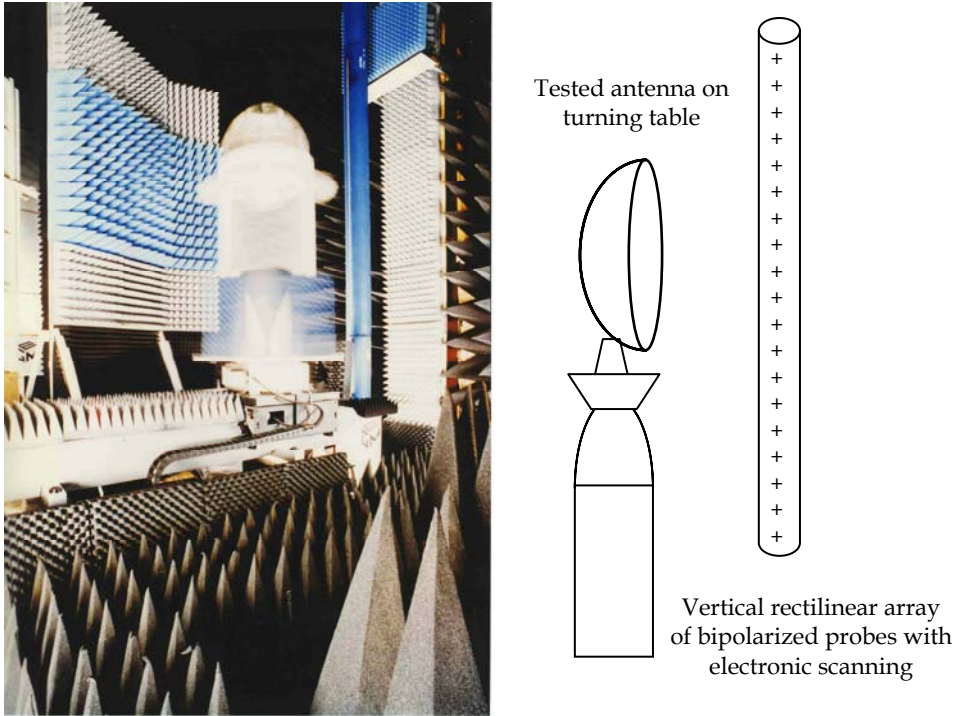


Fig. 15. Rapid near-field range at Supélec and principle of rapid near-field assessment systems

5. Electromagnetic field measurement method

The measurement of the radiation of the antennas is indissociable from the measurement of high frequency electromagnetic field. Primarily four different methods for high frequency electromagnetic field measurement exist. These methods differ primarily by the type of connection between the probe and the receiver, this connection could possibly be the cause of many disturbances. The first method is the simplest one. It consists in using of a small dipole probe connected to a receiver with a coaxial line. In order to limit the parasitic effects of the line on the measurement signal, a balun is placed between the line and the dipole. This method makes it possible the measurement of the local value of one component of the electric or magnetic field.

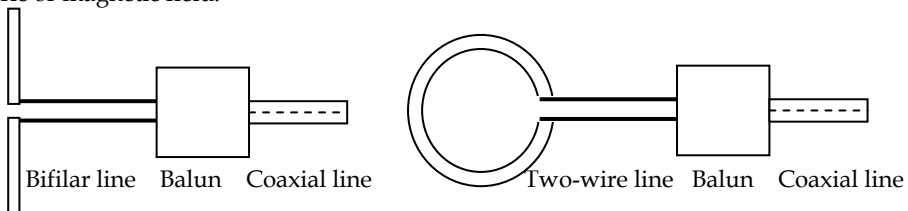


Fig. 17. Measurement of the electric and magnetic field with a dipole probe

In the case of a field whose space variations are very fast, the modulated scattering technique can be used advantageously. This second method consists in the use of a small probe loaded with a nonlinear element like a PIN diode, which is low frequency modulated (Callen & Parr, 1955), (Richmond, 1955), (Bolomey & Gardiol, 2001). The electromagnetic field scattered by this probe is collected by the emitting antenna (monostatic arrangement) or by a specific or auxiliary antenna (bistatic arrangement) called auxiliary antenna. The signal provided by the emitting antenna is proportional to the square of the field radiated at the probe location for the monostatic arrangement, and that provided by the auxiliary antenna is proportional to this field for the bistatic arrangement. These two signals are low frequency modulated like the scattered field, and this amplitude modulation allows one to retrieve this signal among parasitic signals, with coherent detection for example. The low frequency modulation of the diode may be conveyed by resistive lines or by an optical fiber in the case of the optically modulated scattering technique (Hygate & Nye, 1990) so as to limit the perturbations.

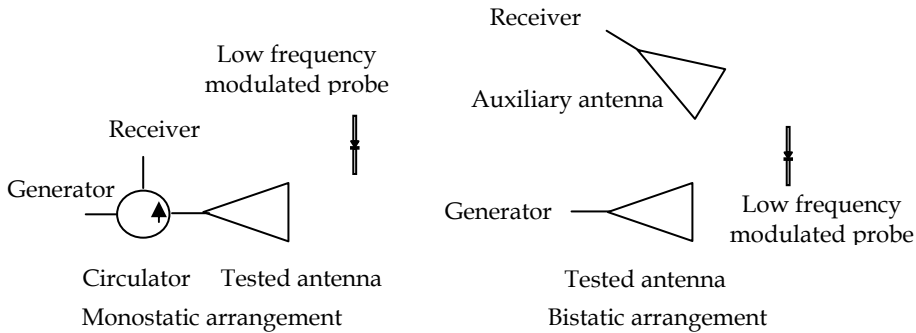


Fig. 18. The modulated scattering technique

The third method uses an electro-optic probe. This probe is a small one like a dipole, and is loaded with an electro-optic crystal like LiNbO_3 . The refraction index of the crystal linearly depends on the radiofrequency electric field which is applied to it. The light of a laser is conveyed by an optical fiber and crosses the crystal. The phase variations of the light transmitted through the crystal are measured and are connected linearly to the radiofrequency electric field applied to the crystal. The calibration of the probe makes it possible to know the proportionality factor between the variation of the phase undergone by the light and the amplitude of the measured radiofrequency electric field. This method makes it possible to produce probes with very broad band performances (Loader et al, 2003). In particular, an electric dipole of this type is an excellent time-domain probe: the measurement signal is proportional to the measured time-domain electric field.

The last method is simpler and less expensive than the two preceding ones while making it possible to carry out very local measurements without the disturbances due to the connection between the probe and the receiver. This method uses detected probes (Bowman, 1973) to measure the local electric field. Such a probe is loaded with a schottky diode and detects the RF currents induced by the electric field, to obtain a continuous voltage. This voltage can be measured by a voltmeter. The lines connecting the dipole and the voltmeter are made highly resistive to reduce their parasitic effect. The main defects of this method are

its poor sensitivity and that it provides only the amplitude of the measured field. If the knowledge of the phase is necessary for the application, it must be obtained by means of phaseless methods.

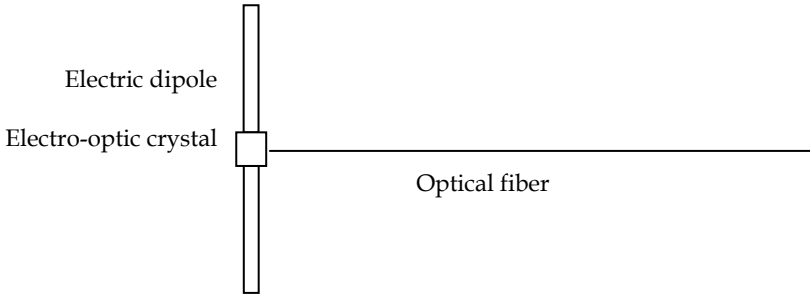


Fig. 19. Electro-optic dipole probe

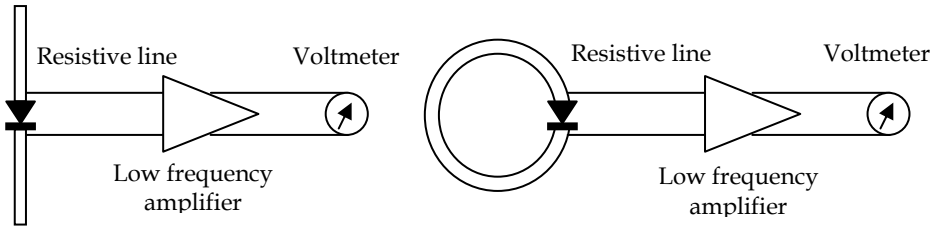


Fig. 20. Detected probe

6. Instrumentation

The instrumentation used for antenna measurements depends on the temporal mode used: time domain or frequency domain. Network or spectrum analyzer and frequency synthesizer are used for frequency domain measurements. Real time or sampling oscilloscope and pulse generator are used for time domain measurements.

Frequency domain antenna measurements

The system of emission-reception the most used for antenna measurements is the vector network analyzer. It allows the measurement of transmission coefficients and it supplies the phase. Its intermediary frequency bandwidth can reach 1MHz, i.e. it allows very high speed measurements, and its dynamic can reach 140dB. It can have several ways of measurement so as to be able to measure simultaneously direct and cross polarizations. Its maximum frequency bandwidth of operation is 30kHz to 1000GHz (with several models). It is also possible to use a scalar network analyzer or a spectrum analyzer coupled to a frequency synthesizer when the measurement of the phase is not necessary as for far-field for example.

Time domain antenna measurements

Antenna measurements in the time domain are less frequent than in the frequency domain. The measurement signal is delivered by a pulse generator. Certain characteristics of the pulse can be adjusted: the rise and fall times, the duration, the repetition rate and the

amplitude. The receiver is a fast oscilloscope. The real time oscilloscope acquires the measured time response in one step, but its sensitivity is limited and it is very expensive. The sampling oscilloscope requires numerous repetitions of the measurement signal to acquire its time response, but its sensitivity is better and its price is lower than those of the real time oscilloscope. In 2009, the maximum frequency of operation for real time oscilloscope is 20GHz and 75GHz for sample oscilloscope.

Probe

Direct far-field measurements use a source antenna. The dimensions of this source antenna are limited by the distance between this antenna and the tested antenna. A large source antenna increases the measurement signal and decreases the parasitic reflections. The measured polarization is the one of the source antenna.

Near-field measurements can use several types of probe: open-ended circular or rectangular metallic waveguide and electric dipole for narrow band operation (half a octave) and ridged waveguide for broad band operation (a decade).

7. Conclusion

Currently it is possible to measure all the characteristics of an antenna with a good accuracy. Far-field ranges do not have a very good accuracy, due to parasitic reflections for the outdoor ranges and because of the limited distance between the source antenna and the tested antenna for the indoor ranges. The compact range allows one to obtain a direct far-field cut in a relatively short time. The near-field techniques are the most accurate and the most convenient for global antenna radiation testing. Their main defect is the duration of the measurement which rises from the large number of necessary space points. Rapid near-field measurement systems allow one to solve this problem, but the accuracy is less good, and the frequency bandwidth is limited. Progress is necessary in this field. Research relates to the rise in frequency, with for solutions the hologram compact antenna test range and the phaseless methods. The hologram compact antenna test range must improve their accuracy while the phaseless methods must improve their reliability. Electromagnetic diagnosis of antenna must be optimized on a case-by-case basis.

8. References

- Ashkenazy, J. et al. (1985). Radiometric measurement of antenna efficiency, *Electronics letters*, Vol.21, N°3, January 1985, pp.111-112, ISSN 0013-5194
- Bolomey, J. C. & Gardiol, F.E. (2001). *Engineering applications of the modulated scatterer technique*, Artech House Inc, ISBN 1-58053-147-4, 685 Canton Street, Norwood, MA 02062 USA
- Bowman, R. R. (1973). Some recent developments in the characterization and measurement of hazardous electromagnetic fields, International Symposium, Warsaw, October 1973, pp217-227
- Callen, A. L. & Parr, J. C. (1955). A new perturbation method for measuring microwave fields in free space, *IEE(GB)*, n°102, 1955, p.836

- Hygate, G. & Nye J. F. (1990). Measurement microwave fields directly with an optically modulated scatterer, *Measurement Science and Technology's*, 1990, pp.703-709, ISSN 0957-0233
- Hirvonen, T. et al. (1997). A compact antenna test range based on a hologram, *IEEE Transactions on Antennas and Propagation*, Vol.AP45, N°8, August 1997, pp.1270-1276, ISSN 0018-926X
- ICNIRP, (1998). Guide pour l'établissement de limites d'exposition aux champs électriques, magnétiques et électromagnétiques, *Health Physics Society*, Vol.74, n°4, 1998, pp.494-522, ISSN 0017-9078
- Isernia, T. & Leone, G. (1994). Phaseless near-field techniques : formulation of the problem and field properties, *Journal of electromagnetic waves and applications*, Vol.8, N°1, 1995, pp.267-284, ISSN 0920-5071
- Isernia, T. & Leone, G. (1995). Numerical and experimental validation of a phaseless planar near-field technique, *Journal of electromagnetic waves and applications*, Vol.9, N°7, 1994, pp.871-888, ISSN 0920-5071
- Johnson, R. C. et al. (1969). Compact range techniques and measurements, *IEEE Transactions on Antennas and Propagation*, Vol.AP17, N°5, September 1969, 568-576, ISSN 0018-926X
- Johnson, R. C. et al. (1973). Determination of far-field antennas patterns from near-field measurements, *Proceeding of the IEEE*, Vol.61, N°12, December 1973, pp.1668-1694, ISSN 0018-9219
- Kenefick, J. F. (1971). Ultra-precise analytics, *Photogrammetry Engineering*, Vol.37, 1971, pp.1167-1187, ISSN 0031-8671
- Kummer, W. & Gillespie, E. (1978). Antenna measurement - 1978, *Proceedings of the IEEE*, Vol.66, N°4, April 1978, 483-507, ISSN 0018-9219
- Lee, J.J. et al. (1988). Near-field probe used as a diagnostic tool to locate defective elements in an array antenna, *IEEE Transactions on Antennas and Propagation*, Vol.AP36, n°6, June 1988, ISSN 0018-926X
- Lemanczyk, H. (1988). Comparison of near-field range results, *IEEE Transactions on Antennas and Propagation*, VolAP36, n°6, June 1988, pp.845-851, ISSN 0018-926X
- Loader, B. G. et al. (2003). An optical electric field probe for specific absorption rate measurements, The 15th International Zurich Symposium, 2003, pp.57-60
- Newell, A. C. (1988). Error analysis techniques for planar near-field measurements, *IEEE Transactions on Antennas and Propagation*, VolAP36, n°6, June 1988, pp.754-768, ISSN 0018-926X
- Picard, D. et al. (1992). Real time analyser of antenna near-field distribution, 22nd European Microwave Conference, Vol..1, pp.509-514, Espoo, Finland, 24-27 August 1992
- Picard, D. et al. (1996). Reconstruction de la loi d'alimentation des antennes réseau à partir d'une mesure de champ proche par la méthode matricielle, Jina 1996, Novembre 1996, Nice
- Picard, D. et al. (1998). Broadband and low interaction rapid cylindrical facility, PIERS 1998, Nantes, France, July 1998, pp.13-17
- Picard, D. & Gattoufi, L. (1998). Diagnostic d'antennes réseau par des méthodes matricielles, *Revue de l'Electricité et de l'Electronique*, n°9, Octobre 1998

- Pozar, D. & Kaufman, B. (1988). Comparison of three methods for the measurement of printed antennas efficiency, *IEEE Transactions on Antennas and Propagation*, Vol.AP36, N°1, January 1988, 136-139, ISSN 0018-926X
- Rahmat Samii, Y. (1985). Microwave holography of large reflector antennas simulation algorithms, *IEEE Transaction on Antennas and Propagation*, Vol.AP33, N°11, November 1985, ISSN 0018-926X
- Rahmat Samii, Y. (1988). Application of spherical near-field measurements to microwave holographic diagnosis of antennas, *IEEE Transaction on Antennas and Propagation*, VolAP36, n°6, June 1988, ISSN 0018-926X
- Richmond, J. H. (1955). A modulated scattering technique for measurement of field distribution, *IRE Transactions on Microwave theory and technique*, Vol.3, 1955, pp.13-17
- Slater, D. (1991). *Near-field antenna measurements*, Artech House Inc, ISBN 0-89006-361-3, 685 Canton Street, Norwood, MA 02062 USA
- Wegrowicz, L.A. & Pokuls, R.. (1991). Inverse problem approach to array diagnostics, IEEE AP-S International Symposium, Ontario, Canada, pp.1292-1295, 24-28 June 1991
- Yaghjian, A.D. (1982). Efficient computation of antenna coupling and fields within the near-field region, *IEEE Transactions on antennas and Propagation*, Vol. AP30, n°1, January 1982, pp113-127, ISSN 0018-926X
- Yaghjian, A. (1986). An overview of near-field antenna measurements, *IEEE Transactions on Antennas and Propagation*, Vol.AP34, N°1, January 1986, 30-45, ISSN 0018-926X
- Ziyyat, A. et al. (2001). Prediction of BTS antennas safety perimeter from near-field to near-field transformation : an experimental validation, AMTA'2001 Symposium, Denver, Colorado, USA, October 2001

The interference between ground plane and receiving antenna and its effect on the radiated EMI measurement uncertainty

Mikulas Bittera, Viktor Smiesko, Karol Kovac and Jozef Hallon
*Slovak University of Technology
Slovakia*

1. Introduction

Despite the fact that the result of the radiated electromagnetic interference (EMI) measurement is two-valued, i.e. „pass / fail“, the measurement is the most complex and the most time-consuming measurement of all of electromagnetic compatibility (EMC) measurements. The main task of such measurement is to recognize whether a maximal value of the radiated disturbance from the equipment under test (EUT) exceeds the maximal value given by a standard – a limit value. These limit values are chosen so that no EMI generated by the EUT exceeds the level, which can disturb the operation other electronic devices of commonly used.

Also the interpretation of the radiated EMI measurement is a very complex problem due to many disturbing influences affecting such a measurement. The problem is more difficult because of the necessity to derive the uncertainty budget of EMI measurement of test laboratories. In general, we can recognize three types of negative effects on the uncertainty of the measurement:

- effect of test site equipment (of the measuring chain);
- effect of test site arrangement;
- effect of the tested equipment.

Except for the effect of the tested equipment, which depends mainly on its cable arrangement, the main problem represents the effect of receiving antenna, if a broadband antenna is used. The antenna brings into measurement additional errors, which increase measurement uncertainty. Some errors are also caused by presence of the ground plane in the test site. They are mainly error of antenna factor and of directivity, which can emphasize or suppress the errors of receiving antenna. These errors and their effect on the entire uncertainty of the measurement are investigated in case of broadband Bilog antenna, a typical receiving antenna for radiated EMI measurement, which covers a frequency range of our interest. Since the mentioned effects cannot be quantified by real measurement or by simple calculation, this investigation is based on numerical calculation – simulation based on “method of moments”.

2. Radiated EMI measurement

2.1 Principle of measurement

A principle of the radiated EMI measurement given by (CISPR 16-2-3) is shown in Fig. 1. The intensity of electric field, generated by EUT, is scanned by the receiving antenna and measured by a rf measuring receiver. The measurement is executed in an open area test site, but it may be performed also in shielded chambers to suppress ambient disturbing signals. As it may be seen also in Fig. 1 the antenna receives radiated disturbance from EUT directly but also by reflected wave from the reference ground plane, which ensures equivalent conditions for all test sites.

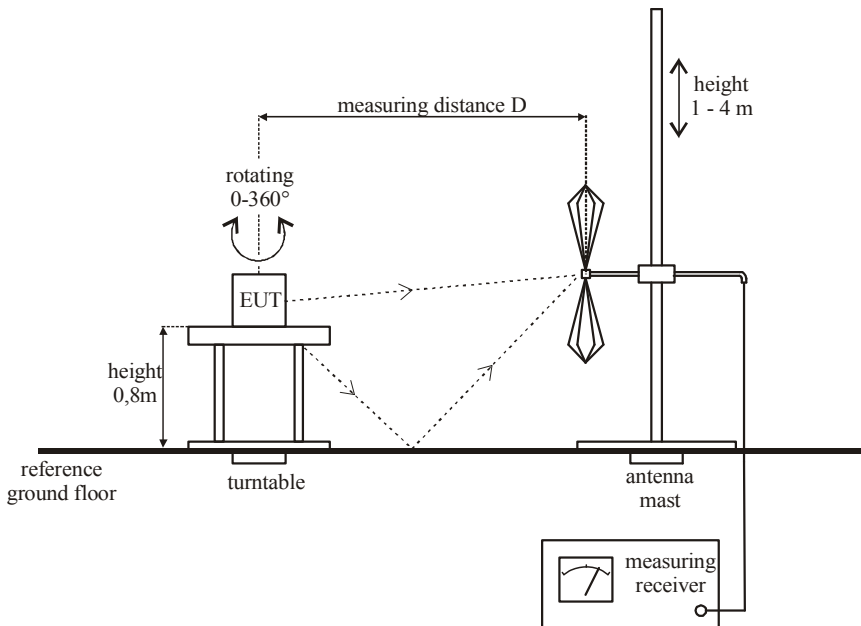


Fig. 1. Scheme of radiated EMI measurement

Measured electromagnetic wave from the EUT is in the point of receiving antenna given by vector sum of direct and reflected wave. Resulting phase of the sum is changing with the varying height over the reference ground plane. Since the maximal radiated disturbance must be found receiving antenna must change its height in the range of 1 m to 4 m and also EUT must rotate to record all directions of possible radiations.

The measurement must be executed for both polarizations of receiving antenna – horizontal and vertical. The radiated disturbance must be recorded in frequency range of 30 MHz to 1000 MHz and a quasi-peak value of this disturbance must be measured by a quasi-peak detector. Such a value does not depend only on amplitude of the measured voltage but also on its repetition frequency, so the resulting value is relative to voltage-time area of disturbing signal.

So, concerning the radiated EMI measurement, it shall be found by the maximal radiated disturbance is given:

- certain arrangement of EUT;
- certain turn of EUT;
- certain height of receiving antenna;
- certain polarization of receiving antenna;
- certain frequency of radiated disturbance.

If such a maximal value does not exceed the given disturbance limit value for the given electric device, the EUT can be stated as electromagnetic compatible in terms of radiated disturbance.

2.2 Uncertainty of measurement

In general, uncertainty of the measurement is as important as the result of measurement itself. The term uncertainty represents a region about an observed value of a measured quantity, which is likely to contain the true value of that quantity. The uncertainty describes deficiencies of quantity knowledge. There are many potential uncertainty contributions, which influence the uncertainty of measurement and which cannot be independent.

The standard CISPR 16-4-2 (CISPR 16-4-2) knows and quantifies following 17 uncertainty contributions that influence the radiated EMI measurement:

- receiver reading;
- attenuation between antenna and receiver;
- antenna factor;
- receiver corrections for sine-wave voltage;
- receiver corrections for pulse amplitude corrections;
- receiver corrections for pulse repetition rate response;
- receiver corrections for noise floor proximity;
- mismatch between antenna and receiver;
- antenna factor frequency interpolation;
- antenna factor height deviations;
- directivity difference of antenna ;
- phase centre location of antenna;
- cross-polarisation of antenna;
- balance of antenna;
- test site imperfections;
- measuring distance between EUT and antenna;
- table or EUT height.

It is important to note, that despite the fact that most of these contributions do not influence the result of measurement, they affect its uncertainty. The combined standard uncertainty may be computed using Gauss's law on the distribution of uncertainty:

$$u_c = \sqrt{\sum_i c_i^2 u^2(x_i)} \quad (1)$$

where c_i is the sensitivity coefficient and $u(x_i)$ the standard uncertainty in decibel of i -th contribution x_i . The expanded measurement uncertainty may be calculated as:

$$U = 2u_c \quad (2)$$

and it should be less than U_{CISPR} , which is given by standard CISPR 16-4-2 and which is 5.2dB. If the uncertainty U is greater than U_{CISPR} all the measurement results have to be increased by the difference ($U-U_{CISPR}$).

3. Receiving antennas

In order to obtain the radiated EMI measurement we should use antennas of various types. An antenna transforms intensity of electromagnetic field to voltage, which is measurable by the measuring receiver. To get the exact value of field intensity, tuned half-wave dipoles shall be used. The dipoles represent basic type of line antennas, more details can be found in (Balanis, 1997).

But nowadays, it is customary to use broadband antennas (biconical, log-periodic, Bilog or horn antenna) to save measurement time. These antennas shall satisfy the standard requirements (CISPR 16-1-4):

- the antennas shall be plane polarized;
- the main lobe of their radiation pattern shall be such that the response in the direction of the direct wave and that in the direction of the wave reflected from the ground do not differ by more than 1 dB;
- the voltage standing-wave ratio of the antenna with the antenna feeder connected and measured from the receiver and shall not exceed 2.0 to 1;

Despite the fact that antennas satisfy the mentioned requirements they bring into measurement additional errors, which increase the whole uncertainty of such a measurement.

Broadband Bilog antennas are widely used in radiated emission measurements. They represent combinations of biconical antenna and log-periodic dipole array, so they are able to cover the frequency range from 30 MHz to 3 GHz (Van Dijk, 2005). By using the proper geometry it is possible to achieve small dimensions of the antenna also at lower frequencies, which is given by the bow-tie part of antenna. On the other hand the log-periodic part determines the antenna properties at higher frequencies (usually over 200 MHz).

In presence of E field, voltage V is induced across a $50\ \Omega$ load at the feed point of the antenna. Then antenna factor AF represents the ratio between the field strength of an incident plane wave E_{in} and induced voltage V :

$$AF = \frac{E_{in}}{V} \quad (3)$$

or expressed in dB terms:

$$AF(dB) = 20 \log_{10} \frac{E_{in}}{V} = E_{in}(dB) - V(dB) \quad (4)$$

Generally antenna factor AF may be expressed also by its parameter:

$$AF = \sqrt{\frac{480\pi}{Z\lambda^2 G}} \quad (5)$$

where Z is load impedance of antenna, l is a wavelength and G is a gain. Such an AF is free space antenna factor determined on basis of the assumption that the antenna is located in free space. In practice, radiated EMI measurements are always performed in presence of a perfectly conducting ground plane. Since antenna like Bilog has large dimensions, there is a not negligible effect of ground plane on antenna properties and also on antenna factor. In this case antenna factor is known as a standard site method antenna factor. This parameter may be obtained theoretically from the standard site attenuation $A(dB)$ using the following expression (Kodali, 1996):

$$AF_{SSM}(dB) = 10\log f - 24.46 + 0.5[E_D^{\max}(dB\mu Vm^{-1}) + A(dB)] \quad (5)$$

where f is frequency in MHz, E_D^{\max} is the maximum E field at the receiving antenna position during scanning (from 1 m to 4 m height) for a half-wave dipole with 1 pW of radiated power.

Other important parameter is the radiation pattern. It refers to the directional (angular) dependence of radiation from the antenna. It is generally known that radiation pattern of half-wave dipole is constant in H plane, but in E plane it is a figure-of-eight pattern. So the directivity F given by sphere angles (θ, φ) can be expressed as:

$$F(\theta, \varphi) = \frac{\cos\left(\frac{kl}{2}\cos\theta\right) - \cos\left(\frac{kl}{2}\right)}{\sin\theta} = \frac{\cos\left(\frac{\pi}{2}\cos\theta\right)}{\sin\theta} \quad (6)$$

where k is wave number ($k=2\pi/\lambda$) and l the length of the dipole (in case of half-wave dipole $l=\lambda/2$). Unfortunately, the radiation patterns of other (broadband) antennas are not known. In addition they vary with changing frequency.

4. Modelling

The whole antenna analysis was executed by means of numerical methods – analytical methods are suitable just for simple problems, while measurement is always affected by auxiliary equipment. Numerical methods can be divided into three categories: frequency domain, time domain and eigenmode or modal solvers. For antenna analysis the most suitable method are solvers in frequency domain. The method of moments (Harrington, 1993) was chosen to analyse the problems.

The numerical model must be created at first to implement analysis by means of numerical simulations. Interaction between dipole antenna and ground plane is known generally, so we focused on popular broadband Bilog antenna. The Bilog antenna analysed in this contribution is 785 mm long and 1660 mm wide, with 15 pairs of dipole elements and a bow-tie part. The scale factor τ and the spacing factor σ of log-periodic dipole array elements are 0.855 and 0.13 (the longest dipole element is 640 mm long). The bow-tie element has the flare angle 37° , the height of triangle is 775 mm and height of feed point is 55 mm. The numerical model of such an antenna is shown in Fig. 2. The presented model is a wire model – wire replacement of antenna – so the model consists just of wire segments.

This model is composed of 191 segments, and elements of antenna are connected to each other by non-radiating transmission lines.

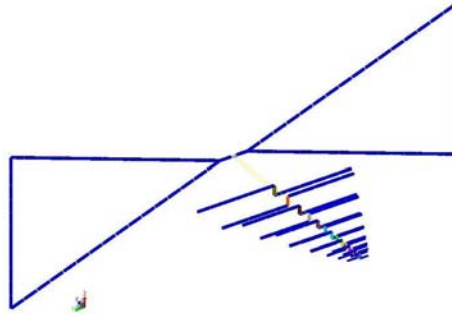


Fig. 2. The numerical model of analysed Bilog antenna.

To use these models, at first we have to validate the numerical model of the Bilog antenna. That means to verify that the obtained results copy sufficiently the properties of real antenna. The antenna factor values are obtained by simulation by placing a source of electromagnetic field e.g. short dipole antenna at adequate distance (ca. 100 m) away from the receiving Bilog antenna. Then antenna factor is given as ratio between known E field values E_{in} and computed induced voltage at antenna output V (Chen & Lin, 2003). The comparison of obtained simulated values of free space antenna factor with the measured values provided by manufacturer is shown in Fig. 3. There is a good correlation between measured and simulated antenna factor values, the small differences below 200 MHz can be caused by omission of balun (balanced-unbalanced network) in case of simulations. At higher frequencies, the effect of sequential activation of log-periodic dipole elements may be seen.

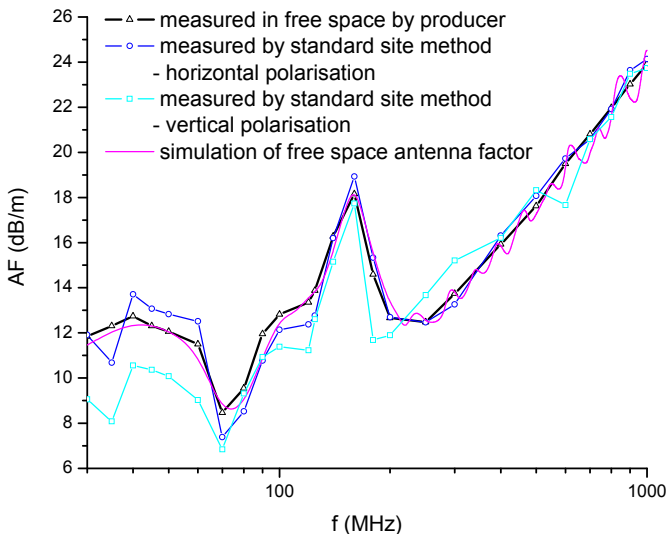


Fig. 3. Comparison of measured and simulated values of antenna factor of Bilog antenna.

Also the simulated radiation patterns of Bilog antenna were compared with measured ones at discrete frequencies. The differences are mainly in back lobe (see Fig. 4), which may be caused by antenna feeder presence during the measurement, or by small errors in numerical computation.

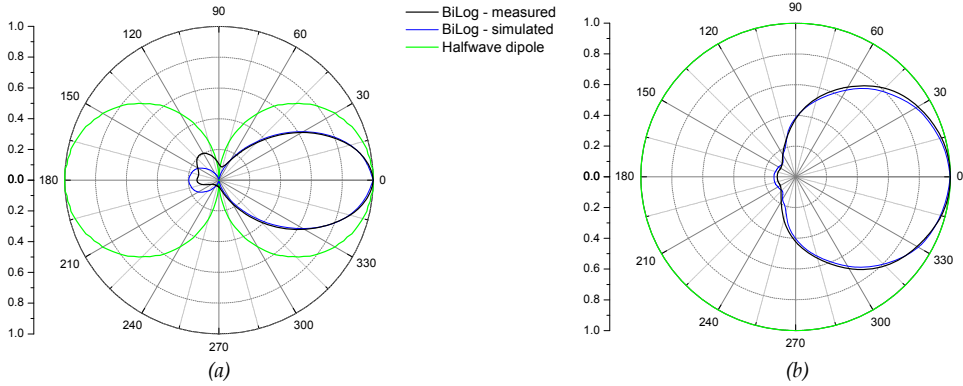


Fig. 4. Comparison of measured and simulated radiation patterns of Bilog antenna at 200 MHz (a) in E plane, (b) in H plane.

5. Methods

From all mentioned uncertainty contributions two of them affected by ground plane presence were chosen for further analysis:

- antenna factor height deviations;
- directivity difference of antenna.

It is known that the presence of ground plane affects the input impedance Z of every antenna. The change of impedance cause change of induced voltage V on antenna, and consequently according to (3) also change of antenna factor AF . This variation may be expressed as error of antenna factor ΔAF :

$$\Delta AF = AF_h - AF_{FS} \tag{7}$$

where AF_{FS} is antenna factor of antenna in free space and AF_h antenna factor of the same antenna, calculated by the same conditions, in the height h over the reference ground plane. It is necessary to ensure the identical height of both antennas (transmitting short dipole and receiving analysed antenna) during the antenna factor calculation. Unfortunately, the error ΔAF is not constant. It changes with varying height of antenna and also with frequency. Therefore it is necessary to consider with range of errors, obtained as intersection of all the errors for height interval from 1 m to 4 m.

Note that the change of antenna impedance due to height variation may cause also additional error in mismatch between antenna and receiver.

Broadband antennas have radiation patterns different from the half-wave dipole and they are additionally frequency dependent. At lower frequencies, the radiation pattern of Bilog antenna is similar to the pattern of half-wave dipole. But with increasing frequency of

radiation the main lobe of radiation pattern becomes more dominant, so there is less similarity between two radiation patterns (see Fig. 5). Hence, there is higher probability that error caused by the real radiation pattern of Bilog antenna is higher than at lower frequencies and the using of such antennas introduces additional error into the measurement.

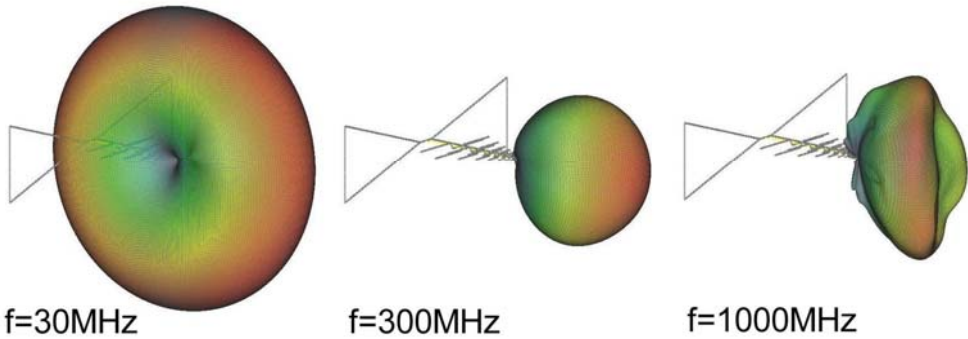


Fig. 5. Radiation pattern of Bilog antenna at frequencies 30 MHz, 300 MHz and 1000 MHz.

In addition, the ground plane also affects the directivity of the antenna. The variation of radiation pattern may be expressed as well simply as the error of antenna factor. If the source of radiation is not situated in front of analysed antenna in direction of maximal radiation (zero angle-wise), but it is moved so that radiation from itself affects the analysed antenna with angles (θ, ϕ) , we obtain the real antenna factor of antenna AF :

$$AF(\theta, \phi) = AF(dB) + F(\theta, \phi) \quad (8)$$

where $AF(dB)$ is known antenna factor and F is directivity of analysed antenna. Then the error, obtained by replacing the half-wave dipole antenna by broadband antenna, may be expressed as error of antenna factor ΔAF defined as:

$$\Delta AF(dB) = AF(\theta, \phi) - AF_D(\theta, \phi) - K \quad (9)$$

where AF and AF_D are antenna factors at the same angles of incidence given by angles (θ, ϕ) . The dependence of antenna factor of half-wave dipole antenna may be obtained by substituting (6) into (8). The parameter K is a correction for neglecting the difference between the values of antenna factors of these antennas.

Since receiving antenna varies its height with respect to height of tested equipment during the measurement from 1 to 4 m, angles of incidence of disturbing electromagnetic waves on measuring antenna vary their values as well. If tested object is assumed to be in 1 m height and the measuring distance is standard (CISPR 16-1-4) recommended 10 m the angle of incidence of direct wave varies from 0° to 17° . In case of shorter distances e.g. 3 m these angles may increase up to 45° . If we consider not only the direct wave incident on the antenna, but also the wave reflected from the reference ground plane, angles of incidence are from 0° up to 27° . Similarly for 3 m measuring distance we have to consider a range of

possible angles of incidence up to 60° or for 30 m just up to 9.5°. The possible errors of antenna factor, which may be included into the entire uncertainty, are shown in Fig. 6 and 7. It is necessary to consider the range of errors, because the real error may vary in value according to angle of incidence, which is unknown.

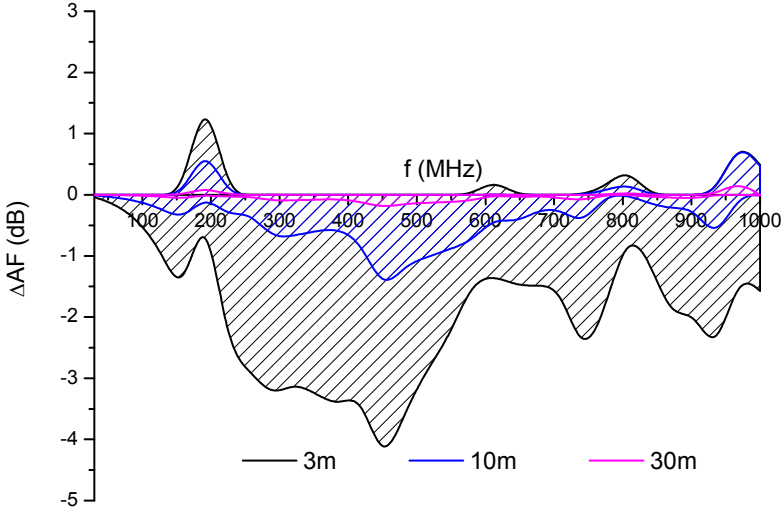


Fig. 6. Possible errors of antenna factor caused by directivity for horizontally polarised Bilog and for different measuring distances

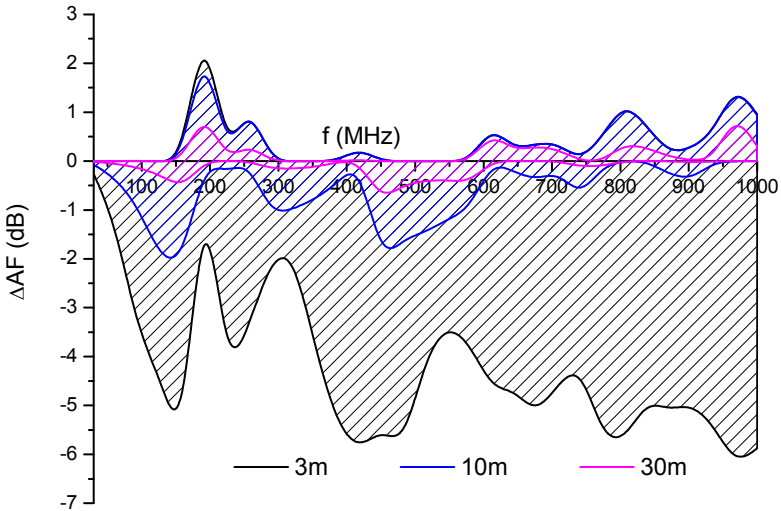


Fig. 7. Possible errors of antenna factor caused by directivity for vertically polarised Bilog and for different measuring distances

Since the radiation pattern of tested equipment and then also the angle of incidence are mostly unknown, we take into account that disturbing electromagnetic field may be received by measuring antenna with the same probability with any angle from given range. Hence, it is necessary to rotate the source of radiation around the analysed measuring antenna with these angles and record the maximal variations (positive and negative) in comparison with zero angle of incidence. This process was performed at multiple discrete points of frequency range of our interest from 30 to 1000 MHz and for both polarizations of antenna. The result is the error of antenna factor ΔAF , respectively its frequency dependence, which represents one of contributions to entire uncertainty of the radiated EMI measurement. The error ΔAF is not single-valued, it may be arbitrary between maximal and minimal range, but we have to consider the maximal error in order to calculate the measurement uncertainty.

6. Results

The perfect ground plane presence near the Bilog antenna affects its input impedance as well as its antenna factor. But it also affects its radiation pattern of Bilog antenna. To obtain the error ΔAF of Bilog antenna, which is influenced by ground plane presence, we have to modify the numerical model of the antenna. Instead of inserting the ground plane into the model, we make use of the mirror principle and below the Bilog we locate its mirror image in distance of double height over the ground plane. In such cases it is necessary to get the maximal and minimal values of error ΔAF at different angles of incidence, which are dependent on the antenna height over the ground plane.

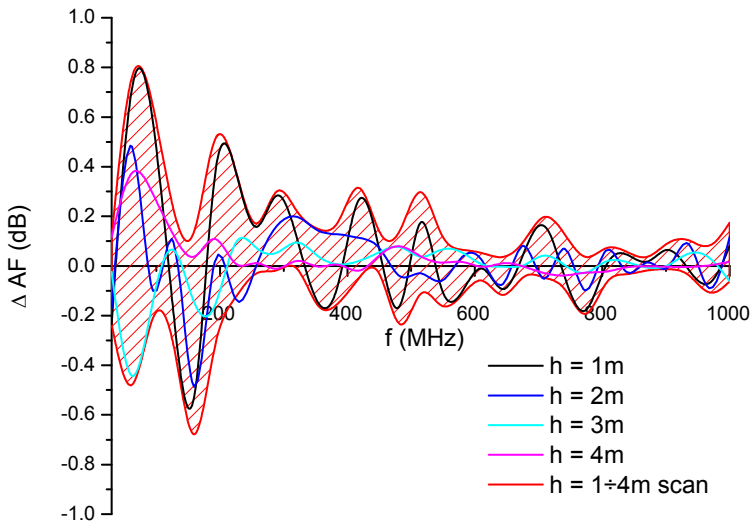


Fig. 8. Possible errors of antenna factor for a horizontally polarized Bilog placed in height h over the ground plane

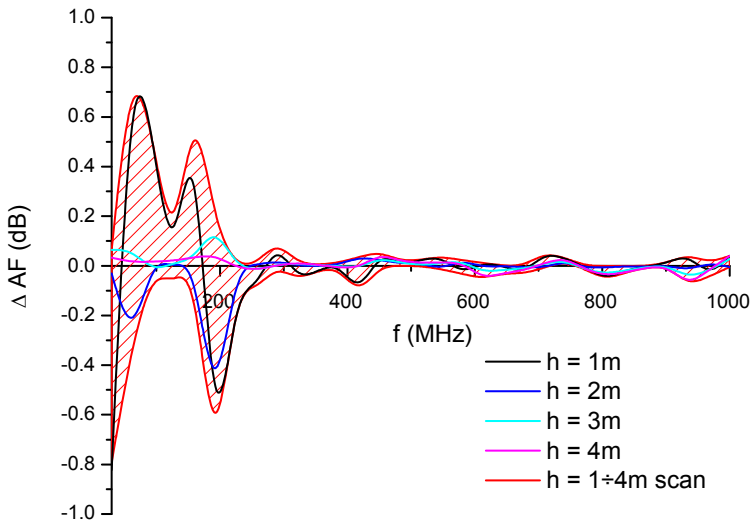


Fig. 9. Possible errors of antenna factor for a horizontally polarized Bilog placed in height h over the ground plane

As the antenna varies its height above the reference ground plane, its antenna factor varies as well. This variation ΔAF is shown in Fig. 8 and 9 according to (7). The error is strongly frequency dependant and it is maximal ± 0.8 dB in case of the lowest height of antenna $h = 1$ m. This is when the mutual coupling between the antenna and the ground plane is maximal. The error is large in the frequency range below 200 MHz, which is the active range of bow-tie part of antenna. The log-periodical part causes a smaller error when mainly vertically polarised. It is consistent with the previous analysis of biconical or log-periodical antennas (Chen & Foegelle 1998), (Chen et al. 1999).

The error ΔAF is dependent also on the angle of incidence. While at zero angle of incidence the error is zero due to correction K , with increasing angles of incidence the error ΔAF also generally increases in value. As we can see in Fig. 6 and 7 the worst situation occurs at short measuring distances of 3 m. A better situation occurs in case of horizontally polarized antenna, the possible error is up to ± 1.4 dB. In case of vertical polarized antenna the error is up to ± 2 dB. With increasing measuring distance the values of error ΔAF descends, at 10 m the maximal error is ± 4.1 dB or ± 6 dB and at 30 m distance ± 0.2 dB or ± 0.8 dB for both polarizations. Such errors are visibly frequency dependent and mostly negative, which means that received signal is smaller than expected

The effect of ground plane presence on directional patterns of Bilog antenna we may be seen in Fig. 10. With increasing height over the ground plane the directional pattern of Bilog antenna becomes smoother – it resembles the directional pattern in free space. On the other hand at low heights also the main lobe of the pattern is crinkled. Even though the ground plane influence on radiation pattern of Bilog cannot be overlooked, this effect is not so evident on frequency characteristics of error ΔAF as a whole, as it is seen in Fig. 11 and 12. More significant is the interference of bow-tie part of Bilog with ground plane in the frequency range from 100 to 200 MHz that causes higher error of antenna factor. The effect

of presence of ground plane increases the maximal error of approximately 0.4 dB at horizontal polarization and of 1.2 dB at vertical polarization. This increase is just in mentioned frequency range, in case of shorter measuring distances and vertically polarized antenna there is even the error ΔAF drop at higher frequencies (Bittera et al., 2008).

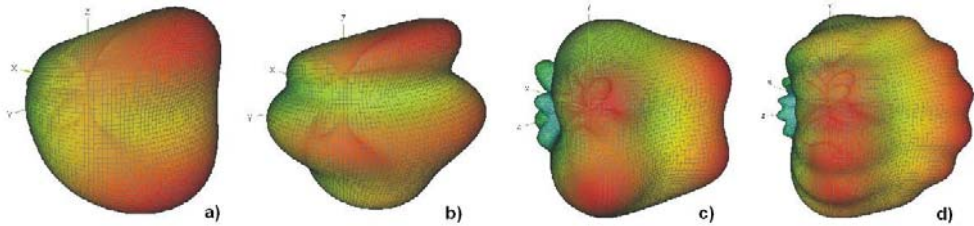


Fig. 10. Radiation pattern of Bilog for 200 MHz : (a) in free space, (b) 1 m over ground plane vertical polarization, (c) 1 m over ground plane horizontal polarization, (d) 4 m over ground plane horizontal polarization

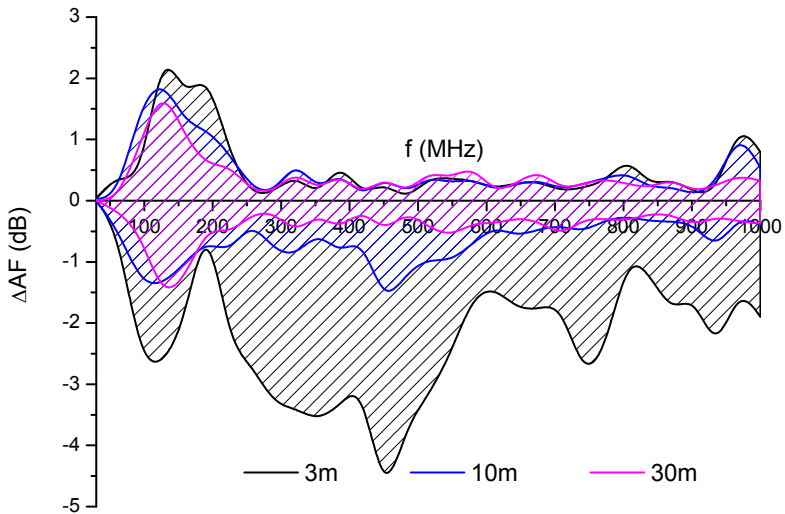


Fig. 11. Possible errors of antenna factor over ground plane caused by directivity for horizontally polarised Bilog

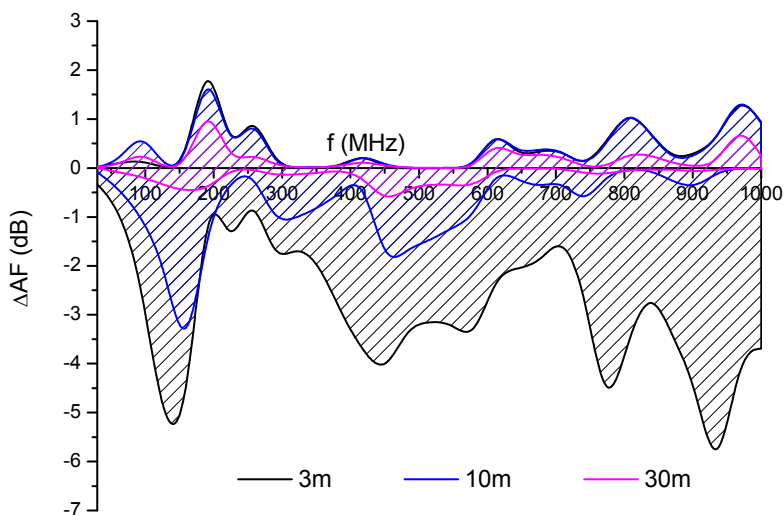


Fig. 12. Possible errors of antenna factor over ground plane caused by directivity for vertically polarised Bilog

7. Conclusion

In comparison with half-wave dipoles, Bilog antennas are more popular among test engineers due to their broadband properties - it is not necessary to change them during the radiated EMI measurement. On the other hand they introduces additional errors into measurement with greater contributions to uncertainty. The entire uncertainty is thus larger. The effect of ground plane on Bilog antenna pattern and consequently the effect of its interference to measurement uncertainty are not measurable. To examine this influence the numerical simulation based on method of moments has been used. The incurred error is computed as the difference between antenna factor of ideal antenna in free space and antenna factor influenced by ground plane presence respectively. In case of directivity effect analysis ideal antenna is represented by half-wave dipole. Due to varying the antenna height over the reference ground plane the uncertainty contribution has to be expressed as maximum of errors at all heights in a scanning range from 1 m to 4 m.

Due to high mutual coupling between antenna and ground plane we get the maximum error when the antenna is in height of 1 m. In case of directivity difference the error is also dependent on the measuring distance. Though ground plane presence affects the radiation pattern of Bilog, its entire effect on the uncertainty is not as significant. It is mainly affected by the Bilog radiation pattern difference itself. Resulting from the analysis, using Bilog antenna is more suitable for larger measuring distance to get lower uncertainties.

From the analysis it is evident that both analysed effects - antenna factor height deviations and directivity difference of antenna are strongly frequency dependent. Therefore we may use the maximal error value as well as frequency dependence of the error for uncertainty calculation. The first consideration is suitable for simpler calculations while in other cases

we need to know all errors as being frequency dependent. However then we may minimize uncertainty of the measurement.

8. References

- CISPR 16-1-4 (Ed.2.0). Specification for radio disturbance and immunity measuring apparatus and methods - Part 1-4: Radio disturbance and immunity measuring apparatus - Ancillary equipment - Radiated disturbances. *IEC Standard*, May 2005, 179 p.
- CISPR 16-2-3 (Ed.2.0). Specification for radio disturbance and immunity measuring apparatus and methods - Part 2-3: Methods of measurement of disturbances and immunity -Radiated disturbance measurements. *IEC Standard*, December 2006, 185 p.
- CISPR 16-4-2 (Ed.1.0). Specification for radio disturbance and immunity measuring apparatus and methods - Part 4-2: Uncertainties, statistics and limit modelling - Uncertainty in EMC measurements. *IEC Standard*, November 2003, 43 p.
- Balanis, C.A. (1997). *Antenna Theory - Analysis and design*, John Wiley & Sons, ISBN 0-471-59268-4, New York
- Harrington, R.F. (1993). *Field computation by moment method*, IEEE Press, ISBN 0-7803-1014-4, Piscataway
- Kodali, V.P. (1996) *Engineering electromagnetic compatibility - Principles, measurements and Technologies*, IEEE Press, ISBN 0-7803-1117-5, New York
- Bittera, M.; Smiesko, V.; Kovac, K. & Hallon, J. (2008). Interference between ground plane and Bilog antenna and its effect on EMI measurement uncertainty, *Proceedings of Asia-Pacific Microwave Conference*, pp. 611-614, ISBN 978-1-4244-2642-3, Hong Kong
- Chen, Z.; Foegelle, M.D. & Harrington, T. (1999). Analysis of log periodic dipole array antennas for site validation and radiated emissions testing, *Proceedings of the 1999 IEEE International Symposium on EMC*, pp. 618-623, ISBN 0-7803-5057-X, Seattle, August 1999, IEEE Press, Piscataway, NJ
- Chen, Z. & Foegelle, M.D. (1998). A numerical investigation of ground plane effects on biconical antenna factor, *Proceedings of the 1998 IEEE International Symposium on EMC*, pp. 618-623, ISBN 0-7803-5015-4, Denver, August 1998, IEEE Press, Piscataway, NJ
- Chen, H.F. & Lin, K.H. (2003). A numerical analysis of antenna factor of Bilog antennas for normalized site attenuation and EMC measurements, *Proceedings of the 2003 IEEE International Symposium on EMC*, pp. 817-821, ISBN 0-7803-7835-0, Boston, August 2003, IEEE Press, Piscataway, NJ
- Van Dijk, N. (2005). Uncertainties in 3-m radiated emission measurement due to the use of different types of receive antennas. *IEEE Transactions on Electromagnetic compatibility*, Vol. 47, No. 1, (February 2005) pp. 77 - 85, ISSN 0018-9375

Analysis of directive sensor influence on array beampatterns

Lara del Val¹, Alberto Izquierdo¹, María I. Jiménez¹,
Juan J. Villacorta¹ and Mariano Raboso²

¹ *Universidad de Valladolid (Departamento de Teoría de la Señal y Comunicaciones e Ingeniería Telemática)*
Spain

² *Universidad Pontificia de Salamanca (Escuela Universitaria de Informática)*
Spain

1. Introduction

Over the past few years, a large number of pattern synthesis techniques of antenna arrays have been studied and developed. Such techniques may be classified into two categories: techniques that optimize the excitation (amplitude and phase) of each element in a uniform array (Van Veen & Buckley, 1988), and techniques that adjust the positions of the elements with uniform excitation, resulting in a non-uniform geometry ("Unz, 1960", "Harrington, 1961", "Skolnik et al., 1964", "Haupt, 1994"). Despite of this classification, both categories are not exclusive; so, it is possible to develop techniques that optimize both the excitations and the positions of the elements ("Akdagli & Guney, 2003", "Kurup et al., 2003", "Kumar & Branner, 2005").

It has been also observed that many of these techniques make a beampattern synthesis only in the case of an array pointing to the broadside. Only a few techniques are designed taking into account other angles further than the broadside ("Bae et al., 2005", "Bray et al., 2002", "Feng & Chen, 2005"), which is the basis of beamforming. The reason is that, these techniques work on the assumption that the array is formed by omnidirectional sensors. In this case, working with the array pattern in the u domain ($u = \sin(\theta)$), a variation of the pointing angle only implies that a shift in the beampattern, without variation of the characteristics of neither the main lobe, nor the sidelobes (Mailloux, 2005). Thus, representing the pattern in the $u-u_0$ domain ($\sin(\theta) - \sin(\theta_0)$, being θ_0 the pointing angle), implies that a variation in the steering angle does not produce any effect on the array beampattern.

The problem arises when the assumption that sensors forming the array are omnidirectional can not be used. There are different types of arrays that employ directive sensors, such as retro-directive (Feng & Chen, 2005), or acoustic arrays (Brandstein & Ward, 2001). In these cases, design methods of array pattern synthesis based on pointing only to the broadside, are not suitable techniques if these arrays are going to be used in beamforming systems

later, because there is no information about the behaviour of the array pointing to angles that are different of the broadside.

The purpose of this paper is to study the influence of the sensor directivity into the array beampattern, in order to test if its effects on the array pattern must be taken into consideration in design methods of pattern array synthesis, and other array design methods. This chapter is organized so that the next section describes the studies accomplished for the analysis, as well as the results found. Finally, some interesting conclusions are shown in section 3.

2. Analysis Results

A linear array with 19 uniformly spaced sensors has been used in this study. The spacing between sensors can vary between $\lambda/4$ and λ . With these spacing we avoid the effects of mutual coupling (Agrawal & Lo, 1972). As this work is based on linear arrays, beampatterns are only represented in azimuth (θ).

The range of variation of θ is $[-90^\circ, 90^\circ]$ with one degree steps. The diagram is represented in the u domain, so the range of azimuth values really is $[-1, 1]$.

This analysis has been carried out employing sensors with a cardioid directive response, which is the most frequently directive response for audio microphones, and working under the assumption that all sensors have the same directive response. This assumption can be done because there are not mutual coupling effects. The employed formula is:

$$D = [1/(1 + C)] \cdot (C + \cos \theta) \quad (1)$$

In this study values of constant C , which has been named Directive Factor, have been varied from 0.25 (most sharp cardioid) to 1 (less sharp cardioid).

A deep analysis of the invariance of ULA beampattern versus the steering angle has been made, using spacing value of $\lambda/2$ of and with a directive factor C with a 1.0 value, verifying that the hypothesis of invariance is not fulfilled with directive sensors. Beampattern for a maximum steering angle, θ_0 , of $\pm 60^\circ$ is evaluated.

Figure 1 shows beampatterns for different positive steering angles θ_0 , where the x -axis, corresponds to variable $u-u_0$, being $u=\sin\theta$ and $u_0=\sin\theta_0$. When steering angle increases from broadside, the contribution of the directive sensors on the beampattern is stronger. This contribution does not affect on the same way to positive and negative $u-u_0$ values. For positive $u-u_0$ values, when the steering angle increases, sidelobes of the beampattern decrease, improving array performance. For $u-u_0$ negative values, beampattern sidelobes increase, reducing array performance.

Besides this behaviour difference between positive and negative $|u-u_0|$ values, another two effects of sensor directivity on array beampattern can be observed:

(a) As the steering angle (θ_0) moves away from the broadside, sensor directivity leads to a higher increase of sidelobe level. This effect can be observed in Figure 2, where the seventh sidelobe on the left of the mainbeam for several steering angles are shown.

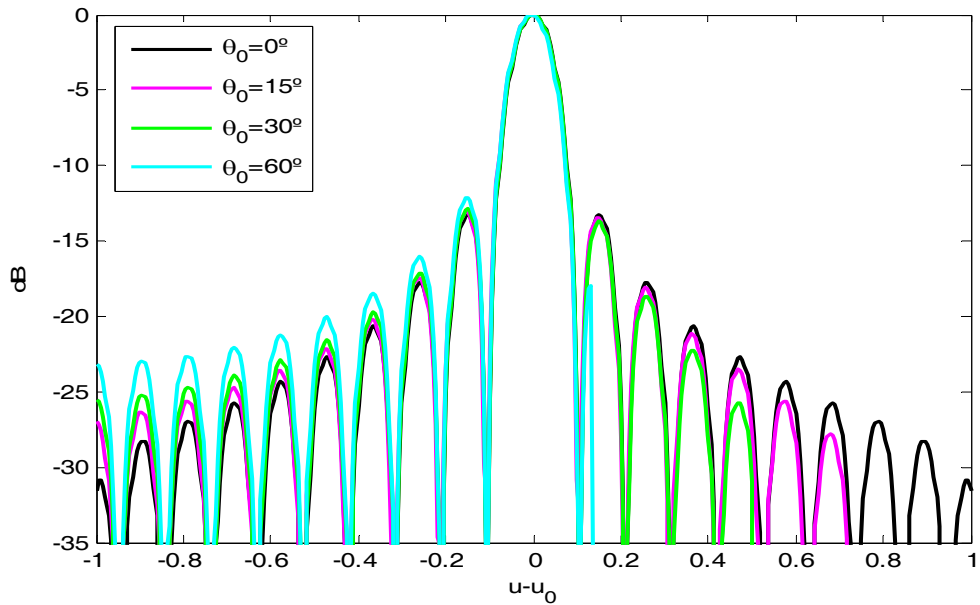


Fig. 1. ULA beampattern in $u-u_0$ space with cardioid sensors

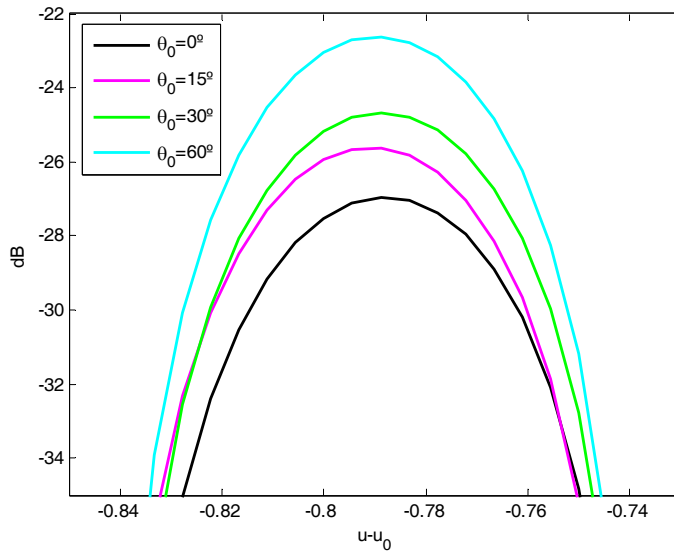


Fig. 2. Sensor directivity effect vs. Steering angle θ_0

(b) For a constant θ_0 value, as $|u-u_0|$ comes to 1, sensor directivity influence is higher, increasing the difference between the omnidirectional and the directive cases. This effect is

shown in Figure 3, where the beam patterns of the omnidirectional and the directive cases for $\theta_0=0$ are shown as an example.

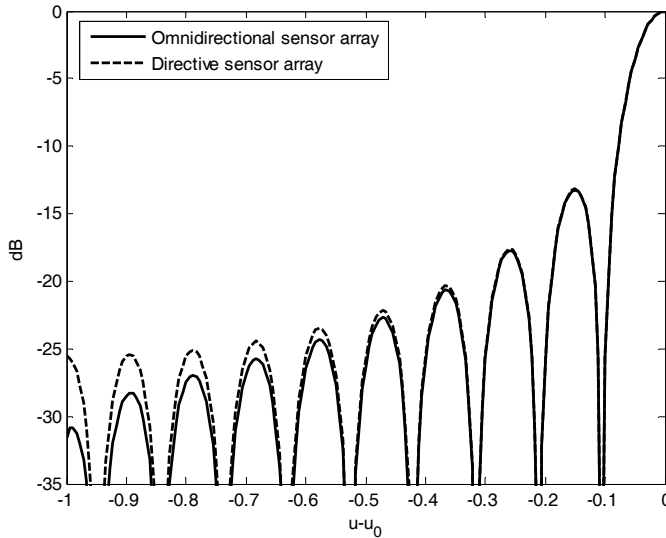


Fig. 3. Sensor directivity effect vs. $|u-u_0|$

In order to characterize absolute variation of sidelobe levels, ΔSLL_i has been defined:

$$\Delta SLL_i = SLL_i(\theta_0 = 60^\circ) - SLL_i(\theta_0 = 0^\circ) \quad (2)$$

Table 1 shows the absolute variation of the 8 first sidelobes located on the left of the mainlobe. It can be observed that moving away from the mainlobe (increasing index i), the variation of the sidelobe level increases. For the fifth sidelobe, ΔSLL is greater than 3dB.

i	1	2	3	4	5	6	7	8
ΔSLL_i	1.51	1.67	2.16	2.63	3.11	3.65	4.25	5.16

Table 1. ΔSLL_i (dB) for the 8 sidelobes on the left of the mainlobe

This section continues with detailed studies for several sidelobe levels, where dependences on the steering angle, sensor spacing and directive factor C are analyzed.

2.1 First Sidelobe Level (SLL_1)

SLL_1 Sensitivity vs. steering angle

Figure 4 shows that increasing steering angles produce higher first sidelobe levels, at the left of the mainlobe. For small steering angles, the first sidelobe level is below the omnidirectional case, but with greater angles the sidelobe level exceeds the omnidirectional one. The reason of this behaviour is that pointing the beam more and more to the right, i.e.

increasing the steering angle, makes beampattern values on the left of the mainbeam be affected by lower and lower sensor directivity values, as it is showed in Figure 5. The effect of sensor directivity over the first sidelobe can vary its level in 1.52dB.

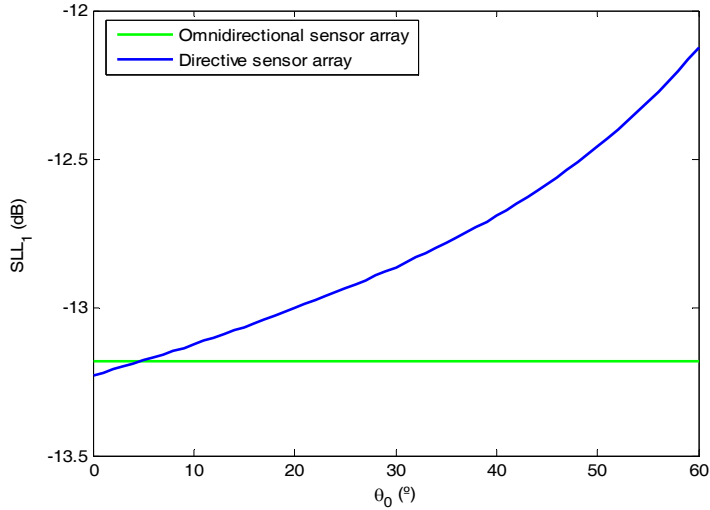


Fig. 4. Left SLL₁ vs. Steering angle

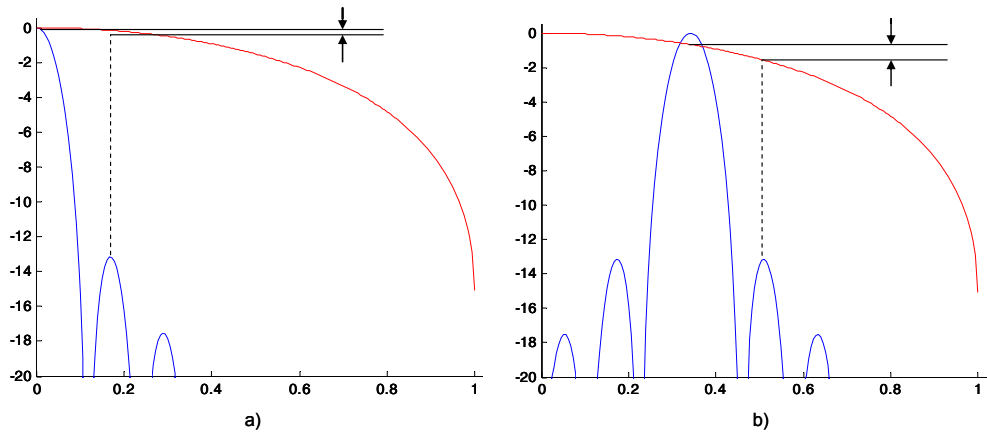


Fig. 5. Sensor directivity effect on first sidelobe level. Spacing= $\lambda/2$. a) $\theta_0=0^\circ$, b) $\theta_0=20^\circ$

SLL₁ Sensitivity vs. sensor spacing:

This first sidelobe level analysis is extended with a study of sensor directivity influence on array beampattern with regard to sensor spacing. This spacing is varied between 0.25λ and 1λ . Directive factor (C) is fixed to 1. Figure 6 shows this influence with regard to sensor spacing. It can be observed that an increase on sensor spacing deals to a SLL₁ decrease.

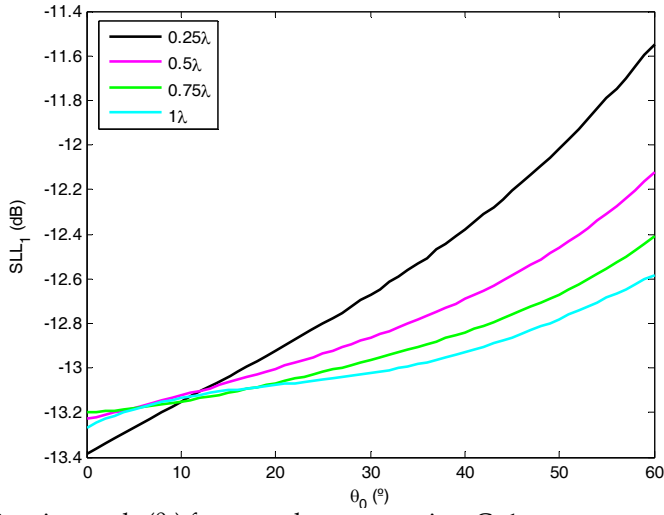


Fig. 6. SLL_1 vs. Steering angle (θ_0) for several sensor spacing. $C=1$.

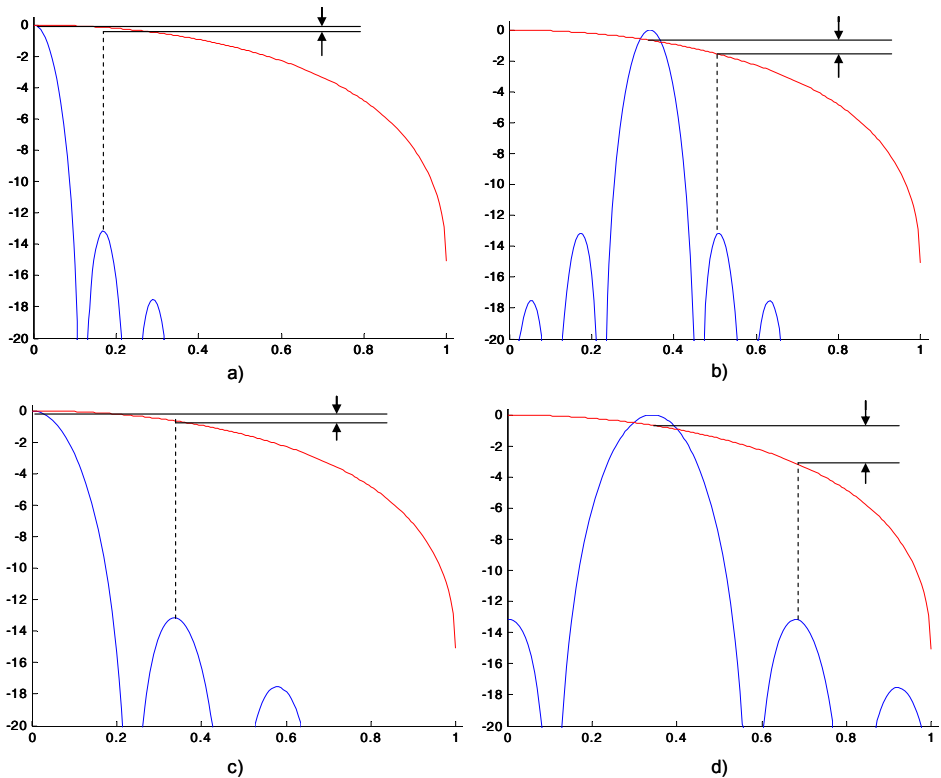


Fig. 7. Sensor directivity effect on first sidelobe level. $C=1$. a) Spacing= $\lambda/2$ and $\theta_0=0^\circ$; b) Spacing= $\lambda/2$ and $\theta_0=20^\circ$; c) Spacing= 0.25λ and $\theta_0=0^\circ$; d) Spacing= 0.25λ and $\theta_0=20^\circ$

The reason of this behaviour is that increasing sensor spacing makes a compression of the beampattern. Figure 7 shows how the first sidelobe is closer and closer to the mainbeam, reducing the difference between the directivity values that affects each of these lobes (first sidelobe and mainlobe).

The variation of SLL_1 (ΔSLL_1) is inversely proportional to sensor spacing, as it can be observed in Figure 8. The sensitivity of ΔSLL_1 versus sensor spacing is lower than the one on steering angle. This effect must be taken into account, since it can increase sidelobe level between 0.68dB and 1.81dB, i.e. a 1.13dB variation.

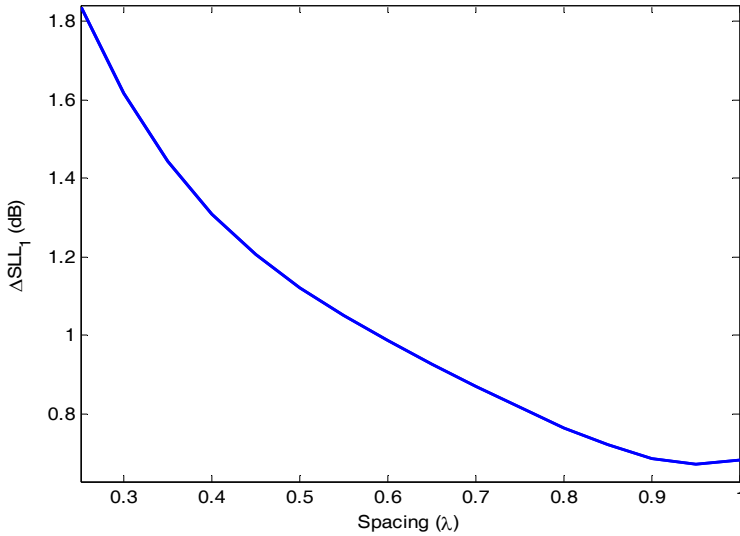


Fig. 8. ΔSLL_1 vs. Sensor spacing

SLL_1 Sensitivity vs. Directive factor C

SLL_1 analysis is finished off with a study of sensor directivity influence on the array beampattern with regard to sensor directive factor (C). This directive factor is varied between 1 and 0.25. Sensor spacing is fixed to 0.5λ . Figure 9 shows this influence. It can be observed that decreasing directive factor, i.e. using more directive sensors, increases SLL_1 .

The reason of this behaviour is that sharper sensor directivity deals to a larger difference between the directivity values that affect first sidelobe and mainlobe, as Figure 10 shows.

The variation of SLL_1 (ΔSLL_1), is inversely proportional to the directive factor, as it can be observed in Figure 11. The sensitivity of SLL_1 versus directive factor is lower than the sensitivity versus sensor spacing. In this case, the effect can be increased from 1.11dB to 2.03dB, i.e. a 0.92dB variation.

These SLL_1 analyses show that SLL_1 is less sensitive to directive factor variations than to spacing and steering angle ones. The highest sensitivity is shown for the steering angle.

All these analyses have been done for positive steering angles. In the case of negative steering angles values, the behaviour would be the symmetric one.

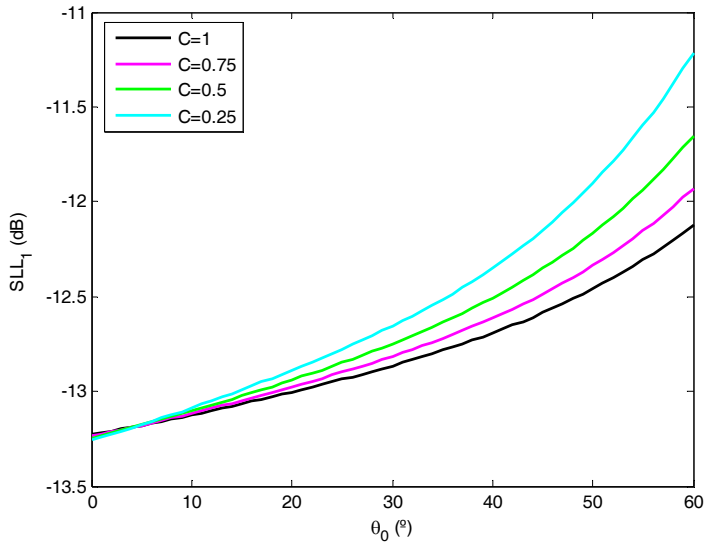


Fig. 9. SLL₁ vs. Steering angle (θ_0) for several directive factors (C). Spacing= $\lambda/2$.

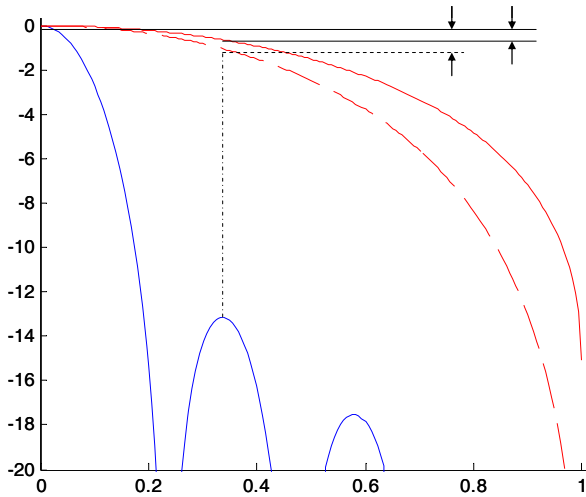


Fig. 10. Sensor directivity effect on first sidelobe level. Spacing= $\lambda/2$. C=1 (—), C=0.25 (---)

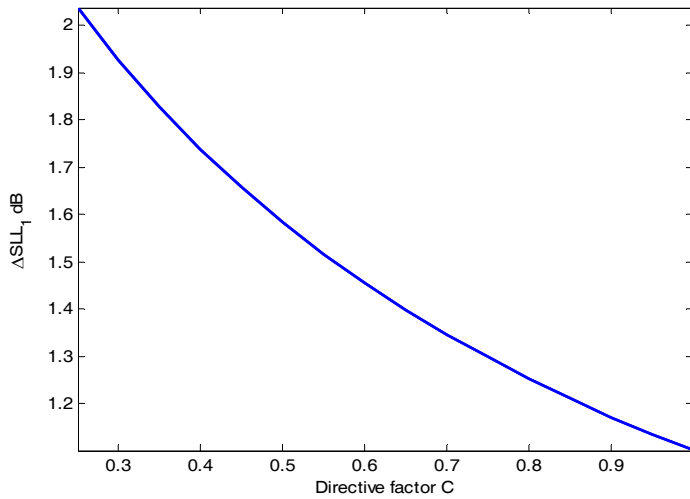


Fig. 11. ΔSLL_1 vs. Directive factor C

2.2 Sidelobe Average Level (\overline{SLL})

The analysis of the average sidelobe level (\overline{SLL}) is similar to the analysis of the first sidelobe level. A sidelobe average level that calculates the average of the first 8 sidelobes on the left of the mainlobe has been taken in consideration. This average level of an array formed by omnidirectional sensors is constant.

Figure 12 shows that, an increase in steering angle causes an increase in \overline{SLL} . Firstly, the average level values for the directional case are below the values of the omnidirectional case, but with an increasing steering angle, average level values of the directional case are over the omnidirectional ones. This average level has a variation ($\Delta\overline{SLL}$) of 3.75dB.

The analyses of the \overline{SLL} sensibility versus sensor spacing and directive factor (C), have been made in the same way than the ones shown for SLL_1 . In this case, an increase on the spacing and/or on the directive factor, also means a decrease of $\Delta\overline{SLL}$, as it can be observed in Figures 13 and 14.

For this sidelobe level, the sensitivity of $\Delta\overline{SLL}$ versus sensor spacing is also lower than the one versus steering angle. Despite this sensitivity is lower, it must be taken into consideration, since it can increase average sidelobe level between 4.48dB and 6.51dB, i.e. a 2.17dB variation.

The sensitivity of $\Delta\overline{SLL}$ versus directive factor is also lower than the sensitivity versus steering angle. In this case, the effect can be increased from 5.52dB to 7.60dB, i.e. a 2.08dB variation.

These analyses show that \overline{SLL} is more sensitive to directive factor variations than to spacing and steering angle ones. The highest sensitivity, as in the SLL_1 analysis, is shown for the steering angle.

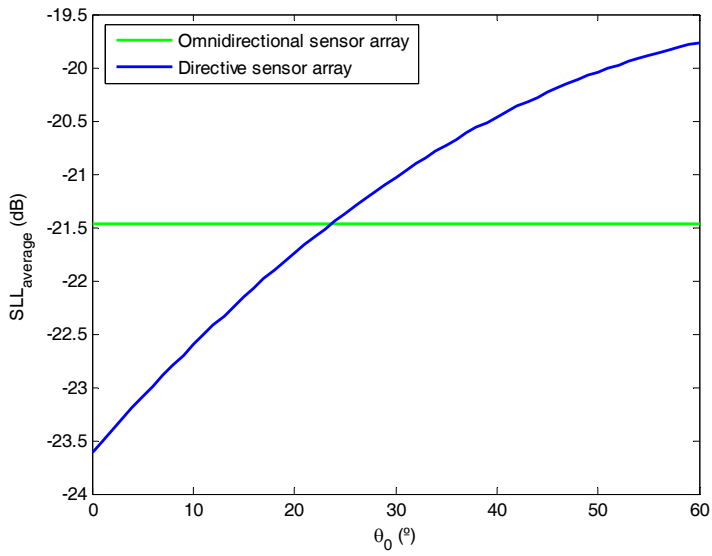


Fig. 12. \overline{SLL} vs. Steering angle

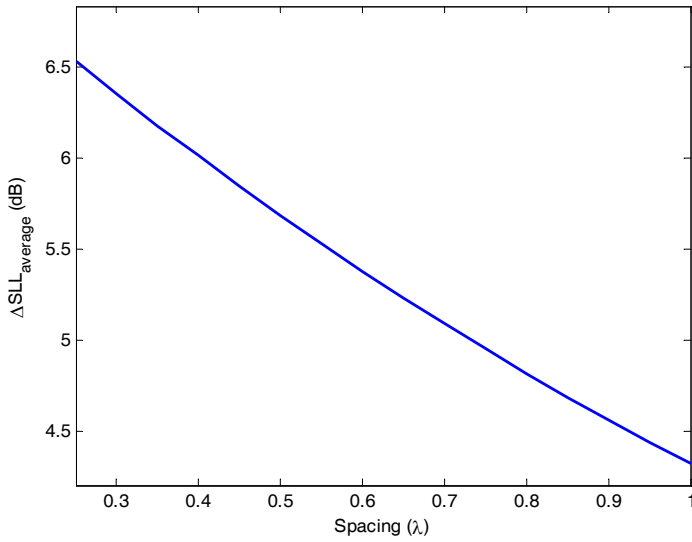


Fig. 13. ΔSLL vs. Sensor spacing

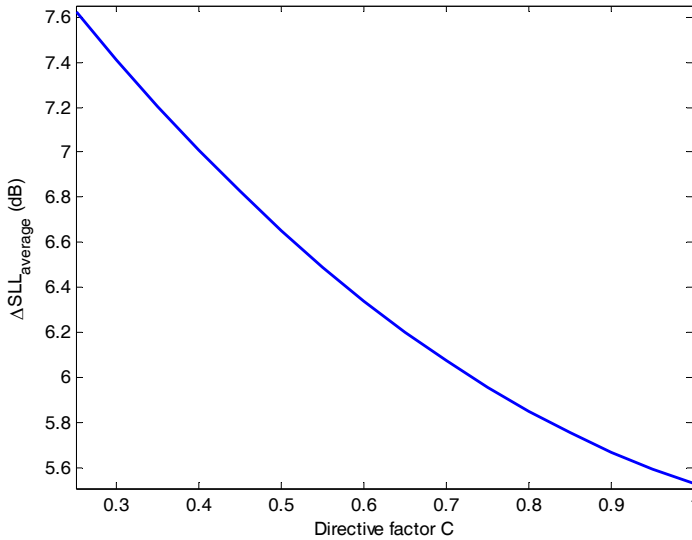


Fig. 14. $\overline{\Delta SLL}$ vs. Directive Factor C

2.3 Maximum Sidelobe Level (SLL_{max})

Lastly, maximum sidelobe level (SLL_{max}), which is related with grating lobes, is analysed. Due to the appearance of grating lobes depends on sensor spacing, the influence of this spacing on the variation of SLL_{max} and steering angle is studied. Figure 15 shows that an increase of steering angle means an increase of SLL_{max} for all spacing.

For spacing greater than $\lambda/2$, there are two different behaviours:

- (a) A first one, with SLL_{max} around -13dB that grows up slowly with increasing steering angle.
- (b) A second one, where SLL_{max} suffers a quite abrupt increase. This increase indicates the existence of grating lobes.

For λ spacing, the behaviour is again unique, because there are grating lobes for all the steering angles.

Comparing Figures 15 and 16, where SLL_{max} performance for an omnidirectional sensor array is shown, it can be observed that the sensor directive response makes grating lobes appearance more gradual and less abrupt than in the omnidirectional case. This is an improvement in array performance, but it is also a problem because it can be even greater than the mainlobe.

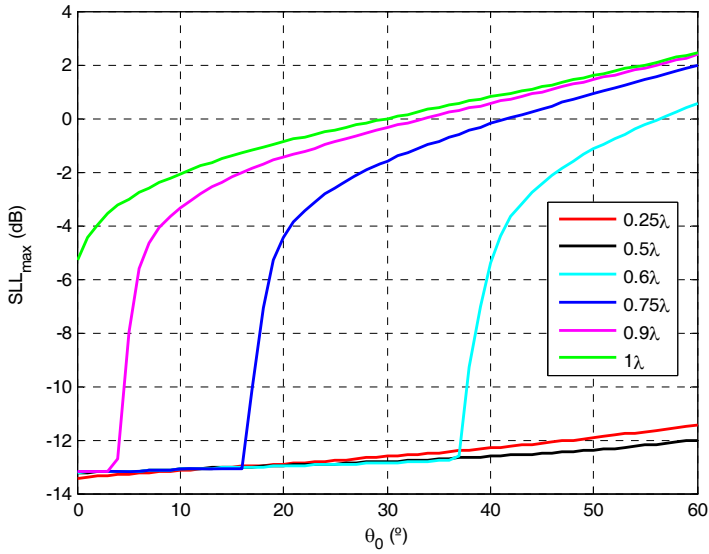


Fig. 15. SLL_{max} vs. Steering angle for several sensor spacing. C=1. Directive sensor array

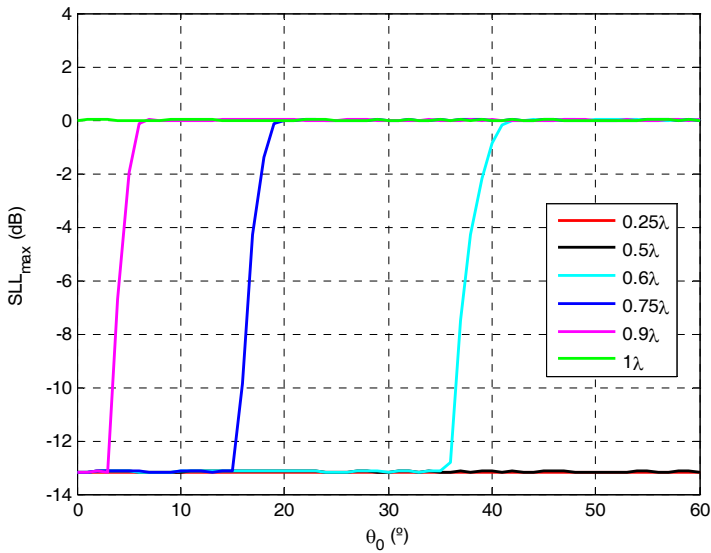


Fig. 16 SLL_{max} vs. Steering angle for several sensor spacing. Omnidirectional sensor array

3. Conclusions

This paper shows that using arrays with directive sensors makes the invariance hypothesis no longer valid. Sidelobe level increments around 5dB can be observed if directive sensors

are used. This effect can be increased depending on the sensor spacing and the directive factor.

In Table 2, ΔSLL_1 and $\overline{\Delta SLL}$ versus steering angle, spacing and directive factor relations are shown. Sidelobes are more sensitive to steering angle variation than to spacing and directive factor variation. \overline{SLL} is more sensitive to parameter variation than SLL_1 , because \overline{SLL} includes effects on several sidelobes, and these effects are larger in sidelobes which are more distant from the main lobe. \overline{SLL} is also more sensitive because it includes grating lobes effect. This effect is also included in maximum sidelobe level. Sensor directivity produces a more gradual appearance of greater grating lobes.

	ΔSLL_1 [dB]	$\overline{\Delta SLL}$ [dB]
Steering angle	1.51	3.22
Sensor spacing	1.13	2.17
Directive factor (C)	0.92	2.08

Table 2. ΔSLL_1 and $\overline{\Delta SLL}$ vs. steering angle, spacing and directive factor (C)

The research has been realized for sensors whose directive response is a cardioids function, but it can be extended as a future work to any other type of directive response. It can be also extended to random arrays, because they are influenced by the sensor directive response.

4. References

- A. Akdagli, and K. Guney (2003). Shaped-Beam Pattern Synthesis of Equally and Unequally Spaced Linear Antenna Arrays Using a Modified Tabu Search Algorithm, *Microwave and Optical Technology Letters*, Vol. 36, No. 1, (Jan. 2003) 16-20, ISSN 0895-2477
- V. Agrawal and Y. Lo (1972). Mutual coupling in phased arrays of randomly spaced antennas, *IEEE Transactions on Antennas and Propagation*, Vol. AP-20, No. 3, (May 1972) 288-295, ISSN 1045-9243
- J. Bae, K. Kim, and C. Pyo (2005). Design of Steerable Linear and Planar Array Geometry with Non-uniform Spacing for Side-Lobe Reduction, *IEICE Transactions on Communications*, Vol. E88-B, No. 1, (Jan. 2005) 345-357, ISSN 0916-8516
- M. Brandstein, and D. Ward (2001). *Microphone Arrays. Signal Processing Techniques and Applications*, Springer-Verlag, ISBN 3-540-41953-5, Berlin
- M. Bray, D. Werner, D. Boeringer, and D. Machuga (2002). Optimization of Thinned Aperiodic Linear Phased Arrays Using Genetic Algorithms to Reduce Grating Lobes During Scanning, *IEEE Transactions on Antennas and Propagation*, Vol. 50, No. 12, (Dec. 2002) 1732-1742, ISSN 1045-9243
- B. Feng, and Z. Chen (2004). Optimization of Three Dimensional Retrodirective Arrays, *Proceedings of the IEEE 3rd Annual Communication Networks and Services Research Conference 2005*, pp. 80-83, ISBN 0-7695-2333-1, Halifax (Nova Scotia, Canada), May 2005, Halifax
- R. Harrington (1961). Sidelobe reduction by nonuniform element spacing, *IRE Transactions on Antennas and Propagation*, Vol. 9, No. 2, (Mar. 1961) 187-192, ISSN 0096-1973

- R. Haupt (1994). Thinned arrays using genetic algorithms, *IEEE Transactions on Antennas and Propagation*, Vol. 42, No. 7, (May 1994) 993-999, ISSN 1045-9243
- B. Kumar, and G. Branner (2005). Generalized Analytical Technique for the Synthesis of Unequally Spaced Arrays with Linear, Planar, Cylindrical and Spherical Geometry, *IEEE Transactions on Antennas and Propagation*, Vol. 53, No. 2, (Feb. 2005) 621-634, ISSN 1045-9243
- D. Kurup, M. Himdi, and A. Rydberg (2003). Synthesis of Uniform Amplitude Unequally Spaced Antenna Arrays Using the Differential Evolution Algorithm, *IEEE Transactions on Antennas and Propagation*, Vol. 51, No. 9, (Sep. 2003) 2210-2217, ISSN 1045-9243
- R. Mailloux (2005). *Phased Array Antenna Handbook* (2nd Ed.), Artech House Inc., ISBN 9781580536905, Norwood, MA
- M. Skolnik, G. Nemhauser, and J. Sherman (1964). Dynamic programming applied to unequally spaced arrays, *IEEE Transactions on Antennas and Propagation*, Vol. AP-12, No. 1, (Jan. 1964) 35-43, ISSN 1045-9243
- H. Unz (1960). Linear arrays with arbitrarily distributed elements, *IRE Transactions on Antennas and Propagation*, Vol. 8, No. 2, (Mar. 1960) 222-223, ISSN 0096-1973
- B. Van Veen, and K. Buckley (1988). Beamforming: A Versatile approach to Spatial Filtering, *IEEE ASSP Magazine*, (Apr. 1988) 4-24

Millimeter-wave Radio over Fiber System for Broadband Wireless Communication

Haoshuo Chen, Rujian Lin and Jiajun Ye
*Shanghai University, Shanghai
 China*

1. Introduction

The wireless networking has attracted much interest in past decades, owing to its high mobility. People can connect their devices such as PDAs, mobile phones or computers to a network by radio signals anywhere in home, garden or office without the need for wires. The global growth of mobile subscribers is much faster than wireline ones, as the Figure 1 shows (Yungsoo et al., 2003). The number of mobile subscribers worldwide has increased from 215 million in 1997 to 946 million (15.5% of global population) in 2001. It is predicted that by the year 2010 there will be 1,700 million terrestrial mobile subscribers worldwide. At present, main wireless standards are Wireless LAN (WLAN), IEEE802.11a/b/g, offering up to 54-Mbps and operating at 2.4-GHz and 5-GHz, and 3-G mobile networks, IMT2000/UMTS, offering up to 2-Mbps and operating around 2-GHz. But with the development of human society, people have higher requirements for the services, such as video, multimedia and other new value-added services. In order to offer these broadband services, wireless systems will need to offer higher data transmission capacities.

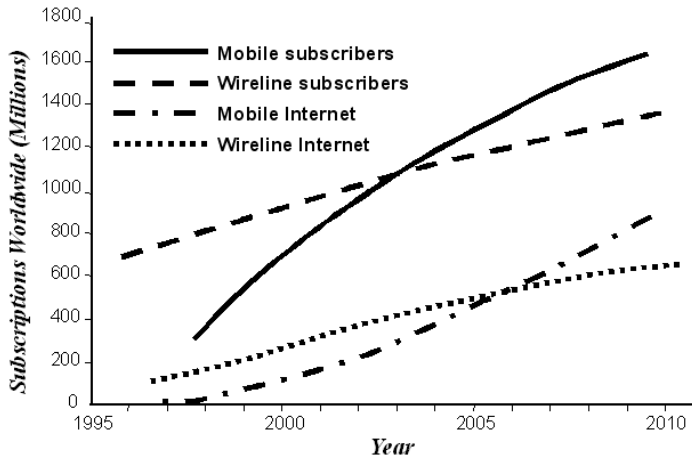


Fig. 1. Global growth of mobile and wireline subscribers.

By increasing operating frequencies of wireless system, a broader bandwidth can be provided to transmit data with higher transmission speed. In Millimeter-wave (mm-wave) band (30-GHz ~300GHz), about 270-GHz bandwidth can be utilized, which is ten times the bandwidth in Centimeter-wave band (3-GHz~30-GHz). Moreover, the increase of operation frequency helps to minimize the size of wireless equipment and improve the antenna directivity. But free space loss increases drastically with frequency and obstacles such as a human body may easily cause a substantial drop of received power at mm-wave band, nullifying the gain provided by the antennas. Besides, the diffraction of mm-wave, the ability to bend around edges of obstacles is weak (Smulders, 2002). Due to the characteristics of mm-wave, the electrical delivery of mm-wave wireless signals over a long distance is not feasible. Many research works have been done to transmit mm-wave over the fiber-optic links, which exploit the advantages of both optical fibers and mm-wave frequencies to realize broadband communication systems and contribute a lot to the development of mm-wave Radio over Fiber (RoF) systems (Sun et al., 1996; Braun et al., 1998; Kitayama, 1998). Figure 2 gives the architecture of mm-wave RoF system. Central Station (CS) and distributed Base Stations (BS) are linked with optical fibers. In each pico-cell, BS communicates with some Mobile Terminals (MT) by wireless signals at mm-wave band.

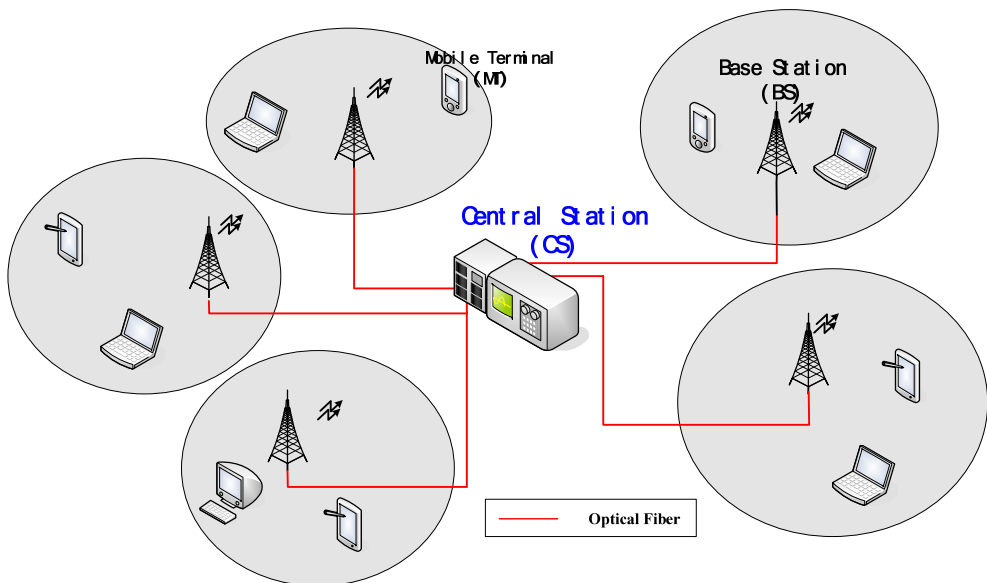


Fig. 2. Architecture of mm-wave RoF system.

Main issues in mm-wave RoF system include the optical methods of generating low noise mm-wave wireless signal and overcoming the influence of fiber chromatic dispersion on the transmission of optical wireless signal. Because of the great amounts of BSs, to reduce the system's capital, installation and maintenance costs, it is imperative to make the distributed BSs as simple as possible. Therefore, the signal processing works, such as modulation/demodulation for information conveying, cross-cell handover control, and etc. should be centralized on CS, making the BS be a simple light-wave to mm-wave converter.

In this chapter, a brief introduction of mm-wave RoF system will be given and the optical techniques of generating mm-wave signals are presented. Unlike the conventional discussions about mm-wave RoF systems focusing on the downlink only, the design of bidirectional mm-wave RoF systems are considered. Two multiplexing techniques, Wavelength Division Multiplexing (WDM) and Subcarrier Multiplexing (SCM) are introduced to realize the distributed BSs. Fiber chromatic dispersion, the main cause of performance degradation in optical communications also affects mm-wave RoF systems, making the mm-wave fade with distance in the fiber links. The influence of fiber chromatic dispersion on different mm-wave generation techniques will be discussed. The Medium Access Control (MAC) protocols suitable for the fast handover of mm-wave systems are also introduced.

2. Techniques of millimeter-wave signal generation in RoF Systems

The generation of mm-wave wireless signal in BS using optical techniques is the key technical issue of mm-wave RoF systems. In the following context, three optical technologies to yield mm-wave signal, such as direct intensity modulation, optical self-heterodyning and Optical Frequency Multiplication (OFM) will be introduced.

2.1 Direct intensity modulation and external intensity modulation

The direct intensity modulation is realized by applying mm-wave directly to the laser and change the intensity of the launched light, the mm-wave signal can be recovered in BS by direct detection. Hartmann et al. (2003) reported the experimental result of using uncooled directly modulated DFB lasers to transmit high data-rate Orthogonal Frequency Division Multiplexing (OFDM) video signals over 1-km multi-mode fiber (MMF). The experimental setup is shown in Figure 3. The video signal is transmitted from a mobile laptop to a desktop PC.

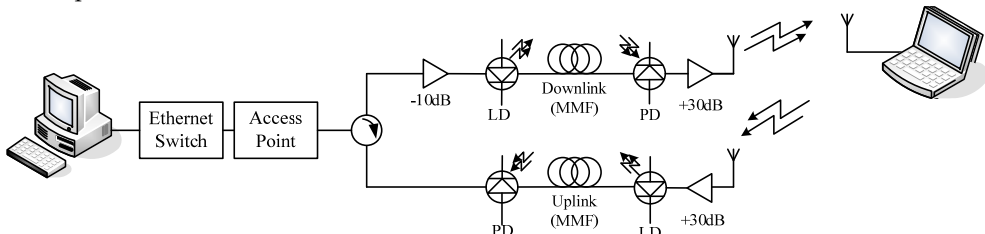


Fig. 3. The experimental setup of direct intensity modulation.

The main drawback of direct intensity modulation is that the bandwidth of modulating signal is limited by the modulation bandwidth of laser.

Another way to realize intensity modulation is to modulate the light launched from a laser which operates in continuous wave (CW) mode in an external intensity modulator, e.g., Mach-Zehnder modulator (MZM) or electro-absorption modulator (EAM). Figure 4 gives the scheme of generating mm-wave signal by using MZM (O'Rcilly et al., 1992).

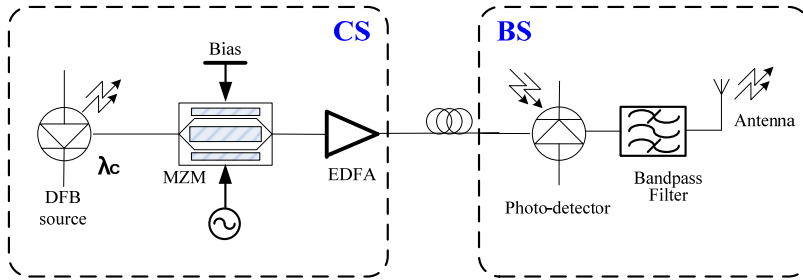


Fig. 4. The usage of MZM as external modulator.

It can be seen that a single laser source is required together with a MZM. By biasing the MZM at V_{π} , the half-wave voltage of MZM, the optical carrier at center wavelength will be suppressed. The beat of upper and lower 1st side-modes will yield required mm-wave signal, whose frequency is twice that of the mm-wave signal applied to MZM. The EAM is also a candidate of external modulator (Kuri et al., 1999). The mm-wave produced by these intensity modulation schemes have some advantages such as no line-width broadening due to the fiber dispersion, but a mm-wave oscillator is required in CS inevitably, which is costly.

2.2 Optical self-heterodyning

The generation of mm-wave signal by self-heterodyning of two-mode light-waves has a good effect to overcome the fiber chromatic dispersion (Gliese et al., 1996).

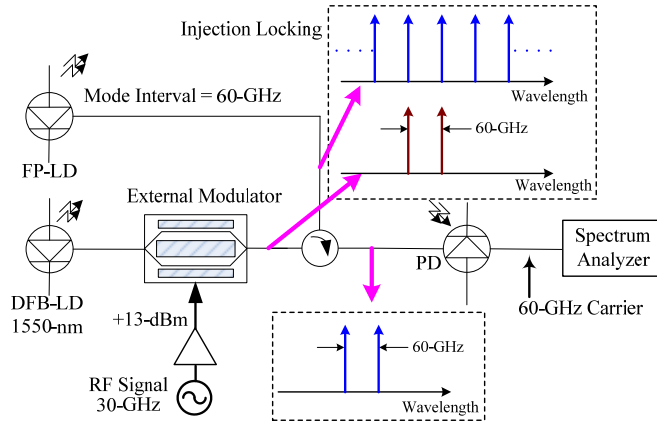


Fig. 5. Configuration of the two-mode injection-locking of a FP LD for optical self-heterodyning

Optical self-heterodyning is based on transmission of two phase-correlated optical signals, at frequencies f_1 and f_2 . The difference of these two frequencies is the frequency of desired mm-wave signal. After opto-electronic conversion at photodiode (PD) in BS, the mm-wave at frequency f_c ($f_c = f_1 - f_2$) is generated. Figure 5 shows the configuration of the two-mode locking of a FP LD to generate 60-GHz mm-wave carrier. The 1st upper and lower side-modes, obtained by applying MZM with 30-GHz radio frequency (RF) signal to modulate

the CW output from a DFB LD are used to lock the two modes of the FP LD, whose mode interval is 60-GHz (Ogusu et al., 2003). The main drawback of optical self-heterodyning is the strong influence of laser phase noise and optical frequency variation on the purity and stability of the generated mm-wave signal. The optical phase-locked loop (OPLL) has been used to reduce the phase noise (Williams et al., 1989; Gliese et al., 1992). Hence the optical self-heterodyning is a costly solution for photonic generation of mm-wave signal because it needs a special laser system.

2.3 Optical Frequency Multiplication (OFM)

2.3.1 OFM by optical frequency sweeping technique

Optical Frequency Multiplication (OFM) is a kind of photonic methods which up-convert low frequency microwave into mm-wave band. The mm-wave generation by OFM is based on a technique called as optical frequency sweeping which is ideally implemented by launching light-wave from a fast tunable laser which is swept periodically at a microwave frequency, but this technique is infeasible, because this kind of tunable laser is unavailable in the market.

Figure 6 gives an arrangement of OFM by an alternate optical frequency sweeping technique. It can be seen that in CS a light-wave is launched by a laser diode operating at CW mode and then phase-modulated in an external phase modulator by a microwave signal at frequency f_s with a large modulation index. The output light-wave becomes an optical frequency-swept signal, having a lot of side modes separated by f_s . This phase spectrum is converted into an intensity spectrum by passing the phase-modulated light-wave through a periodic optical filter such as Mach-Zehnder interferometer (MZI). These intensity side modes beat with each other at the PD in BS producing a series of harmonics of the sweeping signal. In this way, a mm-wave at frequency $2nf_s$ is generated which can be picked up using a narrowband band-pass filter and amplified for radiating into the air via an antenna. In this scheme, the data signal can be intensity-modulated on the optical frequency-swept signal by an external intensity modulator (Ton et al., 2003). The principle of OFM is deduced as below.

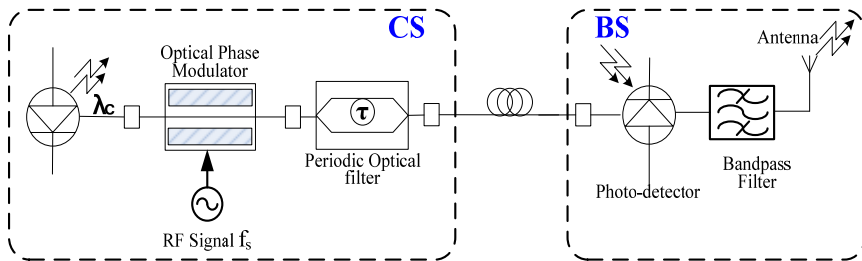


Fig. 6. The basic arrangement of OFM using optical frequency sweeping technique.

The electric field at the output of optical phase modulator is express as

$$E_i(t) = E_c \exp(j\omega_c t + j\beta \sin \omega_s t) \tag{1}$$

where E_c is the amplitude of electric field; ω_c is the central angular frequency of optical source; ω_s is the angular frequency of phase sweeping signal; β is the phase modulation index. After passing through the MZI with delay parameter τ , the electric field becomes

$$E_o(t) = E_c \exp(j\omega_c t + j\beta \sin \omega_s t) + E_c \exp[j\omega_c(t - \tau) + j\beta \sin \omega_s(t - \tau)] \quad (2)$$

The photo-current is proportional to $E_o(t) \times E_o^*(t)$, i.e.

$$\begin{aligned} i_d(t) &= \frac{1}{2} R \{E_o(t) \times E_o^*(t)\} = \frac{1}{2} R E_c^2(t) \{1 + \cos[\omega_c \tau + 2\beta \sin(\frac{\omega_s \tau}{2}) \cos(\omega_s t - \frac{\omega_s \tau}{2})]\} \\ &= \frac{1}{2} R E_c^2(t) \{ \cos(\omega_c \tau) [J_0(2\beta \sin \frac{\omega_s \tau}{2}) + 2 \sum_{n=1}^{\infty} J_{2n}(2\beta \sin \frac{\omega_s \tau}{2}) \cos(2n\omega_s t - n\omega_s \tau)] \\ &\quad - \sin(\omega_c \tau) [2 \sum_{n=1}^{\infty} J_{2n-1}(2\beta \sin \frac{\omega_s \tau}{2}) \cos((2n-1)\omega_s t - \frac{2n-1}{2}\omega_s \tau)] \} \end{aligned} \quad (3)$$

where R is a proportional constant related to the responsivity of PD. $J_n(x)$ is the n -th Bessel function of x . From (3) it is revealed that if $\omega_c \tau = k\pi$, ($k = \text{integer}$) and $\omega_s \tau = \pi$, each of even harmonics in the photo-current approaches its maximum value while all odd harmonics disappear, i.e.

$$i_d(t) = \frac{1}{2} R E_c^2 [J_0(2\beta) + 2 \sum_{n=1}^{\infty} (-1)^n J_{2n}(2\beta) \cos(2n\omega_s t)] \quad (4)$$

This means that the central wavelength λ_c of laser source and the delay constant τ of MZI should be kept to meet a specific relation, otherwise the mm-wave generation will not be effective. For example, the parameters of system in Figure 6 are taken as: $f_s = 5$ GHz, $\tau = 0.1$ ns, $\lambda_c = 2c\tau/k$, where c is the light velocity in vacuum. If $k = 38706, 38707, 38708$, Then $\lambda_c = 1550.147\text{nm}, 1550.107\text{nm}, 1550.067\text{nm}$ respectively. This means that λ_c deviates from its optimum value by 0.02nm will cause the desired harmonic to disappear.

Although this technique does not need any mm-wave oscillator and up-conversion chain both in CS and in BS, the trouble in the real situation exists such as the temperature dependence of τ . If one wants the system stable, the MZI should be temperature stabilized in addition to that the laser should be wavelength-tunable. Hence this kind of OFM configuration for mm-wave generation is not cost-effective (Lin et al., 2008).

2.3.2 OFM by nonlinear modulation of dual-drive Mach-Zehnder modulator

Recognizing that there are two basic processes for OFM: one, optical phase modulation with large modulation index to generate high order optical side-modes; another, phase modulation-to-intensity modulation conversion to make self-heterodyne happen at PD. For the implementation of phase modulation-to-intensity modulation conversion it is necessary to have two laser beams interfering with each other, but MZI optical filter is not the only device to make optical interference.

Actually a dual-drive Mach-Zehnder modulator (DD-MZM) is a parallel combination of two optical phase modulators and its two arms can make optical interference happen. Therefore

an OFM arrangement to generate mm-wave based on high order optical side-modes generation & self-heterodyne using a DD-MZM can be configured as Figure 7.

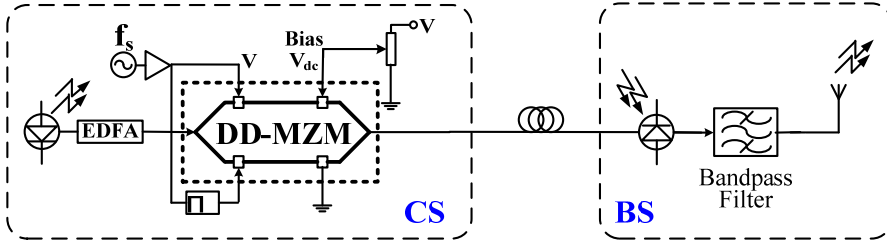


Fig. 7. The basic arrangement of OFM by nonlinear modulation of DD-MZM.

DD-MZM as a commonly used linear intensity modulator can also output optical wave with many harmonics when it is modulated in a nonlinear way, i.e. driven by two large RF signals applied to its two electrodes. Assuming E_c , the amplitude of electric field input to two arms of DD-MZM; τ , the time delay difference between two arms of DD-MZM; θ , the phase difference between two RF signals; $\Delta\varphi_{dc}$, the initial phase difference of light-waves in the two arms of DD-MZM; β , the phase modulation index caused by the RF signals; ω_c and ω_s , the angular frequencies of the light-wave and the RF signal respectively; $\varphi_N(t + \tau)$ and $\varphi_N(t)$, the laser phase noise in two arms of DD-MZM, the electrical field of output light-wave from DD-MZM is

$$E_o = E_c \exp[j\omega_c(t + \tau) + j\beta \cos(\omega_s(t + \tau) + \theta) + \Delta\varphi_{dc} + \varphi_N(t + \tau)] + E_c \exp[j\omega_c t + j\beta \cos \omega_s t + \varphi_N(t)] \quad (5)$$

The photo-current $i_d(t)$ in PD produced by light-wave injection is

$$i_d(t) = \frac{1}{2} RE_o E_o^* = RE_c^2 \{1 + \cos[\beta \cos(\omega_s t + \omega_s \tau + \theta) - \beta \cos \omega_s t + \omega_c \tau + \Delta\varphi_{dc} + \varphi_N(t + \tau) - \varphi_N(t)]\} \quad (6)$$

Setting $\Delta\varphi = \omega_c \tau + \Delta\varphi_{dc}$, $\alpha = \omega_s \tau + \theta$, $i_d(t)$ can be simplified into the form following:

$$i_d(t) = RE_c^2 \{1 + \cos[\beta_1 \cos(\omega_s t + \alpha) - \beta_2 \cos \omega_s t + \Delta\varphi + \varphi_N(t + \tau) - \varphi_N(t)]\} = RE_c^2 + RE_c^2 \{ \cos[\Delta\varphi + \varphi_N(t + \tau) - \varphi_N(t)] \cos[\beta_{12} \cos(\omega_s t + \phi)] - \sin[\Delta\varphi + \varphi_N(t + \tau) - \varphi_N(t)] \sin[\beta_{12} \cos(\omega_s t + \phi)] \} \quad (7)$$

where $\beta_{12} = \beta[(\cos \alpha - 1)^2 + (\sin \alpha)^2]^{1/2}$, $\phi = \text{tg}^{-1}[-\sin \alpha / (\cos \alpha - 1)]$. In a DD-MZM, the two arms are identical in length, therefore $\tau = 0$, the laser phase noise terms in photo-current is

cancelled with each other. In addition, if $\alpha = \omega_s \tau + \theta = \pi$ holds, then β_{12} reaches its maximum value 2β and $\phi = 0$.

Expanding $i_d(t)$ into a series by using Bessel function gives

$$i_d(t) = RE_c^2 + RE_c^2 \left\{ \cos \Delta\varphi [J_0(2\beta) + 2 \sum_{n=1}^{\infty} (-1)^n J_{2n}(2\beta) \cos(2n\omega_s t)] \right. \\ \left. + \sin \Delta\varphi [2 \sum_{n=1}^{\infty} (-1)^n J_{2n-1}(2\beta) \cos((2n-1)\omega_s t)] \right\} \quad (8)$$

The photo-current is composed of a lot of even order harmonics and odd order harmonics of the RF signal. By adjusting the bias voltage V_{dc} to make that $\Delta\varphi = \omega_c \tau + \Delta\varphi_{dc} = \pi V_{dc} / V_\pi = 0$ or π , $\cos \Delta\varphi = \pm 1$ and $\sin \Delta\varphi = 0$, the odd order harmonics disappear, while each even order harmonic reaches its maximum, i.e.

$$i_d(t) = RE_c^2 [1 \pm J_0(2\beta) \pm 2 \sum_{n=1}^{\infty} (-1)^n J_{2n}(2\beta) \cos(2n\omega_s t)] \quad (9)$$

where $\beta = \pi V / V_\pi$, V is the amplitude of RF signal, V_π is the voltage for π phase shift of MZM. If a specific value of (2β) is taken, then the specific order Bessel function reaches its maximum. For example, to generate 40-GHz carrier from 5-GHz signal (multiplying factor $2n=8$), setting $\beta = 4.8$ gives $J_8(9.6) = 0.3244$. The maximum amplitude of generated 40-GHz carrier is $0.6488 \times RE_c^2$.

In comparison with the OFM scheme shown in Figure 6, OFM by nonlinear modulation of DD-MZM has the following advantages:

- (1) The optimum condition to make odd harmonics disappear and even harmonics maximum is independent of the laser wavelength so that the tunable laser is no longer necessary.
- (2) The system does not need any periodic optical filter, such as MZI, to implement PM-IM conversion, so that the system stability is improved by getting rid of temperature-sensitive devices. Even the phase shift in each arm of DD-MZM also depends on the environmental temperature, the two arms with the same length are integrated together in a compact package so that the influences of temperature variation on the two phase modulators are in balance and will be cancelled out.
- (3) Laser phase noise is cancelled out so that the output spectrum of mm-wave is pure.
- (4) The configuration of CS is most simplified by excluding the tunable DFB LD and the MZI, so that cost saving is achieved.

Because the harmonics are generated in the condition that the phase modulation index is high, a high power amplifier is required to amplify the RF signal. Many works have been done to lower the driving voltage of MZM. A push-pull structure MZM with V_π of 0.3V has been proposed by Tsuzuki et al. (2006).

3. Bi-directional mm-wave RoF System based on OFM by using DD-MZM

3.1 Bi-directional mm-wave RoF system based on OFM with IF sub-carrier

In addition to the photonic generation of mm-wave, an important thing is how to convey baseband information on a mm-wave. One technique is to directly modulating the mm-wave by the baseband information, another is to modulate the mm-wave by an intermediate frequency (IF) sub-carrier which conveys the base-band information. The advantages of utilizing an IF signal consist in that first, various modulation/demodulation schemes for conveying the base-band information can be used as required by applications; second, the IF signal inserted in the system can also be a pilot tone to generate a pure mm-wave in BS which will be used as a local reference signal for down-converting the modulated mm-wave received from the antenna back into an modulated IF signal; third, utilization of a group of IF sub-carriers instead of one can more sufficiently exploit the bandwidth of mm-wave.

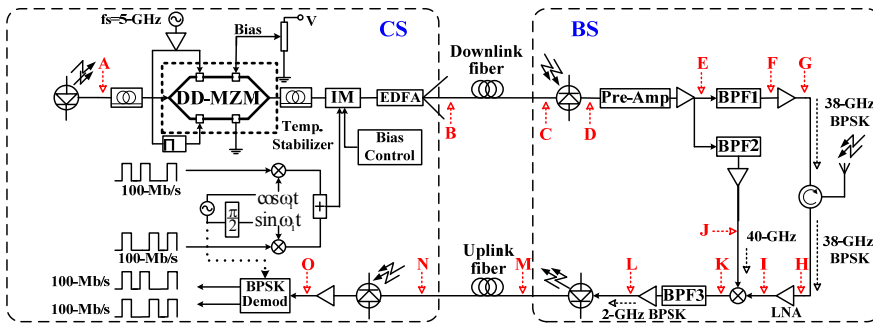


Fig. 8. Bidirectional 38/40-GHz RoF system based on OFM using DD-MZM

Considering the cost-efficiency of bi-directional mm-wave RoF systems, the BS should be configured as simple as possible and no complex electronic circuits, such as mm-wave local oscillator, mm-wave up-conversion chain is needed in both CS and BS. Therefore, the modulated mm-wave signal for radiation in downlink and the mm-wave reference for down-converting the received mm-wave signal into IF signal in uplink need to be generated at the same time after opto-electronic conversion in BS. Then the down-converted signal can be easily modulated on the light-wave launched by a low cost FP laser and sent back to CS. A bidirectional 40-GHz RoF system based on high order optical side-modes generation & self-heterodyne using a DD-MZM can be configured as Figure 8 with observation points A, B, C... O. In downlink, a 1550-nm polarization-adjusted laser beam in CS is injected into a DD-MZM, whose two arms are DC-biased properly and RF-driven separately. Two 5-GHz sinusoidal waves with phase difference π are driving the DD-MZM to carry out optical phase modulation with a large index in each arm. At the combining point of DD-MZM, the two optical beams with different phases interfere with each other converting optical phase modulation into optical intensity modulation with many high order side-modes. These optical modes are re-modulated in another IM by an information-bearing 2-GHz IF signal and then transmitted over a downlink fiber of 20-km. Finally they beat at the PD in BS, generating many electrical harmonics of 5-GHz signal, among which any harmonic can be picked up by a specific narrowband band-pass filter. In this way not only a pure 40-GHz signal, but also a 38-GHz mm-wave carrying 2×100 -Mbps Ethernet data in BPSK format is generated. The latter

will be amplified and radiated into the air via an antenna. In uplink, the 38-GHz signal from the antenna is amplified by a low noise amplifier (LNA) and then mixed with the amplified local 40-GHz signal, resulting in a 2-GHz IF signal. The filtered and amplified IF signal directly modulates a FP LD, being sent back to CS via the uplink fiber and recovered at PD. Eventually the amplified IF signal is BPSK-demodulated into 2×100-Mbps Ethernet data. The modulating IF signal which carries the digital information in phase is expressed as

$$m(t) = \cos(\omega_i t + \phi_1) + \sin(\omega_i t + \phi_0) \quad (10)$$

where ω_i is the angular frequency of IF signal; ϕ_1 and ϕ_0 are the in-phase and quadrature symbols of information carried by the IF signal. Including the modulation effect in IM, the expression of photo-current given in (9) is modified as

$$\begin{aligned} i(t) = & RE_c^2 [1 + km(t)][1 \pm J_0(2\beta) \pm 2 \sum_{n=1}^{\infty} J_{2n}(2\beta) \cos(2n\omega_s t)] \\ & \pm k \left\{ \sum_{n=1}^{\infty} J_{2n}(2\beta) \cos[(2n\omega_s + \omega_i)t + \phi_1] + \sum_{n=1}^{\infty} J_{2n}(2\beta) \cos[(2n\omega_s - \omega_i)t - \phi_1] \right\} \\ & \pm k \left\{ \sum_{n=1}^{\infty} J_{2n}(2\beta) \sin[(2n\omega_s + \omega_i)t + \phi_0] + \sum_{n=1}^{\infty} J_{2n}(2\beta) \sin[(2n\omega_s - \omega_i)t - \phi_0] \right\} \end{aligned} \quad (11)$$

where k is the intensity modulation index in IM. Obviously the photo-current contains not only the IF side-bands centered at each harmonic of the RF signal, but also the pure harmonics of the RF signal. The latter can be used as the local reference signal for down-conversion process in reception from the antenna.

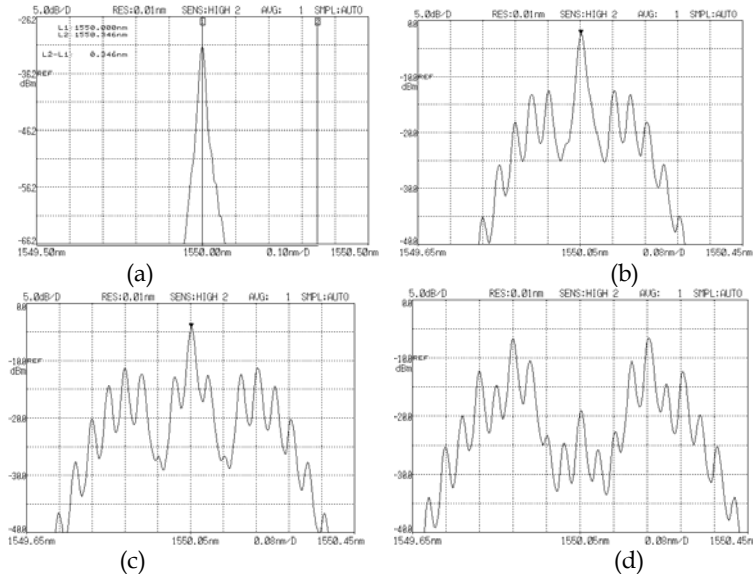


Fig. 9. The optical spectrum of (a) laser source at A, (b) at C when single arm of DD-MZM driven by +24dBm, (c) at C when single arm driven by +27dBm, (d) at C when dual arms driven by +27dBm.

The experimental results are shown below. Figure 9 (a) shows the optical spectrum of the DFB laser. Figures 9 (b) and (c) show the optical spectrum expansion as the optical phase modulation index increases in case that one arm of DD-MZM is driven. When the 5-GHz driving power approaches to +27dBm, the ± 4 th side-modes rise to the highest indicating $\beta=4.8$, as shown in Figure 9 (c). Applying this best driving power to both arms of DD-MZM, the optical spectrum shown in Figure 9 (d) becomes a carrier suppressed type with strong side-modes around ± 20 -GHz.

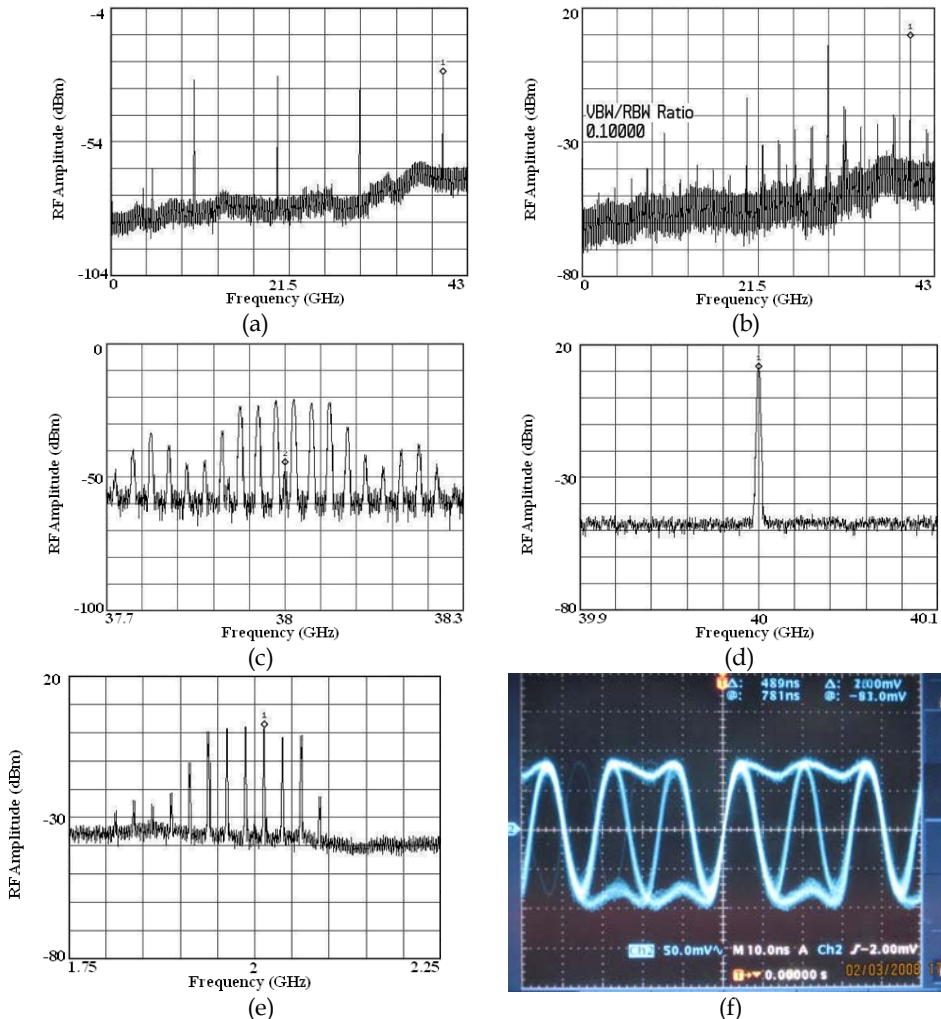


Fig. 10. The electrical spectrum of (a) generated harmonics at D, (b) at D when 2-GHz IF signal is added, (c) 38-GHz BPSK at E, (d) 40-GHz signal at J, (e) 2-GHz BPSK at O, (f) Waveform of demodulated 100-Mbps Ethernet data.

It is expected that strong 40-GHz mm-wave will be generated at PD in BS. This is proved by the RF spectrum at PD output, as shown in Figure 10 (a) where 40-GHz peak is the highest among other harmonics and odd harmonics disappear, because the bias voltage has been adjusted to meet $\Delta\varphi = \pi$. To maintain this optimum operating condition the DD-MZM has been put in a temperature stabilizer. When the BPSK-modulated 2-GHz IF signal is turned on, its spectrum appears around each generated harmonic, as shown in Figure 10 (b). Figure 10 (c) shows the spectrum of 38-GHz BPSK signal at point E in Figure 8. The filtered 40-GHz signal is amplified to above +10-dBm at point J with carrier-to-noise ratio (CNR) larger than 50-dB as shown in Figure 10 (d), and is good as a local signal for the mixer. The 2-GHz BPSK signal from the mixer is amplified, transmitted over the uplink fiber and recovered in CS, as shown in Figure 10 (e). Figure 10 (f) shows the BPSK-demodulated 100-Mbps Ethernet data, giving the evidence that the proposed bidirectional 40-GHz RoF system is successful. In this kind of bidirectional mm-wave RoF systems, the base-band digital information is conveyed by IF signal, on which many modulation/de-modulation schemes, such as PSK, QPSK, M-QAM and even OFDM can be used. In other words, this kind of bidirectional mm-wave RoF systems is transparent to the base-band information and very flexible to various applications. Larrode et al. (2006) demonstrated the generation of a 39.9-GHz mm-wave based on OFM with 1.5-GHz IF sub-carrier, which is 16 or 64 QAM-modulated.

3.2 Bi-directional mm-wave RoF system with QPSK direct modulation

Although bidirectional mm-wave RoF systems based on OFM with IF sub-carrier are advantageous in many respects, the width of an IF band limits very high speed transmission over the RoF system. Quadrature phase-shift keying (QPSK) is much more widely used than BPSK, since QPSK modulation scheme encodes two bits per symbol, which is twice the rate of BPSK. The QPSK-modulated IF signal has been employed in mm-wave RoF system. Now optical QPSK can be used to generate QPSK-modulated mm-wave signal. A system has been realized by using two optical fiber links to transmit I and Q signals separately (Fuster et al., 2001), but two PDs in BS have to be utilized, therefore it is not cost-effective.

Figure 11 gives a new design of 60-GHz bi-directional RoF system, whose modulation scheme is optical QPSK, similar to a previous work (Zhou et al., 2008), but two DD-MZMs in parallel connection are replaced by a four electrodes DQPSK Lithium Niobate (LN) modulator (Doi et al., 2007), which can greatly overcome the problem of interference intensity noise (IIN) caused by the time delay between the two optical paths.

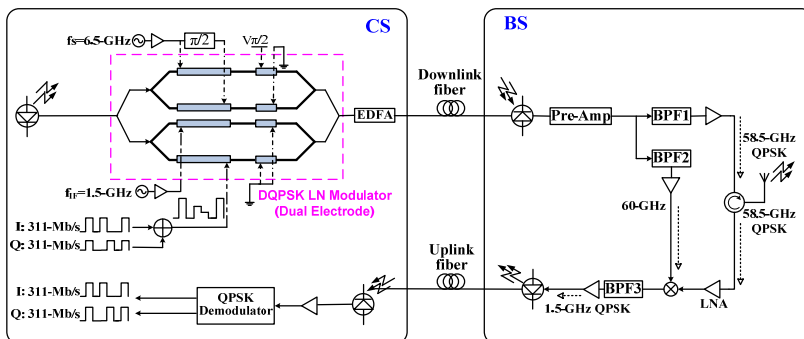


Fig. 11. The basic structure of optical QPSK bidirectional mm-wave RoF system.

As shown in Figure 11, two high-power 6.5-GHz RF signals with phase difference $\pi/2$ are applied to one MZI's two electrodes of DQPSK modulator. And a 1.5-GHz IF signal for generating pure mm-wave tone and 622-Mbit/s baseband signal, after 2 to 4 level conversion drive another MZI's two electrodes respectively. After photo-detection at the PD in BS, the 58.5-GHz QPSK-modulated signal and pure 60-GHz signal are generated. This configuration of mm-wave generation is analyzed as below. The output electric field from the DQPSK modulator is expressed as

$$\begin{aligned}
 E_{out}(t) = & E_c \exp[j\omega_c t + j\beta \cos \omega_s t + j\pi/2 + j\varphi_N(t)] \\
 & + E_c \exp[j\omega_c t + j\beta \sin \omega_s t + j\varphi_N(t)] \\
 & + E_c \exp[j\omega_c t + j\alpha \cos \omega_{IF} t + \varphi_N(t)] \\
 & + E_c \exp[j\omega_c t + j\phi_M + j\varphi_N(t)]
 \end{aligned} \quad (12)$$

where E_c is the amplitude of electric field; ω_c is the angular frequency of light source; ω_s is the the angular frequency of RF signal; ω_{IF} is the the angular frequency of IF signal; β and α are the phase modulation indexes of RF signal and IF signal respectively; $\varphi_N(t)$ is the laser phase noise; ϕ_M is the QPSK phase symbol with random value taken in $\{0, \pi/2, \pi, 3\pi/2\}$. The time delay difference between any two arms in the integrated DQPSK modulator can be neglected.

The photo-current in BS is $i_d(t) = 0.5 \times RE_{out}(t) \times E_{out}^*(t)$. Substituting (12) for $E_{out}(t)$ gives $i_d(t)$ in the expression as following

$$\begin{aligned}
 i_d(t) = & RE_c^2 \{ 2 + 2 \sum_{n=1}^{\infty} J_{2n-1}(\sqrt{2}\beta) \sin[(2n-1)(\omega_s t - \frac{\pi}{4})] + 2 J_0(\alpha) \sum_{n=1}^{\infty} (-1)^n J_{2n-1}(\beta) \cos[(2n-1)\omega_s t] \\
 & + 2 J_1(\alpha) \cos(\omega_{IF} t) [J_0(\beta) + 2 \sum_{n=1}^{\infty} (-1)^n J_{2n}(\beta) \cos(2n\omega_s t)] \\
 & + 2 \cos \phi_M \sum_{n=1}^{\infty} (-1)^n J_{2n-1}(\beta) \cos[(2n-1)\omega_s t] + \sin \phi_M [J_0(\beta) + 2 \sum_{n=1}^{\infty} (-1)^n J_{2n}(\beta) \cos(2n\omega_s t)] \\
 & + J_0(\alpha) [J_0(\beta) + 2 \sum_{n=1}^{\infty} J_{2n}(\beta) \cos(2n\omega_s t)] + 4 J_1(\alpha) \cos(\omega_{IF} t) \sum_{n=1}^{\infty} J_{2n-1}(\beta) \sin[(2n-1)\omega_s t] \\
 & + \cos \phi_M [J_0(\beta) + 2 \sum_{n=1}^{\infty} J_{2n}(\beta) \cos(2n\omega_s t)] + 2 \sin \phi_M \sum_{n=1}^{\infty} J_{2n-1}(\beta) \sin[(2n-1)\omega_s t] \\
 & + \cos \phi_M J_0(\alpha) + 2 \sin \phi_M J_1(\alpha) \cos(\omega_{IF} t) \}
 \end{aligned} \quad (13)$$

where $\cos(\alpha \cos \omega_{IF} t) \approx J_0(\alpha)$ and $\sin(\alpha \cos \omega_{IF} t) \approx 2 J_1(\alpha)$ have been taken, because the function of IF signal in this system is to generate pure mm-wave in BS as local reference signal for reception down-conversion, therefore the modulation index α should be small enough to make the linear modulation of IF signal onto the light-wave.

From (13) it is revealed that only the odd harmonics of RF signal have quadrature components. It means that only the odd harmonics of RF signal can convey the baseband information in QPSK form, whose $(2n-1)^{\text{th}}$ components are expressed as

$$\begin{aligned}
F_{2n-1} = & 2RE_c^2 \{ J_{2n-1}(\sqrt{2}\beta) \sin[(2n-1)(\omega_s t - \frac{\pi}{4})] + J_0(\alpha)(-1)^n J_{2n-1}(\beta) \cos[(2n-1)\omega_s t] \\
& + \cos\phi_M (-1)^n J_{2n-1}(\beta) \cos[(2n-1)\omega_s t] + \sin\phi_M J_{2n-1}(\beta) \sin[(2n-1)\omega_s t] \\
& + J_1(\alpha) J_{2n-1}(\beta) \{ \sin[(2n-1)\omega_s + \omega_{IF}]t + \sin[(2n-1)\omega_s - \omega_{IF}]t \} \}
\end{aligned} \quad (14)$$

where the first two terms are the $(2n-1)$ th harmonics of RF signal; the second two terms represent the QPSK-modulated $(2n-1)$ th harmonics of RF signal; the last two terms represent the IF side-bands centered at the $(2n-1)$ th harmonics of RF signal.

If $n=5$, the 9th harmonics of RF signal are expressed as

$$\begin{aligned}
F_9 = & 2RE_c^2 \{ J_9(\sqrt{2}\beta) \sin(9\omega_s t - \frac{\pi}{4}) - J_0(\alpha) J_9(\beta) \cos(9\omega_s t) \\
& - J_9(\beta) [\cos\phi_M \cos(9\omega_s t) - \sin\phi_M \sin(9\omega_s t)] \\
& + J_1(\alpha) J_9(\beta) \{ \sin[(9\omega_s + \omega_{IF})t] + \sin[(9\omega_s - \omega_{IF})t] \} \}
\end{aligned} \quad (15)$$

Taking $f_s = 6.5\text{GHz}$, $f_{IF} = 1.5\text{GHz}$, $f_9 = 58.5\text{GHz}$, Simulation has been performed using VPI software. Figures 12 (a) and (b) shows the optical spectrum of QPSK-modulated 58.5-GHz signal and 60-GHz reference signal for down-conversion in uplink. The QPSK modulated 1.5-GHz signal resulting from down-conversion is shown in Figure 12 (c). The constellation of demodulated 622-Mbit/s QPSK vector is given in Figure 13.

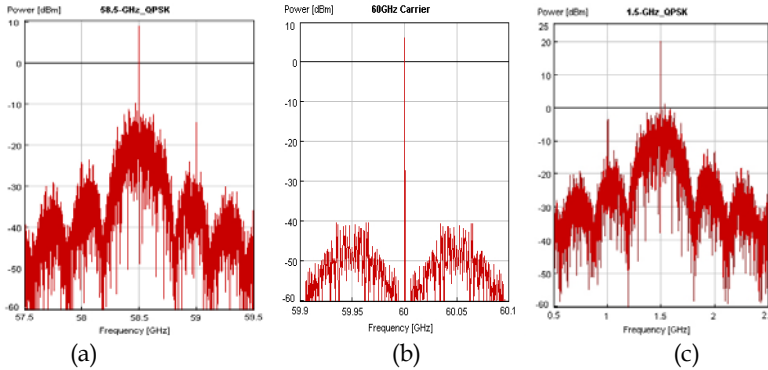


Fig. 12. The electrical spectrum of (a) QPSK-modulated 58.5-GHz signal, (b) pure 60-GHz carrier, (c) QPSK-modulated 1.5-GHz signal after down-conversion.

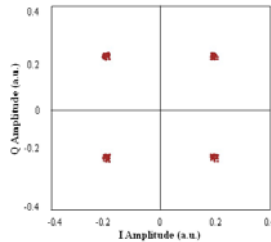


Fig. 13. Constellation of recovered QPSK signal.

3.3 Multiplexing of RoF system

3.3.1 Subcarrier Multiplexing (SCM) in RoF Link

SCM technology has been widely used in analog cable television (CATV) (Olshansky et al., 1989). Optical SCM technology which multiplexes various signals in the RF region and transmitted at a single wavelength can also be helpful to improve the bandwidth utilization of mm-wave provided by mm-wave RoF system. Garcia et al. (2005) proposed to apply optical SCM to RoF system based on optical frequency sweeping technology. In optical frequency sweeping technology, the maximum mm-wave bandwidth supported by one wavelength is limited by half the RF sweep frequency f_{sw} , i.e. if $f_{sw}=5$ -GHz, as described in Section 2.3.1, the maximum mm-wave bandwidth can achieve 2.5-GHz. If the bandwidth of data signals on the sub-carriers exceeds $f_{sw}/2$, overlapping of the double-sided bands obtained at every harmonic occurs. As shown in Figure 14, data channels on sub-carriers below $f_{sw}/2$ can be used to modulate the swept light source.

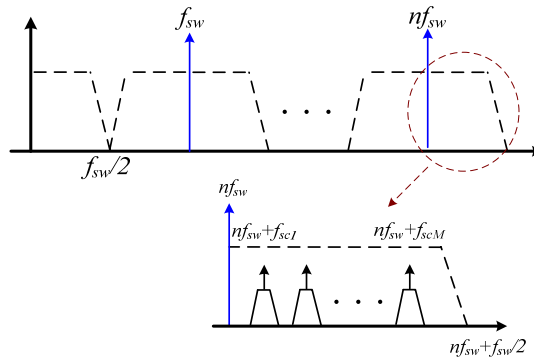


Fig. 14. Bandwidth capacity of optical frequency sweeping technique.

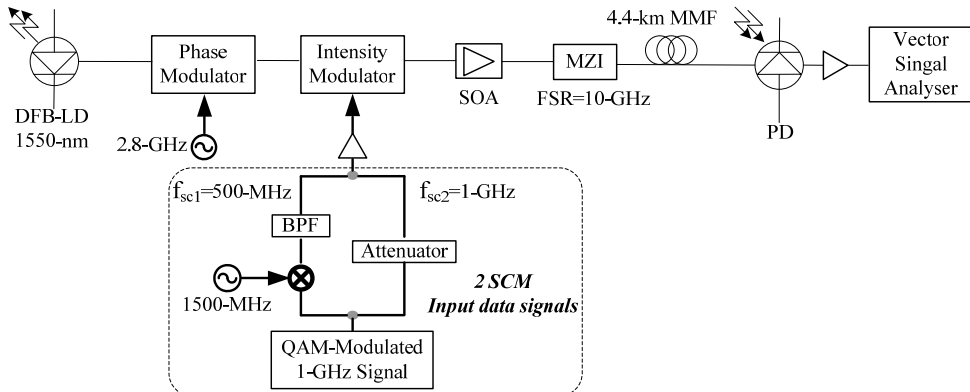


Fig. 15. Experimental setup of SCM RoF system.

Garcia et al. (2005) set up an experiment to demonstrate the feasibility to transmit the multiple RF signals at a single wavelength. The experimental setup is shown in Figure 15. Two 64 QAM-modulated signals on two sub-carriers at 500-MHz and 1-GHz are transmitted simultaneously in a RoF link. After 4.4-km fiber transmission in a RoF link based optical frequency sweeping, these two 64 QAM-modulated signals can be up-converted to 17.3-GHz and 17.8-GHz.

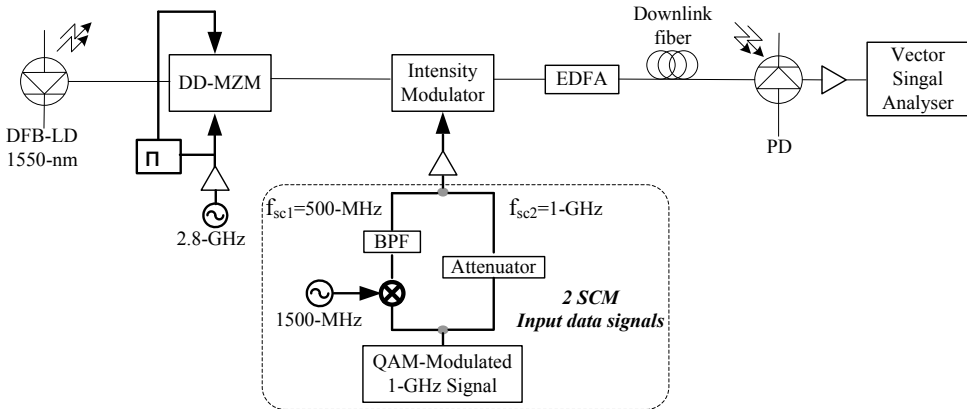


Fig. 16. An alternate setup of SCM RoF system.

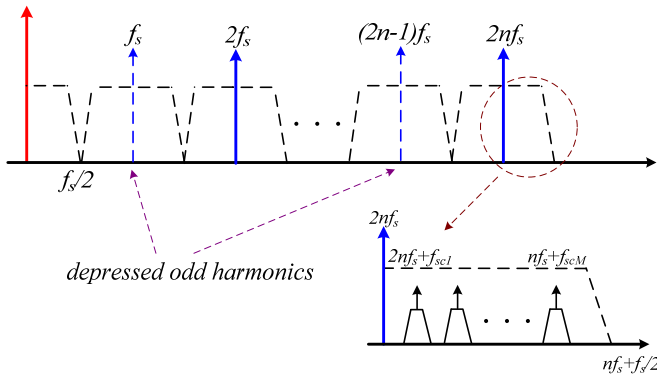


Fig. 17. Bandwidth capacity of OFM by nonlinear modulation of DD-MZM.

In section 2.3.2, it is pointed out that OFM by nonlinear modulation of DD-MZM is much better than OFM by optical frequency sweeping, therefore an alternate setup to Figure 15 is made as Figure 16, where a push-pull driven DD-MZM replaces the phase modulator plus MZI in Figure 15. Although the odd harmonics can be depressed in this scheme, according to equation (9) (in section 2.3.2), the bandwidth capacity of this technique is the same as optical frequency sweeping technique, as shown in Figure 17, f_s is the frequency of RF signal applied to DD-MZM. Because the bandwidth capacity is decided by the bandwidth of each optical side-mode, generated by nonlinear modulation of DD-MZM, rather than that of generated mm-wave harmonics after opto-electronic conversion.

3.3.2 Wavelength Division Multiplexing (WDM) in RoF Link

The bidirectional RoF systems, discussed in Section 3.1 and 3.2, have been demonstrated as a cost-effective scheme to generate mm-wave signal and realize bidirectional transmission. All those proposed systems can also realize the architecture with distributed BSs operating at one wavelength. As depicted in Figure 18, CS broadcasts the data packets at one wavelength to all BSs. Each BS extracts its own packets and transmits the data signals, which are up-converted to mm-wave band, sent to MTs. In other words, CS allocates different time slots for different BSs, and makes the RoF system work in Time Division Multiplexing (TDM) scheme.

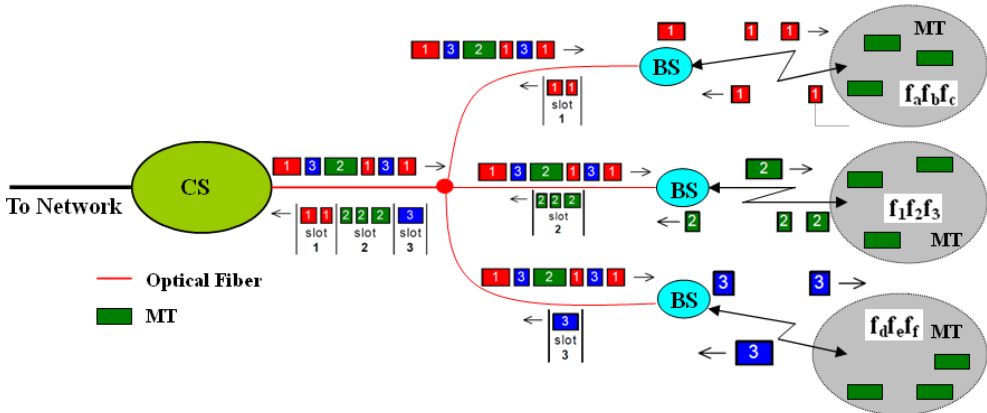


Fig. 18. Principle of bidirectional RoF system with distributed BSs based on TDM.

The basic principle of TDM RoF system is like that of EPON, which is shown in Figure 19. But the realization of TDM in EPON is based on special protocols and techniques and both Optical Line Terminal (OLT) and Optical Network Unit (ONU) need to own the ability of data processing (Kramer, 2006). Because BS in RoF system corresponds to ONU in EPON, if each BS is in charge of data processing instead of a transparent interface, the system can not be cost-effective.

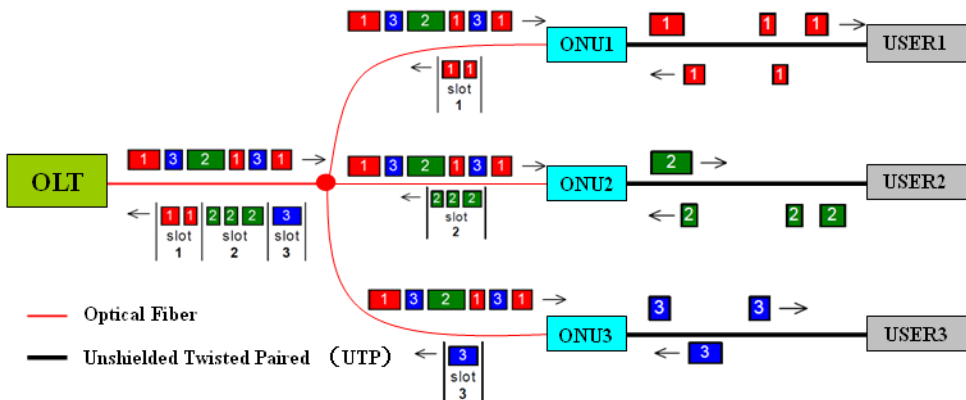


Fig. 19. The basic structure of EPON

Many research works have been done to realize RoF system with distributed BSs incorporating Wavelength Division Multiplexing (WDM) (Stöhr et al., 1998; Griffin et al., 1999). Compared to incorporating TDM, a RoF system based on WDM does not need complex protocols to handle data and can make the structure of BS as simple as possible. The utilization of WDM can simplify the network architecture by using different wavelengths to feed different BSs, and greatly simplify network upgrade and maintenance by enabling the introduction of new services and the deployment of additional BSs (Nirmalathas et al., 2000). Figure 20 shows a star-tree architecture for a RoF system incorporating WDM. In the system, the fiber links from the CS form the star part of the architecture while the tree part is at the remote node (RN) with each branch feeding a different BS pico-cell. Each RN, as one arm of star feeds its group of BSs by its own unique WDM wavelengths for both the downlink and the uplink.

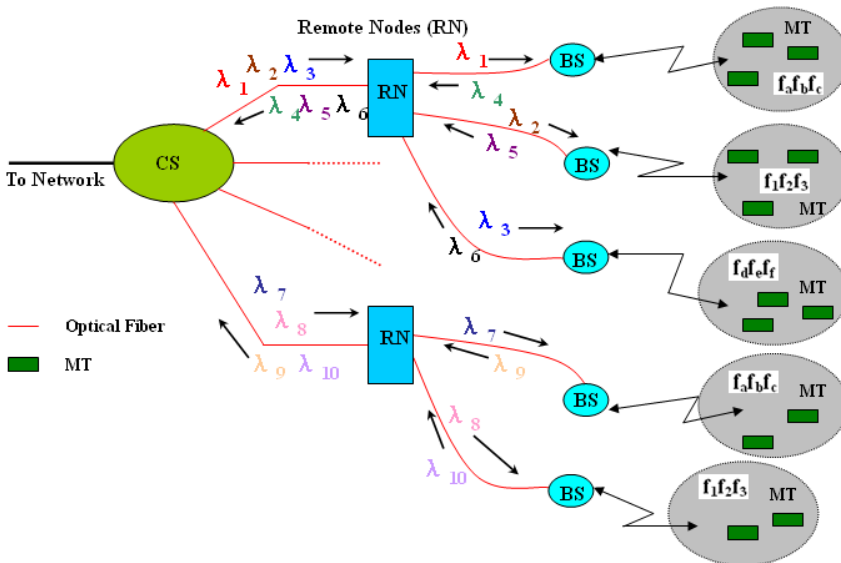


Fig. 20. Star-tree architecture for a RoF system incorporating WDM.

A WDM mm-wave RoF system with a star-tree architecture has been demonstrated (Smith et al., 1998). In this system, three SCM mm-wave signals each carrying 155-Mb/s data are transmitted in the RoF link. An alternative WDM RoF architecture is the ring network shown in Figure 21. The ring topology allows the allocation of a single wavelength to a particular BS and the wavelength routing is enabled via optical add-drop multiplexers (OADMs). The CS provides a number of wavelengths each carrying multiple modulated RF subcarriers. Uplink transmission is achieved by modulating uplink RF signals onto an optical carrier at the same BS wavelength, and adding it back into the ring via the OADM (Nirmalathas et al., 2000).

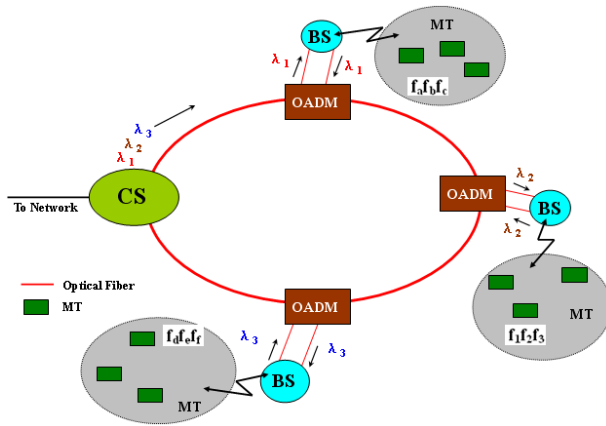


Fig. 21. Ring architecture for a RoF system incorporating WDM.

3.3.3 Distributed mm-wave RoF system incorporating WDM and OFM

OFM techniques have been demonstrated as the efficient ways to yield mm-wave signals, as discussed in section 2.3. In this section, a distributed 40-GHz RoF system and its MT design will be proposed in Figure 22 (The appropriate RF amplifiers are not drawn for simplicity). In this system, a high power 5-GHz RF signal is applied to DD-MZM. The bandwidth capacity of the system can achieve 2.5-GHz. CS broadcasts the downlink optical signals to each BS at one wavelength, which reduces the number of modulators such as DD-MZM and IM in CS. BS as a transparent interface is only in charge of optical-electronic conversion work. In MT, Data Processing Unit demodulated the 2.5-GHz signal and extracted the data frames sent with its ID number (MAC address).

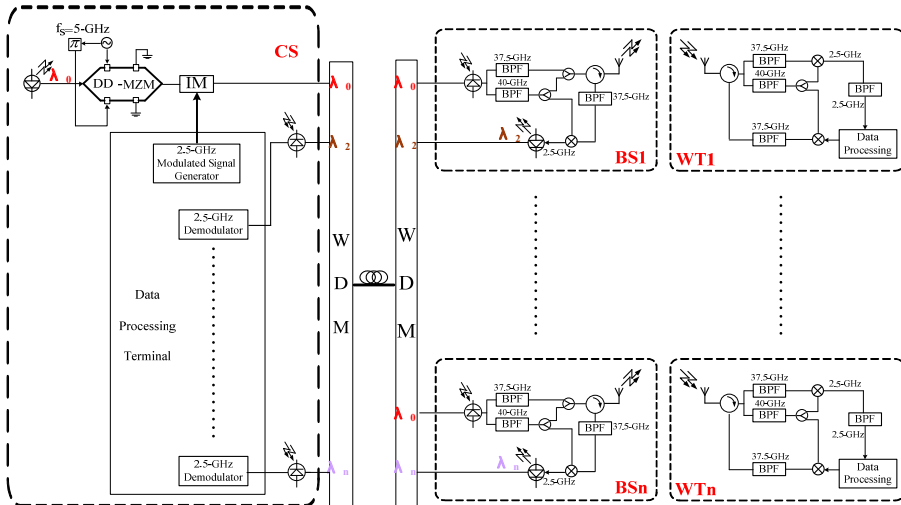


Fig. 22. Architecture of distributed 40-GHz RoF system and the design of MT.

Because the modulation scheme discussed in section 3.2 is adopted, pure 40-GHz reference can be yielded together with the 37.5-GHz modulated signal in BS. Unlike the BS design in section 3.1, both 40-GHz carrier and 37.5-GHz modulated signals are transmitted from BS to MT in this system. Therefore, the 40-GHz carrier can be used as mm-wave reference for both BS and MT. In the uplink, each BS transmits the down-converted 2.5-GHz signal back to CS with a different wavelength.

4. Millimeter-wave fading induced by fiber chromatic dispersion in RoF system

The fiber chromatic dispersion is always one of critical problems in optical communications. Optical components at different frequencies travel through the fiber at different velocities. A pulse of light broadens and becomes distorted after passing through a single-mode fiber (Meslener, 1984). To mm-wave RoF system, the fiber chromatic dispersion causes the remarkable mm-wave fading (Schmuck, 1995).

4.1 Analysis of chromatic dispersion in intensity modulated RoF system

The intensity modulation schemes of yielding mm-wave signal have been introduced in Section 2.1. Those schemes may be sensitive to fiber chromatic dispersion. For example, an external optical modulator (MZM) is used to modulate CW optical signal with a RF signal. The electric field at the output of optical modulator is express as (Schmuck, 1995)

$$E(t) = E_c \cos\left[d \cdot \frac{\pi}{2} + m \cdot \frac{\pi}{2} \cos \omega_m t\right] \cdot \cos \omega_c t \quad (16)$$

where E_c is the amplitude of electric field; ω_c is the central angular frequency of optical source; ω_s is the angular frequency of RF signal; $m = V_m / V_\pi$ is normalized amplitude of the driving RF signal; $d = V_b / V_\pi$ is the normalized bias voltage of the modulator; V_π is the π shift voltage of the modulator.

The electric field for $V_b = V_\pi / 2$, after the transmission over a fiber link can be expressed by Bessel functions

$$E(t) = \frac{E_c}{\sqrt{2}} J_0(\beta) \cos(\omega_c t + \phi_0) - \frac{E_c}{\sqrt{2}} J_1(\beta) \{\cos[(\omega_c - \omega_m)t + \phi_1] + \cos[(\omega_c + \omega_m)t + \phi_2]\} \quad (17)$$

where $\beta = m\pi / 2$; ϕ_0 , ϕ_1 and ϕ_2 represent the different phase delays of the optical components due to the fiber chromatic dispersion.

After photo-detection at the PD, the power of wished mm-wave signal can be approximately expressed as

$$p \propto \cos^2\left[\pi c D \left(\frac{f_m}{f_c}\right)^2 z\right] = \cos^2\left[\frac{\pi D \lambda_c^2 f_m^2 z}{c}\right] \quad (18)$$

where D represents the fiber group velocity dispersion parameter; c is the velocity of light in vacuum; λ_c is wavelength and z is the fiber length. If parameters are chosen as: $c=3 \times 10^8$ -m/s, $D=17$ -ps/(km \times nm), $\lambda_c = 1550$ -nm, $f_m = 40$ -GHz, the relation between the amplitude of mm-wave and the transmission distance in fiber is shown in Figure 16. It shows that the amplitude of mm-wave changes with the transmission distance so fast that this mm-wave generation scheme can not be used in practice.

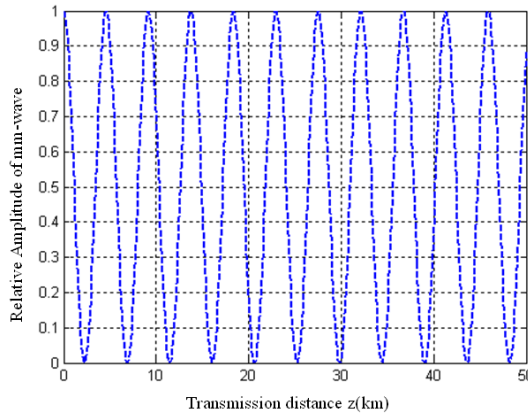


Fig. 16. The relative amplitude of 40-GHz mm-wave varies with the fiber length

Many methods have been proposed to overcome the mm-wave signal fading induced by fiber chromatic dispersion. Smith et al. (1997) proposed a method to generate an optical carrier with single sideband (SSB) modulation by using a DD-MZM, biased at quadrature point, and applied with RF signals, $\pi/2$ out of phase to its two electrodes. The RF power degradation due to fiber dispersion was observed to be only 15-dB when using the technique to send 2 to 20-GHz signals over 79.6-km of fiber. By using an optical filter to depress one sideband. SSB optical modulation is realized and demonstrated by Park et al. (1997). Moreover, stimulated Brillouin scattering (SBS), a nonlinear phenomenon in optical fiber was applied to realize SSB modulation by Yonenaga & Takachio (1993).

4.2 Fiber chromatic dispersion in OFM techniques

In this section, the chromatic dispersion in OFM techniques will be discussed. According to the basic arrangement of optical frequency sweeping technique, shown in Figure 6, the equation (2) can also be expressed as (Walker et al., 1992)

$$E_{in}(t) = f(\omega_s t) \exp(j\omega_c t) = \sum_{n=-\infty}^{+\infty} F_n \exp[j(\omega_c + n\omega_s)t] \quad (19)$$

where the harmonic components F_n is given by:

$$F_n = \frac{1}{2\pi} \int_{-\pi}^{\pi} f(\theta) \exp(-jn\theta) d\theta \quad (20)$$

$$f(\theta) = E_c \exp(j\beta \cos \theta) + E_c \exp[j\beta \cos(\theta - \omega_s \tau) - j\omega_c \tau] \quad (21)$$

The fiber transfer characteristic can be written in the form

$$H(\omega) = \exp[-j(k_0 + k_1(\omega - \omega_c) + \frac{k_2}{2}(\omega - \omega_c)^2 + \dots)z] \quad (22)$$

where the first term is a constant phase shift, the second term is constant propagation delay and the third term is the first order dispersion of optical fiber. At the angular frequencies of side modes in the light-wave, $H(\omega)$ has the values:

$$H_n = H(\omega_c + n\omega_s) = \exp[-j(k_0 + k_1n\omega_s + \frac{k_2}{2}n^2\omega_s^2)z] = \exp[-j(k_0z + k_1n\omega_s z + n^2\varphi)] \quad (23)$$

where $\varphi = k_2\omega_s^2 z/2$ represents the fiber dispersion at the angular frequency of the first side-mode.

The first order dispersion constant D of fiber is related to k_2 by the expression $D = -2\pi ck_2 / \lambda_c^2$, therefore φ is related to D by

$$\varphi = -\frac{\omega_s^2 D \lambda_c^2}{4\pi c} z \quad (24)$$

where c is the light velocity in vacuum, z is the transmission distance in fiber and λ_c is the working wavelength.

The electric field of light-wave at output of the fiber is

$$E_{out}(t) = \sum_{n=-\infty}^{\infty} F_n H_n \exp[j(\omega_c + n\omega_s)t] \quad (25)$$

The photo-current produced in PD is

$$i_d(t) \propto E_{out}(t)E_{out}^*(t) = \sum_{n=-\infty}^{\infty} \sum_{m=-\infty}^{\infty} F_n F_m^* H_n H_m^* \exp[j(n-m)\omega_s t] \quad (26)$$

Setting $p = n - m$ and substituting (20) and (23) for F_n and H_n in (26) gives

$$\begin{aligned} i_d(t) &\propto \sum_{p=-\infty}^{\infty} \frac{1}{2\pi} \int_{-\pi}^{\pi} f(\theta - p\varphi) f(\theta + p\varphi)^* \exp(-jp\theta) d\theta \exp(jp\omega_s(t - k_1 z)) \\ &= \sum_{p=-\infty}^{\infty} I_p \exp(jp\omega_s(t - k_1 z)) \end{aligned} \quad (27)$$

Hence the amplitude of p -th harmonic in photo-current after transmission over the fiber becomes

$$I_p = \frac{1}{2\pi} \int_{-\pi}^{\pi} f(\theta - p\varphi) f(\theta + p\varphi)^* \exp(-jp\theta) d\theta \quad (28)$$

Substituting (21) for $f(\theta)$ in (28) and performing the integration give

$$\begin{aligned}
 I_p = E_c^2 \{ & J_p(2\beta \sin p\varphi) + \exp(-jp\omega_s\tau)J_p(2\beta \sin p\varphi) \\
 & + \exp(j\omega_c\tau - jp\frac{\omega_s\tau}{2})J_p(2\beta \sin(p\varphi - \frac{\omega_s\tau}{2})) \\
 & + \exp(-j\omega_c\tau - jp\frac{\omega_s\tau}{2})J_p(2\beta \sin(p\varphi + \frac{\omega_s\tau}{2})) \}
 \end{aligned} \quad (29)$$

So the p th harmonic can be approximately expressed by

$$F_p = I_p \exp(jp\omega_s t) + I_{-p} \exp(-jp\omega_s t) \quad (30)$$

Applying the parity of Bessel function to equation (38), F_n can be written as

$$\begin{aligned}
 F_p = 2E_c^2 \{ & J_p(2\beta \sin p\varphi) [\cos p\omega_s t + \cos(p\omega_s t - p\omega_s\tau)] \\
 & + J_p(2\beta \sin(p\varphi + \frac{\omega_s\tau}{2})) \cos(p\omega_s t - p\frac{\omega_s\tau}{2} - \omega_c\tau) \\
 & + J_p(2\beta \sin(p\varphi - \frac{\omega_s\tau}{2})) \cos(p\omega_s t - p\frac{\omega_s\tau}{2} + \omega_c\tau) \}
 \end{aligned} \quad (31)$$

The intensity modulation depth M_p is defined as $M_p = |F_p / F_0|$. In the condition that the optimized condition ($\omega_c\tau = k\pi, \omega_s\tau = \pi$) for optical frequency sweeping technique is satisfied, the intensity

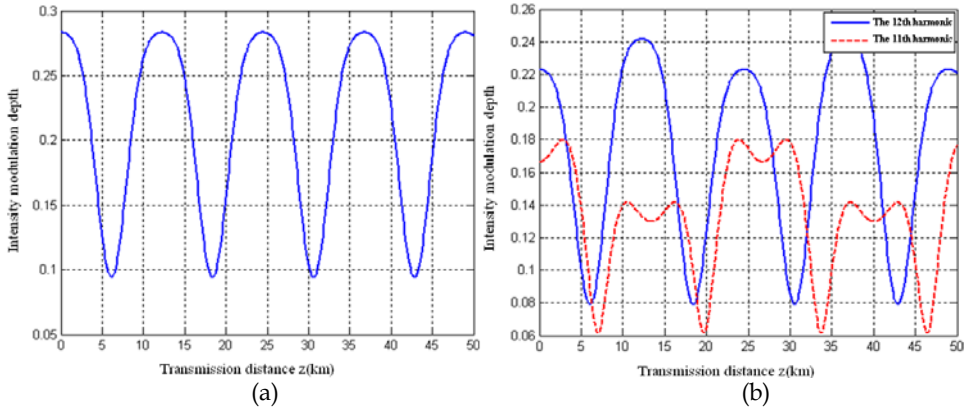


Fig. 17. The intensity modulation depth of 12th harmonic in the (a) satisfied condition, (b) unsatisfied condition.

modulation depth of 12th harmonic with transmission distance is shown in Figure 17 (a). Figure (b) shows the intensity modulation depth in the unsatisfied condition and the odd harmonics appear.

Lin et al. (2008) analyzed the mm-wave fading caused by fiber chromatic dispersion in the OFM scheme using nonlinear modulation of DD-MZM. The result is drawn in Figure 18,

together with the result of double side-modes IM (without carrier depression) for comparison. It can be seen in Figure 18 that in the double side-modes IM scheme the amplitude of generated 40-GHz mm-wave behaves 100% fading with periodic zeros at different fiber lengths. In contrast, in OFM scheme using DD-MZM, the amplitude fading of generated 40-GHz mm-wave is much weaker, only 30% and without zeros. Furthermore, the minimum amplitude happens in much longer period. This means that OFM by using DD-MZM is a good mm-wave generation method with tolerability to fiber chromatic dispersion. Conceptually, OFM by using DD-MZM is such a system that generation of mm-wave is the superposition of several mm-waves generated by self-heterodyne of several pairs of optical side-modes. So the interference of several mm-waves at the same frequency results in only a little amplitude fading.

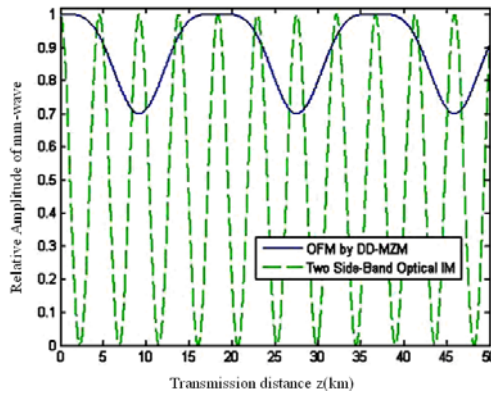


Fig. 18. Amplitude of 40GHz mm-wave varies with fiber length in double side-modes IM scheme and DD-MZM OFM scheme.

5. Fast handover in mm-wave RoF system

There is much more free space loss at mm-wave band than that at 2.4-GHz or 5-GHz, since free space loss increases drastically with frequency. In principle this higher free space loss can be compensated for by the use of antennas with stronger pattern directivity while maintaining small antenna dimensions. When such antennas are used, however, antenna obstruction (e.g., by a human body) and mispointing may easily cause a substantial drop of received power, which may nullify the gain provided by the antennas. This effect is typical for mm-wave signals because the diffraction of mm-wave signals (i.e., the ability to bend around edges of obstacles) is weak (Smulders, 2002), so a mm-wave communication network has many characteristics quite different from conventional wireless LANs (WLANs) operating in 2.4 or 5-GHz bands.

Due to the free space loss of mm-wave signal, the coverage of BS, as pico-cell has been smaller than that of Access Point (AP) in current WLAN. The small size of pico-cell induces the large number of BSs and frequent handovers of MT from one pico-cell to another. As a result, the key point in designing the Medium Access Control (MAC) protocol for mm-wave RoF system is to provide efficient and fast handover support. A MAC protocol based on Frequency Switching (FS) codes can realize fast handover and adjacent pico-cells employ

orthogonal FS codes to avoid possible co-channel interference (Kim & Wolisz, 2003). A moveable cells scheme based on optical switching architecture can realize the handover in the order of ns or μ s (Lannoo et al., 2004), which is suitable to all MTs moving at the same speed, for example in a train scenario. In this way, MT can operate on the same frequency during the whole connection and avoid the fast handovers. Based on moveable cells scheme, Yang & Liu (2008) proposed a further scheme, in which the adjacent pico-cells are grouped as a larger cell, and along the railway all the BS in this larger cell use the same frequency channel. When n adjacent pico-cells are grouped, times of handover can be decreased n -fold.

6. Conclusion

In this chapter, many technical issues about the mm-wave RoF systems are presented. Firstly, three kinds of mm-wave generation techniques are introduced. In those techniques, OFM techniques realized by optical frequency sweeping and nonlinear modulation of DD-MZM are mainly discussed and the latter is proved to be a more stable and cost-efficient way to yield signal at the mm-wave band. Unlike most research works by now only concentrating on the downlink of RoF system, the design of several bidirectional mm-wave RoF systems is described which deals with the uplink as optical transport of IF signal, generated by down-conversion of mm-wave signal. The information-bearing mm-wave for radiation and the reference mm-wave for down-conversion are all generated in BS by OFM. Then, two multiplexing techniques, WDM and SCM are introduced to mm-wave RoF systems. Star-tree and ring architectures are adopted in mm-wave RoF systems to realize the distributed BSs. After showing the large bandwidth capacity at mm-wave band provided by OFM techniques, incorporating SCM to RoF system is demonstrated to improve the utilization ratio of large bandwidth. Considering the influence of chromatic dispersion in fiber on mm-wave fading, a common analysis on the effect of fiber chromatic dispersion to mm-wave generation techniques (i.e., intensity modulation and OFM) are given and OFM by using DD-MZM is proved to be tolerable to fiber chromatic dispersion. Due to the great free space loss of signal at mm-wave band, the coverage of each BS is very small and the handover of MT becomes a problem. To meet the real-time communication requirements for mm-wave systems, several MAC protocols suitable either to efficient and fast handover or to moveable cells schemes, which make the MT avoid the fast handover problem, are introduced.

7. Acknowledgements

This work was supported by the National Natural Science Foundation of China (60377024 and 60877053), and Shanghai Leading Academic Discipline Project (08DZ1500115).

8. References

Braun, R.-P.; Grosskopf, G.; Heidrich, H.; von Helmlolt, C.; Kaiser, R.; Kruger, K.; Kruger, U.; Rohde, D.; Schmidt, F.; Stenzel, R. & Trommer, D. (1998). Optical microwave generation and transmission experiments in the 12- and 60-GHz region for wireless communications, *Microwave Theory and Techniques, IEEE Transactions on*, Vol. 46, No. 4, pp. 320-330.

- Doi, M.; Hashimoto, N. ; Hasegawa, T. ; Tanaka, T. & Tanaka, K (2007). 40 Gb/s low-drive-voltage LiNbO₃ optical modulator for DQPSK modulation format. in *Optical Fiber Communication Conference and Exposition and The National Fiber Optic Engineers Conference*, OSA Technical Digest Series (CD), paper OWH4.
- Elrefaie, A.F.; Wagner, R.E.; Atlas, D.A. & Daut, D.G. (1988). Chromatic dispersion limitations in coherent lightwave transmission systems, *Lightwave Technology, Journal of*, Vol. 6, No. 5, pp. 704-709, 1988.
- Fuster, J.M.; Marti, J.; Candelas, P.; Martinez, F.J. & Sempere, L. (2001). Optical generation of electrical modulation formats, *27th European Conference on Optical Communication (ECOC 2001)*, pp. 536-537, 2001.
- Garcia Larrode, M.; Koonen, A.M.J.; Vegas Olmos, J.J.; Tafur Monroy, I. & Schenk, T.C.W. (2005). RF bandwidth capacity and SCM in a radio-over-fibre link employing optical frequency multiplication, *Conference on Optical Communication, 2005 (ECOC 2005)*, Vol. 3, pp. 681-682, Sep. 25-29, 2005.
- Gliese, U.; Nielsen, T. N.; Bruun, M.; Lintz Christensen, E.; Stubkjaer, K. E.; Lindgren, S. & Broberg, B. (1992). A wideband heterodyne optical phase-locked loop for generation of 3-18 GHz microwave carriers, *IEEE Photonics Technology Letters*, Vol. 4, No. 8, pp. 936-938.
- Gliese, U.; Norskov, S. & Nielsen, T.N. (1996). Chromatic dispersion in fiber-optic microwave and millimeter-wave links, *Microwave Theory and Techniques, IEEE Transactions on*, Vol. 44, No. 10, pp. 1716-1724.
- Griffin, R.A.; Lane, P.M. & O'Reilly, J.J. (1999). Radio-over-fiber distribution using an optical millimeterwave/DWDM overlay, *OFC 1999*, Paper WD6-1, 1999.
- Hartmannor, P. ; Webster, M. ; Wonfor, A. ; Ingham, J.D. ; Penty, R.V. ; White, I.H. ; Wake, D. & Seeds, A.J. (2003). Low cost multimode fibre based wireless LAN distribution system using uncooled, directly modulated DFB laser diodes, *2003 European Conference on Optical Communication (ECOC 2003)*, Sep. 21-25, 2003.
- Juha Rapeli (2001). Future directions for mobile communications business, technology and research, *Wireless Personal Communications*, Vol. 17, No. 2-3, pp.155-173.
- Kim, H.B. & Wolisz, A., Performance evaluation of a MAC protocol for radio over fiber wireless LAN operating in the 60-GHz band, *Global Telecommunications Conference, 2003 (GLOBECOM '03)*, Vol. 5, pp. 2659-2663, Dec. 1-5, 2003.
- Kitayama, K. (1998). Architectural considerations of radio-on-fiber millimeter-wave wireless access systems, *International Symposium on Signals, Systems, and Electronics, 1998 (ISSSE 98)*, pp.
- Kramer, G. (2006). What is next for Ethernet PON?, *The Joint Intenational Conference on Optical Internet and Next Generation Network, 2006 (COIN-NGNCON 2006)*, pp. 49-54, Jul. 9-13, 2006.
- Kuri, T.; Kitayama, K.; Stohr, A. & Ogawa, Y. (1999). Fiber-optic millimeter-wave downlink system using 60 GHz-band external modulation, *Lightwave Technology, Journal of*, Vol. 17, No. 5, pp. 799-806.
- Lannoo, B.; Colle, D.; Pickavet, M. & Demeester, P. (2004). Optical switching architecture to realize "moveable cells" in a radio-over-fiber network, *6th International Conference on Transparent Optical Networks, 2004*, Vol. 2, pp. 2-7, Jul. 4-8, 2004.

- Larrode, M.G.; Koonen, A.M.J.; Olmos, J.J.V.; Verdurmen, E.J.M. & Turkiewicz, J.P. (2006). Dispersion tolerant radio-over-fibre transmission of 16 and 64 QAM radio signals at 40 GHz, *Electronics Letters*, Vol. 42, No. 15, pp. 872-874.
- Lin, Ru-jian; Zhu, Mei-wei; Zhou, Zhe-yun & Ye, Jia-jun (2008). Theoretic and experimental study on mm-wave radio over fiber system based on OFM, *Proc. SPIE*, Vol. 7137, 71371M (2008), DOI:10.1117/12.807835.
- Meslener, G. (1984). Chromatic dispersion induced distortion of modulated monochromatic light employing direct detection, *Quantum Electronics, Journal of*, Vol. 20, No. 10, pp. 1208-1216, 1984.
- Nirmalathas, A.; Lim, C.; Novak, D.; Castleford, D.; Waterhouse, R. & Smith, G. (2000). Millimeter-wave fiber-wireless access systems incorporating wavelength division multiplexing, *Microwave Conference, 2000 Asia-Pacific*, pp. 625-629, 2000.
- Ogusu, M.; Inagaki, K.; Mizuguchi, Y. & Ohira, T. (2003). Carrier generation and data transmission on millimeter-wave bands using two-mode locked Fabry-Perot slave lasers, *IEEE transactions on microwave theory and techniques*, Vol. 51 (1), No. 2, pp. 382-391.
- Olshansky, R.; Lanzisera, V.A. & Hill, P.M. (1989). Subcarrier multiplexed lightwave systems for broad-band distribution, *Lightwave Technology, Journal of*, Vol. 7, No. 9, pp. 1329-1342, 1989.
- O'Rcilly, J.J.; Lane, P.M.; Heidemann, R. & Hofstetter, R. (1992). Optical generation of very narrow linewidth millimetre wave signals, *Electronics Letters*, Vol. 28, No. 25, pp. 2309-2311.
- Park, J.; Sorin, W.V. & Lau, K.Y. (1997). Elimination of the fiber chromatic dispersion penalty on 1550nm millimeter-wave optical transmission, *Electronics Letters*, Vol. 33, No. 6, pp. 512-513, 1997.
- Schmuck, H. (1995). Comparison of optical millimeter-wave system concepts with regard to chromatic dispersion, *Electronics Letters*, Vol. 31, No. 21, pp.1848-1849, 1995.
- Smith, G.H.; Novak, D. & Ahmed, Z. (1997). Techniques for optical SSB generation to overcome dispersion penalties in fibre-radio systems, *Electronics Letters*, Vol. 33, No. 1, pp. 74-75, 1997.
- Smith, G.H.; Novak, D. & Lim, C., A (1998). Millimeter-wave full-duplex fiber-radio star-tree architecture incorporating WDM and SCM, *Photonics Technology Letters, IEEE*, Vol. 10, No. 11, pp. 1650-1652, 1998.
- Smulders, P. (2002). Exploiting the 60 GHz band for local wireless multimedia access: prospects and future directions, *Communications Magazine, IEEE*, Vol. 40, No. 1, pp.140-147.
- Sun, C.K.; Orazi, R.J. & Pappert, S.A. (1996). Efficient microwave frequency conversion using photonic link signal mixing, *IEEE Photonics Technology Letters*, Vol. 8, No. 1, pp. 154-156.
- Stöhr, A.; Kitayama, K. & Jäger, D. (1998). Error-free full-duplex optical WDM-FDM transmission using an EA-transceiver, *International Topical Meeting on Microwave Photonics, 1998 (MWP 98)*, pp. 37-40, Oct. 12-14, 1998.
- Ton Koonen; Anthony Ng'oma; Peter Smulders; Henrie van den Boom; Idelfonso Tafur Monroy & Giok-Djan Khoe (2003). In-house networks using multimode Polymer Optical Fibre for broadband wireless services, *Photonic Network Communications*, Vol. 5, No. 2, pp. 177-187.

- Tsuzuki, K. ; Sano, K. ; Kikuchi, N.; Kashio, N.; Yamada, E.; Shibata, Y.; Ishibashi, T.; Tokumitsu, M. & Yasaka, H. (2006). 0.3 Vpp single-drive push-pull InP Mach-Zehnder modulator module for 43-Gbit/s systems, *Optical Fiber Communication Conference and Exposition and The National Fiber Optic Engineers Conference, Technical Digest (CD) (Optical Society of America, 2006)*, paper OWC2.
- Walker, N.G.; Wake, D. & Smith, I. C. (1992). Efficient millimeter-wave signal generation through FM-IM conversion in dispersive optical fiber links, *Electronics Letters*, Vol. 28, No. 21, pp. 2027-2028, 1992.
- Williams, K.J.; Goldberg, L.; Esman, R.D.; Dagenais, M. & Weller, J.F. (1989). 6-34 GHz offset phase-locking of Nd:YAG 1319 nm nonplanar ring lasers, *Electronics Letters*, Vol. 25, No. 18, pp. 1242-1243.
- Xiu, Ming-lei & Lin, Ru-jian (2007). Report on 40GHz-RoF bidirectional transmission experiment system with pilot tone, *Conference on Lasers and Electro-Optics - Pacific Rim, 2007. CLEO/Pacific Rim 2007*, pp.1-2, Aug. 26-31, 2007.
- Yang, Chunyong & Liu, Deming (2008). Cell extension for fast moving users in a RoF network, *Proc. SPIE 7278, 72781E (2008)*, DOI:10.1117/12.823294.
- Yonenaga, K. & Takachio, N. (1993). A fiber chromatic dispersion compensation technique with an optical SSB transmission in optical homodyne detection systems, *Photonics Technology Letters*, Vol. 5, No. 8, pp. 949-951, 1993.
- Yungsoo Kim; Byung Jang Jeong; Jaehak Chung; Chan-Soo Hwang; Ryu, J.S.; Ki-Ho Kim; Young Kyun Kim (2003). Beyond 3G: vision, requirements, and enabling technologies, *Communications Magazine, IEEE*, Vol. 41, No. 3, pp. 120-124.
- Zhou, Zheyun ; Lin, Rujian & Ye Jiajun (2008). A novel optical QPSK modulation scheme for millimeter-wave Radio-Over-Fiber system, *2008 Asia Optical Fiber Communication and Optoelectronic Exposition and Conference, OSA Technical Digest (CD)*, paper SaK12.
- Zhu, Mei-wei; Lin, Ru-jian; Ye, Jia-jun & Xiu, Minglei (2008). Novel millimeter-wave radio-over-fiber system using dual-electrode Mach-Zehnder modulator for millimeter-wave generation. *Opto-Electronic Engineering*, Vol. 35, No. 4, pp. 126-130.

Measurement and modeling of rain intensity and attenuation for the design and evaluation of microwave and millimeter-wave communication systems

Gamantyo Hendrantoro
Institut Teknologi Sepuluh Nopember
Indonesia

Akira Matsushima
Kumamoto University
Japan

1. Introduction

Rain-induced attenuation creates one of the most damaging effects of the atmosphere on the quality of radio communication systems, especially those operating above 10 GHz. Accordingly, methods have been devised to overcome this destructive impact. Adaptive fade mitigation schemes have been proposed to mitigate the rain fade impact in terrestrial communications above 10 GHz (e.g., Sweeney & Bostian, 1999). These schemes mainly deal with the temporal variation of rain attenuation. When such methods as site diversity and multi-hop relaying are to be used, or when the impact of adjacent interfering links is concerned, the spatial variation of rain must also be considered (Hendrantoro et al, 2002; Maruyama et al, 2008; Sakarellos et al, 2009; Panagopoulos et al, 2006). There is also a possibility of employing a joint space-time mitigation technique (Hendrantoro & Indrabayu, 2005). In designing a fade mitigation scheme that is expected to work well within a specified set of criteria, an evaluation technique must be available that is appropriate to test the system performance against rainy channels. Consequently, a model that can emulate the behavior of rain in space and time is desired.

This chapter presents results that have thus far been acquired from an integrated research campaign jointly carried out by researchers at Institut Teknologi Sepuluh Nopember, Indonesia and Kumamoto University, Japan. The research is aimed at devising transmission strategies suitable for broadband wireless access in microwave and millimeter-wave bands, especially in tropical regions. With regards to modeling rain rate and attenuation, the project has gone through several phases, which include endeavors to measure the space-time variations of rain intensity and attenuation (Hendrantoro et al, 2006; Mauludiyanto et al, 2007; Hendrantoro et al, 2007b), to appropriately model them (e.g., Yadnya et al, 2008a;

Yadnya et al, 2008b), and finally to apply the resulting model in evaluation of transmission system designs (e.g., Kuswidiastuti et al, 2008). Tropical characteristics of the measured rain events in Indonesia have been the focus of this project, primarily due to the difficulty in implementing rain-resistant systems in microwave and millimeter-wave bands in tropical regions (Salehudin et al, 1999) and secondarily because of the lack of rain attenuation data and models for these regions. The design of millimeter-wave broadband wireless access with short links, as typified by LMDS (local multipoint distribution services), is also a central point in this project, which later governs the choice of space-time measurement method. As such, endeavors reported in this chapter offer multiple contributions:

- a. Measurements and analyses of raindrop size distribution, raindrop fall velocity distribution, rain rate and attenuation in maritime tropical regions represented by the areas of Surabaya.
- b. Method to estimate specific attenuation of rain from raindrop size distribution models.
- c. Stochastic model of rain attenuation that can be adopted to generate rain attenuation samples for use in evaluation of fade mitigation techniques.

We start in the next section with the measurement system, raindrop size distribution modeling, estimation of specific attenuation, and the synthetic storm technique. Afterward, we discuss modeling of rain intensity and attenuation, touching upon space-time distribution and the time series models. Finally, examples of evaluation of communication systems are given, followed by some concluding remarks.

2. Measurement of rain intensity and attenuation

2.1 Spatio-temporal measurement of rain intensity

The design of our space-time rain field measurement system is based on several criteria. Firstly, the spatial and temporal scope and resolution of the rain field variation must be taken into account. Another constraint is the available budget and technology. When budget is not a concern, space-time measurement using rain radar can be done, as exemplified by Tan and Goddard (1998) and Hendrantoro and Zawadzki (2003). Radar has its strength in large observation area and feasibility of simulating radio links on radar image. However, due to its weaknesses that include high cost and low time resolution, and due to the relatively small measurement area desired to emulate an LMDS cell, it is decided to employ a network of synchronized rain gauges operated within the campus area of Institut Teknologi Sepuluh Nopember (ITS) in Surabaya, as shown in Fig. 1. The longest distance between rain gauges is about 1.55 km, from site A at the Polytechnic building to site D at the Medical Center. The shortest, about 400 m, is between site B at the Department of Electrical Engineering building and site C at the Library building. The rain gauges, each of tipping-bucket type, are synchronized manually. At site B, an optical-type Parsivel disdrometer is also operated to record the drop size distribution (DSD), as well as a 54-meter radio link at 28 GHz adopted to measure directly rain attenuation.

2.2 Raindrop size distribution measurement and modelling

DSD (raindrop size distribution) is a fundamental parameter that directly affects rainfall rate and rain-induced attenuation. The widely used negative exponential model of DSD

proposed by Marshall and Palmer (1948) derived from measurement in North America might yield inaccurate statistical estimates of rain rate and attenuation when adopted for tropical regions (Yeo et al, 1993). A number of tropical DSD measurements have since been reported and models proposed accordingly. Nevertheless, considering the variety of geographical situations of regions within the tropical belt, each with its own regional sub-climate, more elaborate studies on tropical DSD are deemed urgent.

In this study, we use Parsivel, an optical-type disdrometer that works on a principle of detecting drops falling through the horizontal area of a laser beam. As a result, the instrument is capable of measuring not only the diameter of each falling drop but also its fall velocity. The system consists of the optical detector connected to a computer that records the raw data. Each record comprises the number of detected drops within a certain diameter interval and fall velocity interval. The average DSD ($m^{-3}mm^{-1}$) can be obtained as:

$$\bar{N}(D) = \frac{C(D)}{AT\Delta D} \left(\frac{1}{C(D)} \sum_{k=1}^{C(D)} \frac{1}{v_k(D)} \right) \quad (1)$$

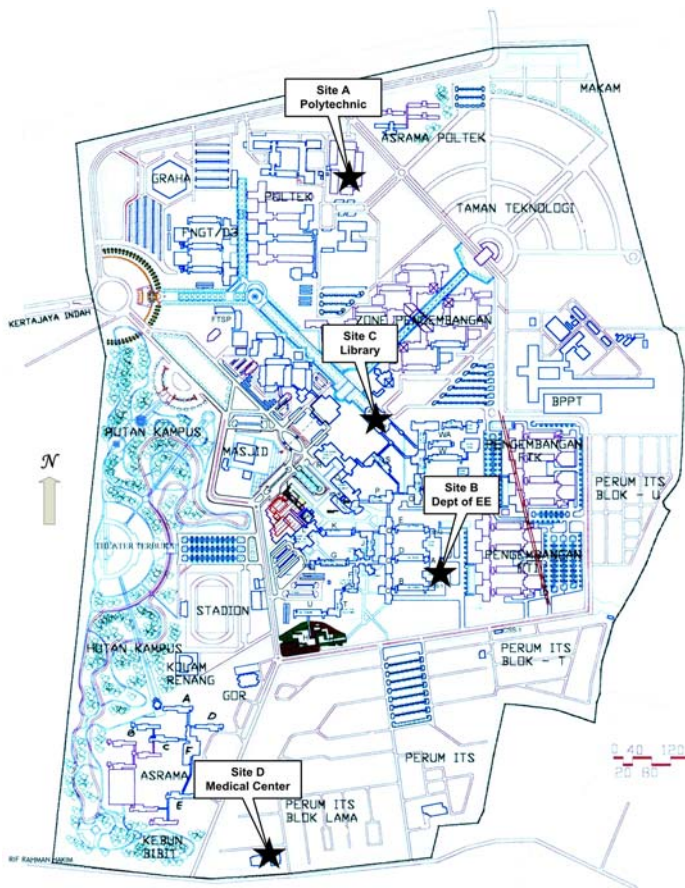


Fig. 1. Map of the measurement area in the campus of ITS in Surabaya.

where $C(D)$ denotes the number of drops detected in the diameter interval $[D-\Delta D/2, D+\Delta D/2]$ given in millimeters, A (m^2) the area of the laser beam, T (seconds) the integration time, $v_k(D)$ the measured velocity in m/s of the k^{th} drop in the diameter interval $[D-\Delta D/2, D+\Delta D/2]$, as opposed to a deterministic diameter-dependent velocity model such as the Gunn-Kinzer (Brussaard & Watson, 1995). From (1) it is apparent that the average DSD is a linear function of the average of the inverse of drop fall velocity, rather than the average velocity itself. This can cause discrepancy of attenuation or radar reflectivity estimates from their actual values. In fact, measurements made using a similar instrument in the US reveal discrepancy of the average fall velocity from the theoretical deterministic value (Tokay et al, 2003). The variations of raindrop fall velocity will be discussed later in this section. In our study, DSD measurements are categorized into bins representing disjoint intervals of rainfall rate, 0-0.5, 0.5-1, 1-2, ..., 256-512 mm/h . An average DSD and an average rain rate are subsequently computed for each bin. Table 1 summarizes the parameter values for each interval. Although the Parsivel is able to detect objects of larger diameters, only those within the diameter range up to 6 mm, relevant to the maximum diameter of stable raindrops (Brussaard & Watson, 1995), are considered. The sampling volume in the table is calculated by assuming the Gunn-Kinzer fall velocity and using the fact that the laser beam area is $3 \text{ cm} \times 18 \text{ cm}$. Table 2 recapitulates the DSD measurements made in Surabaya for the various bins of rain rate. Fig. 2 presents the average DSD curves for all rain rate bins.

Singapore and Surabaya are located in the same region of Southeast Asia and share the same tropical maritime climate. Three models fitted to Singapore DSD reported in the literature are used in this study, two of which are lognormal and gamma fitted to measurements made by Ong et al using a Joss-Waldvogel disdrometer (Timothy et al, 2002). The other is a negative exponential model obtained using the indirect method in which the DSD shape is assumed a priori and it is only the shape parameters that are estimated by fitting the DSD model to measurements of rainfall rate and attenuation (Yeo et al, 1993, Li et al, 1994). The Marshall-Palmer model is also included in the comparison. The DSD evaluation is made for three different values of average rain rate, 11.068, 44.15, and 174 mm/h , representing low, medium, and high intensity, respectively.

As shown in Fig. 3 in general the Surabaya curve stays constantly below the Marshall-Palmer. Comparison with the Singapore models show that, except for the gamma model, the higher the rain rate, the larger the difference between the Singapore models and the Surabaya results, with the Surabaya DSD falling below the Singapore results for almost all drop diameters. For lower rain rates, the difference is not large and Surabaya DSD shows larger concentration of drops with larger diameters yet fewer smaller drops. A previous study in North America reported by Hendratoro and Zawadzki (2003) has found that contribution to attenuation at 30 GHz is dominated by drops of diameters in the 1-3 mm range. This observation suggests that for the same rain rate the induced attenuation at 30 GHz in Surabaya might be lower on average than that in Singapore. It should be stressed herein that all of these disagreements in the detailed shapes of Surabaya DSD from that of either Singapore or Marshall-Palmer might originate from differences in various aspects of the measurement, such as the local climate, the measuring instrument, the number of samples, and the year of measurement. A more in-depth study is required to identify the real causes of the disagreements.

Central Diameter (D , mm)	Interval Width (ΔD , mm)	Sampling Volume (m^3)	
		T = 10 s	T = 60 s
0.062	0.125	0.0058	0.0349
0.187	0.125	0.0357	0.2143
0.312	0.125	0.0661	0.3966
0.437	0.125	0.0965	0.5788
0.562	0.125	0.1252	0.7510
0.687	0.125	0.1522	0.9130
0.812	0.125	0.1792	1.0750
0.937	0.125	0.2062	1.2370
1.062	0.125	0.2292	1.3753
1.187	0.125	0.2477	1.4862
1.375	0.250	0.2742	1.6450
1.625	0.250	0.3068	1.8410
1.875	0.250	0.3366	2.0198
2.125	0.250	0.3636	2.1814
2.375	0.250	0.3876	2.3258
2.750	0.500	0.4183	2.5101
3.250	0.500	0.4493	2.6956
3.750	0.500	0.4641	2.7845
4.250	0.500	0.4641	2.7845
4.750	0.500	0.4641	2.7845
5.500	1.000	0.4641	2.7845

Table 1. Interval Parameter Values of the Optical Disdrometer.

Rain rate interval (mm/hr)	Center value (mm/hr)	Average value (mm/hr)	Number of samples
0 - 0.5	0.25	0.1162	7116
0.5 - 1	0.75	0.7089	1168
1 - 2	1.5	1.447	829
2 - 4	3	2.799	957
4 - 8	6	5.640	892
8 - 16	12	11.06	420
16 - 32	24	22.12	471
32 - 64	48	44.15	382
64 - 128	96	90.19	212
128 - 256	192	174.9	169
256 - 512	384	257.2	80

Table 2. Number of Measured Samples in Each Rain Rate Bin.

For model fitting purpose, the average DSD curves for the lowest two intervals of rain rate are excluded due to irregularities in their shapes that hinder achievement of a good fit to each of the adopted models. This treatment does not bear any significant implication to the

design of millimeter-wave communications since rain events of high intensity are of higher importance. The DSD measurements are fitted to a number of theoretical models, namely, the negative exponential, Weibull, and gamma. Among the three, gamma fits worst, and therefore is not discussed further herein. On the other hand, Weibull slightly outdoes the negative exponential and yields the following equation:

$$N(D) = 281.629 \frac{\eta}{\sigma} \left(\frac{D}{\sigma} \right)^{\eta-1} \exp \left[- \left(\frac{D}{\sigma} \right)^\eta \right] \quad (2)$$

with $\eta = 1.212 R^{0.056}$ and $\sigma = 0.728 R^{0.177}$. Whereas the negative exponential fit gives:

$$N(D) = 1054 \exp(-2.415 R^{-0.14} D) \quad (3)$$

where $N(D)$ is the DSD given in $\text{m}^{-3}\text{mm}^{-1}$ with the drop diameter D expressed in mm and rain rate R in mm/hr.

An examination is also made on the variation of raindrop fall velocity. The Gunn-Kinzer velocity model commonly adopted in the computation of specific attenuation from DSD was obtained from an experiment in an ideal environment. It is therefore of interest to see the actual variation of rainfall velocity and its impact on the rain attenuation induced. Fig. 4 (a) depicts the average fall velocity as detected by the disdrometer for each diameter range compared with that of Gunn-Kinzer. There can be observed a discrepancy for large drops from the Gunn-Kinzer estimate. The probability density function of fall velocity for diameter range of central value 6.5 mm, shown in Fig. 4 (b), indicates as if a large number of drops fall with near-zero velocity. To a lesser extent the same trend can also be observed for other diameter ranges. A correction attempt is made accordingly by omitting drops with velocities that are considered too low for their size. This is done to velocity ranges $v(D) \leq 4$ m/s for $4.25 \text{ mm} \leq D \leq 6.5 \text{ mm}$, $v(D) \leq 2$ m/s for $3.25 \text{ mm} \leq D \leq 3.75 \text{ mm}$, and $v(D) \leq 1$ m/s for $1.062 \text{ mm} \leq D \leq 2.75 \text{ mm}$, and is referred to as correction #1. A second attempt (correction #2) is made by linearizing the density function for velocity ranges stated above starting from zero at zero velocity. Despite the discrepancy of the velocity measurement from that of the Gunn-Kinzer and various corrections thereof (Fig. 4 (c)), it is found that the resulting discrepancy in specific attenuation from that obtained using the Gunn-Kinzer velocity is not significant, as given in Table 3. It is therefore considered safe to use Gunn-Kinzer velocity in subsequent analysis of rain attenuation.

Y_h	Average error magnitude (dB/km)
Measurement	0.0725
Correction #1	0.0250
Correction #2	0.0210

Table 3. Average error magnitude of attenuation for horizontally-polarized waves (Y_h).

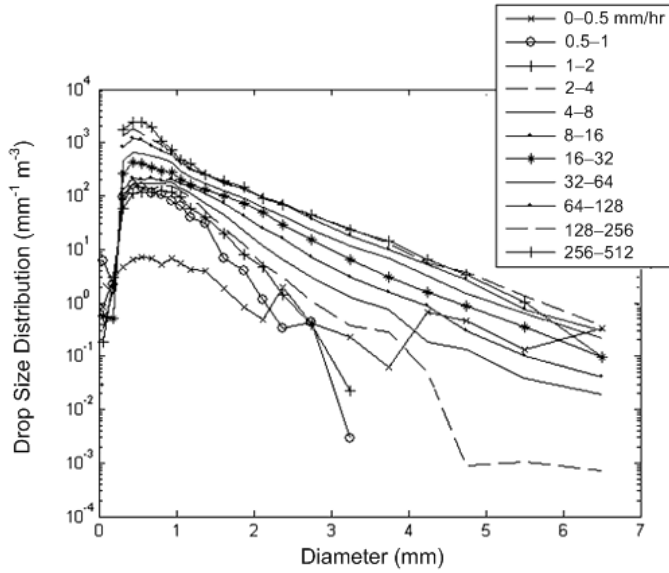


Fig. 2. Curves of average DSD for different intervals of rain rate obtained from measurements made in Surabaya.

2.3 Rain intensity-to-specific attenuation conversion

a. Formulation as scattering problem

Although realistic raindrops are modelled as a deformed body of revolution (Pruppacher et al., 1971), we limit the analysis here to the most fundamental spherical shape. Nevertheless, the final conversion formula is still valid once we could obtain the modal coefficients of far scattered field emerged from arbitrarily shaped body.

As shown in Fig. 5, a set of dielectric spheres having a common relative permittivity ϵ_r is arbitrarily distributed in the air. The number of spheres is Q , and each has an arbitrary radius a_q ($q = 1, 2, \dots, Q$). A position vector is given by $\mathbf{r} = \hat{x}x + \hat{y}y + \hat{z}z = r(\hat{x} \sin \theta \cos \phi + \hat{y} \sin \theta \sin \phi + \hat{z} \cos \theta)$, where \hat{x} , \hat{y} , and \hat{z} are the unit vectors concerning respective coordinate variables. The center of p -th sphere 0_p is denoted by $\mathbf{r} = \mathbf{r}_{p0} = \hat{x}x_{p0} + \hat{y}y_{p0} + \hat{z}z_{p0}$. A position is often measured in terms of the local spherical coordinate system (r_p, θ_p, ϕ_p) with its center located at 0_p as

$$\mathbf{r}_p = \mathbf{r} - \mathbf{r}_{p0} = r_p(\hat{x} \sin \theta_p \cos \phi_p + \hat{y} \sin \theta_p \sin \phi_p + \hat{z} \cos \theta_p) \tag{4}$$

Let us decompose the total electromagnetic fields as

$$(\mathbf{E}, \mathbf{H}) = \begin{cases} \left(\mathbf{E}^i, \mathbf{H}^i \right) + \sum_{q=1}^Q \left(\mathbf{E}^{s(q)}, \mathbf{H}^{s(q)} \right) & \text{(in the air)} \\ \left(\mathbf{E}^{d(p)}, \mathbf{H}^{d(p)} \right) & \text{(in } p\text{-th sphere: } p = 1, 2, \dots, Q) \end{cases} \quad (5)$$

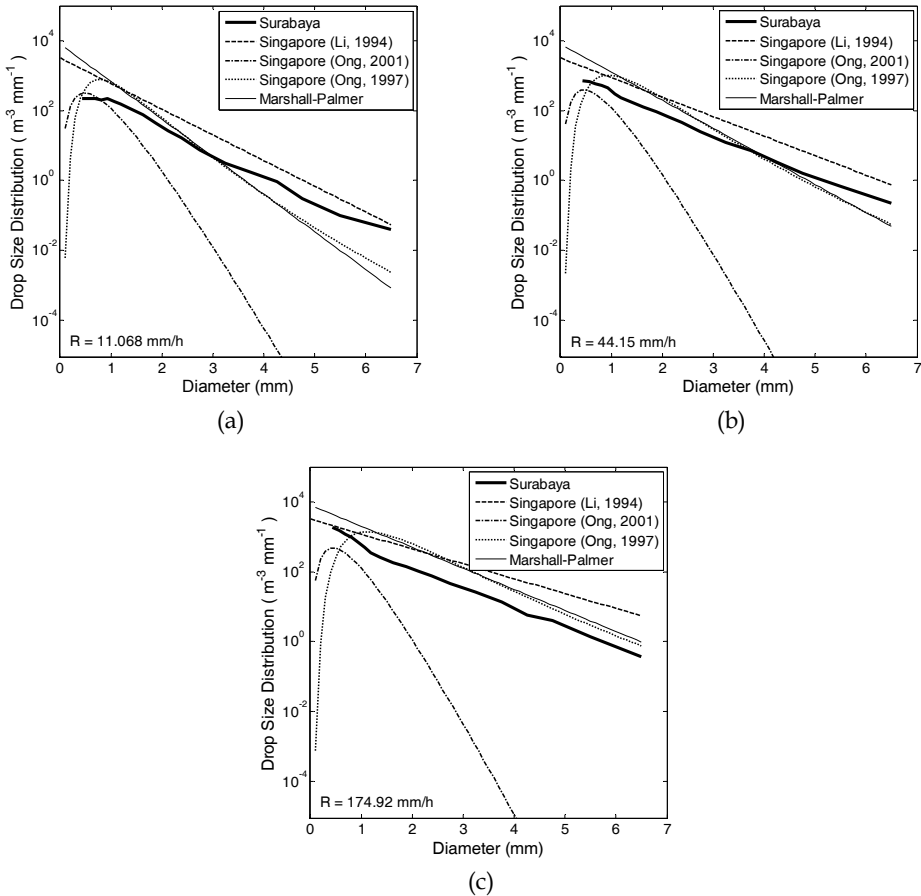


Fig. 3. Comparison of drop size distributions measured in Surabaya and models derived from measurements in Singapore for various rain rates: (a) 11.068 mm/h, (b) 44.15 mm/h, and (c) 174.92 mm/h, which for the Surabaya measurement are average values of intervals 8-16, 32-64, and 128-256 mm/h, respectively.

where the superscripts i , $s(q)$, and $d(p)$ concern the incident field, the scattered field due to the existence of the sphere # q , and the field inside the sphere # p , respectively. With no loss of generality, we can assume that the incident field is x -polarized and propagates in the $+z$

direction. Omitting the time factor $e^{j\omega t}$, we have the expression $E_x^i(\mathbf{r}) = \zeta_0 H_y^i(\mathbf{r}) = e^{-jk_0 z}$, where $k_0 = \omega\sqrt{\epsilon_0\mu_0}$ and $\zeta_0 = \sqrt{\mu_0/\epsilon_0}$.

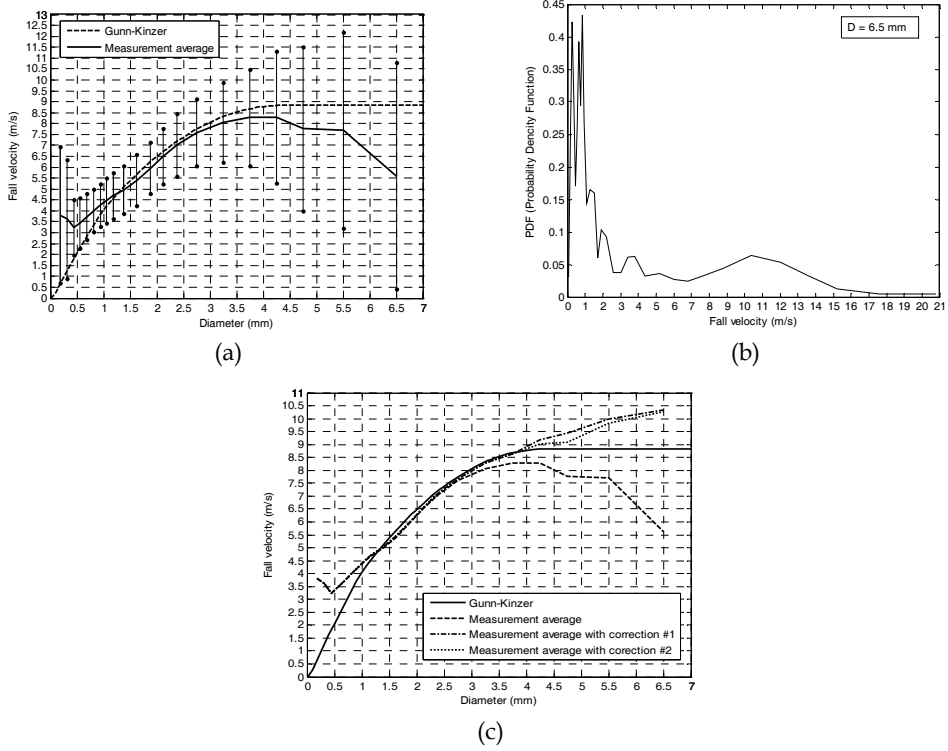


Fig. 4. Drop fall velocity variations shown by (a) the mean \pm variance of fall velocity for every diameter bin, (b) the density function of fall velocity for drop of 6.5 mm diameter and (c) fall velocity curves with corrections.

b. Expression of electromagnetic fields

Let us express the electromagnetic fields in the right hand side of (5) as

$$\begin{pmatrix} E^i(\mathbf{r}) \\ -j\zeta_0 H^i(\mathbf{r}) \end{pmatrix} = e^{-jk_0 z_{p0}} \sum_{n=1}^{\infty} \sum_{m=-n}^n \begin{pmatrix} V_{mn} & U_{mn} \\ U_{mn} & V_{mn} \end{pmatrix} \begin{pmatrix} M_{mn}^{(1)}(k_0 r_p, \theta_p, \phi_p) \\ N_{mn}^{(1)}(k_0 r_p, \theta_p, \phi_p) \end{pmatrix} \quad (6)$$

$$\begin{pmatrix} E^{s(q)}(\mathbf{r}) \\ -j\zeta_0 H^{s(q)}(\mathbf{r}) \end{pmatrix} = \sum_{n=1}^{\infty} \sum_{m=-n}^n \begin{pmatrix} B_{qmn} & A_{qmn} \\ A_{qmn} & B_{qmn} \end{pmatrix} \begin{pmatrix} M_{mn}^{(4)}(k_0 r_q, \theta_q, \phi_q) \\ N_{mn}^{(4)}(k_0 r_q, \theta_q, \phi_q) \end{pmatrix} \quad (7)$$

$$\begin{pmatrix} E^{d(p)}(\mathbf{r}) \\ -j\zeta_0 H^{d(p)}(\mathbf{r}) \end{pmatrix} = \sum_{n=1}^{\infty} \sum_{m=-n}^n \begin{pmatrix} D_{pmn} & C_{pmn} \\ C_{pmn} & D_{pmn} \end{pmatrix} \begin{pmatrix} M_{mn}^{(1)}(k r_p, \theta_p, \phi_p) \\ N_{mn}^{(1)}(k r_p, \theta_p, \phi_p) \end{pmatrix} \quad (8)$$

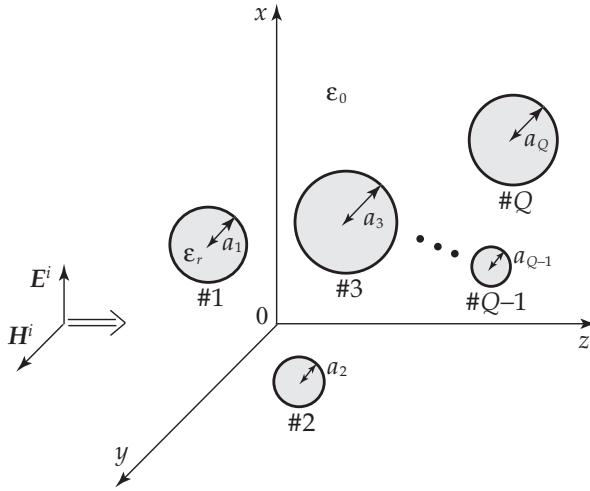


Fig. 5. Dielectric spheres and incident field.

where $k = \omega\sqrt{\epsilon_0\epsilon_r\mu_0}$ and $\zeta = \sqrt{\mu_0/(\epsilon_0\epsilon_r)}$. The vector spherical wave functions are defined as (Stratton, 1941)

$$\mathbf{M}_{mn}^{(l)}(\rho, \theta, \phi) = \frac{\widehat{Z}_n^{(l)}(\rho)}{\rho} \mathbf{m}_{mn}(\theta, \phi) \tag{9}$$

$$\mathbf{N}_{mn}^{(l)}(\rho, \theta, \phi) = \frac{jn(n+1)}{\rho^2} \widehat{Z}_n^{(l)}(\rho) \sin\theta \pi_n^{|m|}(\theta) e^{jm\phi} \hat{\mathbf{r}} + \frac{\widehat{Z}_n^{(l)}(\rho)}{\rho} \mathbf{n}_{mn}(\theta, \phi) \tag{10}$$

where

$$\mathbf{m}_{mn}(\theta, \phi) = \left[-m\pi_n^{|m|}(\theta)\hat{\theta} - j\tau_n^{|m|}(\theta)\hat{\phi} \right] e^{jm\phi}, \quad \mathbf{n}_{mn} = \hat{\mathbf{r}} \times \mathbf{m}_{mn} \tag{11}$$

with the associated Legendre functions $\pi_n^m(\theta) = P_n^m(\cos\theta)/\sin\theta$, $\tau_n^m(\theta) = dP_n^m(\cos\theta)/d\theta$, and the spherical Bessel functions $\widehat{Z}_n^{(l)}(\rho) = \sqrt{\pi\rho/2} Z_{n+1/2}^{(l)}(\rho)$. The function $Z_n^{(l)}$ corresponds to the cylindrical functions $J_n, Y_n, H_n^{(1)},$ and $H_n^{(2)}$ for $l = 1, 2, 3,$ and 4 , respectively. The prime denotes derivative with respect to the variable. As for the incident wave of (6), the spherical wave expansion of a plane wave gives

$$U_{mn} = -\text{sgn}(m)V_{mn} = -j^{-n}(2n+1)\delta_{|m|1}/[2n(n+1)] \tag{12}$$

with $\delta_{|m|1}$ being Kronecker's delta.

c. Mode matching method

The boundary conditions on the dielectric surface are written as

$$\hat{r}_p \times \left(\mathbf{F}^i(\mathbf{r}) + \sum_{q=1}^Q \mathbf{F}^{s(q)}(\mathbf{r}) - \mathbf{F}^{d(p)}(\mathbf{r}) \right) \Big|_{r_p=a_p} = 0 \quad (0 \leq \theta_p \leq \pi, 0 \leq \phi_p < 2\pi; p = 1, 2, \dots, Q) \quad (13)$$

where \mathbf{F} stands for \mathbf{E} and \mathbf{H} . We substitute (6)-(8) into (13) and truncate the infinite series at $n = N_q$ for the q -th sphere ($q = 1, 2, \dots, Q$). The values N_q depend on the electrical size of spheres. This leads us to linear equations including $4 \sum_{q=1}^Q N_q (N_q + 2)$ unknown coefficients

$A_{qmn}, B_{qmn}, C_{pmn},$ and D_{pmn} .

As seen from (6)-(8), the origins of observation points are not unified at this stage. In order to shift the origin of $\mathbf{E}^{s(q)}$ and $\mathbf{H}^{s(q)}$ from 0_q to 0_p , we apply the addition theorem for vector spherical wave functions (Cruzan, 1962)

$$\begin{pmatrix} M_{mn}^{(4)}(k_0 \mathbf{r}_q) \\ N_{mn}^{(4)}(k_0 \mathbf{r}_q) \end{pmatrix} = \sum_{\nu=1}^{\infty} \sum_{\mu=-\nu}^{\nu} \begin{pmatrix} \alpha_{mn,\mu\nu}^{(4)}(k_0 \mathbf{r}_{pq}) & \beta_{mn,\mu\nu}^{(4)}(k_0 \mathbf{r}_{pq}) \\ \beta_{mn,\mu\nu}^{(4)}(k_0 \mathbf{r}_{pq}) & \alpha_{mn,\mu\nu}^{(4)}(k_0 \mathbf{r}_{pq}) \end{pmatrix} \begin{pmatrix} M_{\mu\nu}^{(1)}(k_0 \mathbf{r}_p) \\ N_{\mu\nu}^{(1)}(k_0 \mathbf{r}_p) \end{pmatrix} \quad (14)$$

where the position $(k_0 r_p, \theta_p, \phi_p)$ has been simply written as $k_0 r_p$. The translation coefficients $\alpha_{mn,\mu\nu}^{(4)}$ and $\beta_{mn,\mu\nu}^{(4)}$ are the functions of the shift vector $\mathbf{r}_{pq} = \mathbf{r}_{p0} - \mathbf{r}_{q0}$. Making use of the orthogonal properties of the vector spherical wave functions, and eliminating the coefficients $C_{p\mu\nu}$ and $D_{p\mu\nu}$, we arrive at the set of linear equations

$$\left. \begin{aligned} A_{p\mu\nu} - \sum_{q=1(\neq p)}^Q \sum_{n=1}^{N_q} \sum_{m=-n}^n [A_{qmn} \alpha_{mn,\mu\nu}^{(4)}(k_0 \mathbf{r}_{pq}) + B_{qmn} \beta_{mn,\mu\nu}^{(4)}(k_0 \mathbf{r}_{pq})] \bar{A}_{p\nu} &= U_{\mu\nu} \bar{A}_{p\nu} e^{-jk_0 z_{p0}} \\ B_{p\mu\nu} - \sum_{q=1(\neq p)}^Q \sum_{n=1}^{N_q} \sum_{m=-n}^n [A_{qmn} \beta_{mn,\mu\nu}^{(4)}(k_0 \mathbf{r}_{pq}) + B_{qmn} \alpha_{mn,\mu\nu}^{(4)}(k_0 \mathbf{r}_{pq})] \bar{B}_{p\nu} &= V_{\mu\nu} \bar{B}_{p\nu} e^{-jk_0 z_{p0}} \end{aligned} \right\} \quad (15)$$

$(\nu = 1, 2, \dots, N_p; \mu = -\nu, -\nu + 1, \dots, \nu; p = 1, 2, \dots, Q)$

where

$$\bar{A}_{p\nu} = -\frac{\hat{J}_\nu(k_0 a_p) \hat{J}_\nu'(ka_p) - \sqrt{\epsilon_r} \hat{J}_\nu'(k_0 a_p) \hat{J}_\nu(ka_p)}{\hat{H}_\nu^{(2)}(k_0 a_p) \hat{J}_\nu'(ka_p) - \sqrt{\epsilon_r} \hat{H}_\nu^{(2)'}(k_0 a_p) \hat{J}_\nu(ka_p)} \quad (16)$$

$$\bar{B}_{p\nu} = -\frac{\hat{J}_\nu'(k_0 a_p) \hat{J}_\nu(ka_p) - \sqrt{\epsilon_r} \hat{J}_\nu(k_0 a_p) \hat{J}_\nu'(ka_p)}{\hat{H}_\nu^{(2)'}(k_0 a_p) \hat{J}_\nu(ka_p) - \sqrt{\epsilon_r} \hat{H}_\nu^{(2)}(k_0 a_p) \hat{J}_\nu'(ka_p)} \quad (17)$$

Equation (15) includes the same number of relations as that of unknowns, and thereby, is numerically solved. After that, the other coefficients are computed from

$$C_{p\mu\nu} = \bar{C}_{p\nu} A_{p\mu\nu} / \bar{A}_{p\nu}, \quad D_{p\mu\nu} = \bar{D}_{p\nu} B_{p\mu\nu} / \bar{B}_{p\nu} \quad (18)$$

where

$$\bar{C}_{pv} = \frac{j\sqrt{\varepsilon_r}}{\widehat{H}_v^{(2)}(k_0 a_p) \widehat{J}_v'(ka_p) - \sqrt{\varepsilon_r} \widehat{H}_v^{(2)'}(k_0 a_p) \widehat{J}_v(ka_p)} \quad (19)$$

$$\bar{D}_{pv} = -\frac{j\sqrt{\varepsilon_r}}{\widehat{H}_v^{(2)'}(k_0 a_p) \widehat{J}_v(ka_p) - \sqrt{\varepsilon_r} \widehat{H}_v^{(2)}(k_0 a_p) \widehat{J}_v'(ka_p)} \quad (20)$$

Equations (16), (17), (19), and (20) are called Mie's coefficients (Harrington, 1961). It should be noted that the terms including the translation coefficients in (15) represent the effect of multiple scattering among spheres. If raindrops are so sparsely distributed that the multiple effect is very weak, the approximate solutions of (15) are directly derived as

$$A_{qmn} \approx U_{mn} \bar{A}_{qn} e^{-jk_0 z_{q0}}, \quad B_{qmn} \approx V_{mn} \bar{B}_{qn} e^{-jk_0 z_{q0}} \quad (21)$$

d. Scattering and absorption cross sections

Employing the large argument approximations $\widehat{H}_n^{(2)}(k_0 r_q) \approx j\widehat{H}_n^{(2)'}(k_0 r_q) \approx j^{n+1} e^{-jk_0 r_q}$ and $r_q = r - \mathbf{r} \cdot \mathbf{r}_{q0} / r$ in (7), we can write the far scattered field in the form of inhomogeneous spherical waves as

$$\begin{pmatrix} E_\theta^s(\mathbf{r}) \\ E_\phi^s(\mathbf{r}) \end{pmatrix} \approx \zeta_0 \begin{pmatrix} H_\phi^s(\mathbf{r}) \\ -H_\theta^s(\mathbf{r}) \end{pmatrix} \approx \frac{e^{-jk_0 r}}{k_0 r} \begin{pmatrix} f_\theta(\theta, \phi) \\ f_\phi(\theta, \phi) \end{pmatrix} \quad (r \rightarrow \infty) \quad (22)$$

where the scattering pattern functions are

$$\begin{pmatrix} f_\theta(\theta, \phi) \\ f_\phi(\theta, \phi) \end{pmatrix} = \sum_{q=1}^Q \sum_{n=1}^{N_q} \sum_{m=-n}^n j^n (A_{qmn} \hat{\theta} + jB_{qmn} \hat{\phi}) \cdot \begin{pmatrix} \mathbf{n}_{mn}(\theta, \phi) \\ \mathbf{m}_{mn}(\theta, \phi) \end{pmatrix} e^{-jk_0 \mathbf{r} \cdot \mathbf{r}_{q0} / r} \quad (23)$$

The total scattered power is computed from

$$\begin{aligned} P^s &= \frac{1}{2} \operatorname{Re} \left[\int_0^{2\pi} \int_0^\pi \left[\mathbf{E}^s(\mathbf{r}) \times \mathbf{H}^{s*}(\mathbf{r}) \right] \cdot \hat{\mathbf{r}} \Big|_{r \rightarrow \infty} r^2 \sin\theta \, d\theta \, d\phi \right] \\ &\approx \frac{1}{2\zeta_0^2 k_0^2} \int_0^{2\pi} \int_0^\pi \left[|f_\theta(\theta, \phi)|^2 + |f_\phi(\theta, \phi)|^2 \right] \sin\theta \, d\theta \, d\phi \end{aligned} \quad (24)$$

where the asterisk denotes complex conjugate. The integrals with respect to θ and ϕ in above are numerically evaluated by the Gauss-Legendre quadrature rule and the trapezoidal formula, respectively. Since the power density of incident field is $W^i = 1/(2\zeta_0)$, the total scattering cross section is given by $\sigma^s = P^s / W^i = 2\zeta_0 P^s$.

On the other hand, the power absorbed inside the spheres is computed from

$$\begin{aligned}
 P^a &= \frac{1}{2} \operatorname{Re} \sum_{q=1}^Q \left[\int_0^{2\pi} \int_0^\pi \left[E^{d(q)}(\mathbf{r}) \times \mathbf{H}^{d(q)*}(\mathbf{r}) \right] \cdot (-\hat{r}) \Big|_{r \rightarrow a_q} a_q^2 \sin \theta \, d\theta \, d\phi \right] \\
 &\approx \frac{\pi}{k_0^2 \zeta_0} \operatorname{Re} \frac{1}{j \sqrt{\epsilon_r}} \sum_{n=1}^{N_q} \sum_{m=-n}^n \frac{2n(n+1)(n+m)!}{(2n+1)(n-m)!} \\
 &\quad \times \sum_{q=1}^Q \left[|C_{qmn}|^2 \hat{J}_n'(ka_q) \hat{J}_n^*(ka_q) - |D_{qmn}|^2 \hat{J}_n(ka_q) \hat{J}_n^*(ka_q) \right]
 \end{aligned} \tag{25}$$

The absorption cross section is given by $\sigma^a = P^a / W^i = 2\zeta_0 P^a$.

The optical theorem or the extinction theorem states that the diffracted field in the forward direction, which is related to $f_\theta(0,0)$, should be attenuated due to the scattering and absorption. This is based on the law of energy conservation. The amount of this attenuation is called the extinction cross section and expressed as

$$\begin{aligned}
 \sigma^e &= \sigma^s + \sigma^a = -\frac{4\pi}{k_0^2} \operatorname{Im} [f_\theta(0,0)] \\
 &= \frac{2\pi}{k_0^2} \sum_{n=1}^{N_q} n(n+1) \operatorname{Im} \left\{ j^{n+1} \sum_{q=1}^Q [A_{q1n} + A_{q(-1)n} - B_{q1n} + B_{q(-1)n}] e^{jk_0 z_{q0}} \right\}
 \end{aligned} \tag{26}$$

e. Specific rain attenuation

Suppose that Q spheres are randomly allocated inside the volume V (m^3). By using σ^e (m^2) in Eq. (26), the specific rain attenuation is given by $\gamma = \sigma^e / V$ (m^{-1}). From a practical viewpoint, the unit is often converted via

$$\gamma [\text{dB/km}] = \gamma [\text{m}^{-1}] \times 10^3 \times 10 \log_{10} e = 4343 \sigma^e / V \tag{27}$$

If we can neglect the multiple scattering among spheres, the approximate cross section

$$\sigma^e \approx -\frac{2\pi}{k_0^2} \operatorname{Re} \sum_{n=1}^\infty (2n+1) = \sum_{q=1}^Q (\bar{A}_{qn} + \bar{B}_{qn}) \tag{28}$$

is applied to Eq. (27) with the aid of Eqs. (16) and (17). We will use this formula in the later computations.

Let us determine the series of realistic radii a_q as a function of rainfall intensity R (mm/h). Each distribution model proposes a function $N(a)$ ($\text{m}^{-3} \text{mm}^{-1}$), which is a number of raindrops having the radius between a and $a + da$ (mm) per unit volume. Then the integral

$$\tilde{N}(a) = \int_0^a N(a') da' \quad [\text{m}^{-3}] \tag{29}$$

gives a number of raindrops, the radius of which are less than a (mm), per unit volume. The value $\tilde{N}(\infty)$ denotes the total number. When we deal with Q raindrops in the numerical computation, the q -th radius a_q (mm) is sampled by the rule

$$\frac{\tilde{N}(a_q)}{\tilde{N}(\infty)} = \frac{q-1/2}{Q} \quad (q = 1, 2, \dots, Q) \tag{30}$$

with $V = Q/\tilde{N}(\infty)$. Among a lot of proposed models, we select exponential and Weibull distribution models and the related formulas are arranged in Table 4.

Raindrop distribution model	Density function $N(a)$ ($\text{m}^{-3} \text{mm}^{-1}$)	Sampled radius a_q (mm) by (30)
	Parameters	
Exponential (Marshall et al., 1948)	$N_0 e^{-\Lambda a}$	$-\frac{1}{\Lambda} \log\left(1 - \frac{q-1/2}{Q}\right)$
	$N_0 = 16000 \text{ m}^{-3} \text{mm}^{-1}$ $\Lambda = 8.2 R^{0.21}$ $\tilde{N}(\infty) = N_0 / \Lambda$	
Weibull (Sekine et al., 1987)	$N_0 \frac{\eta}{\sigma} \left(\frac{a}{\sigma}\right)^{\eta-1} e^{-(a/\sigma)^\eta}$	$\sigma \left[-\log\left(1 - \frac{q-1/2}{Q}\right)\right]^{1/\eta}$
	$N_0 = 1000 \text{ m}^{-3} \text{mm}^{-1}$ $\eta = 0.95 R^{0.14}$ $\sigma = 0.13 R^{0.44}$ $\tilde{N}(\infty) = N_0$	

Table 4. Representative two distribution models. The rainfall R is measured in mm/h.

f. Numerical examples

Examples of the radius a_q by the above models are given in Table 5 for fixed R and Q . The exponential distribution proposed by Marshall and Palmer predicts that, compared with Weibull model, smaller raindrops are concentrated inside a smaller volume.

Fig. 6 shows the convergence of attenuation γ as Q increases based on the Weibull distribution up to 1000 GHz. The relative complex permittivity of water is a function of temperature and frequency. One of the effective formulas (Liebe et al., 1991) gives, at 25°C, $\epsilon_r = 78.1-j3.8, 62.8-j29.9, 7.8-j13.8,$ and $4.2-j2.3$ for 1, 10, 100, and 1000 GHz, respectively. Slight irregularity at $Q = 2$ stems from internal resonance in the dielectric media, which is relaxed for larger Q due to the averaging effect. Roughly speaking, the distance between adjacent curves becomes halved as Q is doubled, which results in good convergence. Hereafter we will fix as $Q = 32$.

Model	Radii a_q (mm)									V (cm^3)
Exponential	0.02	0.06	0.10	0.16	0.23	0.32	0.46	0.77		1800
Weibull	0.14	0.28	0.40	0.52	0.65	0.80	0.99	1.35		8000

Table 5. Radii of raindrops at $R = 50$ mm/h and $Q = 8$.

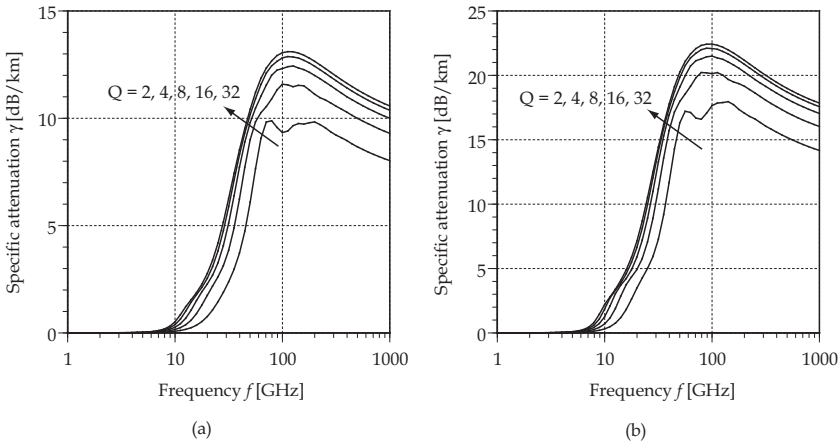


Fig. 6. Convergence of specific attenuation at 25°C by Weibull distribution as the number of sampled raindrops Q is increased. (a) $R = 25$ mm/h and (b) $R = 50$ mm/h.

Fig. 7 shows comparisons of attenuation γ between the exponential and Weibull distribution for four values of rainfall R . At low frequencies the exponential distribution predicts lower attenuation, probably because electrically small raindrops work as weak scatterers and absorbers. These drops contribute, in turn, to attenuation at high frequencies, since they are now electrically large and densely allocated. Fig. 8 shows the effect of changing temperature. The deviation of specific attenuation behaves in a different manner between the frequency bands 10-20 GHz and 30-100 GHz. This is explained by the permittivity of the water. In the lower frequency band around 15 GHz, the real part of ϵ_r is large at high temperatures, which leads large scattering loss. On the other hand, in the millimeter wave around 50 GHz, the increase in the permittivity makes the raindrops electrically large, which promotes the electromagnetic transparency of rain medium and results in low attenuation.

2.4 Synthetic storm technique

Synthetic storm technique (SST) is a method to obtain estimates of rain attenuation statistics for links of a given length, whenever a real radio link is inexistent. Given measurements of wind velocity and time series of rain intensity at a site, statistics of rain attenuation on a hypothetical link passing through or nearby that site can be estimated by dividing the link into segments, each of length equal the distance travelled over by the rain structure as it is blown by the wind during one sampling period of rain rate measurement. At each sampling time, rain attenuation is obtained as the sum of specific attenuation estimates (dB/km) multiplied by the segment length (km). That is, the n -th sample of rain attenuation is:

$$A(n) = \sum_{m=0}^{N-1} k [R(n-m)]^a \delta_m \quad (31)$$

with $R(n)$ denoting the n -th sample of rain rate measurement, k and a the power-law coefficients that depend on radio frequency, wave polarization, temperature, drop shape

and size distribution, such as those given by ITU-R Rec. P.838 (ITU-R, 2005), N the number of segments constituting the link, and δ_m the length of the m -th segment of the link. That is,

$$N = \left\lceil \frac{L \cos \theta}{vT} \right\rceil \tag{32}$$

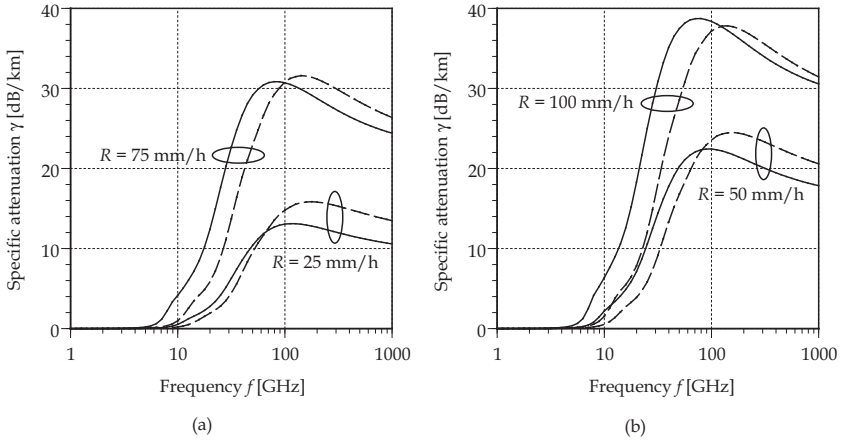


Fig. 7. Specific attenuation at 25°C by two models with sampled 32 raindrops. Dashed curves: exponential distribution, Solid curves: Weibull distribution.

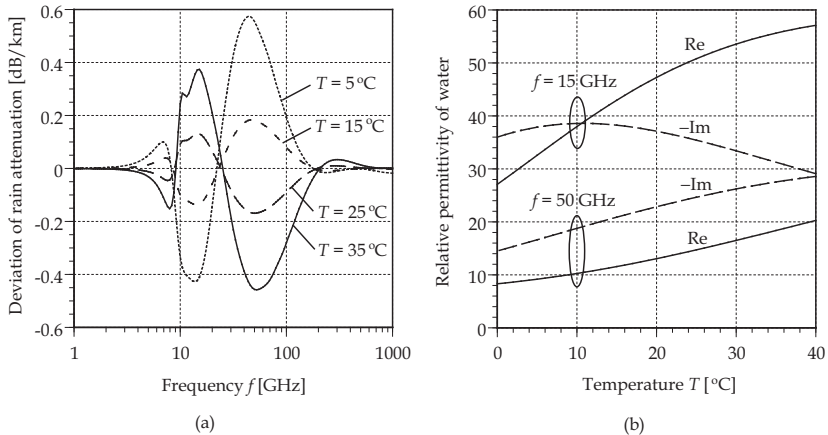


Fig. 8. Temperature dependence of specific attenuation by Weibull distribution with sampled 32 raindrops at $R = 50$ mm/h. (a) Deviation $\gamma(T) - \gamma(20^\circ\text{C})$ and (b) Real and Imaginary parts of relative permittivity ϵ_r .

$$\delta_m = \begin{cases} \frac{vT}{\cos\theta} & m = 0, \dots, N - 2 \text{ and } \theta \neq 90^\circ \\ L - \frac{(N-1)vT}{\cos\theta} & m = N - 1 \text{ and } \theta \neq 90^\circ \\ L & \text{all } m \text{ and } \theta = 90^\circ \end{cases} \quad (33)$$

with v representing wind velocity, T the rain rate sampling period and θ angular difference between the wind direction and link orientation. The situation is graphically described in Fig. 9. The SST does not yield estimates of the actual rain attenuation, but it proves to give a good estimate of the attenuation statistics (Matricciani & Riva, 2005). It can also be used to acquire good statistical estimates of fade dynamics (Matricciani, 2004; Sánchez-Lago et al, 2007). Mahmudah et al (2008) and Suwadi et al (2009) use SST to examine the performance of cell-site diversity in a network of converging, short links.

Eqn. (31) indicates that rain attenuation samples can be straightforwardly obtained by convolving the rectangular-windowed time series of the specific attenuation and that of the segment length. This fact has been pointed out first by Matricciani (1996) and is also confirmed in our own study. When the wind direction and link orientation are perpendicular, the link comprises only a single segment and the convolution becomes multiplication. In this case, the resulting attenuation statistics tend to be higher due to the absence of moving-average effects.

Before proceeding to use the SST results in subsequent analyses, a comparison is made on the different results arising from the use of different values of wind velocity. In this case, we consider three different statistics, namely, the daily average, the daily maximum, and the monthly average. It is shown in Fig. 10 that the distributions of attenuation for the case of daily average and monthly average wind velocity, respectively, are almost identical, whereas the one obtained using daily maximum value tend to give an upper bound (Hendrantoro et al, 2007b). It can also be observed that for probabilities of being exceeded less than 0.1%, the SST results are higher than the value predicted by the ITU-R method.

An attempt to confirm the applicability of SST for short links is made by comparing the attenuation statistics on a hypothetical link from the SST exercise using rain rate measurements with that estimated using a simple segmentation method. The latter makes use of the fact that the measurement sites are almost aligned in an almost North-South orientation (see Fig. 1). Using this method and recognizing that the fictitious link A-D would be 1.55 km long, the rain attenuation estimate at the n^{th} sampling time is:

$$A(n) = 1.55k \sum_{m=1}^3 [R_m(n)]^{\alpha} \Delta l_m \text{ dB} \quad (34)$$

with indexes $m = 1, \dots, 3$ referring to sites A, B and D (rain gauge at site C is inactive during the observation), $\Delta l_1 = \Delta l_3 = 0.25$, $\Delta l_2 = 0.5$, and all other variables defined previously. This scenario is depicted in Fig. 11. It is assumed that each rain gauge represents an area of homogeneous instantaneous rain rate. Results shown in Table 6 indicate that there is no significant difference among the percentiles for various methods, sources, and link orientations. This has also been confirmed through a Kolmogorov-Smirnov test in which the

distribution curves are shown to reside within the upper and lower bounds for lognormality with 80% confidence interval. For low probabilities of being exceeded, SST results for the North-South oriented link tend to surpass those for the East-West. This phenomenon owes to the fact that about 67% of the wind velocity measurements made simultaneously with those of rain rate and subsequently used in the SST are of East-West direction, i.e., perpendicular to the North-South link orientation, which might result in higher statistics as previously discussed.

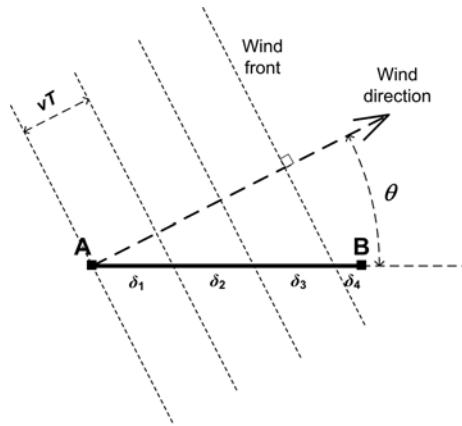


Fig. 9. Segmentation of a hypothetical link A-B according to the wind velocity v and averaging time of rain rate measurement T .

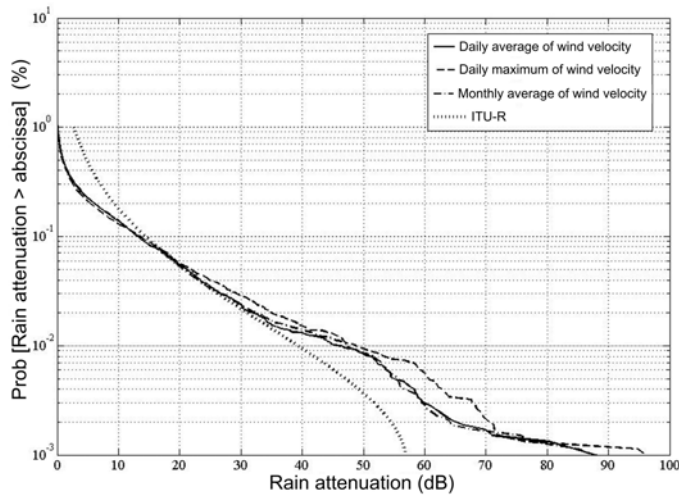


Fig. 10. Complementary cumulative distribution of rain attenuation along a 2 km link obtained using various statistics of wind velocity compared to that obtained using ITU-R method.

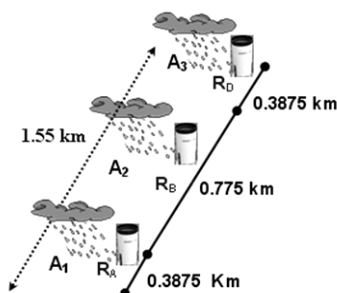


Fig. 11. Use of multiple rain gauges to compute rain attenuation estimates on a fictitious radio link.

Percentiles of attenuation (dB)	Synthetic Storm						Segmented Link
	East-West oriented			North-South oriented			
	A	B	D	A	B	D	
A_1	0	0	0	0.13	0	0	0.22
$A_{0.5}$	1.40	1.36	1.19	1.68	1.31	1.47	1.35
$A_{0.1}$	15.01	13.98	14.55	13.66	12.86	13.02	12.73
$A_{0.05}$	22.34	19.96	21.89	21.64	20.78	21.49	19.84
$A_{0.01}$	38.95	37.11	36.67	36.85	35.92	35.73	34.96
$A_{0.005}$	42.32	38.56	41.03	39.38	39.26	38.49	38.56
$A_{0.001}$	51.27	58.10	49.93	47.59	47.82	44.04	49.96
$A_{0.0005}$	53.65	60.18	53.21	48.84	48.36	45.29	50.93

Table 6. Percentiles of attenuation (dB) obtained from SST on East-West and North-South links compared to those from the three-segment link.

3. Modelling of rain intensity and attenuation

3.1 Space-time distribution of rain intensity and attenuation

A number of efforts have been made by researchers around the globe to model and characterize the space-time variation. Maseng-Bakken model of temporal characteristics of rain attenuation (Maseng & Bakken, 1981) is commonly used as a starting point in doing so. For instance, Burgueno et al (1990) has adopted the model to describe the 49-years of rain rate measurement in Barcelona, Spain. Paulson (2002) and Gremont (2004) have expanded the Maseng-Bakken model into a space-time one of rain field involving correlation function of rain rate. Other than that, different forms of spatial correlation have also been proposed separately by Lin (1975), Morita and Higuti (1978), and Capsoni et al (1981) from measurements made in the U.S., Japan and Europe, respectively. Kanellopoulos and Koukoulas (1987) use the first two models to estimate the correlation of attenuations on two links converging into a common end.

In a similar investigation performed in Surabaya, measurements of rain rate made in 2006-2007 are classified into stratiform and convective types (Hendrantoro et al, 2007b). A simple criterion is adopted in this classification, that is, an event is considered “convective” if it contains samples with intensity higher than 25 mm/hr (Bogush, 1989). The time correlation for each of the two types of rain is subsequently compared with the result from 49 years of data obtained in Barcelona, Spain. It can be seen from Fig. 12 that the convective type exhibits correlation of rain rate that decreases with time lag more rapidly than the stratiform. In addition, both types of rain observed in Surabaya shows slower decrease in correlation with time lag compared to the result from Barcelona. Despite the vast difference in the length of the measurement period, this finding might indicate that even the convective rain events in Surabaya last longer than average rain events in Barcelona. When time-to-space conversion using SST is concerned, it leads to a strong indication that rain cells in Surabaya are larger than those occurring in Barcelona.

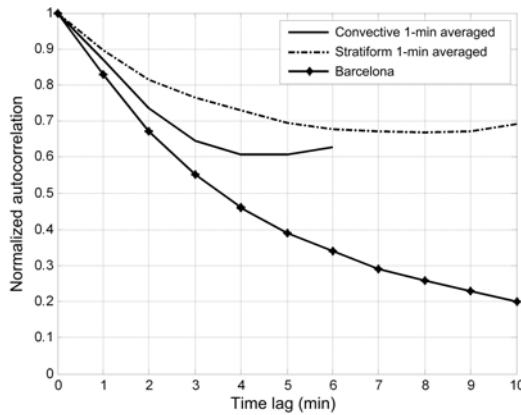


Fig. 12. Average autocorrelation functions for the stratiform and convective events in Surabaya compared with the function for all events in Barcelona.

The latter observation is supported by a spatial correlation analysis of rain rate and specific attenuation in Surabaya. In this analysis, the rain events are classified into four groups according to the quartiles of either the space-time maximum or average of the squares of rain rate. The two different criteria yield different results, and hence, both are considered separately. With measurements made in four different sites of various distances in-between, correlation coefficients of rain rate are obtained for six pairs of sites of different distances, namely, 0.4, 0.55, 0.70, 0.95, 1.00 and 1.55 km. For rain rate analysis, average correlation between two sites of distance d km according to Morita-Higuti (MH) model:

$$\rho_R(d) = e^{-\alpha\sqrt{d}} \quad (35)$$

with a being the model parameter whose value lies in the range of 0.2-0.3 $\text{km}^{-1/2}$, and Capsoni-Matricciani-Mauri (CMM) model:

$$\rho_R(d) = e^{-\beta d} \quad (36)$$

with β equal to 0.46 km^{-1} , are used as reference. For the specific attenuation, which is calculated by applying the power-law relation with ITU-R coefficients for 30 GHz horizontally polarized waves (ITU-R, 2005), Lin model is adopted:

$$\rho_r(d) = \frac{G}{\sqrt{G^2 + d^2}} \tag{37}$$

with G being the characteristic distance that lies in the range of 1.5–3 km. The rain rate and specific attenuation quartiles together with the parameter values of the HM, CMM and Lin models obtained through fitting to (35)–(37) are shown in Tables 7 and 8, while the correlation curves are pictorially depicted in Fig. 13. For the lower quartiles the value of a is in the same range as the MH model, but is generally lower for the greater quartiles. For the CMM model, the values of β are all less than 0.46 obtained in Europe. These findings suggest that rain cells in Surabaya, especially those formed during the heaviest rain events, possess larger dimension than their Japanese and European counterparts.

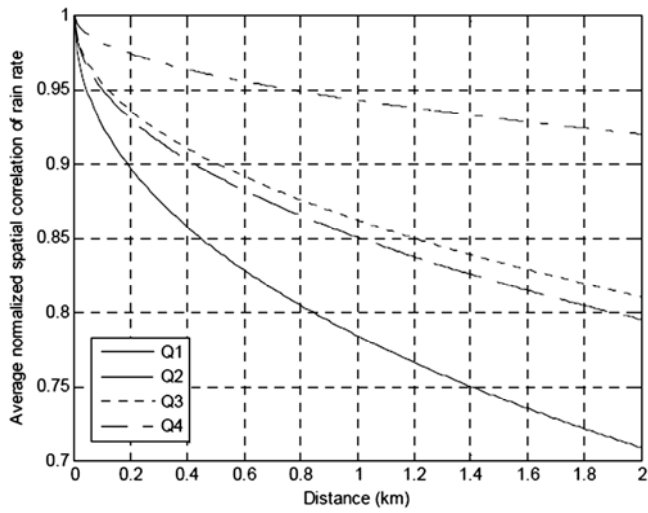
Conclusions that can be drawn from this investigation are manifold. Firstly, it is apparent that categorization of rain events into quartiles based on maximum and mean squared values of rain rate yields different sets of correlation function. It indicates that events with high maximum values do not necessarily possess high mean square values. An extreme exemplary case of such a condition is an event comprising a very long drizzle preceded by a brief high-intensity storm. Secondly, it can be observed that events with high mean square values, i.e., greater than 49.7 (mm/h)^2 , tend to produce high spatial correlation of rain rates between two sites up to 2 km apart. It suggests that the average size of rain cells having long intense rain is relatively large.

Q	Maximum rain rate criterion			Mean squared rain rate criterion		
	Range	a	β	Range	a	β
I	$R_{\max} \leq 32.1$	0.25	0.24	$\langle R^2 \rangle \leq 49.7$	0.24	0.23
II	$32.1 < R_{\max} \leq 61.1$	0.21	0.22	$49.7 < \langle R^2 \rangle \leq 253.5$	0.16	0.17
III	$61.1 < R_{\max} \leq 101.4$	0.18	0.19	$253.5 < \langle R^2 \rangle \leq 730.5$	0.15	0.16
IV	$101.4 < R_{\max}$	0.073	0.074	$730.5 < \langle R^2 \rangle$	0.059	0.062

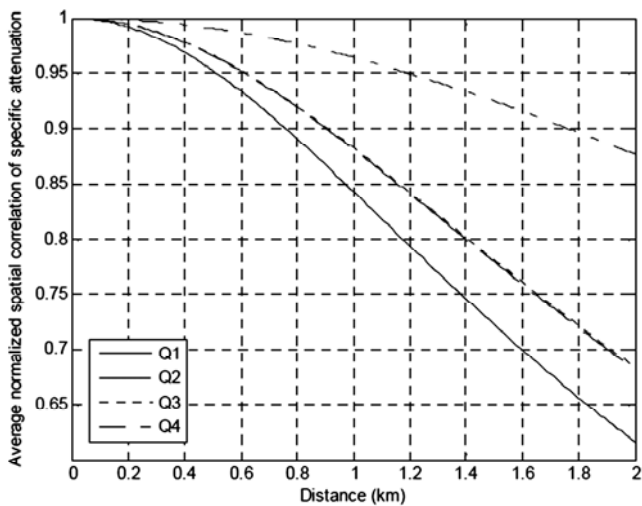
Table 7. HM and CMM model parameter estimation from Surabaya measurements.

Q	Maximum specific attenuation criterion		Mean squared specific attenuation criterion	
	Range	G	Range	G
I	$A_{H,\max} \leq 7.11$	1.54	$\langle A_H^2 \rangle \leq 1.95$	1.56
II	$7.11 < A_{H,\max} \leq 12.75$	1.72	$1.95 < \langle A_H^2 \rangle \leq 10.38$	1.86
III	$12.75 < A_{H,\max} \leq 21.76$	1.93	$10.38 < \langle A_H^2 \rangle \leq 29.92$	1.88
IV	$21.76 < A_{H,\max}$	3.19	$29.92 < \langle A_H^2 \rangle$	3.64

Table 8. Lin model parameter estimation from Surabaya measurements.



(a)



(b)

Fig. 13. Spatial correlations of (a) rain rate according to MH model and (b) specific attenuation of 30 GHz horizontally polarized waves according to Lin, both obtained by regression with respect to the correlations from measurements for four quartiles of mean squared values.

3.2 ARIMA modeling of rain rate and attenuation

The short-term variation of rain attenuation is of great interest to millimeter-wave system designers as it determines the capability of the system required to handle the induced fades. In particular, two parameters are commonly used as a measure of fade dynamics, namely

fade duration and fade slope (van de Kamp & Castanet, 2002). A time series model is sought to demonstrate fade dynamics characteristics that approach those of actual measurements. A number of models have been proposed and tested by various researchers. In stochastic signal processing, it is of interest to obtain an appropriate time series model for stationary random processes. Such models that might be useful and appropriate to describe rain fade dynamics are of the ARMA family. The ARMA model has been proposed for modelling rain attenuation in both single- and multiple-link configuration (Hendrantoro et al, 2006, Yadnya et al, 2008a, 2008b). The underlying assumption is that the rain field is stationary, at least during the rain event under consideration, both in time and space. The temporal stationarity assumption assures that the ARMA model order does not change during the event, whereas the spatial stationarity is necessary for the applicability of the multi-variate version to the case of multiple-link system. The latter is deemed acceptable for a configuration with very short links located nearby, such as the macro-diversity access links of a millimeter-wave cellular system. Considering the statistics of rain cell diameter, which is approximately in the order of 4-5 km (extrapolation of spatial correlation of specific attenuation for the 4th quartile in Fig. 13 (b) up to about 0.5), it is motivating to obtain a more realistic, non-stationary model. Consequently, studies are made on various possible models, including those of ARIMA family.

To determine the appropriate ARIMA(p, d, q) model parameters, where p , d and q denote the orders of the AR part, the differencing process and the MA, respectively, firstly the stationarity in both variance and mean of the event is evaluated following Box-Jenkins (Box et al, 1994). The test for stationarity in variance is intended to determine the appropriate transformation required to make the event stationary, if necessary. Whereas the test for stationarity in mean is meant to specify the order of differencing d . Next, the orders of the AR and MA parts are identified and diagnosed for the whiteness and normality of the residual. If necessary, outliers can be detected and discarded to increase the model accuracy as measured by the mean squared error (MSE). The resulting model parameters can be used to generate time series samples of rain attenuation following the characteristics of the particular event upon which the model is developed. To produce a more generic model, a large database of rain events must be used, from which various values of model parameters can be identified and clustered to yield a complete stochastic model. Such a model, for instance, must be capable of determining the statistics of appearance of a given set of model parameter values. Expansion into space-time model can also be made by invoking, for example, the VARIMA (Vector ARIMA) model using simultaneous measurements at several spatially distributed rain gauges (for rain rate) or radio links (for attenuation).

An illustration of the ARIMA model application involving a number of rain events is given as follows. During an event, rain attenuation at 28 GHz on the 54 meter link is recorded with one-second sampling period. For verification purposes, attenuation is also estimated from rainfall rate measured during the event by invoking the conversion method outlined in ITU-R Rec. P.838 for vertically polarized radio wave at 30 GHz (ITU-R, 2005). Shown below is the cumulative distribution function (CDF) of rain attenuation estimates on February 10, 2009 obtained through three fashions: direct measurement of attenuation, measurement of rain rate followed by conversion using the ITU-R method and computer generation of time series samples according to the ARIMA modelling result. It is found out that the most appropriate model for this particular event is ARIMA (0, 1, 1). However, for different events, ARIMA model of different orders might result.

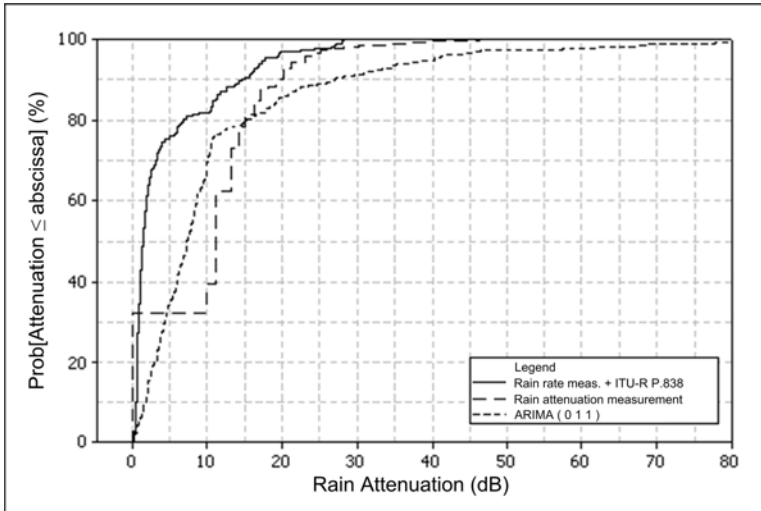


Fig. 14. The cumulative distribution function of rain attenuation estimates obtained through three different methods.

4. Examples of evaluation of communication systems

4.1 Cell-site diversity with adaptive modulation for cellular systems

In this example, evaluation is made upon cell-site diversity on the downlink involving two base stations making a 180° spacing around a user terminal (Hendrantoro et al, 2007a), as shown in Fig. 15 (a). The downlinks are of identical lengths $L_1 = L_2$ and experiencing correlated rain attenuation of A_{R1} and A_{R2} , respectively, that are generated from the bivariate AR model (Hendrantoro et al, 2006). The links employ separate yet identical adaptive M-QAM modulators with fixed power, implying fixed clear-sky SNR on both links. Herein it is assumed to be 44.8 dB, 38.8 dB, 35.3 dB and 32.8 dB for a pair of equal-length links of 1, 2, 3 and 4 km, respectively. The system model is given in Fig. 15 (b), whereas the scenario for adaptive modulation following the output SNR of the combiner at the user side is presented in Table 9, which is devised to attain bit error rate of 10^{-11} . Three different methods of combining are considered, namely, selection (SC), equal-gain (EGC) and maximal-ratio combining (MRC).

Results shown in Fig. 16 demonstrate the system performance, mainly in terms of average bit error rate and probability of outage. Fig. 16 (a) shows the complementary cumulative distribution function of bit error rate for 1 km links, which is kept approximately 10^{-11} . Fig. 16 (b) shows the outage probabilities for different combining techniques and link lengths. It can be seen that with any combining scheme, the outage can be suppressed down to 0.06% or less (corresponding to availability of 99.94% or higher), even for links of 4 km. With adaptive M-QAM modulation, the outage is compensated for by adopting lower modulation level, which leads to lower bandwidth efficiency. From another result not shown here, the actual degradation in the average efficiency is actually not significant. Fig. 16 (d) also reveals

that diversity might only be necessary for user terminals positioned near the border of cells having radius of about 4 km.

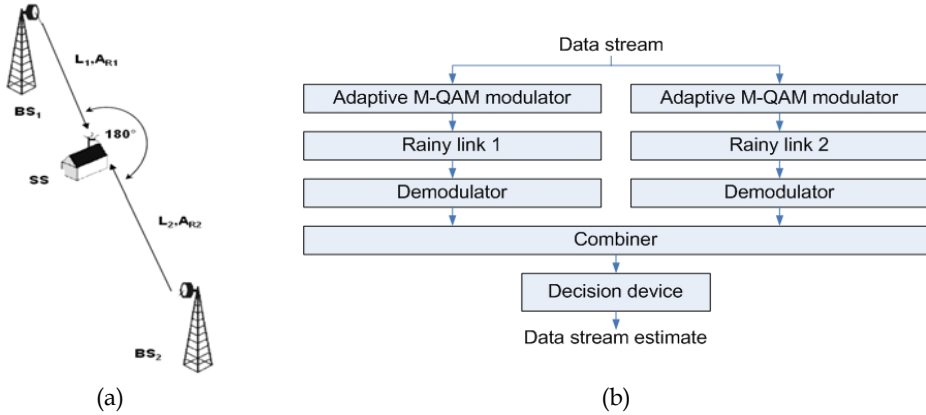


Fig. 15. Simulated communication system: (a) physical configuration and (b) system model.

SNR (dB)	< 13.6	13.6 - 20.6	20.6 - 26.8	> 26.8
Modulation	No Transmission (M_0)	4-QAM ($M_1=4$)	16-QAM ($M_2=16$)	64-QAM ($M_3=64$)

Table 9. Scenario used in adaptive modulation

4.2 Channel capacity of LMDS applying distributed MIMO

MIMO (multi-input multi-output) wireless systems with distributed antennas (D-MIMO) has been studied as a way to improve the system capacity (Lioli et al, 2009). Herein we explain the evaluation of the Shannon capacity performance of a 2x2 D-MIMO, with link configuration as used in the previous section, especially in rainy conditions. Fig. 17 shows the improvement in channel capacity due to adoption of D-MIMO. A significant increase in capacity over the SISO case can be realized when the links involved are of equal length, that is, 1 km as in Fig. 17 (a). Lower increases in capacity happen when the other link is longer, as seen in Fig. 17 (b), with positive improvement occurs only when the clear-sky SNR is about 12 dB or larger. However, it can be observed in all cases that the destructive impact of rain on the achieved capacity is not so significant.

5. Concluding remarks

A number of issues have been discussed throughout this chapter. First, raindrop size distribution measurements made in Surabaya have been found to slightly differ from that of the M-P model and those derived from Singapore measurements. Fits to Weibull and gamma have subsequently been made from the Surabaya measurements. It has also been found that large variation also occurs in raindrop fall velocity distribution, deviating from the commonly used Gunn-Kinzer model, but does not significantly change the specific attenuation estimates computed accordingly.

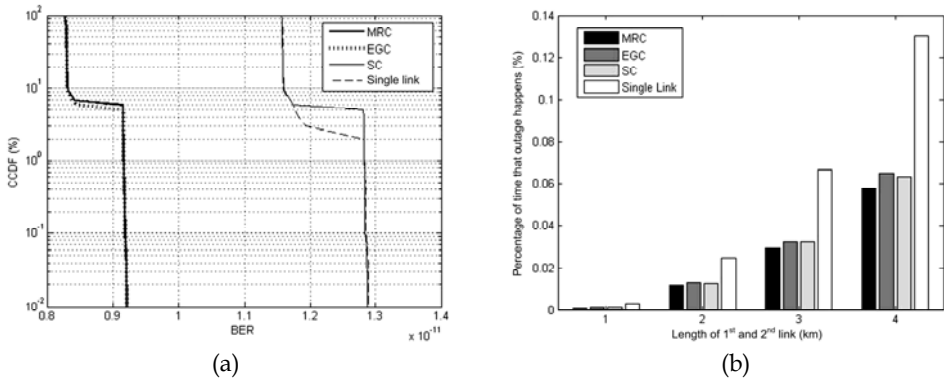


Fig. 16. Performance of dual-link systems with adaptive modulation and diversity with various combining schemes in terms of (a) CCDF of bit error rate for 1 km links and (b) outage probability for various link lengths and diversity combining techniques.

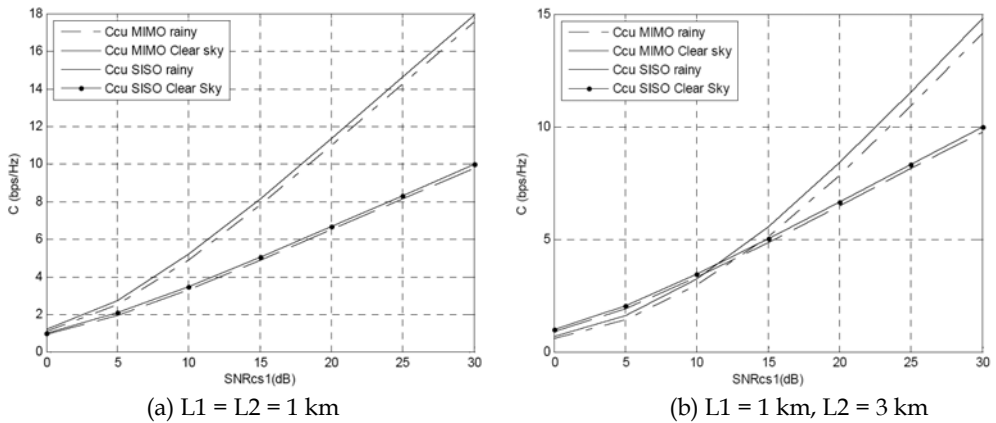


Fig. 17. The capacity of D-MIMO and SISO systems for (a) links of 1 km both and (b) unbalanced links of 1 km and 3 km.

Secondly, the solution based on spherical mode expansion has been developed to yield a set of linear equations that includes whole multiple scattering effects. Assuming that this effect is weak, we derived approximate but effective formulas for specific rain attenuation based on the exponential and Weibull models for realistic raindrop distribution. Numerical results were shown for the frequency dependence of specific attenuation at several values of rainfall and temperature. The discrepancy of the results by two models and the deviation due to temperature change were discussed.

Thirdly, a look into synthetic storm technique has shown its applicability for short links and the effects of using different statistics of wind velocity on the attenuation statistics. Attenuation statistics tend to be higher when the wind blows perpendicular to the link orientation.

Fourthly, an examination of space-time variation shows that on average convective rain events in Surabaya last longer than those in Barcelona. A deeper study into the spatial variation indicates that the spatial correlation depends on the intensity of the rain. Events with high mean squared rain rate tend to produce high spatial correlation between two sites up to 2 km apart, which suggests that the average rain cells having long intense rain are relatively large. ARMA and ARIMA modeling of rain events has also been discussed and given an example. The ARIMA model has been chosen particularly due to its ability to describe the non-stationarity of rain events.

Finally, examples have been given on the use of rain model to evaluate the performance of millimeter-wave communication systems under the impact of rain attenuation. The first example involves cell-site diversity with adaptive modulation implemented in cellular systems, while the second concerns LMDS applying distributed MIMO scheme. In particular, average bit error rate, probability of outage and channel capacity are taken as performance indicators.

6. Acknowledgement

Our studies are made possible by a research grant from JICA through the PREDICT-ITS project and a 2009 Hibah Kompetensi grant from the Indonesian Ministry of National Education. We wish to acknowledge the contribution and assistance to the reported work from our colleagues and students: Achmad Mauludiyanto, Suwadi, Muriani, Lince Markis, Haniah Mahmudah, Ari Wijayanti, Made S. Yadnya, Devy Kuswidiastuti, Adelina Hapsari, Kartika Ramadhani, Ninik Dwi Yundariani and Taufiq Ramadhany at Institut Teknologi Sepuluh Nopember, as well as Eko Setijadi and Naoki Tanaka at Kumamoto University.

7. References

- Bogush, A. J. (1989) *Radar and the Atmosphere*, Artech House, ISBN: 0-89006-222-6, Boston.
- Box, G. E. P.; Jenkins, G. M. & Reinsel, G. C (1994). *Time Series Analysis*, Prentice-Hall, ISBN-10: 0130607746.
- Brussaard, G. & Watson, P. (1995) *Atmospheric Modelling and Millimetre-Wave Propagation*, Chapman-Hall, ISBN: 0-412-56230-8, London.
- Burgueno, A.; Vilar, E. & Puigcerver, M. (1990) Spectral Analysis of 49 Years of Rainfall Rate and Relation to Fade Dynamics, *IEEE Transactions on Communications*, Vol. 38, No. 9, September 1990, 1359-1366, ISSN: 0090-6778.
- Capsoni, C., Matriccioni, E. & Mauri, M. (1981) Radar Derived Statistics of Rain Profile Slant Path, *Proceedings of URSI 20th General Assembly*, 50-57, Washington, D. C., 1981.
- Cruzan, O. R. (1962). Translation addition theorem for spherical vector wave functions, *Quarterly of Applied Mathematics*, Vol. 20. 33-40, ISSN: 0033569X.
- Drufuca, G. (1974) Rain Attenuation Statistics for Frequencies Above 10 GHz from Raingauges Observations, *Journal de Recherches Atmospherique*, Vol. 8, No. 1-2, 1974, 399-411, ISSN: 0021-7972.
- Gremont, B. C. (2004) Spatio-Temporal Rain Attenuation Model for Application to Fade Mitigation Techniques, *IEEE Transactions on Antennas and Propagation*, Vol. 52, No. 5, May 2004, 1245-1256, ISSN: 0018-926X.

- Harrington, R. F. (1961). *Time-Harmonic Electromagnetic Fields*, 292-298, McGraw-Hill, ISBN-10: 0070267456, New York
- Hendrantoro, G.; Bultitude, R. J. C. & Falconer, D. D. (2002) Use of Cell-Site Diversity in Millimeter-Wave Fixed Cellular Systems to Combat the Effects of Rain Attenuation, *IEEE Journal on Selected Areas in Communications*, Vol. 20, No. 3, April 2002, 602-614, ISSN: 0733-8716.
- Hendrantoro, G. & Zawadzki, I. (2003). Derivation of Parameters of Y-Z Power Relation from Raindrop Size Distribution Measurements and Its Application in the Calculation of Rain Attenuation from Radar Reflectivity Factor Measurements. *IEEE Transactions on Antennas and Propagation*, Vol. 51, No. 1, January 2003, 12-22, ISSN: 0018-926X.
- Hendrantoro, G. & Indrabayu (2005). A Multichannel Autoregressive Model of Rain Attenuation on Multiple Radio Links and Its Application in Assessment of Fade Mitigation Schemes in Fixed Wireless Systems Above 10 GHz, *Proceedings of URSI General Assembly*, New Delhi, September 2005.
- Hendrantoro, G.; Indrabayu; Suryani, T. & Mauludiyanto, A. (2006). A Multivariate Autoregressive Model of Rain Attenuation on Multiple Short Radio Links, *IEEE Antennas and Wireless Propagation Letters*, Vol. 5, 2006, 54-57, ISSN: 1536-1225.
- Hendrantoro, G.; Mauludiyanto, A. & Yundariani, N. D. (2007a), Application of Adaptive QAM Modulation and Diversity Scheme for 30 GHz Cellular Communications under the Impact of Rain Attention in Indonesia (in Indonesian), *IPTEK: The Journal for Technology and Science*, Vol. 18, No. 3, September 2007, 82-88.
- Hendrantoro, G.; Muriani; Cahyono, D.; Mauludiyanto, A. & Matsushima, A. (2007b) Measurement of Time-Varying Rainfall Rate in Surabaya and Estimation of Attenuation Statistics by Synthetic Storm Technique, *Proceedings of Korea-Japan Microwave Conference*, Okinawa, November 2007.
- ITU-R (2005) Specific Attenuation Model for Rain for Use in Prediction Methods, Rec P.838-3, January 2005.
- Kanellopoulos, J. D. & Koukoulas, S. G. (1987) Analysis of the Rain Outage Performance of Route Diversity Systems, *Radio Science*, Vol. 22, No. 4, July-August 1987, 549-565, ISSN: 0048-6604.
- Kuswidiastuti, D.; Suwadi & Hendrantoro, G. (2008) LMDS Channel Capacity Enhancement using D-MIMO under the Impact of Rain Attenuation, *Proceedings of Indonesian Students Scientific Meeting*, Delft, May 2008.
- Li, L. W.; Yeo, T. S.; Kooi, P. S. & Leong, M. S. (1994). Comment on Raindrop Size Distribution Model. *IEEE Transactions on Antennas and Propagation*, Vol. 12, No. 9, Sep. 1994, 1360, ISSN: 0018-926X.
- Liebe, H. J.; Hufford, G. A. & Manabe, T. (1991). A Model for the complex permittivity of water at frequencies below 1 THz, *International Journal of Infrared and Millimeter Waves*, Vol. 12, No. 7, 1991, 659-675, ISSN: 01959271.
- Lin, S. H. (1975). A Method for Calculating Rain Attenuation Distribution on Microwave Paths, *Bell System Technical Journal*, Vol. 54, No. 6, 1975, 1051-1086, ISSN: 00058580.

- Liolis, K. P.; Panagopoulos, A. D.; Cottis, P. G. & Rao, B.D. (2009) On the applicability of MIMO principle to 10-66GHz BFWA networks: capacity enhancement through spatial multiplexing and interference reduction through selection diversity, *IEEE Transactions on Communications*, Vol. 57, No. 2, February 2009, 530-541, ISSN: 0090-6778.
- Mahmudah, H.; Wijayanti, A.; Mauludiyanto, A.; Hendrantoro, G. & Matsushima, A. (2008) Evaluation of Millimeter Wave Cell Site Diversity using Synthetic Storm, *Proceedings of URSI General Assembly*, Chicago, August 2008.
- Marshall, J. S. & Palmer, W. M. (1948). The distribution of raindrops with size, *Journal of Meteorology*, Vol. 5, 1948, 165-166, ISSN: 00959634
- Maruyama, T.; Shirato, Y.; Akimoto, M. & Nakatsugawa, M. (2008) Service Area Expansion of Quasi-Millimeter FWA Systems Through Site Diversity Based on Detailed Rainfall Intensity Data, *IEEE Transactions on Antennas and Propagation*, Vol. 56, No. 10, Oct. 2008, 3285 - 3292, ISSN: 0018-926X.
- Maseng, T. & Bakken, P. M. (1981) A Stochastic Dynamic Model of Rain Attenuation, *IEEE Transactions on Communications*, Vol. COM-29, No. 5, May 1981, 660-669, ISSN: 0090-6778.
- Matricciani, E. (1996) Physical-Mathematical Model of the Dynamics of Rain Attenuation Based on Rain Rate Time Series and a Two-Layer Vertical Structure of Precipitation, *Radio Science*, Vol. 31, No. 2, March-April 1996, 281-295, ISSN: 0048-6604.
- Matricciani, E. (2004) Service Oriented Statistics of Interruption Time Due to Rainfall in Earth-Space Communication Systems, *IEEE Transactions on Antennas and Propagation*, Vol. 52, No. 8, August 2004, 2083-2090, ISSN: 0018-926X.
- Matricciani, E. & Riva, C. (2005) The Search for the Most Reliable Long-Term Rain Attenuation CDF of a Slant Path and the Impact on Prediction Models, *IEEE Transactions on Antennas and Propagation*, Vol. 53, No. 9, September 2005, 3075-3079, ISSN: 0018-926X.
- Mauludiyanto, A; Muriani; Markis, L.; Hendrantoro, G. & Matsushima, A. (2007) Preliminary Results from the Study of Raindrop Size Distribution and Rainfall Rate in Indonesia for the Development of Millimetre-Wave Systems in Tropical Regions, *Proceedings of International Symposium on Antennas and Propagation*, Niigata, 2007.
- Morita, K. & Higuti, I. (1976) Prediction Methods for Rain Attenuation Distributions of Micro- and Millimeter Waves, *Review of the Electronic Communication Laboratory*, Vol. 24, No. 7-8, July-August 1976, 651-668.
- Morita, K. & Higuti, I. (1978). Statistical Studies on Rain Attenuation and Site Diversity Effect on Earth to Satellite Links in Microwave and Millimeter Wavebands, *Transactions of The IECE of Japan*, Vol. E 61, No. 6.
- Panagopoulos, A.D.; Skouloudakis, P.V. & Cottis, P.G. (2006) Quality of Service of Broadband Fixed Wireless Access QPSK Channels Interfered by Adjacent Terrestrial Links, *IEEE Transactions on Antennas and Propagation*, Vol. 54, No. 11, Nov. 2006, 3317 - 3326, ISSN: 0018-926X.
- Paulson, K. S. (2002) The Spatial-Temporal Statistics of Rain Rate Random Fields, *Radio Science*, Vol. 37, No. 5, September 2002, ISSN: 0048-6604.
- Pruppacher, H. R. & Pitter, R. L. (1971). A semi-empirical determination of the shape of cloud and rain drops, *Journal of the Atmospheric Sciences*, Vol. 28, No. 1, 1971, 86-94, ISSN: 00224928

- Sakarellos, V. K.; Skraparlis, D.; Panagopoulos, A. D. & Kanellopoulos, J. D. (2009) Optimum Placement of Radio Relays in Millimeter-Wave Wireless Dual-Hop Networks, *IEEE Antennas and Propagation Magazine*, Vol. 51, No. 2, April 2009, 190 – 199, ISSN: 1045-9243.
- Salehudin, M.; Hanantasena, B. & Wijdeman, L. (1999). Ka-Band Line-of-Sight Radio Propagation Experiment in Surabaya Indonesia. *Proceedings of 5th Ka-Band Utilization Conference*, Taormina, 1999.
- Sánchez-Lago, I.; Fontán, F. P.; Mariño, P. & Fiebig, U. -C. (2007) Validation of the Synthetic Storm Technique as Part of a Time-Series Generator for Satellite Links, *IEEE Antennas and Wireless Propagation Letters*, Vol. 6, 2007, 372-375, ISSN: 1536-1225.
- Sekine, M.; Chen, C. D. & Musha, T. (1987). Rain attenuation from log-normal and Weibull rain-drop distributions, *IEEE Transactions on Antennas and Propagation*, Vol. 35, No. 3, March 1987, 358-359, ISSN: 0018926X.
- Stratton, J. A. (1941). *Electromagnetic Theory*, 392-423, McGraw-Hill, ISBN-10: 0070621500, New York.
- Suwadi; Hendratoro, G.; Murdaningtyas, C. D. (2009) Performance of Selection Combining and Adaptive Coded Modulation in Millimeter-Wave Wireless Communication Systems under the Impact of Rain Attenuation in Indonesia (in Indonesian), *Proceedings of National Seminar on Electrical Engineering, Informatics and Education*, Malang, July 2009.
- Sweeney, D. G. & Bostian, C. W. (1999) Implementing Adaptive Power Control as a 30/20-GHz Fade Countermeasure, *IEEE Transactions on Antennas and Propagation*, Vol. 47, No. 1, January 1999, 40-46, ISSN: 0018-926X.
- Tan, J. & Goddard, J. W. F. (1998). Radar-derived area coverage, *Proceedings of 8th URSI Commission F Triennial Open Symposium on Wave Propagation and Remote Sensing*, Aveiro, Portugal, Sept. 22-25, 1998, 51-54.
- Timothy, K. I.; Ong, J. T. & Choo, E. B. L. (2002) Raindrop Size Distribution Using Method of Moments for Terrestrial and Satellite Communication Applications in Singapore. *IEEE Transactions on Antennas and Propagation*, Vol. 15, No. 10, October 2002, 1420-1424, ISSN: 0018-926X.
- Tokay, A.; Wolff, K. R.; Bashor, P. & Dursun, O. K. (2003). On the Measurement Errors of the Joss-Waldvogel Disdrometer. *Proceedings of 31st Int. Conf. on Radar Meteorology*, Seattle, August 2003.
- van de Kamp, M. M. J. L. & Castanet, L. (2002) Fade Dynamics Review, *Proceedings of COST 280 1st International Workshop*, Malvern, July 2002.
- Yadnya, M. S.; Mauludiyanto, A.; Hendratoro, G. (2008a). ARMA Modeling of Rain Rate in Surabaya (In Indonesian), *Proceedings of Seminar on Intelligent Technology and Its Application*, Surabaya, May 2008.
- Yadnya, M.S.; Mauludiyanto, A.; Hendratoro, G. (2008b) ARMA Modeling from rain rate Measurement to Simulation Communication Channel Modeling for Millimeter Wave in Surabaya, *The 6th Kumamoto University Forum*, Surabaya, November 5-6, 2008.
- Yeo, T. S.; Kooi, P. S. & Leong, M. S. (1996). A Two-Year Measurement of Rainfall Attenuation of CW Microwaves in Singapore. *IEEE Transactions on Antennas and Propagation*, Vol. 41, No. 6, June 1993, 709-712, ISSN: 0018-926X.

High-Temporal Global Rainfall Maps from Satellite Passive Microwave Radiometers

Shoichi Shige
Kyoto University
Japan

Satoshi Kida & Tomoya Yamamoto
Osaka Prefecture University
Japan

Takuji Kubota
Japan Aerospace Exploration Agency
Japan

Kazumasa Aonashi
Meteorological Research Institute
Japan

1. Introduction

High-precision and high-temporal global rainfall maps are very important for scientific studies for global water cycle and practical applications for water resources. However, rainfall has been poorly measured by ground-based observations. In particular, very few in situ measurements of rainfall are available for over the oceans owing to sparse observations. Therefore, satellite remote sensing is the only way to measure rainfall globally. Historically, the earliest satellite observations of the Earth were made in the visible and infrared regions. Therefore, cloud-top temperature and cloud patterns from visible and infrared radiometers had been used to estimate rainfall globally based on an empirical relationship with ground-level rain rate (e.g. Arkin & Meisner 1987).

A more direct measure of rainfall can be obtained using passive microwave radiometers (MWRs) because its ability to penetrate clouds and measure the emitted radiation from rainwater and the scattering caused by cloud ice and snow. During the past three decades, passive MWRs have evolved from single-channel radiometers with low spatial resolution such as the Electronically Scanning Microwave Radiometer (ESMR) on Nimbus-5 to higher-resolution sensors with many channels such as the Advanced Microwave Scanning Radiometer for the Earth Observing System (AMSR-E; Kawanishi et al. 2003) aboard the *Aqua* satellite. Since the launch of the first Special Sensor Microwave Imager (SSM/I; Hollinger et al. 1990; Colton & Poe 1999) on the Defense Meteorological Satellite Program (DMSP), passive MWRs have been a standard instrument in global rainfall retrieval. The problems of passive MWR rainfall retrieval algorithms lie in the fact they are not fully constrained. Since brightness temperatures (Tbs) measured by

passive MWRs are the end product of the integrated effects of electromagnetic absorption/emission and scattering through a precipitating cloud along the sensor viewpath, a priori model or database for the three-dimensional (3D) properties of precipitating clouds are required to establish relationship between Tbs and rain rates.

A new age of active microwave remote sensing of precipitation from space began with the launch of the Tropical Rainfall Measuring Mission (TRMM; Simpson et al. 1988, 1996) which carries the first space-borne radar (Precipitation Radar (PR); Kozu et al. 2001; Okamoto 2003; Okamoto & Shige 2008) together with the TRMM Microwave Imager (TMI; Kummerow et al. 1998). The PR has enabled us to directly obtain vertical profiles of precipitation over the global Tropics (Iguchi 2007; Iguchi et al. 2000, 2009). Information obtained by the TRMM PR accelerated the development of passive MWR rainfall retrieval algorithms (Viltard et al. 2006; Kummerow et al. 2007). One algorithm using precipitation-related variable models and retrieval methods based on TRMM observation studies is the Global Satellite Mapping of Precipitation (GSMaP) algorithm (Aonashi et al. 2009; Kubota et al. 2007). The GSMaP algorithm has been applied to MWRs currently in orbit such as SSM/I, TMI, and AMSR-E to produce global precipitation maps. Despite the improved rainfall estimates using data from passive MWRs, the challenge remains to further fill information gaps through more frequent satellite observations. Passive MWRs are generally of two types: imagers and sounders. Microwave imagers (MWIs) such as the SSM/I, TMI and AMSR-E, and have channels suitable for monitoring precipitation. Microwave sounders (MWSs) such as the Advanced Microwave Sounding Unit (AMSU) (Mo 1996; Saunders et al. 1995) aboard the National Oceanic and Atmospheric Administration (NOAA) satellites and the first satellite of the Meteorological Operational satellite program (MetOp-A) are primarily developed for profiling atmospheric temperature and moisture using opaque spectral regions. Two AMSU-based rainfall retrieval algorithms have been developed. One is a neural-network-based algorithm developed at the Massachusetts Institute of Technology, Cambridge (Surussavadee & Staelin 2008a,b). The algorithm is trained using a cloud-resolving model. The other is the Microwave Surface and Precipitation Products System (MSPPS) Day-2 rainfall algorithm for the AMSU and has been developed at NOAA (Ferraro et al. 2005).

Because there have been four AMSU instruments in orbit since the launch of NOAA18 in 2005, together with five MWIs (TMI, AMSR-E, and SSM/I), there have been more observations of rainfall in time and space, with swaths being ~2200 km wide. Another advantage of the four AMSU sensors on the NOAA satellites and MetOp-A is that they are typically spaced about 4 h in time, thus giving a better representation of the diurnal cycle.

Kubota et al. (2009) demonstrated effective performance of the merger of the MWSs in addition to the MWIs by the ground-radar validation around Japan. However, the multitude of satellite data sources does not come without its problem. Bias errors in the retrieved rain rates that vary between MWIs and MWSs are troublesome for many applications. The only way to try to overcome this problem is to develop a consensus algorithm applicable to both MWIs and MWSs based on the same physical principle. Recently, Shige et al. (2009) developed an over-ocean rainfall retrieval algorithm for MWS (GSMaP_MWS) that shares at a maximum a common algorithm framework with the GSMaP algorithm for MWI (GSMaP_MWI; Aonashi et al. 2009; Kubota et al. 2007). The purpose of this paper is to briefly describe GSMaP_MWS algorithm and provide examples of rainfall maps from MWRs (MWIs + MWSs).

2. Overview of retrieval algorithm

A flowchart of the GSMaP_MWI and GSMaP_MWS algorithms is shown in Fig. 1. Here, the TMI version of GSMaP_MWI (GSMaP_TMI) and the AMSU version of GSMaP_MWS (GSMaP_AMSU) are described. Similar to the GSMaP_MWI algorithm, the GSMaP_MWS algorithm consists of two parts: the forward calculations for making the lookup tables (LUTs) showing the relationship between rainfall rates and Tbs with a radiative transfer model (RTM), and the retrieval part to estimate precipitation rates from the observed Tbs using the LUTs. The GSMaP_MWS algorithm shares information required for the RTM calculation with the GSMaP_MWI algorithm. Also in the retrieval process, the GSMaP_MWS algorithm retains the basic structure of the GSMaP_MWI algorithm.

2.1 Forward calculation

The RTM calculation requires information on atmospheric variables, as well as precipitation-related variables. Atmospheric temperature, freezing-level height (FLH), surface winds, and surface temperature are adapted from the Japan Meteorological Agency (JMA) global analysis (GANAL). Similarly, sea surface temperature is adapted from JMA merged satellite and *in situ* data global daily sea surface temperatures in the global ocean. As for relative humidity, the constant value of 100% is assumed.

The convective and stratiform precipitation models for precipitation-related variables (hydrometer profiles, drop-size distribution (DSD), etc.) are constructed for ten precipitation types. Precipitation types are determined in terms of stratiform pixel ratio, stratiform rain ratio, precipitation area, precipitation top height, rain intensity, and diurnal cycle from the PR data, together with the ratio between PR precipitation rates and TRMM lightning imaging sensor flash rates (Takayabu & Katayama 2004; Takayabu 2006, 2008). Precipitation types consist of six land types (severe thunderstorm, afternoon shower, shallow convection, extratropical cyclone, organized convection, and highland rain) and four ocean types (shallow convection, extratropical cyclone, transition zone, and organized convection). Global distributions of the precipitation types in $2.5^\circ \times 2.5^\circ$ latitude-longitude boxes are statistically classified trimonthly.

The convective and stratiform precipitation profiles of PR data are averaged over prescribed precipitation ranges for each precipitation type. In this averaging, profiles relative to FLH are used to exclude the influence of atmospheric temperature variations (Kubota et al. 2007). The database of precipitation types and profiles makes it possible for the algorithm to deal with trimonthly variation of typical hydrometeor profiles.

For rain DSD, a gamma distribution of rain drop size is assumed:

$$N(D) = N_0 D^\mu \exp(-\Lambda D) \quad (1)$$

where $N(D)$ is the number concentration for particles with diameter D , $\mu=3$, N_0 and Λ are parameters to be determined. For convective precipitation, N_0 and Λ are determined using DSD parameter estimated from the “ α -adjustment” method of PR algorithm (Kozu et al. 2009). For stratiform precipitation, the standard values of N_0 and Λ assumed in PR algorithm is used.

On the other hand, conventional models were used for frozen and mixed-phase particle-size distribution that could not be estimated from the TRMM PR observation. The exponential distribution is used for the DSD model of snow and graupel. The refractivity of convective

and stratiform frozen particles is calculated, assuming them as the mixture of ice and air with an empirically prescribed constant density (200 kg m^{-3}). Particle-size distribution and refractivity for mixed-phase stratiform precipitation (between FLH minus 1 km and FLH) were parameterized in terms of atmospheric temperature (Nishitsuji et al. 1983; Takahashi & Awaka 2005), while mixed-phase convective precipitation was neglected.

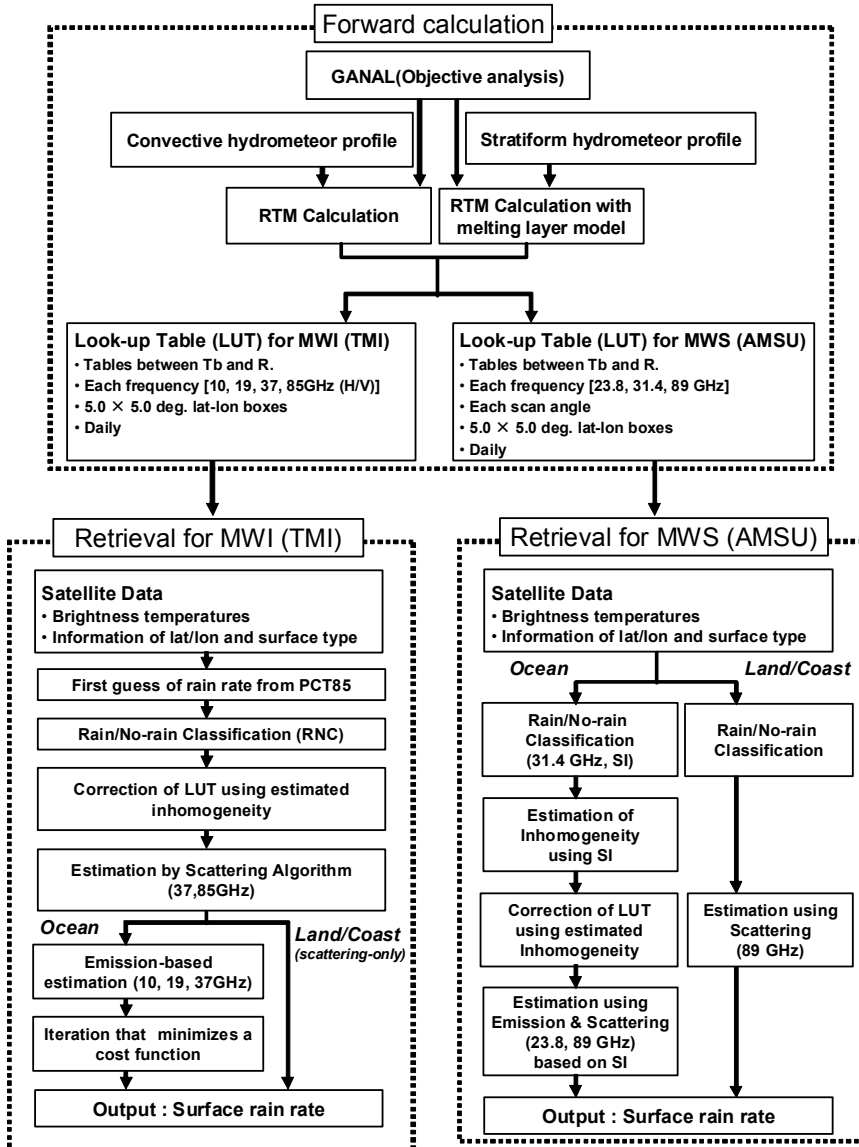


Fig. 1. Flowchart for the GSMaP algorithm for microwave imager (MWI) and microwave sounder (MWS)

From forward calculations with a four-stream RTM (Liu 1998), LUTs showing the relationship between rainfall rates and Tbs were computed daily in $5.0^\circ \times 5.0^\circ$ latitude-longitude boxes. While conical scanning radiometers such as the TMI preferentially scan at a constant slant path angle, the AMSU radiometer uses cross-track scanning to view the Earth. The variations in path lengths through which the atmosphere is viewed by cross-track scanning should be taken into account. For the AMSU, the received polarization also varies with scan angle because of the rotating-reflector/fixed-feed horn antenna design. This is different from that of imagers using a conical scanning mechanism, which receive a fixed polarization independent of the scan. At a given scan angle θ_s , the normalized surface emitted radiation (i.e., emissivity) ε_s seen by the AMSU contains mixed vertical ε_V and horizontal ε_H polarizations (the very small cross-polarized contribution due to imperfect cross-polarization isolation in the antenna is neglected), i.e.,

$$\varepsilon_s = \varepsilon_V(\theta) \cos 2\theta_s + \varepsilon_H(\theta) \sin 2\theta_s \quad (2)$$

where the local zenith angle θ (LZA) varies as a function of scan angle θ_s (Grody et al. 2001). The LUTs are produced for each scan angle from RTM calculations using (2). For a sea surface, the emissivity components ε_V and ε_H are calculated using the Fresnel formula for calm seas (Guillou et al. 1998), together with an empirical model that includes the effects of wind-driven foam and surface roughness on emissivity (Schuessel & Luthardt 1991), while for a land surface, they are set at 0.9.

2.2 Retrieval

The retrieval process of the GSMaP_MWS has been developed, retaining the basic structure of the GSMaP_MWI algorithm. Emission signatures are mainly used to determine rainfall, while scattering signatures are used to help define the nature of precipitation. Taking advantage of 150 GHz of AMSU, an SI is defined as follows:

$$SI = (Tb_{89} - Tb_{89_{LUT0}}) - (Tb_{150} - Tb_{150_{LUT0}}). \quad (3)$$

where $Tb_{89_{LUT0}}$ and $Tb_{150_{LUT0}}$ are Tb_{89} and Tb_{150} at 0 mm h^{-1} in the LUTs, respectively. Because the response to snow and graupel lowers the Tb and increases strongly with frequency, the Tb reduction is higher at 150 GHz than at 89 GHz. Thickness between precipitation top height and freezing level height increases with AMSU-B SI (Fig. 6 of Shige et al. 2009). In the retrieval process, SI is used as a key parameter.

Similar to the GSMaP_MWI algorithm, rain or no-rain flags are identified by deterministic methods at the beginning of this process. Then, the horizontal inhomogeneity of rainfall within rather large AMSU FOVs is taken into account by the algorithm in order to properly compensate for nonlinearities in the Tbs versus water content relationships. The LUTs at 23 GHz and 89 GHz are corrected using the horizontal inhomogeneity of rainfall estimated from SI for AMSU-A and AMSU-B FOVs, respectively. Using the corrected LUTs, rain rates are retrieved from Tb_{23} and Tb_{89} , and these estimates are combined depending SI to give the rainfall estimate at AMSU-B FOV.

3. Results

3.1 The matched TRMM and NOAA-15(NK) case

In principle, rainfall retrievals using data from the PR and TMI aboard the TRMM satellite are superior to those using data from AMSU instruments, which have coarser FOVs and channels for profiling atmospheric temperature and moisture instead of precipitation. The PR provides height information based upon the time delay of the precipitation-backscattered return power and allows vertical profiles of precipitation to be obtained directly. The TMI is equipped with channels suitable for monitoring precipitation; in particular, 10 GHz channel has nearly linear relationship between rainfall rates and T_b s. Thus, a comparison of AMSU estimates against TRMM estimates is very useful for the development and validation of AMSU rainfall retrievals.

Figure 2 shows rain-rate maps from PR, GSMaP_TMI, and GSMaP_AMSU for the matched TRMM and NOAA-15(NK) case on 25 July 2005 over Atlantic Ocean, together with that from the Microwave Surface and Precipitation Products System (MSPPS) Day-2 rainfall algorithm for the AMSU. The MSPPS Day-2 rainfall algorithm for the AMSU (hereinafter NOAA_AMSU) was developed at NOAA (Ferraro et al. 2005). A simultaneous retrieval of the ice water path (IWP) and ice-particle effective diameter (D_e) from T_b data at 89 and 150 GHz was performed through two processes: simplifying the radiative transfer equation into a two-stream approximation and estimating the cloud-base and cloud-top T_b s through the use of AMSU measurements at 23.8 and 31.4 GHz. The rain rate was computed based on an IWP and rain-rate relation derived from the GPROF algorithm database, which contains the profiles of various hydrometeors generated from the cloud-resolving models. The weakness of the NOAA_AMSU algorithm was that only precipitation that is detectable from a scattering signature can be estimated (Huffman et al. 2007, Joyce et al. 2004). Recently, a new correction has been developed for the AMSU-A cloud liquid water content to fill in the gaps of NOAA_AMSU retrievals over ocean (Vila et al. 2007). Rain estimates shown in Fig. 2 d were derived using the improved NOAA_AMSU algorithm.

It can be seen with AMSU has much wider swath (~ 2200 km; Fig. 2c, d) than PR (~ 220 km; Fig. 2a) and TMI (~ 760 km; Fig. 2b), giving more observation of rainfall in time and space. Both GSMaP_AMSU and NOAA_AMSU depict similar large-scale structure with PR and GSMaP_TMI. However, there is considerable disagreement between GSMaP_AMSU and NOAA_AMSU at the finescale. GSMaP_AMSU detects scattered rain pixels, while NOAA_AMSU does not. The rain/no-rain classification method in GSMaP_AMSU uses not only the AMSU-A data but also SI from the AMSU-B data, leading to detection of scattered rain pixels.

3.2 Combined microwave estimates

Figure 3 shows combined precipitation estimate for the 3-h period from MWIs (SSM/I on three DMSP satellites, TMI on TRMM and AMSR-E on *Aqua*). The coverage of these MWIs is about 60 % of the earth's surface in the latitude band 60°N-S . On the other hand, Fig. 4 shows combined precipitation estimate for the 3-h period from passive MWIs and MWSs (i.e. AMSU). The addition of AMSU allows for better coverage (about 90 %), thus adding improved global rainfall retrieval. The data voids in the latitude band $45^\circ\text{S-}60^\circ\text{S}$ arise not from the lack of the data from MWIs and MWSs, but from unfavorable condition. The

current GSMaP algorithm mask sea ice regions where rain retrievals are not possible using AMSR-E Sea Ice Concentration product (Comiso 2009).

Combined precipitation estimate for the 3-h period from MWIs and MWRs has been obtained by Joyce et al. (2004) and Huffman et al. (2007; their Fig. 1). Different precipitation retrieval algorithms were applied to MWIs and MWSs. For example, in the study of Huffman et al. (2007), passive microwave FOVs from the TMI, AMSR-E, and SSM/I were converted to precipitation estimates with the Goddard Profiling Algorithm (GPROF) (Kummrow et al. 1996, 2001; Olson et al. 2006; Wilheit et al. 2003), while those from AMSU were converted to precipitation estimates with the NOAA_AMSU algorithm (Ferraro et al. 2005). The primary difference from the previous studies is that the combined precipitation estimate shown in Fig. 4 is deduced from the algorithms for MWIs and MWSs that share information required for the RTM calculation and the basic structure of retrieval process (Fig. 1).

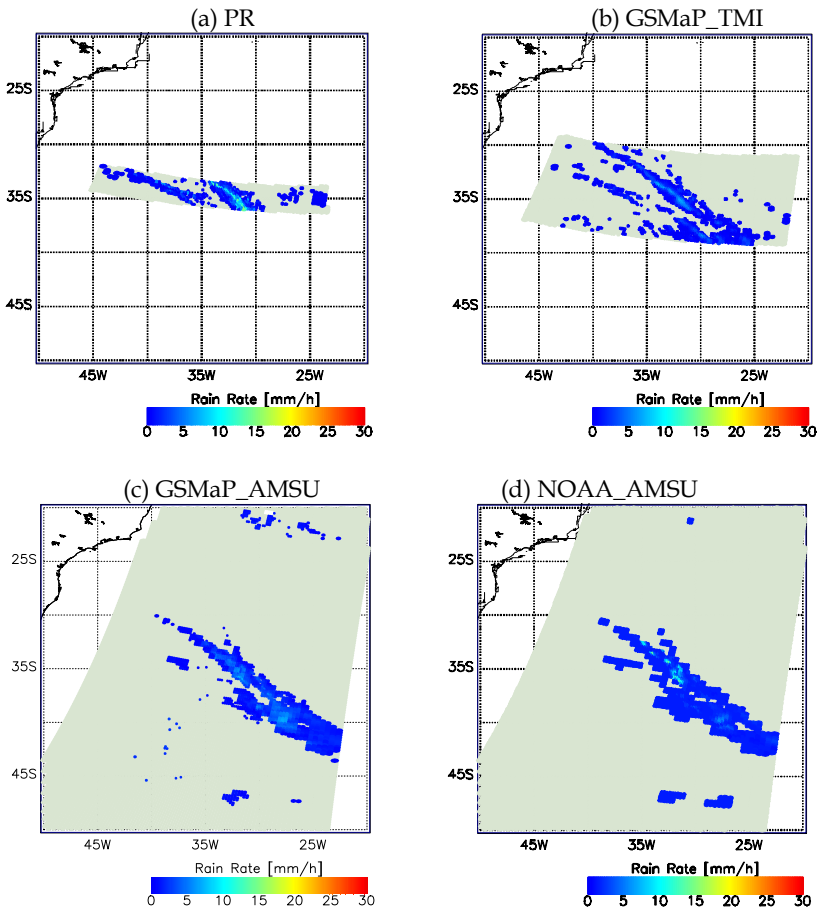


Fig. 2. Rain-rate maps from PR (a), GSMaP_TMI (b) and GSMaP_AMSU (c) for the matched TRMM and NOAA-15(NK) case on 25 July 2005.

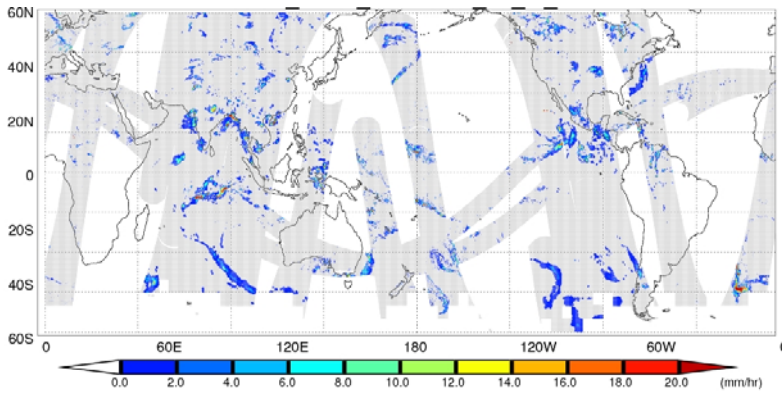


Fig. 3. Combined microwave precipitation estimate at $0.1^\circ \times 0.1^\circ$ for the 3-h period centered at 0130 UTC 25 July 2005 in mm h^{-1} from the TMI, SSM/I, and AMSR-E. Whited-out areas denote regions that lack reliable estimates. (TMI, SSM/I, and AMSR-E are averaged where overlaps occur.)

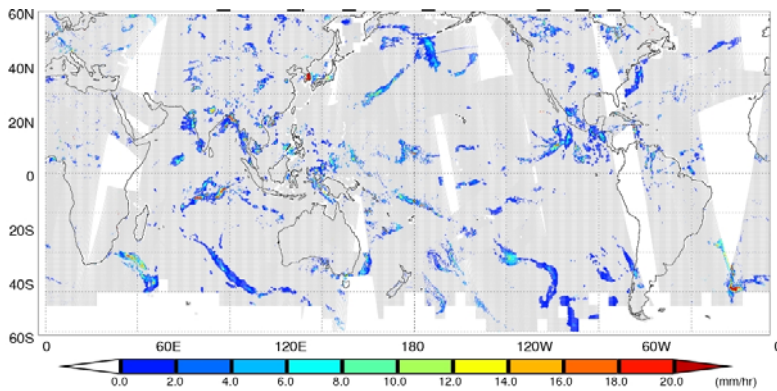


Fig. 4. Same as Fig. 3, but for combined microwave precipitation estimate from the TMI, SSM/I, AMSR-E and AMSU. (TMI, SSM/I, AMSR-E, and AMSU are averaged where overlaps occur.)

4. Discussion and Future Work

As already noted, rainfall retrievals using data from MWIs such as TMI are superior to those using data from MWSs such as AMSU. Figure 5 compares GSMaP_TMI-retrieved and GSMaP_AMSU-retrieved rain rates at $0.1^\circ \times 0.1^\circ$ with rain rates estimated from the ground-based radar at Kwajalein Island, Republic of the Marshall Islands (Wolff et al. 2005). Although it is hard to tell whether the pattern of the GSMaP_TMI rain rates is biased with respect to the Kwajalein radar estimated-rain rates, the GSMaP_AMSU algorithm clearly overestimates (underestimates) rainfall at light (heavy) rain rates. While the TMI scan at a

constant slant path angle, the AMSU radiometer uses cross-track scanning to view the Earth, resulting in the variations in the size of individual FOVs. This variation may lead to less agreement with KR-estimated rain and should be corrected.

Both the GSMaP_MWI and GSMaP_MWS algorithms have been developed using information obtained by the TRMM PR in the latitude band 35°N-35°S. Therefore, uncertainties should be large in the regions where the TRMM PR data is unavailable. The upcoming Global Precipitation Measurement (GPM) core satellite will carry dual-wavelength precipitation radar (DPR) with Ku/Ka-band (13.6/35.5 GHz) and cover the latitude band 65°N-65°S (Senbokuya et al. 2004). Information obtained by the GPM DPR will be used to improve precipitation estimates in the future.

Recently, a new type of MWR suitable for precipitation retrieval and temperature and moisture sounding, such as the Special Sensor Microwave Imager-Sounder (SSMIS; Kunkee et al. 2008), has been carried by satellites. The GPM Microwave Imager, which will be carried by the GPM core satellite together with DPR, also will employ 166 GHz and 183.31 GHz band channels in addition to channels suitable for monitoring precipitation. Thus, it is important to develop the GSMaP algorithm for this type of MWRs.

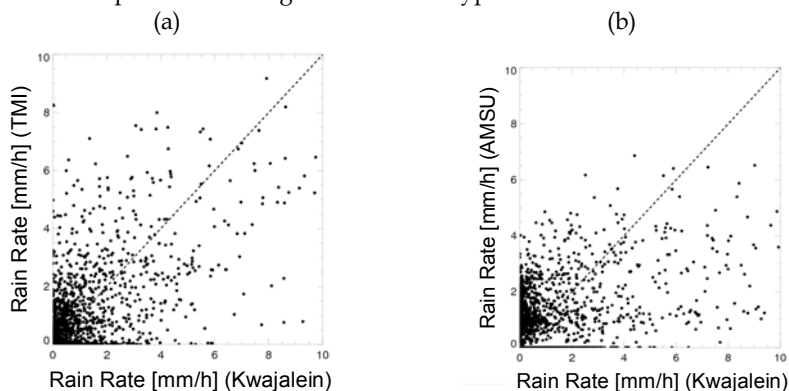


Fig. 5. Scatterplots comparing (a) GSMaP_TMI-retrieved and (b) GSMaP_AMSU-retrieved rain rates to KR-estimated rain rates at $0.1^\circ \times 0.1^\circ$. Dashed line shows 1:1 relation.

5. Acknowledgements

This study has been supported by the Japan Aerospace Exploration Agency under the 5th TRMM RA and the Mitsui & Co., Ltd. Environment Fund.

6. References

- Aonashi, K.; Awaka, J.; Hirose, M.; Kozu, T.; Kubota, T.; Liu, G.; Shige, S.; Kida, S.; Seto, S.; Takahashi, N. & Takayabu, Y. N. (2009). GSMaP passive microwave precipitation retrieval algorithm: algorithm description and validation, *J. Meteor. Soc. Japan*, vol. 87A, pp. 119-136.
- Arkin, P. A. & Meisner, B. N. (1987). The relationship between largescale convective rainfall and cold cloud over the Western Hemisphere during 1982-84. *Mon. Wea. Rev.* vol. 115, pp. 51-74.

- Colton, M. C. & Poe, G. A. (1999). Intersensor calibration of DMSP SSM/I's: F-8 to F-14, 1987–1997, *IEEE Trans. Geosci. Remote Sens.*, vol. 37, no. 1, pp. 418–439.
- Comiso, J. C. (2009). Enhanced sea ice concentrations and ice events from AMSR-E data, *J. Remote Sens. Soc. Japan*, vol. 29, no. 1, pp. 195–215.
- Ferraro, R. F.; Weng, F.; Grody, N.; Zhao, L.; Meng, H.; Kongoli, C.; Pellegrino, P.; Qiu, S. & Dean, C. (2005). NOAA operational hydrological products derived from the Advanced Microwave Sounding Unit (AMSU), *IEEE Trans. Geosci. Remote Sens.*, vol. 43, no. 5, pp. 1036–1049.
- Grody, N.; Zhao, J.; Ferraro, R.; Weng, F. & Boers, R. (2001). Determination of precipitable water and cloud liquid water over oceans from the NOAA 15 Advanced Microwave Sounding Unit, *J. Geophys. Res.*, vol. 106, no. D3, pp. 2943–2954, 10.1029/2000JD900616.
- Guillou, C.; Ellison, W.; Eymard, L.; Lamkaouchi, K.; Prigent, C.; Delbos, G.; Balana, G. & Boukabara, S. A. (1998). Impact of new permittivity measurements on sea surface emissivity modeling in microwaves, *Radio Sci.*, vol. 33, no. 3, pp. 649–667.
- Hollinger, J. P.; Peirce, J. L. & Poe, G. A. (1990). SSM/I instrument evaluation, *IEEE Trans. Geosci. Remote Sens.*, vol. 28, no. 5, pp. 781–790.
- Huffman, G.; Adler, R.; Bolvin, D.; Gu, G.; Nelkin, E.; Bowman, K.; Hong, Y.; Stocker, E. & Wolff, D. (2007). The TRMM Multisatellite Precipitation Analysis (TMPA): Quasi-global, multiyear, combined-sensor precipitation estimates at fine scales, *J. Hydrometeorol.*, vol. 8, no. 1, pp. 38–55.
- Iguchi, T.; Kozi, T.; Meneghini, R.; Awaka, J. & Okamoto, K. (2000). Rain profiling algorithm for the TRMM precipitation radar, *J. Appl. Meteorol.*, vol. 39, no. 12, pp. 2038–2052.
- Iguchi, T. (2007). Spaceborne radar algorithms, in *Measuring Precipitation From Space – EURAINSAT and the Future*, V. Levizzani, P. Bauer, and F. J. Turk, Eds. New York: Springer-Verlag, pp. 199–212, 2007.
- Iguchi, T.; Kozi, T.; Kwiatkowski, J.; Meneghini, R.; Awaka, J. & Okamoto, K. (2009). Uncertainties in the rain profiling algorithm for the TRMM precipitation radar, *J. Meteorol. Soc. Japan*, vol. 87A, pp. 1–30.
- Joyce, R. J.; Janowiak, J. E.; Arkin, P. A. & Xie, P. (2004). CMORPH: A method that produces global precipitation estimates from passive microwave and infrared data at high spatial and temporal resolution, *J. Hydrometeorol.*, vol. 5, no. 3, pp. 487–503.
- Kawanishi, T.; Sezai, T.; Ito, Y.; Imaoka, K.; Takeshima, T.; Ishido, Y.; Shibata, A.; Miura, M.; Inahata, H. & Spencer, R. W. (2003). The Advanced Microwave Scanning Radiometer for the Earth Observing System (AMSR-E), NASDA's contribution to the EOS for global energy and water cycle studies, *IEEE Trans. Geosci. Remote Sens.*, vol. 41, no. 2, pp. 184–194.
- Kozi, T.; Kawanishi, T.; Kuroiwa, H.; Kojima, M.; Oikawa, K.; Kumagai, H.; Okamoto, K.; Okumura, M.; Nakatsuka, H. & Nishikawa, K. (2001). Development of precipitation radar onboard the Tropical Rainfall Measuring Mission satellite, *IEEE Trans. Geosci. Remote Sens.*, vol. 39, no. 1, pp. 102–116.
- Kozi, T.; Iguchi, T.; Kubota, T.; Yoshida, N.; Seto, S.; Kwiatkowski, J. & Takayabu, Y. N. (2009). Feasibility of raindrop size distribution parameter estimation with TRMM precipitation radar, *J. Meteorol. Soc. Japan*, vol. 87A, pp. 53–66.

- Kubota, T.; Shige, S.; Hashizume, H.; Aonashi, K.; Takahashi, N.; Seto, S.; Hirose, M.; Takayabu, Y. N.; Nakagawa, K.; Iwanami, K.; Ushio, T.; Kachi, M. & Okamoto, K. (2007). Global precipitation map using satelliteborne microwave radiometers by the GSMaP project: Production and validation, *IEEE Trans. Geosci. Remote Sens.*, vol. 45, no. 7, pp. 2259–2275.
- Kubota, T.; Ushio T.; Shige S.; Kida S.; Kachi, M. & Okamoto K. (2009). Verification of high resolution satellite-based rainfall estimates around Japan using gauge-calibrated ground radar dataset. *J. Meteor. Soc. Japan*, vol. 87A, pp. 203–222.
- Kummerow, C.; Barnes W.; Kozu T.; Shiue J. & Simpson J. (1998). The Tropical Rainfall Measuring Mission (TRMM) sensor package, *J. Atmos. Ocean. Technol.*, vol. 15, no. 3, pp. 809–817.
- Kummerow, C.; Olson, W. S. & Giglio, L. (1996). A simplified scheme for obtaining precipitation and vertical hydrometeor profiles from passive microwave sensors, *IEEE Trans. Geosci. Remote Sens.*, vol. 34, no. 5, pp. 1213–1232.
- Kummerow, C. D.; Hong, Y.; Olson, W. S.; Yang, S.; Adler, R. F.; McCollum, J.; Ferraro, R.; Petty, G.; Shin, D. B. & Wilhelm, T. T. (2001). The evolution of the Goddard profiling algorithm (GPROF) for rainfall estimation from passive microwave sensors, *J. Appl. Meteorol.*, vol. 40, no. 11, pp. 1801–1820.
- Kummerow, C.; Masunaga, H. & Bauer, P. (2007). A next-generation microwave rainfall retrieval algorithm for use by TRMM and GPM, in *Measuring Precipitation From Space – EURAINSAT and the Future*, V. Levizzani, P. Bauer, and F. J. Turk, Eds. New York: Springer-Verlag, pp. 235–252, 2007.
- Kunkee, D. B.; Poe, G. A.; Boucher, D. J.; Swadley, S. D.; Hong, Y.; Wessel, J. E. & Uliana, E. A. (2008). Design and evaluation of the first Special Sensor Microwave Imager/Sounder, *IEEE Trans. Geosci. Remote Sens.*, vol. 46, no. 4, pp. 863–883.
- Liu, G. (1996). A fast and accurate model for microwave radiance calculation, *J. Meteorol. Soc. Japan*, vol. 76, no. 2, pp. 335–343.
- Mo, T. (1996). Prelaunch calibration of the Advanced Microwave Sounding Unit-A for NOAA-K, *IEEE Trans. Microw. Theory Tech.*, vol. 44, no. 8, pp. 1460–1469.
- Nishitsuji, A.; Hoshiyama, M.; Awaka, J. & Furuhashi, Y. (1983). An analysis of propagative character at 34.5 GHz and 11.5 GHz between ETS-II satellite and Kasima station—On the precipitation model from stratus, *IEICE Trans. Commun.*, vol. J66-B, no. 9, pp. 1163–1170, (in Japanese).
- Okamoto, K. (2003). A short history of the TRMM precipitation radar, *Meteorol. Monogr.*, vol. 29, no. 51, pp. 187–195.
- Okamoto, K. & Shige, S. (2008). TRMM precipitation radar and its observation results, *IEICE Trans. Commun.*, vol. J91-B, no. 7, pp. 723–733, (in Japanese).
- Olson, W. S.; Kummerow, C. D.; Song, Y.; Petty, G. W.; Tao, W.-K.; Bell, T. L.; Braun, S. A.; Yansen, W.; Lang, S. E.; Johnson, D. E. & Chiu, C. (2006). Precipitation and latent heating distributions from satellite passive microwave radiometry. Part I: Improved method and uncertainty estimates, *J. Appl. Meteorol. Climatol.*, vol. 45, no. 5, pp. 702–720.
- Saunders, R. W.; Hewison, T. J.; Stringer, S. J.; & Atkinson, N. C. (1995). The radiometric characterization of AMSU-B, *IEEE Trans. Microw. Theory Tech.*, vol. 43, no. 4, pp. 760–771.
- Schluessel, P. & Luthardt, H. (1991). Surface wind speeds over the North Sea from special sensor microwave/imager observations, *J. Geophys. Res.*, vol. 96, no. C3, pp. 4845–4853.

- Senbokuya Y.; Satoh S; Furukawa K; Kojima M; Hanado H; Takahashi N; Iguchi T. & Nakamura K. (2004). Development of the spaceborne dual-frequency precipitation radar for the Global Precipitation Measurement. *IGARSS '04*, 5, pp. 3566-3569.
- Shige, S.; Yamamoto, T.; Tsukiyama, T.; Kida, S.; Ashiwake, H.; Kubota, T.; Seto, S.; Aonashi, K. & Okamoto, K. (2009). The GSMaP precipitation retrieval algorithm for microwave sounders. Part I: Over-ocean algorithm. *IEEE Trans. Geosci. Remote Sens.*, vol. 47, No. 9, pp. 3084-3097.
- Simpson, J.; Adler, R. F. & North, G. R. (1988). A proposed satellite Tropical Rainfall Measuring Mission (TRMM). *Bull. Amer. Meteor. Soc.*, vol. 69, no. 3, pp. 278-295
- Simpson, J.; Adler, R. F.; Kummerow, C.; W.-K. Tao & R. F. Adler, 1996: On the Tropical Rainfall Measuring Mission (TRMM). *Meteor. Atmos. Phys.*, vol. 60, pp., 19-36.
- Surussavadee, C. & Staelin, D. H. (2008a). Global millimeter-wave precipitation retrievals trained with a cloud-resolving numerical weather-prediction model. Part I: Retrieval design, *IEEE Trans. Geosci. Remote Sens.*, vol. 46, no. 1, pp. 99-108.
- Surussavadee, C. & Staelin, D. H. (2008b). Global millimeter-wave precipitation retrievals trained with a cloud-resolving numerical weather-prediction model. Part II: Performance evaluation, *IEEE Trans. Geosci. Remote Sens.*, vol. 46, no. 1, pp. 109-118.
- Takahashi N. & Awaka, J. (2005). Introduction of a melting layer model to a rain retrieval algorithm for microwave radiometers, in *Proc. 25th IGARSS*, pp. 3404-3409.
- Takayabu Y. N. & Katayama, M. (2004). Low-latitudes rainfall characteristics and its meteorological factors analyzed with mesoscale statistics of TRMM PR data, presented at the 1st AOGS, Singapore, Paper 57-OOA-A1683.
- Takayabu, Y. N. (2006). Rain-yield per flash calculated from TRMM PR and LIS data and its relationship to the contribution of tall convective rain, *Geophys. Res. Lett.*, vol. 33, No. 18, p. L18705, DOI:10.1029/2006GL027531.
- Takayabu, Y. N. (2008). Observing rainfall regimes using TRMM PR and LIS data, *GEWEX News*, vol. 18, no.2, pp. 9-10.
- Vila, D.; Ferraro, R. & Joyce, R. (2007). Evaluation and improvement of AMSU precipitation retrievals, *J. Geophys. Res.*, vol. 112, no. D20, p. D20119, DOI: 10.1029/2007JD008617.
- Viltard, N.; Burland, C. & Kummerow, C. (2006). Rain retrieval from TMI brightness temperature measurements using a PR-based database, *J. Appl. Meteor. and Climatol.*, vol. 45, pp. 455-466.
- Wilheit, T.; Kummerow, C. D. & Ferraro, R. (2003). Rainfall algorithms for AMSR-E, *IEEE Trans. Geosci. Remote Sens.*, vol. 41, no. 2, pp. 204-214.
- Wolff, D. B., Marks, D. A.; Amitai, E.; Silberstein, D. S.; Fisher, B. L.; Tokay, A.; Wang, J. & Pippitt, J. L. (2005). Ground validation for the Tropical Rainfall Measuring Mission (TRMM). *J. Atmos. Oceanic Technol.*, vol. 22, No. 4, pp. 365-380.

A Dual-Frequency Metallic Waveguide System

Yoshihiro Kokubo

*Graduate School of Engineering, University of Hyogo, Himeji-shi, Hyogo
Japan*

1. Introduction

Conventional metallic waveguides have several major advantages, including low propagation losses and high power transmissions in the microwave frequency range. One disadvantage of metallic waveguides is that the propagation frequency band is limited at frequencies above the cutoff frequency f_c . The usable frequency range is therefore restricted to $f_c < f < 2f_c$, because the TE₂₀ mode can exist in rectangular metallic waveguides at frequencies higher than $2f_c$. A ridge waveguide (or a double-ridge waveguide) (Cohn, 1947) has the advantage that it can extend the propagating frequency range by reducing the cutoff frequency for the TE₁₀ mode. However, it has disadvantages in that it has a small and complex structure and a high attenuation constant.

We investigated a new type of waveguide in which single-mode propagation is possible at frequencies higher than $2f_c$ using two arrays of dielectric rods with a dielectric constant of between 20 and 30 (Shibano et al., 2006 ; Kokubo et al., 2007a).

This chapter introduces a system that uses a dual-frequency band waveguide. Firstly, we present the fundamental principles of this dual-frequency band waveguide in which a dual in-line dielectric array is installed. Since the electromagnetic reflection coefficient of a periodic array of dielectric rods is frequency dependent, at low frequencies electromagnetic waves may pass through the dual in-line dielectric rods located near the sidewalls, while at high frequencies electromagnetic waves may be reflected between them. Higher modes are suppressed in the waveguide when the space between two dielectric arrays is narrower than the space between the metal sidewalls.

Secondly, if this type of waveguide contains a corner bend and a straight portion with even symmetry (including the power source), then the dielectric rods are only required in the corner bends of the waveguide, because odd-symmetry modes (such as TE₂₀) are not excited (Kokubo et al., 2007b). As an example, a 90° bend waveguide is considered and its S-parameters are calculated. Another thick dielectric rod is located at the boundary between regions with and without dielectric rods, as reflection occurs there. This dielectric rod functions as a dielectric lens, concentrating electromagnetic waves at the center of the waveguide.

Thirdly, we introduce a frequency multiplexer or demultiplexer that mixes or separates electromagnetic waves with wide band frequencies (Kokubo & Kawai, 2008). A coaxial waveguide converter is usually used for introducing electromagnetic waves into a waveguide. However, there is no converter that can match the impedance over such a wide

frequency range. Accordingly, two converters are required for low and high frequency ranges, and electromagnetic waves must be separated into these two frequency ranges using a frequency demultiplexer.

Finally, the rods must span the entire waveguide without any gaps at the top or bottom which presents problems for fabrication. To overcome these problems, holes with diameters slightly larger than the rods were fabricated at the top of the waveguide and the dielectric rods were inserted into these holes.

2. Structure of dual-frequency waveguide and calculation method

Since the electromagnetic reflection coefficient of the imaginary wall shown in Fig. 1 is frequency dependent, at low frequencies electromagnetic waves may pass through the two imaginary walls located near the sidewalls, while at high frequencies electromagnetic waves may be reflected between them. Higher modes are suppressed in the waveguide as the space between two imaginary walls is narrower than the space between the metal sidewalls. This type of imaginary wall can be realized by an array of dielectric rods. The transmittance of electromagnetic waves for a single row of dielectric rods as a function of frequency is shown in Fig. 2 for four different incident angles. The transmittance is calculated using the cylindrical wave expansion method (Maradudin & McGurn, 1993 ; Tayeb & Maystre, 1997). The dielectric rods are assumed to be made of LaAlO_3 (dielectric constant $\epsilon_r = 24$) and their radius is $r = 0.09a$, where a is the spatial period of the rods, and the electric field is parallel to the rod axes. The transmittance of electromagnetic waves is high at low frequencies ($\omega a / 2\pi c \approx 0.2$) and is low at high frequencies ($\omega a / 2\pi c \approx 0.45$), although it varies depending on the incident angle. An array of dielectric rods can function as an imaginary wall.

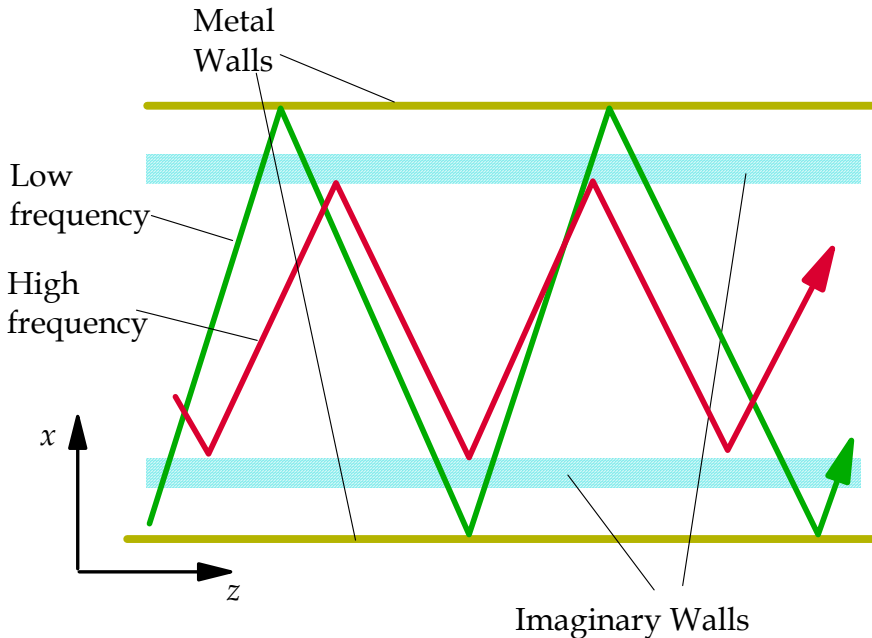


Fig. 1. Imaginary walls in a metallic waveguide.

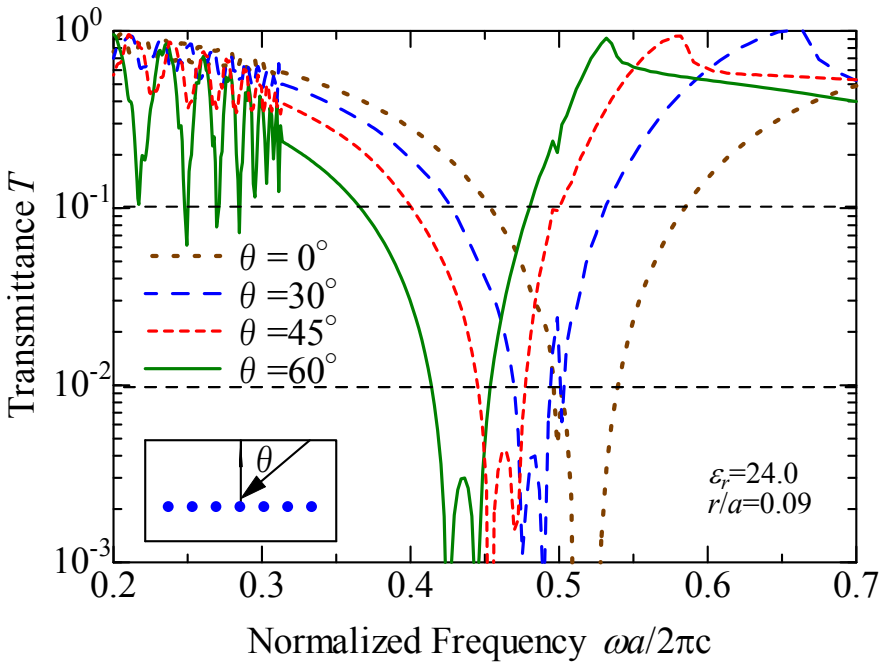


Fig. 2. Transmittance of electromagnetic waves for a single row of dielectric rods for four different incident angles between 0 and 60 degrees for $\epsilon_r=24$ and $r/a=0.09$.

The propagation modes in this waveguide differ from those in conventional metallic waveguides. They can be calculated by the supercell approach (Benisty, 1996) by applying appropriate periodic Bloch conditions at the boundary of the unit cell (Boroditsky et al., 1998). Fig. 3(a) shows the detailed profile of the waveguide with dielectric arrays. The computational domain (super cell) shown in Fig. 3(b) is excited by a modulated Gaussian pulse and observed somewhere within the unit cell. Such observation points are located out of symmetry planes for the lattice to avoid the possibility of probing a null value of the possible propagation modes. The circumference of the unit cell is terminated by applying Bloch boundary conditions at the lateral surfaces $z = \pm a/2$, $x = 0$, and $x = w_1$. At $x = 0$ and $x = w_1$, however, boundary conditions are employed that enforce the electric walls. Maxwell's equations are solved and the field is determined at various points in the computational domain for each value of the wave vector \mathbf{k} , which is normally selected along the edges of the Brillouin zone. The Fourier transform of the computed signal has peaks at frequencies of modes that can propagate in the structure for a given value of the wave vector \mathbf{k} .

In fact, the periodic boundary conditions include the wave vector \mathbf{k} , and can be expressed in the frequency domain as:

$$\mathbf{E}(\mathbf{r} + \mathbf{R}; t) = \mathbf{E}(\mathbf{r}; t) \cdot \exp(j\mathbf{k} \cdot \mathbf{R}) \tag{1}$$

$$\mathbf{H}(\mathbf{r} + \mathbf{R}; t) = \mathbf{H}(\mathbf{r}; t) \cdot \exp(j\mathbf{k} \cdot \mathbf{R}) \tag{2}$$

where \mathbf{R} represents a lattice constant vector.

The above equations may be implemented in the time domain in several ways, but to achieve stable results it is convenient to introduce two electromagnetic fields, with time dependences $\sin(\omega t)$ and $\cos(\omega t)$, denoted by $[\mathbf{e}_1(\mathbf{r};t), \mathbf{h}_1(\mathbf{r};t)]$ and $[\mathbf{e}_2(\mathbf{r};t), \mathbf{h}_2(\mathbf{r};t)]$, respectively. (Boroditsky et al., 1998)

$$\mathbf{E}(\mathbf{r};t) = \mathbf{e}_1(\mathbf{r};t) + j\mathbf{e}_2(\mathbf{r};t) \tag{3}$$

$$\mathbf{H}(\mathbf{r};t) = \mathbf{h}_1(\mathbf{r};t) + j\mathbf{h}_2(\mathbf{r};t) \tag{4}$$

The periodic boundary conditions in equations (1) and (2) may then be written in the time domain as:

$$\mathbf{e}_1(\mathbf{r} + \mathbf{R};t) = \mathbf{e}_1(\mathbf{r};t) \cdot \cos(\mathbf{k} \cdot \mathbf{R}) - \mathbf{e}_2(\mathbf{r};t) \cdot \sin(\mathbf{k} \cdot \mathbf{R}) \tag{5}$$

$$\mathbf{e}_2(\mathbf{r} + \mathbf{R};t) = \mathbf{e}_1(\mathbf{r};t) \cdot \sin(\mathbf{k} \cdot \mathbf{R}) + \mathbf{e}_2(\mathbf{r};t) \cdot \cos(\mathbf{k} \cdot \mathbf{R}) \tag{6}$$

$$\mathbf{e}_1(\mathbf{r};t) = \mathbf{e}_1(\mathbf{r} + \mathbf{R};t) \cdot \cos(\mathbf{k} \cdot \mathbf{R}) + \mathbf{e}_2(\mathbf{r} + \mathbf{R};t) \cdot \sin(\mathbf{k} \cdot \mathbf{R}) \tag{7}$$

$$\mathbf{e}_2(\mathbf{r};t) = -\mathbf{e}_1(\mathbf{r} + \mathbf{R};t) \cdot \sin(\mathbf{k} \cdot \mathbf{R}) + \mathbf{e}_2(\mathbf{r} + \mathbf{R};t) \cdot \cos(\mathbf{k} \cdot \mathbf{R}) \tag{8}$$

These relations, together with analogous ones for the magnetic field, allow the field to be updated at the periodic boundaries of the computational domain. It is worth emphasizing that equations (5-8) introduce the direction of propagation and the value of the phase constant into the computations (Boroditsky et al., 1998).

The calculated results for $r = 0.09a$, $w_1 = 2.5a$, and $w_2 = 1.8a$ are shown in Fig. 4, where w_1 is the width of the waveguide and w_2 is the distance between two dielectric arrays. If the rectangular waveguide is a WR-90 waveguide (22.9×10.2 mm; $f_c \approx 6.55$ GHz), a is determined from $w_1/2.5 = 9.16$ mm. As expected, a single mode is available between 5.93 and 9.26 GHz, and between 12.33 and 17.55 GHz.

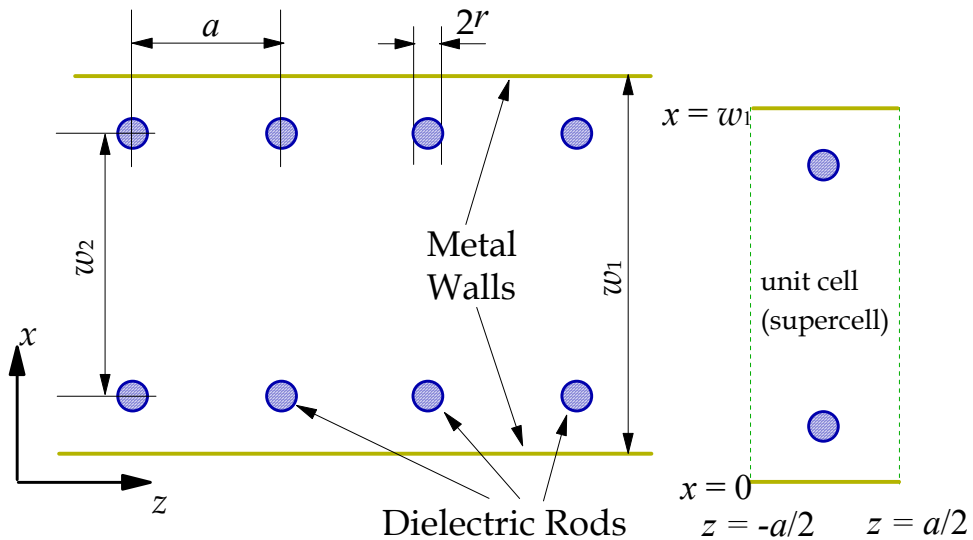


Fig. 3 (a) Detailed profile of the dual band waveguide. (b) Computational domain in real space for the calculating of the dispersion diagram.

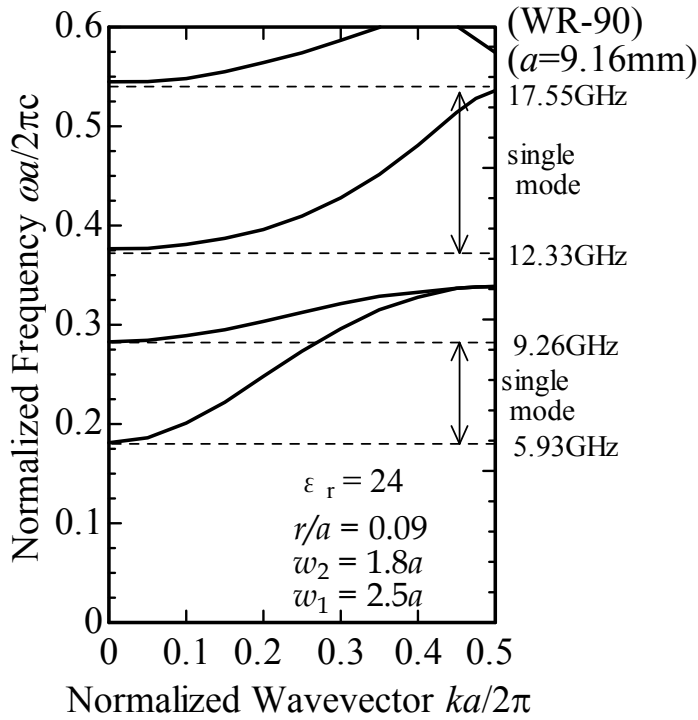


Fig. 4 Eigenvalue dispersion along the guide axis.

3. 90-degree bend waveguide

If this type of waveguide contains a corner bend and a straight portion with even symmetry (including the power source), then dielectric rods are only required in the corner bend of the waveguide, because odd-symmetry modes (such as TE_{20}) are not excited (Kokubo et al., 2007b). The proposed waveguide structure does not have dielectric rods in the straight portion; rather it has them only in the corner bend, as shown in Fig. 5(a). Firstly, the reflection coefficients $|S_{11}|$ are calculated using HFSS (Ansoft Corporation, 2005). Secondly, a scheme for reducing the reflection coefficients is proposed.

The metallic waveguide is assumed to be a WR-90 waveguide (22.9×10.2 mm, cutoff frequency $f_c \approx 6.55$ GHz). The material constants and dimensions are as follows; $\epsilon_r = 24$, $a = 9.16$ mm, $r = 0.09a$, and $w_1 = 2.5a$ ($= 22.9$ mm), and $w_2 = 1.8a$ (≈ 16.5 mm). In this case, single mode propagation is available between 5.93 and 9.26 GHz and between 12.33 and 17.55 GHz. Two arrays of dielectric rods are located in the corner bend of the waveguide and one pair of rods is placed at the end of the corner in the straight portion. The radius of curvature, R , is defined as the distance from the center of the circle to the center of the waveguide. If we assume that there is an integer number of dielectric rods in the 90° bend waveguide structure while maintaining a constant distance, a , between the outer dielectric rods, then

there will be the same number of inner rods as outer rods. This setup is depicted in Fig. 5(b). The reflection coefficients $|S_{11}|$ are calculated by HFSS (Ansoft Corporation, 2005). Values of $|S_{11}|$ for the case when $R = 38.5$ mm are shown by the dotted line in Fig. 6. Although $|S_{11}|$ are not as high as expected, they are not sufficiently small to make the waveguide practical.

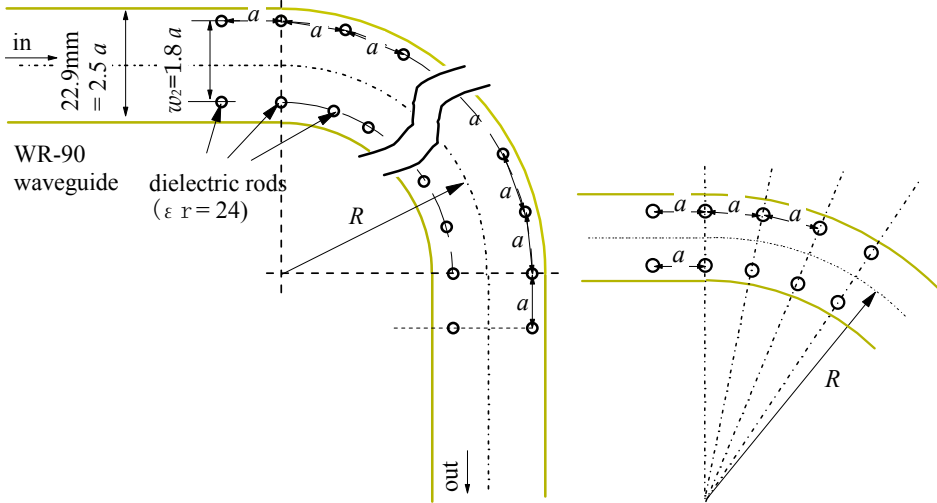


Fig. 5. (a) 90° bend waveguide with dual in-line dielectric rods. (b) Configuration of the dielectric rods in the waveguide. There is the same number of inner arrays as outer arrays.

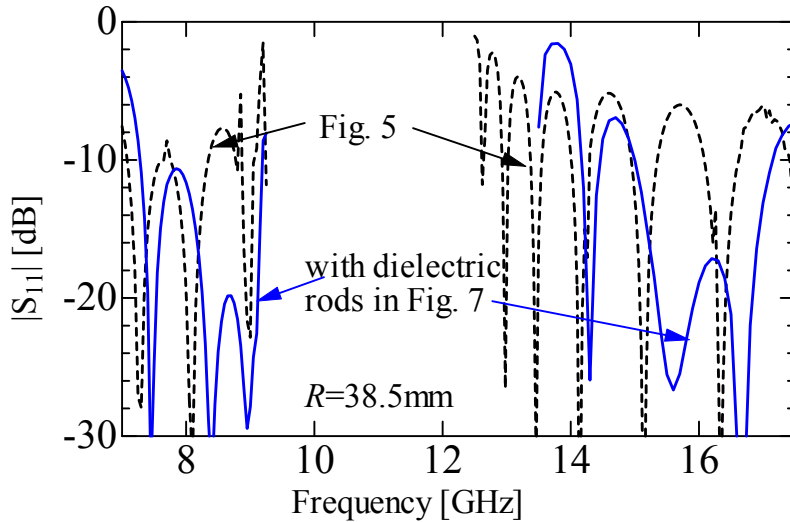


Fig. 6. Reflection coefficient $|S_{11}|$ at the corner bend of the waveguide. Solid and dotted lines denote the cases for type A and type B illustrated in Fig. 9, respectively.

4. Reduction of the reflection coefficient

Other dielectric rods are set at both ends of the dielectric arrays, as shown in Fig. 7, in order to reduce the reflection $|S_{11}|$. The new dielectric rod is assumed to be Teflon. The dielectric constant and radius of the rods are $\epsilon_r = 2.08$ and $r = 2.85$ mm, respectively. These dielectric rods function as a dielectric lens, concentrating electromagnetic waves at the center of the waveguide. The reflection coefficient calculation results for this configuration are shown by the solid line in Fig. 6.

Mode conversion may occur after passing through the corner bend, because dielectric arrays are absent in the straight waveguide portion. Only the TE_{20} mode need be considered, because the TE_{30} mode is under the cutoff condition below 19.6 GHz. The power ratio of the TE_{20} to TE_{10} electromagnetic waves is obtained. Fig. 8 shows the results for this case with new dielectric rods. The power of the TE_{20} mode is very low at frequencies higher than $2f_c$.

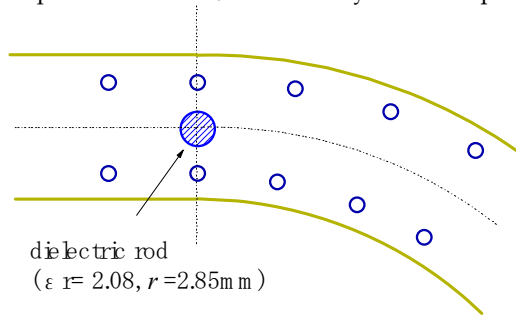


Fig. 7. Addition of another dielectric rod.

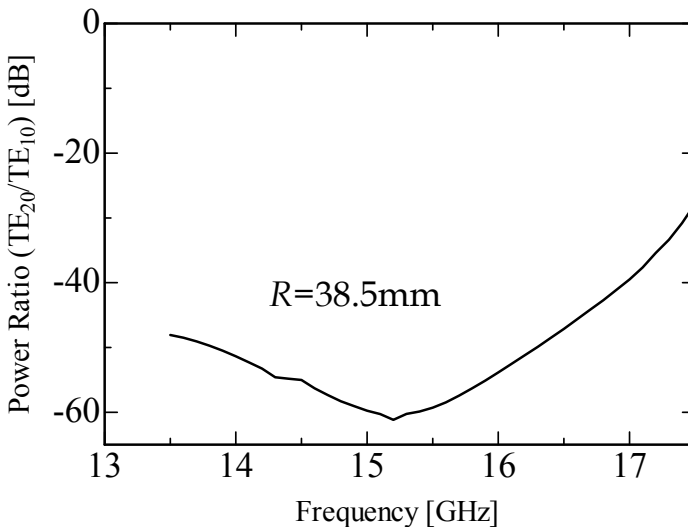


Fig. 8. Power ratio of TE_{20} to TE_{10} after passing through the waveguide.

5. Simple fabrication method

In order to fabricate of a dual-frequency band waveguide, such as the type A dual-frequency band waveguide illustrated in Fig. 9, it is necessary to locate the dielectric rods in the waveguide without a gap at the top and bottom. Such a structure may be difficult to fabricate. To overcome this problem, holes with diameters slightly larger than the rods were fabricated at the top of the waveguide and the dielectric rods were inserted into them (type B, Fig. 9). Opening a large hole in the top of the metallic waveguide, however, may be difficult since the wall current at a large hole will disturb the electromagnetic waves.

Firstly, the thick Teflon rod needs to be replaced by a thin LaAlO_3 rod. Fig. 10 shows an improved structure over that shown in Fig. 7. The thick dielectric rod is replaced by three LaAlO_3 rods having radii of 0.35 mm. The S-parameters calculated by HFSS are shown by the solid lines in Fig. 11. Secondly, S-parameters are calculated for type B in Fig. 9 with the three thin LaAlO_3 rods shown in Fig. 10. The diameter for inserting three thin rods is assumed to be 0.8 mm. The S-parameters calculated by HFSS are shown as dotted lines in Fig. 11. The results depicted by the solid and dotted lines are almost the same.

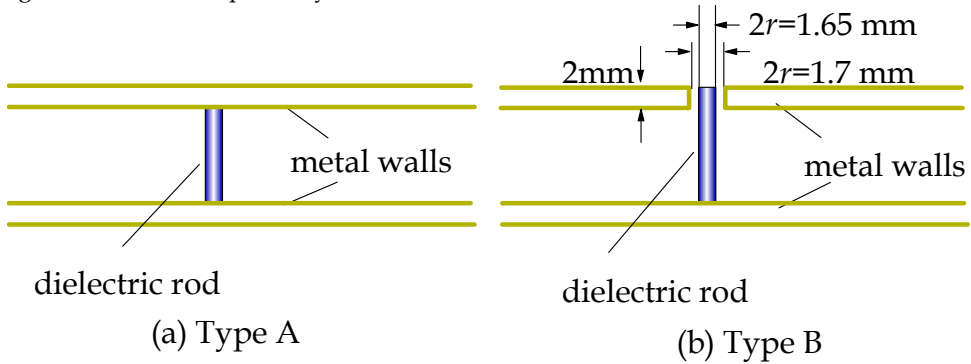


Fig. 9. (a) Dielectric rod located in a waveguide that does not have gaps at top and bottom. (b) Dielectric rod inserted in a hole made at the top of the waveguide with a diameter 0.1 mm larger than the rod diameter.

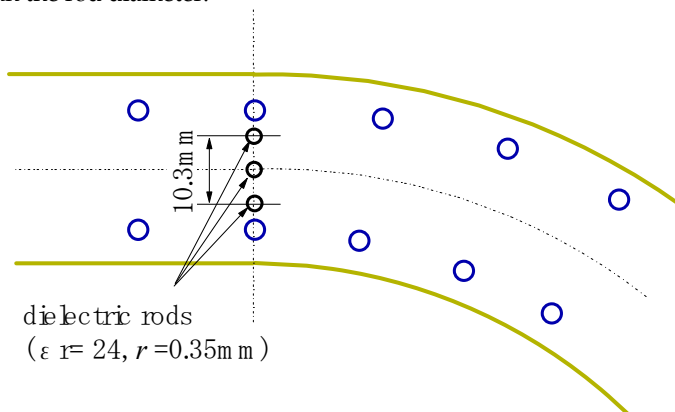


Fig. 10. Three thin LaAlO_3 rods that replace the thick Teflon rod shown in Fig.7

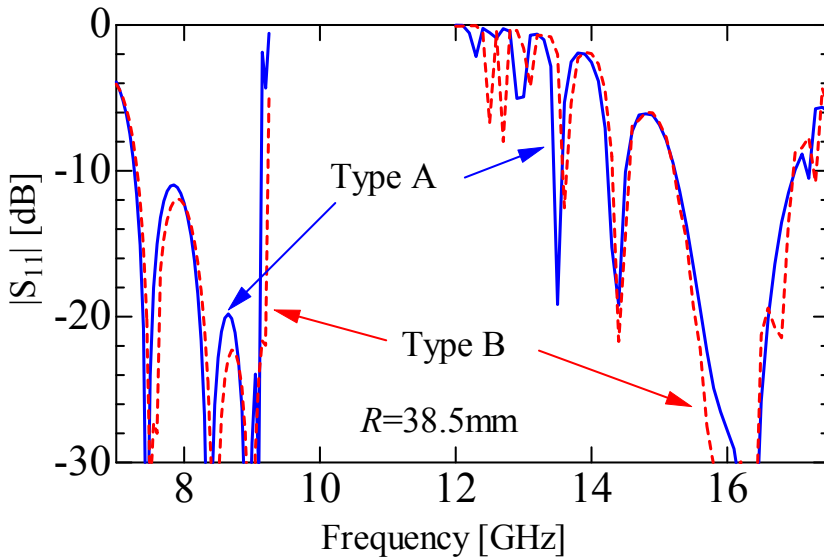


Fig. 11. Reflection coefficient $|S_{11}|$ at the corner bend of the waveguide. Solid and dotted lines denote the cases for type A and type B illustrated in Fig.9, respectively.

6. Frequency multiplexer/demultiplexer

A frequency multiplexer/demultiplexer is required to introduce electromagnetic waves into the waveguide (Kokubo & Kawai, 2008). The frequency multiplexer/demultiplexer has a height of 10.2 mm, which is same as that of a WR-90 waveguide. The basic concept of the waveguide is shown in Fig. 12. Electromagnetic waves in the low-frequency region (f_1 : 5.93-9.26 GHz) propagate between ports 1 and 2, and electromagnetic waves in the high-frequency region (f_2 : 12.33-17.55 GHz) pass between ports 1 and 3. Ports 1 and 2 are part of the WR-90 waveguide and port 3 is formed from a WR-62 waveguide (15.8×7.9 mm: $f_c = 9.49$ GHz), which is narrower than the WR-90 waveguide and is connected to the WR-90 waveguide by a tapered waveguide. Two arrays of dielectric rods are not necessary in the straight portion, because mode conversion does not occur there. We mentioned in the previous section that dielectric arrays are not necessary in the straight portion with a 90° bend waveguide. Except for two pairs of rods, all the dielectric rods were all removed from the straight portion. Accordingly, the structure of the frequency multiplexer/demultiplexer is shown in Fig. 12. Rod A, with a radius of 2.3 mm, is assumed to be made of Teflon ($\epsilon_r = 2.08$) and is used to reduce the reflection. The S-parameters $|S_{11}|$ ($=|S_{22}|$) for low frequencies and $|S_{11}|$, $|S_{21}|$, $|S_{31}|$, and $|S_{33}|$ for high frequencies are calculated using HFSS. $|S_{31}|$ and $|S_{32}|$ must be zero for low frequencies, because port 3 is under the cutoff condition below 9.49 GHz and $|S_{22}|$ is not important in the high frequency region, because the design ensures that there are no high frequency components from the port 2.

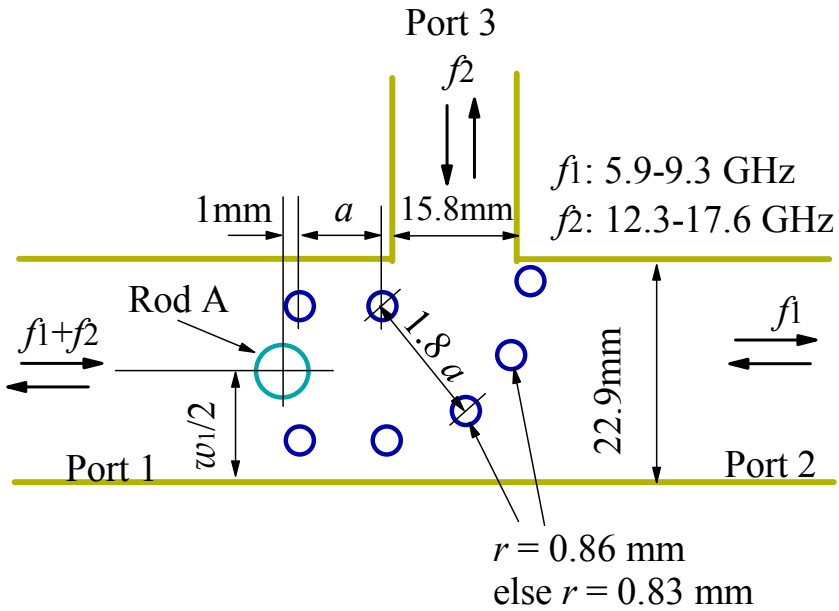


Fig. 12. Basic concept of the frequency multiplexer/demultiplexer.

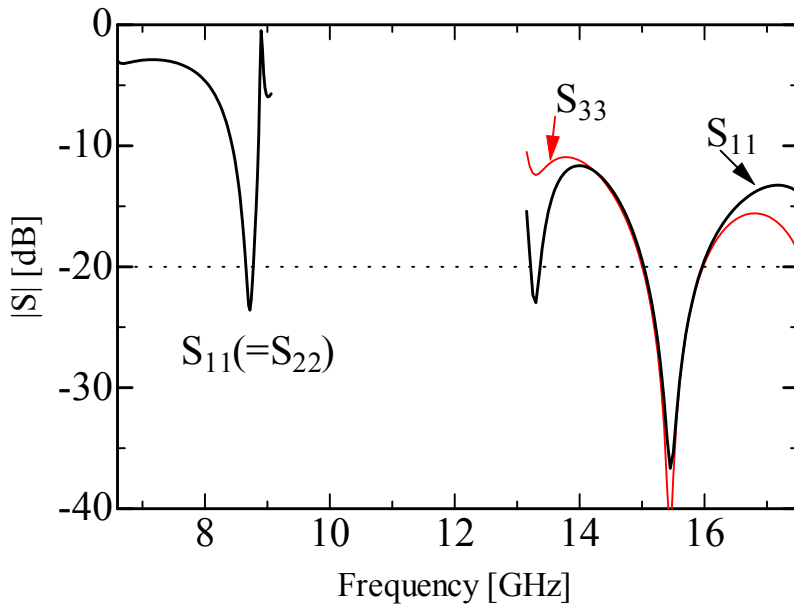


Fig. 13. Reflection coefficient $|S_{11}|$ ($=|S_{22}|$) for low frequencies and $|S_{11}|$ and $|S_{33}|$ for high frequencies.

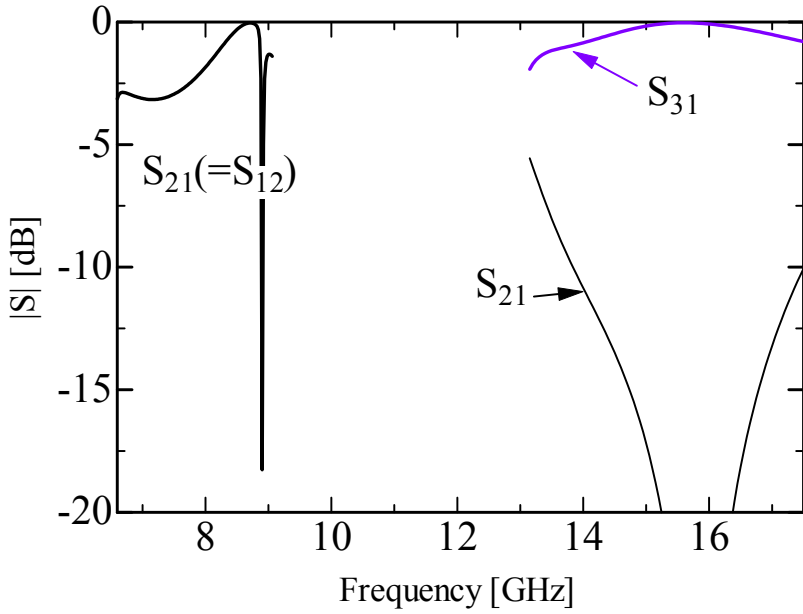


Fig. 14. $|S_{21}|$ ($=|S_{12}|$) for low frequencies and $|S_{21}|$ and $|S_{31}|$ for high frequencies.

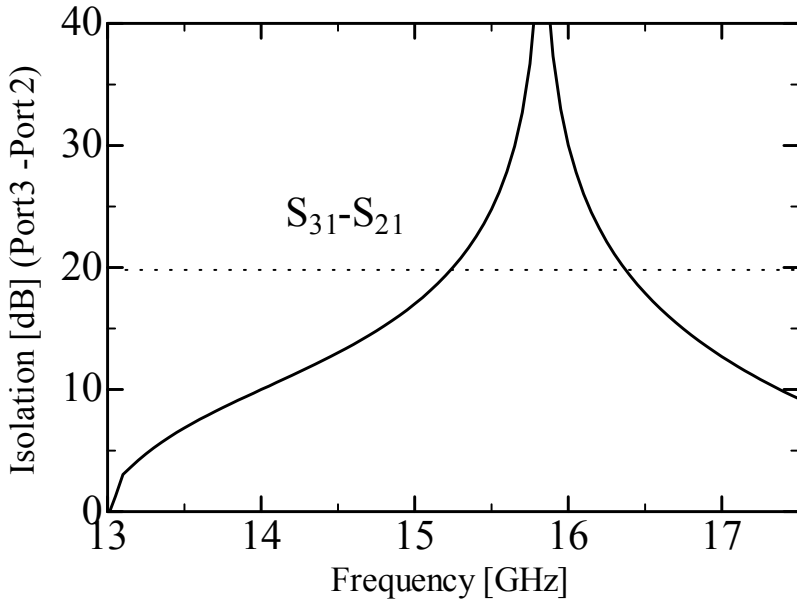


Fig. 15. Port isolation between two output ports.

The calculated results are shown in Figs. 13 and 14. If the criterion of reflection is -20 dB, then the bandwidth of $|S_{11}|$ in the low-frequency region is rather narrow. However, $|S_{21}|$ is rather small and almost all of the power from port 1 is led to port 3 at high frequencies. Port isolation between ports 2 and 3 is larger than 20 dB at frequencies between 15.3 and 16.3 GHz, as shown in Fig. 15.

7. Confirmation of mode conversion

Mode conversion of the electromagnetic waves may occur after passing through the bend from port 3 to port 1 because dielectric arrays are absent in the straight waveguide portion. Only the TE_{20} mode needs to be considered, because the TE_{30} mode is under the cutoff condition below 19.6 GHz. The power ratio of the TE_{20} to TE_{10} electromagnetic wave is obtained at port 1. The calculated results are shown in Fig. 16. Since the power of the TE_{20} mode is very low at frequencies higher than 13.1 GHz, mode conversion will not occur without dielectric rods in the straight portion.

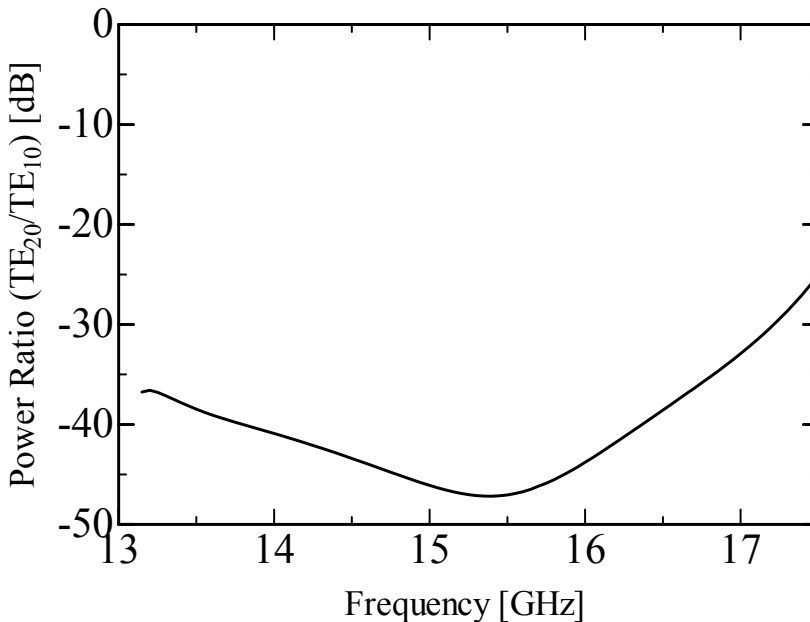


Fig. 16. Power ratio of TE_{20} to TE_{10} at port 1.

8. Simple fabrication method

As shown in the previous section, holes with diameters slightly larger than the rods will be fabricated at the top of the waveguide and the dielectric rods will be inserted (Type B, Fig. 11).

Firstly, the thick Teflon rod needs to be replaced by a thin LaAlO_3 rod. Fig. 17 shows an improved structure over that shown in Fig. 12. The coordinates and radii of the dielectric rods are shown in Table 1. A thick dielectric rod will be replaced by two thin LaAlO_3 rods having radii of 0.36 mm at separated by 7.9 mm. The S-parameters calculated by HFSS are shown by the solid lines in Figs. 18 and 19. Secondly, S-parameters are calculated for type B in Fig. 11 with two thin LaAlO_3 rods inserted from the top of the waveguide. The diameter for inserting three thin rods is assumed to be 0.8 mm. The S-parameters calculated by HFSS are shown by the dotted lines in Figs. 18 and 19. The results for the solid and dotted lines are almost the same. Port isolation between ports 2 and 3 is shown in Fig. 20.

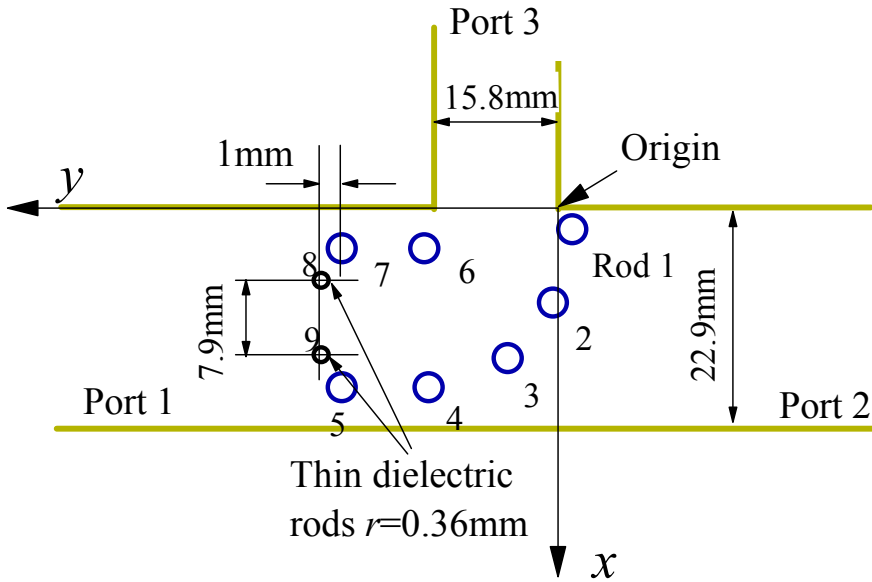


Fig. 17. Improved structure of the frequency multiplexer/demultiplexer. Two thin LaAlO_3 rods are used to reduce reflections.

Rod No.	Coordinate x [mm]	Coordinate y [mm]	Radius r [mm]
1	1.26	-0.29	0.83
2	10.3	1.2	0.86
3	17.1	7.3	0.86
4	19.7	16.1	0.83
5	19.7	25.2	0.83
6	3.2	16.1	0.83
7	3.2	25.2	0.83
8	7.5	26.2	0.36
9	15.4	26.2	0.36

Table 1. Coordinates and radii of dielectric rods illustrated in Fig. 17

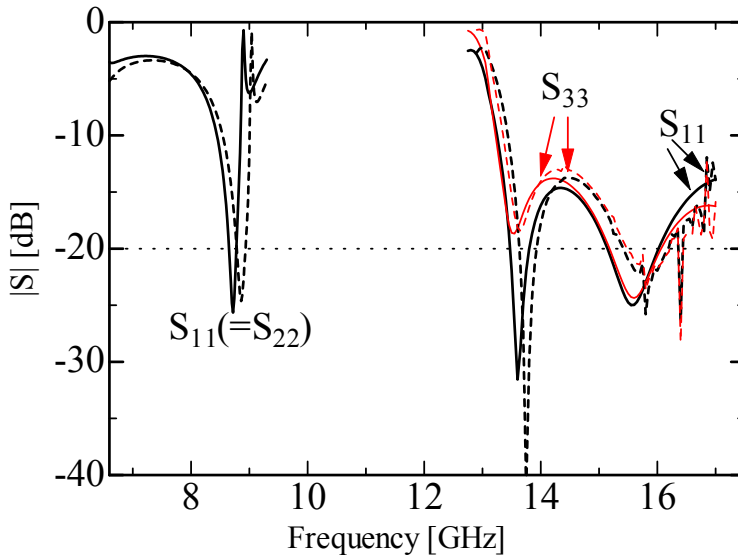


Fig. 18. Reflection coefficient $|S_{11}|$ ($=|S_{22}|$) for low frequencies and $|S_{11}|$ and $|S_{33}|$ for high frequencies. Solid and dotted lines denote the cases for type A and type B illustrated in Fig.9, respectively.

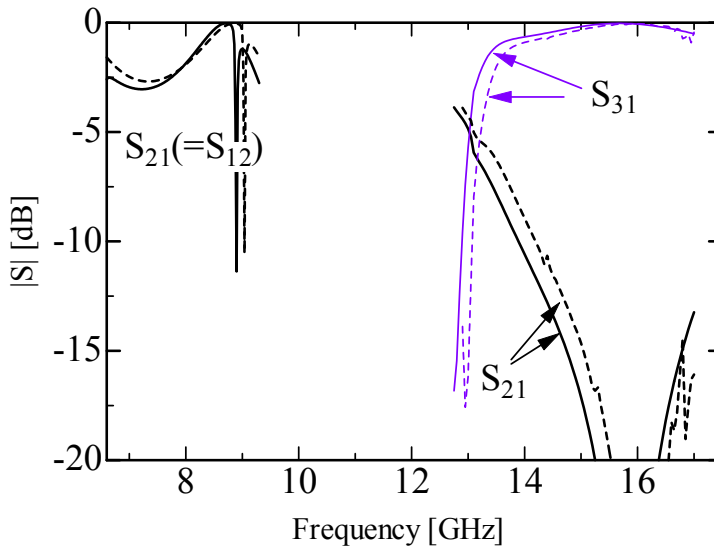


Fig. 19. $|S_{21}|$ ($=|S_{12}|$) for low frequencies and $|S_{21}|$ and $|S_{31}|$ for high frequencies. Solid and dotted lines denote the cases for type A and type B illustrated in Fig.9, respectively.

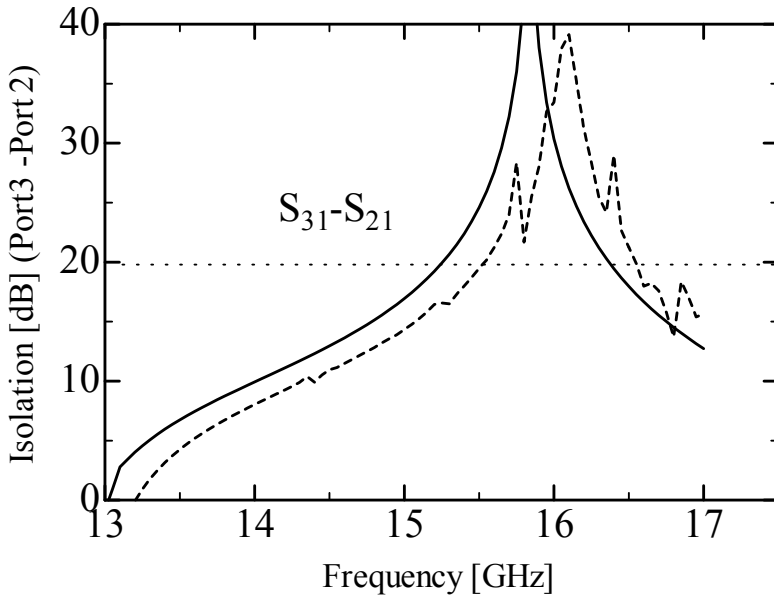


Fig. 20. Port isolation between two output ports. Solid and dotted lines denote the cases for type A and type B illustrated in Fig.9, respectively.

9. Conclusion

Electromagnetic waves were propagated in a waveguide with dual in-line dielectric rods made of LaAlO_3 and without higher modes above $2f_c$. Firstly, an economically feasible setup for this type of waveguide system was proposed including 90° bend waveguide. Reflection coefficients $|S_{11}|$ smaller than -18 dB were obtained at frequencies between 8.2 and 9.1 GHz and between 15.3 and 16.8 GHz by calculation. The electromagnetic wave includes less than -40 dB of the TE_{20} component in the straight portion in the case of a radius of curvature $R \geq 38.5$ mm at frequencies below 17 GHz, so that dielectric rods are not required in the straight portion.

Secondly, a sample structure for a frequency multiplexer/demultiplexer is proposed for introducing electromagnetic waves from a coaxial cable. Reflection of electromagnetic wave occurs without dielectric rods in the straight portion; therefore, another rod, made of LaAlO_3 or Teflon, is introduced to reduce reflection and the calculated S-parameters. The bandwidths for reflections smaller than -20 dB are still narrow; however, optimization of the design may enable the bandwidth to be expanded.

10. References

- Ansoft Corporation (2005). Introduction to the Ansoft Macro Language, HFSS v10.
- Benisty, H. (1996). Modal analysis of optical guides with two-dimensional photonic band-gap boundaries, *Journal of Applied Physics*, 79, 10, (1996) pp.7483-7492, ISSN 0021-8979.
- Boroditsky, M.; Coccioli, R. & Yablonovitch, E. (1998). Analysis of photonic crystals for light emitting diodes using the finite difference time domain technique, *Proceedings of SPIE*, Vol. 3283, (1998) pp.184-190, ISSN 0277-786X.
- Cohn, S., B. (1947). Properties of Ridge Wave Guide, *Proceedings of the IRE*, Vol.35, (Aug. 1947) pp. 783-788, ISSN 0096-8390.
- Kokubo, Y.; Maki, D. & Kawai, T. (2007a). Dual-Band Metallic Waveguide with Low Dielectric Constant Material, *37th European Microwave Conference Proceedings*, pp.890-892, ISBN 978-2-87487-000-2, Munich, Germany, Oct. 2007, EuMA, Belgium.
- Kokubo, Y.; Yoshida, S. & Kawai, T. (2007b). Economic Setup for a Dual-band Metallic Waveguide with Dual In-line Dielectric Rods, *IEICE Transactions on Electronics*, Vol.E90-C, No.12, (Dec. 2007) pp.2261-2262, ISSN 0916-8524.
- Kokubo, Y. & Kawai, T. (2008). A Frequency Multiplexer/Demultiplexer for Dual Frequency Waveguide, *38th European Microwave Conference Proceedings*, (Oct. 2008) pp.24-27, ISBN 978-2-87487-005-7, Amsterdam, The Netherland, Oct. 2008, EuMA, Belgium.
- Maradudin, A. A. & McGurn, A. R. (1993). Photonic band structure of a truncated, two-dimensional, periodic dielectric medium, *Journal of the Optical Society of America B*, Vol.10, No.2, (1993) pp. 307-313, ISSN 0740-3224.
- Shibano, T.; Maki, D. & Kokubo, Y. (2006). Dual Band Metallic Waveguide with Dual in-line Dielectric Rods, *IEICE Transactions on Electronics*, Vol.J89-C, No.10, (Oct. 2006) pp.743-744, ISSN 1345-2827 (Japanese Edition) ; Correction and supplement, *ibid*, Vol.J90-C, No.3, (Mar. 2007) p.298, ISSN 1345-2827. (Japanese Edition).
- Tayeb, G. & Maystre, D. (1997). Rigorous theoretical study of finite-size two-dimensional photonic crystals doped by microcavities, *Journal of the Optical Society of America A*, Vol. 14, No.12, (Dec. 1997) pp. 3323-3332, ISSN 1084-7529.

Applications of On-Chip Coplanar Waveguides to Design Local Oscillators for Wireless Communications System

Ramesh K. Pokharel, Haruichi Kanaya
and Keiji Yoshida
*Kyushu University
Japan*

1. Introduction

On-chip distributed transmission line resonators in CMOS technology have become the interest of research subjects recently (Ono et al. 2001; Umeda et al., 1994; Kanaya et al., 2006; Wolf, 2006) because of their size which becomes more compact, as the frequency of application increases. Among the various transmission lines, coplanar waveguide (CPW) has more engineering applications (Toyoda, 1996; Civello, 2005) because it is easy to fabricate by LSI technology since the signal line and ground plane exist on the same plane so that no via holes are required for integrating active components such as transistors on Si-substrate (Toyoda, 1996).

The applications of the CPW were reported for many on-chip LSI components. The CPW was exploited as an inductor and used to design a conventional-type matching circuit for LNA (Ono et al., 2001) in microwave-band frequency, and they are most popular in monolithic microwave integrated circuit (MMIC) (Umeda et al., 1994). However, the application of CPW lines as an inductor takes larger space than the conventional spiral inductors (Umeda et al., 1994). Some of the present authors have also implemented the on-chip CPW impedance-matching circuit for a 2.4 GHz RF front-end (Kanaya et al., 2006) and for 5GHz band power amplifier (Pokharel et al., 2008) using impedance inverters. In designing the matching circuits using impedance inverters and quarter wavelength resonators realized by on-chip CPW (Kanaya et al, 2006; Pokharel et al., 2008) the size of the matching circuits becomes compact thus reducing the chip area by about 30% than using spiral inductors for 2.4GHz-band applications and 40% for 5 GHz-band applications.

However, the applications of on-chip CPW resonators in designing other components such as a voltage-controlled oscillator (VCO) have not been reported yet. A conventional VCO consists of a LC-resonator to produce an oscillation at the frequency band of interest, and this LC-resonator may be replaced by a CPW resonator. Such possibilities are investigated in this paper. In a conventional VCO, the performance such as phase noise of the VCO depends on the quality (Q) factor of the LC resonator. Usually, a spiral inductor is used in

the resonator and these have quite low Q 's of around 3-5 at GHz frequency range and on the other hand, it takes large on-chip area in the expensive silicon substrate. The inductor can be either resonated with the device drain capacitance or by adding a shunt capacitor (on chip or off). Using bond wires instead of on-chip spiral inductors allows the design of low phase noise oscillators but makes the fabrication more difficult as it is difficult to precisely set the length of the bond wire. Also for use in Phase Locked Loop (PLL) applications it is necessary to have variable frequency or so called higher frequency tuning range (FTR). Therefore, it is not a wise practice to use bond wires in designing a VCO due to design difficulties in estimating the bond wires inductances.

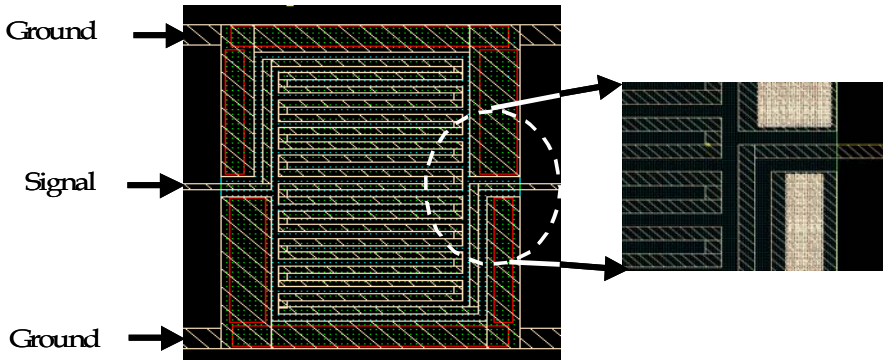
In this paper, first, we propose a design method of a VCO using on-chip CPW resonator thus replacing an LC-resonator. First, transmission characteristics of the on-chip meander CPW resonator fabricated using TSMC 0.18 μm CMOS technology are investigated experimentally and an equivalent circuit is developed. Later, the application of on-chip resonator is also demonstrated to design 10 bits digitally-controlled oscillator (DCO). The derived equivalent circuit is used to carry out the post-layout simulation of the chip. One of the advantages of the proposed method to design VCO and DCO using on-chip CPW resonator than using a LC-resonator is smaller chip area.

2. Design of On-Chip CPW Resonator and Its Equivalent Circuits

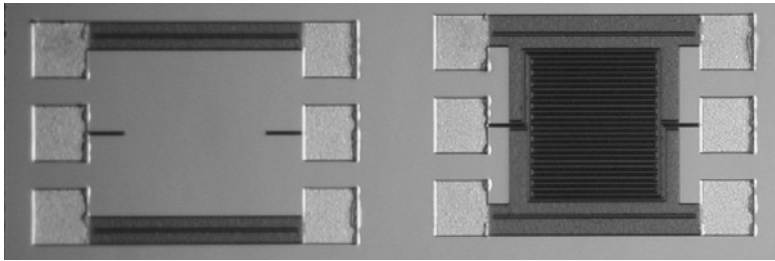
In this paper, we use Advanced Design System (ADS2008A, Agilent Technologies) for designing active elements and Momentum (Agilent Technologies) for passive elements for schematic design. Co-simulation option was used for electromagnetic characterization of hybrid structures consisting of active and passive elements together. We first develop the equivalent circuit for on-chip meander CPW resonator using experimental results and latter, the circuit is used to carry out the post-layout simulation of the chip.

The on-chip meander CPW resonator is designed, fabricated, and measured using TSMC 0.18 μm CMOS technology. This process has 1-poly and 6-metal layers and the thickness of the top metal is 3.1 μm . The conductance of the metal and dielectric permittivity (ϵ_r) of the SiO_2 are $4.1 \times 10^7 \text{ S/m}$ and 4.1, respectively. The upper layer is covered by lamination whose relative permittivity is 7.9.

Fig. 1 shows the layout and chip photos of on-chip CPW resonator designed and characterized by EM simulator. In Fig. 1(a), the enlarged portion of the layout is illustrated to show its structure in detail where the signal line and slot size is 5 μm each, respectively. Bottom metal (Metal-1) is used as ground plane covering all portion of CPW to reduce the losses. Therefore, we prefer to call this CPW as conductor-backed CPW. Total length of the resonator is 3300 μm which is supposed to be shorter than a quarter-wavelength resonator at 5.2 GHz. The chip photo of the on-chip CPW resonator is shown in Fig. 1(b) and Fig. 1(c). Please note that a small stub at the center CPW pad (dummy pad of right side) in Fig. 1(b) is to de-embed the interconnect between metal 6 terminal of the CPW resonator and the pad. The microwave characteristics are measured by using air coplanar probes (Cascade Microtech, GSG150) and vector network analyzer (HP, HP8722C) in Air coplanar probe station (Cascade Microtech Inc.). The CPW pads are 100 μm square and have coplanar configurations so that characteristic impedance is 50 Ω .



(a) Layout of CPW resonator showing enlarged section for illustration of its structure



(b) Dummy chip

(c) On-chip CPW meander resonator

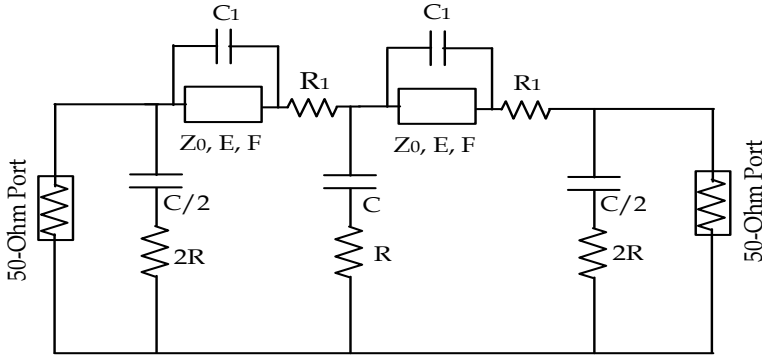
Fig. 1. Layouts and chip photographs of CPW resonator.

The measured data must be de-embedded in order to remove the parasitic effects of interconnects, pads and contacts surrounding the device (Civello, 2005). Therefore, in Fig. 1(b), chip photo of a dummy pad and in Fig. 1(c), chip photo of the CPW resonator are shown. In order to de-embed the measured raw data, at first, we measure S-parameters of total (Fig. 1(c)) and open dummy chip (Fig. 1(b)), respectively. Next, S-parameters are transformed into Y-parameters according to Equation (1) to get the Y-parameters (Y_{TML}) of the transmission-line resonator only.

$$[Y]_{TML} = [Y]_{total} - [Y]_{dummy} \quad (1)$$

Y-parameters are then converted to Z-parameters in order to compare the results between simulation using the Equivalent circuits of Fig. 2. In Fig. 2, two equivalent circuits are developed using 2-stages and 5-stages for CPW resonator in meander structure, where ideal transmission lines are represented by the parameters such as characteristic impedance (Z_0), electrical length of each part (E), and frequency (F). Furthermore, C_1 represents the mutual capacitance between the meander lines, R_1 is the resistive loss of the line in each segment, and the parameters R (resistance), C (Capacitance) represent the silicon substrate of the corresponding segment. In Fig. 2(b), where 5-stage model of equivalent circuit is shown, the meander line is divided into shorter segments, therefore parameters of each segment of the model such as R_1 , C_1 , E will differ from 2-stage model of Fig. 2(a). Each parameters in both models are noted below each figure. Here, model parameters for Si-substrate (R , C) are

estimated by the dielectric characteristics, and the rest of the parameters of the meander line are estimated by fitting to the measured results, because our main goal is to develop a simple model which can be incorporated in ADE simulation to carry out the post-layout simulation of the chip that consists of on-chip CPW resonators.



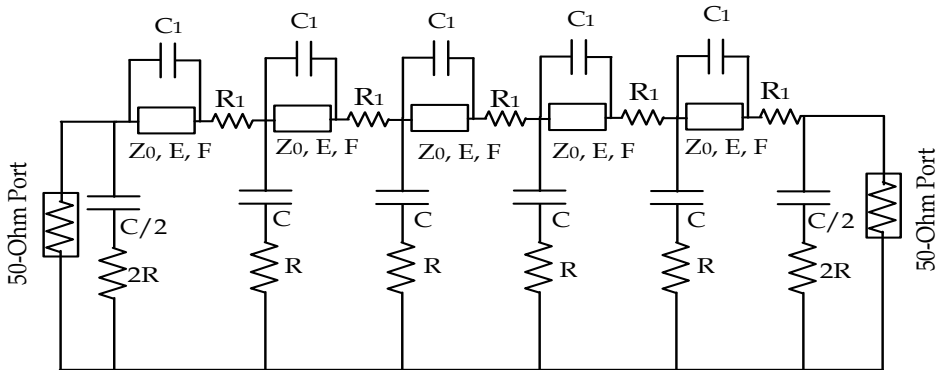
Parameters

$$Z_0 = 32 \Omega ; E = 22.5 \text{ degrees}; F = 1 \text{ GHz}$$

$$C = 30 \text{ fF}; R = 8.3 \text{ k} \Omega$$

$$C_1 = 0.46 \text{ fF}; R_1 = 14 \Omega$$

(a) 2-stage equivalent circuit



Parameters

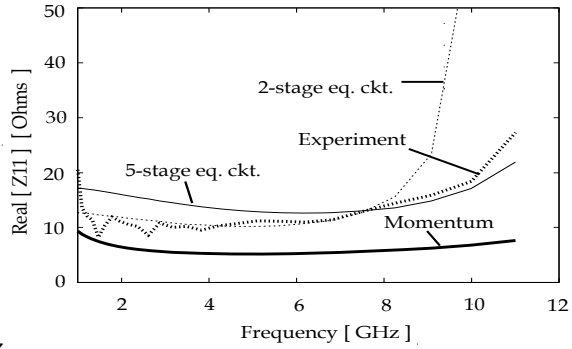
$$Z_0 = 32 \Omega ; E = 9 \text{ degrees}; F = 1 \text{ GHz}$$

$$C = 11.5 \text{ fF}; R = 3.3 \text{ k} \Omega$$

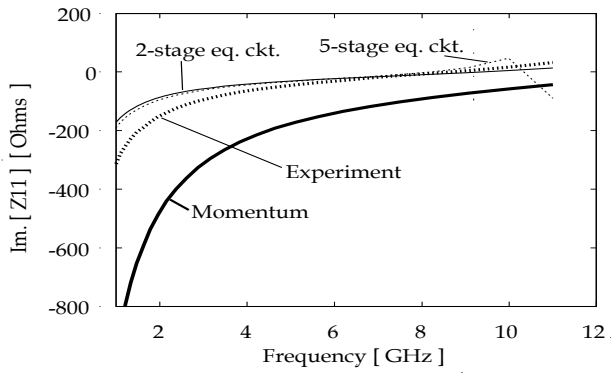
$$C_1 = 1.1 \text{ fF}; R_1 = 5.7 \Omega$$

(b) 5-stage equivalent circuit

Fig. 2. Two types of equivalent circuits using various stages for on-chip CPW meander resonator

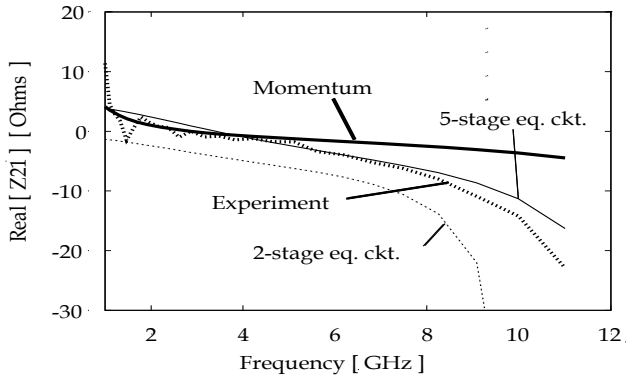


(a) Real part of Z_{11}

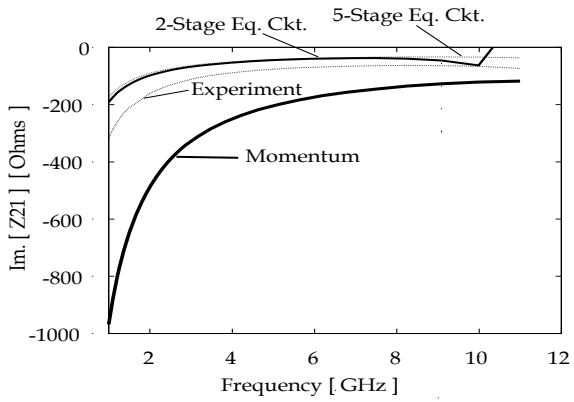


(b) Imaginary part of Z_{11}

Fig. 3. Comparison of simulated Z_{11} -parameters using two-types of equivalent circuit models with Momentum-simulation and measured results



(a) Real part of Z_{21}



(b) Imaginary part of Z_{21}

Fig. 4. Comparison of simulated Z_{21} -parameters using two-types of equivalent circuit models with Momentum-simulation and measured results

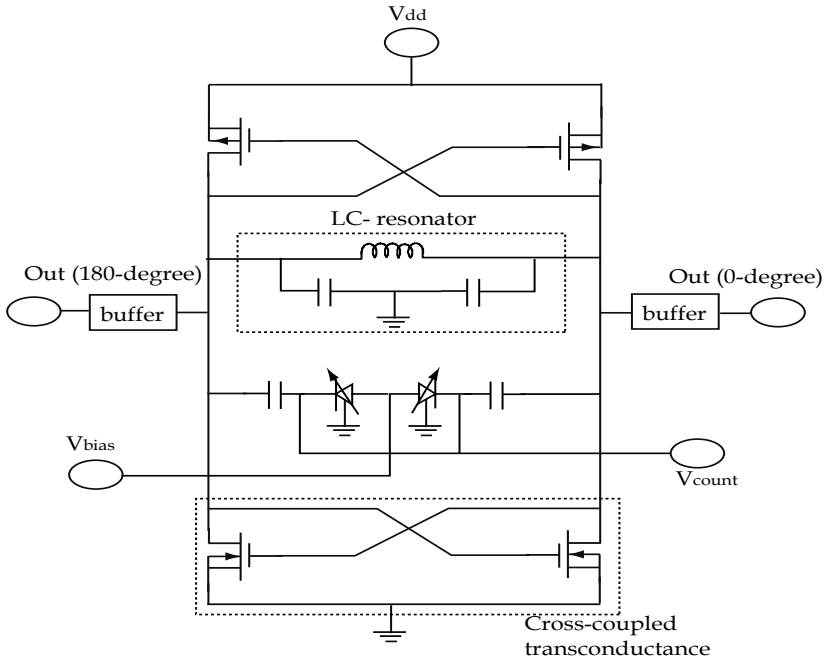


Fig. 5. Schematic of conventional VCO employing LC-resonator

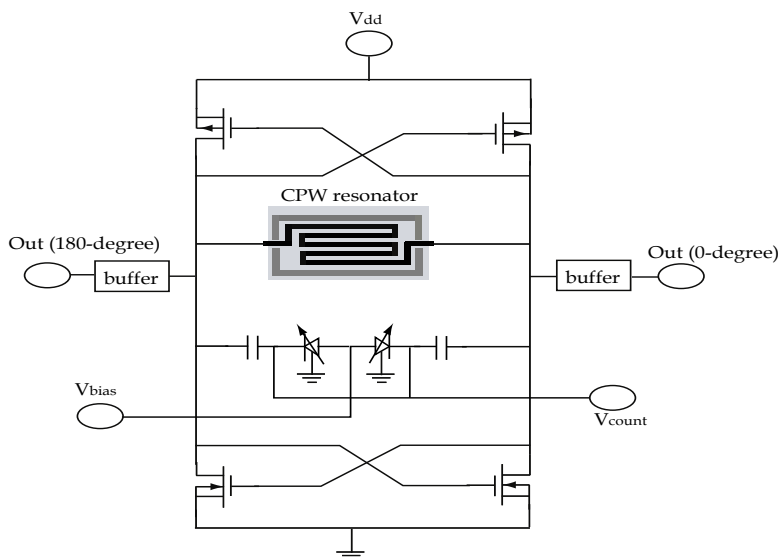
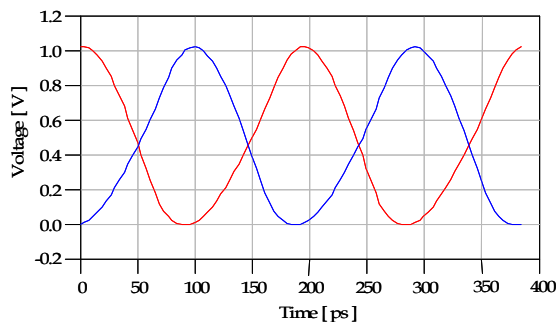
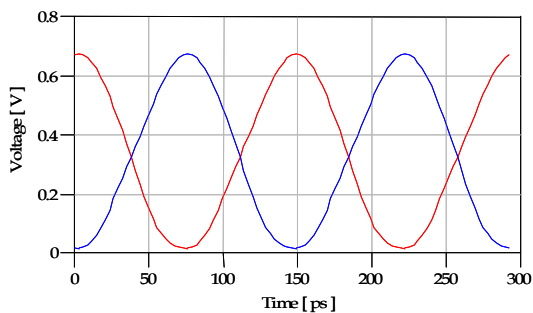


Fig. 6. Schematic of Proposed VCO employing on-chip CPW resonator



(a) Simulation results of VCO using LC-resonator having differential output waveforms



(b) Simulation results of VCO using on-chip CPW-resonator having differential output waveforms

Fig. 7. Output voltage waveforms of designed VCOs

Finally, the Z-parameters which are transformed from S-parameters are compared with measured results and simulation by Momentum in Fig. 3 and Fig. 4, respectively. Here we choose Z-parameters because of the simplicity to illustrate the comparison in closer range in linear scale. In Fig. 3, real and imaginary parts of Z_{11} -parameters are compared where circuit simulation results using the proposed equivalent circuits will reproduce more closely with measured results than the simulation by Momentum. This tendency is also similar in Fig. 4 where real and imaginary parts of Z_{21} -parameters are compared. Up to 7 GHz, both equivalent circuits produce good agreement with the experiment results, therefore in this paper, 2-stage equivalent circuit of Fig. 2(a) is used onwards in ADE simulation to carry out the post-layout simulation of the whole chip of VCO employing on-chip CPW resonator.

3. Design of VCO Using On-Chip CPW Resonator

A conventional VCO (Dai & Harjani, 2003; Hajimiri & Lee, 2004) mainly consists of three parts such as (i) LC-resonator (ii) Varactor (iii) Cross-coupled transconductance circuit as shown in Fig. 5 where the LC tank circuit determines the frequency of oscillation and form the drain loads. Frequency dependant signals at the drains are then 'cross-coupled' to the other devices' gate, which creates a negative impedance of value $-1/g_m$ at the drain terminals. As VCO is usually used in a phase-locked loop (PLL) in a wireless transceiver, it is necessary to have variable frequency, which is measured in terms of frequency tuning range (FTR) corresponding to center frequency. To make the fixed frequency oscillator into a variable frequency oscillator, it is necessary to tune the capacitive load and for this purpose, a voltage-tuned capacitor known as varactor is added into the resonator.

Fig. 5 and Fig. 6 show the schematics of the designed VCOs. In Fig. 5, schematic of LC-VCO is shown and that of using the proposed CPW resonator is shown in Fig. 6. In Fig. 5, the parasitic capacitances of the $1/g_m$ devices will increase the minimum capacitance of the varactor reducing the tuning range of the VCO whereas in Fig. 6, the equivalent capacitance of the varactor and CPW resonator will decrease which results in the higher FTR of the proposed VCO using on-chip CPW resonator which is to be illustrated in Fig. 11.

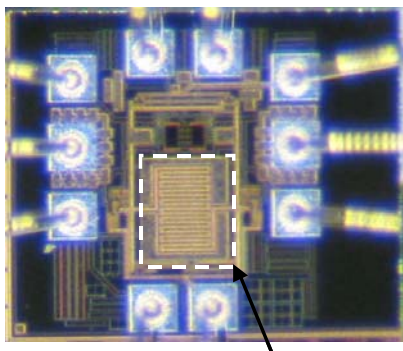
Fig. 7 shows the post-layout simulation of waveforms of the maximum voltage swing of the designed VCO where the maximum peak voltage of LC-VCO is greater than that of the VCO using on-chip CPW resonator and this is clearly reflected in the performance of the phase noise of the VCO in Table 1 to be discussed later.

4. Fabricated Chips and Measurement Results

We designed, fabricated and measured two VCOs as shown in the schematics of Fig. 5 and Fig. 6, respectively for comparison purpose. However, from onward, we will present the graphs of measured results of the proposed VCO using on-chip CPW resonator only and will summarize the final results of both VCOs in Table 1.

Fig. 8 shows the chip photo of the proposed VCO that employs on-chip CPW resonator. The output of both VCOs is designed with buffer circuits so that it provides good matching with the measurement equipments such a spectrum analyzer. Phase noise of the VCO is measured using a Signal Source Analyzer (E5052B SSA, Agilent Technologies) and keeping the chip inside a shield box. While measuring the phase noise of the VCO, the chip was placed inside a small shield room to protect the phase noise from the effect of the low-

frequencies inference, therefore we designed both VCOs with SMA connector rather than CPW probes because, if we design the VCO with the pads for the CPW coplanar probes, we can not measure inside a shield box.



CPW resonator

Fig. 8. Chip photograph of designed VCO using on-chip CPW resonator in TSMC 0.18 μ m CMOS

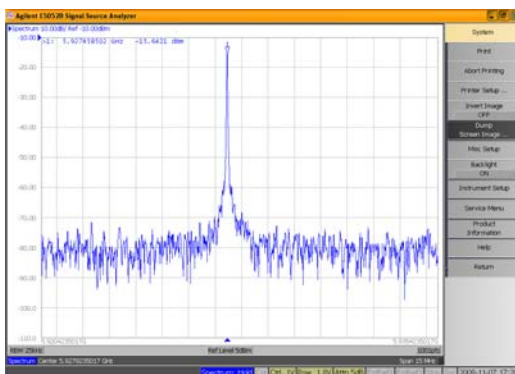


Fig. 9. Spectrum of output power of the VCO employing on-chip CPW resonator measured by SSA

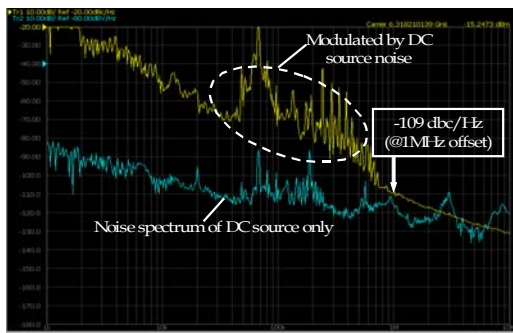


Fig. 10. Phase noise of the proposed VCO using on-chip CPW resonator with noise of DC source only measured by SSA

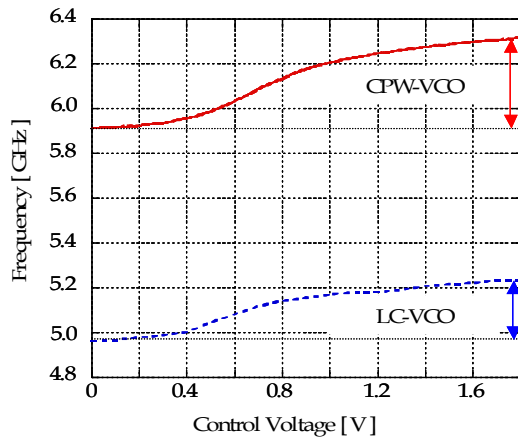


Fig. 11. Measured frequency-tuning range (FTR) showing comparison between FTR of the proposed VCO with that of LC-VCO

	LC resonator	CPW resonator
Center Frequency [GHz]	5.2	5.9
FTR [%]	5.4	10.9
Phase noise [dBc/Hz@1MHz]	-114	-109
Area [m^2]	1.4×10^{-7}	1.1×10^{-7}

Table 1. Comparison of measured parameters between two vcOs using lc resonator and on-chip cpw resonator, respectively. [ftr=frequency-tuning range]

The output power spectrum is measured by SSA which is shown in Fig. 9. Fig. 10 shows the measured phase noise of the proposed VCO. The phase noise measurement demands a dc sources free from any low-frequencies noise. Among them, the relatively pure two DC sources can be obtained from SSA but our VCO layout needs three DC sources for biasing. Therefore, we use two DC sources from SSA and a commercial DC source for remaining one. Due to this impure DC source, the spectrum of phase noise below 900KHz-offset frequency in Fig. 10 is affected by noise of the DC source. The long wires that connects the DC source and the chip that placed inside a shield box when completes a ground path with SSA, acts as a inductance and in turn becomes a loop antenna, which is the main reason of the modulated phase noise below 900MHz-offset frequency in Fig. 10. To clarify this issue, we also plotted the noise spectrum of DC source only in Fig. 10 with phase noise of the VCO and it validates the explanation above. Therefore, it is inferred that a pure DC source is inherent to measure the phase noise of a VCO and the wires that connect the DC source and the chip should be as short as possible.

The comparison of measured FTR of the proposed VCO employing on-chip CPW resonator with that of LC-VCO is shown in Fig. 11 where FTR of the proposed VCO has larger FTR than that of LC-VCO. To make the fixed frequency oscillator into a variable frequency

oscillator, varacter is connected as a capacitive load to a resonator. But the parasitic capacitances of the 1/gm devices will increase the minimum capacitance of the varacter reducing the tuning range of the conventional LC-VCO whereas in the proposed VCO, the equivalent capacitance of the varacter and CPW resonator will decrease which results in the higher FTR of the proposed VCO in Fig. 11.

Table 1 show the comparison of the parameters of the proposed VCO using on-chip CPW resonator with VCO employing LC-resonator. From the table, it is noted that the VCO using CPW resonator has advantages in terms of chip size and frequency-turning range (FTR). On the other hand, it has slightly poor performance in terms of phase noise but this design technique can be implemented for higher frequency applications whereas in designing a LC-VCO, the self-resonance of inductor prevents its applications beyond that frequency.

5. Application of On-Chip CPW Resonator to Design a Digitally Controlled Oscillator

5.1 Introduction of Digitally Controlled Oscillator (DCO)

Scaling down of CMOS technology and reduction in supply voltage complicates the implementation of RF integrated circuits in deep submicron CMOS process and demands the use of digital-assisted approaches in their circuit implementation (Matsuzawa, 2008). An oscillator, being a critical component of all digital phase locked loop (ADPLL) for future generation wireless transceiver, is necessary to be implemented using digital signals to control its frequency tuning characteristics.

Recently, various types of DCO architectures were proposed and implemented in deep submicron CMOS technology (Staszewski et al., 2005, Fahs et al., 2009). The DCO implemented in ring structure (Fahs et al., 2009) gives poor phase noise performance with high power consumption, and they are, therefore, hardly suitable for multi-GHz wireless applications. In a DCO implemented using a LC-resonator (Staszewski et al., 2005), on-chip inductor (L) is inherent which increases the chip size and in turn, results in high price. In this Section, we will propose a 10bit DCO using on-chip CPW resonator and MIM capacitors instead of the LC-resonator.

5.2 Design, Fabrication, and Experimental Results of 10 bit DCO

The proposed schematic of the designed 10 bit DCO is shown in Fig. 12 where the core of the DCO is similar to the VCO explained in chapter 3 which employed the on-chip CPW resonator instead of LC resonator. Furthermore, varacters are replaced by a capacitor bank made of MIM capacitors which are controlled by 10 bit digital signals so that wide tuning range is realized. Figure 13 shows the chip photograph of the proposed DCO to test the proposed concept of designing a DCO using on-chip CPW resonator. The control pins were wire bonded to a package and the package was placed on a PCB and externally controlled similarly as in the VCO. The output of DCO is designed with buffer circuits to provide a good matching to the measurement equipments. The measured DC power consumed by the DUT was about 75.8 mW at 1.8 V supply, and simulation shows that about 61% of total power was consumed by the buffer circuits only. The exact power consumption of the proposed DCO can be predicted when two separate DC supply source were designed for DCO core and buffer circuits, respectively. Figure 14 shows the one of the signal spectrums measured which verifies the DCO is operating at 5.2 GHz producing the power of -16 dBm.

Phase noise of the DCO was measured similarly as VCO previously. The chip was wire bonded to PCB as shown in Figure 13 and then to SMA connectors to facilitate to measure the phase noise inside the shield box. The digital controls bits are inputted through the digital pads. Figure 15 shows the phase noise of the DCO where the phase noise was to be -114 dBc/Hz (@1 MHz offset frequency).

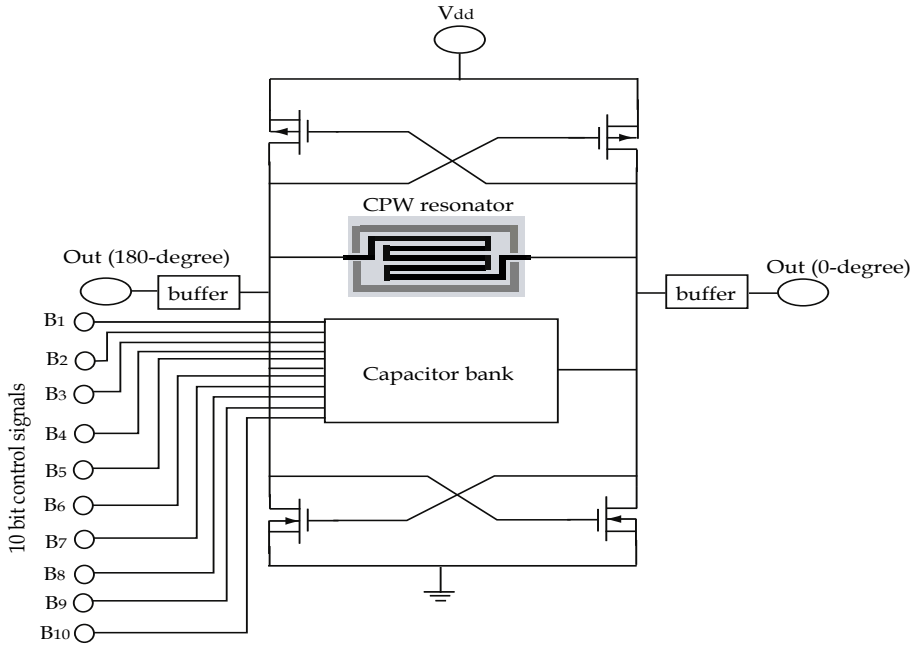


Fig. 12. Schematic diagram of 10 bit DCO using on-chip CPW resonator

We observed some modulated waves from the offset of 100 kHz to 800 kHz, and this is mainly due to the noise introduced along with the digital signals and through the interconnecting cables to the control pins.

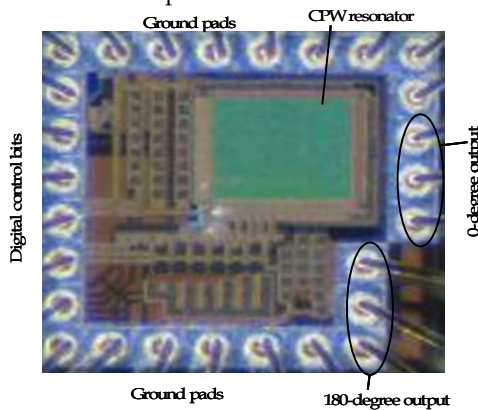


Fig. 13. Schematic diagram of 10 bit DCO using on-chip CPW resonator

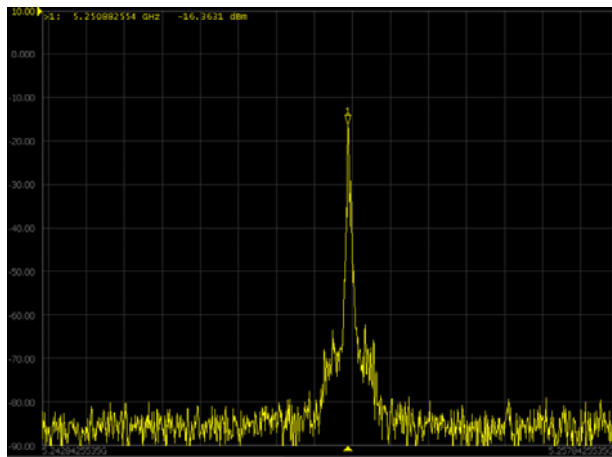


Fig. 14. Measured signal spectrum of 10 bit DCO using on-chip CPW resonator

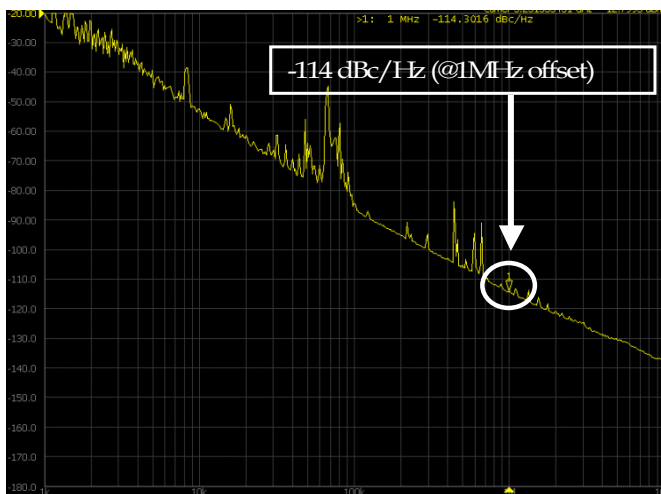


Fig. 15. Measured phase noise of 10 bit DCO using on-chip CPW resonator

	Central freq. [GHz]	Tuning step [kHz]	Power dissipation [mW]	Phase noise [dBc/Hz]	Chip size [mm ²]
Proposed TML DCO	5.0	400	75.8	-114	0.18
LC-DCO	5.0	400	75.6	-115	0.23

Table 2. Comparison of performance of the proposed TML DCO and that of a conventional LC-DCO

Table 1 shows the comparison of the performances of the proposed 10 bit DCO and another one is conventional 10 bit DCO that employed LC resonator which was also designed and tested by the authors to compare the performance with the proposed DCO. In the table, it shows that the proposed DCO has about 30% less chip area than the conventional DCO using LC resonator under similar other parameters.

6. Conclusion

The applications of on-chip CPW resonator was demonstrated to design a VCO and DCO at 5 GHz band. First, we examined the characteristics of the on-chip resonator in meander structure theoretically and experimentally in 0.18 μm CMOS technology. Then, a VCO employing on-chip CPW resonator instead of LC-tank resonator is proposed, designed and fabricated using the same technology and latter a 10 bit DCO. The advantages of employing CPW resonator is the wide frequency-tuning range, and it also saves about 30% of chip size whereas the measured other performance of the proposed oscillators are comparable to that of an oscillator using LC resonator. The design technique is applicable for higher frequencies. Furthermore, the CPW resonator in meander structure can be designed to exploit the vacant space of the layout so the chip size can be further reduced.

An equivalent circuit is developed to reproduce the experimental results of the on-chip CPW resonator whose model parameters are useful to extract RCX (Resistance-Capacitance extraction) of the chip.

7. Acknowledgement

This work was partly supported by a grant of Knowledge Cluster Initiative implemented by Ministry of Education, Culture, Sports, Science and Technology (MEXT), JSPS.KAKENHI (Wakate-B and Kiban-B), and JST-Seeds Excavation (B). This work was also partly supported by VLSI Design and Education Center (VDEC), the University of Tokyo in collaboration with CADENCE Corporation and Agilent Technologies.

8. References

- Ono, B.; Suematsu, N.; Kubo, S.; Nakajima, K.; Iyama, Y. and Ishida, O. (2001). Si substrate resistivity design for on-chip matching circuit based on electro-magnetic simulation, *IEICE Trans. Electron.*, Vol. E84-C, No. 7, (July 2001), pp. 923-929
- Umeda, Y.; Enoki, T. and Ishii, Y. (1994). Sensitivity analysis of 50-GHz MMIC-LNA on gate recess depth with InAlAs/InGaAs/InP HEMTs. *IEEE MTT-S Int. Microwave Symp. Dig.*, pp.123-126, San Diego, May 1994, IEEE
- Kanaya, H.; Pokharel, R. K.; Koga, F. and Yoshida, K. (2006). Design and verification of on-chip impedance matching circuit using transmission line theory for 2.4 GHz band wireless receiver front-end. *IEICE Trans. on Electron.*, Vol.E89-C, No.12, (December 2006), pp.1888-1895
- Pokharel, R. K.; Kanaya, H. and Yoshida, K. (2008). Design of 5GHz-band power amplifier with on-chip matching circuits using CPW impedance (K) inverters. *IEICE Trans. Electron.*, Vol. E91-C, No. 11, (November 2008), pp. 1824-1827
- Wolff, I. (2006). Coplanar microwave integrated circuits, pp. 10-90, Wiley Interscience, 2006.

- Toyoda, I. (1996). Circuit design using coplanar waveguides, *Digest of Microwave Workshops and Exhibitions (MWE'96)*, pp. 461-469, Pacific Yokohama, December 1996
- Civello, J. (2005). Addressing the challenges of RF device modeling for successful high-frequency design, *Microwave Engineering Europe*, (January 2005), pp.21-28
- Dai, L. & Harjani, R. (2003). Design of high-performance CMOS voltage controlled oscillators, Kluwer Academic Publishers, 2003
- Hajimiri, A. & Lee, T. H., (2004). The design of low noise oscillators, Kluwer Academic Publishers, 2004
- Matsuzawa, A. (2008). Digital-centric RF CMOS technologies, *IEICE Trans. Electron.*, vol. E91-C, no. 11, (November 2008), pp. 1720-1725
- Staszewski, R. B.; Hung, C.; Barton, N.; Lee M. and Leipold, D. (2005). A digitally controlled oscillator in a 90 nm Digital CMOS process for mobile phones, *IEEE J. Solid-State Circuits*, vol. 40, (Nov. 2005), pp 2203-2211
- Fahs, B.; Ali-Ahmad, W. Y. and Gamand, P. (2009). A two-stage ring oscillator in 0.13-um CMOS for UWB impulse radio. *IEEE Microwave Theory and Techniques*, vol. 57, no. 5, (May 2009), pp. 1074-1082

Design Techniques for Microwave and Millimeter Wave CMOS Broadband Amplifiers

Shawn S. H. Hsu and Jun-De Jin

*Dept. of Electrical Engineering, National Tsing Hua University
Taiwan*

1. Introduction

The microwave and millimeter wave broadband amplifier is one of the key circuit blocks for high-speed optical communication systems. It is also of extreme importance for wideband wireless communications operating within microwave frequency range. Previously reported results were mostly designed using compound semiconductor III-V (Majid-Ahy et al., 1990; Masuda et al., 2003; Shigematsu et al., 2001) or SiGe (Mullrich et al., 1998; Weiner et al., 2003) technologies to take advantage of the superior transistor characteristics. Lately, CMOS technology with continuously scaled feature sizes attracts much attention of circuit designers for wideband amplifier applications owing to the impressive cut-off and maximum oscillation frequencies (Chan et al., 2008). Considering the requirements of modern integrated circuit design such as low cost, low power consumption, and high integration level with other circuit blocks, CMOS technology is of great potential for microwave and millimeter wave broadband amplifier applications.

This chapter provides the fundamental design concepts of broadband amplifier using the modern CMOS technology. Various design techniques are introduced for achieving high performance microwave broadband amplifiers. The main design considerations and current trends are also discussed. We will give a brief overview about the applications of broadband amplifiers and background information in section 1. Section 2 discusses the considerations of transistors and inductive components in standard CMOS process for broadband amplifier design. Section 3 reviews different design techniques for broadband amplifiers with an emphasis on the inductor peaking technique. The bandwidth enhancement ratio (BWER) of each approach is calculated. In section 4, recent advances on CMOS broadband amplifier design for microwave applications are reported. We propose a pi-type inductive peaking (PIP) technique to realize a 40 Gb/s transimpedance amplifier (TIA) in 0.18- μm CMOS technology (Jin & Hsu, 2008). We also propose an asymmetrical transformer peaking (ATP) technique to achieve a miniaturized 70 GHz broadband amplifier in 0.13- μm CMOS technology (Jin & Hsu, 2008). The core area is only $\sim 0.05 \text{ mm}^2$ and the Gain-Bandwidth Product (GBP) is up to 231 GHz which is among the highest compared with other reported works with similar or even more advanced technologies. Finally, section 5 provides the closing remarks of this chapter and also some recommendations of further study on CMOS broadband amplifiers for microwave and millimeter wave applications.

1.1 Applications of microwave and millimetre wave broadband amplifiers

The block diagram of a typical fiber-optic communication system is shown in Fig. 1(a). In the transmitter side, the laser driver (LD) amplifies the signal to modulate the laser diodes for converting the electrical signal to optical signal. In the receiving end, a photo detector converts the weak optical signal that transmits through the fiber back to the electrical signal, followed by a transimpedance amplifier (TIA) and limiting amplifier (LA) to amplify the photo current. Among the front-end circuit blocks in a fiber-optic communication system, the LD, TIA, and LA are all broadband amplifiers. Currently, the data rate of the system increases from 10-Gb/s (OC-192) to 40-Gb/s (OC-768) or even up to 80-Gb/s (OC-1536), and the demands increase as well for these amplifiers with a bandwidth up to microwave and millimeter frequency range.

Another main application of broadband amplifiers is for wireless communications. The concept of broadband communication is to transmit the data in a certain bandwidth such that the data rate can increase and the emitted power can reduce. The wider the bandwidth, the greater the information-carrying capacity. There are some specific bands for the broadband communications such as multichannel multipoint distribution service (MMDS, 2-3 GHz), worldwide interoperability for microwave access (WiMax, 2-11 GHz), ultra-wide band (UWB, 3.1-10.6 GHz and 57-64 GHz), and radio astronomy (9 KHz-275 GHz). A typical block diagram of a wireless communication system is shown in Fig. 1(b). For broadband applications, the two front-end amplifiers including the low noise amplifier (LNA) and the power amplifier (PA) both have a wideband frequency response.

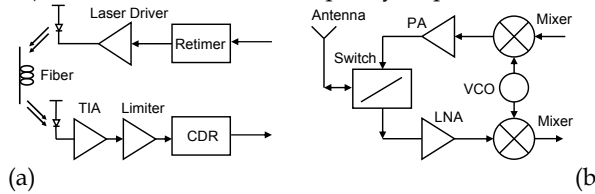


Fig. 1. (a) Block diagram of a typical fiber-optic communication system (b) block diagram of a typical wireless communication system.

2. Design considerations for CMOS broadband amplifiers

2.1 MOS transistors

Transistors play an extremely critical role in microwave circuit design, since the circuit consists of only a few transistors in most cases. Figure 2 shows the small-signal model of a MOSFET, where R_g is the poly gate resistance and R_s is due to the junction resistance. The four terminals are gate (G), drain (D), source (S), and body (B). The gate-source capacitance C_{gs} and gate-drain capacitance C_{gd} are important to the high frequency response of the transistor. The capacitances C_{sb} and C_{db} represent the paracitic capacitances of the body node to the source and drian terminals, respectively.

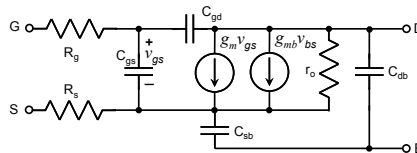


Fig. 2. Equivalent circuit model of a MOS transistor.

By neglecting the source parasitic resistance and the second order effect from the body node, the unity current gain cut-off frequency f_T and maximum oscillation frequency f_{max} of a transistor can be expressed as:

$$f_T = \frac{g_m}{2\pi(C_{gs} + C_{gd})} \quad (1)$$

$$f_{max} = \frac{f_T}{2\sqrt{(R_g)(g_{ds} + 2\pi f_T C_{gd})}} \quad (2)$$

where g_m is the transconductance and g_{ds} is the output conductance ($1/r_o$). According to the equations, the resistive and capacitive parasitics are the main limitation of the transistor f_T and f_{max} , which can be minimized through the transistor layout and selection of transistor geometry. In general, the gate resistance R_g can be reduced by employing the transistors with a multi-finger topology and a short width of each finger. The gate width W_g of each finger typically used is in a range of 1 to 3 μm for RF design if f_{max} is the major design consideration. A large finger number n can increase the transconductance for high-gain amplifier design, while f_{max} reduces with the increased total gate width due to the increase of parasitics. Note that f_T is relatively less sensitive to the increased finger number since the increase of g_m compensates the additional parasitic capacitances. Figure 3 shows the f_T and f_{max} of 0.13- μm NMOS as functions of W_g and n based on the foundry provided transistor model. As shown in the figure, the transistors of a longer W_g (5 μm) have higher f_T compared to that of a shorter W_g (1.2 μm) with the same n , which can be attributed to the increase rate of g_m is higher than that of the parasitic capacitances as W_g increases from 1.2 μm to 5 μm . It can also be observed that f_T does not increase significantly with n . On the other hand, the transistors with a shorter W_g present higher f_{max} resulting from the lower gate resistance R_g , smaller output conductance g_{ds} , and also the lower C_{gd} (under the same n). As the total finger number increases, f_{max} decreases significantly mainly due to the increased parasitic capacitance C_{gd} and output conductance g_{ds} .

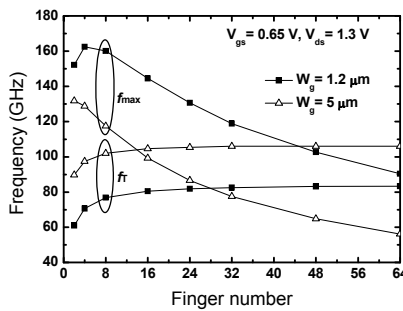


Fig. 3. Transistor (0.13- μm NMOS) f_T and f_{max} as functions of the finger width W_g and finger number n . ($W_g = 1.2 \mu\text{m}$ and $5 \mu\text{m}$)

The parasitics can also be reduced by the interconnect layout in the transistors. The wiring effect could be significant on the corresponding parasitic capacitances and resistances

especially for advanced technology with a small feature size (Chan et al., 2008). For transistors with a small gate length such as 65 nm, the parasitics originated from the transistor interconnects are critical to the overall frequency response. By changing the source, drain and gate interconnects in the transistor, the capacitive and resistive parasitics can be reduced effectively leading to improved cut-off frequency f_T and maximum oscillation frequency f_{max} . For example, we propose using the ring-type gate structure and the reduced number of interconnect layers in 65 nm N-MOSFET. The f_T and f_{max} are improved up to 21% and 22% respectively without changing any process steps. Figure 4 shows the comparison of the typical layouts using the meander-type gate with four interconnect metal layers ($M_1 \sim M_4$) from the foundry and the proposed transistor layout with the ring-type gate and only two interconnect layers ($M_1 \sim M_2$). The corresponding cross sections are also presented as indicated in the figure (A-A', B-B', and C-C'). As can be seen, the minimized metal interconnect layer can significantly reduce the sidewall parasitic capacitances and the via induced parasitic resistances leading to improved f_T and f_{max} . The improved transistor characteristics are beneficial to broadband amplifier performance.

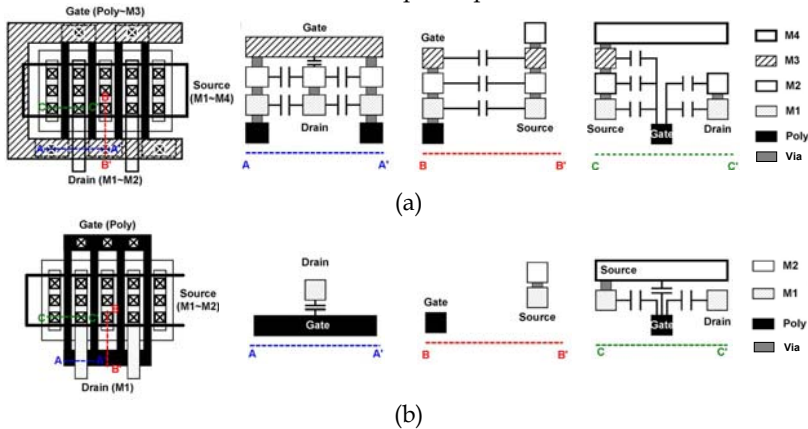


Fig. 4. Transistor layouts and the corresponding cross sections (a) typical foundry provided layout (b) proposed layout approach. The sidewall parasitic capacitances and the via induced parasitic resistances are both reduced in (b).

2.2 Inductive components

Compared with the low frequency amplifiers using analog circuit design approaches, one major difference for microwave amplifiers is the use of inductive passive components. In general, the inductive components are utilized for the matching network in microwave circuits. In addition, with inductive components, the parasitic capacitances which limit the high speed operation of a MOSFET can be resonated out to achieve wideband characteristics. For CMOS IC design, the inductive components such as inductors and transformers are usually designed as a spiral shape to maximize the inductance while minimize the chip area. Design of spiral inductor mainly considers the width w of the line, spacing s between the lines, and the metal thickness t . The foundry often provides a thick top metal layer for high Q inductor design, which has a range around $2 \mu\text{m}$ to $3 \mu\text{m}$. The spacing is limited by the technology, and the minimum value is usually employed for high inductance and small chip area. The minimum width of the metal line is also limited by the technology. The consumed

chip area reduces if using a small w , whereas the parasitic resistance could increase and the inductor quality factor (Q factor) could drop. For a wider line, a higher Q factor may be achieved, but the parasitic capacitance could limit the operation frequency. Figure 5 compares the square and octagonal inductors for the inductance and Q based on EM simulations. With the same chip area ($100\ \mu\text{m} \times 100\ \mu\text{m}$), the octagonal design has a slightly smaller overall length and thus a smaller inductance. The octagonal design also has less resistive parasitics resulting in a higher Q . Note that the square type inductor is more suitable for wideband applications owing to its lower Q and therefore a wider bandwidth for LC resonance.

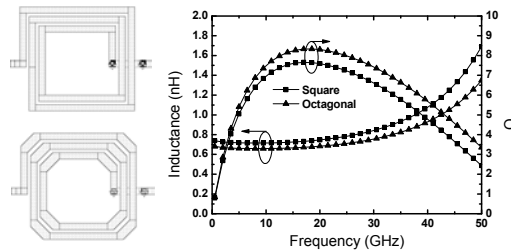


Fig. 5. Comparison of spiral inductors with two different shapes. ($w = 4\ \mu\text{m}$, $s = 2\ \mu\text{m}$, $t = 2.3\ \mu\text{m}$, inner diameter = $40\ \mu\text{m}$)

On-chip transformers are also widely used for microwave and millimeter wave amplifier design. Transformers provide flexible matching and inductive peaking capability with variable coupling ratio and alterable polarity. In some cases, a transformer is essentially equivalent to two inductors with additional mutual inductance but consumes an area similar to one inductor. The transformer layout is also similar to a symmetrical spiral inductor with a turn ratio close to one. Figure 6 shows different layouts of transformers for small turn ratio design. The black line represents the primary coil and grey line represents the secondary coil. The layout of type (a) has a small coupling factor because of less mutual inductance, and is relatively simple to achieve the desired coupling factor. The design of type (b) has a moderate coupling factor. Type (c) has a large coupling factor while the quality factor is smaller due to the capacitive parasitics. Note that the secondary side consists of several coils connected in parallel to obtain a small turn ratio. For these transformers with the winding in the same metal layer, the maximum achievable coupling factor mainly depends on the minimum metal spacing. Another design shown in Fig. 6(d) uses two adjacent metal layers for the winding of the coils. A high coupling factor can be achieved if a thin dielectric layer is between the two metals. Note that the parasitic capacitance is relatively large, which could limit the operation frequency. A general representation of the equivalent circuit model for an on-chip transformer is shown in Fig. 6(e), where R_1 and R_2 represent the ohmic losses due to the resistivity of the inductor metal lines; C_p is the parasitic capacitance of each coil originated from the spiral routing; C_m represents the coupling capacitance between the primary and secondary coils; C_{ox} is the oxide layer parasitic capacitance and C_{si} and R_{si} represent the coupling and ohmic losses due to the silicon substrate. The coefficient M describes the inductive coupling between the primary and the secondary coils.

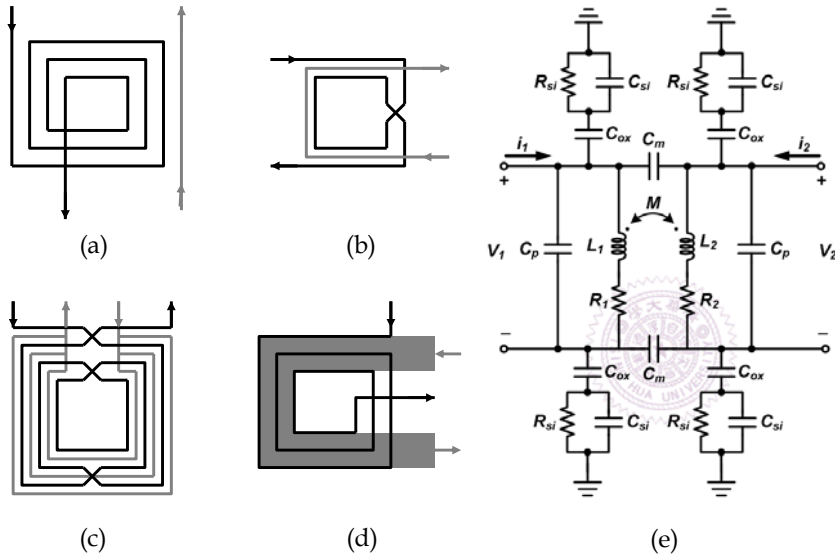


Fig. 6. (a)-(d) different designs of transformers (e) equivalent circuit model of an on-chip transformer.

It is worth mentioning that co-design of active and passive components is a useful approach to optimize the performance of microwave circuits. For the operation frequencies up to tens of GHz, the undesired resistive and capacitive components can seriously degrade the amplifier performance. As mentioned earlier, interconnect in a transistor is a critical issue for its frequency response and the inductive components are useful for bandwidth enhancement. By co-design of the transistor interconnect and the inductive components, the parasitics can be effectively minimized to enhance circuit performance. More details will be discussed later using the proposed broadband amplifier as an example, in which the transformer design considers with the transistor interconnect layout simultaneously to reduce the parasitics.

3. Design Techniques for Broadband Amplifiers

For the broadband amplifiers designed by MOSFETs, the circuit bandwidth is ultimately limited by the intrinsic capacitances of the transistors. Different approaches were proposed for bandwidth extension such as f_T doubler (Galal & Razavi, 2003), negative impedance converter (Galal & Razavi, 2003), negative Miller capacitance (Galal & Razavi, 2003; Mataya et al., 1968), distributed amplifier (DA) (Arbabian & Niknejad, 2008; Chien & Lu, 2007), and inductive peaking technique (Mohan et al., 2000; Galal & Razavi, 2003; Galal & Razavi, 2004), as shown in Fig. 7. The main design concept in these techniques is all related to how to reduce the impact of the parasitic capacitances on the circuit. Compared with the conventional differential amplifier, the f_T doubler topology reduces the input capacitance roughly to half and thus the f_T extends out to twice of the frequency. The negative impedance converter can generate negative impedance to cancel the undesired parasitics for

bandwidth enhancement. The negative Miller capacitance technique uses the similar concept to cancel the gate-drain capacitance of the transistor to extend the bandwidth. Compared with the bandwidth enhancement using passive components, these techniques utilize active components with a smaller chip area while consume additional power. Note that the effectiveness of the bandwidth extension is sensitive to the bias condition and could induce undesired oscillation problems.

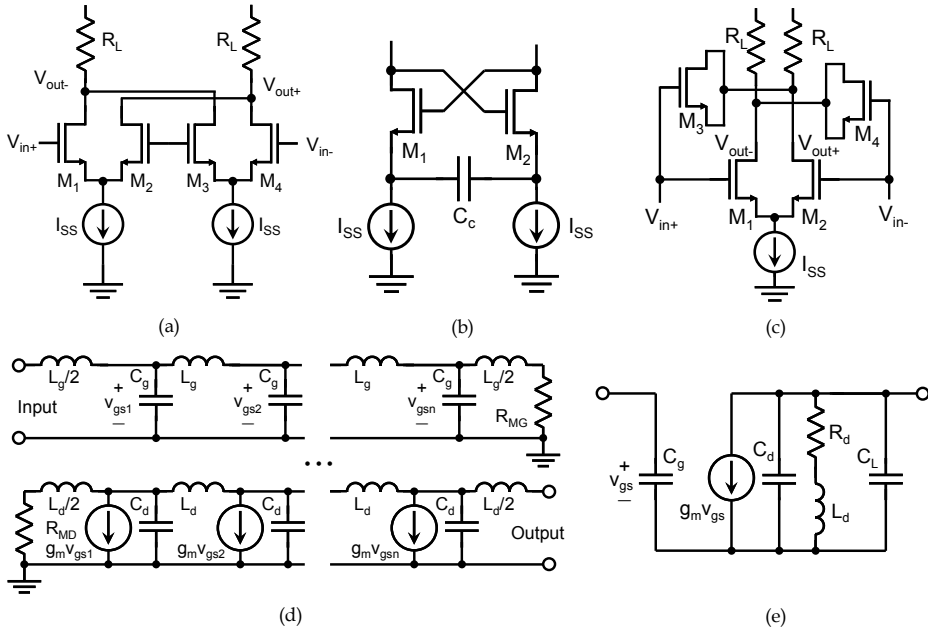


Fig. 7. Bandwidth enhancement techniques: (a) f_T doubler (b) negative impedance converter (c) negative Miller capacitance (d) distributed amplifier (DA), and (e) inductive peaking.

The DA configuration is a popular technique and Fig. 7(d) shows the simplified circuit scheme for a MOS distributed amplifier. The resistors R_{MG} and R_{MD} terminate the gate and drain lines to minimize the destructive reflection for stability and gain flatness. With the inductors L_g and L_d , the input and output artificial transmission lines are constructed by incorporating the equivalent gate and drain capacitances C_g and C_d , respectively. By a proper design of the transmission line delay, the output signal from each stage is added in phase resulting in a gain-bandwidth product much greater than that of an individual amplifier. It should be mention that the DA architecture normally consumes a large DC power and occupies a considerable amount of chip area for obtaining a high gain-bandwidth product.

Another attractive design approach is the inductive peaking technique. The fundamental idea is to introduce a zero by an inductor to cancel the original RC pole and extend the circuit bandwidth. Figure 7(e) shows a simple example of the inductive peaking topology, which is a common-source (CS) amplifier with shunt inductor peaking. With a peaking inductor L_d connected in series with the load resistor R_d , the capacitive parasitics can be

resonated out at the frequency around the original pole to extend the circuit bandwidth. The inductive peaking technique can achieve a large bandwidth while maintain a small power consumption. Various inductor peaking configurations such as shunt peaking, shunt-series peaking (Fig. 8(a)), and T-coil peaking techniques (Fig. 8(b)) will be analyzed together with the discussion of the bandwidth enhancement ratio (BWER) of each technique. Note that the comparison is based on a fundamental cascaded common-source topology, which is widely used for high frequency broadband amplifiers. The proposed wideband design techniques as will be illustrated in Section 4 also employ the cascade configuration. One fundamental difference between the DA and the cascade topology is the overall gain of each stage for the former sums up whereas that for the latter multiplies. As a result, the power consumption and chip area can be effectively reduced using the cascade configuration.

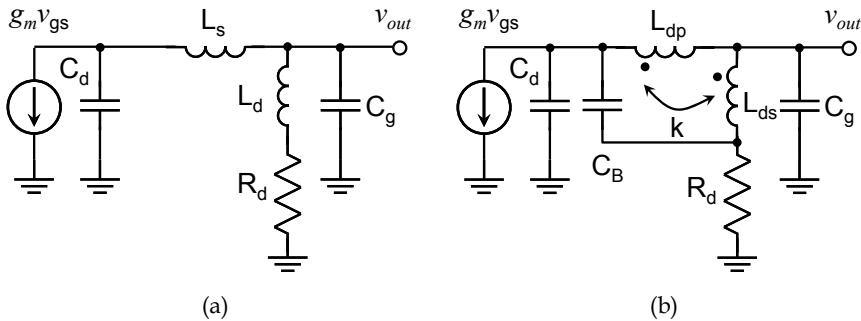


Fig. 8. (a) shunt-series inductive peaking (b) T-coil inductive peaking.

3.1 Shunt Peaking

For the small-signal equivalent circuit model of a cascaded CS amplifier, as shown in Fig. 9, the 3-dB bandwidth of each stage is determined by the drain resistance R_d , equivalent drain capacitance C_d , and equivalent gate capacitance C_g of the next stage. The ratio of C_g to C_d can be determined from the foundry provided model for a more practical estimation, which is between 2.5 and 3.5 (0.5 ~ 60 GHz) in 0.18- μm CMOS technology. Note that the gate-to-drain capacitance C_{gd} is split by the Miller theorem and included in C_g and C_d in this case. To simplify the circuit analysis, C_g/C_d is set to be 3 for the following analysis.

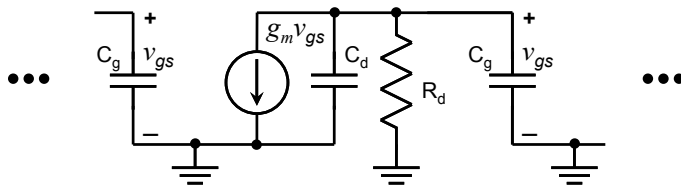


Fig. 9. Small-signal equivalent circuit model of a cascaded common-source amplifier.

The most straightforward bandwidth enhancement technique is probably shunt peaking (Mohan et al., 2000), as shown in Fig. 7(e). By connecting an inductor L_d in series with R_d , the parasitic capacitance of the drain node can be resonated out by a shunt LC resonance. An

alternative explanation is that the peaking inductor introduces a zero to extend the circuit bandwidth. Based on the transimpedance transfer function, the design equation for L_d can be derived and written as:

$$L_d = m_d R_d^2 (C_d + C_g) \quad (3)$$

With an m_d of 0.71, the maximum achievable BWER is 1.85 with a gain peaking of 1.5 dB, as shown in Fig. 10, *curve* (ii). Note that *curve* (i) is the normalized frequency response of this circuit without any bandwidth enhancement method applied.

3.2 Shunt-series Peaking

The second technique is shunt-series peaking (see Fig. 8(a)) which employs two inductors, one inductor L_d is connected in series with R_d and the other inductor L_s is in series with C_g . The design equation for both inductors can be written as:

$$L_d = \frac{L_s}{2} = \frac{R_d^2 (C_d + C_g)}{4} \quad (4)$$

The circuit analysis presented in the original publication (Galal & Razavi, 2004) shows a BWER up to 3.46 with a gain peaking of 1.8 dB based on the assumption that C_g/C_d is one. However, the BWER reduces to 1.83 when C_g/C_d of 3 is used, as shown in Fig. 10, *curve* (iii).

3.3 T-Coil Peaking

A more effective technique is the T-coil peaking (Galal & Razavi, 2003) which utilizes one transformer and one capacitor as shown in Fig. 8(b). The primary coil L_{dp} is connected between the drain node and C_g , and the secondary coil L_{ds} is between R_d and C_g . In addition, the bridge capacitor C_B is connected between the drain node and R_d . By neglecting C_d , the design equations for the transformer and capacitor can be written as:

$$L_{dp} = L_{ds} = \frac{C_g R_d^2}{4} \left(1 + \frac{1}{4\zeta^2} \right) \quad (5)$$

$$k = \frac{4\zeta^2 - 1}{4\zeta^2 + 1} \quad (6)$$

$$C_B = \frac{C_g}{16\zeta^2} \quad (7)$$

For a flat group delay response, a ζ of $\sqrt{3}/2$ results in a BWER of 2.82 if C_d is neglected. Note that the BWER obtained in Fig. 10, *curve* (iv) is reduced to 2.40 since C_d is taken into account for a fair comparison.

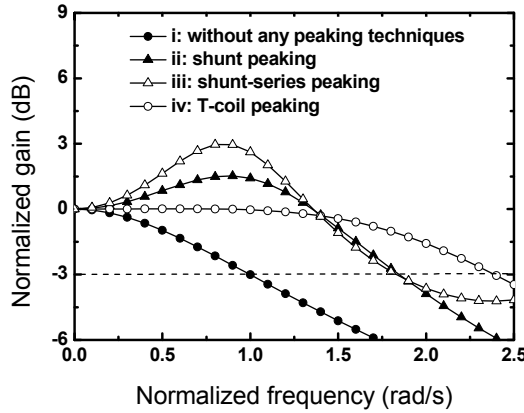


Fig. 10. Frequency response of using different inductive peaking techniques for bandwidth improvement.

4. Proposed Broadband Design Techniques

The above discussed bandwidth enhancement techniques are effective and have been used in many CMOS broadband amplifiers. In this section, we introduce two different inductive peaking techniques for wideband amplifier design.

4.1 π -type Inductor Peaking (PIP)

Figure. 11 shows the small-signal equivalent circuit model of a cascaded CS stage including the proposed PIP inductors (L_{d1} , L_{s1} , and L_{d2}), where R_{d1} and R_{d2} are the drain bias resistors. An improved BWER up to 3.31 can be obtained using the PIP inductor peaking technique by including the drain capacitance C_d , and under an assumption that the ratio of C_g/C_d is 3. The bandwidth improvement by adding each peaking inductor is described as follows.

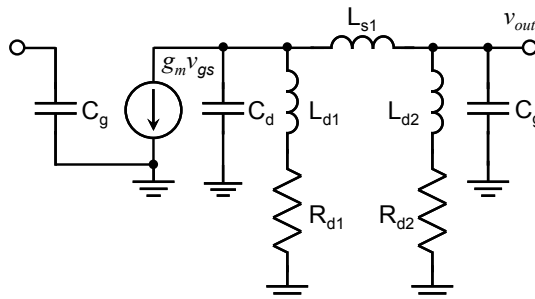


Fig. 11. The equivalent circuit model of one gain stage with the pi-type inductor peaking (PIP) technique.

If not considering the inductors, the drain current $g_m v_{gs}$ flows into C_d , C_g , R_{d1} , and R_{d2} , and generates the output voltage v_{out} . In this case, the 3-dB bandwidth ω_0 is limited by the resistive and capacitive loads. By inserting L_{d2} in series with R_{d2} , the bandwidth is increased by a parallel resonance with C_d and C_g . If L_{s1} is also added, the bandwidth can be further enhanced by a series resonance with C_g at higher frequencies, which forces more drain current to flow through L_{s1} and reach the output terminal. Finally, by introducing one more inductor L_{d1} , C_d and C_g can be resonated in parallel with L_{d1} at even higher frequencies to obtain a further improved bandwidth. According to the circuit shown in Fig. 11, Fig. 12 is the frequency response of the above four conditions, where ω_0 and the DC gain are both normalized. The gradually improved bandwidth can be observed as adding the three peaking inductors step by step. An improved BWER up to 3.31 can be obtained with the three PIP inductors.

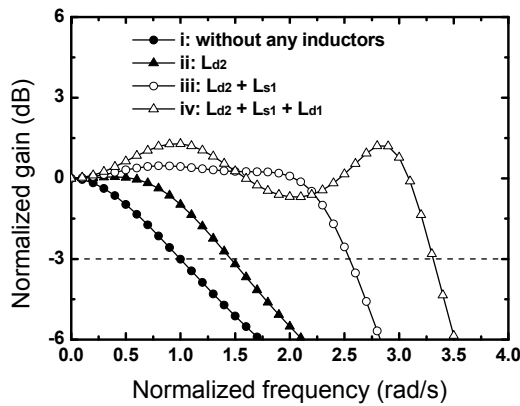


Fig. 12. Comparison of the bandwidth enhancement results using PIP technique under different numbers of peaking inductors, where $C_g = 3C_d$ and $R_{d1} = R_{d2}$.

Based on the circuit in Fig. 11, the transimpedance transfer function $Z_{PIP}(s)$ can be derived as follows:

$$Z_{PIP}(s) = \frac{v_{out}}{-g_m v_{gs}} = R_{d1} R_{d2} \frac{1 + s \left(\frac{L_{d1}}{R_{d1}} + \frac{L_{d2}}{R_{d2}} \right) + s^2 \frac{L_{d1} L_{d2}}{R_{d1} R_{d2}}}{D_0 + s D_1 + s^2 D_2 + s^3 D_3 + s^4 D_4 + s^5 D_5} \quad (8)$$

where

$$\begin{aligned} D_0 &= R_{d1} + R_{d2} \\ D_1 &= L_{d1} + L_{d2} + L_{s1} + R_{d1} R_{d2} (C_d + C_g) \\ D_2 &= (C_d + C_g) (R_{d1} L_{d2} + R_{d2} L_{d1}) + R_{d1} L_{s1} C_d + R_{d2} L_{s1} C_g \\ D_3 &= L_{d1} C_d (L_{d2} + L_{s1}) + L_{d2} C_g (L_{d1} + L_{s1}) + R_{d1} R_{d2} L_{s1} C_d C_g \\ D_4 &= L_{s1} C_d C_g (R_{d1} L_{d2} + R_{d2} L_{d1}) \\ D_5 &= L_{d1} L_{d2} L_{s1} C_d C_g \end{aligned} \quad (9)$$

The required inductances for bandwidth improvement can be determined analytically from the transfer function. The numerator includes two zeros (R_{d1}/L_{d1}) and (R_{d2}/L_{d2}) and the denominator contains two pairs of complex conjugate poles. By solving the transfer function with properly designed damping factors (< 0.707), these zeros and poles can enhance the bandwidth effectively. The properties of the poles and zeros as adding the three peaking inductors step by step are summarized in Table 1. Note that these values are obtained by assuming the gain flatness is smaller than 2.0 dB.

	without PIP	L_{d2}	$L_{d2} + L_{s1}$	$L_{d2} + L_{s1} + L_{d1}$
Zero	—	$\omega_{z1} = 1.33$	$\omega_{z1} = 1.33$	$\omega_{z1} = 1.33$ $\omega_{z2} = 2.50$
Pole	$\omega_{p1} = 1.00$	—	—	$\omega_{Ld1,p3} = 1.39$
Complex pole	—	$\omega_{Ld2,p1} = \omega_{Ld2,p2} = 1.15$	$\omega_{Ls1,p1} = \omega_{Ls1,p2} = 1.21$ $\omega_{Ls1,p3} = \omega_{Ls1,p4} = 2.37$	$\omega_{Ld1,p1} = \omega_{Ld1,p2} = 1.28$ $\omega_{Ld1,p4} = \omega_{Ld1,p5} = 3.01$
Damping factor	—	$\xi_{Ld2,p1} = 0.79$	$\xi_{Ls1,p1} = 0.82$ $\xi_{Ls1,p3} = 0.28$	$\xi_{Ld1,p1} = 0.63$ $\xi_{Ld1,p4} = 0.14$

Table 1. Properties of the poles and zeros of one gain stage with PIP under different numbers of peaking inductors, where ξ and ω_n are the damping factor and the corner frequency of the complex poles, respectively.

Based on the proposed PIP technique, a transimpedance amplifier targeting at 40-Gb/s for OC-768 applications is realized in standard 0.18- μm CMOS technology. The 40-Gb/s TIA composes of four cascaded CS stages for high transimpedance gain, as shown in Fig. 13. Identical resistance for the drain bias resistor R_D of each stage is employed, and the input and output impedances are designed as 50 Ω through the resistors $R_{M1} \sim R_{M4}$. For a high-gain consideration, a large R_D is preferred while the required peaking inductances for PIP topology increases as well. A trade-off exists here since a large inductor not only occupies more chip area but also has lower operation frequency. The resistive parasitics associated with a large inductor also degrade the circuit performance. In practical design, R_D is ~ 200 ohm and the inductors are designed to be smaller than the calculated values to reduce the resistive loss.

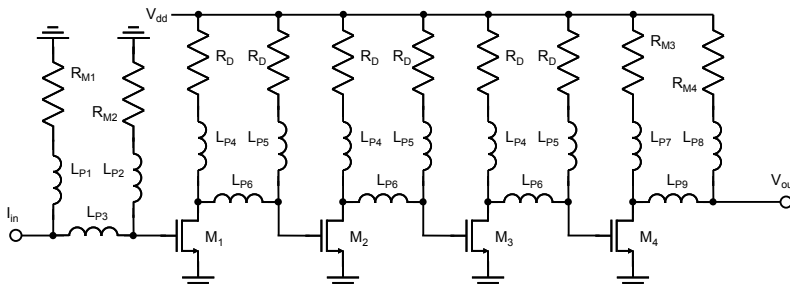


Fig. 13. Circuit topology of the proposed 40-Gb/s CMOS TIA with PIP.

Figure 14 compares the design of a TIA with and without using the proposed PIP technique. With a transimpedance gain Z_T of 51 dB Ω , the simulated bandwidth for the TIA with PIP is improved by a factor up to ~ 11 (33.8 GHz/3.1 GHz) compared to that without applying the PIP inductors.

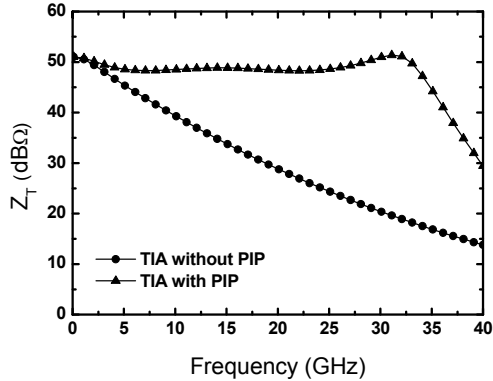


Fig. 14. Simulated frequency response for the TIA with and without PIP.

The TIA was fabricated in 0.18- μm CMOS technology with a chip area of $1.17 \times 0.46 \text{ mm}^2$ and measured on-wafer with coplanar ground-signal-ground (GSG) probes. The measured transimpedance gain Z_T is shown in Fig. 15 (a). The gain and the 3-dB bandwidth are 51 dB Ω and 30.5 GHz in the presence of an on-chip C_{pd} of 50 fF at the input, respectively. Note that the C_{pd} placed at the input is to take the photodiode parasitic capacitance into consideration. Under a 1.8 V supply voltage, the amplifier consumes 60.1 mW, and a gain-bandwidth product per DC power figure-of-merit (GBP/P_{dc}) of 180.1 GHz Ω /mW is achieved. To measure the transient response of the 40-Gb/s TIA, a high speed $2^{31}-1$ PRBS is applied. With an input current swing of 740 μA_{pp} , the output eye diagram at 40-Gb/s is shown in Fig. 15 (b) with an output voltage swing of 263 mV $_{pp}$.

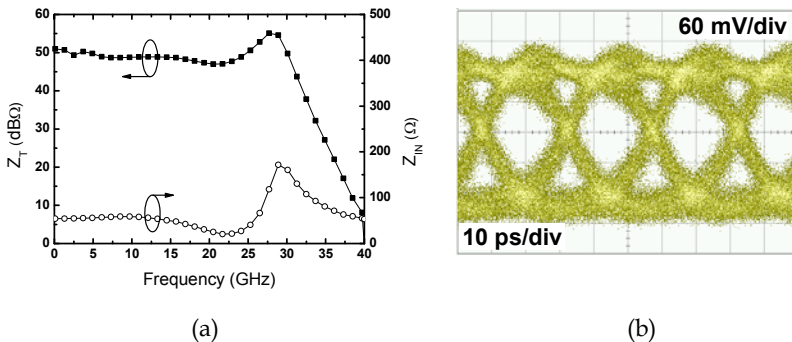


Fig. 15 Measured (a) transimpedance gain Z_T and (b) eye diagram at 40 Gb/s ($2^{31}-1$ PRBS) of the amplifier using PIP technique.

4.2 Asymmetrical Transformer Peaking (ATP)

Transformers are very useful for enhancing the microwave circuit performance owing to the mutual inductance. Amplifiers designed with transformers also allow operation under a low supply voltage. Compared to the inductor peaking technique, peaking with transformer can extend the bandwidth whereas with an improved area efficiency. Figure 16 shows the proposed asymmetrical transformer peaking (ATP) technique for broadband amplifier design. The basic design is also the cascaded common-source (CS) configuration to enhance the gain-bandwidth product. Compared with the typically used cascode topology as a unit gain block for microwave amplifier design, the CS design is easier for achieving low power design owing to the low supply voltage. Similar to other inductor peaking techniques, the basic idea of ATP is to resonate out the parasitic capacitance for bandwidth enhancement. Moreover, the transformer has the advantage of additional mutual inductor to reduce the required area of inductors. The asymmetrical primary and secondary coils can also accommodate the unequaled parasitic loading capacitances in a transistor. Based on the foundry provided transistor model and ideal inductive components, Fig. 17 shows the comparison of three designs with the same basic five-stage CS configurations. The results indicate that these designs present a similar low-frequency gain but with an obvious bandwidth difference. Without applying any peaking technique, the bandwidth is only 7.0 GHz (*curve (i)*), while the bandwidth can be significantly enhanced up to 69.7 GHz (*curve (ii)*) if the transformer is symmetrical. With the further improvement with asymmetrical coils in transformer design, the bandwidth increases up to around 80 GHz (*curve (iii)*).

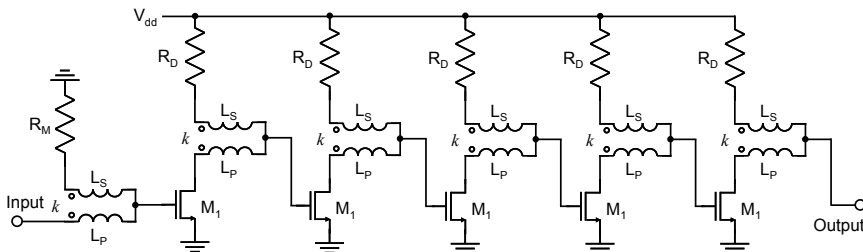


Fig. 16. The proposed broadband amplifier using asymmetrical transformer peaking (ATP) technique.

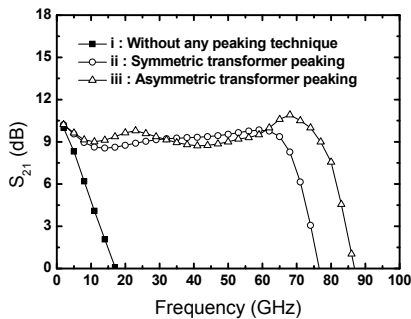


Fig. 17. Simulated frequency response with different inductive peaking techniques.

The small-signal equivalent circuit model for one gain stage in the cascaded CS configuration using transformer peaking technique is shown in Fig. 18, where C_g is the gate capacitance of the next stage and k is the coupling factor. Based on this model, the transimpedance transfer function $Z_T(s)$ from the current source $g_m v_{gs}$ to the output voltage v_{out} can be derived as:

$$Z_T(s) = \frac{v_{out}}{-g_m v_{gs}} = R \frac{1 + s(L_S - k\sqrt{L_P L_S})/R}{1 + sR(C_d + C_g) + s^2(L_P C_d + L_S C_d + L_S C_g) + s^2(-2k\sqrt{L_P L_S} C_d) + s^3 R L_P C_d C_g + s^4 L_P L_S C_d C_g (1 - k)} \quad (10)$$

As can be observed from (10), one zero (numerator) and two pairs of complex poles (denominator) are introduced, and the damping factors of the poles could be smaller than 0.707 if the circuit is properly designed. For the case of $L_P = L_S$, the design is not optimized due to the inherently unequal loading capacitances ($C_d \neq C_g$) from each side of the transformer.

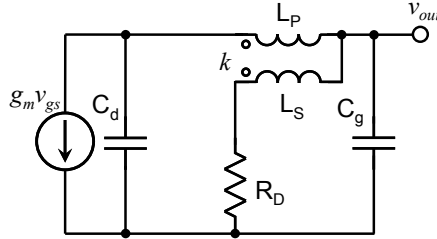


Fig. 18. Small-signal equivalent circuit model for one gain stage using transformer peaking technique.

The polarity of the transformer is also critical in this design. With a similar configuration but opposite transformer polarity, the derived Z_T from (10) can be applied directly except that all the signs need to be inverted for the k -related terms. In other words, the coupling coefficient k becomes negative in the original equation. This difference reduces the frequencies of the zero and the complex poles resulting in a smaller BWER. Based on the above analysis, the unequal inductances and an appropriate transformer polarity are both beneficial for bandwidth extension. By using the asymmetric transformer T_D , the circuit bandwidth can be enhanced up to 80.6 GHz with a gain flatness of ± 1.1 dB by $L_P = 0.11$ nH, $L_S = 0.2$ nH, and $k = 0.3$, as shown in Fig. 17, curve (iii).

It should be mentioned that a co-design approach is adopted to minimize the undesired parasitics and further enhance the amplifier performance. For millimeter wave design, layout is critical for circuit performance. In this study, the transformer layout is co-designed with the transistors for reducing the loss from interconnect parasitics and minimizing the chip area. In the adopted 0.13- μm CMOS technology, one-poly and eight-metal layers (1P8M) with various metal thicknesses and line spacings are available for transformer design. In typical design, the top layer M8 is employed for inductive components owing to the thicker metal for a lower conductor loss. However, if considering the interconnects and the overall circuit performance, M3 is a better choice for the transformer winding. By using M3 instead of M8, the additional loss introduced by the metal/via connections from M3 to M8 can be

eliminated, which can be significant at the frequency of interest. In addition, the minimum metal spacing of M8 is restricted to $2\ \mu\text{m}$, whereas the M3 layer provides a spacing of $0.21\ \mu\text{m}$ enabling a transformer with an enhanced coupling coefficient. Although the thickness of M3 is smaller than M8, the skin effect as operating at tens of GHz makes the metal thickness not that critical. For achieving the desired inductance ratio while maintaining design simplicity, two individually wound inductors are closely placed to form a transformer, as shown in Fig. 19 (a). Figure 19 (b) is the chip micrograph of the five-stage CS broadband amplifier with asymmetrical transformer peaking. The circuit area including the DC and RF probing pads is $0.66 \times 0.59\ \text{mm}^2$, and the core area is only $0.48 \times 0.11\ \text{mm}^2$ ($\sim 0.05\ \text{mm}^2$).

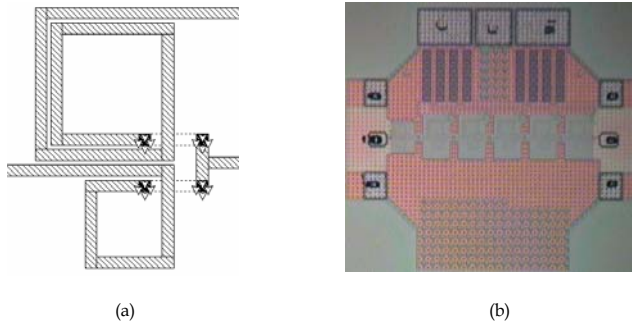
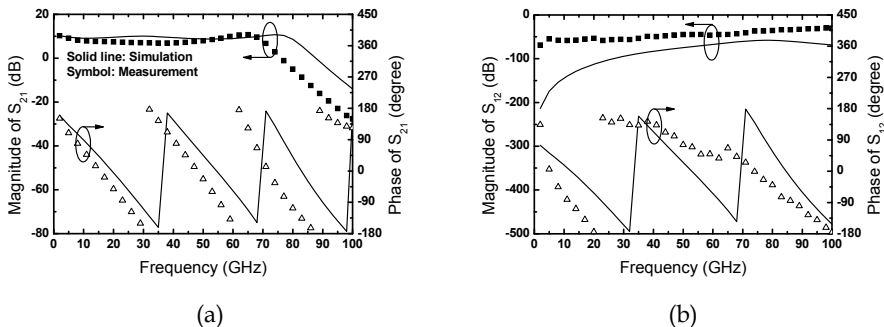


Fig. 19. (a) On-chip asymmetric transformer layout (b) chip micrograph (area: $0.66 \times 0.59\ \text{mm}^2$, core area: $0.48 \times 0.11\ \text{mm}^2$)

The broadband amplifier was fabricated in a standard 1P8M $0.13\text{-}\mu\text{m}$ CMOS process. The ground-signal-ground (GSG) RF probes were used for the on-wafer S-parameters measurement from 2 GHz to 100 GHz, as shown in Fig. 20 together with the simulated results. The measured S_{21} at low frequencies is 10.3 dB and the circuit bandwidth is 70.6 GHz under a power consumption P_{DC} of 79.5 mW. A gain-bandwidth product of 231 GHz and a GBP/P_{DC} of 2.9 GHz/mW are achieved. The measured reverse isolation S_{12} is well below $-30\ \text{dB}$ up to 100 GHz. In addition, the measured S_{11} and S_{22} are below $-6.1\ \text{dB}$ and $-10.8\ \text{dB}$ respectively within the circuit bandwidth. The measured output 1-dB compression points $P_{1dB,out}$ are 0.2 dBm, $-0.2\ \text{dBm}$, and $-1.0\ \text{dBm}$ at 5 GHz, 10 GHz, and 20 GHz, respectively.



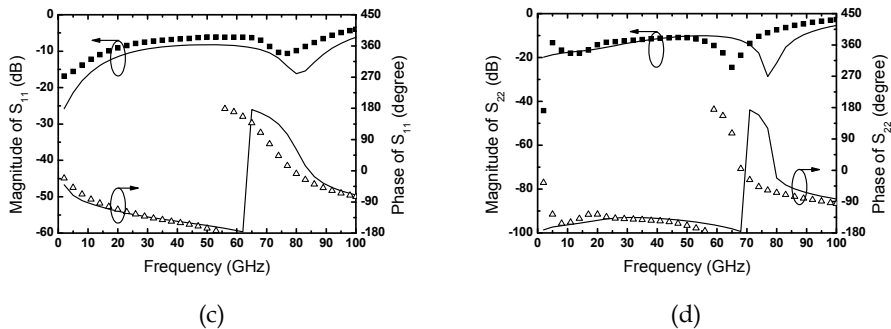


Fig. 20. Measured and simulated S-parameters of the proposed broadband amplifier using the proposed asymmetric transformer peaking (ATP).

5. Conclusion

In this chapter, various aspects for the design of microwave and millimeter wave broadband amplifiers using modern CMOS technology were discussed. Section 1 briefly introduced the applications of broadband amplifiers in wireline/wireless communication systems. Section 2 illustrated the design considerations of transistors and inductive components using standard CMOS process. The transistor geometry and interconnect were shown to be critical to its high frequency response. The design tradeoffs were also analyzed for spiral inductors and transformers in CMOS technology. In section 3, different design techniques for broadband amplifiers were reviewed. Three inductor peaking techniques including shunt, shunt-series, and T-coil approaches were compared in details. Section 4 focused on the bandwidth enhancement techniques that we proposed for CMOS broadband amplifier design. With the proposed π -type inductive peaking (PIP) technique, a 40 Gb/s transimpedance amplifier (TIA) was realized in 0.18- μm CMOS technology. We also proposed an asymmetrical transformer peaking (ATP) technique to achieve a miniaturized 70 GHz broadband amplifier in 0.13- μm CMOS technology with a core area of only ~ 0.05 mm². The PIP and ATP design techniques can be utilized for many high-speed building blocks in wireline/wireless communications systems, such as laser/modulator driver, multiplexer/de-multiplexer, and low noise amplifier/power amplifier. The successfully demonstrated design techniques for enhancing the performance of CMOS integrated amplifiers at microwave and millimeter wave frequencies enable further studies for various applications.

6. References

- Arbaban, A. & Niknejad, A. M. (2008). A broadband distributed amplifier with internal feedback providing 660GHz GBW in 90nm CMOS. *IEEE ISSCC Dig. Tech. Paper*, pp. 196-197, Feb. 2008
- Chan, C. et al. (2008). Wiring effect optimization in 65-nm low-power NMOS. *IEEE Electron Device Letters*, 29, 11, (Nov. 2008) page numbers (1245-1248)

- Chien, J.-C. & Lu, L.-H. (2007). 40Gb/s high-gain distributed amplifiers with cascaded gain stages in 0.18 μ m CMOS. *IEEE ISSCC Dig. Tech. Paper*, pp. 538-539, Feb. 2007
- Galal, S. & Razavi B. (2003). 10-Gb/s limiting amplifier and laser/modulator driver in 0.18- μ m CMOS technology. *IEEE J. Solid-State Circuits*, 38, 12, (Dec. 2003) page numbers (2138-2146)
- Galal, S. & Razavi B. (2003). Broadband ESD protection circuits in CMOS technology. *IEEE J. Solid-State Circuits*, 38, 12, (Dec. 2003) page numbers (2334-2340)
- Galal, S. & Razavi B. (2004). 40-Gb/s amplifier and ESD protection circuit in 0.18- μ m CMOS technology. *IEEE J. Solid-State Circuits*, 39, 12, (Dec. 2004) page numbers (2389-2396)
- Jin, J.-D. & Hsu, S. S. H. (2008). A 40-Gb/s transimpedance amplifier in 0.18- μ m CMOS technology. *IEEE J. Solid-State Circuits*, 43, 6, (June 2008) page numbers (1449-1457)
- Jin, J.-D. & Hsu, S. S. H. (2008) A miniaturized 70-GHz broadband amplifier in 0.13- μ m CMOS technology. *IEEE Trans. Microw. Theory Tech.*, 56, 12, (Dec. 2008) page numbers (3086-3092)
- Majidi-Ahy, R. et al. (1990). 5-100 GHz InP coplanar waveguide MMIC distributed amplifier. *IEEE Trans. Microw. Theory Tech.*, 38, 12, (Dec. 1990) page numbers (1986-1993)
- Masuda, S. et al. (2003). An over-110-GHz InPHEMT flip-chip distributed baseband amplifier with inverted microstrip line structure for optical transmission system. *IEEE J. Solid-State Circuits*, 38, 9, (Sept. 2003) page numbers (1479-1484)
- Mataya, J. A. Et al. (1968). IF amplifier using Cc compensated transistors. *IEEE J. Solid-State Circuits*, SC-3, 4, (Dec. 1968) page numbers (401-407)
- Mohan, S. S. et al. (2000). Bandwidth extension in CMOS with optimized on-chip inductors. *IEEE J. Solid-State Circuits*, 35, 3, (Mar. 2000) page numbers (346-355)
- Mullrich, J. et al. (1998). 40Gbit/s transimpedance amplifier in SiGe bipolar technology for the receiver in optical fibre TDM links. *Electron. Lett.*, 34, 5, (Mar. 1998) page numbers (452-453)
- Shigematsu, H. et al. (2001). A 49-GHz preamplifier with a transimpedance gain of 52 dB Ω using InP HEMTS. *IEEE J. Solid-State Circuits*, 36, 9, (Sept. 2001) page numbers (1309-1313)
- Weiner, J. S. et al. (2003). SiGe differential transimpedance amplifier with 50-GHz bandwidth. *IEEE J. Solid-State Circuits*, 38, 9, (Sept. 2003) page numbers (1512-1517)

MULTI-PORT TECHNOLOGY AND APPLICATIONS

Moldovan Emilia¹, Bosisio G. Renato², Wu Ke² and Tatu Serioja O.¹

¹*Institut National de la Recherche Scientifique INRS-EMT Montreal*

²*Ecole Polytechnique de Montreal
Canada*

1. Introduction

This chapter is dedicated to the description of emerging multi-port circuit designs based on various technologies and their related applications in wireless communication systems and radar sensors.

The multi-port circuit theory was first developed in the 1970s by Engen and other scientists, for accurate automated measurements of the complex reflection coefficient in microwave network analysis. These multi-port pioneers highlighted its usefulness in micro-wave low-cost circuit characterizations (S-parameters). The multi-port techniques were further proposed and developed by Professor R. G. Bosisio and collaborators, for use as a microwave and millimeter wave demodulator in connection with homodyne and heterodyne receivers since 1994. Several multi-port architectures for specific applications have been developed and demonstrated.

Basically, the multi-port is composed of several couplers interconnected by transmission lines and phase shifters. The multi-port acts as an interferometer; its output signals are linear combinations of phase shifted reference and input unknown signals. By using appropriate power detectors at each output and simple analogue signal processing, this circuit can provide I/Q down-conversion or direct modulation.

The chapter describes and analyzes several multi-port circuit implementations and their advantages versus the conventional approaches. Taking benefit of the advancements in fabrication technologies at microwave and millimeter wave frequencies, bulky waveguide circuits have been integrated into various Substrate Integrated Circuits (SICs), including synthesized metallic and dielectric waveguides. For example, Substrate Integrated Waveguides (SIW) consist of a new design scheme based on the concept that a standard metallic rectangular waveguide can be synthesized by two linear arrays of metalized via holes or slots, which are made on the same planar substrate, along with other planar circuits. Despite its dimensional limitations, the conventional Rectangular Waveguide (RWG) technology is still necessary to connect all these SICs to standard millimeter-wave equipment and circuits. Various multi-port circuit schemes and practical realizations, including Miniature Hybrid Microwave Integrated Circuit (MHMIC) and Monolithic Microwave Integrated Circuit (MMIC) implementations, are presented.

Multi-port implementations in Ka-band and V-band receivers for Wireless Local Area Networks (WLANs) dedicated to high data-rate communications are discussed. The multi-port interferometer is an innovative approach, due to its intrinsic properties, such as wide bandwidth, reduced local oscillator power required to perform efficient down-conversion, excellent isolation between input RF ports, and very good suppression of harmonic and spurious products. Multi-ports have been successfully used to demodulate various QAM/PSK signals at hundreds of Mb/s data rates.

Furthermore, multi-port W-band automotive Continuous Wave (CW), V-band Frequency Modulated CW (FMCW), and Phase Coded CW (PCCW) radar sensors with their related relative velocity and distance measurement principles are discussed and compared.

Computed Aided Design (CAD) tools, such as Advanced Design Systems (ADS) of Agilent Technologies and High Frequency Structure Simulator (HFSS) of Ansoft have been used for circuit designs and system simulations. Test bench prototype photographs, and comparative analysis between simulation and measurement results enforce the presentation.

2. The Multi-port Reflectometer

The multi-port, actually a “six-port” circuit, was first developed by Cohn and Weinhouse (1964) to evaluate the phase of a microwave signal, and extended by Engen (1972, a.1977) and other scientists, for accurate automated measurements of the complex reflection coefficient in microwave network analysis. Between 1972 and 1994, similar researches were pursued by other laboratories, including Poly-Grames Research Center of Ecole Polytechnique of Montreal.

The proposed six-port is a passive circuit, composed of hybrid couplers and/or power dividers, connected by transmission lines. It has two inputs, one for the unknown signal and other for the reference one, and four outputs. The output signals represent linear combinations between the input signals. The evaluation of the reflexion coefficient is based on the measurement of output signal power levels, $|b_i|^2$, where $i = 1, \dots, 4$, as follows:

$$P_1 = |b_1|^2 = |Aa + Bb|^2 \quad (1)$$

$$P_2 = |b_2|^2 = |Ca + Db|^2 \quad (2)$$

$$P_3 = |b_3|^2 = |Ea + Fb|^2 \quad (3)$$

$$P_4 = |b_4|^2 = |Ga + Hb|^2 \quad (4)$$

The A to H are complex constants based on multi-port calibration, and \mathbf{a} and \mathbf{b} are the incident and the reflected wave, respectively, at the measurement point. Taking into account that each output signal linearly depends on the incident wave power $|a|^2$, and choosing the port 4 as reference, the output signal power levels will only depend on \mathbf{a} . Hence, if $H=0$,

$$P_4 = |G|^2 |a|^2 \quad (5)$$

and the normalized output powers of ports 1 to 3 are:

$$p_1 = P_1/P_4 = |A|^2 |a|^2 |\Gamma - q_1|^2 \quad (6)$$

$$p_2 = P_2/P_4 = |C|^2 |a|^2 |\Gamma - q_2|^2 \quad (7)$$

$$p_3 = P_3/P_4 = |E|^2 |a|^2 |\Gamma - q_3|^2 \quad (8)$$

where $q_1 = -B/A$, $q_2 = -D/C$, $q_3 = -F/E$, and A to F are known, due to calibration process. Hence, the reflexion coefficient can be easily obtained using the output power readings. In order to illustrate the previous theoretical considerations, the bloc diagram of a six-port reflectometer based on four hybrid couplers is presented in Fig. 1.

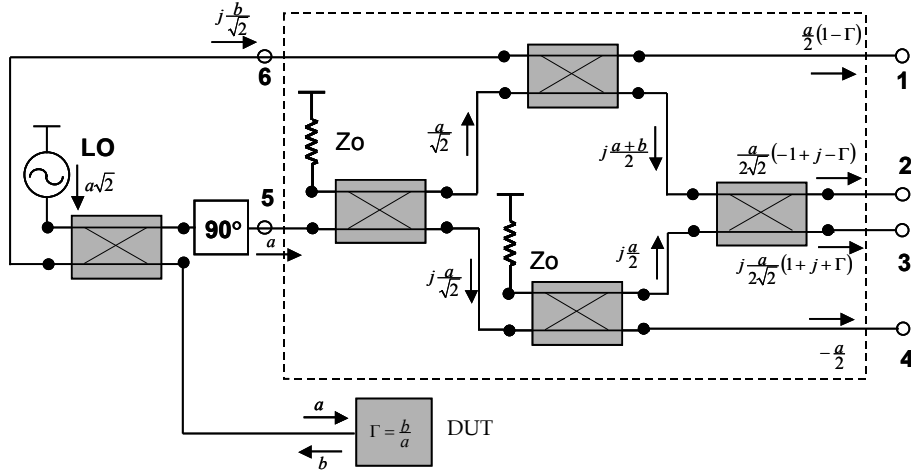


Fig.1. The block diagram of a six-port reflectometer

The reference signal is generated by a local oscillator. $\Gamma = b/a$ represents the reflexion coefficient of the device under test (DUT). The output powers can be expressed as follows:

$$P_1 = (|a|^2/4) |\Gamma - 1|^2 \tag{9}$$

$$P_2 = (|a|^2/8) |\Gamma - (-1 + j)|^2 \tag{10}$$

$$P_3 = (|a|^2/8) |\Gamma - (-1 - j)|^2 \tag{11}$$

$$P_4 = |a|^2/4 \tag{12}$$

By choosing the power of port 4 as reference, due to its non-dependence on Γ , the normalized powers are:

$$p_1 = P_1 / P_4 = |\Gamma - 1|^2 \tag{13}$$

$$p_2 = P_2 / P_4 = 1/2 |\Gamma - (-1 + j)|^2 \tag{14}$$

$$p_3 = P_3 / P_4 = 1/2 |\Gamma - (-1 - j)|^2 \tag{15}$$

Hence, three circles in complex plan Γ are obtained:

$$|\Gamma - 1|^2 = \sqrt{p_1} \tag{16}$$

$$|\Gamma - (-1 + j)|^2 = \sqrt{2p_2} \tag{17}$$

$$|\Gamma - (-1 - j)|^2 = \sqrt{2p_3} \tag{18}$$

These circles, presented in Fig. 2, are centered at $q_1 = 1$, $q_2 = -1 + j$ and $q_3 = -1 - j$.

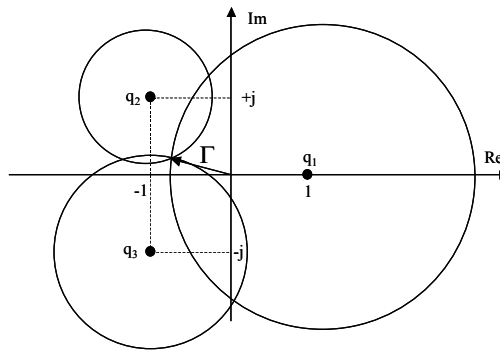


Fig. 2. The family circles in Γ plane

The reflection coefficient Γ is determined by the intersection of these three circles, whose radii are obtained by power measurements. The q_i points depend on the six-port architecture. Ideally, they should be located at the vertices of an equilateral triangle whose center is at the origin. Consequently, $|q_1| = |q_2| = |q_3|$, while the arguments differ by $\pm 120^\circ$ (Engen, b. 1977).

3. The Multi-port Interferometer

In the nineties, the idea of a multi-port circuit to be used in direct conversion microwave receivers was proposed for the first time at the PolyGrames Research Center of Ecole Polytechnique de Montreal, Canada, by Professor R.G. Bosisio and his collaborators. The first reported changes were for narrow-band single-carrier demodulation of digital data (Li et al., 1994, 1995, 1996). The multi-port architecture was very similar to the original approach and a calibration process was needed to perform measurements.

The idea of a multi-port interferometer with no need of calibration appeared in 2001 (Tatu et al, 2001). Especially for microwave and millimeter wave frequency, the multi-port successfully replace the conventional I/Q mixers in the receiver front-ends.

3.1 The Multi-port Interferometer Operating Principle

The multi-port circuit presented in Fig. 3, is composed of three 90° hybrid couplers and a Wilkinson power divider. This architecture is typical for a multi-port microstrip implementation. When a standard rectangular waveguide realization is suitable, four 90° hybrid couplers and a 90° phase shifter must be used. The 90° phase shifter will be implemented using a quarter of wave length line, in order to obtain in-phase power split signals, as done by a Wilkinson power divider.

This circuit is designed to perform phase and amplitude measurements without a calibration procedure (Tatu et al, 2005). The phase shift and relative amplitude between RF unknown and reference input signals, a_6 and a_5 , respectively, will be obtained by output power measurements.

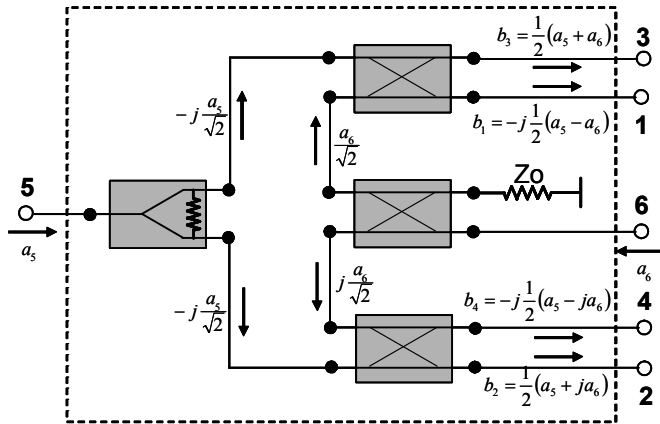


Fig. 3. The multi-port circuit

In a general case, the output signals, b_i , can be expressed in function of the multi-port dispersion parameters (S_{ij}):

$$b_i = \sum_{j=1}^6 S_{ij} a_j, \quad i = 1, \dots, 6 \tag{19}$$

The scattering matrix of the proposed multi-port phase discriminator can be easily obtained using the diagram of Fig. 3 as follows:

$$\begin{bmatrix} b_1 \\ b_2 \\ b_3 \\ b_4 \\ b_5 \\ b_6 \end{bmatrix} = \frac{1}{2} \begin{bmatrix} 0 & 0 & 0 & 0 & -j & j \\ 0 & 0 & 0 & 0 & 1 & j \\ 0 & 0 & 0 & 0 & 1 & 1 \\ 0 & 0 & 0 & 0 & -j & -1 \\ -j & 1 & 1 & -j & 0 & 0 \\ j & j & 1 & -1 & 0 & 0 \end{bmatrix} \cdot \begin{bmatrix} a_1 \\ a_2 \\ a_3 \\ a_4 \\ a_5 \\ a_6 \end{bmatrix} \tag{20}$$

Supposing a perfect match ($a_1 = a_2 = a_3 = a_4$), the two normalized input waves having α amplitude ratio and $\Delta\varphi = \varphi_6(t) - \varphi_5$ phase difference, can be expressed as follows:

$$a_5 = a \exp(j \varphi_5) \tag{21}$$

$$a_6 = \alpha a \exp[j \varphi_6(t)] = \alpha a_5 \exp(j \Delta\varphi) \tag{22}$$

Therefore, the four normalized output waves can be expressed in function of input waves and scattering (S) parameters:

$$b_i = a_5 S_{5i} + a_6 S_{6i}, \quad i = 1, \dots, 4 \tag{23}$$

More specifically:

$$b_1 = a/2 \exp[j (\varphi_5 - \pi/2)] \{1 - \alpha \exp[j (\Delta\varphi + \pi)]\} \tag{24}$$

$$b_2 = a/2 \exp(j \varphi_5) \{1 + \alpha \exp[j (\Delta\varphi + \pi/2)]\} \quad (25)$$

$$b_3 = a/2 \exp(j \varphi_5) \{1 + \alpha \exp(j \Delta\varphi)\} \quad (26)$$

$$b_4 = -a/2 \exp[j(\varphi_5 + \pi/2)] \{1 + \alpha \exp[j (\Delta\varphi - \pi/2)]\} \quad (27)$$

In order to obtain the DC output signals, four power detectors are connected to the multiport outputs. As known, the DC output voltage of an ideal power detector is proportional to the square magnitude of the RF input signal:

$$V_i = K_i |b_i|^2, i = 1, \dots, 4 \quad (28)$$

Supposing that identical power detectors are used, $K_i = K$, the DC output voltages will be:

$$V_1 = K |b_1|^2 = K a^2/4 [1 + \alpha^2 - 2\alpha \cos (\Delta\varphi)] \quad (29)$$

$$V_2 = K |b_2|^2 = K a^2/4 [1 + \alpha^2 - 2\alpha \sin (\Delta\varphi)] \quad (30)$$

$$V_3 = K |b_3|^2 = K a^2/4 [1 + \alpha^2 + 2\alpha \cos (\Delta\varphi)] \quad (31)$$

$$V_4 = K |b_4|^2 = K a^2/4 [1 + \alpha^2 + 2\alpha \sin (\Delta\varphi)] \quad (32)$$

Each function $V_i (\Delta\varphi)$ is periodical of 2π and the output minimum voltages are shifted by $\pi/2$ one to other. The normalized DC output voltage variations in a 360° input signal phase difference shift are presented in Fig. 4 ($v_i = V_i/K |b_i|^2, i = 1, \dots, 4$). The input signals are considered of the same amplitude ($\alpha = 1$).

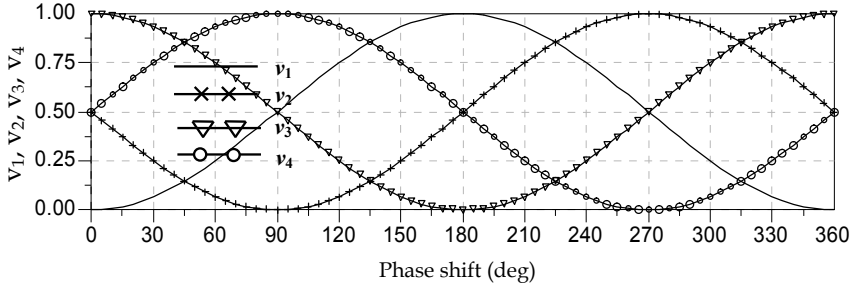


Fig. 4. Normalized DC output voltage variations for a 360° shift of input signal phase difference

As seen, the minimal values are shifted by 90° multiples. In addition, the output voltages at ports 1 and 3, and 2 and 4, respectively, are phase opposites. Therefore, the output quadrature signals I/Q can be obtained using a differential approach.

In the I/Q complex plane, a Γ vector can be defined based on the four output voltages:

$$\Gamma = (V_3 - V_1) + j(V_4 - V_2) \quad (33)$$

and the I/Q signals are:

$$I = V_3 - V_1 = \alpha K a^2 \cos (\Delta\varphi) \quad (34)$$

$$Q = V_4 - V_2 = \alpha K a^2 \sin (\Delta\varphi) \quad (35)$$

Previous equations show that, theoretically, the output signal DC offset is equal to zero. In practice, this value is not null, but can be reduced by a rigorous design of the multi-port circuit and its power detectors.

Based on previous equations, the Γ vector can be expressed as:

$$\Gamma = \alpha K a^2 \exp(j \Delta\varphi) \quad (36)$$

It is to be noted that the Γ magnitude is proportional to the amplitude ratio between the input signals and its phase represents their phase difference:

$$\varphi_{\Gamma} = \Delta\varphi = \varphi_6 - \varphi_5 \quad (37)$$

This biunique correspondence between RF and baseband domains proves that the multi-port circuit can act as a phase discriminator.

In the same time, it can be demonstrated that this circuit can also act as an amplitude discriminator. If the input signal is PSK modulated, the Γ circle radius is a function of the input multi-port power, as expected. As known, the input RF power is equal to the square magnitude of the normalized input wave. According to equation (36) and the normalized wave definition, the magnitude of Γ became:

$$|\Gamma| = \alpha K |a|^2 = (P_{IN}/P_{REF})^{1/2} K P_{REF} = K (P_{IN}P_{REF})^{1/2} \quad (38)$$

where P_{IN} and P_{REF} represent the powers of the RF input and local oscillator reference signals, respectively. Supposing a variation of RF input signal power from P_{IN1} to P_{IN2} , and assuming a constant local oscillator power, this will be proportional to a variation of Γ magnitude:

$$|\Gamma_1| / |\Gamma_2| = (P_{IN1}/P_{IN2})^{1/2} \quad (39)$$

For a dB quantification of this relation:

$$20 \log(|\Gamma_1| / |\Gamma_2|) = 20 \log[(P_{IN1}/P_{IN2})^{1/2}] = 10 \log(P_{IN1}/P_{IN2}) \quad (40)$$

and

$$|\Delta\Gamma|_{dB} = \Delta P_{IN \text{ dB}} \quad (41)$$

The previous equation shows that the amplitude variation of the baseband signal in complex plane is equal to the RF input signal power variation in the same time range, for a constant reference signal. This property proves the capability of the multi-port circuit to also act as an amplitude discriminator.

Equations (37) and (41) represent the fundament of multi-port theory, proving the potential of this circuit to demodulate various PSK and QAM modulated signals.

3.2 The Multi-port Practical Implementations

The multi-port circuit was implemented in various architectures and technologies. The choice of the fabrication technology depends on the operating frequency and application.

Microstrip Monolithic Microwave Integrated Circuits (MMIC) and Miniature Hybrid Microwave Integrated Circuits (MHMIC) were preferred for prototypes at Ka and V band frequencies, for various communication receivers and radar sensors, in homodyne and heterodyne implementations. The Substrate Integrated Waveguide (SIW) and Standard Rectangular Waveguide (SRW) technologies were used at W band frequencies, to support higher power levels, requested in radar sensors and phase noise measurement applications.

3.2.1 MHMIC and MMIC Microstrip Multi-port Implementations

During the time, various multi-port circuits were designed and fabricated in microstrip technology, for different applications. The typical topology of the circuit was illustrated in Fig. 3. This multi-port circuit is designed as the core of an I/Q demodulator, using three 90° hybrid couplers and a Wilkinson power divider.

The relative power reading of the output signals gives sufficient information to determine the phase shift between the two RF inputs, thereby realizing a QPSK demodulator.

The Momentum of Advanced Design System (ADS) software of Agilent Technology was used for the circuit design in microstrip implementations.

A good design targets the reflection and insertion loss, and the isolation between the RF and reference signal. It is to be mentioned that, due to its architecture, the insertion loss of an ideal multi-port is 6 dB. The isolation of the inputs is a very important criterion of the communication systems. The phase difference between the two input signals is evaluated by linear combinations of four output signals, detected at ports 1, 2, 3 and 4. In order to reduce the DC offset caused by the multiple reflections at the outputs, related return losses at the operating frequency must be excellent.

3.2.1. a. Ka-band Microstrip Implementations

At the beginning, a multi-port circuit was designed at Ka-band frequencies, in MHMIC and MMIC technologies, to be used in a direct conversion receiver for high speed QPSK communications (Tatu et al., 2001).

The circuit was first designed and fabricated in hybrid technology, on a 250 μm ceramic substrate with a relative permittivity $\epsilon_r = 9.9$. The layout and related photograph of the MHMIC multi-port Ka-band implementation are shown in Fig. 5.

The distributed parameter multi-port, composed of three compact 90° hybrid couplers and a Wilkinson power divider, is placed in the middle of the circuit layout. Surface-mounted RF Schottky diodes and related wide-band matching circuit networks are connected to multi-port outputs. The MHMIC chip outer dimensions are 23 x 23 mm.

At the central operating frequency, the measured reflection coefficients S_{11} to S_{66} are less than -24 dB and the measured isolation between RF and reference ports, S_{56} , is found to be at least -27 dB. The measured transmission coefficients are close to the theoretical predicted value of -6 dB. The detection circuit is designed to cope with a wideband operation (23 to 31 GHz) using HSCH-9161 type zero-bias Schottky diodes.

The MMIC multi-port module is fabricated on a 100 micron TriQuint's GaAs substrate with a relative permittivity $\epsilon_r = 12.9$ (Tatu et al., 2002).

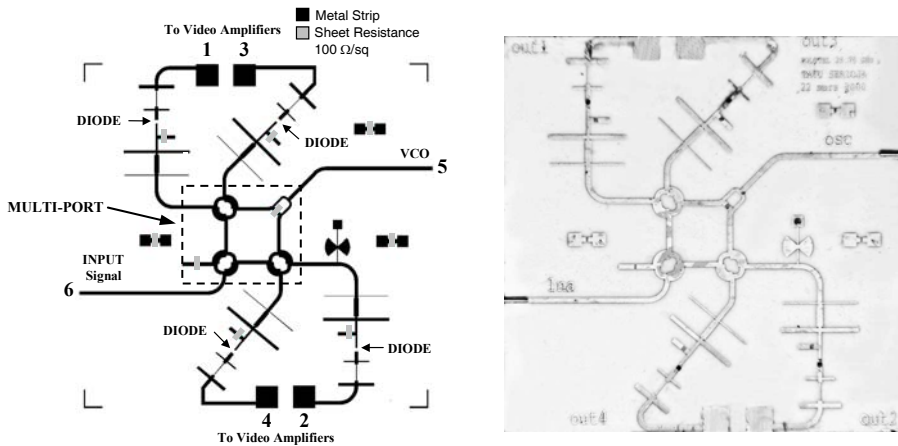


Fig 5. MHMIC Ka-band layout (and photograph) of multi-port circuit with power detectors

Three different implementations of the 90° hybrid coupler in a frequency range of 6 GHz, between 24 and 30 GHz, with distributed parameters, discrete components, and a combination of both methods, are realized and compared. The distributed parameter implementation is large in size (1.39 mm²), but it has excellent S parameter performances. The discrete element coupler has a very small size, but the fabrication process tolerances at this frequency range lead to poor S parameter performances. The hybrid implementation using high impedance transmission lines and capacities leads to very good S parameter performances.

Fig. 6.a shows the RF topology of a wideband millimeter wave MMIC distributed parameter multi-port circuit with integrated RF Schottky diodes (marked by arrows) and related matching networks, using 50 Ω transmission lines. The circuit is realized in a 100 micron GaAs substrate. Its size is about 4 x 4 mm.

In order to reduce the size of the MMIC circuit, a new approach is proposed. The couplers are realized using high impedance transmission lines and discrete components (shunt capacitors of 200 fF, loaded near the ports of the hybrid couplers). The diameter of these couplers is 600 microns, representing 45% of the first implementation, with a diameter of 1330 microns. The same RF Schottky diodes are used in this implementation. Their matching networks are also realized using shunt capacitors and high impedance transmission lines.

Fig. 6.b shows the RF topology of this hybrid circuit. Its size is reduced to 2 x 3 mm, representing about 37% of the first implementation.

In order to characterize the MMIC multi-port circuit, a study of its S parameters in a 6 GHz range around the central frequency, was made. The magnitude and phase of the S parameters versus the operating frequency are close to the predicted values. The results of both implementations (see Figs. 6.a and b) are practically similar.

In the operating band, the magnitudes of the transmission coefficients, illustrated in Figs. 7.a and b, are close to the theoretically predicted values of -6 dB. The phase shifts between the same parameters are multiples of 90° over the considered frequency band (6 GHz), as seen in Figs. 8.a and b.

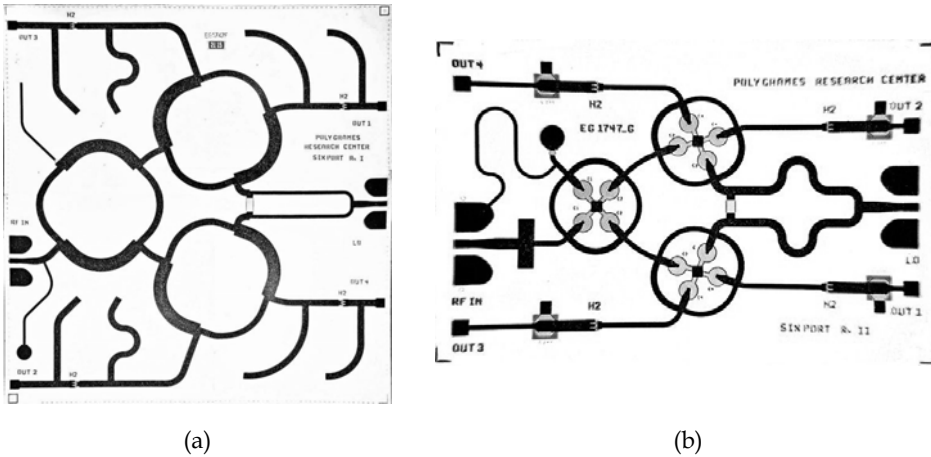


Fig. 6. MMIC multi-port module: (a) distributed parameters; (b) hybrid implementation

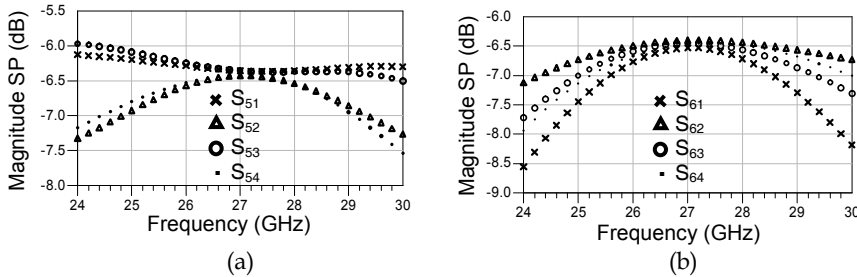


Fig.7. Magnitude of transmission coefficients vs. the operating frequency: (a) LO; (b) RF

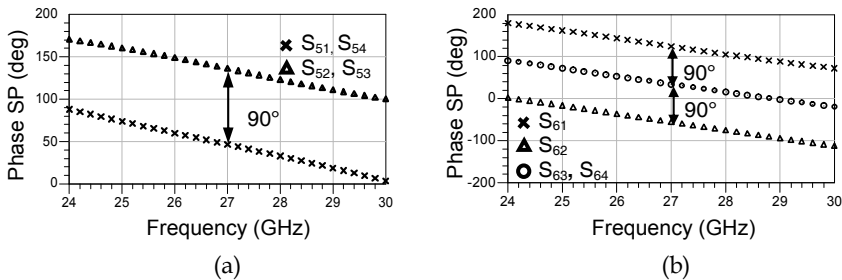


Fig. 8. Phase of transmission coefficients vs. the operating frequency: (a) LO; (b) RF

Fig. 9 shows excellent return loss and isolation of RF inputs (S_{55} , S_{66} , S_{56}) in the considered frequency band, for the MMIC multi-port module, including the Schottky diodes. Therefore, as for the MHMIC circuit, it can be concluded that the influence of DC offsets in the demodulating process is significantly minimized.

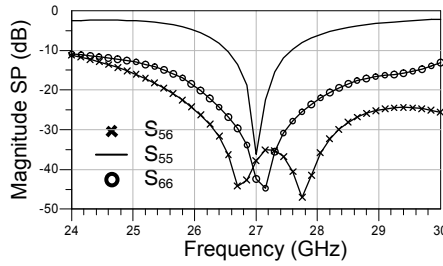


Fig. 9. Return loss and isolation of input ports vs. the operating frequency

Considering a QPSK modulation, the RF design of the multi-port circuit is such that only one of four possible modulation states is correctly identified, at any given time, by an analogue decoder. Harmonic balance simulation of the MMIC multi-port module is shown in Fig. 10. The local oscillator (LO) and RF input power levels were both set at -3 dBm. As seen, each output voltage of the multi-port has a single maximum value over a 360° phase-shift between input signals.

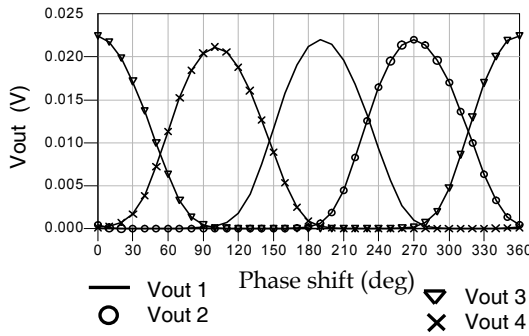


Fig. 10. MMIC multi-port output voltages vs. the phase difference of input signals

3.2.1. b. V-band Microstrip Implementation

A V-band multi-port circuit was designed in MHMIC technology using a $125 \mu\text{m}$ ceramic substrate, having a relative permittivity of 9.9 (Boukari et al., 2009). The circuit topology is based on four 90° hybrid couplers connected by 50Ω microstrip transmission lines, as seen in the microphotograph of Fig. 11. In order to avoid reflections at the two unused ports of the multi-port circuit, 50Ω loads are connected to open circuited quarter-wave transmission lines (representing virtual RF short-circuits). The hybrid coupler connected to LO port (5) together with the 90° phase shifter (implemented using an additional quarter-wave transmission line on curved branch) is equivalent to an in-phase 3 dB power divider.

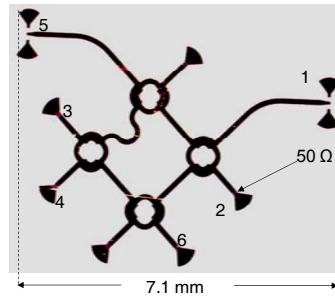


Fig. 11. The microphotograph of the V-band MHMIC multi-port

On-wafer multi-port S parameter measurements are performed using an Agilent PNA millimeter-wave network analyzer, over 4 GHz band, between 60 and 64 GHz. Fig. 12 presents typical S parameter variations for this multi-port circuit.

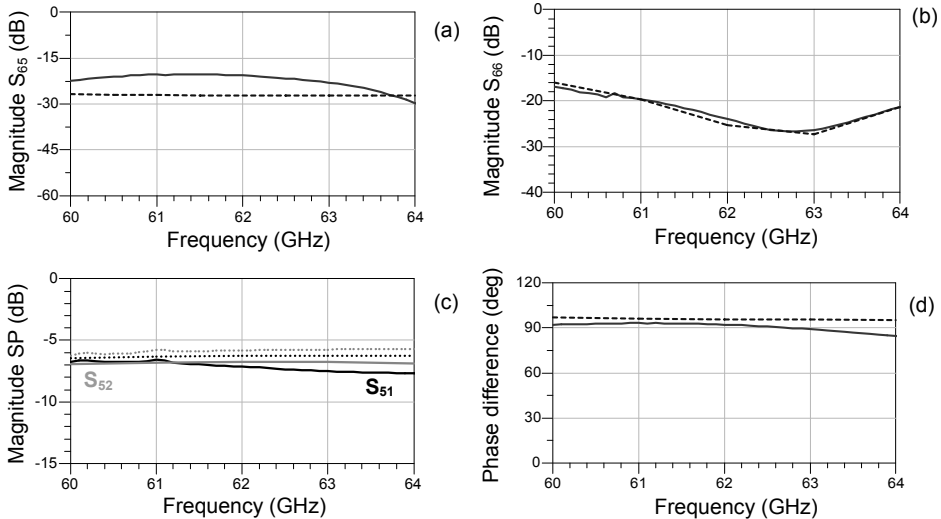


Fig. 12. Simulated (dotted line) and measured (continuous line) S-parameters of the V-band multi-port

As seen, good results are obtained for return loss and isolation between the RF input ports. In addition, power split is quasi-constant over the band and close to the theoretical value of -6 dB. The use of the V-band hybrid couplers determines a quasi-constant 90° phase difference over a wide band, suitable for a good I/Q mixer.

In order to demonstrate that the multi-port is a four “qi points” circuit having all points spaced by 90° , a harmonic balance simulation is performed at 60 GHz using a multi-port model based on S-parameter measurement results. Power detectors are connected at the four outputs. The phase difference between the millimeter-wave inputs is swept in a 360° range and the RF input signal power is set to 0 dBm.

The multi-port detected output voltages versus the phase difference are shown in Fig. 13. As seen, the output voltage minimum values are shifted by 90° multiples, as requested for this multi-port architecture. In addition, the output voltages at ports 1 and 3, and 2 and 4, respectively, are phase opposites. Therefore, I/Q output signals can be obtained using a differential approach, as illustrated by equations (34) and (35).

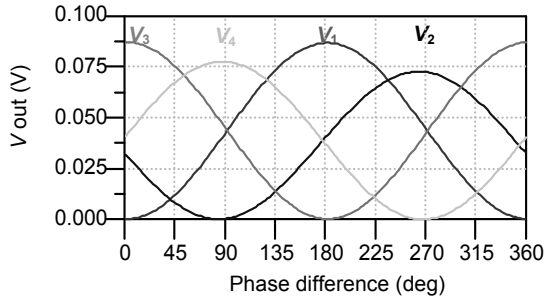


Fig. 13. Multi-port detected voltages vs. input phase difference

Two multi-port implementations were designed and fabricated for automotive radar applications (Boukari et al., 2009). Different topologies are used: three Hybrid and one Wilkinson couplers, and two hybrid and two rat-race couplers, respectively. Their microphotographs are showed in Figs. 14.a and b.

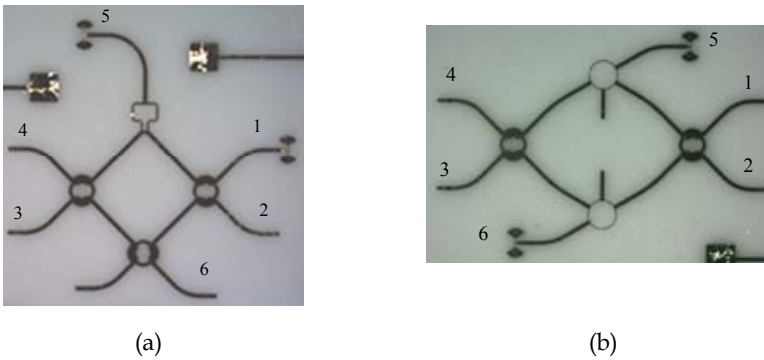


Fig. 14. Microphotographs of multi-ports implemented using: (a) hybrid and Wilkinson couplers; (b) hybrid and rat-race couplers

On-wafer multi-port S parameter measurements were performed using an Agilent PNA millimeter-wave network analyzer, over 30 GHz band, between 60 and 90 GHz.

Fig. 15 presents some typical S parameters of the multi-port presented in Fig. 14 (a). Both isolation and return loss have very good values at the operating frequency of 77 GHz (Figs. 15.a and b). Fig. 15.c shows the power splitting between the LO port and two adjacent output ports (S_{51} and S_{52}). The error of related phase difference from 90° is minimal at the operating frequency (Fig. 15.d). In addition, Fig. 16 presents the same S parameters for the multi-port presented in Fig. 15 (b). As in the previous case, measures are presented in

continuous line and simulations in dotted line. Similar conclusions can be drawn at the operating frequency and over the whole 30 GHz band.

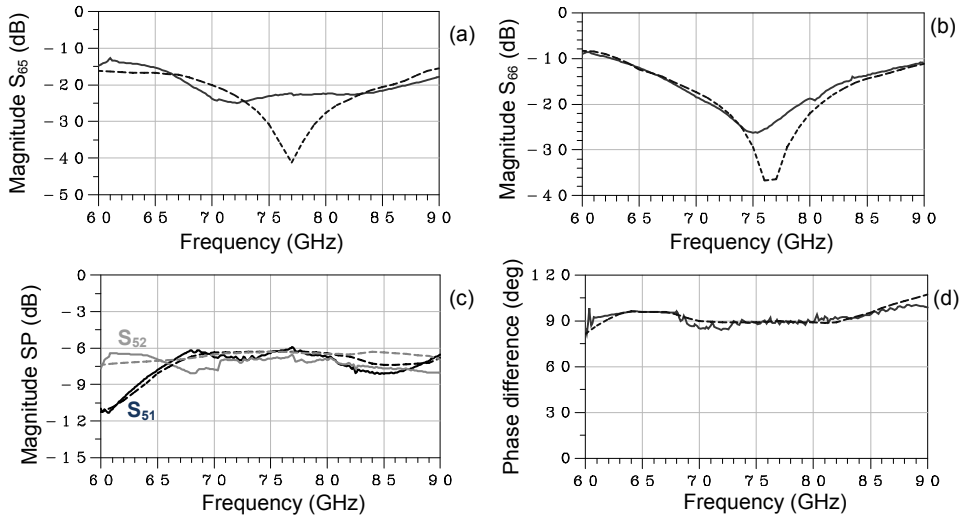


Fig. 15. Simulated (dotted line) and measured (continuous line) S parameters of the multi-port of Fig. 15 a

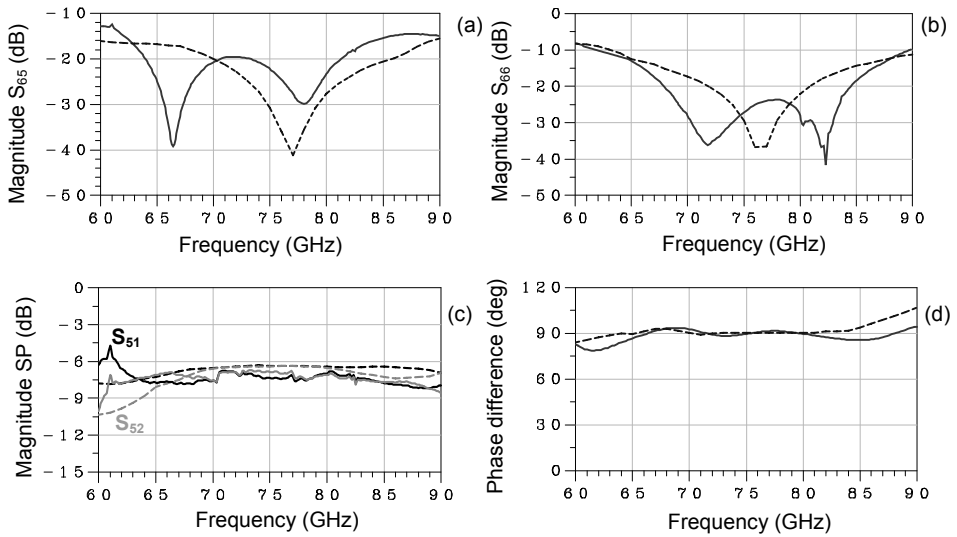


Fig. 16. Simulated (dotted line) and measured (continuous line) S parameters of the multi-port of Fig. 15. b

3.2.2 Rectangular Waveguide Multi-port Implementation

The circuit was designed using the High Frequency Structure Simulator (HFSS) software of Agilent Technologies, and fabricated in a metal block of brass using a computer numerically controlled (CNC) milling machine. The operating frequency was selected at 94 GHz, related to a specific radar sensor application. WR-10 standard rectangular waveguide corresponding to W frequency band was used to generate the circuit and to connect it to the network analyzer, or other front-end components, such as antennas, power and low-noise amplifiers, power detectors, couplers or phase shifters. For this implementation, a four hybrid coupler topology was used. The photographs of the RWG multi-port and related hybrid coupler are presented in Fig. 17.

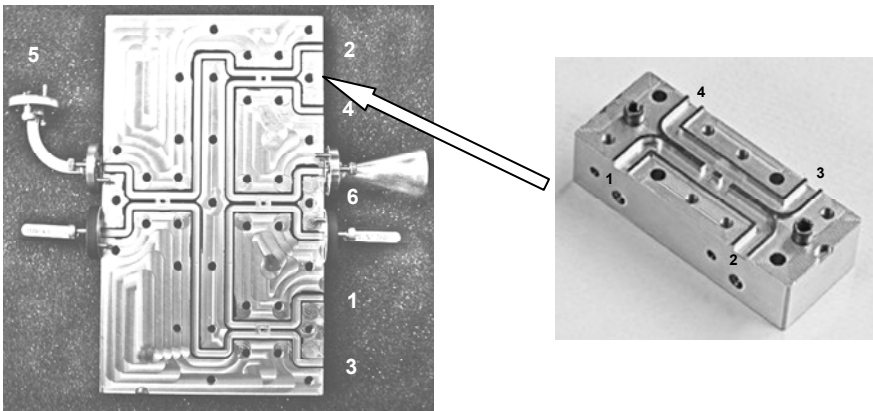


Fig. 17. Photographs of RWG multi-port and related hybrid coupler

An Anritsu 37397C Network Analyzer was used to measure the S-parameters (Moldovan et al, 2004). Due to the geometrical limitations, as seen in the circuit photography, it was impossible to measure all specific S-parameters (e.g. 6-4, 1-3, 2-4) using the standard network analyzer equipment. Fig. 18 shows the measured return losses and the isolation related to the input ports. A maximal isolation of -26 dB is obtained at 94.6 GHz and less than -20 dB were obtained for both RF and LO input return losses, at 95 GHz.

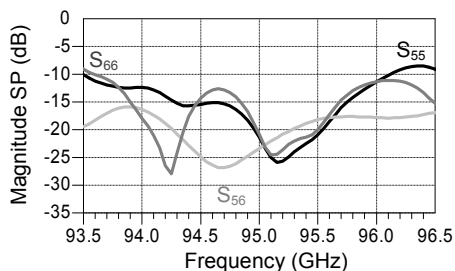


Fig. 18. Return losses and isolation related to the input ports

Output matches and isolation between output ports have also been measured, as seen in Figs. 19.a and b. The return losses are less than -15 dB, over a 1.5 GHz band, between 94.2 and 95.7 GHz. A minimum isolation of -25 dB between output ports 2 and 4 at 94.7 GHz is obtained. Typical measured transmission coefficients are also presented in Figs. 20.a and b. The magnitudes of the measured transmission S-parameters S_{51} , S_{54} and S_{62} are about -7.5 dB between 94.6 and 95 GHz. Therefore, a supplementary insertion loss of 1.5 dB, comparative to the ideal value of -6 dB, is obtained.

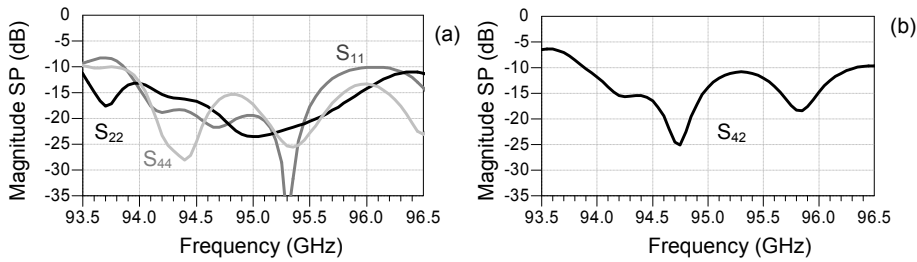


Fig. 19. (a) Return losses at output ports 1, 2 and 4; (b) isolation between outputs 2 and 4

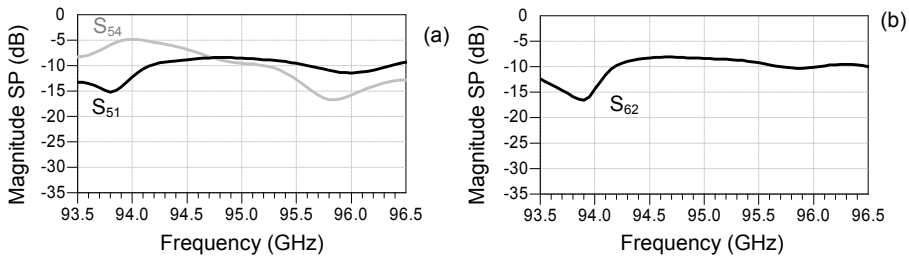


Fig. 20. Transmission coefficients between: (a) LO input and outputs 1 and 4; (b) RF input and output 2

3.2.3 Substrate Integrated Waveguide Multi-port Implementation

The substrate integrated waveguide (SIW) technology, that is part of the substrate integrated circuit family, presents a new design scheme based on the concept that a standard metallic waveguide can be synthesized and fabricated with linear arrays of metalized via holes or posts, which are realized on the same planar substrate along with other planar circuits such as micro-strip and coplanar waveguides.

This dielectric-filled integrated waveguide presents a similarity to its rectangular counterpart even though it has a non-conventional width/height aspect ratio and different guided-wave modal behaviors. The SIW technology allows a high degree of integration of millimeter-wave circuits at low cost, as compared to the standard waveguide technology. The resulting size of circuits can be significantly reduced due to the inherent dielectric effects (Moldovan et al., 2006).

The multi-port circuit, to be used in the RF module of a millimeter wave radar sensor, is designed and fabricated on a low-cost standard 254 μm alumina substrate. Commercial full-wave software (High Frequency Structure Simulator - HFSS version 9.1) of Ansoft

Corporation is used for the design and simulation. To measure the S-parameters in W-band, an Anritsu 37397C Network Analyzer is used.

The multi-port architecture is based on four 90° hybrid couplers. Photographs of the SIW multi-port circuit alone and integrated in the metallic fixture, are presented in Figs. 21. a and b.

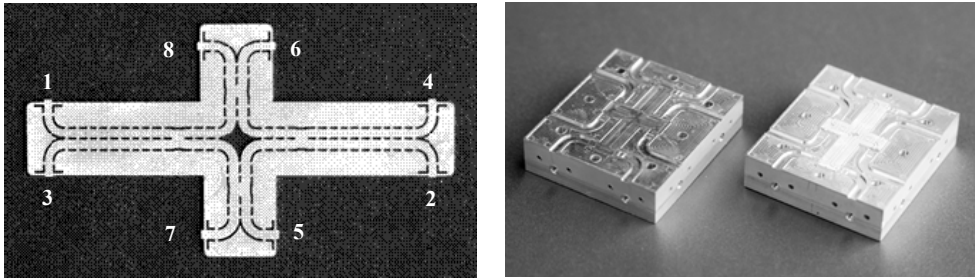


Fig. 21. Photographs of the SIW multi-port circuit

The outer dimensions of the SIW multi-port circuit, of 18.6 by 35.7 mm, are related to WR-10 standard flanges. The circuit is mounted on a metallic fixture, providing SIW to WR-10 transitions, in order to perform S-parameter measurements and to allow the connections to other millimeter wave circuits. The outer dimensions of the fixture, of 43 by 50 mm, are restricted by the physical dimensions of the standard WR-10 flanges, having a diameter of 19 mm. The machined rectangular waveguide part is fabricated in a metal block of brass using a computer numerically controlled milling machine. In order to accommodate the SIW alumina circuit, the metal block provides a central cavity. The alumina substrate is processed using laser micromachining equipment. The slots, the top and the bottom of the circuit are metalized.

The simulations and measurements are performed over a 4 GHz frequency band, between 92 and 96 GHz. In order to improve the sensor performances, the input ports must be isolated from each other as much as possible. The leakage of the reference signal to port 6 must be negligible as compared to the received signal. Fig. 22 shows comparative simulation (continuous line) and measured (dotted line) results of the input isolation over the frequency band. At least 20 dB of isolation is obtained in a wide band, covering the operating frequency of 94 GHz.

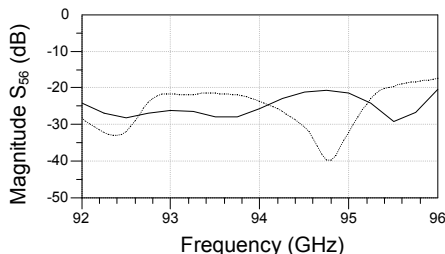


Fig. 22. Simulated and measured (dotted line) isolation between input ports

Using the same convention, comparative simulation and measurement results of return losses related to all output ports are presented in Fig. 23. It can be seen that about 20 dB of the return loss magnitude is obtained at the operating frequency of 94 GHz.

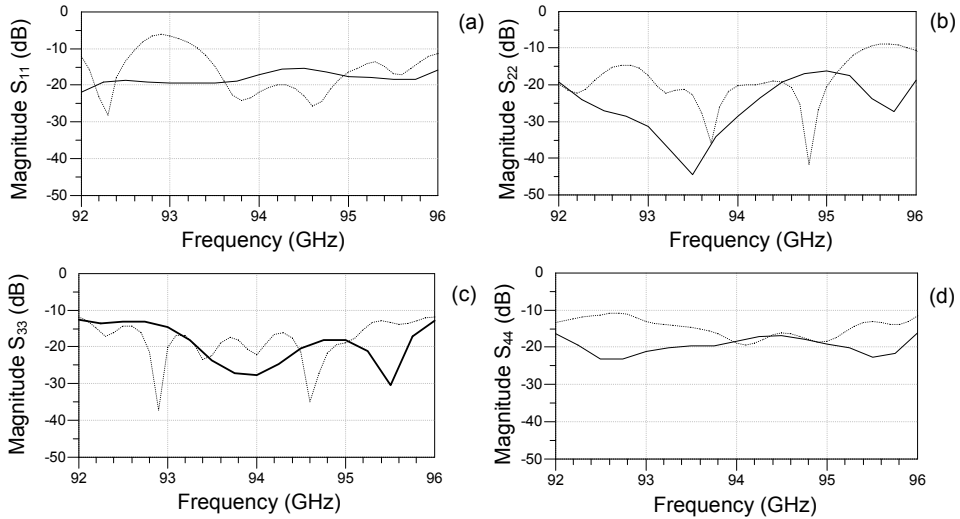


Fig. 23. Simulated (continuous line) and measured (dotted line) output return losses

It is to be noted that, because each RF input signal passes through two hybrid couplers, an ideal multi-port circuit has an equal split of 6 dB of the input signal at the central frequency. Simulation results presented in Fig. 24 are very close to this theoretical value. In the case of the proposed multi-port circuit, equipped with SIW to WR-10 rectangular wave guide transitions to all the ports, an additional loss of around 4 dB must be considered. Therefore, as seen in the figures below, a measured insertion loss of about 10 dB is achieved.

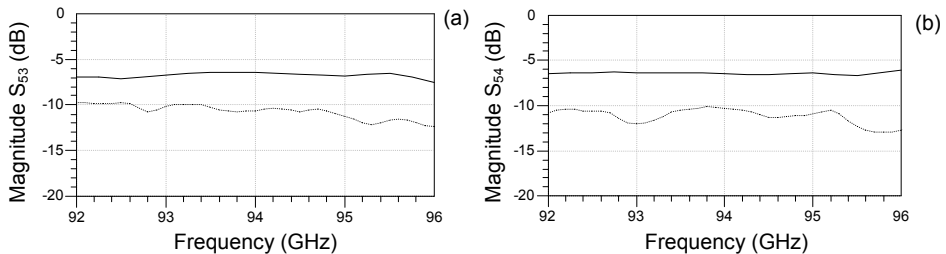


Fig. 24. Simulated and measured (dotted line) transmissions: LO port to outputs: (a) 3; (b) 4

Due to the use of 90° hybrid couplers, the phase difference between the transmission S-parameters must be multiples of 90° . Fig. 25 presents a typical phase measurement of two consecutive transmissions between the reference ports and output ports 3 and 4. As it can be seen in this figure, an equal phase difference of around 90° is obtained in the frequency band.

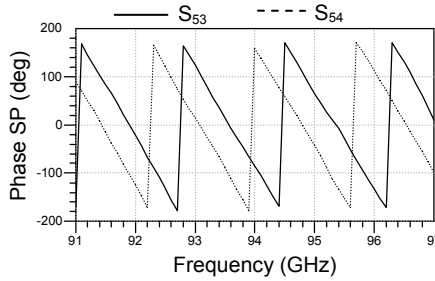


Fig. 25. Measured S parameter phases of consecutive transmission parameters S_{53} and S_{54}

According to equations (29) to (32), the multi-port output waves are linear combinations of the input waves. Measured S-parameters are used to calculate one of these output magnitudes versus the phase shift between the RF input waves. As illustrated in Fig. 26, for each output wave, periodical maximum and minimum values are obtained. The period of the output wave is 360° . In this calculation, the power of each RF input signal was set to 0 dBm. Due to the constructive and destructive interferences, the output signals oscillate between a minimum and a maximum. The minimum value is theoretically zero. However, in practice, due to the constructive errors, this is a non-zero value and it represents a criterion of quality of the multi-port design. As shown by this diagram, the output minimum value is less than 3% of its maximum. So, it can be concluded that very good measurement results are obtained.

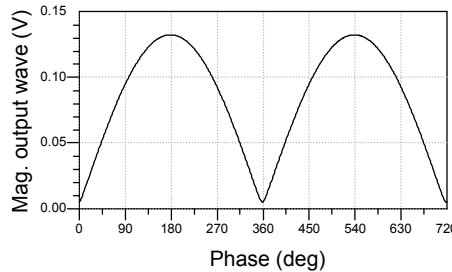


Fig. 26. Calculated output wave variation vs. input signal phase difference

4. The Multi-port Quadrature Demodulator

Similarly as in the analysis of the multi-port interferometer, we assume that there are two normalized input waves, a reference one, a_5 , generated by a local oscillator, and a_6 , an RF time dependent signal, of different amplitude, phase and even frequency (heterodyne case). Therefore, the output I/Q signals are:

$$i(t) = v_3(t) - v_1(t) = K \alpha(t) |a|^2 \cos[-\Delta\omega t + \Delta\phi(t)] \tag{42}$$

$$q(t) = v_4(t) - v_2(t) = K \alpha(t) |a|^2 \sin[-\Delta\omega t + \Delta\phi(t)] \tag{43}$$

Previous equations show that the multi-port circuit, together with four power detectors and two differential amplifiers can successfully replace a conventional I/Q mixer.

In practice, for a multi-port heterodyne receiver, the carrier frequency ω is close to the local oscillator frequency ω_0 . Therefore, these are low IF heterodyne receivers. However, if $\omega_0 = \omega$, I/Q conversion is obtained in a homodyne architecture. Hence, $\Delta\omega = 0$ and the quadrature output signals are:

$$i(t) = v_3(t) - v_1(t) = K \alpha(t) |a|^2 \cos[\Delta\varphi(t)] \quad (44)$$

$$q(t) = v_4(t) - v_2(t) = K \alpha(t) |a|^2 \sin[\Delta\varphi(t)] \quad (45)$$

This aspect can be considered as an important advantage of the proposed receivers compared to the conventional ones, because the same multi-port front-end can be used for both heterodyne and homodyne architectures. In addition, signal to noise ratio is improved and the cost of additional hybrid couplers and the two Schottky diodes is compensated by the reduced cost of the IF stage (IF mixers instead of the conventional IF I/Q ones).

4.1 Communication System Applications

In order to validate the previous theoretical results, a test bench using available equipments and a prototype based on Ka-band multi-port of Fig.5, is built.

Fig. 27 shows the block diagram and the photography of this test bench. The PSK/QAM modulated signal and the reference signal of 250 MHz are generated using an HP-8782 vector signal generator. This generator can provide various PSK/QAM modulated signals. The Ka-band modulated signal and the reference signal are obtained using a local oscillator LO (Wiltron frequency synthesizer model 6740B), a Wilkinson power divider (W) and two SU26A21D side-band up-converters. The direct conversion and analog splitting are simultaneously obtained using the Ka-band multi-port demodulator. The demodulated signal constellation can be directly visualized using an oscilloscope.

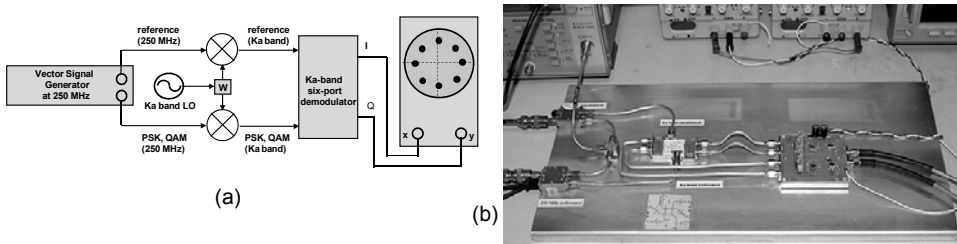


Fig. 27. Block diagram (a) and photograph (b) of the Ka-band demodulator test bench

Fig. 28 shows various demodulated constellations of 40 Mb/s PSK/QAM signals, on oscilloscope screen, using previously described Ka-band prototype (Tatu et al (2005)). As seen, all clusters of demodulated constellations are very well positioned and individualized, validating the multi-port approach.

Fig. 29 (a) shows simulated and measured Bit Error Ratio (BER) in the case of QPSK signals, as a function of E_b/N_o , where E_b is the average energy of a modulated bit and N_o is the noise power spectral density. It can be seen that the BER is less than $1.0E^{-6}$ for E_b/N_o higher than

11 dB over the operating band (23 – 31 GHz). However, outside the upper and lower limits of the operating bandwidth, the BER rises up rapidly, as it is measured to be greater than $1.0E^{-4}$ at 22 GHz and 32 GHz for the same value of E_b/N_0 .

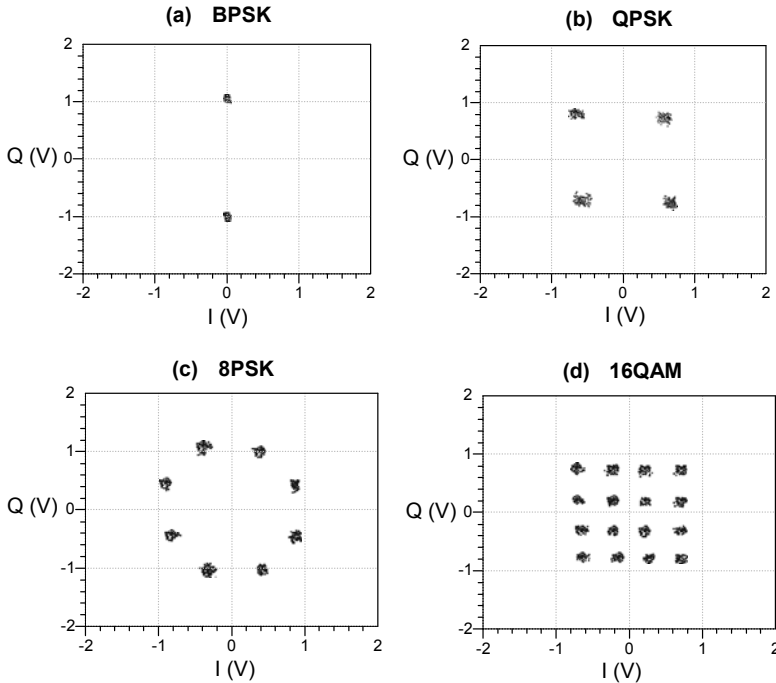


Fig. 28. Measurement results of various PSK/QAM modulated signals using a Ka-band multi-port demodulator

In addition, Fig. 29 (b) shows simulated and measured results on QPSK signals BER vs. the phase shift from synchronism between the carrier and LO signals, when both frequencies are set at 27 GHz. The simulated and measured BER is less than $1.0 E^{-6}$ for LO phase shift from the synchronism smaller than $\pm 35^\circ$ and $\pm 30^\circ$, respectively.

Fig. 30 shows the schematic block diagram of a 60 GHz wireless link using a multi-port module (MPM) (Moldovan et al., 2008). The receiver uses a multi-port heterodyne architecture with rapid analog carrier recovery loop at IF. Two IF differential amplifiers (IFDA) will generate quadrature IF signals. A second down-conversion, IF to baseband, is performed using two conventional mixers and the carrier recovery module (CRM). This CRM generates the IF coherent signal of 900 MHz.

A rapid analog carrier recovery loop was chosen for synchronous demodulation, in order to follow the inherent frequency/phase shift of the millimeter-wave frequency local oscillator (LO) and the eventual Doppler shift due to relative movements between transmitter and receiver. After low pass filtering (LPF) and baseband amplification (BBA), the quadrature baseband demodulated signals are obtained at the outputs of the sample and hold circuits (SHC). A clock recovery circuit generates an

in-phase clock at the symbol rate using one of the outputs. The use of two limiters improves the demodulated QPSK signals at the baseband module (BBM) output.

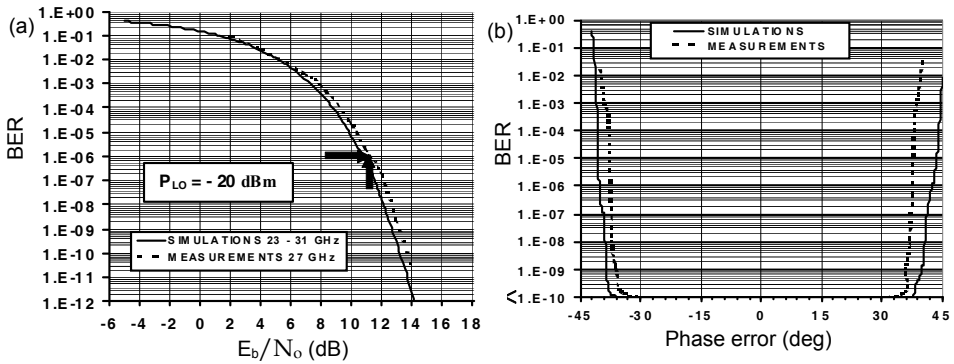


Fig. 29. BER results of QPSK modulated signals versus E_b/N_0 ratio (a) and phase error from synchronism (b)

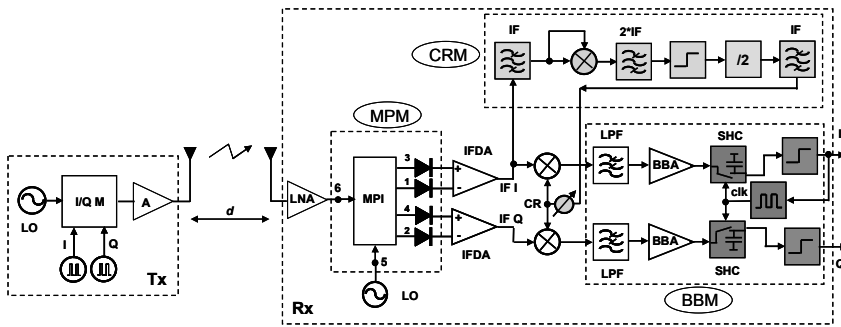


Fig. 30. Schematic block diagram of 60 GHz wireless link using a multi-port heterodyne architecture with carrier recovery loop at IF

Simulations are performed using a 60 GHz carrier frequency and a pseudorandom signal, which drives the direct millimeter-wave QPSK modulator. The bit-rate is chosen at 500 Mb/s with a corresponding symbol rate of 250 MHz. The transmitter power is set at 10 dBm, and the antenna gains are 10 dBi. A loss-link model based on the Friis equation is used to simulate the signal propagation over the distance d of 10 m. In order to obtain realistic results, the multi-port model is based on measurement results of the V-band circuit (see Figs. 11 and 12).

Bit error rate analysis is also performed using an appropriate length pseudorandom bit stream and various Doppler shifts. Fig. 31 shows the BER results versus the energy per bit to the spectral noise density (E_b/N_0), in the case of an ideal QPSK demodulator, a Doppler shift up to 200 KHz, and a Doppler shift of 600 KHz. The simulation results show a very good performance of the proposed wireless link: the BER is 10^{-6} for an E_b/N_0 ratio of 10.4 dB,

similar to the ideal demodulator, if the Doppler shift is less than 200 KHz (circles on the BER diagram). For a Doppler shift of 600 KHz, corresponding to a millimeter-wave LO frequency stability of 10^{-5} , the BER is less than 10^{-6} for an E_b/N_o ratio of around 13.5 dB. Therefore, the E_b/N_o ratio of the received 600 KHz Doppler shift signal must increase with 3 dB for similar results, as in the ideal case. The BER value deteriorates from 10^{-6} to around 10^{-3} for a E_b/N_o ratio of 10.4, remaining at a reasonable level. Transmission on range up to 10 m, as required for UWB short range WPAN, has been demonstrated using previous simulations based on S-parameters measurement results of a ceramic V-band multi-port. A multi-port receiver prototype based on previous results is currently under design.

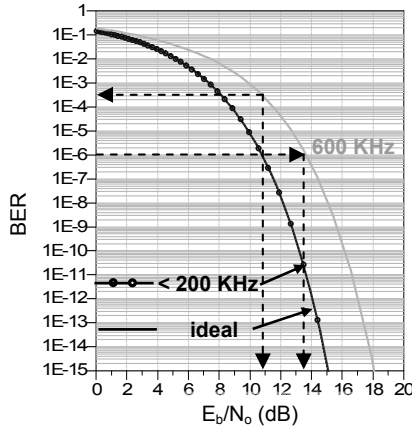


Fig. 31. BER simulation results for various Doppler shifts

4.2 Radar Sensor Applications

4.2.1 Two-tone CW W-band Multi-port Radar

This method uses two CW signals to measure both relative speed and distance to the target (Moldovan et al, 2007).

The relative speed of the target is obtained by measuring one of the I or Q signal frequency, according to the equation:

$$v = \frac{c}{2} \cdot \frac{\omega - \omega_0}{\omega_0} \tag{46}$$

where c is the speed of light, and ω and ω_0 are the transmitted and reflected signal frequencies, respectively.

The direction of target movement is obtained by a simple observation; the sense of rotation of $\Gamma = I + jQ$ phasor in the complex plane, clockwise or counter clockwise, is related to the sign of the Doppler frequency.

The distance measurement is obtained using two adequately spaced CW frequencies ω_{01} and ω_{02} . The distance to the target is calculated using the measured difference between the phases of the two corresponding echo signals $\Delta\theta_1$ and $\Delta\theta_2$ respectively:

$$d = \frac{c}{2} \cdot \frac{\Delta\theta_1 - \Delta\theta_2}{\omega_{01} - \omega_{02}} \quad (47)$$

A radar sensor prototype (see Fig. 32) operating at 94 GHz was built using the SIW circuit in brass fixture of Fig. 21, external components as wave-guide antennas, attenuator (Att), phase shifter (PhSh) and a baseband module to generate I/Q signals according to multi-port theory (Moldovan et al., 2007). The metallic target is placed in the vicinity of the sensor. Therefore the CW signal frequencies are spaced by 50 MHz, corresponding to a maximum unambiguous range of 3 m. A distance measurement error of 2% is obtained validating the operating principle of this radar sensor.

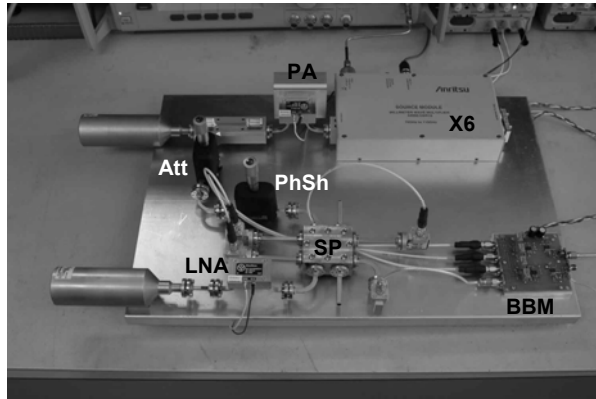


Fig. 32. Two-tone W-band multi-port radar sensor prototype

4.2.2 FMCW and PCCW V-band Multi-port Radar

Frequency modulated (FM) and phase coded (PC) CW radar sensor architectures are explored in conjunction with the V-band multi-ports presented in Fig. 15 (Cojocaru et al., 2008, 2009).

The FMCW radars transmit linear modulated continuous wave signals, which are positive and negative modulated, alternatively. The frequency difference of the transmitted and received signals is used to obtain relative speed and the distance to the target.

It is to be noted that phase coded (PC) waveforms comparative to FM waveforms differ in the sense that the transmitted pulse is subdivided into a number of equal length sub-pulses. The phase of each sub-pulse is chosen according to an optimal binary code sequence. An optimal binary code consists of a sequence of +1s and -1s (i.e. the phase alternates between 0° and 180°), and it has some remarkable features. Firstly, the peak side lobe of the autocorrelation function is the minimum possible for a given sequence length and secondly, the compression ratio is equal to the number of elements of the code. Thus, upon reception, the compressed pulse obtained through the correlation will enable the range to target evaluation.

In order to obtain initial validation of the proposed architectures, system simulations are performed using multi-port computer models based on S-parameter measurements in an ADS co-simulation platform. These results show relative speed and range measurements

with a good accuracy. The principle of the Doppler shift sign detection, related to multi-port properties is demonstrated. The proposed PCCW architecture effectively rejects the Doppler frequency from the range channel, before the correlation takes place, providing an accurate pulse compression.

Two prototype front-ends are currently under design and fabrication.

5. Conclusion

The chapter illustrates the interferometric concept in quadrature down-conversion for communication and radar sensor applications. Various millimeter-wave multi-port circuits covering the Ka, V and W bands are presented and analyzed. In addition, a Ka band demodulator and a W-band radar sensor prototype are presented. Present and future works are focused on UWB multi-port receivers and V-band radar sensors for automotive applications.

The multi-port circuits can successfully replace conventional quadrature mixers and the proposed architectures exploit the advantages of millimeter-wave interferometry, as presented in this chapter.

6. References

- Boukari, B., Hammou, D., Moldovan, E., Bosisio, R., Wu, K. & Tatu, S.O. (2009). MHMICs on Ceramic Substrate for Advanced Millimeter wave Systems, *Proceedings of IEEE Microwave Theory and Techniques Symposium*, pp. 1025-1028, Boston, June 7-12, 2009.
- Cojocaru, R.I., Moldovan, E., Boukari, B., Affes, S. & Tatu, S.O. (2008). A New 77 GHz Automotive Phase Coded CW Multi-port Radar Sensor Architecture. *Proceedings of 5th European Radar Conference European Microwave Week*, pp. 164-167, Amsterdam, October 27-31, 2008.
- Cojocaru, R.I., Boukari, B., Moldovan, E. & Tatu, S.O. (2009). Improved FMCW Multi-Port Technique, *Proceedings of 6th European Radar Conference 2009 European Microwave Week*, Rome, September 28 - October 2, 2009, pp. 290-293.
- Cohn, S.B. & Weinhouse, N.P. (1964). An Automatic Microwave Phase Measurement System. *Microwave Journal*, Vol. 7, pp. 49-56, February 1964.
- Engen, G.F. & Hoer, C.A. (1972). Application of an Arbitrary 6-Port Junction to Power-Measurement Problems. *IEEE Transactions on Instrumentation and Measurement*, Vol. 21, No. 11, pp. 470-474, November 1972.
- Engen, G.F. (1977). a. The Six-Port Reflectometer. An Alternative Network Analyzer. *IEEE Transactions on Microwave Theory and Techniques*, Vol. 25, No. 12, pp. 1075-1077, December 1977.
- Engen, G.F. (1977). b. An Improved Circuit for Implementing the Six-Port Technique of Microwave Measurements. *IEEE Transactions on Microwave Theory and Techniques*, Vol. 25, No. 12, pp. 1080-1083, December 1977.
- Li, J., Wu, Ke & Bosisio, R.G. (1994). A Collision Avoidance Radar Using Six-Port Phase/Frequency Discriminator (SPFD). *Proceedings of IEEE Microwave Theory and Techniques Symposium*, pp. 1553-1556, 1994.

- Li, J., Bosisio, R.G. & Wu, K. (1995). Computer and Measurement Simulation of a New Digital Receiver Operating Directly at Millimeter-Wave Frequencies. *IEEE Transactions Microwave Theory Techniques*, Vol. 43, pp. 2766-2772, December 1995.
- Li, J., Bosisio, R.G. & Wu, K. (1996). Dual-Ton Calibration of Six-Port Junction and Its Application to the Six-Port Direct Digital Millimetric Receiver. *IEEE Transactions Microwave Theory Techniques*, Vol. 44, pp. 93-99, January 1996.
- Moldovan, E., Tatu, S.O., Gaman, T., Wu, Ke & Bosisio, R.G. (2004). A New 94-GHz Six-Port Collision-Avoidance Radar Sensor. *IEEE Transactions on Microwave Theory and Techniques*, Vol. 52, No. 3, pp. 751-759, March 2004.
- Moldovan, E., Bosisio, R.G. & Wu, Ke (2006). W-Band Multiport Substrate-Integrated Waveguide Circuits. *IEEE Transactions on Microwave Theory and Techniques*, Vol. 54, No. 2, pp. 625-632, February 2006.
- Moldovan, E., Tatu, S.O., Affes, S, Wu, K. & Bosisio, R. (2007). W-band Substrate Integrated Waveguide Radar Sensor Based on Multi-port Technology, *Proceedings of 4th European Radar Conference, European Microwave Week*, pp. 174-177, Munich, October 8 - 12, 2007.
- Moldovan, E., Affes, S. & Tatu, S.O. (2008). A 60 GHz Multi-Port Receiver with Analog Carrier Recovery for Ultra Wideband Wireless Personal Area Networks, *Proceedings of European Microwave Conference, European Microwave Week*, pp. 1779-1782, Amsterdam, October 27-31, 2008.
- Tatu, S.O., Moldovan, E., Wu, Ke & Bosisio, R.G. (2001). A New Direct Millimeter Wave Six-Port Receiver. *IEEE Transactions on Microwave Theory and Techniques*, Vol. 49, No. 12, pp. 2517-2522, December 2001.
- Tatu, S.O., Moldovan, E., Brehm, G., Wu, Ke & Bosisio, R.G. (2002). Ka-Band Direct Digital Receiver. *IEEE Transactions on Microwave Theory and Techniques*, Vol. 50, No. 11, pp. 2436-2442, November 2002.
- Tatu, S.O., Moldovan, E., Wu, Ke, Bosisio, R.G. & Denidni, T. (2005). Ka-Band Analog Front-End for Software - Defined Direct Conversion Receiver. *IEEE Transactions on Microwave Theory and Techniques*, Vol. 53, No. 9, pp. 2768-2776, September 2005.
- Tatu, S.O. & Moldovan, E. (2007). V-Band Multiport Heterodyne Receiver for High-Speed Communication Systems. *EURASIP Journal on Wireless Communications and Networking*, Vol. 2007, Article ID 34358, 7 pages, Hindawi Publishing Corp., 2007

Wideband Representation of Passive Components based on Planar Waveguide Junctions

Fermín Mira¹, Ángel A. San Blas², Vicente E. Boria³ and Benito Gimeno⁴

¹*Centre Tecnològic de Telecomunicacions de Catalunya (CTTC),*

²*Universidad Miguel Hernández de Elche,*

³*iTEAM - Universidad Politècnica de Valencia,*

⁴*ICMUV-Universidad de Valencia,*

Spain

1. Introduction

Modern microwave and millimeter-wave equipment, present in mobile, wireless and space communication systems, employ a wide variety of waveguide components (Uher et al., 1993; Boria & Gimeno, 2007). Most of these components are based on the cascade connection of waveguides with different cross-section (Conciauro et al., 2000). Therefore, the full-wave modal analysis of such structures has received a considerable attention from the microwave community (Sorrentino, 1989; Itoh, 1989). The numerical efficiency of these methods has been substantially improved in (Mansour & MacPhie, 1986; Alessandri et al., 1988; Alessandri et al., 1992) by means of the segmentation technique, which consists of decomposing the analysis of a complete waveguide structure into the characterization of its elementary key-building blocks, i.e. planar junctions and uniform waveguides.

The modeling of planar junctions between waveguides of different cross-section has been widely studied in the past through modal analysis methods, where higher-order mode interactions were already considered (Wexler, 1967). For instance, in order to represent such junctions, the well-known mode-matching technique has been typically formulated in terms of the generalized scattering matrix (Safavi-Naini & MacPhie, 1981; Safavi-Naini & MacPhie, 1982; Eleftheriades et al., 1994). Alternatively, the planar waveguide junction can be characterized using a generalized admittance matrix or a generalized impedance matrix, obtained either by applying the general network theory (Alvarez-Melcón et al., 1996) or by solving integral equations (Gerini et al., 1998). A common drawback to all the previous techniques is that any related generalized matrix must be recomputed at each frequency point.

In the last two decades, several works have been focused on avoiding the repeated computations of the cited generalized matrices within the frequency loop. For instance, frequency independent integral equations have been set up when dealing, respectively, with inductive (or H-plane) and capacitive (or E-plane) discontinuities (Guglielmi & Newport,

1990; Guglielmi & Alvarez-Melcón, 1993), steps (Guglielmi et al., 1994; Guglielmi & Gheri, 1994), and posts (Guglielmi & Gheri, 1995). On the other hand, following the Boundary Integral-Resonant Mode Expansion (BI-RME) technique developed at the University of Pavia (Italy), a generalized admittance matrix in the form of pole expansions has been derived for arbitrarily shaped H-plane (Conciauro et al., 1996) and E-plane components (Arcioni et al., 1996), as well as for 3-D resonant waveguide cavities (Arcioni et al., 2002).

The objective of this chapter will be to describe a new method for the analysis of passive waveguide components, composed of the cascade connection of planar junctions. This new method extracts the main computations out of the frequency loop, thus reducing the overall CPU effort for solving the frequency-domain problem. The key points to reach such objectives are:

- Starting from the integral equation technique for the representation of planar waveguide junctions (Gerini et al., 1998), we propose a novel formulation of the generalized impedance and admittance matrices in the form of quasi-static terms and a pole expansion. A convergence study of this novel algorithm will be presented, where the two formulations in form of impedance and admittance matrices are compared in terms of efficiency and robustness.
- Once the generalized matrices of planar junctions are expressed in the form of pole expansions, a novel technique that provides the wideband generalized impedance or admittance matrix representation of the whole structure in the same form will be presented. For this purpose, the structure is segmented into planar junctions and uniform waveguide sections, which are both characterized in terms of wideband impedance/admittance matrices. Then, an efficient iterative algorithm for combining such matrices, and finally providing the wideband generalized impedance matrix of the complete structure, is followed (Arcioni & Conciauro, 1999). A special formulation will be derived for two-dimensional structures in order to obtain more optimized algorithms for this kind of geometries widely employed in practical designs.

Finally, the proposed method will be validated through the presentation of several practical designs. The results provided by our novel method will be compared with those provided by the previous methods commonly employed for the analysis of such passive devices, as well as with the results provided by commercial software.

2. Generalized Z and Y matrices of Planar Waveguide Steps

The structure under study is the planar junction between two arbitrarily shaped waveguides shown in Fig. 1. Following the integral equation technique described in (Gerini et al., 1998), such junction can be represented in terms of a generalized Z or Y matrix, and two sets of asymptotic modal admittances or impedances (see Fig. 1), which are determined as follows

$$\hat{Y}_m^{(\delta)} = \lim_{m \rightarrow \infty} Y_m^{(\delta)} = \begin{cases} \kappa_m^{(\delta)} / (jk\eta) & \text{TE modes} \\ jk / (\kappa_m^{(\delta)}\eta) & \text{TM modes} \end{cases} \quad (1)$$

$$\hat{Z}_m^{(\delta)} = \lim_{m \rightarrow \infty} (1 / Y_m^{(\delta)}) = \begin{cases} jk\eta / \kappa_m^{(\delta)} & \text{TE modes} \\ \kappa_m^{(\delta)}\eta / (jk) & \text{TM modes} \end{cases} \quad (2)$$

where $Y_m^{(\delta)}$ represents the modal admittance of the m -th mode at at waveguide port δ ($\delta=1,2$)

$$Y_m^{(\delta)} = \begin{cases} \gamma_m / (jk\eta) & \text{TE modes} \\ jk / (\gamma_m\eta) & \text{TM modes} \end{cases} \quad \gamma_m = \sqrt{\kappa_m^{(\delta)} - k^2} \quad (3)$$

and $\kappa_m^{(\delta)}$ is the cutoff wavenumber (Conciauro et al., 2000).

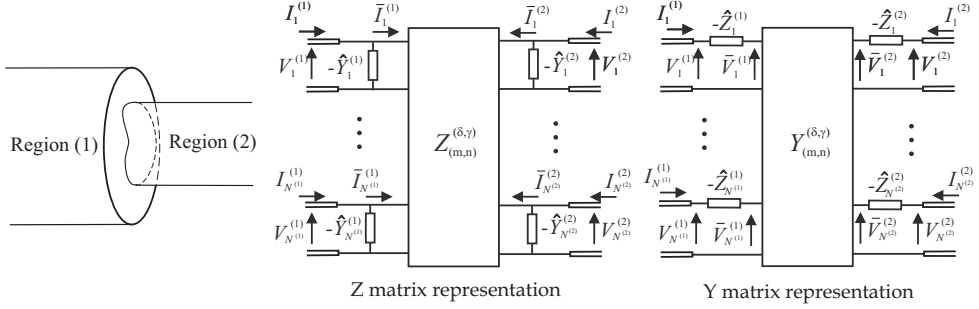


Fig. 1. Planar junction between two waveguides and multimode equivalent circuit representation in form of generalized Z and Y matrices.

2.1 Generalized Z matrix formulation

In order to derive the expressions for the elements of the generalized Z matrix of the planar junction (see Fig. 1), the next integral equation set up for the magnetic field at the junction plane must be solved (see more details about its derivation in (Gerini et al., 1998))

$$\mathbf{h}_n^{(\gamma)}(s) = \int_{S^{(2)}} \sum_{\zeta=1}^2 \left[\sum_{m=1}^{\infty} \hat{Y}_m^{(\zeta)} \mathbf{h}_m^{(\zeta)}(s) \mathbf{h}_m^{(\zeta)}(s') - \sum_{m=N^{(\zeta)}+1}^{\infty} \hat{Y}_m^{(\zeta)} \left(1 - \frac{Y_m^{(\zeta)}}{\hat{Y}_m^{(\zeta)}} \right) \mathbf{h}_m^{(\zeta)}(s) \mathbf{h}_m^{(\zeta)}(s') \right] \cdot \mathbf{M}_n^{(\gamma)}(s') ds' \quad (4)$$

where $\mathbf{h}_n^{(\gamma)}$ is the normalized magnetic field related to the n -th mode at waveguide γ (Conciauro et al., 2000), and $\mathbf{M}_n^{(\gamma)}$ is the unknown magnetic current related to the electric field at the junction plane

$$\mathbf{z} \times \mathbf{E} = \sum_{n=1}^{N^{(1)}} \bar{\mathbf{I}}_n^{(1)} \mathbf{M}_n^{(1)} - \sum_{n=1}^{N^{(2)}} \bar{\mathbf{I}}_n^{(2)} \mathbf{M}_n^{(2)} \quad (5)$$

If we want to find an expression for the Z matrix in the form of pole expansions, we must express the kernel of the previous integral equation as a sum of terms depending on k and $1/k$. Taking into account (1), the first summation of (4) fulfills such condition directly. Regarding the second summation in (4), since $Y_m^{(\zeta)} \rightarrow \hat{Y}_m^{(\zeta)}$ when $m \rightarrow \infty$, we can approximate the term within parenthesis by its Taylor series

$$\left(1 - \frac{Y_m^{(\zeta)}}{\hat{Y}_m^{(\zeta)}} \right) \approx \sum_{r=1}^R c_r \left(\frac{k}{\kappa_m^{(\zeta)}} \right)^{2r} \quad (6)$$

where the values of the first coefficients c_r for the TE and TM modes are shown in Table 1. Then, if we consider a k^2 frequency dependency for TE modes and all contributions from TM

modes are set to be frequency independent (due to the definitions of the asymptotic modal admittances given in (1) and the expression for the second summation in (4)), we can rewrite the previous Taylor series as follows

$$\left(1 - \frac{Y_m^{(\zeta)}}{\hat{Y}_m^{(\zeta)}}\right) \approx \begin{cases} \left(\frac{k}{k_0}\right)^2 \sum_{r=1}^R c_r \left(\frac{k_0}{\kappa_m^{(\zeta)}}\right)^{2r} & \text{TE} \\ \sum_{r=1}^R c_r \left(\frac{k_0}{\kappa_m^{(\zeta)}}\right)^{2r} & \text{TM} \end{cases} \quad (7)$$

where k_0 corresponds to the value of k at the center point of the frequency range. Proceeding in this way, we manage to express the second series of (4) as the required combination of terms with k and $1/k$ dependence. By introducing the value of k_0 into (7), we reduce the number of accessible modes $N^{(r)}$ required to obtain an accurate representation of the planar junction in the whole frequency range.

r	TE (Z matrix) TM (Y matrix)	TM (Z matrix) TE (Y matrix)
1	1/2	-1/2
2	1/8	-3/8
2	1/16	-5/16

Table 1. Values of the first coefficients c_r for TE and TM modes.

Then, making use of eqs. (1) and (7) into (4), we can easily obtain the next integral equation

$$\mathbf{h}_n^{(r)}(s) = \int_{s^{(2)}} \sum_{\zeta=1}^2 \left[\frac{1}{jk\eta} \sum_{m^{\text{TE}}=1}^{\infty} \kappa_m^{(\zeta)} \mathbf{h}_m^{(\zeta)}(s) \mathbf{h}_m^{(\zeta)}(s') + \frac{jk}{\eta} \left(\sum_{m^{\text{TM}}=1}^{\infty} \frac{\mathbf{h}_m^{(\zeta)}(s) \mathbf{h}_m^{(\zeta)}(s')}{\kappa_m^{(\zeta)}} \right. \right. \\ \left. \left. + \sum_{m^{\text{TE}}=N^{(\zeta)+1}}^{\infty} \mathbf{h}_m^{(\zeta)}(s) \mathbf{h}_m^{(\zeta)}(s') \sum_{r=1}^R \frac{c_r k_0^{2r-2}}{(\kappa_m^{(\zeta)})^{2r-1}} - \sum_{m^{\text{TM}}=N^{(\zeta)+1}}^{\infty} \mathbf{h}_m^{(\zeta)}(s) \mathbf{h}_m^{(\zeta)}(s') \sum_{r=1}^R \frac{c_r k_0^{2r}}{(\kappa_m^{(\zeta)})^{2r+1}} \right) \right] \cdot \mathbf{M}_n^{(r)}(s') ds' \quad (8)$$

where the original summations in m have been divided into the contributions of TE (m^{TE}) and TM (m^{TM}) modes.

Now, we can solve the previous integral equation by means of the Method of Moments (MoM). Expanding the unknown magnetic current in terms of the modes of the waveguide with a smaller cross-section (note that $\mathbf{z} \times \mathbf{E} = 0$ out of the intersection of the two waveguides)

$$\mathbf{M}_n^{(r)}(s') = \sum_{q=1}^Q \alpha_{q,n}^{(r)} \mathbf{h}_q^{(2)}(s') \quad (9)$$

and using the Galerkin approach, we finally obtain the following linear system of equations

$$\mathbf{P} \cdot \boldsymbol{\alpha}^{(r)} = \mathbf{Q}^{(r)} \quad (10)$$

where $\boldsymbol{\alpha}^{(r)}$ contains the unknown coefficients $\alpha_{q,n}^{(r)}$, whereas $\mathbf{Q}^{(r)}$ and \mathbf{P} matrix elements are computed as indicated next

$$Q_{p,n}^{(\gamma)} = \int_{S^{(2)}} \mathbf{h}_p^{(2)}(s) \mathbf{h}_n^{(\gamma)}(s) ds = \begin{cases} \sigma_{p,n} & (\gamma) = (1) \\ \delta_{p,n} & (\gamma) = (2) \end{cases} \quad (11)$$

$$\mathbf{P} = \frac{1}{jk\eta} (\mathbf{R} - k^2 \mathbf{S}) \quad (12)$$

$$R_{p,q} = \sum_{m^{TE}=1}^{\infty} \kappa_m^{(1)} \sigma_{p,m} \sigma_{q,m} + \kappa_p^{(2)} \delta_{p,q}^{TE} \quad (13)$$

$$S_{p,q} = \frac{\delta_{p,q}^{TM}}{\kappa_p^{(2)}} + \sum_{m^{TM}=1}^{\infty} \frac{\sigma_{p,m} \sigma_{q,m}}{\kappa_m^{(1)}} + F_p \left(\delta_{p,q}^{TE} - \left(\frac{k_0}{\kappa_p^{(2)}} \right)^2 \delta_{p,q}^{TM} \right) \sum_{r=1}^R \frac{c_r k_0^{2r-2}}{(\kappa_p^{(2)})^{2r-1}} \\ + \sum_{m^{TE}=N^{(1)+1}}^{\infty} \sigma_{p,m} \sigma_{q,m} \sum_{r=1}^R \frac{c_r k_0^{2r-2}}{(\kappa_m^{(1)})^{2r-1}} - \sum_{m^{TM}=N^{(1)+1}}^{\infty} \sigma_{p,m} \sigma_{q,m} \sum_{r=1}^R \frac{c_r k_0^{2r}}{(\kappa_m^{(1)})^{2r+1}} \quad (14)$$

where $\delta_{p,q}$ stands for the Kronecker's delta (i.e. $\delta_{p,q} = 1$ if $p = q$ and $\delta_{p,q} = 0$ if $p \neq q$), and

$$F_p \equiv \begin{cases} 0 & p < N^{(2)} + 1 \\ 1 & p \geq N^{(2)} + 1 \end{cases} \quad (15)$$

It is interesting to see that \mathbf{R} and \mathbf{S} can be expressed as the following block matrices

$$\mathbf{R} = \begin{bmatrix} \mathbf{R}_{11} & \mathbf{0}_{12} \\ \mathbf{0}_{21} & \mathbf{0}_{22} \end{bmatrix} \quad \mathbf{S} = \begin{bmatrix} \mathbf{S}_{11} & \mathbf{S}_{12} \\ \mathbf{S}_{21} & \mathbf{S}_{22} \end{bmatrix} \quad (16)$$

where the subscript 1 corresponds with the TE modes, and the subscript 2 with the TM modes, used in (9). Notice that the elements $R_{p,q}$ are zero whenever p or q are related to TM modes, since the coupling coefficients $\sigma_{p,m}$ are zero when p is a TM mode and m is a TE mode (Guillot et al., 1993). Therefore, the matrix \mathbf{P} can be written as

$$\mathbf{P} = \frac{1}{jk\eta} \begin{bmatrix} \mathbf{R}_{11} - k^2 \mathbf{S}_{11} & -k^2 \mathbf{S}_{12} \\ -k^2 \mathbf{S}_{12}^T & -k^2 \mathbf{S}_{22} \end{bmatrix} \quad (17)$$

For solving the linear system defined in (10), the \mathbf{P} matrix must be inverted. Following (Zhang, 1999), we can say that

$$\mathbf{P}^{-1} = jk\eta \begin{bmatrix} \mathbf{P}_{11}^{-1} & -\mathbf{P}_{11}^{-1} \mathbf{S}_{12} \mathbf{S}_{22}^{-1} \\ -\mathbf{S}_{22}^{-1} \mathbf{S}_{12}^T \mathbf{P}_{11}^{-1} & \mathbf{S}_{22}^{-1} \mathbf{S}_{12}^T \mathbf{P}_{11}^{-1} \mathbf{S}_{12} \mathbf{S}_{22}^{-1} - \mathbf{S}_{22}^{-1} / k^2 \end{bmatrix} \quad (18)$$

where $\mathbf{P}_{11} = \mathbf{R}_{11} - k^2 (\mathbf{S}_{11} - \mathbf{S}_{12} \mathbf{S}_{22}^{-1} \mathbf{S}_{12}^T)$. The inverse of this block can be easily obtained after solving the generalized eigenvalue problem shown next

$$\mathbf{R}_{11} \mathbf{x} = k^2 (\mathbf{S}_{11} - \mathbf{S}_{12} \mathbf{S}_{22}^{-1} \mathbf{S}_{12}^T) \mathbf{x} \quad (19)$$

If the matrix $\mathbf{X} = (\mathbf{x}_1, \mathbf{x}_2, \dots, \mathbf{x}_{Q_1})$, whose Q_1 columns are the eigenvector solutions of the previous problem (Q_1 being the number of the total Q basis functions in (9) corresponding to TE modes), is normalized as follows

$$\mathbf{X}_T \mathbf{R}_{11} \mathbf{X} = \mathbf{\Lambda} = (k_1^2, k_1^2, \dots, k_{Q_1}^2) \quad (20)$$

$$\mathbf{X}_T (\mathbf{S}_{11} - \mathbf{S}_{12} \mathbf{S}_{22}^{-1} \mathbf{S}_{12}^T) \mathbf{X} = \mathbf{U} = \text{diag}(1, 1, \dots, 1) \quad (21)$$

where k_i is the i -th eigenvalue solution of the previous problem, we can easily write that

$$\mathbf{P}_{11}^{-1} = \sum_{i=1}^{Q_1} \frac{\mathbf{x}_i \{\mathbf{x}_i\}^T}{k_i^2 - k^2} \quad (22)$$

Finally, if we extract the limit value of the previous summation when $k \rightarrow 0$, which is obviously equal to \mathbf{R}_{11}^{-1} , we obtain the following expression

$$\mathbf{P}_{11}^{-1} = \mathbf{R}_{11}^{-1} + k^2 \sum_{i=1}^{Q_1} \frac{\mathbf{x}_i \{\mathbf{x}_i\}^T}{k_i^2 (k_i^2 - k^2)} \quad (23)$$

where the series in (23) converges with a very low number of terms, rather smaller than Q_1 , due to the previous extraction of the low-frequency term in the matrix \mathbf{P}_{11}^{-1} .

Introducing now (23) into (18), we obtain the next expressions for the different blocks of the \mathbf{P}^{-1} matrix

$$(\mathbf{P}^{-1})_{11} = jk\eta \mathbf{R}_{11}^{-1} + jk^3 \eta \sum_{i=1}^{Q_1} \frac{\mathbf{x}_i \{\mathbf{x}_i\}^T}{k_i^2 (k_i^2 - k^2)} \quad (24)$$

$$(\mathbf{P}^{-1})_{12} = -jk\eta \mathbf{R}_{11}^{-1} \mathbf{S}_{12} \mathbf{S}_{22}^{-1} - jk^3 \eta \sum_{i=1}^{Q_1} \frac{\mathbf{x}_i \{\mathbf{x}'_i\}^T}{k_i^2 (k_i^2 - k^2)} \quad (25)$$

$$(\mathbf{P}^{-1})_{22} = \frac{\eta}{jk} \mathbf{S}_{22}^{-1} + jk\eta \mathbf{S}_{22}^{-1} \mathbf{S}_{12}^T \mathbf{R}_{11}^{-1} \mathbf{S}_{12} \mathbf{S}_{22}^{-1} + jk^3 \eta \sum_{i=1}^{Q_1} \frac{\mathbf{x}'_i \{\mathbf{x}'_i\}^T}{k_i^2 (k_i^2 - k^2)} \quad (26)$$

where $\mathbf{x}'_i = \mathbf{S}_{22}^{-1} \mathbf{S}_{12}^T \mathbf{x}_i$. Once the \mathbf{P} matrix has been successfully inverted, the elements of the generalized Z matrix of the planar step can be obtained through the evaluation of

$$\mathbf{Z}_{m,n}^{(\delta,\gamma)} = \sum_{q=1}^Q \alpha_{q,n}^{(\gamma)} \int_{S^{(2)}} \mathbf{h}_q^{(2)} \mathbf{h}_m^{(\delta)} ds = \{\mathbf{Q}^{(\delta)}\}^T \mathbf{P}^{-1} \mathbf{Q}^{(\gamma)} \quad (27)$$

thus obtaining the following final expressions for all possible combinations of TE and TM modes

$$\mathbf{Z}_{\text{TE-TE}}^{(\delta,\gamma)} = jk\eta \{\mathbf{Q}_{11'}^{(\delta)}\}^T \mathbf{R}_{11}^{-1} \mathbf{Q}_{11'}^{(\gamma)} + jk^3 \eta \sum_{i=1}^{Q_1} \frac{\mathbf{y}_i^{(\delta)} \{\mathbf{y}_i^{(\gamma)}\}^T}{k_i^2 (k_i^2 - k^2)} \quad (28)$$

$$\mathbf{Z}_{\text{TE-TM}}^{(\delta,\gamma)} = jk\eta \{\mathbf{Q}_{11'}^{(\delta)}\}^T \mathbf{R}_{11}^{-1} \mathbf{E}_{12'}^{(\gamma)} + jk^3 \eta \sum_{i=1}^{Q_1} \frac{\mathbf{y}_i^{(\delta)} \{\mathbf{y}_i^{(\gamma)}\}^T}{k_i^2 (k_i^2 - k^2)} \quad (29)$$

$$\mathbf{Z}_{\text{TM-TE}}^{(\delta,\gamma)} = jk\eta \{\mathbf{E}_{12'}^{(\delta)}\}^T \mathbf{R}_{11}^{-1} \mathbf{Q}_{11'}^{(\gamma)} + jk^3 \eta \sum_{i=1}^{Q_1} \frac{\mathbf{y}_i^{(\delta)} \{\mathbf{y}_i^{(\gamma)}\}^T}{k_i^2 (k_i^2 - k^2)} \quad (30)$$

$$\mathbf{Z}_{\text{TM-TM}}^{(\delta,\gamma)} = \frac{\eta}{jk} \{\mathbf{Q}_{22'}^{(\delta)}\}^T \mathbf{S}_{22}^{-1} \mathbf{Q}_{22'}^{(\gamma)} + jk\eta \{\mathbf{E}_{12'}^{(\delta)}\}^T \mathbf{R}_{11}^{-1} \mathbf{E}_{12'}^{(\gamma)} + jk^3 \eta \sum_{i=1}^{Q_1} \frac{\mathbf{y}_i^{(\delta)} \{\mathbf{y}_i^{(\gamma)}\}^T}{k_i^2 (k_i^2 - k^2)} \quad (31)$$

where we have that $\mathbf{y}_i^{(\delta)} = \{\mathbf{Q}_{11'}^{(\delta)}\}^T \mathbf{x}_i$ and $\mathbf{y}_i^{n(\delta)} = \{\mathbf{E}_{12'}^{(\delta)}\}^T \mathbf{x}_i$, $\mathbf{E}_{12'}^{(\delta)} = \mathbf{Q}_{12'}^{(\delta)} - \mathbf{S}_{12} \mathbf{S}_{22}^{-1} \mathbf{Q}_{22'}^{(\delta)}$, k_i and \mathbf{x}_i are, respectively, the eigenvalues and eigenvectors related to the inversion of the matrix \mathbf{P} , the subscripts 1 and 2 refer, respectively, to TE and TM modes, and Q_1 is the number of the \mathbf{Q} vector basis functions corresponding to TE modes.

2.1.1 Generalized Z matrix formulation for H-plane waveguide steps

In the previous section we derived the general formulation for any planar junction. The objective of this section is to detail the Z matrix for the H-plane waveguide junction shown in Fig. 2.

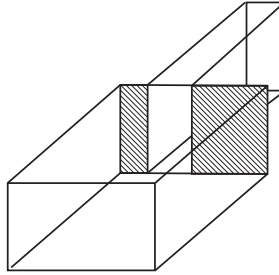


Fig. 2. H-plane junction between two waveguides.

Taking into account that only TE modes are excited in our case (H-plane junction), and considering an adequate high number of accessible modes ($N^{(s)}$) in (4), such integral equation could be simplified by neglecting the second term of the kernel, thus giving place to the classical formulation collected in (Guglielmi et al., 1994). However, in order to reduce the number of accessible modes needed to get very accurate results, and therefore increasing the computational efficiency of our analysis method, we will not reject any term in the kernel of (4).

Now, with the aim of avoiding the inversion of frequency dependent matrices, the previous integral equation should be expressed in the following way

$$\mathbf{h}_n^{(r)}(s) = \frac{1}{jk\eta} \int_{s^{(2)}} \mathbf{K}(s, s') \cdot \mathbf{M}_n^{(r)}(s') ds' \quad (32)$$

being \mathbf{K} a static (frequency independent) kernel. Recalling (1), it is easily verified that the first summation of (4) can be directly written as required. Regarding the second summation in (4), we can approximate the term within parenthesis by its Taylor series

$$\left(1 - \frac{Y_m^{(\zeta)}}{\hat{Y}_m^{(\zeta)}} \right) \approx \sum_{r=1}^R c_r \left(\frac{k_0}{\kappa_m^{(\zeta)}} \right)^{2r} \quad (33)$$

where the original frequency dependence k has been substituted by k_0 (see (7)), and c_r are the coefficients of the cited Taylor expansion for TE modes (see Table 1). As it has been explained before, if a rather high number of accessible modes is chosen for modeling the junction, we can approximate the Taylor series in (33) by zero, and then obtain the same integral equation provided by the more classical formulation (Guglielmi et al., 1994).

Thus, after introducing (1) and (33) into (4), we derive the following expression for the aforementioned static kernel

$$\mathbf{K}(s, s') = \sum_{\zeta=1}^2 \sum_{m=1}^{\infty} \kappa_m^{(\zeta)} \mathbf{h}_m^{(\zeta)}(s) \mathbf{h}_m^{(\zeta)}(s') - \sum_{\zeta=1}^2 \sum_{m=N^{(\zeta)}+1}^{\infty} \mathbf{h}_m^{(\zeta)}(s) \mathbf{h}_m^{(\zeta)}(s') \sum_{r=1}^R \frac{c_r k_0^{2r}}{\left(\kappa_m^{(\zeta)}\right)^{2r-1}} \quad (34)$$

Next, we can apply the Method of Moments to solve the integral equation proposed in (32) in the same way that for the general case, thus obtaining the next linear system of equations

$$\mathbf{P} \cdot \boldsymbol{\alpha}^{(\gamma)} = jk\eta \mathbf{Q}^{(\gamma)} \quad (35)$$

where

$$P_{p,q} = \sum_{m=1}^{\infty} \kappa_m^{(1)} \sigma_{m,p} \sigma_{m,q} \left[1 - F_m^{(1)} \sum_{r=1}^R c_r \left(\frac{k_0}{\kappa_m^{(1)}} \right)^{2r} \right] + \delta_{p,q} \kappa_p^{(2)} \left[1 - F_p^{(2)} \sum_{r=1}^R c_r \left(\frac{k_0}{\kappa_m^{(2)}} \right)^{2r} \right] \quad (36)$$

and $Q_{p,n}^{(\gamma)}$ has the same expression shown in (11).

Then, the matrix \mathbf{P} can be inverted outside the frequency loop, thus obtaining an expression for the generalized Z matrix with a linear frequency dependence

$$\mathbf{Z}^{(\delta,\gamma)} = jk\eta \{ \mathbf{Q}^{(\delta)} \}^T \mathbf{P}^{-1} \mathbf{Q}^{(\gamma)} \quad (37)$$

2.2 Generalized Y matrix formulation

In order to derive the expressions for the elements of the generalized Y matrix of the planar waveguide junction (see Fig. 1), the next integral equation set up for the electric field at the junction plane must be solved (Gerini et al., 1998)

$$\mathbf{e}_n^{(\gamma)}(s) = \int_{s^{(\zeta)}} \sum_{\zeta=1}^2 \left[\sum_{m=1}^{\infty} \hat{Z}_m^{(\zeta)} \mathbf{e}_m^{(\zeta)}(s) \mathbf{e}_m^{(\zeta)}(s') - \sum_{m=N^{(\zeta)}+1}^{\infty} \hat{Z}_m^{(\zeta)} \left(1 - \frac{Z_m^{(\zeta)}}{\hat{Z}_m^{(\zeta)}} \right) \mathbf{e}_m^{(\zeta)}(s) \mathbf{e}_m^{(\zeta)}(s') \right] \cdot \mathbf{J}_n^{(\gamma)}(s') ds' \quad (38)$$

where $\mathbf{e}_n^{(\gamma)}$ is the electric field related to the n -th mode at waveguide γ , whereas $\mathbf{J}_n^{(\gamma)}$ is the unknown electric current at the junction plane related to the magnetic field

$$-(\mathbf{z} \times \mathbf{H}) = \sum_{n=1}^{N^{(1)}} \bar{V}_n^{(1)} \mathbf{J}_n^{(1)} - \sum_{n=1}^{N^{(2)}} \bar{V}_n^{(2)} \mathbf{J}_n^{(2)} \quad (39)$$

In order to obtain a suitable expression for the pole expansion, we can approximate the term within parenthesis in (38) by its Taylor series (see Table 1)

$$\left(1 - \frac{Z_m^{(\zeta)}}{\hat{Z}_m^{(\zeta)}} \right) \approx \sum_{r=1}^R c_r \left(\frac{k}{\kappa_m^{(\zeta)}} \right)^{2r} \quad (40)$$

Taking into account (2), the term within parenthesis in (38) must be frequency independent for TE modes and k^2 for TM modes, so we rewrite (40) by using the wavenumber at the center of the frequency band as follows

$$\left(1 - \frac{Z_m^{(\zeta)}}{\hat{Z}_m^{(\zeta)}}\right) \approx \begin{cases} \sum_{r=1}^R c_r \left(\frac{k_0}{\kappa_m^{(\zeta)}}\right)^{2r} & \text{TE} \\ \left(\frac{k}{k_0}\right)^2 \sum_{r=1}^R c_r \left(\frac{k_0}{\kappa_m^{(\zeta)}}\right)^{2r} & \text{TM} \end{cases} \quad (41)$$

Now, by introducing (2) and (41) in (38), we obtain

$$\mathbf{e}_n^{(\gamma)}(s) = \sum_{\zeta=1}^2 \int_{s^{(\zeta)}} \mathbf{J}_n^{(\gamma)}(s') \cdot \left[jk\eta \sum_{m^{\text{TE}}=1}^{\infty} \frac{\mathbf{e}_m^{(\zeta)}(s)\mathbf{e}_m^{(\zeta)}(s')}{\kappa_m^{(\zeta)}} + \frac{\eta}{jk} \sum_{m^{\text{TM}}=1}^{\infty} \kappa_m^{(\zeta)} \mathbf{e}_m^{(\zeta)}(s)\mathbf{e}_m^{(\zeta)}(s') - jk\eta \sum_{m^{\text{TE}}=N^{(\zeta)+1}}^{\infty} \mathbf{e}_m^{(\zeta)}(s)\mathbf{e}_m^{(\zeta)}(s') \sum_{r=1}^R \frac{c_r k_0^{2r}}{(\kappa_m^{(\zeta)})^{2r+1}} + jk\eta \sum_{m^{\text{TM}}=N^{(\zeta)+1}}^{\infty} \mathbf{e}_m^{(\zeta)}(s)\mathbf{e}_m^{(\zeta)}(s') \sum_{r=1}^R \frac{c_r k_0^{2r-2}}{(\kappa_m^{(\zeta)})^{2r-1}} \right] ds' \quad (42)$$

The previous integral equation can be solved by means of the Method of Moments. In this case, expanding the unknown electric current in terms of the modes of the waveguide with a bigger cross-section

$$\mathbf{J}_n^{(\gamma)}(s') = \sum_{q=1}^Q \alpha_{q,n}^{(\gamma)} \mathbf{e}_q^{(1)}(s') \quad (43)$$

and using the Galerkin approach, we finally obtain the following linear system of equations in the form of (10) where

$$Q_{p,n}^{(\gamma)} = \int_{s^{(\gamma)}} \mathbf{e}_p^{(1)}(s) \mathbf{e}_n^{(\gamma)}(s) ds = \begin{cases} \delta_{p,n} & (\delta) = (1) \\ \sigma_{p,n} & (\delta) = (2) \end{cases} \quad (44)$$

$$\mathbf{P} = \frac{\eta}{jk} (\mathbf{R} - k^2 \mathbf{S}) \quad (45)$$

$$R_{p,q} = \kappa_p^{(1)} \delta_{p,q}^{\text{TM}} + \sum_{m^{\text{TM}}=1}^{\infty} \kappa_m^{(2)} \sigma_{p,m} \sigma_{q,m} \quad (46)$$

$$S_{p,q} = \frac{\delta_{p,q}^{\text{TE}}}{\kappa_p^{(1)}} + \sum_{m^{\text{TE}}=1}^{\infty} \frac{\sigma_{p,m} \sigma_{q,m}}{\kappa_m^{(2)}} + F_p \left(\delta_{p,q}^{\text{TM}} - \left(\frac{k_0}{\kappa_p^{(1)}}\right)^2 \delta_{p,q}^{\text{TE}} \right) \sum_{r=1}^R \frac{c_r k_0^{2r-2}}{(\kappa_p^{(1)})^{2r-1}} - \sum_{m^{\text{TE}}=N^{(2)+1}}^{\infty} \sigma_{p,m} \sigma_{q,m} \sum_{r=1}^R \frac{c_r k_0^{2r}}{(\kappa_m^{(2)})^{2r+1}} + \sum_{m^{\text{TM}}=N^{(2)+1}}^{\infty} \sigma_{p,m} \sigma_{q,m} \sum_{r=1}^R \frac{c_r k_0^{2r-2}}{(\kappa_m^{(2)})^{2r-1}} \quad (47)$$

Now, we express \mathbf{R} and \mathbf{S} as the following block matrices

$$\mathbf{R} = \begin{bmatrix} \mathbf{0}_{11} & \mathbf{0}_{12} \\ \mathbf{0}_{21} & \mathbf{R}_{22} \end{bmatrix} \quad \mathbf{S} = \begin{bmatrix} \mathbf{S}_{11} & \mathbf{S}_{12} \\ \mathbf{S}_{21} & \mathbf{S}_{22} \end{bmatrix} \quad (48)$$

where the elements $R_{p,q}$ are zero whenever p or q are related to TE modes, since the coupling coefficients $\sigma_{p,m}$ are zero when p is a TE mode and m is a TM mode (Guillot et al., 1993).

Therefore, the matrix \mathbf{P} can be written as

$$\mathbf{P} = \frac{\eta}{jk} \begin{bmatrix} -k^2 \mathbf{S}_{11} & -k^2 \mathbf{S}_{12} \\ -k^2 \mathbf{S}_{12}^T & \mathbf{R}_{22} - k^2 \mathbf{S}_{22} \end{bmatrix} \quad (49)$$

Following the same procedure that for the Z matrix computation, we obtain the inverse of the matrix \mathbf{P} in the form of pole expansion

$$(\mathbf{P}^{-1})_{11} = \frac{1}{jk\eta} \mathbf{S}_{11}^{-1} + \frac{jk}{\eta} \mathbf{S}_{11}^{-1} \mathbf{S}_{12} \mathbf{R}_{22}^{-1} \mathbf{S}_{12}^T \mathbf{S}_{11}^{-1} + \frac{jk^3}{\eta} \sum_{i=1}^{Q_2} \frac{\mathbf{x}'_i \{\mathbf{x}'_i\}^T}{k_i^2 (k_i^2 - k^2)} \quad (50)$$

$$(\mathbf{P}^{-1})_{12} = -\frac{jk}{\eta} \mathbf{S}_{11}^{-1} \mathbf{S}_{12} \mathbf{R}_{22}^{-1} - \frac{jk^3}{\eta} \sum_{i=1}^{Q_2} \frac{\mathbf{x}'_i \{\mathbf{x}'_i\}^T}{k_i^2 (k_i^2 - k^2)} \quad (51)$$

$$(\mathbf{P}^{-1})_{22} = \frac{jk}{\eta} \mathbf{R}_{22}^{-1} + \frac{jk^3}{\eta} \sum_{i=1}^{Q_2} \frac{\mathbf{x}_i \{\mathbf{x}_i\}^T}{k_i^2 (k_i^2 - k^2)} \quad (52)$$

where $\mathbf{x}'_i = \mathbf{S}_{11}^{-1} \mathbf{S}_{12} \mathbf{x}_i$. Once the \mathbf{P} matrix has been successfully inverted, the elements of the \mathbf{Y} matrix of the planar step can be obtained through the evaluation of

$$Y_{m,n}^{(\delta,\gamma)} = \sum_{q=1}^Q \alpha_{q,n}^{(\gamma)} \int_{S^{(\gamma)}} \mathbf{e}_q^{(1)} \mathbf{e}_m^{(\delta)} ds = \{\mathbf{Q}^{(\delta)}\}^T \mathbf{P}^{-1} \mathbf{Q}^{(\gamma)} \quad (53)$$

thus obtaining the following final expressions for all possible combinations of TE and TM modes

$$\mathbf{Y}_{\text{TE-TE}}^{(\delta,\gamma)} = \frac{1}{jk\eta} \{\mathbf{Q}_{11'}^{(\delta)}\}^T \mathbf{S}_{11}^{-1} \mathbf{Q}_{11'}^{(\gamma)} + \frac{jk}{\eta} \{\mathbf{E}_{21'}^{(\delta)}\}^T \mathbf{R}_{22}^{-1} \mathbf{E}_{21'}^{(\gamma)} + \frac{jk^3}{\eta} \sum_{i=1}^{Q_2} \frac{\mathbf{y}_i^{n(\delta)} \{\mathbf{y}_i^{n(\gamma)}\}^T}{k_i^2 (k_i^2 - k^2)} \quad (54)$$

$$\mathbf{Y}_{\text{TE-TM}}^{(\delta,\gamma)} = \frac{jk}{\eta} \{\mathbf{E}_{21'}^{(\delta)}\}^T \mathbf{R}_{22}^{-1} \mathbf{Q}_{22'}^{(\gamma)} + \frac{jk^3}{\eta} \sum_{i=1}^{Q_2} \frac{\mathbf{y}_i^{n(\delta)} \{\mathbf{y}_i^{r(\gamma)}\}^T}{k_i^2 (k_i^2 - k^2)} \quad (55)$$

$$\mathbf{Y}_{\text{TM-TE}}^{(\delta,\gamma)} = \frac{jk}{\eta} \{\mathbf{Q}_{22'}^{(\delta)}\}^T \mathbf{R}_{22}^{-1} \mathbf{E}_{21'}^{(\gamma)} + \frac{jk^3}{\eta} \sum_{i=1}^{Q_2} \frac{\mathbf{y}_i^{r(\delta)} \{\mathbf{y}_i^{n(\gamma)}\}^T}{k_i^2 (k_i^2 - k^2)} \quad (56)$$

$$\mathbf{Y}_{\text{TM-TM}}^{(\delta,\gamma)} = \frac{jk}{\eta} \{\mathbf{Q}_{22'}^{(\delta)}\}^T \mathbf{R}_{22}^{-1} \mathbf{Q}_{22'}^{(\gamma)} + \frac{jk^3}{\eta} \sum_{i=1}^{Q_2} \frac{\mathbf{y}_i^{r(\delta)} \{\mathbf{y}_i^{r(\gamma)}\}^T}{k_i^2 (k_i^2 - k^2)} \quad (57)$$

where we have that $\mathbf{y}_i^{r(\delta)} = \{\mathbf{Q}_{22'}^{(\delta)}\}^T \mathbf{x}_i$ and $\mathbf{y}_i^{n(\delta)} = \{\mathbf{E}_{21'}^{(\delta)}\}^T \mathbf{x}_i$, $\mathbf{E}_{21'}^{(\delta)} = \mathbf{Q}_{21'}^{(\delta)} - \mathbf{S}_{12}^T \mathbf{S}_{11}^{-1} \mathbf{Q}_{11'}^{(\delta)}$. As it has been explained before, the series in (54)-(57) also converge with a number of terms rather smaller than Q_2 .

3. Segmentation Scheme for Passive Components based on Planar Waveguide Junctions

The structure under study is composed of the cascade connection of planar junctions between two different waveguides of lengths l_1 and l_2 (see Fig. 3), with the equivalent circuit for a Z matrix representation. Our aim is to represent each basic building block of this equivalent circuit in terms of a wideband Z matrix in the form of pole expansions

$$\mathbf{Z} = \frac{\eta}{jk} \mathbf{A} + jk\eta \mathbf{B} + jk^3\eta \mathbf{C}(\Delta^2 - k^2\mathbf{U})^{-1} \mathbf{C}^T \quad (58)$$

where $k = \omega\sqrt{\mu\varepsilon}$, $\eta = \sqrt{\mu/\varepsilon}$, and \mathbf{A} , \mathbf{B} , \mathbf{C} , Δ and \mathbf{U} are frequency independent matrices (the meaning and structure of these matrices are detailed in (Arcioni & Conciauro, 1999) for the dual case of the wideband admittance matrix formulation). In particular, \mathbf{A} and \mathbf{B} are square symmetric matrices of size N (N being the total number of accessible modes considered in each building block), \mathbf{C} is a matrix of size $N \times Q$, with Q the number of terms included in the pole expansion, Δ is a diagonal matrix with the values of the poles, and \mathbf{U} is the identity matrix of size Q .

According to Fig. 3, we will compute the wideband impedance matrix in the form of pole expansions for the uniform waveguide sections (\mathbf{Z}_{w1} and \mathbf{Z}_{w2}), for each planar junction (\mathbf{Z}_{st}), and also for the two sets of asymptotic modal admittances generated by the integral equation technique, which are denoted as \mathbf{Z}_{a1} and \mathbf{Z}_{a2} , respectively.

Although this method can be applied to building blocks in the form of Y matrix, in this chapter we will focus our attention in the Z matrix representation, whereas the Y matrix representation of uniform waveguides and the efficient cascade connection of Y matrices can be found in (Arcioni & Conciauro, 1999). Next, we concentrate on the novel aspects related to the efficient computation of all such matrices.

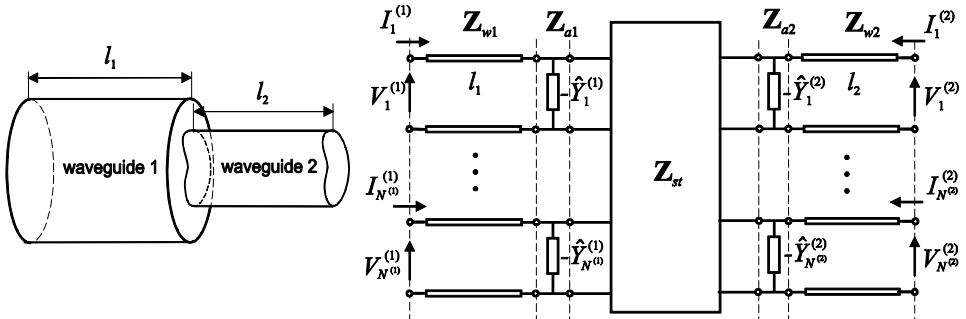


Fig. 3. Planar junction between two waveguides of lengths l_1 and l_2 , and equivalent circuit for the multimode Z matrix representation.

3.1 Planar waveguide steps

If we recall the expression for the generalized impedance matrix in the form of a pole expansion (28)-(31), we find the following frequency independent blocks for the planar waveguide junction under study (\mathbf{Z}_{st})

$$\mathbf{A}^{(\delta,\gamma)} = \begin{bmatrix} \mathbf{0}_{11} & \mathbf{0}_{12} \\ \mathbf{0}_{21} & \{\mathbf{Q}_{22}^{(\delta)}\}^T \mathbf{S}_{22}^{-1} \mathbf{Q}_{22}^{(\gamma)} \end{bmatrix} \quad (59)$$

$$\mathbf{B}^{(\delta,\gamma)} = \begin{bmatrix} \{\mathbf{Q}_{11}^{(\delta)}\}^T \mathbf{R}_{11}^{-1} \mathbf{Q}_{11}^{(\gamma)} & \{\mathbf{Q}_{11}^{(\delta)}\}^T \mathbf{R}_{11}^{-1} \mathbf{E}_{12}^{(\gamma)} \\ \{\mathbf{E}_{12}^{(\delta)}\}^T \mathbf{R}_{11}^{-1} \mathbf{Q}_{11}^{(\gamma)} & \{\mathbf{E}_{12}^{(\delta)}\}^T \mathbf{R}_{11}^{-1} \mathbf{E}_{12}^{(\gamma)} \end{bmatrix} \quad (60)$$

$$\mathbf{C} = \begin{bmatrix} \mathbf{Y}^{(1)} \Delta^{-1} \\ \mathbf{Y}^{(1)} \Delta^{-1} \\ \mathbf{Y}^{(2)} \Delta^{-1} \\ \mathbf{Y}^{(2)} \Delta^{-1} \end{bmatrix} \quad \Delta = \text{diag}\{k_1, \dots, k_{Q_1}\} \quad (61)$$

where $\mathbf{Y}^{(\delta)} = [\mathbf{y}_1^{(\delta)} \dots \mathbf{y}_{Q_1}^{(\delta)}]$ and $\mathbf{Y}^{n(\delta)} = [\mathbf{y}_1^{n(\delta)} \dots \mathbf{y}_{Q_1}^{n(\delta)}]$ for $\delta = 1, 2$.

3.2 Asymptotic admittances

Each set of asymptotic modal admittances in Fig. 3 can be seen as a two-port network, which can be easily characterized by a generalized Z matrix (\mathbf{Z}_a) whose elements are defined as follows

$$Z_{m,n}^{(\delta,\gamma)} = -\frac{\delta_{mn}}{\hat{Y}_m} = \delta_{mn} \begin{cases} -\frac{jk\eta}{\kappa_m^{(\delta)}} & \text{TE} \\ -\frac{\kappa_m^{(\delta)}\eta}{jk} & \text{TM} \end{cases} \quad (62)$$

The previous expression is suitable for the representation of the generalized impedance matrix as indicated by (58). In this case, the pole expansion is not present and therefore

$$A_{mn}^{(\delta,\gamma)} = \delta_{mn} \begin{cases} 0 & \text{TE} \\ -\kappa_m^{(\delta)} & \text{TM} \end{cases} \quad (63)$$

$$B_{mn}^{(\delta,\gamma)} = \delta_{mn} \begin{cases} -1/\kappa_m^{(\delta)} & \text{TE} \\ 0 & \text{TM} \end{cases} \quad (64)$$

3.3 Uniform waveguide sections

Now, we derive the expressions for the generalized impedance matrix of a uniform waveguide section of length l . Since the modes of this element are uncoupled, the only non-zero entries of such Z matrix (\mathbf{Z}_w) are those relating voltages and currents of the same mode, which are computed as

$$Z_{mn}^{(1,1)} = Z_{mn}^{(2,2)} = \delta_{mn} Z_m \coth \gamma_m l \quad (65)$$

$$Z_{mn}^{(1,2)} = Z_{mn}^{(2,1)} = \delta_{mn} Z_m \text{csch } \gamma_m l \quad (66)$$

where $\gamma_m = \sqrt{\kappa_m^2 - k^2}$, and κ_m and Z_m are, respectively, the cutoff wavenumber and the characteristic impedance of the m -th mode considered in the waveguide section.

Considering that the modes of the waveguide section can be of type TE or TM, we obtain the following expressions

$$Z_{mn}^{(1,1)} = \delta_{mn} \begin{cases} jk\eta \frac{\coth \gamma_m l}{\gamma_m} = jk\eta f_r^{\text{TE}}(k^2) & \text{TE} \\ \frac{\eta}{jk} \gamma_m \coth \gamma_m l = \frac{\eta}{jk} f_r^{\text{TM}}(k^2) & \text{TM} \end{cases} \quad (67)$$

$$Z_{mn}^{(1,2)} = \delta_{mn} \begin{cases} jk\eta \frac{\text{csch } \kappa_m l}{\gamma_m} = jk\eta f_i^{\text{TE}}(k^2) & \text{TE} \\ \frac{\eta}{jk} \gamma_m \text{csch } \kappa_m l = \frac{\eta}{jk} f_i^{\text{TM}}(k^2) & \text{TM} \end{cases} \quad (68)$$

In order to express the Z matrix elements of the waveguide section in the form of the pole expansion collected in (58), we will make use of the theorem of Mittag-Leffler (Spiegel, 1991)

$$f(k^2) = f(0) + \sum_{p=1}^{\infty} \text{Res}(f, z_p) \frac{k^2}{z_p(k^2 - z_p)} \quad (69)$$

where $\text{Res}(f, z_p)$ are the residues of the function f related to their poles z_p , which in our case are defined as

$$z_p \equiv k_{ms}^2 = (\kappa_m^{(1)})^2 + (s\pi/l)^2 \quad (70)$$

with $s=0,1,2,\dots$ for TE modes and $s=1,2,3,\dots$ for TM modes. It can be seen that the values for the poles are directly related to the resonant wavenumbers of the open-circuited waveguide.

Then, applying the theorem of Mittag-Leffler to the functions f in equations (67) and (68), we can obtain

$$f_r^{\text{TE}}(k^2) = \frac{\coth \kappa_m l}{\kappa_m} + k^2 \sum_{s=0}^{\infty} \frac{\varepsilon_s}{l} \frac{1}{k_{ms}^2 (k_{ms}^2 - k^2)} \quad (71)$$

$$f_r^{\text{TM}}(k^2) = \kappa_m \coth \kappa_m l - k^2 \frac{2}{l} \sum_{s=1}^{\infty} \frac{(s\pi/l)^2}{k_{ms}^2 (k_{ms}^2 - k^2)} \quad (72)$$

$$f_t^{\text{TE}}(k^2) = \frac{\text{csch } \kappa_m l}{\kappa_m} + k^2 \sum_{s=0}^{\infty} \frac{\varepsilon_s}{l} \frac{(-1)^s}{k_{ms}^2 (k_{ms}^2 - k^2)} \quad (73)$$

$$f_t^{\text{TM}}(k^2) = \kappa_m \text{csch } \kappa_m l - k^2 \frac{2}{l} \sum_{s=1}^{\infty} \frac{(-1)^s (s\pi/l)^2}{k_{ms}^2 (k_{ms}^2 - k^2)} \quad (74)$$

where ε_s means the Neumann's factor (i.e. $\varepsilon_s = 1$ if $s=0$ and $\varepsilon_s = 2$ if $s \neq 0$).

For the case of the f_r^{TM} and f_t^{TM} functions we need further treatment of the previous expressions. In particular, we must extract the low frequency contribution from the series in (72) and (74). Then, after solving analytically the infinite summations when $k \rightarrow 0$ (Gradstheyn and Ryzhik, 1980), we can obtain that

$$f_r^{\text{TM}}(k^2) = \kappa_m \coth \kappa_m l - k^2 \frac{l}{2} \left(\frac{\coth \kappa_m l}{\kappa_m l} - \text{csch}^2 \kappa_m l \right) - k^4 \frac{2}{l} \sum_{s=1}^{\infty} \frac{(s\pi/l)^2}{k_{ms}^4 (k_{ms}^2 - k^2)} \quad (75)$$

$$f_t^{\text{TM}}(k^2) = \kappa_m \text{csch } \kappa_m l - k^2 \frac{l}{2} \text{csch } \kappa_m l \left(\frac{1}{\kappa_m l} - \coth \kappa_m l \right) - k^4 \frac{2}{l} \sum_{s=1}^{\infty} \frac{(-1)^s (s\pi/l)^2}{k_{ms}^4 (k_{ms}^2 - k^2)} \quad (76)$$

Finally, if we introduce the previous expansions (71), (73), (75) and (76) into (67) and (68), we obtain the Z matrix representation in the form of (58), where the entries of the frequency independent matrices are

$$A_{m,n}^{(1,1)} = \delta_{mn} \begin{cases} 0 & \text{TE} \\ \kappa_m \coth \kappa_m l & \text{TM} \end{cases} \quad A_{m,n}^{(1,2)} = \delta_{mn} \begin{cases} 0 & \text{TE} \\ \kappa_m \operatorname{csch} \kappa_m l & \text{TM} \end{cases} \quad (77)$$

$$B_{m,n}^{(1,1)} = \delta_{mn} \begin{cases} \frac{\coth \kappa_m l}{\kappa_m} & \text{TE} \\ \frac{1}{2} \left(\frac{\coth \kappa_m l}{\kappa_m l} - \operatorname{csch}^2 \kappa_m l \right) & \text{TM} \end{cases} \quad B_{m,n}^{(1,2)} = \delta_{mn} \begin{cases} \frac{\operatorname{csch} \kappa_m l}{\kappa_m} & \text{TE} \\ \frac{1}{2} \operatorname{csch}^2 \kappa_m l \left(\frac{1}{\kappa_m l} - \coth \kappa_m l \right) & \text{TM} \end{cases} \quad (78)$$

$$C = \begin{bmatrix} C^{(1)} \\ C^{(2)} \end{bmatrix} \quad C_{m,ns}^{(1)} = \delta_{mn} \begin{cases} \sqrt{\frac{\epsilon_s}{l}} \frac{1}{k_{ms}} & \text{TE} \\ \sqrt{\frac{2}{l}} \frac{(s\pi/l)}{k_{ms}^2} & \text{TM} \end{cases} \quad C_{m,ns}^{(2)} = (-1)^s C_{m,ns}^{(1)} \quad (79)$$

4. Efficient Cascade Connection of Z Matrices

Once the expressions for the generalized Z matrices of all basic blocks of the structure shown in Fig. 3 have been presented, we proceed to combine them in order to determine the wideband Z matrix representation of the complete structure. For such purpose, we first outline a procedure to solve the combination of two cascaded Z matrices in the form of pole expansions, which follows a dual formulation to the one derived in (Arcioni & Conciauro, 1999) for the admittance matrix case. Then, a novel efficient algorithm, which allows to reduce the effective number of poles to be considered after connecting two wideband Z matrices, is fully described.

4.1 Combination of two generalized Z matrices

Let us consider two cascaded building blocks of the structure shown in Fig. 3, whose generalized Z matrices (named as Z_I and Z_{II} in Fig. 4) are given in the previous form of (58). As it can be inferred from Fig. 4, the voltages and the currents at the external ports are grouped into the vectors $\mathbf{v}^{(1)}$, $\mathbf{i}^{(1)}$, $\mathbf{v}^{(2)}$ and $\mathbf{i}^{(2)}$, and the currents at the connected ports are collected into the vector $\mathbf{i}^{(c)}$. If we consider that the currents $\mathbf{i}^{(1)}$ and $\mathbf{i}^{(2)}$ are incoming, respectively, to the blocks I and II, and the currents $\mathbf{i}^{(c)}$ are incoming to the block II, we can write

$$\mathbf{v} = \mathbf{Z}^{ee} \mathbf{i} + \mathbf{Z}^{ec} \mathbf{i}^{(c)} \quad (80)$$

$$\mathbf{Z}^{ec} \mathbf{i}^{(c)} = -\{\mathbf{Z}^{ec}\}^T \mathbf{i} \quad (81)$$

where

$$\mathbf{v} = \begin{bmatrix} \mathbf{v}^{(1)} \\ \mathbf{v}^{(2)} \end{bmatrix} \quad \mathbf{i} = \begin{bmatrix} \mathbf{i}^{(1)} \\ \mathbf{i}^{(2)} \end{bmatrix} \quad (82)$$

and the matrices \mathbf{Z}^{ee} , \mathbf{Z}^{ec} and \mathbf{Z}^{cc} are given by

$$\mathbf{Z}^{ee} = \begin{bmatrix} \mathbf{Z}_I^{(1,1)} & 0 \\ 0 & \mathbf{Z}_{II}^{(2,2)} \end{bmatrix} \quad \mathbf{Z}^{ec} = \begin{bmatrix} -\mathbf{Z}_I^{(1,c)} \\ \mathbf{Z}_{II}^{(2,c)} \end{bmatrix} \quad \mathbf{Z}^{cc} = \mathbf{Z}_I^{(c,c)} + \mathbf{Z}_{II}^{(c,c)} \quad (83)$$

Our final goal is to obtain the overall matrix \mathbf{Z}_{tot} , relating the vectors \mathbf{v} and \mathbf{i} , in the same form of (58). For such purpose, we first express the matrices \mathbf{Z}^{ee} , \mathbf{Z}^{ec} and \mathbf{Z}^{cc} in the form of pole expansions. Taking into account the following definitions of the matrices

$$\mathbf{A}^{ee} = \begin{bmatrix} \mathbf{A}_I^{(1,1)} & \mathbf{0} \\ \mathbf{0} & \mathbf{A}_{II}^{(2,2)} \end{bmatrix} \quad \mathbf{B}^{ee} = \begin{bmatrix} \mathbf{B}_I^{(1,1)} & \mathbf{0} \\ \mathbf{0} & \mathbf{B}_{II}^{(2,2)} \end{bmatrix} \quad \mathbf{C}^{ee} = \begin{bmatrix} \mathbf{C}_I^{(1)} & \mathbf{0} \\ \mathbf{0} & \mathbf{C}_{II}^{(2)} \end{bmatrix} \quad (84)$$

$$\mathbf{A}^{ec} = \left[\mathbf{A}_I^{(e,c)} + \mathbf{A}_{II}^{(e,c)} \right] \quad \mathbf{B}^{ec} = \left[\mathbf{B}_I^{(e,c)} + \mathbf{B}_{II}^{(e,c)} \right] \quad \mathbf{C}^c = \left[-\mathbf{C}_I^{(c)} \quad \mathbf{C}_{II}^{(c)} \right] \quad (85)$$

$$\mathbf{A}^{ec} = \begin{bmatrix} -\mathbf{A}_I^{(1,c)} \\ \mathbf{A}_{II}^{(2,c)} \end{bmatrix} \quad \mathbf{B}^{ec} = \begin{bmatrix} -\mathbf{B}_I^{(1,c)} \\ \mathbf{B}_{II}^{(2,c)} \end{bmatrix} \quad \Delta = \begin{bmatrix} \Delta_I & \mathbf{0} \\ \mathbf{0} & \Delta_{II} \end{bmatrix} \quad (86)$$

we can easily write that

$$\mathbf{Z}^{ee} = \frac{\eta}{jk} \mathbf{A}^{ee} + jk\eta \mathbf{B}^{ee} + jk^3 \eta \mathbf{C}^c (\Delta^2 - k^2 \mathbf{U})^{-1} \{\mathbf{C}^c\}^T \quad (87)$$

$$\mathbf{Z}^{ec} = \frac{\eta}{jk} \mathbf{A}^{ec} + jk\eta \mathbf{B}^{ec} + jk^3 \eta \mathbf{C}^c (\Delta^2 - k^2 \mathbf{U})^{-1} \{\mathbf{C}^c\}^T \quad (88)$$

$$\mathbf{Z}^{cc} = \frac{\eta}{jk} \mathbf{A}^{cc} + jk\eta \mathbf{B}^{cc} + jk^3 \eta \mathbf{C}^c (\Delta^2 - k^2 \mathbf{U})^{-1} \{\mathbf{C}^c\}^T \quad (89)$$

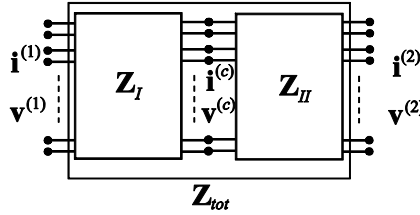


Fig. 4. Two elementary building blocks connected in cascade.

Then, the currents at the connected ports can be arranged in the following way

$$\mathbf{i}^{(c)} = \begin{bmatrix} \mathbf{i}_1^c \\ \mathbf{i}_2^c \end{bmatrix} \quad (90)$$

where \mathbf{i}_1^c and \mathbf{i}_2^c contain, respectively, the currents corresponding to TE (subscript 1) and TM (subscript 2) modes. According to such arrangement, the related matrices of (84)-(86) can be partitioned as indicated below

$$\mathbf{A}^{cc} = \begin{bmatrix} \mathbf{0} & \mathbf{0} \\ \mathbf{0} & \mathbf{A}_{22}^{cc} \end{bmatrix} \quad \mathbf{B}^{cc} = \begin{bmatrix} \mathbf{B}_{11}^{cc} & \mathbf{B}_{12}^{cc} \\ \{\mathbf{B}_{12}^{cc}\}^T & \mathbf{B}_{22}^{cc} \end{bmatrix} \quad \mathbf{C}^c = \begin{bmatrix} \mathbf{C}_1^c \\ \mathbf{C}_2^c \end{bmatrix} \quad (91)$$

$$\mathbf{A}^{ec} = \begin{bmatrix} \mathbf{0} & \mathbf{A}_2^{ec} \end{bmatrix} \quad \mathbf{B}^{ec} = \begin{bmatrix} \mathbf{B}_1^{ec} & \mathbf{B}_2^{ec} \end{bmatrix} \quad (92)$$

where zero matrices appear in the partitioning of \mathbf{A}^{cc} and \mathbf{A}^{ec} when TE modes are involved (remember the expressions collected in (59), (63) and (77)). At this point, the problem to be solved is completely dual to the one considered in (Arcioni & Conciauro, 1999) for the admittance matrix formulation. Therefore, following a dual procedure, we can easily deduce

the Z matrix for the cascaded connection of the building blocks in the required form of pole expansions

$$\mathbf{Z}_{tot} = \frac{\eta}{jk} \mathbf{A}_{tot} + jk\eta \mathbf{B}_{tot} + jk^3 \eta \mathbf{C}_{tot} (\mathbf{K}^2 - k^2 \mathbf{U})^{-1} \mathbf{C}_{tot}^T \quad (93)$$

where

$$\mathbf{A}_{tot} = \mathbf{A}^{ee} - \mathbf{A}_2^{ec} \{\mathbf{A}_{22}^{cc}\}^{-1} \{\mathbf{A}_2^{ec}\}^T \quad (94)$$

$$\mathbf{B}_{tot} = \mathbf{E} + \mathbf{A}_2^{ec} \mathbf{X}_i \mathbf{K}^{-4} \mathbf{X}_i^T \{\mathbf{A}_2^{ec}\}^T - \mathbf{A}_2^{ec} \{\mathbf{A}_{22}^{cc}\}^{-1} \mathbf{F}^T - \mathbf{F} \{\mathbf{A}_{22}^{cc}\}^{-1} \{\mathbf{A}_2^{ec}\}^T \quad (95)$$

$$\mathbf{C}_{tot} = \mathbf{F} \mathbf{X}_i + \mathbf{G} \mathbf{X}_w - \mathbf{A}_2^{ec} \mathbf{X}_i \mathbf{K}^{-2} \quad (96)$$

and

$$\mathbf{E} = \mathbf{B}^{ee} - \mathbf{B}_1^{ec} \{\mathbf{B}_{11}^{cc}\}^{-1} \{\mathbf{B}_1^{ec}\}^T \quad (97)$$

$$\mathbf{F} = \mathbf{B}_2^{ec} - \mathbf{B}_1^{ec} \{\mathbf{B}_{11}^{cc}\}^{-1} \mathbf{B}_{12}^{cc} \quad (98)$$

$$\mathbf{G} = \mathbf{C}^e - \mathbf{B}_1^{ec} \{\mathbf{B}_{11}^{cc}\}^{-1} \mathbf{C}_1^c \quad (99)$$

Furthermore, the matrix $\mathbf{K} = \text{diag}\{k_i\}$ is a diagonal matrix with the eigenvalues, and \mathbf{X}_i and \mathbf{X}_w are matrices with the eigenvectors, corresponding to the solution of the problem

$$\left(\begin{bmatrix} \mathbf{A}_{22}^{cc} & 0 \\ 0 & \Delta^2 \end{bmatrix} - k^2 \begin{bmatrix} \mathbf{P} & \mathbf{R} \\ \mathbf{R}^T & \mathbf{Q} \end{bmatrix} \right) \begin{bmatrix} \mathbf{i}_2^c \\ \mathbf{w}^c \end{bmatrix} = 0 \quad (100)$$

where

$$\mathbf{P} = \mathbf{B}_{22}^{cc} - \{\mathbf{B}_{12}^{cc}\}^T \{\mathbf{B}_{11}^{cc}\}^{-1} \mathbf{B}_{12}^{cc} \quad (101)$$

$$\mathbf{Q} = \mathbf{U} - \{\mathbf{C}_1^c\}^T \{\mathbf{B}_{11}^{cc}\}^{-1} \mathbf{C}_1^c \quad (102)$$

$$\mathbf{R} = \mathbf{C}_2^c - \{\mathbf{B}_{12}^{cc}\}^T \{\mathbf{B}_{11}^{cc}\}^{-1} \mathbf{C}_1^c \quad (103)$$

and the auxiliary vector \mathbf{w}^c is defined as follows

$$\mathbf{w}^c = k^2 (\Delta^2 - k^2 \mathbf{U})^{-1} (\{\mathbf{C}^e\}^T \mathbf{i} + \{\mathbf{C}_1^c\}^T \mathbf{i}_1^c + \{\mathbf{C}_2^c\}^T \mathbf{i}_2^c) \quad (104)$$

4.2 Efficient characterization of passive structures

When two building blocks of a structure are cascaded, the number of terms in the resulting pole expansion is equal to the number of poles for each block plus the number of TM accessible modes at the common port (see the generalized eigenvalue problem raised in (100), as well as the definition and partitioning of the involved matrices in (84)-(86), (91) and (92)). If the structure is composed of many blocks, the total number of poles will become very high, thus reducing the efficiency of the algorithm due to the size of the successive eigenvalue problems.

For avoiding such drawback, we propose to limit the number of eigenvalues considered after each connection. When two different blocks are connected, we obtain the entries of the generalized Z matrix in the following form

$$Z_{mn}^{(\delta, \gamma)} = \frac{\eta}{jk} A_{mn}^{(\delta, \gamma)} + jk\eta B_{mn}^{(\delta, \gamma)} + jk^3 \eta \sum_{i=1}^Q \frac{C_{mi}^{(\delta)} C_{ni}^{(\gamma)}}{k_i^2 - k^2} \quad (105)$$

In this equation, the higher terms of the sum have a lower contribution to the final result. Due to this fact, we can only consider Q' eigenvalues in the sum, and approximate the contribution of the remaining $Q - Q'$ eigenvalues by

$$jk^3\eta \sum_{i=Q'+1}^Q \frac{C_{mi}^{(\delta)}C_{ni}^{(\gamma)}}{k_i^2 - k^2} \approx jkk_0^2\eta \sum_{i=Q'+1}^Q \frac{C_{mi}^{(\delta)}C_{ni}^{(\gamma)}}{k_i^2 - k_0^2} \quad (106)$$

where k_0 corresponds to the value of k at the center point of the frequency band. Proceeding in such a way, the eigenvalues with lower weight are included within the linear term

$$Z_{mn}^{(\delta,\gamma)} \approx \frac{\eta}{jk} A_{mn}^{(\delta,\gamma)} + jk\eta \left(B_{mn}^{(\delta,\gamma)} + k_0^2 \sum_{i=Q'+1}^Q \frac{C_{mi}^{(\delta)}C_{ni}^{(\gamma)}}{k_i^2 - k_0^2} \right) + jk^3\eta \sum_{i=1}^{Q'} \frac{C_{mi}^{(\delta)}C_{ni}^{(\gamma)}}{k_i^2 - k^2} \quad (107)$$

thus obtaining a reduced size for the eigenvalue problem to be solved during the next connection, whereas very good accuracy is still preserved. This technique can also be applied to reduce the number of poles involved in the Z matrix characterization of each single building block, i.e. waveguide steps and uniform waveguide sections.

5. Optimized Cascade Connection for H-plane Waveguide Components

The method proposed in the previous section is general and can be simplified for the analysis of H-plane components, where only TE modes are present. However, the absence of TM modes involves that the \mathbf{A} matrices for all the building blocks are zero. For this reason, we introduce a new general expression for the building blocks where an additional low frequency term depending on k^3 has been extracted

$$\mathbf{Z} = jk\eta\mathbf{A} + jk^3\eta\mathbf{B} + jk^5\eta\mathbf{C}(\Delta^2 - k^2\mathbf{U})^{-1}\mathbf{C}^T \quad (108)$$

The purpose of this new formulation is to obtain new expressions of the matrix \mathbf{C} with a stronger attenuation for higher terms in the pole expansion. In this way, a lower number of poles will be necessary for recovering a given accuracy.

The proposed cascade connection in section 4.1 can be applied since (108) can be expressed in the following way

$$\mathbf{Z} = k^2 \left(\frac{\eta}{jk} (-\mathbf{A}) + jk\eta\mathbf{B} + jk^3\eta\mathbf{C}(\Delta^2 - k^2\mathbf{U})^{-1}\mathbf{C}^T \right) \quad (109)$$

5.1 Uniform waveguide section for H-plane waveguide components

Equations (71) and (73) provide the expression for $f_r^{\text{TE}}(k^2)$ and $f_i^{\text{TE}}(k^2)$ for a Z matrix expression in the form of (58). However, in order to obtain the Z matrix in the form of (108) for H-plane components, an additional low frequency term must be extracted from the series in (71) and (73). Then, after solving analytically the infinite summations when $k \rightarrow 0$ (Gradstheyn and Ryzhik, 1980), we obtain the following expressions for the functions f^{TE}

$$f_r^{TE}(k^2) = \frac{\coth \kappa_m l}{\kappa_m} + k^2 \frac{l}{2(\kappa_m)^2} \left[\frac{\coth \kappa_m l}{\kappa_m l} + \operatorname{csch}^2 \kappa_m l \right] + k^4 \sum_{s=1}^{\infty} \frac{\varepsilon_s}{l} \frac{1}{k_{ms}^4 (k_{ms}^2 - k^2)} \quad (110)$$

$$f_t^{TE}(k^2) = \frac{\operatorname{csch} \kappa_m l}{\kappa_m} + k^2 \frac{1 + \kappa_m l \coth \kappa_m l}{2\kappa_m^3 \sinh^2 \kappa_m l} + k^4 \sum_{s=1}^{\infty} \frac{\varepsilon_s}{l} \frac{(-1)^s}{k_{ms}^4 (k_{ms}^2 - k^2)} \quad (111)$$

Finally, after introducing the previous expansions (110) and (111) into (67) and (68), it can be easily identified the entries of the frequency independent blocks corresponding to the wideband Z matrix representation of the waveguide section

$$A_{m,n}^{(1,1)} = \delta_{mn} \frac{\coth \kappa_m l}{\kappa_m} \quad A_{m,n}^{(1,2)} = \delta_{mn} \frac{\operatorname{csch} \kappa_m l}{\kappa_m} \quad (112)$$

$$B_{m,n}^{(1,1)} = \delta_{mn} \frac{l}{2\kappa_m^2} \left(\frac{\coth \kappa_m l}{\kappa_m l} + \operatorname{csch}^2 \kappa_m l \right) \quad B_{m,n}^{(1,2)} = \delta_{mn} \frac{1 + \kappa_m l \coth \kappa_m l}{2\kappa_m^3 \sinh^2 \kappa_m l} \quad (113)$$

$$C_{m,ns}^{(1)} = \delta_{mn} \sqrt{\frac{\varepsilon_s}{l}} \frac{1}{k_{ms}^2} \quad C_{m,ns}^{(2)} = (-1)^s C_{m,ns}^{(1)} \quad (114)$$

If the expression of the C entries in (114) is compared with (79), the new entries depend on $1/k_{ms}^2$ instead of $1/k_{ms}$, thus reducing the required number of poles because of the stronger attenuation of the terms in the series.

6. Validation Results

First of all, we have performed a detailed convergence study of the impedance and admittance formulations of the original integral equation technique proposed in (Gerini et al., 1998). From this study, we conclude that accurate and stable results are obtained in both cases, provided that the same number of modes in the bigger and smaller waveguides is used with each formulation, and that the higher number of modes is always chosen for the bigger waveguide. Note that in the Z matrix (Y matrix) formulation, the basis functions are the modes of the smaller (bigger) cross-section waveguide, whereas the infinite series involve the modes of the bigger (smaller) waveguide. This means that the number of basis functions in the Y matrix formulation should be equal to the number of terms considered in the infinite series present in the Z matrix representation, and vice versa. Since the classical integral equation technique needs to invert a matrix of size equal to the number of basis functions per each frequency point, the Y matrix formulation provides the slowest convergent results. To accelerate such convergence rate, we propose the wideband representation just outlined in this work.

For verification purposes, we have first analyzed a simple planar junction between two rectangular waveguides (see the geometry in Fig. 5). First of all, we proceed to validate the Z matrix formulation through comparison with the original integral equation technique. In Fig. 5 (left), we show the results obtained for 1, 8 and 15 accessible modes (N), whereas the total number of basis functions (Q) is equal to 100 ($Q_1=58$), $R=3$ in (7), and the infinite series in (13) and (14) are summed up with 600 terms. With regard to the convergent evaluation of the frequency-dependent series in (28)-(31), only the first 25 terms (poles) have been required. For comparative reasons, we also include the results for $k_0=0$ in (7), which

correspond to the ones provided by the method proposed in (Mira et al., 2006), and the convergent results obtained with the original integral equation technique using only 1 accessible mode. It can be concluded that the use of k_0 clearly improves the convergence rate of our method, thus involving a reduction in the required number of accessible modes (N) when compared to the previous approach of (Mira et al., 2006).

In terms of numerical efficiency, the CPU time required by our method to solve the considered waveguide step in the whole frequency range (201 frequency points) has been equal to 0.10 s for the worst case ($N=15$). However, the original integral equation technique needed 1.01 s for solving the same planar junction. Therefore, the analysis method of planar waveguide junctions proposed in this paper involves a substantial reduction in the related computational effort, without degrading the accuracy of results.

In Fig. 5 (right) we compare the obtained results for Z matrix and Y matrix formulations. As it can be noticed, with an adequate number of accessible modes (i.e. $N=15$) the Y matrix formulation provides the same accurate results. Only small differences can be observed for 1 accessible mode, because of the different approximations proposed in (7) and (41). In terms of numerical efficiency, the CPU time required by using the Y matrix formulation to solve the waveguide step in the whole frequency range has been equal to 0.55 s for the worst case. The original integral equation technique would need 108 s following the Y matrix formulation.

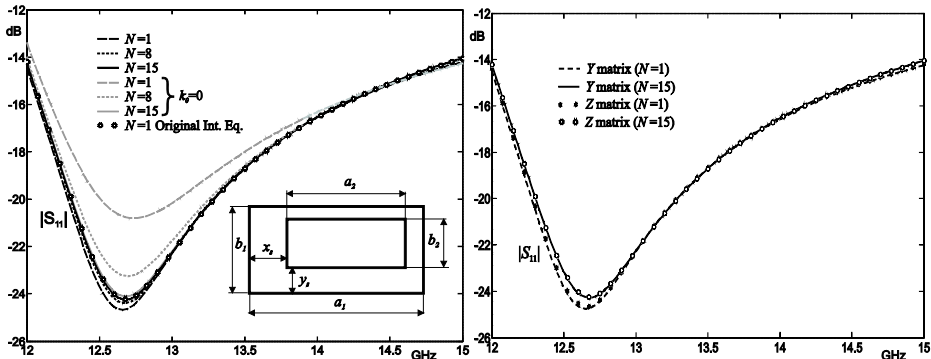


Fig. 5. Convergence study of the new method for a single waveguide step, whose dimensions are $a_1=19.05$ mm, $b_1=9.525$ mm, $a_2=13.0$ mm, $b_2=5.5$ mm, $x_s=4.0$ mm and $y_s=3.0$ mm.

Once the algorithm for the analysis of single waveguide steps has been successfully verified, the analysis of several waveguide filters will be shown for validating the overall performance of the proposed technique. Our first example deals with the full-wave analysis of a 4-pole direct-coupled cavity filter in WR-75 waveguide ($a=19.05$ mm, $b=9.525$ mm). The dimensions of the coupling windows (see Fig. 6) are $w_1=9.55$ mm, $w_2=6.49$ mm and $w_3=5.89$ mm, $h_1=h_2=h_3=6.0$ mm and $d=2.0$ mm, whereas the lengths of the WR-75 waveguide cavities are $l_1=11.95$ mm and $l_2=13.37$ mm. In order to get an accurate modelling of all waveguide

¹All reported CPU times have been obtained with a Pentium 4 at 3.2 GHz.

steps involved in this example, we have considered $N=9$, $Q=450$ and 75 terms in the series (Z matrix formulation), where the symmetries of the structure have been taken into account.

The practical application of the iterative algorithm of Section 4 has been implemented in the same way for all the filter examples. First, the cascade connection of the generalized matrices representing each waveguide step, and their related two sets of asymptotic admittances (see Fig. 3), has been solved. Next, the generalized matrices representing the uniform waveguide sections have been added. Finally, all these basic building blocks are cascaded in order to obtain the overall Z matrix for the whole structure. In order to reduce the overall number of poles, the algorithm proposed in Section 4.2 has been applied after each cascade connection. In this example, the final number of poles related to the last cascade connection was equal to 60.

In Fig. 6, we successfully compare the set of S parameters obtained with our pole expansion technique (solid lines) with those provided by the well-known commercial software Ansoft HFSS (v.10.0) based on the Finite Elements Method (FEM). In order to evaluate the numerical efficiency related to the analysis technique proposed in this paper, we have also made use of a traditional approach based on frequency-by-frequency (point-to-point) calculations for solving the cascade connection of Z matrices (see for instance (Boria et al., 1997)). As it can be concluded from Fig. 6 (see results with stars), the same accurate response can be obtained with the point-to-point cascade connection technique. However, the CPU effort required by such traditional approach to compute the electrical response for 301 frequency values was equal to 0.54 s, whereas following the method proposed in this paper was reduced to only 0.23 s. If the original integral equation technique is used to analyze the planar waveguide steps, together with the point-to-point connection technique, the same accurate results from Fig. 6 can be recovered in 2.68 s, and 1490 s with HFSS (fast sweep).

Therefore, it can be concluded that our novel analysis technique is the most efficient one in terms of computational effort. Furthermore, we have verified that the CPU time required by our method remains rather stable with the required number of frequency points, thus making it very appropriate for dense simulations in the frequency domain. Finally, we have also included in Fig. 6 the results obtained when $k_0=0$ in (7) and (107). As it could be expected, such results converge more slowly than those provided by our analysis technique. The analysis by means of Y matrix formulation has been also performed, but in this case only with the point-to-point connection technique. In this case the total CPU time was 1.20 s with our new formulation, and 239 s following the classical Y matrix formulation.

The second example consists of a triple-mode filter proposed in (Lastoria et al., 1998), whose topology is shown in Fig. 7. The input and output sections of this filter are standard WR-75 waveguides, and the dimensions of the five inner waveguides are $a_1=12.2$ mm, $a_2=19.6$ mm, $a_3=19.6$ mm, $a_4=15.6$ mm and $a_5=5.0$ mm for the widths, $b_1=5.0$ mm, $b_2=15.6$ mm, $b_3=19.6$ mm, $b_4=19.6$ mm and $b_5=12.2$ mm for the heights, $l_1=5.3$ mm, $l_2=4.0$ mm, $l_3=8.6$ mm, $l_4=4.0$ mm and $l_5=5.3$ mm for the lengths. The input and output coupling windows are centered with regard to the central cavity.

The analysis (see Fig. 7) was performed with 150 basis functions and 800 terms in the series (Z matrix), 20 accessible modes and 100 poles in the last cascade connection. Our results (solid lines) are well compared with those provided by the commercial software HFSS (circles). The same accurate results (see stars in Fig. 7) can be obtained if the frequency-by-frequency (point-to-point) technique for cascading Z matrices is used. However, our novel analysis method provides such results in only 1.13 s for 301 frequency points, whereas the

CPU effort is raised to 2.93 s when using the point-to-point connection technique. Finally, the combination of the original integral equation technique with the cited point-to-point connection technique would provide the same accurate results in 29 s. Regarding HFSS, the CPU time was of 467 s (fast sweep).

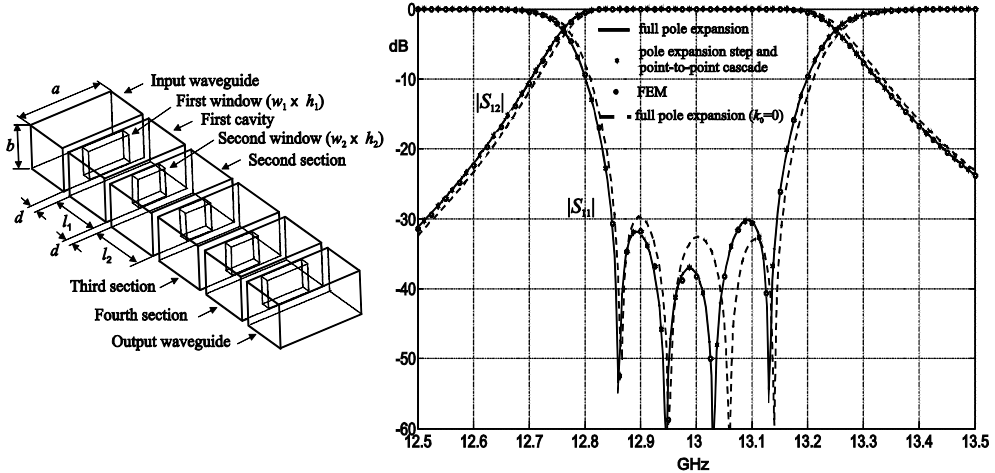


Fig. 6. Geometry and S parameters of a four pole filter in rectangular waveguide technology.

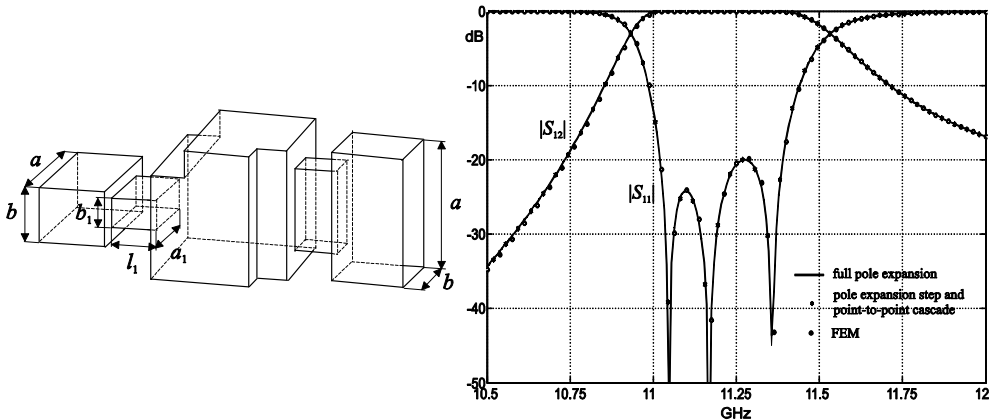


Fig. 7. Geometry and S parameters of a triple-mode filter in rectangular waveguide technology.

Next, we have studied the accuracy of the proposed method when used to predict the out-of-band response of the triple-mode filter just considered before. In Fig. 8, we compare the S parameters of such structure in a very wide frequency band (1000 points comprised between 8 and 18 GHz) when k_0 in (7) and (107) is chosen to be 0 and equal to the value of the in-band center frequency. As it can be observed, both results are less accurate at very high frequencies (far from the center frequency of the filter), and more accuracy is preserved when additional terms are considered in (107), i.e. when $k_0 \neq 0$. In order to recover more accurate results, even at very high frequencies, it has been needed to increase the number of

accessible modes to 25 and the total number of poles to 250, thus involving a CPU effort (1000 points) of 4.9 s.

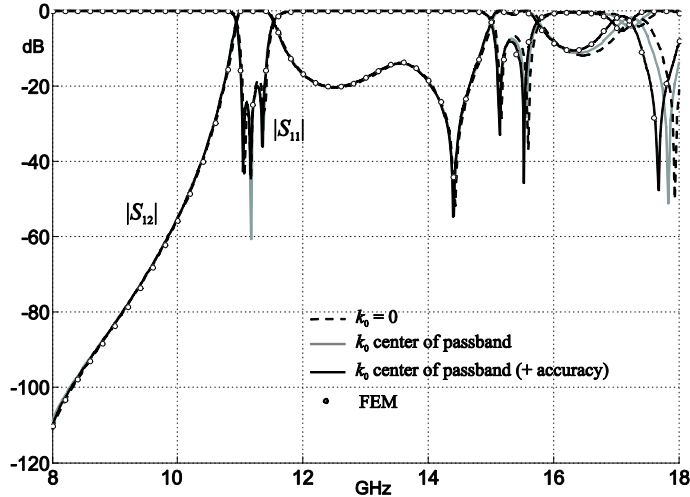


Fig. 8. Out-of-band response of the triple-mode cavity filter.

Now, we apply our novel technique to the analysis of H-plane filters. We have first solved the full-wave analysis of a symmetrical 8-pole inductive filter in WR-137 waveguide ($a=34.85$ mm, $b=15.85$ mm), whose topology is included in Fig. 9. The dimensions of the first half (symmetric structure) of coupling windows (with thickness always equal to 2.0 mm) are $w_1=22.04$ mm, $w_2=16.33$ mm, $w_3=14.59$ mm, $w_4=14.12$ mm and $w_5=14.03$ mm, and of the cavities are $l_1=24.34$ mm, $l_2=28.31$ mm, $l_3=29.38$ mm and $l_4=29.65$ mm. The analysis was performed taking into account the symmetries, where $N=4$ accessible modes were considered for each cascade connection. The waveguide steps were computed with 30 basis functions, and 150 terms in the series. The final number of poles for the whole filter was 60.

In Fig. 9, we successfully compare the S parameters provided by our pole expansion technique (solid lines) with the results obtained by the commercial software HFSS (circles) and by a traditional frequency-by-frequency cascade connection (stars). The CPU effort required by such traditional approach to compute the electrical response for 301 frequency values was equal to 0.26 s, whereas the method proposed in this paper only needed 0.09 s. Regarding the results obtained with HFSS, for an optimal convergence we employed a mesh with 67026 tetrahedra with a CPU time of 56 s for each frequency point.

The second example under consideration is an H-plane dual-mode filter topology proposed in (Guglielmi et al., 2001), whose geometry can be seen in Fig. 10. The input and output sections of this filter are WR-75 waveguides, and the widths and lengths of the three coupling windows are, respectively, $w_1=10.931$ mm, $w_2=10.782$ mm and $w_3=10.956$ mm, $d_1=3.0$ mm, $d_2=12.481$ mm and $d_3=3.0$ mm. The first and last coupling windows are centered, respectively, with regard to the input and output waveguide sections, whereas the offsets between the apertures and the upper walls of the cavities are $o_1=18.146$ mm, $o_2=18.295$ mm, $o_3=17.915$ mm and $o_4=18.101$ mm. As regards the two resonant cavities of this filter, their widths and lengths are, respectively, $a_1=30.077$ mm, $a_2=29.567$ mm, $l_1=28.306$ mm and $l_2=28.852$ mm.

The selected configuration for this filter was 5 accessible modes, 60 basis functions, 300 terms in the series and 25 poles after the last cascade connection. Fig. 10 shows our results (solid lines) with those provided by the commercial software HFSS (circles) and by a point-to-point connection technique (stars). Our novel analysis method provides accurate results in only 0.11 s for 301 frequency points, whereas the CPU effort is raised to 0.22 s when using the point-to-point connection technique. The simulation with HFSS was performed with 236994 tetrahedra due to the high sensitivity of this filter, and the CPU time was 279 s for each frequency point. Finally, the results obtained when $k_0=0$ in (33) and (107) are shown in Fig. 10. As it should be expected, the results computed with such approach converge more slowly than those obtained with our wideband analysis method.

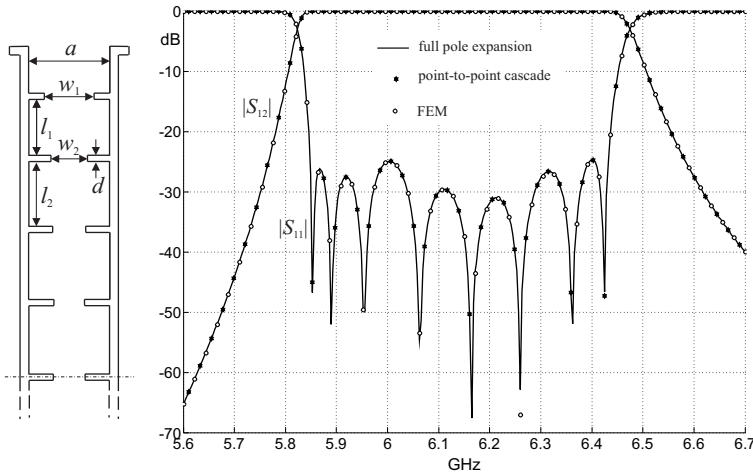


Fig. 9. Geometry and S parameters of a symmetrical 8-pole H-plane filter in rectangular waveguide technology.

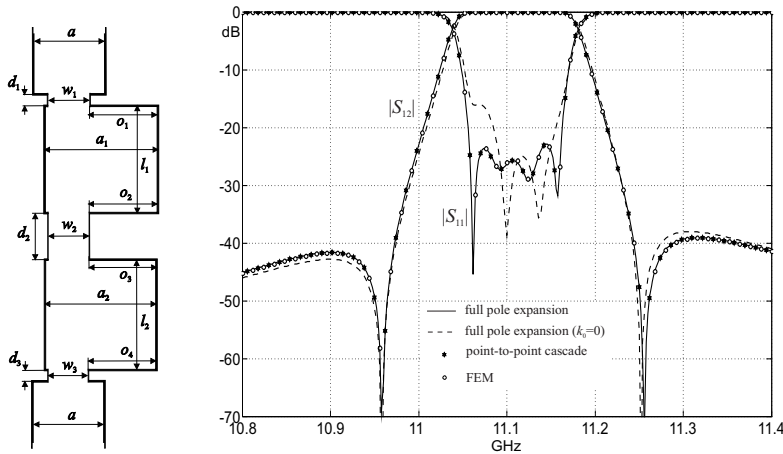


Fig. 10. Geometry and S parameters of an H-plane dual-mode filter in rectangular waveguide technology.

The proposed method has been also applied to predict the out-of-band response of the dual-mode filter just considered before. In Fig. 11, we compare the S parameters of such structure in a very wide frequency band (1000 points comprised between 8 and 18 GHz) when k_0 is chosen to be 0 and equal to the value of the in-band center frequency. As it can be observed, both results are slightly less accurate at very high frequencies (far from the center frequency of the filter), and more accuracy is preserved when additional terms are considered in (107), i.e. when $k_0 \neq 0$. In order to recover very accurate results in a very wide frequency band, it has been needed to increase the total number of poles to 75, thus involving a global CPU effort (1000 points) of 0.39 s.

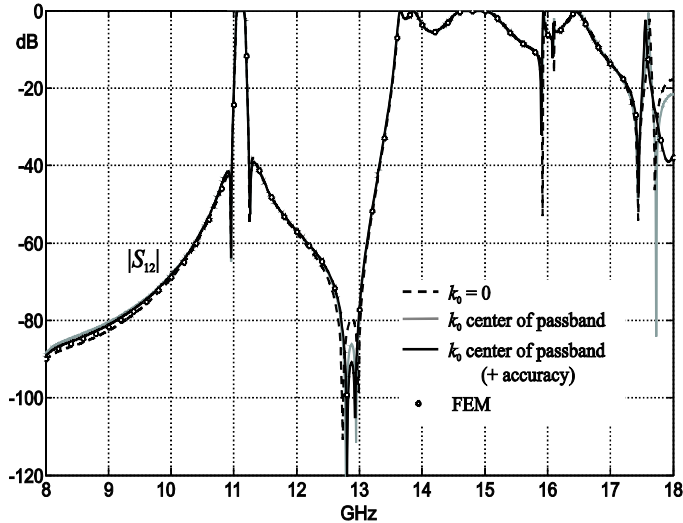


Fig. 11. Out-of-band response of the H-plane dual-mode filter.

7. Conclusions

In this chapter, we have presented a very efficient procedure to compute the wideband generalized impedance and admittance matrix representations of cascaded planar waveguide junctions, which allows to model a wide variety of real passive components. The proposed method provides the generalized matrices of waveguide steps and uniform waveguide sections in the form of pole expansions. Then, such matrices are combined following an iterative algorithm, which finally provides a wideband matrix representation of the complete structure. Proceeding in this way, the most expensive computations are performed outside the frequency loop, thus widely reducing the computational effort required for the analysis of complex geometries with a high frequency resolution. The accuracy and numerical efficiency of this new technique have been successfully validated through the full-wave analysis of several waveguide filters.

With regard to the analysis of single waveguide steps, the Z matrix representation offers a better computational efficiency than the Y matrix representation. However, our novel technique for the admittance case can even provide a better performance than the original integral equation formulated in terms of the Z matrix. The Y matrix representation is useful

when the devices under study include building blocks (i.e. arbitrarily shaped 3D cavities) whose analysis through the BI-RME method typically provides admittance matrices. In this way, a wideband cascade connection of Y matrices can be applied.

8. References

- Alessandri, F., G. Bartolucci, and R. Sorrentino (1988), Admittance matrix formulation of waveguide discontinuity problems: Computer-aided design of branch guide directional couplers, *IEEE Trans. Microwave Theory Tech.*, 36(2), 394-403.
- Alessandri, F., M. Mongiardo, and R. Sorrentino (1992), Computer-aided design of beam forming networks for modern satellite antennas, *IEEE Trans. Microwave Theory Tech.*, 40(6), 1117-1127.
- Alvarez-Melcón, A., G. Connor, and M. Guglielmi (1996), New simple procedure for the computation of the multimode admittance or impedance matrix of planar waveguide junctions, *IEEE Trans. Microwave Theory Tech.*, 44(3), 413-418.
- Arcioni, P., and G. Conciauro (1999), Combination of generalized admittance matrices in the form of pole expansions, *IEEE Trans. Microwave Theory Tech.*, 47(10), 1990-1996.
- Arcioni, P., M. Bressan, G. Conciauro, and L. Perregrini (1996), Wideband modeling of arbitrarily shaped E-plane waveguide components by the boundary integral-resonant mode expansion method, *IEEE Trans. Microwave Theory Tech.*, 44(11), 2083-2092.
- Arcioni, P., M. Bozzi, M. Bressan, G. Conciauro, and L. Perregrini (2002), Frequency/time-domain modeling of 3D waveguide structures by a BI-RME approach, *Int. Journal of Numer. Modeling: Electron. Networks, Devices and Fields*, 15(1), 3-21.
- Boria, V. E., and B. Gimeno (2007), Waveguide filters for satellites, *IEEE Microwave Magazine*, 8(5), 60-70.
- Boria, V. E., G. Gerini, and M. Guglielmi (1997), An efficient inversion technique for banded linear systems, in *IEEE MTT-S Int. Microw. Symp. Digest*, pp. 1567-1570, Denver.
- Conciauro, G., P. Arcioni, M. Bressan, and L. Perregrini (1996), Wideband modelling of arbitrarily shaped H-plane waveguide components by the boundary integral-resonant mode expansion method, *IEEE Trans. Microwave Theory Tech.*, 44(7), 1057-1066.
- Conciauro, G., M. Guglielmi, and R. Sorrentino (2000), *Advanced Modal Analysis - CAD Techniques for Waveguide Components and Filters*, Wiley, Chichester.
- Eleftheriades, G., A. Omar, L. Katehi, and G. Rebeiz (1994), Some important properties of waveguide junction generalized scattering matrices in the context of the mode matching technique, *IEEE Trans. Microwave Theory Tech.*, 42(10), 1896-1903.
- Gerini, G., M. Guglielmi, and G. Lastoria (1998), Efficient integral equation formulations for impedance or admittance representation of planar waveguide junction, in *IEEE MTT-S Int. Microw. Symp. Digest*, pp. 1747-1750, Baltimore.
- Guillot, P., P. Couffignal, H. Baudrand, and B. Theron, "Improvement in calculation of some surface integrals: Application to junction characterization in cavity filter design", *IEEE Trans. Microwave Theory Tech.*, vol. 41, no. 12, pp. 2156-2160, Dec. 1993.
- Gradstheyn, I. S., and I. M. Ryzhik (1980), *Table of Integrals, Series and Products*, Academic Press.
- Guglielmi, M., and A. Alvarez-Melcón (1993), Rigorous multimode equivalent network representation of capacitive discontinuities, *IEEE Trans. Microwave Theory Tech.*, 41(6/7), 1195-1206.

- Guglielmi, M., and G. Gheri (1994), Rigorous multimode network representation of capacitive steps, *IEEE Trans. Microwave Theory Tech.*, 42(4), 622-628.
- Guglielmi, M., and G. Gheri (1995), Multimode equivalent network representation of inductive and capacitive multiple posts, *IEE Proc. Microwave Antennas Propag.*, 142(1), 41-46.
- Guglielmi, M., and C. Newport (1990), Rigorous multimode equivalent network representation of inductive discontinuities, *IEEE Trans. Microwave Theory Tech.*, 38(11), 1651-1659.
- Guglielmi, M., G. Gheri, M. Calamia, and G. Pelosi (1994), Rigorous multimode network numerical representation of inductive step, *IEEE Trans. Microwave Theory Tech.*, 42(2), 317-326.
- Guglielmi, M., P. Jarry, E. Kerherve, O. Roquebrum, and D. Schmitt (2001), A new family of all-inductive dual-mode filters, *IEEE Trans. Microwave Theory Tech.*, 49(10), 1764-1769.
- Itoh, T. (1989), *Numerical Techniques for Microwave and Millimeter-Wave Passive Structures*, Wiley, New York.
- Lastoria, G., G. Gerini, M. Guglielmi, and F. Emma (1998), CAD of triple-mode cavities in rectangular waveguide, *IEEE Microwave and Guided Wave Letters*, 8(10), 339-341.
- Mansour, R., and R. MacPhie (1986), An improved transmission matrix formulation of cascaded discontinuities and its application to E-plane circuits, *IEEE Trans. Microwave Theory Tech.*, 34(12), 1490-1498.
- Mira, F., A. A. San Blas, V. E. Boria, B. Gimeno, M. Bressan, and L. Perregri (2006), Efficient pole-expansion of the generalized impedance matrix representation of planar waveguide junctions, in *IEEE MTT-S Int. Microw. Symp. Digest*, pp. 1033-1036, San Francisco.
- Safavi-Naini, R., and R. MacPhie (1981), On solving waveguide junction scattering problems by the conservation of complex power technique, *IEEE Trans. Microwave Theory Tech.*, 29(4), 337-343.
- Safavi-Naini, R., and R. MacPhie (1982), Scattering at rectangular-to-rectangular waveguide junctions, *IEEE Trans. Microwave Theory Tech.*, 30(11), 2060-2063.
- Sorrentino, R. (1989), *Numerical Methods for Passive Microwave and Millimeter-Wave Structures*, IEEE Press, New York.
- Spiegel, M. R. (1991), *Complex Variables*, Mc Graw-Hill.
- Uher, J., J. Bornemann, and U. Rosenberg (1993), *Waveguide Components for Antenna Feed Systems: Theory and CAD*, Artech-House, Norwood.
- Wexler, A. (1967), Solution of waveguide discontinuities by modal analysis, *IEEE Trans. Microwave Theory Tech.*, 15(9), 508-517.
- Zhang, F., *Matrix Theory*, Springer-Verlag, New York, 1999.

Study and Application of Microwave Active Circuits with Negative Group Delay

Blaise Ravelo, André Pérennec and Marc Le Roy
 UEB France, University of Brest,
 Lab-STICC, UMR CNRS 3192,
 France

1. Introduction

Since the early of 1970s, the interpretation of the negative group delay (NGD) phenomenon has attracted considerable attention by numerous scientists and physicists (Garrett & McGumber, 1970; Chu & Wong, 1982; Chiao et al., 1996; Mitchell & Chiao, 1997 and 1998; Wang et al., 2000). Several research papers devoted to the confirmation of its existence, in particular in electronic and microwave domains, have been published (Lucyszyn et al., 1993; Broomfield & Everard, 2000; Eleftheriades et al., 2003; Siddiqui et al., 2005; Munday & Henderson, 2004; Nakanishi et al., 2002; Kitano et al., 2003; Ravelo et al., 2007a and 2008a). In these papers, both theoretical and experimental verifications were performed. The NGD demonstrators that exhibit NGD or negative group velocity were based either on passive resonant circuits (Lucyszyn et al., 1993; Broomfield & Everard, 2000; Eleftheriades et al., 2003; Siddiqui et al., 2005) or on active ones (Chiao et al., 1996; Munday & Henderson, 2004; Nakanishi et al., 2002; Kitano et al., 2003). In practice, it was found that the investigated NGD passive circuits proved to be systematically accompanied with losses sometimes greater than 10 dB. While the active ones which use essentially classical operational amplifiers in feedback with R, L and C passive network were limited at only some MHz. Through experiments with these electronic active circuits, it was pointed out (Mitchell & Chiao, 1997 and 1998; Eleftheriades et al., 2003; Kitano et al., 2003) that the apparition of this counterintuitive phenomenon is not at odds with the causality principle. These limitations, i.e. losses and/or restriction on the frequency range drove us to develop the new NGD cell presented in Fig. 1 (Ravelo, Pérennec and Le Roy, 2007a, 2007b, 2007c, 2008a and 2008b).

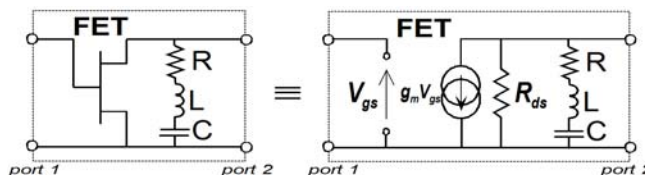


Fig. 1. NGD active cell and its low-frequency model; g_m : transconductance and R_{ds} : drain-source resistor.

This NGD active cell is composed of a field effect transistor (FET) terminated with a shunt RLC series network. We remark that this cell corresponds typically to the topology of a classical resistive amplifier, but here, focus is only on the generation of the NGD function together with gain. In this way, we recently demonstrated (Ravelo et al., 2007a, 2007b) that the group delay of this NGD cell is always negative at its resonance frequency, $\omega_0 = 1/\sqrt{LC}$. Furthermore, as FETs operating in different frequency ranges are available, the cell is potentially able to operate at microwave wavelengths and over broad bandwidths (Ravelo et al., 2007b). The *a priori* limitations rely on the operating frequency band of the lumped RLC components. By definition, the group delay is given by the opposite of the transmission phase, $\varphi(\omega) = \angle S_{21}(j\omega)$ derivative with respect to the angular frequency, ω :

$$\tau(\omega) = \frac{-\partial \angle S_{21}(j\omega)}{\partial \omega}. \quad (1)$$

Analytical demonstrations and frequency measurements had previously allowed us to state that, in addition to NGD, this active cell can generate amplification with a good access matching. The present chapter is organized in two main sections. The fundamental theory permitting the synthesis of this NGD cell is developed in details in Section 2. Then, through a time domain study based on a Gaussian wave pulse response, the physical meaning of this phenomenon at microwave wavelengths is provided (Ravelo, 2008). From a second effect caused by the gain shape of the NGD active cell shown in Fig. 1, an easy method to realize pulse compression (PC) is also developed and examined. To illustrate the relevance and highlight the benefits of this innovative NGD topology, Section 3 deals with a new concept of frequency-independent active phase shifter (PS) used in recent applications (Ravelo et al., 2008b). This NGD PS is mainly composed of a positive group delay device set in cascade with a negative one of similar absolute value. To validate this innovative PS principle, a hybrid planar prototype was fabricated and tested. The measurements proved to well-correlate to the simulations and showed a phase flatness less than $\pm 10^\circ$ over a relative frequency band of 100%. Further to the use of two NGD cells, the results of the simulations run with a second PS showed an improvement of the relative constant-phase bandwidth up to about 125%. These innovative PSs were also used to design and investigate a broadband active balun (Ravelo et al., 2007c). Finally, applications of this microwave NGD active device in telecommunication equipments are proposed, and further improvements are discussed.

2. Theoretical and experimental study of the proposed NGD active topology

This Section deals with the analytical and experimental studies of the NGD active cell schematized in Fig. 1. After a brief recall of the S-parameters analysis, the synthesis relations appropriated to this cell are given in Subsection 2.1. Then, Subsection 2.2 is focused on the time-domain response of this cell in the case-study of a Gaussian input-wave pulse; the basic theory evidencing the associated pulse compression phenomenon is proposed. Subsection 2.3 is devoted to the description of experimental results obtained in both frequency- and time-domains; explanations about the process in use to design the NGD active device under test are also provided.

2.1 S-parameters analysis and synthesis relations

As established in Ravelo et al., 2007a and 2007b, by using the low-frequency classical model of a FET, the scattering matrix of the ideal NGD cell presented in Fig. 1 is expressed as:

$$S_{11}(j\omega) = 1, \quad (2)$$

$$S_{12}(j\omega) = 0, \quad (3)$$

$$S_{21}(j\omega) = \frac{-2ZZ_0g_mR_{ds}}{[Z_0R_{ds} + Z(Z_0 + R_{ds})]}, \quad (4)$$

$$S_{22}(j\omega) = \frac{ZR_{ds} - Z_0(Z + R_{ds})}{Z_0R_{ds} + Z(Z_0 + R_{ds})}, \quad (5)$$

where

$$Z = R + j[L\omega - 1/(C\omega)]. \quad (6)$$

Z_0 is the port reference impedance, usually 50Ω . At the resonance angular frequency, $\omega = \omega_0 = 1/\sqrt{LC}$, one gets $Z = R$, and then equations (4) and (5) become:

$$|S_{21}(\omega_0)| = \frac{2RZ_0g_mR_{ds}}{[Z_0R_{ds} + R(Z_0 + R_{ds})]}, \quad (7)$$

$$|S_{22}(\omega_0)| = \frac{|RR_{ds} - Z_0(R + R_{ds})|}{|Z_0R_{ds} + R(Z_0 + R_{ds})|}. \quad (8)$$

At this frequency, it was demonstrated (Ravelo et al., 2007a and 2007b) that the group delay expressed in equation (1) is always negative:

$$\tau(\omega_0) = \frac{-2LZ_0R_{ds}}{R[RR_{ds} + Z_0(R + R_{ds})]}. \quad (9)$$

The synthesis relations relative to the NGD cell are extracted from equations (8) and (9). As shown hereafter, they depend on the given gain magnitude and group delay (S_{21} and τ_0 , respectively) at the resonance, ω_0 :

$$R = \frac{S_{21}Z_0R_{ds}}{[2g_mZ_0R_{ds} - S_{21}(Z_0 + R_{ds})]}, \quad (10)$$

$$L = \frac{-\tau_0R[RR_{ds} + Z_0(R + R_{ds})]}{(2Z_0R_{ds})}. \quad (11)$$

Then, the C synthesis relation is deduced from the expression of the resonance angular frequency:

$$C = \frac{1}{(L\omega_0^2)}. \quad (12)$$

As previously mentioned, in addition to this NGD property, this circuit allows compression of the width of a modulated Gaussian pulse centred at ω_0 . The compression theory will be developed in the next section.

2.2 Study of the Gaussian-pulse response: evidence of time domain advance and pulse compression (PC)

Fig. 2 illustrates the configuration under consideration in the time-domain study. It consists of a black box of the NGD circuit S-parameters excited by a sine carrier, $f_0 = \omega_0/(2\pi)$, modulated by a Gaussian pulse. In order to evidence the principle of this NGD phenomenon, let us consider the input signal expressed as:

$$x(t) = e^{-\frac{(t-t_0)^2}{2\Delta T_x^2}} \times e^{j\omega_0 t}. \quad (13)$$

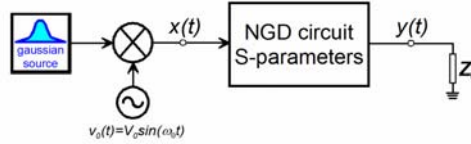


Fig. 2. Block diagram of the understudied configuration considered in time-domain ($Z_0 = 50 \Omega$).

ΔT_x is the standard deviation (half width at $1/e$ of the maximal input value) and t_0 is the central time of the Gaussian pulse. It ensues that the Fourier transform of such a signal is defined as:

$$X(j\omega) = \Delta T_x \sqrt{2\pi} e^{-0.5\Delta T_x^2(\omega-\omega_0)^2 - j(\omega-\omega_0)t_0}. \quad (14)$$

According to the signal processing theory, this function is also Gaussian, and its angular frequency standard deviation is:

$$\Delta\omega_x = 1/\Delta T_x. \quad (15)$$

It means that the pulse compression in time domain involves a pulse expansion in frequency domain and vice versa. Then, the standard deviation of the Gaussian output is compared, at first theoretically, with the input one through the transmittance, $H(j\omega)$. To highlight this analytical approach, let us consider the black box system shown in Fig. 2. As its transfer function, $H(j\omega)$, is excited by $X(j\omega)$, the output Fourier transform is:

$$Y(j\omega) = H(j\omega)X(j\omega) = e^{\ln|H(j\omega)| + j\text{Arg}[H(j\omega)]} X(j\omega). \quad (16)$$

A simplified and approximated analytical study is proposed hereafter in order to analyze the behaviour of this output. First, we consider the Taylor series expansion of the magnitude, $\ln|H(j\omega)|$, around the resonant angular frequency, ω_0 :

$$\ln|H_a(j\omega)| \approx \ln|H(\omega_0)| + \frac{H'(\omega_0)}{H(\omega_0)}(\omega - \omega_0) + \frac{H''(\omega_0)}{2H(\omega_0)}(\omega - \omega_0)^2 + O[(\omega - \omega_0)^3], \quad (17)$$

where $H'(\omega_0)$ and $H''(\omega_0)$ are respectively the first- and second-order derivatives of $|H(j\omega)|$ with respect to ω . Then, application of the same procedure to the transmission phase, $\varphi(\omega) = \angle S_{21}(j\omega)$ leads to the following approximated expression:

$$\begin{aligned} \varphi_a(\omega) &\approx \varphi(\omega_0) + \varphi'(\omega_0)(\omega - \omega_0) + 0.5\varphi''(\omega_0)(\omega - \omega_0)^2 + O[(\omega - \omega_0)^3] \\ &= \varphi(\omega_0) - \tau(\omega_0)(\omega - \omega_0) - 0.5\tau'(\omega_0)(\omega - \omega_0)^2 + O[(\omega - \omega_0)^3] \end{aligned} \quad (18)$$

At resonance, $\varphi(\omega_0) = 0$, and in the vicinity of ω_0 , one gets $\tau'(\omega_0) \approx 0$, this implies that:

$$\varphi_a(\omega) \approx -\tau(\omega_0)(\omega - \omega_0) + O[(\omega - \omega_0)^3]. \quad (19)$$

One should note that the terms of higher order can be ignored if the input signal bandwidth is small enough compared to the NGD bandwidth. As this phase response is relatively linear, the $Y(j\omega)$ -magnitude is unaffected. So, the output modulus can be written as:

$$|Y(j\omega)| \approx |H(\omega_0)| e^{\frac{H'(\omega_0)}{H(\omega_0)}(\omega - \omega_0) + \frac{H''(\omega_0)}{2H(\omega_0)}(\omega - \omega_0)^2} \times |X(j\omega)|. \quad (20)$$

By substituting for $X(j\omega)$ from equation (14) in equation (20), one gets:

$$|Y(j\omega)| \approx |H(\omega_0)| \Delta T_x \sqrt{2\pi} e^{\frac{H'(\omega_0)}{H(\omega_0)}(\omega - \omega_0) - \frac{1}{2} \left[\Delta T_x^2 - \frac{H''(\omega_0)}{H(\omega_0)} \right] (\omega - \omega_0)^2}. \quad (21)$$

The magnitude of the insertion gain is defined as:

$$|H(j\omega)| = \frac{2Z_0 g_m R_{ds} \sqrt{R^2 + [(L\omega - 1/(C\omega))]^2}}{\sqrt{[Z_0 R_{ds} + R(Z_0 + R_{ds})]^2 + (Z_0 + R_{ds})^2 [(L\omega - 1/(C\omega))]^2}}. \quad (22)$$

At ω_0 , this expression becomes:

$$|H(\omega_0)| = \frac{2g_m R_{ds} Z_0 R}{R_{ds} R + Z_0 (R + R_{ds})}, \quad (23)$$

and the first- and second-order derivatives are expressed as follows:

$$H'(\omega_0) = \left. \frac{\partial |H(j\omega)|}{\partial \omega} \right|_{\omega=\omega_0} = 0, \quad (24)$$

$$|H(\omega_0)|'' = \left. \frac{\partial^2 |H(j\omega)|}{\partial \omega^2} \right|_{\omega=\omega_0} = \frac{8g_m R_{ds}^2 Z_0^2 L^2 [R_{ds} Z_0 + 2R(Z_0 + R_{ds})]}{R [R_{ds} R + Z_0 (R + R_{ds})]^3} > 0. \quad (25)$$

It ensues that the output amplitude of equation (21) can be simplified as follows:

$$|Y(j\omega)| \approx |H(\omega_0)| \Delta T_x \sqrt{2\pi} e^{-0.5[\Delta T_x^2 - H''(\omega_0)/H(\omega_0)](\omega - \omega_0)^2}. \quad (26)$$

In fact, thanks to the second-order expansion expressed in equation (26), the output Fourier transform also behaves as a Gaussian pulse:

$$|Y(j\omega)| \approx Y_{\max} e^{-(\omega - \omega_0)^2 / (2\Delta\omega_y^2)}, \quad (27)$$

of amplitude:

$$Y_{\max} = \frac{2g_m R_{ds} Z_0 R}{R_{ds} R + Z_0 (R + R_{ds})} \Delta T_x \sqrt{2\pi}. \quad (28)$$

and with an angular frequency standard deviation such as:

$$\Delta\omega_y = \frac{1}{\sqrt{\Delta T_x^2 - H''(\omega_0)/H(\omega_0)}} = \frac{\Delta\omega_x}{\sqrt{1 - H''(\omega_0)/[H(\omega_0)\Delta T_x^2]}}. \quad (29)$$

Furthermore, the pulse width is expanded in the frequency domain ($\Delta\omega_x > \Delta\omega_y$). In the time domain, the approximated output signal inferred from the inverse Fourier transform of equation (26) is written as:

$$y(t) = \frac{|H(\omega_0)| \Delta T_x}{\sqrt{\Delta T_x^2 - H''(\omega_0)/H(\omega_0)}} e^{-\frac{0.5[t-t_0 - \tau(\omega_0)]^2}{\Delta T_x^2 - H''(\omega_0)/H(\omega_0)}} \times e^{j\omega_0 t}. \quad (31)$$

It can be seen that this output behaves as a modulated Gaussian that exhibits a time advance whenever $\tau(\omega_0) < 0$; moreover, the standard deviation is expressed as:

$$\Delta T_y = \sqrt{\Delta T_x^2 - \frac{4L^2 R_{ds} Z_0 [R_{ds} Z_0 + 2R(Z_0 + R_{ds})]}{R^2 [R_{ds} R + Z_0 (R + R_{ds})]^2}}. \quad (32)$$

This is obviously an approximated expression because it comes from a first-order limited expansion of equation (17). Due to the intrinsic behaviour of linear devices, the higher order terms ensure that ΔT_y cannot tend to zero.

Hence, in practice, equation (32) corresponds to a compression of the pulse width in the time domain. Furthermore, compared to the input pulse, $x(t)$, the output one, $y(t)$ is amplified by the quantity:

$$\alpha = |H(\omega_0)| \cdot \Delta T_x / \Delta T_y . \quad (33)$$

As reported by Cao and co-workers (2003), if ΔT_x is getting closer to $\Delta T_{x\min}$, it goes along with a significant PC.

- *Remarks on the PC phenomenon:* Various PC techniques have been developed at optical- and microwave-wavelengths in order to convert a long-duration pulse into a shorter one. One should note that the principles and methods proposed in the literature depend on whether the applications under study are dedicated to low or high power (Gaponov-Grekhov & Granatstein, 1994; Thumm & Kasparek, 2002). For example, PC was investigated in ultra-fast laser systems (Li et al., 2005), then its use has become more and more common thanks to the development of chirped pulse amplification (Arbore, 1997; Wang & Yao; 2008a and 2008b). The next step was the compression of a pulse in a Mach-Zehnder-interferometer geometry achieved by passing a broadband ultra-short pulse through two chirped fibre Bragg gratings with different chirp rates (Zeitouny et al., 2005). In radar and communication systems, PC has been used to enhance the range resolution. In order to elevate microwave power, investigations by several authors have been focused on a microwave pulse compressor based on a passive resonant cavity (Burt et al., 2005; Baum, 2006). The prerequisites are that the compressor cavity must present a high Q-factor; in addition, the constituting waveguides should operate with an oversized mode of the field in order to increase the power strength, and the power microwave sources should be narrow-band. This set of requirements is met by quasi-optical cavities, particularly by the ring-shaped multi-mirror ones, where the energy is sent to the cavity via corrugated mirror (Kuzikov et al., 2004). But, as in practice the implementation of such a technique is usually very complex and at high cost, a new and much simpler PC technique based on the use of NGD structure was recently proposed (Cao et al., 2003) by using a classical operational amplifier. Though application of this technique to rather low power devices remains possible, one should be aware that it is intrinsically restricted to low frequencies.

The PC method proposed here is close to this latter study, but it is able to operate in the microwave frequency range.

All of these predictions from theory have to be experimentally verified; but prior to the discussion of the corresponding experimental results, it is worth describing the design process of the NGD devices under study.

2.3 Experimental study

(a) Design process:

The flow chart displayed in Fig. 3 lists the sequence of actions to be followed to design NGD active circuits. One should note that the proposed process is well-suited to the use of classical circuit simulator/designer software such as, for example, ADS software from Agilent™.

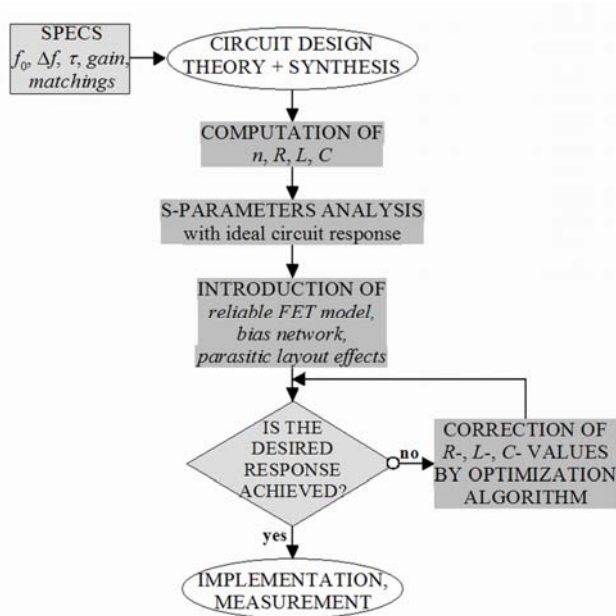


Fig. 3. Flow chart of the NGD-device design process (n is the number of NGD cells).

The technique used to design these devices is similar to the one developed in the case of classical microwave devices (filter, amplifier, coupler ...). During the synthesis of the circuit under study, focus is on the NGD level and the gain value at the centre frequency of the operating band. If the FET characteristics, g_m and R_{ds} , are known, the synthesis relations (10), (11) and (12) introduced in section 2.1 can be used to calculate the values of the RLC resonant-network components included in the NGD active cell. For a more realistic approach, it is worth taking into account a reliable (complete linear or non-linear) model of the employed FET including bias network, the effects of distributed interconnect lines and the actual manufacturing details. The combined use of a circuit simulator with an electromagnetic simulation tool such as Momentum from $ADST^M$ provides more accurate responses. To get acceptable final responses, slight optimizations may be needed prior to implementation and measurements.

(b) Implementation of the proposed prototype: To check for the validity of the aforementioned theoretical predictions on NGD and PC, a proof-of-principle device consisting of an NGD active circuit with three resonant cells (Figs. 4) was designed, fabricated and tested. One should note that the measurement instruments available within our laboratory to evidence both the NGD and PC phenomena had to be considered prior to the selection of the operating band.

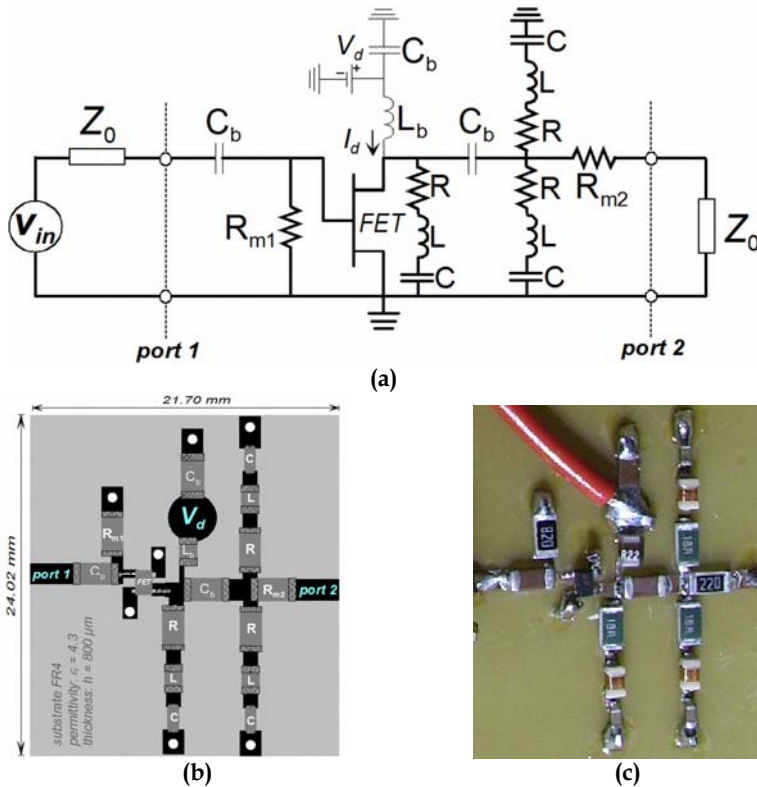


Fig. 4. Fabricated NGD active device: (a) Schematic (bias circuit in thin line), FET (ATF-34143 biased at $V_d = 2\text{V}$, $I_d = 100\text{ mA}$), $R_{m1} = 82\ \Omega$, $R_{m2} = 22\ \Omega$, $R = 18\ \Omega$, $L = 51\ \text{nH}$, $C = 0.5\ \text{pF}$, $C_b = 1\ \text{nF}$, $L_b = 220\ \text{nH}$; (b) layout; (c) photograph.

As pictured in Figs. 4(b) and 4(c), it is a hybrid planar circuit fabricated with surface mount chip components and printed on an FR4 substrate with relative permittivity, $\epsilon_r = 4.3$ and thickness, $h = 800\ \mu\text{m}$. The active element is a PHEMT FET (ATF-34143) mounted in plastic package from *Avago Technology*TM. The implemented circuit is biased through an RF-choke inductance (biasing point: $V_d = 2\text{V}$, $I_d = 100\ \text{mA}$) and cascaded with three RLC series resonant cells in shunt. These three cells were used in order to evidence, with the components at our disposal, both the compression and the NGD effects. The transconductance and the drain-source resistance, $g_m = 226\ \text{mS}$ and $R_{ds} = 27\ \Omega$, respectively, were extracted from the S-parameters of the FET non linear model provided by the manufacturer and further used to synthesize the NGD-cell component values. Then, these values were optimized through electromagnetic and schematic co-simulations carried out with *Momentum* software from *ADSTM*.

(c) *Results of frequency-domain measurements:* Figs 5(a) and 5(b) describe the results of the frequency measurements made with an *EB364A Agilent Vector Network Analyzer*.

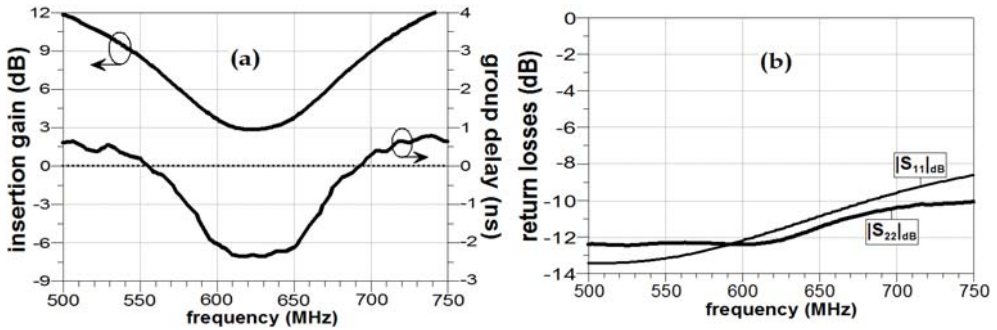


Fig. 5. Measured results: (a) insertion gain/group delay, and (b) return losses.

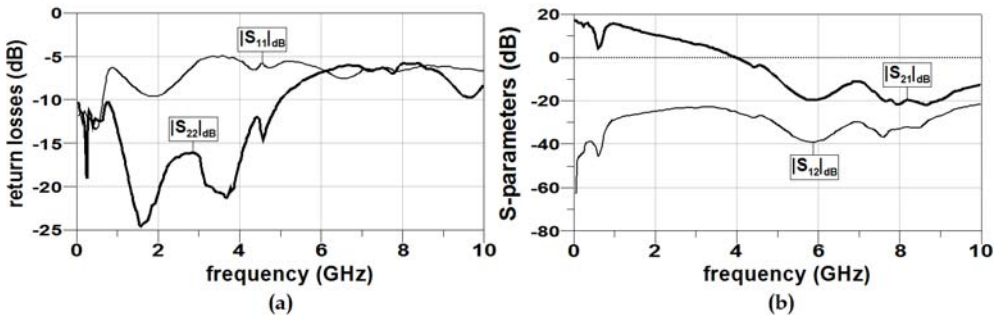


Fig. 6. Wide band frequency responses of the tested NGD device: (a) return losses and (b) S_{21} -parameter and isolation loss.

Fig. 5(a) shows that, in a frequency band of about 135 MHz in width and centred around 622 MHz, the gain and the group delay are better than 2 dB and lower than -2 ns, respectively. In the same frequency band, Fig. 5(b) indicates that the matching level for this NGD device is better than -9 dB. Furthermore, the necessary, but not sufficient, condition for stability is also confirmed by measurements over a wider band (Fig. 6(a)) with return losses $|S_{11}|_{dB}$ and $|S_{22}|_{dB}$ better than 5 dB. In addition, Fig. 6(b) shows that the gain, $|S_{21}|_{dB}$, and isolation loss, $|S_{12}|_{dB}$, exhibited by this NGD device are, respectively, lower than 18 dB and -20 dB over the range from DC to 10 GHz.

At this stage, for a more comprehensive study of NGD-induced effects, let us continue with the time-domain experimental characterization.

(d) Time-domain measurements: In order to allow operation in the specified frequency band and to meet the conditions stated in section 2.2, time-domain measurements were made for a Gaussian wave pulse (8.4 ns as standard deviation) modulating a 622 MHz carrier. This signal was provided by a vector signal generator *Rhode & Schwarz SMJ 100A* and measured with a 2 Gs/s *LeCroy* Digital Oscilloscope.

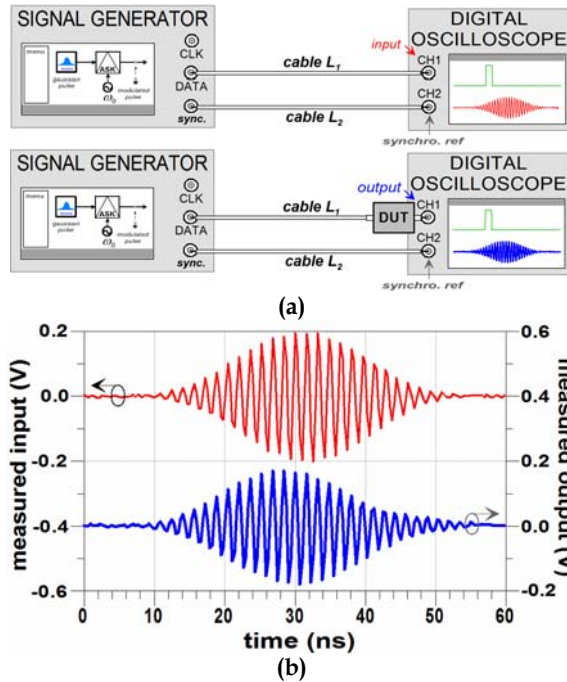


Fig. 7(a). Experimental setup diagram and (b) response by the circuit shown in Fig. 4 in the case of a 622-MHz carrier modulated by a Gaussian input (about 8.4 ns as standard deviation).

Figs. 7 show that the measured output behaves as a Gaussian pulse and is slightly compressed because of the gain shape around the resonance as previously demonstrated. As explained in Fig. 7(a), to avoid cable and connector influences, the first signal to be recorded was the input one. Then it was replaced by the output one (connected to CH1). In both cases, the synchronization reference signal was the same (connected to CH2). Then, the recorded input modulated pulse and NGD DUT output (see thin red line and thick blue one, respectively, in Fig. 7(b)) were resynchronized from the same reference signal (CH2 channel). It is interesting to note that the input-pulse width was the shortest one that the signal generator in use could generate. These results indicate that the pulse width needs to be smaller to better evidence the effects by NGD- and compression. For that reason, we propose the following simulations.

(e) Time domain simulations: These transient simulations were run on using the S-parameters issued from measurements. The input pulse was Gaussian and such that its standard deviation was equal to $\Delta T_x \approx 4.0$ ns; it modulated a 622 MHz sine carrier, corresponding to the centre frequency of the NGD circuit response (see Figs. 2 and 5(a)). In the frequency domain, it gives a Gaussian pulse (dotted line in Fig. 8(a)) with $\Delta f_x \approx 40$ MHz as frequency standard deviation. As shown in Fig. 8(a), the resulting output spectrum (in blue solid line) can be approximated to a Gaussian pulse with a frequency standard deviation of about $\Delta f_y \approx 50$ MHz (or $\Delta T_x \approx 3.3$ ns). In frequency domain, the output pulse

width is thus expanded of about 125% and amplified of about 3.86 dB with respect to the input pulse one.

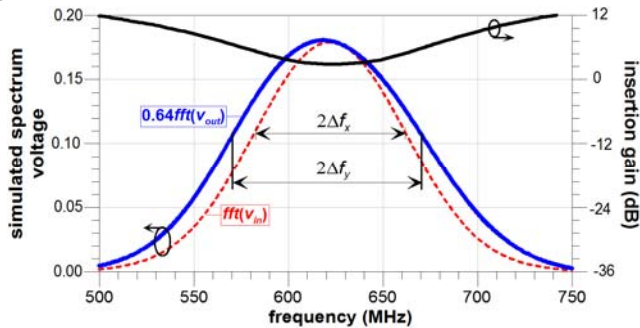


Fig. 8(a). Simulated spectra of the input and output voltage (Fourier transforms) issued from simulations run on using the measured S-parameters.

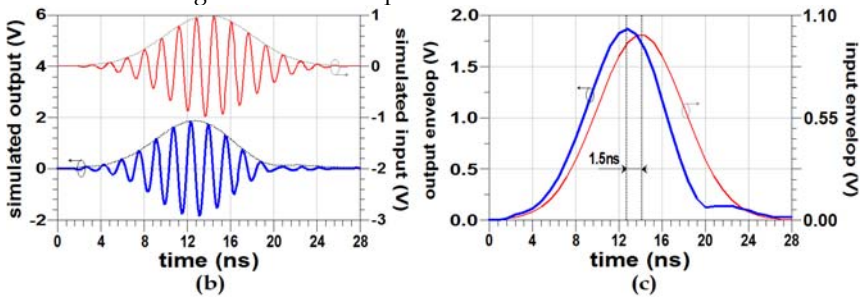


Fig. 8. Simulated results run on using the measured S-parameters: (b) transient- and (c) envelop-voltages.

Figs. 8(b) and 8(c) show that the PC is about 80% in time-domain; moreover, a comparison of the maxima of the input and output pulse envelopes (Fig. 8c) demonstrates that the time advance induced by the NGD effect is about 1.5 ns. As reported in (Ravelo et al., 2008a) further to the implementation of a two-stage NGD circuit, the NGD value was higher over a wide bandwidth centred at about 1 GHz. This means that the pulse-peak advance and PC values can be both improved when several NGD stages are used.

As experiments led, as expected, to the simultaneous generation of both NGD and gain over a rather wide bandwidth at microwave frequencies, it is now worth focusing on the design of microwave devices through use of these properties.

3. Design of frequency-independent phase shifter (PS) and -balun based on NGD active circuits

We recently reported on the use of such NGD active circuits in the design of a frequency-independent phase shifter (PS) (Ravelo, 2008). Let us, at first, recall the underlying innovative and simple fundamental principle. Then, a preliminary study on the influence of RLC-element variations on the PS-responses will be detailed and discussed. The design of a proof-of-concept PS through use of a single stage of NGD active cell will be described prior

to the analysis and discussion of the experimental results. Then, simulations of a two-stage NGD PS will be reported to illustrate both the possibility of achieving broadband of constant phase and the relative insensitivity of the response versus the component tolerances. The last part will deal with the design and simulations of a broadband active balun based on the use of these NGD PSs.

3.1 Principle of the proposed frequency-independent PS

Figs. 9(a) and 9(b) illustrate the fundamental principle of this NGD PS. As shown in Fig. 9(a), the block diagram of the NGD PS under study is composed of two devices set in cascade. The former block, e.g. a transmission line (TL), exhibits a constant positive group delay (PGD) and the latter has of course, a negative one (NGD) of equal magnitude in the desired operating frequency band (see Figs 9(b)).

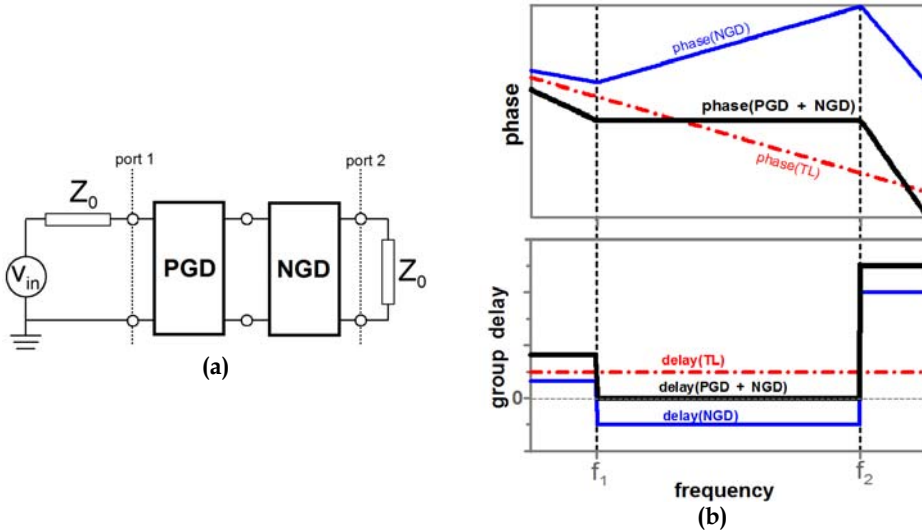


Fig. 9(a). Architecture of the proposed NGD PS and (b) ideal behaviour of the phase and group delay responses (Z_0 : reference impedance).

In the case of a perfect matching between the PGD- and NGD-blocks and on the condition that the phase slopes of these PGD- and NGD-blocks are alike in absolute value, but of unlike signs, the phase response of the whole circuit will be constant as depicted in Fig. 9(a). It implies that the corresponding group delay, $\tau(\omega) = -\partial\phi(\omega)/\partial\omega$ is mathematically equal to zero. When denoting by τ_p and τ_n , the group delays of the considered PGD- and NGD-blocks, respectively, the analytical expressions of their phase responses are:

$$\Phi_p(f) = -2\pi\tau_p(f - f_1) + \Phi_p(f_1), \quad (34)$$

$$\Phi_n(f) = -2\pi\tau_n(f - f_1) + \Phi_n(f_1), \quad (35)$$

As previously argued, in the ideal case of a perfect impedance matching, the total phase response, Φ_t is merely the sum of Φ_p and Φ_n . This implies the total phase response:

$$\Phi_t(f) = -2\pi(\tau_n + \tau_p)(f - f_1) + [\Phi_p(f_1) + \Phi_n(f_1)]. \quad (36)$$

Since the operating principle implies that the group delay absolute values are equal ($\tau_p = -\tau_n$), this quantity can be simplified as:

$$\Phi_t(f) = \Phi_p(f_1) + \Phi_n(f_1). \quad (37)$$

The synthesis relations of the proposed PS were previously detailed in Ravelo et al., 2008b. To illustrate and validate the proposed principle, the following section will deal with the design of a proof-of-concept PS and analysis of simulation- and measurement-results.

3.2 Designs, simulations and experimental results of frequency independent PSs by using NGD active circuits

A PS prototype with one NGD cell (Fig. 10) was designed on using the NGD cell synthesis relations established in section 2.1 in order to investigate the influence of the RLC component values on the magnitude- and phase-responses of S_{21} -parameter. Then, another one-stage NGD PS prototype was fabricated to validate the principle of the PS under study and to assess its performances through measurements. In order to improve the frequency bandwidth of constant phase, a two-stage NGD device was designed through simulations and subjected to a Monte-Carlo sensitivity analysis.

(a) Study of RLC-element variations: In this paragraph, the aim is to gain more insight into the evolution of the S_{21} -magnitude and -phase behaviours versus the component values. This preliminary sensitivity analysis may serve as an initial study for the design of a reconfigurable PS.

The circuit under study is depicted in Fig. 10, the FET was modelled by its non-linear model; moreover, the biasing network and the interconnect lines were both taken into account in the simulations. As preliminary remark, due to the non-reciprocity of the FET, S_{11} is unaffected by variations of any element of the RLC-network. On the other hand, a significant change of the R -value can induce a variation of the S_{22} -output return loss.

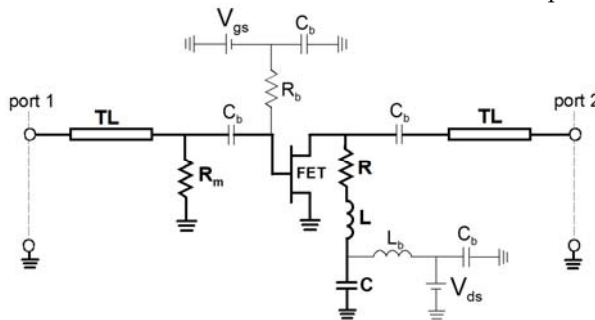


Fig. 10. Detailed schematic of the simulated NGD PS (biasing network in thin line): $R_m = 51 \Omega$, $C_b = 22 \text{ nF}$, $L_b = 390 \text{ nH}$, $R_b = 1 \text{ k}\Omega$, FET/EC-2612 ($V_{gs} = -0.1 \text{ V}$, $V_{ds} = 3 \text{ V}$, $I_{ds} = 30 \text{ mA}$) and TL ($w = 952 \mu\text{m}$, $d = 3.7 \text{ mm}$) printed on an FR4 substrate with relative permittivity, $\epsilon_r = 4.3$, and thickness, $h = 508 \mu\text{m}$.

- *Effects of R variations:* Figs. 11(a) and 11(b) show that the gain and flatness are both affected by variations on R . Increase of R -value leads to a simultaneous enhancement of the gain value and flatness. Then, the phase slope is affected, but, logically, with no change on the centre frequency of the PS.

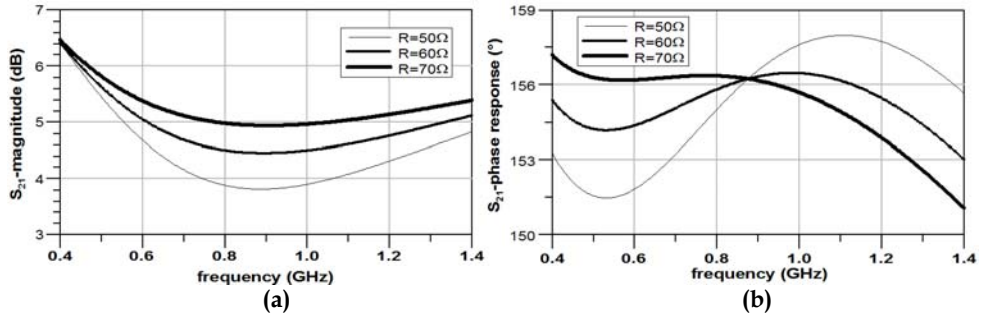


Fig. 11. Simulations of the circuit presented in Fig. 10: influence of R -variations on the gain (a), and on the phase (b) when $L = 6.2$ nH and $C = 5$ pF.

- *Effects of L variations:* Figs. 12 highlight a shift of the NGD cell resonance frequency ($\omega_0 = 1/\sqrt{LC}$) induced by L -variation as well as the shift of the PS centre frequency. In fact, according to equation (9), the modification of the self value affects linearly the group delay, and thus the phase form.

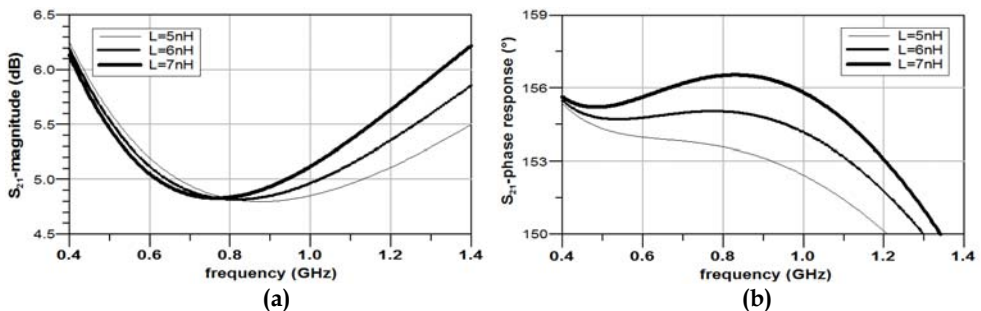


Fig. 12. Simulations of the circuit presented in Fig. 10: influence of L -variations on the gain (a) and the phase (b) when $R = 68 \Omega$ and $C = 5$ pF.

- *Effects of C variations:* Contrarily to the two previous cases, Figs. 13 show that the form of the frequency responses (gain and phase) are rather unaffected by C -variation. On the other hand, it has a significant impact on both the centre frequency and the constant phase value.

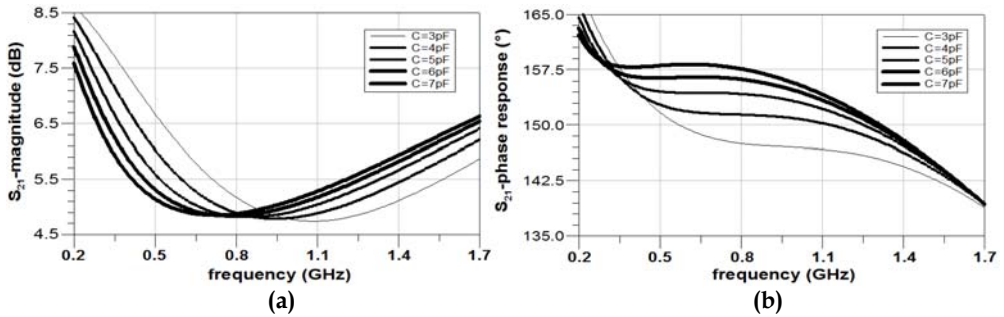


Fig. 13. Simulations of the circuit presented in Fig. 10: influence of C-variation on the gain (a) and the phase (b) when $R = 68 \Omega$ and $L = 6.2 \text{ nH}$.

(b) Experimental results of a PS prototype using one NGD cell:

Fig. 14(a) presents the schematic of the fabricated NGD PS. It relies on the use of a PHEMT FET (EC-2612) manufactured by *Mimix Broadband™* with characteristics, $g_m = 98.14 \text{ mS}$ and $R_{ds} = 116.8 \Omega$ in inductive bias ($V_{gs} = -0.1 \text{ V}$, $V_{ds} = 3 \text{ V}$ and $I_{ds} = 30 \text{ mA}$). For this proof-of-concept circuit, the objective was to reach a constant value of 90° in the operating frequency band. It was voluntarily centred below 2.5 GHz in order to minimize the spurious effects induced by low lumped component values. As indicated by the layout and the photograph respectively pictured in Figs. 14(b) and 14(c), this prototype was implemented in planar hybrid technology printed on an FR4-substrate with permittivity, $\epsilon_r = 4.3$ and thickness, $h = 508 \mu\text{m}$. About the S_{21} -transmission phase and the group delay, Fig. 15(a) illustrates the good agreement between the results of simulations and measurements especially from 0.5 to 1.8 GHz. In addition, the phase measurement shows a flatness of about $\pm 5^\circ$ around 90° from 1.08 to 2.42 GHz. It corresponds to a 76.5% relative bandwidth which is wider than the one obtained by simulation. Moreover, the relative bandwidth increases up to 100% if a $\pm 10^\circ$ variation around 90° is considered.

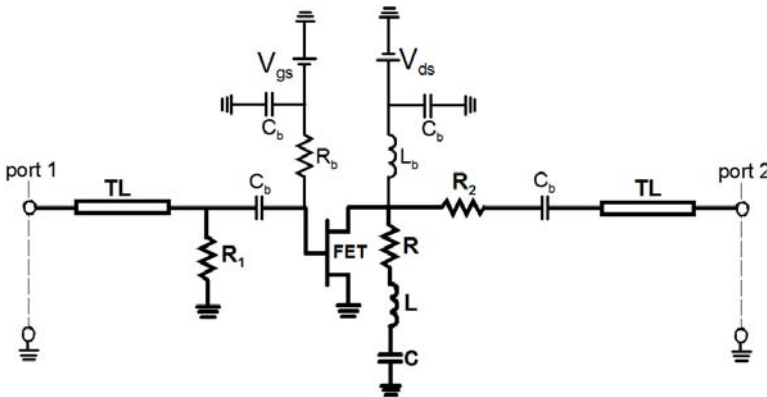


Fig. 14(a): Detailed schematic (biasing network in thin line) of the tested NGD PS : $R_1 = 51 \Omega$, $R_2 = 22 \Omega$, $R = 33 \Omega$, $L = 4.7 \text{ nH}$, $C = 1 \text{ pF}$, $C_b = 22 \mu\text{F}$, $L_b = 220 \text{ nH}$, $R_b = 1 \text{ k}\Omega$, FET (EC-2612 biased at $V_{gs} = -0.1 \text{ V}$, $V_{ds} = 3 \text{ V}$ and $I_{ds} = 30 \text{ mA}$) and TL ($w = 952 \mu\text{m}$, $d = 6.2 \text{ mm}$).

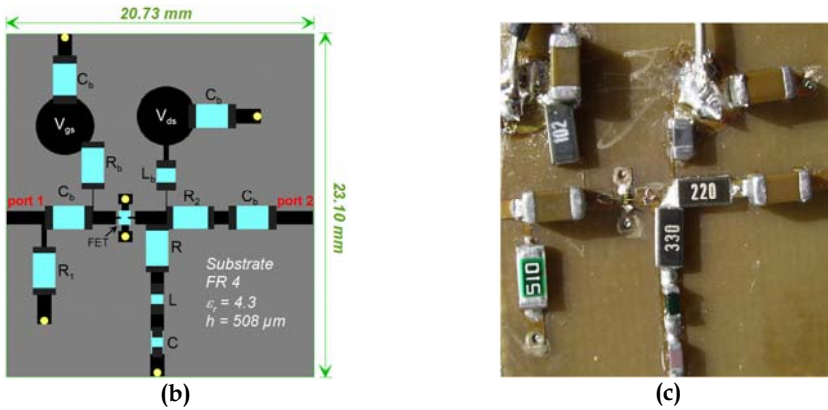


Fig. 14. Tested NGD phase shifter: (b) layout and (c) photograph.

Fig. 15(a) shows that the group delay of the PS under test is fairly negative around 1.7 GHz. Furthermore, in the frequency band of concern, its average value is in practice lower than the group delay generated by a passive device of similar physical length such as a classical transmission line. Fig. 15(b) shows that the flatness of S_{21} -magnitude is about 4 dB around 0 dB. The difference on the gain level likely comes from the dispersion of the values chosen for the passive components and from the transistor model. In fact, the value of gain obtained by measurement is, on average, 2 dB lower than by simulation one; about the group delay flatness, one should note that the measurement gives a better value than the simulation. Moreover, Fig. 15(c) about the comparison between simulations and measurements of the S_{11} input- and S_{22} output- reflection coefficients shows that the input and output matching levels are better than -10 dB from 1.1 GHz to 2.0 GHz. Thanks to the non-reciprocity of the transistor in use, the fabricated phase shifter presents an excellent isolation. Moreover, as explained by Fig. 15(c), a significant access-matching margin is obtained up to 4 GHz. But, these results are not sufficient to guarantee PS stability. So, from simulations run with ADS and by using S-probe components, the stability of this PS was analyzed by checking that the magnitude of the input and output reflection coefficients of the FET was kept below one from 1 GHz up to 10 GHz

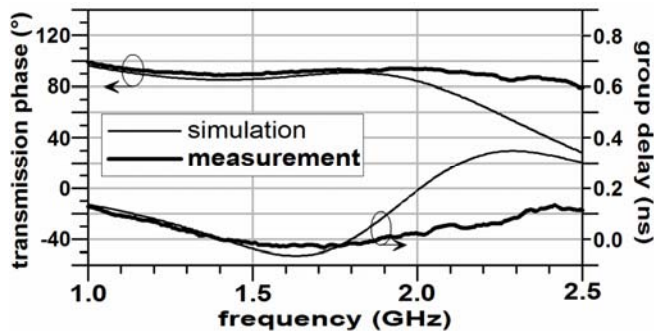


Fig. 15(a). Comparisons of the transmission phase/group delay values obtained by simulations and measurements.

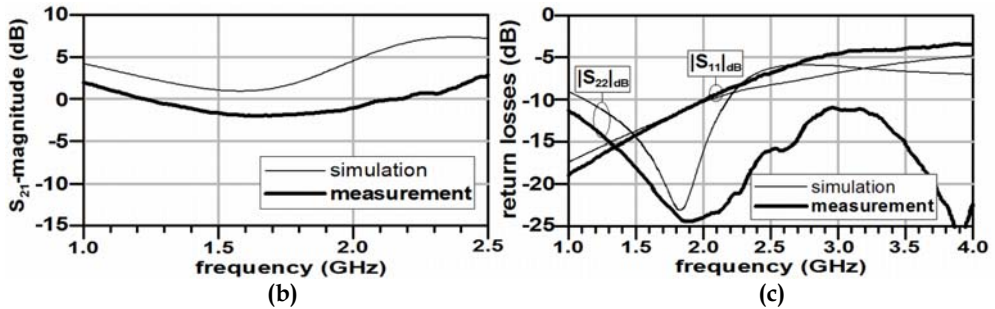


Fig. 15. Comparisons of simulation- and measurement-results about S_{21} -magnitudes (b) and return losses (c).

These results are particularly encouraging and validate both the principle and the design process; and moreover, the PS performances may be further improved as illustrated in the following section.

(c) *Simulations and sensitivity analysis of a two-stage broadband NGD PS*: To enlarge the bandwidth of constant phase while keeping a significant gain, the two-stage prototype schematized in Fig. 16(a) was designed and simulated. As previously, it relies on the use of EC-2612 FETs biased via passive networks. The electromagnetic and schematic co-simulations with *Momentum/ADSTTM* were run on considering the layout presented in Fig. 16(b). The results of simulation, i.e. S-parameter magnitudes, the transmission phase and the group delay are displayed in Figs. 17(a) and (b) together with the results of a 30-trial Monte Carlo sensitivity analysis carried out to gain insight into the impact of the component tolerances on the circuit responses. Indeed, the parameters, R , L and C , of the resonant networks and the transmission line lengths, d , were subjected to random variations of $\pm 5\%$ around their nominal values according to the Gaussian statistical distribution.

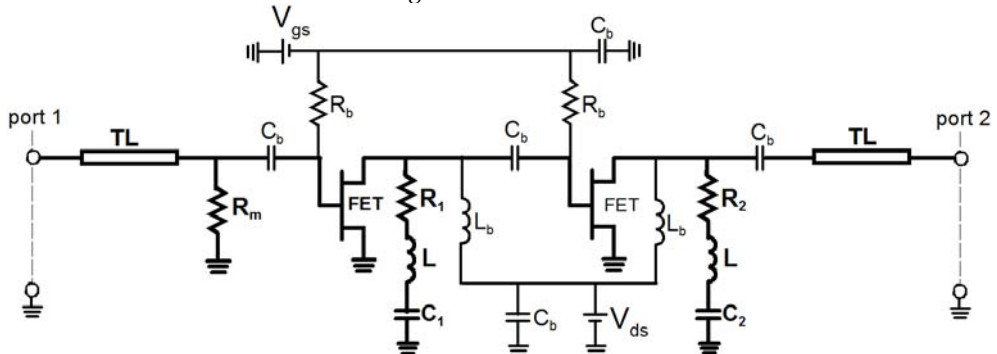


Fig. 16(a). Schematic of the simulated PS with a two-stage NGD circuit (EC-2612 FETs biased at $V_{gs} = -0.1$ V, $V_{ds} = 3$ V): $R_i = 62 \Omega$, $R_o = 120 \Omega$, $R_1 = 43 \Omega$, $R_2 = 75 \Omega$, $L = 2.2$ nH, $C_1 = 3.3$ pF, $C_2 = 1$ pF, $C_b = 1 \mu\text{F}$, $L_b = 330$ nH, $R_b = 1$ k Ω and TL ($w = 952 \mu\text{m}$, $d = 4.80$ mm) printed on an FR4-substrate ($\epsilon_r = 4.3/h = 508 \mu\text{m}$).

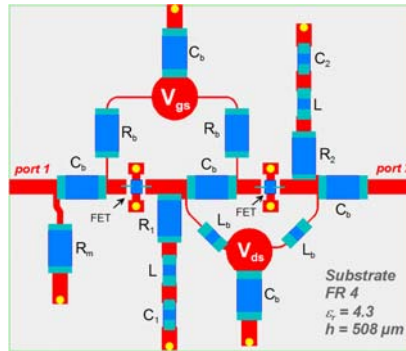


Fig. 16(b). Layout of the simulated NGD PS.

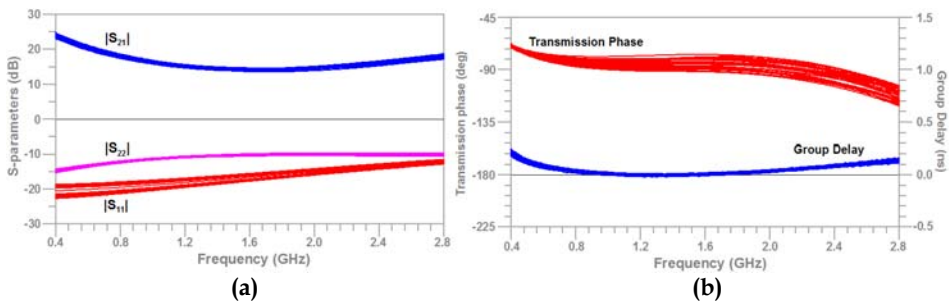


Fig. 17(a). S-parameters magnitudes and (b) transmission phase and group delay with a Monte Carlo analysis as a function of R, L, C and d .

Let us first analyze the results of simulations for the nominal values: the $-90^\circ \pm 10^\circ$ constant phase extends from 0.6 GHz to 2.6 GHz (125% in relative). In this band, the gain is kept between 12 and 18 dB, the return losses are better than 10 dB and the group delay remains below 100 ps. The Monte-Carlo analysis shows that the S-parameters, S_{11} , S_{21} and S_{22} , are within envelop limits with absolute differences less than 3 dB. Input- and output-matchings and gain flatness are kept. This confirms the relevance of cascading different NGD cells to widen the PS operating bandwidth. In a nutshell, this prototype of NGD PS is not sensitive to a variation of 5% on the passive element values and the transmission phase flatness is kept. One should note that a different trade-off could allow a slight increase of the constant phase bandwidth together with a decrease of the gain.

It is worth underlining that getting phase values between -180° and 0° is easier (smaller line) with an even number of cells; and between 0° and 180° with an odd number.

(d) Potential applications of the under study NGD PS: Compared to most of the PS available in the literature, this new PS configuration presents the following advantages:

- a constant transmission phase, which mathematically corresponds to a zero group delay, and generating in practice, a smaller value than that of a passive circuit of equivalent length,
- a possibility of implementation in very compact size,
- a faculty to achieve a broad operating bandwidth of constant phase,

- an easy way to achieve loss compensation or even an amplification thanks to the active circuit characteristics,
- the FET non-reciprocity entails a good isolation but this may be a drawback for certain applications,
- and the proposed topology provides a constant transmission phase and not a constant phase shift between the input and the output or between two outputs as it is often the case with many microwave PS.

These benefits lead us to envisage applications in electronic systems and notably the following ones in the telecommunication areas:

- integration in broadcasting systems such as active phased array antenna, as introduced in many papers (Wang et al., 1996 or Ko et al., 2003 for mobile satellite broadcasting),
- a good candidate for the improvement of modulator/demodulator functions in analog/digital communication systems (Phelan, 1975) such as PSK (phase shift keying), including BPSK (binary PSK), QPSK (Quadrature PSK), and MPSK (M-ary PSK, N bits),
- owing the faculty to provide gain, this NGD PS has an opportunity to operate as multifunction device (loss compensation, constant phase, delay reduction),
- integration in front-end RF architectures, for the synchronization of multipath systems,
- and thanks to the possibility of achieving flat or linear phase value at any levels, this PS is also promising to be useful in particular function such as frequency convertor, balun (Ravelo et al., 2007c), PLL, ...

In this optic of applications, a developed study on the design of a balun using the presented frequency-independent PS is proposed in the next subsection.

3.3 Design of a broadband active balun

The proposed three-port balun architecture is described in Fig. 18 (Ravelo et al., 2007c, 2008b). It presents an input, v_{in} (port 1) and outputs, v_{out}^- (port 2) and v_{out}^+ (port 3). We recall that by definition, a balun is a three-port device with the same amplitude and opposite phases at the two output ports:

$$|v_{out}^+| = |v_{out}^-|, \tag{38}$$

$$|\varphi_{v_{out}^+} - \varphi_{v_{out}^-}| = 180^\circ. \tag{39}$$

Similar to many multi-port microwave devices, it should be associated with good return losses and isolation between the output ports.

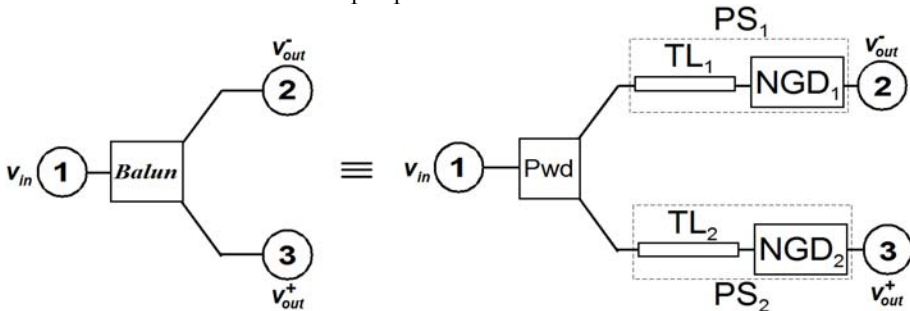


Fig. 18. Proposed architecture of balun with NGD active circuits (*Pwd*: Power divider).

To achieve the above specified functions, we use a power divider, Pwd in cascade with an NGD PS (a classical transmission line, TL, cascaded with an NGD circuit) in each of its output branches. The power divider ensures an equal power split. Then, to get the opposite phases at the output of the balun, the first branch exhibits, for a specified frequency band, a phase shift of -270° and the second one -90° . Here, in each branch of the splitter, a transmission line of negative phase slope is associated with an NGD active circuit of positive phase slope in order to finally get the desired constant phase value over a broadband defined between two frequencies, f_1 and f_2 for both outputs. Fig. 19 shows the schematic of the designed balun with two-stage of the NGD cells. In most of the cases (Antoniades & Eleftheriades, 2005; Lee et al., 2005), Wilkinson dividers are used, but they may restrict the operating bandwidth. In order to operate over a broad bandwidth, a 6 dB resistive splitter composed of a tree of identical resistors equal to $Z_0/3$ is used.

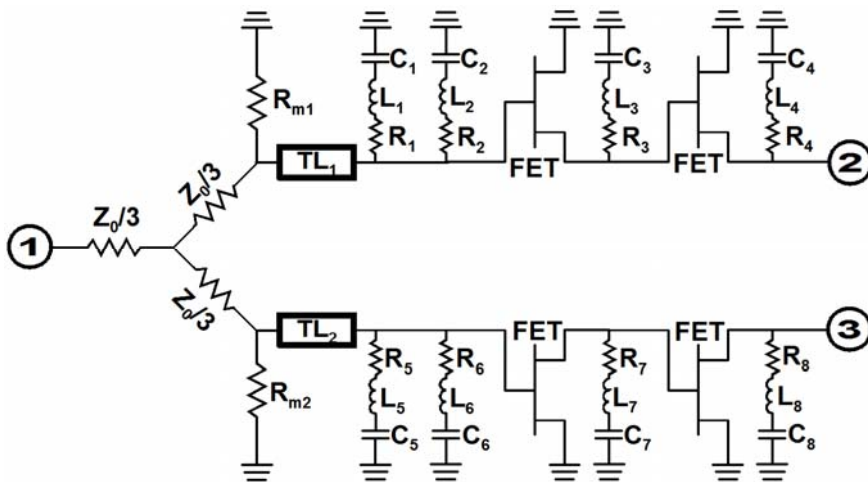


Fig. 19. Schematic of the simulated NGD active balun: $Z_0 = 50 \Omega$, $R_1 = 83 \Omega$, $R_2 = 120 \Omega$, $R_3 = 22 \Omega$, $R_4 = 42 \Omega$, $R_5 = 40 \Omega$, $R_6 = 43 \Omega$, $R_7 = 12 \Omega$, $R_8 = 36 \Omega$, $R_{m1} = 120 \Omega$, $R_{m2} = 150 \Omega$, $L_1 = 1 \text{ nH}$, $L_2 = 320 \text{ pH}$, $L_3 = 270 \text{ pH}$, $L_4 = 531 \text{ pH}$, $L_5 = 3.3 \text{ nH}$, $L_6 = 6.5 \text{ nH}$, $L_7 = 1.3 \text{ nH}$, $L_8 = 3 \text{ nH}$, $C_1 = 2.8 \text{ pF}$, $C_2 = 2.6 \text{ pF}$, $C_3 = C_4 = 2.4 \text{ pF}$, $C_5 = 0.6 \text{ pF}$, $C_6 = 0.1 \text{ pF}$, $C_7 = 0.7 \text{ pF}$, $C_8 = 0.6 \text{ pF}$, TL_1 ($d_1 = 4.49 \text{ mm}$, $Z_{c1} = 50 \Omega$), and TL_2 ($d_2 = 24.89 \text{ mm}$, $Z_{c2} = 50 \Omega$) printed on a RF35 substrate ($\epsilon_r = 3.5$, $h = 508 \mu\text{m}$), FETs: EC-2612 biased at $V_{gs} = -0.1 \text{ V}$, $V_{ds} = 3 \text{ V}$.

The transmission lines TL_i ($i = \{1, 2\}$) are defined by their lengths, d_i , and their characteristic impedances, Z_{c_i} which are set at Z_0 . R_{m1} and R_{m2} allow the matching between the splitter outputs and the input accesses. It is worth pointing out that, in order to achieve a constant phase value with a difference of 180° , d_2 is set longer than d_1 . As illustrated in Fig. 20(a), the top branch (TL_1 and NGD_1) shows a nearly flat phase value of $-90^\circ \pm 10^\circ$ whereas that of the bottom one (TL_2 and NGD_2) is $-270^\circ \pm 10^\circ$ from 3.0 to 6.0 GHz. Figs. 20(a) and 20(b) show that the differential phase output is $180^\circ \pm 9^\circ$, and the insertion losses, $|S_{21}|_{\text{dB}}$ and $|S_{31}|_{\text{dB}}$, are greater than 2.4 dB. Thanks to the non-reciprocity of the employed FET, the isolation levels are better than -59 dB between all ports. In addition, the return losses $|S_{11}|_{\text{dB}}$ and $|S_{22}|_{\text{dB}}$ are better than 11 dB from 3.0 to 6.0 GHz, and the output return loss $|S_{33}|_{\text{dB}}$ is kept over

9 dB. Finally, the differential flatness, $||S_{31}|_{\text{dB}} - |S_{21}|_{\text{dB}}|$, is less than 1.1 dB from 3.5 to 6.0 GHz.

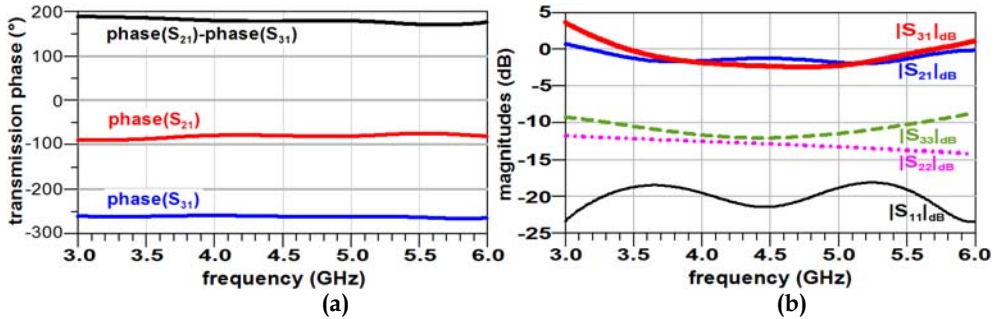


Fig. 20. Phases (a) and magnitudes (b) of the balun simulated S-parameters.

Table 1 summarizes the performances of the understudied balun shown in Fig. 19. More precisely, it deals with S_{21} - and S_{31} -magnitude and phase variations through the two output branches from 3.5 GHz to 5.5 GHz. We remark that they present magnitude and phase flatnesses respectively lower than 2.2 dB and 5°.

Insertion loss	Magnitude (dB)		Phase (deg.)	
	Min.	Max.	Min.	Max.
S_{21}	-1.94	-1.24	-87.50	-79.00
S_{31}	-2.40	-0.24	-263.50	-260.00

Table 1. Simulated balun: phase and magnitude variations from 3.5 GHz to 5.5 GHz.

For such an active multi-port device, the stability must be ensured at every frequency. As previously, this circuit stability analysis was made by carefully verifying that the magnitude of the input and output reflexion coefficients of each transistor was kept below one up to 10 GHz.

On the other hand, in order to conclude about the noise factor of the balun under study, we intend to characterize a balun prototype through experiments carried out in frequency- and time-domains. These measurements should allow us to quantify the noise contribution. Nevertheless, it was verified by time-domain measurements (Fig. 7(a)) that the noise effect is not favoured by the NGD effect. Nevertheless, an increase of a possible noise contribution can be avoided by acting on the positions of the RLC-resonant network and of the transistors of the NGD circuit. Then, a trade-off with the matching level should be set.

The main assets of this compact broadband balun are its very low delay value, the possibility of loss compensation and its good isolation compared to most of the baluns described in the literature (Van Raay & Kompas, 2000; Kuylenstierna & Linner, 2004; Viallon et al., 2005; Antoniadis & Eleftheriades, 2005; Lee et al., 2005).

4. Conclusion and future works

A simple topology of an NGD active circuit consisting in a FET terminated by a shunt RLC-resonant network and dedicated to the microwave signals was proposed and extensively studied. To our knowledge, this experimental demonstration in the time domain of the ability of a circuit to exhibit simultaneously gain and NGD in microwave domain is the first one available in the literature. By injecting in the NGD circuit a sufficiently smoothed input short-pulse modulating a sine carrier, we showed that the output has an envelop peak in advance compared to the input one. Of course, this phenomenon is not in contradiction with the causality principle. It is also worth emphasizing that the circuit under test meets all of the criteria required for classical active microwave devices, i.e. gain, matching and stability. As predicted by theory (Ravelo et al., 2007a, 2007b, 2007c and 2008a), for a prototype implemented in planar technology, measurements showed that, in the time-domain, the pulse peak advance was about -2 ns or 24% of the $1/e$ -input pulse half-width with no attenuation. It is also worth noting that this experiment confirmed that the occurrence of time-domain advance induced by the NGD active circuit was not suppressed by the input noise contribution.

Moreover, thanks to the S_{21} -magnitude form, the NGD circuit under test demonstrated its ability to exhibit a pulse compression phenomenon together with a possibility of amplification. Then, it should be worth using the presented NGD active topology to compensate for dispersion effects and especially to reduce the intersymbol interference (ISI) in certain telecommunication channels.

As a potential application of this NGD circuit, we proposed a new principle of frequency-independent phase shifter. Cascading a classical transmission line with this NGD circuit allowed us to get a constant phase value. The efficiency of this principle was demonstrated by measurement. Indeed, a constant phase value of $90^\circ \pm 5^\circ$ was obtained within a 76% relative frequency band centred at about 1.5 GHz. The impacts of the PS parameter variations were described and a sensitivity analysis was performed and discussed. The main benefits of this NGD active PS are its compactness and also the facility to generate very low group delay, and the broad band characteristics. Besides, a two-stage NGD PS was also designed; the simulation results showed a bandwidth enhancement of the constant phase up to 125% ($-90^\circ \pm 10^\circ$). Some fields of applications such as the design of a broadband active balun for RF front end architectures are discussed.

As ongoing researches, design of reconfigurable devices dedicated to telecommunication applications is planned. Future investigations will be devoted to the design of NGD devices able to operate at higher frequencies through the use of distributed elements. In this prospect, implementation of MMIC devices based on distributed elements is envisaged.

5. References

- Antoniades, M. A. & Eleftheriades, G. V. (2005). A broadband Wilkinson balun using microstrip metamaterial lines, *IEEE Ant. Wireless Propagation Lett.*, Vol. 4, Issue 1, pp. 209-212.
- Arbore, M. A. (1997). Engineerable compression of ultrashort pulses by use of second-harmonic generation in chirped-period-poled lithium niobate, *Opt. Lett.*, Vol. 22, No. 17, pp. 1341-1343.

- Baum, C. E. (2006). Coupling ports in waveguide cavities for multiplying fields in pulse-compression schemes, *Circuit and Electromagnetic System Design Note* 52.
- Broomfield, C. D. & Everard, J. K. A. (2000). Broadband negative group delay networks for compensation of oscillators, filters and communication systems, *Electron. Lett.*, Vol. 23, pp. 1931-1933.
- Burt, G.; Samsonov, S. V.; Phelps, A. D. R.; Bratman, V. L.; Ronald, K.; Denisov, G. G.; He, W.; Young, A. R.; Cross, A. W. & Konoplev, I. V. (2005). Microwave pulse compression using a helically corrugated waveguide, *IEEE Trans. On Plasma Science*, Vol. 33, No. 2, pp. 661-667.
- Cao, H.; Dogariu A.; & Wang, L. J. (2003). Negative group delay and pulse compression in superluminal pulse propagation, *IEEE J. Sel. Top. Quantum Electron.*, Vol. 9, No.1, pp. 52-58.
- Chiao, R. Y.; Bolda, E. L.; Bowie, J.; Boyce, J. & Mitchell, M. W. (1996). Superluminality and amplifiers, *Prog. Crystal Growth Charact. Mat.* 33, pp. 319-325.
- Chu, S. & Wong, S. (1982). Linear pulse propagation in an absorbing medium, *Phys. Rev. Lett.*, Vol. 48, pp. 738-741.
- Eleftheriades, G. V.; Siddiqui, O. & Iyer, A. K. (2003). Transmission line for negative index media and associated implementations without excess resonators, *IEEE MWC Lett.*, Vol. 13, No. 2, pp. 51-53.
- Gaponov-Grekhov, A. V. & Granatstein, V. L. (1994). Applications of high-power microwaves, Ed. Hardcover, Pages No. 364, Artech House, ISBN: 0-89006-699-x, Boston, MA.
- Garrett, C. G. B. & McGumber, D. E. (1970). Propagation of a gaussian light pulse through an anomalous dispersion medium, *Phys. Rev. A*, Vol. 1, pp. 305-313.
- Kitano, M.; Nakanishi, T. & Sugiyama, K. (2003). Negative group delay and superluminal propagation: an electronic circuit approach, *IEEE J. Sel. Top. Quantum Electron.*, Vol. 9, No. 1, pp. 43-51.
- Ko, Y. J.; Park, J. Y. & Bu, J. U. (2003). Integrated RF MEMS phase shifters with constant phase shift, *IEEE MTT-S Symp. Dig.*, Philadelphia, pp. 1489-1492, June 2003.
- Kuylentierna, D. & Linner, P. (2004). Design of broad-band lumped-element baluns with inherent impedance transformation, *IEEE MTT*, Vol. 52, No. 12, pp. 2739-2745.
- Kuzikov, S. V.; Danilov, Y. Y.; Denisov, G. G.; Shegokov D. Y. & Vikharev, A. A. (2004). Multi-mode sled-II pulse compressors, *Proc. LINAC2004*, Lübeck Germany, THP28, pp. 660-662.
- Lee, S.; Lim, J-S.; Yang H-S. & Nam, S. (2005). A novel design of balun using left handed transmission line, *Proceedings of ISAP2005*, Seoul, Korea.
- Li, P.; Chen, X.; Chen, Y. & Xia, Y. (2005). Pulse compression during second-harmonic generation in engineered aperiodic quasi-phase-matching gratings, *Optics Express*, Vol. 13, No. 18, pp. 6807-6814.
- Lucyszyn, S.; Robertson, I. D. & Aghvami, A. H. (1993). Negative group delay synthesiser, *Electron. Lett.*, Vol. 29, pp. 798-800.
- Mitchell, M. W. & Chiao, R. Y. (1997). Negative group delay and 'fronts' in a causal systems: an experiment with very low frequency bandpass amplifiers, *Phys. Lett. A*, Vol. 230, pp. 133-138.
- Mitchell, M. W. & Chiao, R. Y. (1998). Causality and negative group delays in a simple bandpass amplifier, *Am. J. Phys.* 66, pp. 14-19.

- Munday, J. N. & Henderson, R. H. (2004). Superluminal time advance of a complex audio signal, *Appl. Phys. Lett.*, Vol. 85, pp. 503-504.
- Nakanishi, T.; Sugiyama, K. & Kitano, M. (2002). Demonstration of negative group delays in a simple electronic circuit, *Am. J. Phys.*, Vol. 70, Issue 11, pp. 1117-1121.
- Phelan, H. R. (1975). Dual polarization spiral antenna, *U.S. patent No. 3,906,514*, Sep. 16.
- Ravelo, B. (Dec. 2008). Negative group delay active devices: theory, experimental validations and applications, *Ph. D. thesis (in French)*, Lab-STICC, UMR CNRS 3192, UEB, University of Brest, France.
- Ravelo, B.; Pérennec, A.; Le Roy, M. & Boucher, Y. (2007a). Active microwave circuit with negative group delay, *IEEE MWC Lett.*, Vol. 17, Issue 12, pp. 861-863.
- Ravelo, B.; Pérennec, A. & Le Roy, M. (2007b). Synthesis of broadband negative group delay active circuits, *IEEE MTT-S Symp. Dig., Honolulu (Hawaii)*, pp. 2177-2180.
- Ravelo, B.; Pérennec, A. & Le Roy, M. (2007c). Broadband balun using active negative group delay circuit, *Proc. of the 37th EuMC*, Munich, Germany, 8-12 Oct. 2007, pp. 466-469.
- Ravelo, B.; Pérennec, A. & Le Roy, M. (2008a). Negative group delay active topologies respectively dedicated to microwave frequencies and baseband signals, *Journal of the EuMA*, Vol. 4, pp. 124-130.
- Ravelo, B.; Pérennec, A. & Le Roy, M. (2008b). Application of negative group delay active circuits to the design of broadband and constant phase shifters, *Microwave And Optical Technology Lett.*, Vol. 50, No. 12, pp. 3078-3080.
- Siddiqui, O. F.; Erickson, S. J.; Eleftheriades G. V. & Mojahedi, M. (2004). Time-domain measurement of negative group delay in negative-refractive-index transmission-line metamaterials, *IEEE Trans. MTT*, Vol. 52, No. 5, pp. 1449-1454.
- Thumm, M. K. & Kasperek, W. (2002). Passive high-power microwave components, *IEEE Trans. Plasma Sci.*, Vol. 30, No. 3, pp. 755-786.
- Van Raay, F. & Kompa, G. (2000). Design and stability test of a 2-40 GHz frequency doubler with active balun, *IEEE MTT-S Symp. Dig., Honolulu (Hawaii)*, Vol. 3, Boston, MA, pp. 1573-1576.
- Viallon, C.; Venturin, D.; Graffeuil, J. & Parra, T. (2005). Design of an original K-band active balun with improved broadband balanced behavior, *IEEE MWC Lett.*, Vol. 15, No.4, pp. 280-282.
- Wang, C. & Yao, J. (2008a). Photonic generation of chirped millimeter-wave pulses based on nonlinear frequency-to-time mapping in a nonlinearly chirped fiber Bragg grating, *IEEE Tran. MTT*, Vol. 56, No. 2, pp. 542-553.
- Wang, C. & Yao, J. (2008b). Photonic generation of chirped microwave pulses using superimposed chirped fiber Bragg gratings, *IEEE Photon. Technol. Lett.*, Vol. 20, No. 11, pp. 882-884.
- Wang, L. J.; Kuzmich, A. & Dogariu, A. (2000). Gain-assisted superluminal light propagation, *Nature* 406, pp. 277-279.
- Wang, J. J. H.; Tillery, J. K.; Thompson, G. T.; Bohannon, K. E.; Najafabadi, R. M. & Acre, M. A. (1996). A multioctave-band photonicly-controlled, low-profile, structurally-embedded phased array with integrated frequency independent phase-shifter, *IEEE Int. Symp. on Phased Array Syst. Technol.*, pp. 68-73, Oct. 15-18, 1996, Boston, MA.
- Zeitouny, A.; Stepanov, S.; Levinson, O. & Horowitz, M. (2005). Optical generation of linearly chirped microwave pulses using fiber Bragg gratings, *IEEE Photon. Technol. Lett.*, Vol. 17, No. 3, pp. 660-662.

Broadband GaN MMIC Power Amplifiers design

María-Ángeles González-Garrido and Jesús Grajal

Departamento de Señales, Sistemas y Radiocomunicaciones, ETSIT, Universidad Politécnica de Madrid, Ciudad Universitaria s/n, 28040, Madrid, Spain

1. Introduction

Monolithic microwave integrated circuits (MMIC) based on gallium nitride (GaN) high electron mobility transistors (HEMT) have the advantage of providing broadband power performance (Milligan et al., 2007). The high breakdown voltage and high current density of GaN devices provide higher power density than the traditional technology based on GaAs. This allows the use of smaller devices for the same output power, and since impedance is higher for smaller devices, broadband matching becomes easier.

In this chapter, we summarise the design procedure of broadband MMIC high power amplifiers (HPA). Although the strategy is quite similar for most semiconductors used in HPAs, some special considerations, as well as, experimental results will be focused on GaN technology.

Apart from design considerations to achieve the desired RF response, it is essential to analyse the stability of the designed HPA to guarantee that no oscillation phenomena arises. In first place, the transistors are analysed using Rollet's linear K factor. Next, it is also critical to perform nonlinear parametric and odd stability studies under high power excitation. The strategy adopted for this analysis is based on pole-zero identification of the frequency response obtained at critical nodes of the final circuit (Barquintero et al., 2007).

Finally, to avoid irreversible device degradation, thermal simulations are required to accurately predict the highest channel temperature and thermal coupling between transistors.

2. AlGaIn/GaN HEMT Technology

First of all, MMIC GaN technology has to be evaluated. High power GaN devices operate at high temperature and high-dissipated power due to the high power density of performance. Therefore, the use of substrates with high thermal conductivity like the silicon carbide (SiC) is preferred.

GaN technological process is still immature and complex. However, gate lithography resolution lower than 0.2 μm and AlGaIn/GaN epi-structures on 100-mm SiC substrates are already available (Milligan et al., 2007).

Wide band gap semiconductors such as GaN and SiC are very promising technologies for microwave high power devices. The advantages of these materials over conventional semiconductors, GaAs and Si, include high breakdown field (E_g), high saturation electron velocity (v_{sat}), and high thermal conductivity. GaN/AlGaN high electron mobility transistors (HEMTs) offer even higher power performance due to the higher carrier sheet density and the higher saturation velocity of the bidimensional electron gas channel (2DEG) compared to SiC metal semiconductor field effect transistors (MESFETs). The diagram in Fig. 1 summarizes GaN-HEMT properties and its benefits.

This technology has demonstrated a power density of 30 W/mm using devices with dimensions of $0.55 \times 246 \mu\text{m}^2$ at 4 GHz when biased at 120 V (Wu et al., 2004).

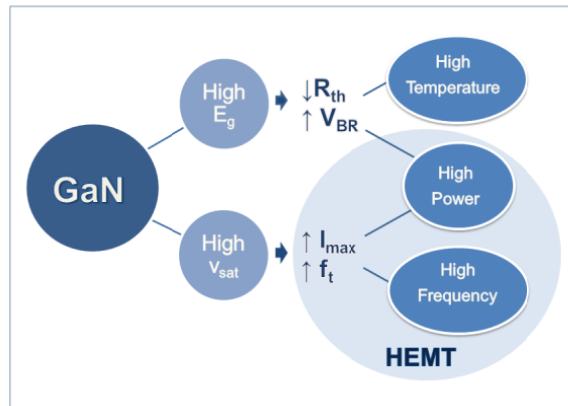


Fig. 1. GaN HEMT properties and benefits.

In a HEMT the conduction channel is confined to the interface between two materials with different band gap. This region known as 2DEG has very few ionized impurities to scatter the electrons, resulting in a very high mobility device. AlGaN/GaN heterostructures have a high sheet carrier density in the 2DEG interface without intentional doping of the structure. The spontaneous and piezoelectric polarization effects are the key factors for the charge distribution in the AlGaN/GaN HEMT (Ambacher et al., 2000).

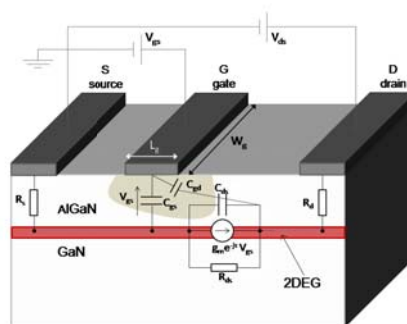


Fig. 2. AlGaN/GaN HEMT model.

The model of a HEMT that shows the small-signal parameters and the 2DEG channel is depicted in Fig. 2. Source and drain ohmic contact, as well as Schottky gate can be observed. The gate voltage (V_{gs}) controls the current (I_{ds}) that flows between the source and the drain. When V_{gs} reaches pinch-off voltage the electrons below the gate are depleted and no current can flow from drain to source.

Since AlGaIn/GaN HEMTs for HPA applications work under high power conditions, nonlinear models have to be used to simulate the transistor performance. The success of the design depends on the precision of the model fitting. A widely used approach is based on Angelov analytical expressions (Angelov et al., 1992). The model parameters are extracted from load pull, S-parameters, and pulse IV measurements. For instance, the nonlinear current source is characterized fitting DC and pulsed IV-measurements. The voltage controlled gate-source and gate-drain capacitance functions (C_{gs} and C_{gd}) are determined from bias dependent hot-FET S-parameter measurements. Finally, the parasitic elements of the HEMT model are extracted with cold-FET S-parameters measured from pinch-off to open channel bias conditions. The high temperature performance of GaN-HPAs demands the use of electro-thermal models (Nuttinck et al., 2003). Otherwise, power estimation will be too optimistic in CW operation.

The design methodology evaluated in this chapter is based on the experience reported by the design of several 2-6 GHz HPAs. The active devices used are 1-mm gate-periphery HEMTs fabricated using AlGaIn/GaN heterostructures and gate length (L_g) technology of 0.5 μm from Selex Sistemi Integrati S.p.A foundry (Costrini et al., 2008) within Korrigan project (Gauthier et al., 2005). The HEMT cells consist of 10 fingers, each with a unit gate width (W_g) of 100 μm . The maximum measured oscillation frequency (f_{max}) of these transistors is about 39 GHz.

A considerable dispersion between wafers is still observed because of GaN technology immaturity. Table 1 shows the main characteristics (device maximum current I_{dss} , pinch-off voltage V_p , breakdown voltage V_{bgd} , C_{gs} , sheet resistance R_s and contact resistance R_c) of two wafers fabricated for the 2-6 GHz HPAs (wafer 1 and 2) and the wafer used for extracting the nonlinear electrical models (wafer 0) for the 1st-run designs. From the results in Table 1, an important deviation between the model and the measurements is expected. For instance, C_{gs} mismatch will produce a poor S11 fitting.

Wafer	I_{dss} mA/mm	V_p (V)	V_{bgd} (V)	C_{gs} (pF/mm)	R_s (Ω /sq)	R_c (Ω mm)
Wafer 0	972	-6.4	>70	3.2	355	0.44
Wafer 1	794	-4.7	50	2.24	456	0.47
Wafer 2	567	-2.7	71	2.88	440	0.36

Table 1. GaN wafers comparison.

Regarding passive technology, the foundries provide microstrip and coplanar models for typical MMIC components such as transmission lines, junctions, inductors, MIM capacitors and both NiCr and GaN resistors.

3. Design

The design process of a broadband HPA is described in this section. Special attention should be paid on broadband matching network synthesis and device stability.

3.1 Amplifiers Topology

The first step in an HPA design is to choose the most appropriated topology to fulfil design specifications. Single or multi-stage topology will be used depending on the gain target. In order to achieve high output power, several devices must be combined in parallel.

The classical combination topologies are the balanced and the corporative HPA. Balanced structures are made with $\lambda/4$ -lines, which become quite large in designs below X-band. Furthermore, multi-stage approach for broadband design will enlarge the circuit even more. On the other hand, the corporate topology based on two-way splitters seems to be a more versatile solution for broadband designs. It can be designed with compact lumped broadband filters in frequencies below X-band while transmission lines can be used at higher frequencies.

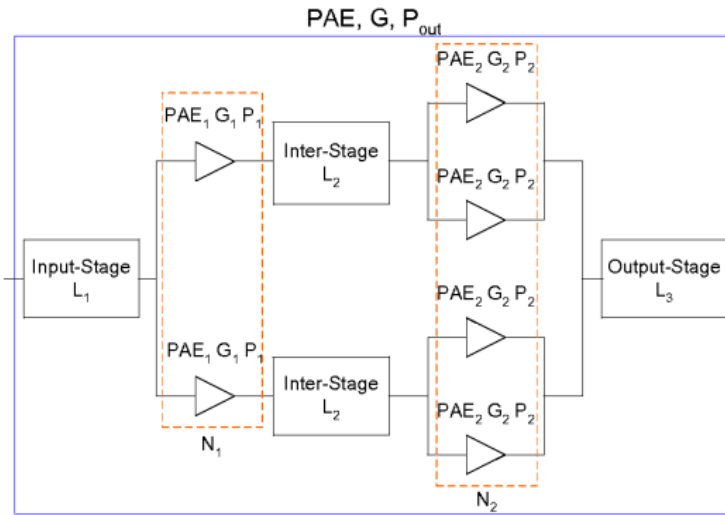


Fig. 3. Two-stage corporative topology amplifier.

The two-stage corporative topology, such as the one in Fig. 3, is widely used to design HPAs, because it offers a good compromise between gain and power. Note that the first stage consists of two unit cells which drive the output stage, composed of four equal cells. This power amplifier has three matching networks: input-, inter-, and output-stage. The labels displayed in Fig. 3 represent the loss of each matching network (L_i), the number of combined cells (N_i), the power added efficiency (PAE_i), the gain (G_i), and the output power (P_i) at the i^{th} -stage.

Output stage loss, L_3 , is critical to the HPA output power ($P_{out}=N \cdot P_{HEMT} \cdot L_3$). Besides, network loss has to be minimised mainly in the output network, because it is essential to maximise power added efficiency (PAE_{total}). Equation (1) is used to calculate PAE_{total} of a corporative topology with 2^n transistors at the output stage. The representation of equation (1) in Fig. 4 confirms the higher influence of L_3 in PAE_{total} .

$$PAE_{total} = \frac{PAE_1 PAE_2 (L_1 L_2 L_3 G_1 G_2 - 1)}{PAE_1 L_1 L_2 G_1 (G_2 - 1) + PAE_2 L_1 (G_1 - 1)} \tag{1}$$

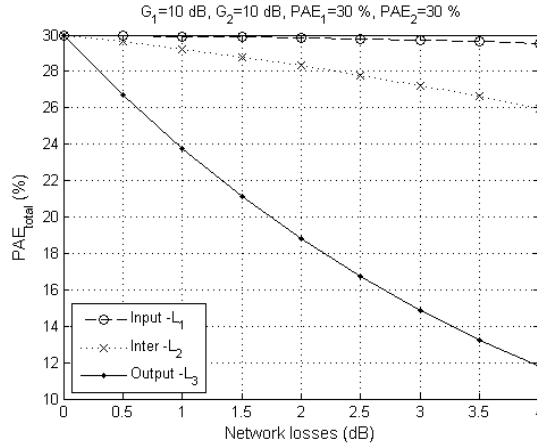


Fig. 4. PAE_{total} versus input-, inter-, and output-stage network loss. To analyse the influence of each network the loss of the other networks are set to 0 dB.

High efficiency operation is especially important for power devices, because thermal issues can degrade the amplifier performance. Dissipated power (P_{dis}) is inversely proportional to the HPA efficiency, see equation (2).

$$P_{dis} \approx P_{out} \cdot ((PAE_{total})^{-1} - 1) \tag{2}$$

P_{dis} and temperature increase (ΔT) are related in equation (3) through the thermal resistance (R_{th}). This parameter gives an idea of the thermal flow through a material or a stack of materials from a hot spot to another observation point. Therefore, R_{th} depends on the thermal conductivity of the materials and the final HPA set-up.

$$\Delta T = P_{diss}R_{th} \tag{3}$$

3.2 Unit transistor cell

The unit transistor cell size selection is based on a compromise between gain and power, because large devices have higher power, but lower gain (Walker, 1993). Moreover, input and output impedances decrease for larger devices, making the design of broadband matching networks difficult. The lack of power of small devices can be solved by combining several devices in parallel. It is worth noting that the complexity of the design increases with the number of cells to be combined.

Once the transistor size is selected, the available unit cells have to be evaluated at different bias operating conditions (Snider, 1967). The optimum operation class of a power amplifier depends on the linearity, efficiency or complexity of the design specifications. In the conventional operation classes, A, B, AB and C, the transistor works like a voltage controlled current source. On the contrary, there are some other classes, such as D, E and F, where amplifier efficiency improves by working like a switch. In the diagram of Fig. 5, different operation classes have been represented, indicating the IV-curves, the load-lines and the

conduction angle (Φ) of each one. The conduction angle defines the time that the transistor is in the on-state.

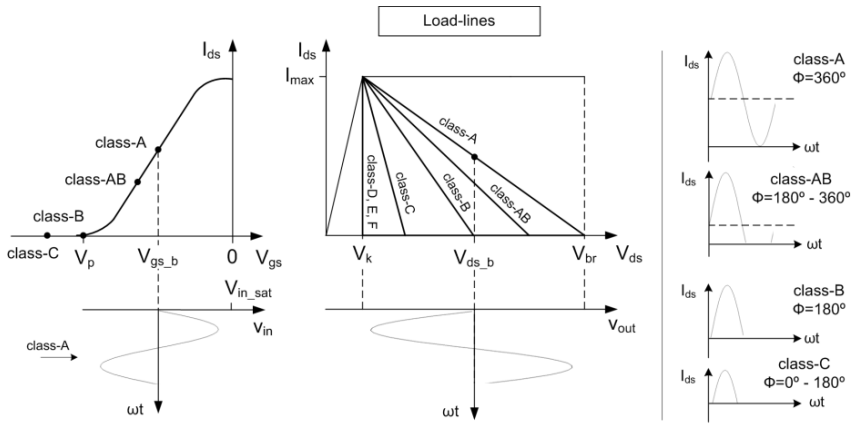


Fig. 5. HPA bias operation classes.

The maximum drain efficiency ($\eta = P_{out}/P_{dc}$) and the maximum output power of a transistor versus the conduction angle can be calculated under ideal conditions, as shown in Fig. 6, where the knee voltage (V_k) is assumed to be 0 V and RF compression is not considered. This representation shows that drain efficiency is inversely proportional to Φ , and that output power is almost constant between class AB and class A. Class-AB operation quiescent point at $30\%I_{max}$ provides simultaneously maximum power and a considerable high drain efficiency, therefore this seems to be an optimum bias point.

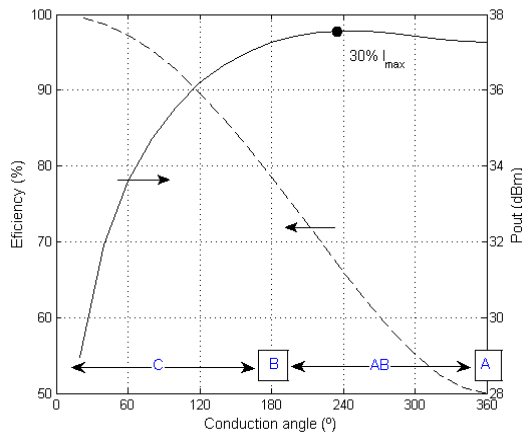


Fig. 6. Output power and drain efficiency versus the conduction angle (Φ) calculated for $V_{ds}=25V$ and $I_{max}=850mA$.

Given an operation class, the RF power drive determines the actual drain efficiency. Efficiency and linearity are opposite qualities. Therefore, a compromise has to be assumed depending on the HPA design application.

3.3 Unit cell stabilization

An in-depth analysis of the stability is necessary to guarantee that no oscillation phenomena arise. Firstly, the transistors are analysed using the classical approach for linear stability based on the Rollet’s (Rollet, 1962) formulas over a wide frequency band. This theorem stands that the transistor is unconditionally stable if the real part of the impedance at one port is positive ($Re(Z_{ii}) > 0$) for any real impedance at the opposite port. The Rollet’s K factor as a function of the two-port network inittance parameters ($y_{ii}=Z_{ii}=Y_{ii}$) is the following:

$$K = \frac{2Re(\gamma_{11})Re(\gamma_2) - Re(\gamma_{12}\gamma_{21})}{|\gamma_{12}\gamma_{21}|} > 1 \tag{4}$$

The easiest way to increase K to achieve $K > 1$ is increasing the input impedance of the transistor. This can be done by adding a frequency dependent resistance (R_{stab}) at the transistor input port: $Z'_{11}=Z_{11}+R_{stab}$. Stability can also be improved with a resistor at the transistor output, but this would reduce the maximum output power. The series stabilization resistance can be calculated from equation (5).

$$R_{stab} = \frac{K|Z_{12}Z_{21}| + Re(Z_{12}Z_{21})}{2Re(Z_{22})} - Re(Z_{11}) \tag{5}$$

Another useful way to write R_{stab} is as a function of the small-signal parameters of the transistor:

$$R_{stab} = \frac{2\omega C_{ds}C_{gs}(K - 1) + C_{gd}g_m K}{2\omega C_{gd}g_m(C_{gd} + C_{gs})} \tag{6}$$

Parallel RC networks in series with the transistor gate make it possible to synthesize R_{stab} in a wide frequency band, see Fig. 7.

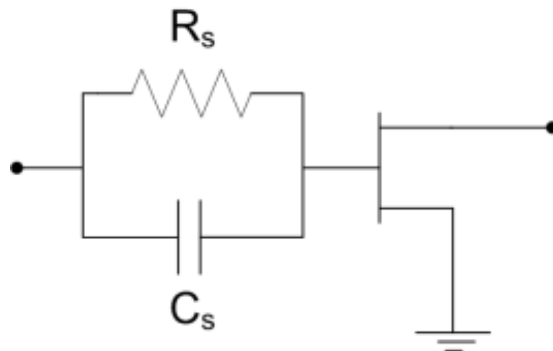


Fig. 7. Stabilization parallel RC networks in series with the transistor gate.

As an example, we take an unstable transistor ($K < 1$) at frequencies under 12.5 GHz. The ideal stabilization resistance to make this transistor unconditionally stable (with $K = 1.2$) at any frequency is plotted in Fig. 8 (left). In the same plot, the R_{stab} traces obtained with two different RC networks have been included. The new K factor (K_{new}) recalculated taking into account the cascade of the series RC networks and the transistors are represented in Fig. 8 (right).

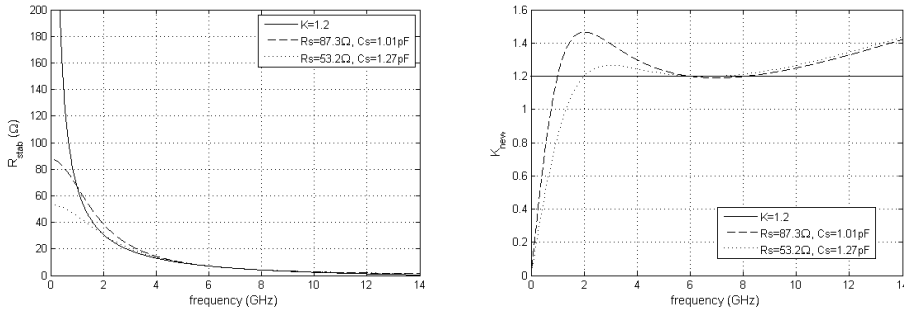


Fig. 8. R_{stab} and K_{new} calculated with an ideal network for $K=1.2$ and two different RC networks.

RC networks cannot be used to stabilize a transistor at low frequencies because the resulting resistor becomes too large or the capacitor too small to be feasible in MMIC technology. Therefore, off-chip stabilization networks are sometimes required to avoid the use of big components in the chip. Another solution is to add a parallel resistor (R_p) in the internal stabilization network. This resistor can be included in the gate bias path (L_b) as depicted in Fig. 9. L_b should be chosen high enough to have no influence in the frequency band of the design.

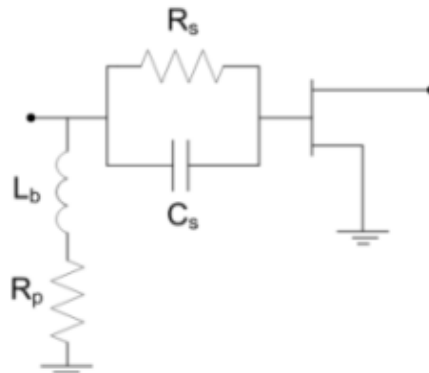


Fig. 9. Combination of a parallel RC networks in series with the transistor and a parallel resistor in the bias path to achieve unconditional stability at any frequency.

In Fig. 10 it is shown the comparison between K_{new} calculated with the series RC network of Fig. 7 and the network of Fig. 9 that combines a series and a parallel resistor. The last solution makes the transistor unconditionally stable even at low frequencies.

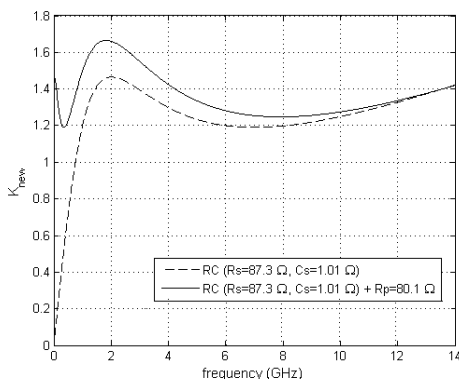


Fig. 10. K_{new} obtained with a single RC networks and with the combination of an RC network and a parallel resistor at the gate bias path.

As Fig. 8 shows, the stabilization networks introduce dissipative loss decreasing with frequency, what also contributes to compensate the device gain slope. The maximum available gain (MAG) after stabilization is obtained as:

$$MAG = \left| \frac{Z_{21}}{Z_{12}} \right| \left(K_{new} - \sqrt{K_{new}^2 - 1} \right) \tag{7}$$

The comparison between the original MAG of the transistor and the MAG obtained with the proposed stabilization networks is shown in Fig. 11.

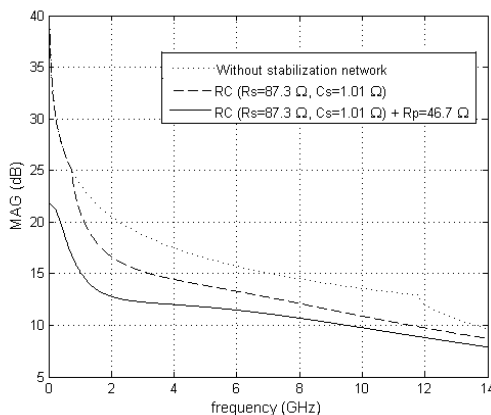


Fig. 11. Comparison of the transistor MAG without any stabilization network and with both a single RC networks and the combination of an RC network and R_p .

RC networks are also used to prevent parametric and out-of-band oscillations (Teeter et al., 1999).

3.4 Networks synthesis

The HPA matching networks (input-, inter-, and output-stage) are synthesized from filter theory and implemented with both lumped elements and transmission lines. These networks are designed to provide optimum impedances at the transistor output and conjugated matching at its input, as well as, matching the HPA input and output to 50Ω . Stabilization networks and DC bias networks have to be included and considered in the synthesis process.

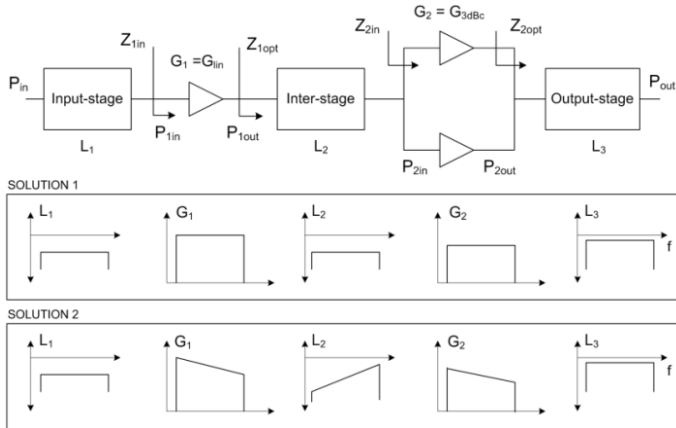


Fig. 12. Two-stage HPA design process.

Two different strategies can be followed in the HPA design as indicated in the diagram in Fig. 12; in the first solution, the transistor and the gain equalization network are considered a single block and the matching networks have to be designed with a flat frequency response. This approach is easily adopted when the stabilization network introduces frequency dependent loss. In the second solution, gain compensation is performed by the inter-stage matching network.

The following steps describe the HPA design process:

- Firstly, the transistor optimum loads for maximum power (Z_{2opt}) are calculated using load-pull techniques. The most precise method to obtain the optimum loads is by means of load-pull measurements. However, load-pull measurement equipment is expensive and, the measurement process could be tedious and long for broadband design, because many load measurements are required. If nonlinear models of the transistor are available, load-pull simulation could be done in CAD simulators. The accuracy of this option depends on the precision of the nonlinear models. When only the transistor lineal-model and the IV-curves are available, the load-pull contours have to be estimated by the Cripps method (Cripps, 1983).
- Next, the output-stage network has to be designed. This network transforms Z_{2opt} to the 50Ω impedance of the HPA output-port and combines the power of the 2nd-stage transistors. The drain DC-bias is included in this network and it is done through a parallel inductance of a value calculated to provide the imaginary part of Z_{2opt} at the design centre frequency. Network loss (L_3) must be minimised, mainly in this output-stage because it is critical to maximise power and PAE.

- Later, the inter-stage network loads are calculated; firstly, the input impedance of the second-stage transistors loaded with the output-stage network (Z_{2in}); secondly, the optimum loads for maximum gain at the first-stage transistors (Z_{1opt}). It is important to calculate the impedances at the expected high power working conditions.
- Then, the inter-stage network is designed to synthesize the optimum loads for the first-stage (Z_{1opt}) and to match the second-stage input (Z_{2in}). The design complexity of this network is higher because two complex impedances have to be matched over a broad frequency bandwidth. Moreover, if it is required, the transistor gain roll-off should be compensated by frequency dependent losses in this network (L_2). This can be done with a RC network, as it was described in section 3.3. First-stage drain DC-bias is also done through a parallel inductance that provides the imaginary part of Z_{1opt} at the design centre frequency.
- Finally, the input-stage network is designed to match the HPA-input of 50Ω to the first-stage transistors input (Z_{1in}). In this case, the input impedance of the transistors is also calculated loading them with the inter- and output-stage networks.

The matching networks can be designed as two-port networks. Anyhow, it is worth noting that the input impedance has to be scaled by the number of transistors to be combined (N). Then, the network can be transformed into a $(N+1)$ -port network. The transformation is done by dividing the two-port network in different sections and scaling them depending on the branching level in the power combination (or division) network. Fig. 13 shows a diagram where the transformation process is schematized.

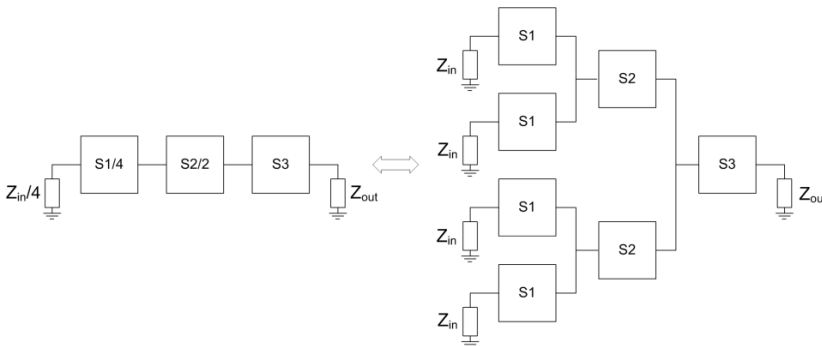


Fig. 13. Transformation of two-port to N-port networks.

4. Global stability analysis

Multistage HPAs are prone to parametric oscillations that are function of the input-power drive. The origin of these instabilities is the nonlinear capacitance of the transistor input impedance, which varies with the input-drive. Odd-mode oscillations are also frequent due to the presence of multiple active elements and the circuit symmetry. Subharmonic oscillations at $f_{in}/2$, where f_{in} is the input signal frequency, are very common in transistors due to the nonlinear capacitance nature. However, spurious oscillations at non-harmonically related frequency f_a are also observed.

Two-port network techniques cannot be applied for HPA stability analysis due to the existence of multiple feedback loops. The standard harmonic-balance (HB) simulators used

for HPA design do not include tools for high-power stability analysis either. Fortunately, there are several techniques that perform a nonlinear stability study based on the circuit linearization around the large-signal steady state obtained with HB. The method proposed by Mons (Mons et al., 1999) is rigorous and complete, but it requires the verification of the Nyquist stability criteria for every nonlinear element, what becomes tedious in complex circuits. From the design process point of view, faster stability analysis is preferred. Therefore, it is proposed a technique based on the insertion of an external small-signal perturbation in a circuit node. This way, it is possible to obtain the closed-loop transfer function provided by the impedance calculated at the observation node in a certain frequency range. Pole-zero identification of the resultant transfer function is used to verify the stability of the circuit (Jugo et al., 2003). This study can be done in both small-signal and large-signal conditions. Different observation nodes must be considered to ensure the detection of masked instabilities, because of pole-zero cancellation in certain nodes. At least, an analysis per each HPA stage is required.

Parametric simulations at different working conditions are advisable to see the evolution of critical poles. If any complex conjugated poles cross to the right half plane an oscillation is detected.

In circuits with N active devices, N modes of performance coexist. There are $N-1$ odd-modes and one even-mode simultaneously. For instance, in the second-stage of the HPA in Fig. 3, three odd-modes and one even-mode coexist. However, due to the symmetry, two odd-modes are equivalent, so only the odd-modes $[+ - + -]$ and $[+ + - -]$, and the even-mode $[+ + + +]$ have to be studied. Using different perturbation configurations, the stability of each mode can be determined by means of the pole-identification technique. Instead of a single perturbation generator, one generator at the input of each transistor is introduced and the phase of the perturbation signals is shifted 180° depending on the excitation mode (Anakabe et al. 2005).

In Fig. 14, the frequency responses of an even-mode (left) and an odd-mode $[+ - + -]$ (right) are depicted. Both responses have been obtained at the same operating conditions ($P_{in}=19\text{dBm}$, $f_{in}=4\text{GHz}$, $V_{ds}=26\text{V}$ and $V_{gs}=-4.2\text{V}$), and it can be seen that the odd-mode presents a resonance at $f_{in}/2$ that indicates the presence of a possible subharmonic oscillation. This means the transfer function may have poles with positive real part.

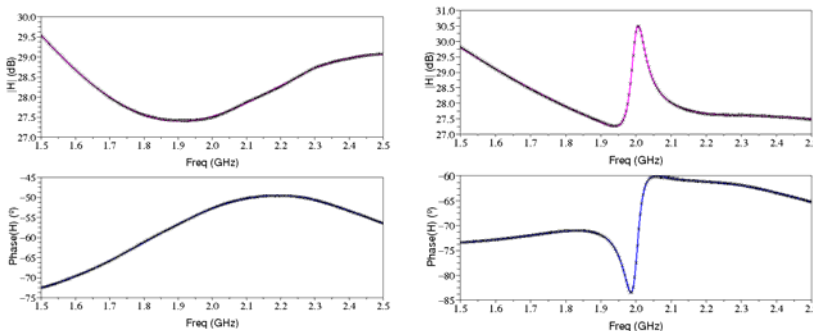


Fig. 14. Closed-loop transfer function calculated with even-mode $[+ + + +]$ (left) and odd-mode $[+ - + -]$ (right) excitation. The HPA operation conditions are $P_{in}=19\text{dBm}$, $f_{in}=4\text{GHz}$, $V_{ds}=26\text{V}$ and $V_{gs}=-4.2\text{V}$

Once an oscillation is found, the instability margin has to be determined through a parametric study about the critical operation conditions. Frequency and power of the input signal, as well as the HPA DC-bias (V_{ds} and V_{gs}) are common parameters that affect stability. The evolution with frequency and V_{ds} of the poles at $f_{in}/2$ corresponding to the frequency response in Fig. 14 are represented in Fig. 15. The HPA is unstable between 3.97 GHz and 4.03 GHz at $V_{ds} = 26$ V.

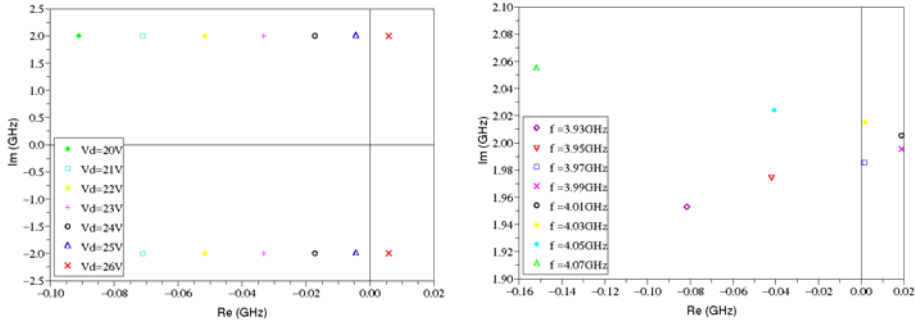


Fig. 15. Evolution of the poles at $f_{in}/2$ versus V_{ds} (left) and f_{in} (right). The HPA initial operation conditions are $P_{in}=19dBm$, $f_{in}=4GHz$, $V_{ds}=25V$ and $V_{gs}=-4.2V$

Once the stability nature has been determined, the HPA circuit has to be corrected to avoid oscillations that may invalidate the design. Usually, the instability is cancelled using notch filters (like RC networks (Teeter et al., 1999)) at the oscillation frequency or resistors to add loss in the oscillation feedback loop. For instance, resistors between the transistors (R_o) can be added to prevent odd-mode oscillations, see Fig. 16.

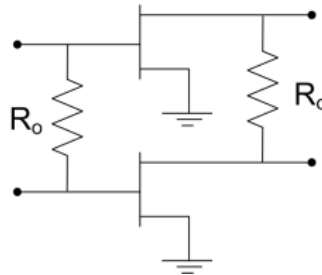


Fig. 16. Resistors to prevent odd oscillations.

5. Thermal characterization

Thermal characterization with different techniques is of crucial interest in GaN-HPAs, because it is still necessary to analyse the influence of the high power dissipated in this leading technology (Nuttinck et al., 2003).

Thermal resistances, R_{thv} at different working conditions can be calculated with commercial software like COMSOL Multiphysics (FEMLAB) or Ansys. The simulations can be

performed for the unit transistor cell to obtain the maximum channel temperature (T_{chann}), or for the final HPA to characterize the thermal coupling between the transistors. Fig. 17 shows the thermal resistance of a unit transistor cell of 1mm, and the results for an HPA with 8x1mm transistors at the output-stage. The simulation has been performed in ideal conditions and taking into account the real mounting fixture of the device on a cooper carrier.

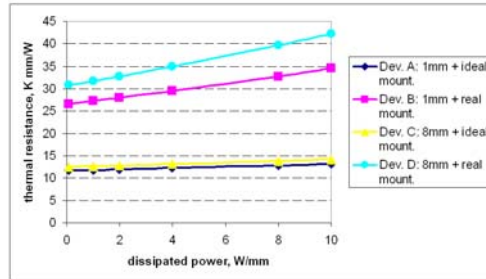


Fig. 17. Comparison between the simulated thermal resistance of a 1mm-transistor and of an HPA with 8x1mm transistors at the output-stage, in ideal and real mounting conditions.

R_{th} in the range of 13.5 °C/W has been obtained at 6W dissipated power (P_{dis}) for the ideal mounting of the 1mm-transistor. From these calculations, an estimated gradient (ΔT) around 81°C is expected between the channel and the backside temperature. However, the real assembly increases R_{th} to 32 °C/W, which means a temperature gradient of 192 °C. Thus, we see that a test fixture mounted on a cooling platform is necessary in order to provide the amplifier with a proper heat dissipation system.

6. Broadband HPA examples

Two fully monolithic broadband HPAs with an output-stage active periphery of 4 mm and 8 mm are presented in the photos of Fig. 18. They have been fabricated at Selex Sistemi Integrati S.p.A.

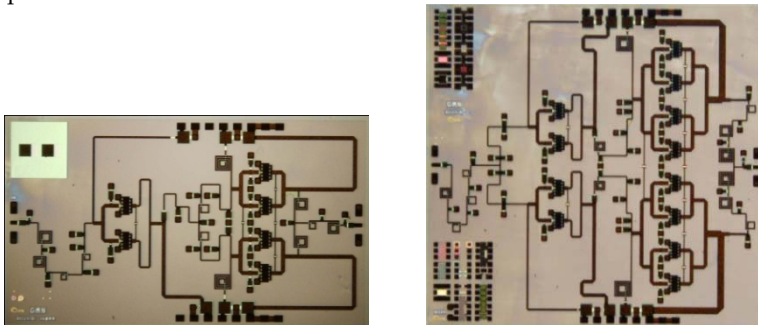


Fig. 18. Photograph of the 4 mm (left) and 8 mm (right) HPAs. The chip size is 6.6x3.7 mm² and 6.6x 6.0 mm², respectively.

Several MMIC HPAs were characterized in CW and pulsed conditions. All chips were tested at drain-source voltage, V_{ds} , from 20 to 25 V and $I_d=30\%I_{max}$.

Typical measured small-signal gain and input return loss of the 4 mm-HPA are shown in Fig. 19. Over the 2-6 GHz frequency range, gain was about 18 dB and the input return loss was lower than -7 dB. Simulated results are also shown for comparison. Mismatch between simulated and measured input return loss exists because the transistor model was extracted from a previous wafer and the technological process is still in development.

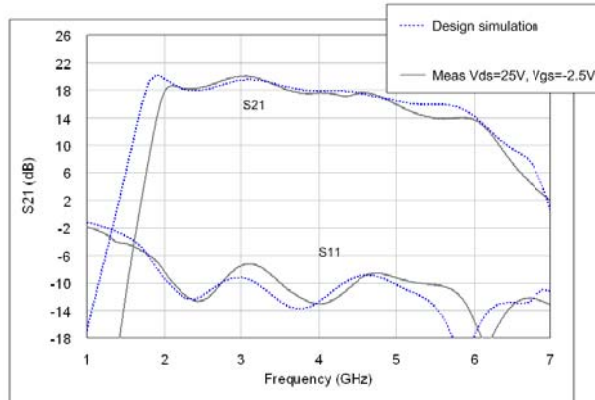


Fig. 19. Comparison of gain and input return loss measurements and simulation of the 4mm-HPA.

Pulsed and CW characterization of the 8mm-HPAs from two different wafers (see Table 1) at 4.5 GHz and $V_{ds}=25V$ are shown in Fig. 20. The pulsed measurements were performed with short pulses of 20 μm length and 1% duty cycle. The HPA from Wafer 1 exhibited higher output power in pulsed-mode, whereas the power capacity in CW is similar. Saturation power is about 15 W in CW with better than 20% PAE and, reaching 26 W and 25% in pulsed-mode.

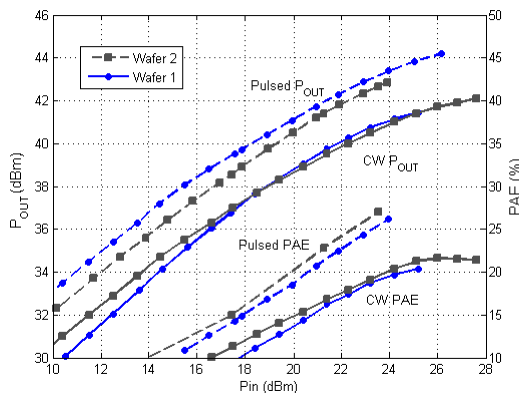


Fig. 20. CW and pulsed output power and PAE versus input power of the 8mm- HPA from Wafer 1 and Wafer 2 at 4.5 GHz, $V_{ds}=25V$ and $30\%I_{DSS}$.

Typical broadband performance of both 4mm-HPA and 8mm-HPA in CW and pulsed-mode is shown in Fig. 21. Pulsed measurements in the lower frequency band are not available because the set-up works above 3 GHz. The 4mm-HPA has greater than 40 dBm (2.5 W/mm) output power in 50% of the band in CW, and greater than 41.4 dBm (3.5 W/mm) in pulsed conditions. On the other hand, the 8mm-HPA delivers 41.2 dBm (2 W/mm) in CW and 44 dBm (3.5 W/mm) in pulsed-mode. Thermal problems are more significant for the 8mm-HPA in CW.

To characterise the power degradation due to thermal heating, the HPAs have been measured in pulsed-mode at different duty cycles and pulse lengths. The duty cycle has higher influence than the pulse length in the HPA performance. The results of this analysis with a pulse length of 100 μ s are depicted in Fig. 22. The output power and PAE at V_{ds} =20 and 25 V are shown for both HPAs. As expected, the power and efficiency degradation is higher for the 8mm-HPA. This device losses approximately 40% of the power capacity from 1% to 50% duty cycle, while the 4mm-HPA falls only 30%.

There is still margin to increase CW power if the test-jig is improved to reduce its thermal resistance.

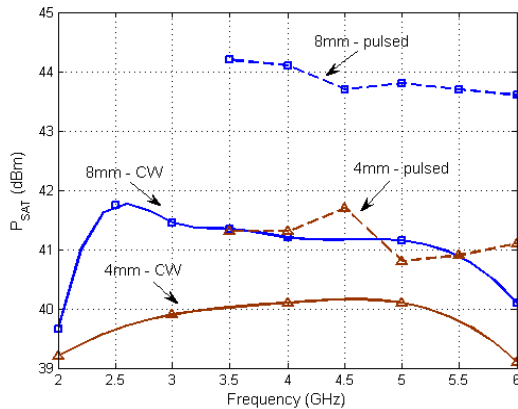


Fig. 21. CW and pulsed output power versus frequency of both 4mm-HPA and 8mm-HPA at V_{ds} =25 V and 30% I_{DSS} .

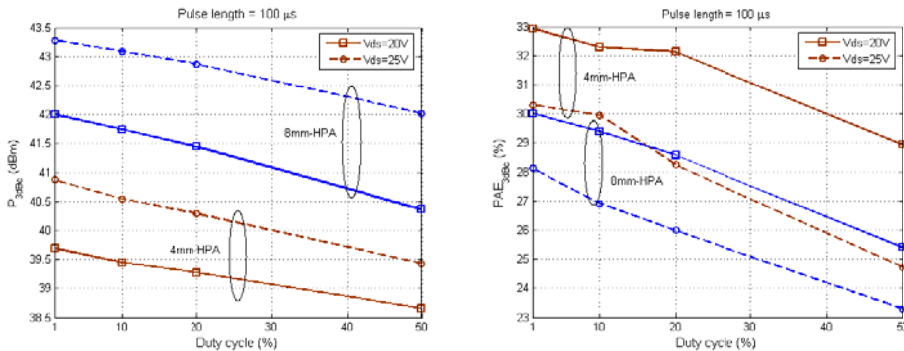


Fig. 22. Output power and PAE versus duty cycle of both 4mm-HPA and 8mm-HPA. Measurements with pulses of 100 μ s length at V_{ds} =20, 25 V and 30% I_{DSS} .

7. Conclusion

This chapter makes a brief introduction of the GaN-HEMT technological process development. Based on this technology, it is established a design procedure for broadband high power amplifiers. The design is focused on the synthesis of the matching and stabilization networks of a two-stage amplifier. It is highlighted the need for nonlinear stability analysis to avoid parametric and odd-mode oscillation. Thermal characterization is also critical due to the high power dissipated in high power GaN devices. Finally, we present the analysis of results of two broadband HPA demonstrators.

8. Acknowledgment

This work has been supported by the Spanish National Board of Scientific and Technology Research under the project TEC2008-021481TEC.

9. References

- Ambacher, O.; Foutz, B.; Smart, J.; Shealy, J. R.; Weimann, N. G.; Chu, K.; Murphy, M.; Sierakowski, A. J.; Schaff, W. J.; Eastman, L. F.; Dimitrov, R.; Mitchell, A.; Stutzmann, M. (2000). Two dimensional electron gases induced by spontaneous and piezoelectric polarization in undoped and doped AlGaIn/GaN heterostructures. *Journal of Applied Physics*, Vol. 87, No. 1, 2000, pp. 334
- Anakabe, A., Collantes, J.M.; Portilla, J.; Mons, S.; Mallet, A. (2005). Detecting and Avoiding Odd-Mode Parametric Oscillations in Microwave Power Amplifiers. *International Journal on RF and Microwave Computer-Aided Engineering*, Vol. 15, No. 5, September 2005, pp. 469-478, ISSN:1096-4290
- Angelov, I.; Zirath, H.; Rosman, N. (1992). A new empirical nonlinear model for HEMT and MESFET devices, *IEEE Trans. Microw. Theory Tech.*, Vol. 40, No. 12, December 1992. pp. 2258-2266, ISSN: 0018-9480
- Barquinero, C.; Suarez, A.; Herrera, A.; Garcia, J.L. (2007). Complete Stability Analysis of Multifunction MMIC Circuits. *IEEE Trans. on Microwave Theory and Tech.*, Vol. 55, No. 10, October 2007, pp. 2024-2033, ISSN: 0018-9480
- Costrini, C.; Calori, M.; Cetronio, A.; Lanzieri, C.; Lavanga, S.; Peroni, M.; Limiti, E.; Serino, A.; Ghione, G.; Melone, G. (2008). A 20 watt micro-strip X-band AlGaIn/GaN HPA MMIC for Advanced Radar Applications," *EUMIC 2008*. pp. 566-569, October 2008
- Cripps, S. (1983). A Theory for the Prediction of GaAs FET Load-Pull Power Contours. *Proceedings of the IEEE Intl. Microwave Symp. Dig.*, Vol. 83, No. 1, 1983, pp. 221- 223
- Gauthier, G.; Mancuso, Y.; Murgadella, F. (2005). KORRIGAN - a comprehensive initiative for GaN HEMT technology in Europe, *EGASS 2005*, pp. 361-363, ISBN: 8890201207
- Jugo, J.; Portilla, J.; Anakabe, A.; Suárez, A.; Collantes, J. M. (2003). Closedloop stability analysis of microwave amplifiers. *Electron. Letters*, Vol. 37, Feb.y 2003, pp. 226-2228
- Milligan, J.W.; Sheppard, S.; Pribble, W.; Wu, Y.-F.; Muller, StG.; Palmour, J.W. (2007). SiC and GaN Wide Bandgap Device Technology Overview. *IEEE Radar Conference*, April 2007, pp. 960-964, ISSN: 1097-5659

- Mons, S.; Nallatamby, J.-C.; Quere, R.; Savary, P.; Obregon, J. (1999). A unified approach for the linear and nonlinear stability analysis of microwave circuits using commercially available tools. *IEEE Trans. Microw. Theory Tech*, 1999, pp. 2403-2409, ISSN 00189480
- Nuttinck, S.; Wagner, B.K.; Banerjee, B.; Venkataraman, S.; Gebara, E.; Laskar, J.; Harris, H.M. (2003), Thermal analysis of AlGa_N-Ga_N power HFETs. *IEEE Trans. on Microw. Theory and Tech.*, Vol. 51, No.12, Dec. 2003, pp. 2445-2452, ISSN: 0018-9480
- Rollett, J. (1962). Stability and Power-Gain Invariants of Linear Twoports. *IRE Transactions on Circuit Theory*, Vol. 9, No. 1, march 1962, pp. 29-32, ISSN 0096-2007
- Snider, D.M. (1967). A theoretical analysis and experimental confirmation of the optimally loaded and overdriven RF power amplifier. *IEEE Transactions on Electron Devices*, Vol. 14, No. 12, Dec 1967, pp. 851-857, ISSN: 0018-9383
- Teeter, D.; Platzker, A.; Bourque, R. (1999). A compact network for eliminating parametric oscillations in high power MMIC amplifiers. *IEEE MTT-S International Microwave Symposium Digest*, Vol. 3, 1999, pp. 967-970, ISBN: 0-7803-5135-5
- Walker, J. L. B. (1993). *High-Power GaAs FET amplifier*, Artech House, 1993, ISBN: 0890064792
- Wu, Y.-F.; Saxler, A.; Moore, M.; Smith, R.P.; Sheppard, S.; Chavarkar, P.M.; Wisleder, T.; Mishra, U.K.; Parikh, P. (2004). 30-W/mm Ga_N HEMTs by field plate optimization. *IEEE Electron Device Letters*, 2004, pp. 117-119, ISSN: 0741-3106

Magnetron Based Radar Systems for Millimeter Wavelength Band – Modern Approaches and Prospects

Vadym Volkov
Institute of Radio Astronomy of National Academy of Sciences of Ukraine
Ukraine

In honor of my mother, Ninel.

1. Introduction

Historically magnetrons were one of the first devices used to build radar systems. Namely, successful development and utilization of the magnetrons in radars had assisted essentially Allies to win battle for air and sea during World War II (Brown, 1999). And definitely they were the first devices, which have allowed developing the radars operating within millimeter wavelengths region. It had happened due to these microwave sources are characterized by a number of advantages. They are rather simple in production. The magnetrons provide both high peak and average power at relatively low operational voltages as well a fair frequency potential. Because of the above advances, the magnetron remains the most utilized type of microwave vacuum tubes until now. Namely, by virtue of the utilization magnetrons in ovens, millions people over whole world have learned the word “microwave”!

However by the middle of 60th magnetron based radar systems had ceased to meet increasing performance requirements and their development had been curtailed. They had moved considerably to a niche of simple, low cost radars for great demand applications like that for marine navigation. It had happened due to both fundamental peculiarities of the magnetron operation and issues concerning their manufacturing. At first, the magnetron is an oscillator providing no modulation capabilities except the simplest case of pulse modulation. It results in difficulties to introduce advanced signal processing into the magnetron based radars. Next, uncertainty in the conceptual ability of the magnetron to produce oscillations with appropriate short-term frequency stability; considerable difficulties to develop the corresponding highly stable modulators; as well as an analog implementation of a coherence-on-receiver technique did not allow to fetch an actual potential of magnetron based system out. It resulted in the strong opinion that the magnetrons are generally not suitable to build radar systems with relevant Doppler capabilities. Further, a high spatial resolution of magnetron based systems can be achieved practically only by reducing the duration of radiated RF pulse. However, it leads to the

following difficulties: (i) the magnetron is a highly resonant device, which limits a minimal possible pulse duration; and (ii) in order to keep the radar potential, pulse repetition rate should be high enough respectively, which reduces unambiguous radar range or requires utilization of dedicated technique to resolve range ambiguity. Further, the first millimeter wavelengths magnetrons demonstrated a low reliability making the result of their utilization rather discouraging in the most cases. Thus, appearance by the middle of 60th efficient power amplifiers based on both vacuum tubes and solid-state devices and great expectations for a rapid progress in their development as well as the introduction a pulse compression technique had given up the magnetrons for lost to use in the high performance radars.

However, since recent time, magnetrons are considered again as a rather attractive choice to develop systems for millimeter wavelengths band namely. This turn has become possible due to: (i) a lack or low availability of other power devices operating within the indicated frequency range; (ii) a significant improvement in magnetrons characteristics, partially, incredible increase in their lifetime; (iii) a dramatic progress in digital signal processing technique; (iv) achievements in the development of high voltage modulators and millimeter wavelengths technique; and (v) a strong demand for millimeter wavelengths radars from non-military applications, which means a great interest in cost effective solutions.

Despite a rather simple internal structure, the magnetron is characterized by a great complexity of the processes taken place inside it. There is no a more or less comprehensive theory of magnetrons until now. Numerical simulation can be accounted as very superficial. In general we prefer to treat the magnetron as something like a magic box characterized often by unpredictable and even surprising behavior. Thus, generally development of modern magnetron based radar, especially operating within millimeter wavelength region, requires profound understanding of principles of the magnetron operation, a great experience, and the utilization of specific design approaches, at a system level partially. However, often the magnetron is considered as old, well known device and respectively radars based on it are designed in a humble way. It results in a humble performance certainly. Probably, a rather uptight attitude to utilize the magnetrons to build contemporary high performance radars is caused by the above reason.

In this paper we do not try to review comprehensively the current state of affairs or to cover as much as possible wide range of issues concerning the development of both millimeter wavelengths magnetrons and radars based on them. Instead, relying on own experience we draw attention to the fact that some noted disadvantages preventing the magnetron utilization in the high performance radar systems are essentially weakened until now, whereas others can be managed successfully by gaining from the achievements of modern electronics. The corresponding design approaches, which have assisted us to develop successfully a number of contemporary magnetron based radar systems operating within millimeter wavelength band and addressed to different application areas, will be disclosed more or less systematically. We hope that the bellow consideration will be helpful for radar designers to keep always in mind the possibilities providing by good old magnetron!

2. Magnetrons in radars – brief overview

We would not like to discuss here the physical principles of magnetron operation. They can be found in a variety of manuscripts (Okress, 1961;Tsimring, 2007). For us it is important

that the magnetron is a vacuum crossed field tube, which is capable to produce high power microwave oscillations with a high efficiency, and hence can be adopted conceptually to use in radar transmitter. As fairly noticed in (Skolnik, 2008), a choice of electronic device for the transmitter end stage defines practically completely radar structure and design approaches. Thus, let us outline the most important peculiarities of the magnetrons as related to their utilization in the radars. At first, the magnetrons are characterized fundamentally by a high both peak and average power. Typical values exceed 100 kW and 100 W for Ka band and 4 kW and 4 W for W and G bands correspondingly. It allows utilizing constant frequency pulse, being the simplest possible among radar signals, while keeping an appropriate radar sensitivity without the usage of a sophisticated signal processing technique. Next, any magnetron is an oscillator rather than an amplifier. It means partially that its output signal depends only on the physical layout of the magnetron internals and the parameters of its circumstance, i.e. applied voltage, a strength of magnetic fields, a value of voltage standing wave ratio at the output flange etc. In addition it is practically impossible to manipulate either parameter of the magnetron output signal independently from the other. Further, the magnetron is characterized by a highly resonant design basically. The magnetron oscillations frequency is essentially defined by electromagnetic properties of its internal layout and can be varied within a wide enough range only by changing a mechanical configuration of such layout, i.e. slowly. All above constrict evidently modulation capabilities providing by the magnetron. Three types of modulation are used in modern radar systems commonly – pulse (as a particular type of amplitude); frequency; and phase modulation respectively. Practically it may be considered that the magnetron by itself provides no ability for a fast, highly reproducible, and well-controlled phase/frequency modulation and adopts only the simplest pulse modulation. Probably only a bandwidth of electrical frequency chirp provided by W and G band magnetrons may appeal to use in the high resolution radars (see Section 0). Notice, since the magnetron output pulse is shaped at a radio frequency directly, it occupies it twice wider frequency band than it is required to ensure a definite spatial resolution.

As for any other oscillator the magnetron oscillation frequency is subjected to fluctuations. According to common approach, fast and slow fluctuations are considered separately and referred as phase noise and frequency stability respectively. Concerning to radar performance the first defines quality of Doppler processing whereas the second is not so important generally except a number of rather special cases. Certainly, the total frequency variation range should not be too big as well as matching between transmitter and receiver frequencies should be ensured ever. Usually the related magnetron performance is characterized as poor and this fact is a byword to utilize such devices in the radars. On other hand the maximum possible variation of magnetron operational frequency including manufacturing tolerances is less than $\pm 1\%$ over all millimeter wavelength bands in use even for non-tunable devices and cannot be considered as a serious issue. As for the phase noise, which is referred as a pulse-to-pulse frequency instability in the magnetron based systems, reflecting peculiarities of Doppler processor implementation, the following should be mentioned. *Prima facie*, it seems to be difficult actually expecting a high pulse-to-pulse frequency stability for the magnetrons. Q-factor of the magnetron resonant system is relatively low even for coaxial devices especially within millimeter wavelengths band as well as frequency pushing is rather big due to a high electron density inside an interaction space. Generally, the behavior of electron cloud has a considerable noise component and not

well predictable at all. Initial conditions to produce successive pulses may not coincide resulting in increase in a value of the pulse-to-pulse frequency instability. This effect observed experimentally when even a single pulse altered the state of magnetron cathode surface (private communication with magnetron developers). Probably it is due to a harsh operational conditions featured by a very high peak power dissipated on as well as a high voltage applied to the elements the magnetron comprises of.

On other hand, in general it is not easily to predict even very roughly what ultimate value of pulse-to-pulse frequency stability of the magnetron can be expected for each definite case. Numerical simulation is hardly useful as well as an independent direct measurement of magnetron frequency stability meets also significant difficulties if achievement of a high accuracy is mandatory. It is due to conceptually pulsed operational mode of the magnetron at rather short pulse duration as well as difficulties relating to ensure an extremely precision and reproducible shape of the high voltage pulse across the magnetron. For this reason, as we have found, despite the above seemingly evident factors, the magnetrons demonstrate a rather good performance in Doppler radar systems, certainly if appropriate design approaches are utilized (see Section 0).

All above can be summarized as follows: (i) magnetron based radars operate always in a pulsed mode; (ii) a spatial resolution is determined by the duration of output magnetron pulse resulting in high peak power requirement to keep a radar potential at an appropriate level under a very low duty cycle operational condition; (iii) since each RF pulse is characterized by an arbitrary phase, a special procedure should be introduced in order to provide Doppler processing capability for the radar; and (iv) especial attention should be drawn to provide as much as possible stable magnetron operational conditions in order to achieve relevant Doppler processing performance. As related to the latter two points, it should be noticed that there is a possibility to lock the phase and frequency of magnetron oscillations with highly stable external oscillator. Unfortunately, an extremely low gain provided, i.e. relation between the output peak magnetron power and the required power of locking signal, especially for millimeter wavelengths frequency region prevent the above possibility to be used in practice.

Next, magnetron life time is considered traditionally to be a serious factor limiting its usability in high performance radar systems. It reflects essentially a state of affair existing in the past, when the magnetron demonstrated actually rather low reliability caused essentially by a limited cathode lifetime. It should be noticed that the magnetron cathode operates at very high current densities as compared with other microwave tubes. In addition, the magnetron cathode is exposed strongly to electron back bombardment inherent to cross-field devices (Okress, 1961) as far as it is sited inside an interaction space. On one hand, such effect results in increase in the emission capabilities of cathode greatly due to secondary emission induced. On other hand it causes cathode overheating and affects the condition of cathode surface. It is considered that the cathode dissipates about 10 % of anode power. It means that a peak power may be as high as several kilowatts. It leads to necessity to reduce the magnetron filament power depending on a value of the anode current. The problem is such induced overheating is not well controlled and depends on many parameters.

Ab initio oxide cathodes are used in the magnetrons. Due to above reasons they demonstrated a poor performance especially for millimeter wavelengths devices owing to a fine internal layout inherent to them. Our experience exposed that lifetime of W band magnetron equipped with oxide cathode was as short as several hours only! Next step was

the usage so called impregnated cathodes (Okress, 1961) in the magnetrons. It has allowed increasing in the magnetrons lifetime up to several hundred hours for Ka band devices. However despite magnetrons equipped with such cathode kept its output power and the ability to start oscillating stably within the above period, we experienced a significant frequency drift even for coaxial magnetrons caused by evaporation of the substance, from which the cathode was made of, with further absorption on the surface of magnetron cavity. Relative failures to manufacture highly reliable magnetrons have coincided with the aforementioned global drop in the interest in the development of magnetron based radars caused by other reasons. On other hand the millimeter wavelengths magnetrons are considered usually as devices for military application exclusively, and for some such applications the achieved life time seems to be more or less suitable. All above have resulted in the development of magnetron and partially investigations in cathode manufacturing have been curtailed worldwide excepting probably the former USSR. The investigations carried over there have given a new lease of life into the development of millimeter wavelengths magnetron and allowed considerable improvement of their characteristics by the end of 80th. It has been achieved due to: (i) utilization of metallic alloy cathodes; (ii) successes in the development of the magnetrons with cold secondary emission cathodes; and (iii) utilization of spatial harmonics different from π type. The latter was especially important for W and G band magnetrons since it has allowed to enlarge dimensions of the magnetron interaction space and the cathode diameter, which results in a considerable increase in peak and average power as well as the maximal pulse duration. In addition, the usage of samarium cobalt magnet system has allowed reducing the magnetron dimensions and weight as well as developing rather miniature devices. The parameters of several millimeter wavelengths magnetrons developed with utilization of above approaches are summarized in Table I.

Frequency band	Ka	Ka	W	G
Peak output power, kW	50	3	4	10
Maximal duty cycle, %	0.2	0.1	0.1	0.085
Anode voltage, V	14000	6300	10000	5
Efficiency	> 33%	> 20%	> 4%	> 5%
Type	Coaxial	No information	Spatial Harmonic	Spatial Harmonic
Type of cathode	Metallic alloy	Cold with spike autoemitters	Cold with auxiliary thermionic cathode	Metallic alloy (?)
Frequency agility	Yes	No	No	No
Life time, hours				No information
Producer specified	>2000	>2000	>1000	
Reached during utilization	>10000 >30000		>5000 >10000	
Average				
Maximal				
Cooling	Forced-air	Forced-air	Forced-air	Liquid
Production status	Full production	Full production	Pre production	Full production

Table I. Parameters of millimeter wavelengths magnetrons.

The indicated values for lifetime of Ka band magnetrons have been obtained during the utilization of a line of Ka band meteorological radars (see Section 0), whereas W-band magnetrons were tested in course of a particular procedure. Achieved value of the magnetron lifetime can be qualified literally as outstanding! It should be noticed that above results were absolutely unexpected for us – we considered reaching 4000 hours only in the best case for Ka band magnetrons. There were no selection for Ka band magnetrons – either among them demonstrates similar performance. Why it has become possible? Beside of the above advances in the cathode manufacturing the overall improvement in production technology should be mentioned, which ensure keeping a high vacuum condition inside the magnetron during whole utilization term. In addition we dare to claim that an advanced design of a magnetron modulator helps significantly the magnetrons exposing its actual potential by automating providing as much as possible safe and optimal operational mode. Since W band magnetrons in question are manufactured in one of branch of Institute of Radio Astronomy of National Academy of Sciences of Ukraine we would like to describe their development and production in some more detail. The first millimeter wavelengths devices had been developed in the middle of 60th (Usikov, 1972). Ab initio they utilize operation at spatial harmonics different from π type. Such magnetron demonstrates excellent performance e.g. peak output power achieved was 80 kW and 10 kW for 3 mm and 2 mm wavelengths devices correspondingly. However due to L type oxide cathode was used in the magnetrons, their life time was limited by a value of several tens hours only. In order to overcome this problem, a cold secondary emission cathode has been introduced in the magnetron design. An auxiliary thermionic cathode placed aside an interaction space was used to provide an initial electron density in the magnetron and ensure oscillation running at the front of modulation pulse. Despite such magnetrons demonstrates inherently a lower efficiency, they are much more promising to extend their lifetime. As a result W band 1 kW device has been developed and industrialized by the middle of 80th (Naumenko et al, 1999). It characterized by a guaranteed life time of 2000 hours. By the end of 90th essential efforts has been concentrated to develop W band magnetrons with expected life time of several thousand hours at peak power of 4 kW, pulse duration of 200 nsec, and duty cycle of 0.1 % for meteorological radars and, a bit later, 1 kW devices with target life time of 10000 hours for airport debris radar. These efforts have resulted in a stable output of W band magnetrons characterized by peak power within the range from 1000 to 4000 W and expected lifetime of 10000 hours (Gritsaenko et al, 2005). At the time being every third manufactured magnetron satisfies technical specification and there are serious reasons to expect an improvement of this ratio. Such fact can be considered as a serious claim on further industrialization. The following problems have been solved to extend the magnetron life time: (i) optimal design of the auxiliary thermionic cathode; (ii) correct choice of an operational spatial harmonics; and (iii) equipping the magnetron with a magnetic-discharge vacuum pump. The latter increases the magnetron dimension but is mandatory to ensure its long life operation especially at a heavy operational conditions, such as a long pulse width, a large duty cycle, or a high pulse repetition rate (see Section 0). A photo of 4 kW W band magnetron produced in the Institute of Radio Astronomy is depicted in Fig. 1. During recent time a low voltage, compact Ka band magnetrons with cold secondary emission cathode are under

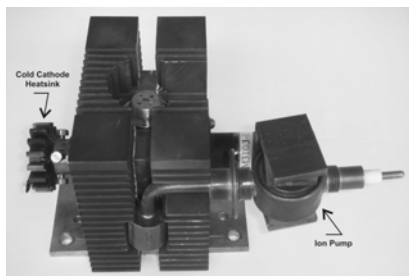


Fig. 1. 4 kW, W band magnetron with cold secondary emission cathode and extended life time.

development. They are intended to be used in low-cost meteorological radar sensors, which are especially convenient for network applications.

Above we have considered the peculiarities of the magnetron utilization in the radars as well as demonstrated that the life time is not an issue preventing magnetrons from usage in high performance radars. Now we would like to discuss further benefits and disadvantages of such approach in a comparative manner. Table II provides a brief comparison between some high power millimeter wavelengths devices available at the time being in respect to their possible usage in the radars. A comprehensive review of current state of the development of power millimeter wavelengths sources can be found in (Barker et al, 2005). Some remarks should be done in addition. As usual the possibility to introduce a sophisticated signal modulation is mentioned as the essential benefit provided by using an amplifier in the radar transmitter. Actually the utilization of a pulse compression technique allows attaining the highest possible resolution for the radars, which is of centimeters grade now. Certainly, the magnetron based radars cannot provide a similar performance level. However for the most applications an extreme resolution is not required and pulse compression is used only to ensure suitable radar sensitivity.

	Magnetron	Traveling wave tube	Klystron with extended interaction	Solid state power amplifier
Peak (average) output power, kW(W) Ka band W band	70 (100) ¹ 4 (4) ¹	1 (300) ¹ [50 (500)] ² 1 (10) ¹ [3 (300)] ²	3 (300) ¹ 1.5 (90) ¹ [1.5 (150)] ²	0.004 (0.004) (single chip) 0.0002 (0.0002) (single chip)
Type	Oscillator	Amplifier	Amplifier	Amplifier
Resolution achievable	High	Highest	Highest	Highest
Life time	Long	Long	Long	Long
Cost	Low	High	High	Low (single chip)
Mandatory options of signal processing	Coherence on receiver	Pulse compression	Pulse compression	Pulse compression; Power combining
Total system cost at similar specifications	Low/moderate	High	High	Very High

Table II. Parameters of power microwave devices.

¹ Air or conductive cooling

² Water cooling

In this case an inherent adverse effect of pulse compression utilization, namely, appearance of spurious targets or, instead, masquerading low RCS targets in presence of that with a strong reflectivity due to side-lobes of the autocorrelation function, should be always taken into consideration. For example, the necessity to monitor simultaneously meteorological phenomena (clouds, precipitation) with a reflectivity range of about 100 dB restricts essentially the application of pulse compression technique for weather radars. Certainly the utilization of such technique providing a relevant performance level requires much more complicated signal processing hardware. Relatively inexpensive implementation of such hardware, suitable to use in mainstream commercial radars, has become to be allowable since very recent time.

Next issue, mentioned usually to accent benefits of truly coherent systems based on utilizing an amplifier in the transmitter, is much higher quality of Doppler processing in this case. However recently developed magnetron based radar systems (see Section 3) demonstrates a competitive Doppler performance within at least Ka band where coaxial magnetrons are available. In addition, further advances in the magnetron modulator design as well as the utilization of a sophisticated digital signal processing allows us to expect over and above improvements in this area, especially for W band radars. The accuracy achieved currently for the phase processing in the magnetron based radars allows us to suggest retrieving appropriate performance even for applications requiring the utilization of synthetic aperture. Interestingly, the approach, based on sampling the radiated signal to provide an enhanced signal processing, inherent to the magnetron based radars, can be useful to improve processing of compressed pulses by avoiding the influence of the distortions introduced by Tx/Rx chains (Zhu, 2008). It is an extra sign that signal processing approaches and, then, capabilities providing by both truly and pseudo coherent radars become closer.

Probably the only area the magnetron based radars cannot compete beyond any doubts with truly coherent systems is radars requiring fast frequency agility.

It should be noticed that despite a low power produced by a single chip, solid state devices allows conceptually developing the most advanced radar systems ever with an unprecedented performance level due to utilization of active phased array technique. Certainly, within millimeter wavelength band such approach is on the technology edge currently and requires enormous efforts to be implemented.

All above mentioned allow us to declare that the achievable performance level of the magnetron based radars is appropriate to meet the most requirements for mainstream applications. Their relatively low cost and complexity make them being very attractive solution especially in the case if the radar system benefits essentially from a shorter wavelengths, as for meteorological applications ($1/\lambda^2$ law for the reflectivity of meteors). Applications where dimensions and weight is among major requirements can be considered also as the area of preferable utilization of the magnetron based radars especially operating within W and G bands.

3. Magnetron based radar systems – development experience

Development of the magnetron based radar systems had started in the Institute of Radio Astronomy of National Academy of Sciences of Ukraine since the middle of 90th of the last century. By the time indicated we experienced with success during many years in the

development and manufacturing of millimetre wavelengths magnetrons with cold secondary emission cathode (Gritsaenko et al, 2005). At the same time, it was clear that existing circumstance for the magnetron usage did not meet modern requirements and did not allow disclosing an actual potential of such devices in radar applications. Then considerable efforts were made in order to develop advanced modulators to drive the above magnetrons, which require furthermore a tighter control of modulation pulse shape as compared to traditional types. Such situation has coincided with a growing interest in radars for environmental investigations operating within millimeter wavelength band. In the course of above tendency the first magnetron based radar sensor has been developed and tested by us (Jenett et al, 1999). It was a rather simple Ka and W band double frequency airborne side looking system intended to detect oil spills on water surface. Since this task benefits strongly from the wavelengths shortening, the utilization of magnetrons has allowed developing the radar rapidly by using simple non coherent signal processing. Nevertheless it demonstrated unexpectedly good performance and was capable to detect a rather weak oil spills even under a low waves condition inherent for internal reservoirs. Obtained experience has allowed us to proceed with radar development and, naturally, the next step was the introduction of Doppler processing capabilities in the radar (Schunemann et al, 2000). After the first usage of a traditional analogue coherence-on-receiver technique, its digital implementation has been introduced. Experiments with a prototype of Ka band meteorological radar demonstrated a good Doppler performance, which was appropriate for the most atmospheric researches as well as to monitor atmospheric conditions. In addition, a capability of the magnetron to work continuously during over several thousand hours has been proven. However our first full functional Doppler polarimetric meteorological radar was equipped with two magnetron based transmitters in order to ensure its reliable unattended continuous operation for at least several months interval. The experience of first year utilization of this radar has disclosed a surprisingly high stability of the magnetron operation. It has allowed to lead off developing a line of high performance magnetron based meteorological radars. It includes both vertically pointed and scanning systems with a high mobility as depicted in Fig. 2. Until now



Fig. 2. Ka band magnetron based meteorological radars.

seven radars has been produced and delivered in cooperation with METEK GmbH (Elmshorn, Germany). Some of them are included into European weather radar network.

Coaxial magnetrons are used in the radars (see Table I). Many improvements have been brought into design with every new item including a double frequency conversion in the receiver; a digital automatic frequency control; a digital receiver technique implementation; modifications in receiver protection circuitry; introduction of the circuits ensuring more magnetron operation safety etc. The essential parameters of most recent radars are summarized in Table III.

The quality of Doppler processing provided by such radars is illustrated by Fig. 3 where Doppler spectrum obtained from a stationary target located at the distance of about 5.5 km is depicted. Signal processing parameters were as follows: pulse repetition frequency - 10 kHz; fast Fourier transform length - 512; spectrum averaging - 10 (dwell time - 0.5 sec). As follows from this figure, Doppler dynamical range exceeds 60 dB, which corresponding to the value of wideband noise floor of -73 dBc/Hz. From this data it is possible to estimate a value of the magnetron pulse-to-pulse frequency instability. Actually, the total power of the received signal can be considered as a sum of coherent P_{coh} and incoherent P_{incoh} components respectively. According to general principles of Doppler processing in radars (Skolnik, 2008), taking into account that the above data are product of a discrete Fourier transform (DFT), and assuming that the magnetron introduces a noise distributed evenly in frequency domain, the ratio between the above components for the signal backscattered by a stationary target, producing definitely monochromatic response, can be set down as:

$$\frac{P_{incoh}}{P_{coh}} = NFl \cdot PRF, \quad (1)$$

where NFl is the noise floor of the radar Doppler processing and PRF is pulse repetition frequency of the radar. On other hand, the phase lag of the signal reflected from a stationary target located at a fixed distance R is $\frac{4\pi R}{\lambda_0} + \Delta\lambda_i$, where $\Delta\lambda_i$ is the deviation of the wavelengths for i th pulse from a constant value of λ_0 . Assuming that $\Delta\lambda_i \ll \lambda_0$, the corresponding discrete time complex signal S at the input of DFT may be written as follows:

$$S_i = A \cdot \left((\sin \varphi_0 + i \cdot \cos \varphi_0) + \varphi_0 \cdot \frac{\Delta\lambda_i}{\lambda_0} \cdot (\sin \varphi_0 - i \cdot \cos \varphi_0) \right), \quad (2)$$

where $\varphi_0 = \frac{4\pi R}{\lambda_0}$. The second term in the above equation reflects the entity of incoherent components in the received signal due to the magnetron pulse-to-pulse frequency instability and determines the value of noise floor NFl on

Operating frequency, GHz	35.5±0.15
Peak transmitter power, kW	30
Average power (max), W	50
Losses, dB, Tx path	1
Rx path	2.5
Pulse duration, nsec	100, 200, 400
Pulse repetition rate, kHz	5...10
Receiver noise figure, dB	3.0
Radar instantaneous dynamical range including STC, dB	>80
Distance for sensitivity, m	
at -10 dB	180
at -1 dB	330

Antenna gain	>50 dB
Polarization decoupling	>40 dB
Total impressed composite wideband noise of Doppler processing @ 5 km, dBc/Hz	-70
Number of range bins	500
Volume	
Transmitter	9U
Receiver	4U
Weight of Tx/Rx units, kg	40

Table III. Parameters of Ka band meteorological radars.

Doppler spectrum assuming that the contribution from other sources like a local oscillator is negligible. Thus finally from formulas (1) and (2), the following expression for the magnetron pulse-to-pulse frequency instability reads as:

$$(3)$$

Substitution of variables in (3) with the above values, namely, noise floor of -73 dBc/Hz, PRF of 10 kHz, of 8.2 mm, and R of 5.5 km results in pulse-to-pulse frequency instability of about

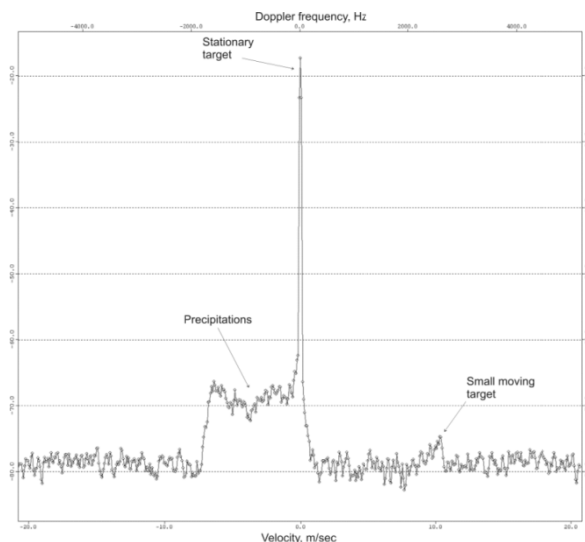


Fig. 3. Doppler spectrum from stationary target located at 5.5 km distance retrieved with Ka band meteorological radar.

Another type of a compact magnetron based Ka band radar is airborne multipurpose radar (Volkov et al, 2007).The developed radar system has been designed especially for applications related to enhancing helicopter flight safety including the detection of power lines and other obstacles, monitoring meteorological conditions, and providing secure landing. But the achieved radar performance enables us to consider it as a versatile sensor, which can be used for other applications. The radar benefits from some novel and cost-

effective solutions including a low-noise; digital receiver; an electrically switchable slotted waveguide antenna array as well as a multifunctional data acquisition and signal processing system. The radar outline; a simplified block diagram; and antenna pattern are depicted in Fig. 4 a, b, and c

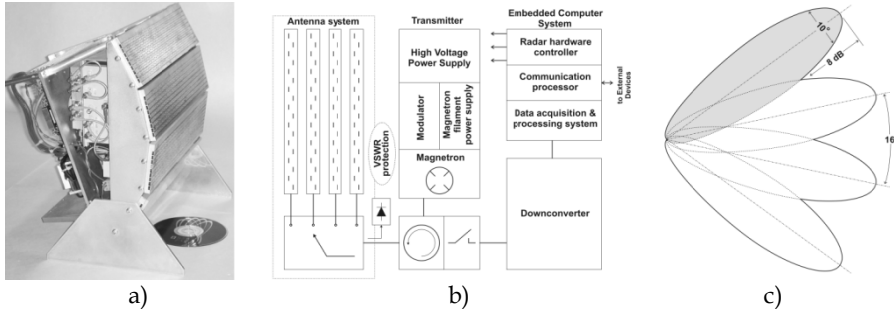


Fig. 4. Outline (a), block diagram (b), and antenna pattern (c) of Ka band airborne scanning radar.

correspondingly. In the radar there is no a separate channel to sample the radiated pulse for coherence-on-receiver implementation. Instead the signal leaked through the receiver protection circuitry is used for this purpose (see Section 0). Single frequency conversion as well as a local oscillator based on a direct digital synthesizer has been used in the radar. The essential radar parameters are summarized in Table IV.

Operating frequency, GHz	35±0.2
Peak transmitter power, kW	2.5
Losses, dB,	
Tx path	1.5
Rx path	2.5
Pulse duration, nsec	50...500
Pulse repetition rate, kHz	1...10
Receiver noise figure, dB	3.0
Receiver dynamical range (max), dB	>90 dB
Time-variation gain control range	24 dB
Minimal distance for full sensitivity, m	50
Antenna	4-sections
Antenna polarization	vertical
Antenna section switching	electrical
Antenna section switching time, μsec	1
Antenna switch decoupling, dB	> 25
Single-pulse sensitivity at 2 km, dBm ²	-13
Total impressed composite wideband noise of Doppler processing @ 3 km, dBc/Hz	-53
Primary power supply, V	18-32 DC
Power consumption (max), W	70
Volume, litre	12
Weight, kg	12

Table IV. Parameters of airborne Ka band scanning radar

A prototype of meteorological W band radar has been developed in the Institute of Radio Astronomy of National Academy of Sciences of Ukraine (Vavriv et al, 2002). It utilizes a proprietary magnetron with cold secondary emission cathode. (see Table I). It is featured by: (i) two separate antennas; (ii) a separate downconverter to sample the radiated signal; and (iii) a high power quasi-optical polarization rotators both in Tx and Rx channels. The radar characteristics are summarized in Table V.

It should be noticed that the radar in question has been developed several years ago and unfortunately no modifications have been provided till now due to our effort were concentrated on the radars operating within Ka band essentially.

Operating frequency, GHz	94
Peak power (max), kW	4
Pulse width, ns	50 - 400
Pulse repetition frequency, kHz	2.5 - 10
Receiver noise temperature, K	1200
Total dynamical range, dB	70
Polarization	HH, VV, HV, VH
Cross-polarization isolation, dB	-25
Antenna diameter, m	0.5
Antenna beam width, deg	0.45
Total impressed composite wideband noise of Doppler processing @ 5 km, dBc/Hz	-47
Sensitivity at 5 km with the integration time of 0.1 sec, dBZ	-41

Table V. Parameters of prototype of W band meteorological radar.

Therefore a serious improvement of its parameter may be expected due to: (i) utilization of a single antenna due to increase in availability of high power circulators and P-i-N switches for the receiver protection circuitry; (ii) an introduction of digital receiver technique as well as a digital frequency control similarly to the above Ka band radars; (iii) the introduction of a low noise amplifier, which have become available during resent time; (iv) the introduction of a synthesized local oscillator; and (v) the introduction of an advanced magnetron modulator.

And at last we would like to provide a brief description W band short pulse transmitter for airport debris radar (Belikov et al, 2002). As known debris are very serious problem to provide enough flight safety. A high resolution as well as a high reliability is a mandatory requirement conceptually for such radars. In the case of magnetron based radar an appropriate resolution may be achieved in a rather simple way, without the utilization of pulse compression. The magnetron with cold-secondary emission cathode used in the transmitter in question provides in addition an extended life time of 10000 hours at least. The parameters of the transmitter are given in Table VI.

Parameter	Measure Unit	Measured Value
Output Frequency(25°C)	GHz	95.086
Frequency Temperature Coefficient	MHz/°C	-1.75
RF Pulse Width (@-3dB, 25°C)	ns	17.5
RF Pulse Width (@-6dB, 25°C)	ns	20
RF Output Peak Power	kW	2

RF Pulse Jitter	ns	3
PRF	kHz	3...30
Supply Voltage min	V	18...32
Current consumption, max @ 28 V	A	14.1
Weight	kg	25
Dimensions		19", 5U unit

Table VI. Parameters of W band short pulse magnetron transmitter.

In the next section some design approaches used in the above mentioned radars are described briefly.

4. Magnetron based radars – design approaches

4.1 General consideration

Let us to remind briefly that any magnetron based radar is featured as follows: (i) a pulsed operational mode is used; (ii) each RF pulse is characterized by an arbitrary phase; and (iii) the spectrum of RF oscillation depends strongly on a shape of modulation voltage as well as on the parameters of external microwave circuits. On other hand, radar operation consists conceptually in locating the received signal as respect to the radiated one in a corresponding space of signal parameters depending of the radar measurement capabilities. For example in the simplest case of non-coherent pulsed radar this space is two dimensional, with coordinates of amplitude and time respectively. For Doppler radar the phase and frequency dimensions should be added. In truly coherent radar systems the exact location of radiated signal in the space of signal parameters is known a priori. Instead, the above peculiarities attending the magnetron utilization in the radars require introduction of specific approaches to provide a precise location of radiated signal in such space and extend its dimensions, i.e. measurement capabilities of the radar.

The most evident but comprehensive method to ensure exact location of the radiated signal is simply to measure its parameters. It is the only way to get phase information, which is a key issue to implement Doppler processing. Thus each magnetron based Doppler radar should be provided with corresponding circuits to sample a small portion of radiated signal in order to measure its parameters like it is depicted in Fig. 5. The magnetron oscillation frequency is next important parameter, whose measurement accuracy affects strongly the overall radar performance. At first, it determines how precisely a target velocity can be measured.

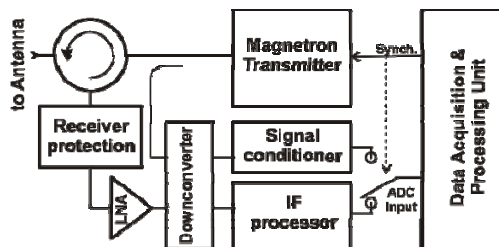


Fig. 5. Typical block-diagram of magnetron based radar.

It does not require a great accuracy and may be implemented relatively easily. Practically in the most cases no measurements are required at all due to a specified magnetron frequency deviation does not exceed a portion of percent in the worst case. A different matter is a pulse-to-pulse frequency deviation. This parameter introduces both non-coherent (noise) and regular components (spurs) into Doppler signal processing (see Fig. 3). In part it determines the ability of the radar to resolve targets with different velocities and reflectivity in the same range bin, e.g. clouds in a strong rain or a moving target in presence of a much stronger reflection from a clutter. As it has been exposed above, the magnetron frequency should be measured with accuracy of about 10^{-7} for a period of several hundred nanoseconds typically or even less, if a higher spatial resolution is required, in order to provide 70 dB spectral dynamical range for Ka band radar and the distance of 5 km. The indicated accuracy is on the edge of contemporary technical capabilities or beyond them, not even to mention the situation inherent to very recent time. Thus at the time being, achieving the maximal possible Doppler performance is the responsibility for the radar circuits, which should ensure as much as possible tight control of magnetron operational parameters – voltage, filament, loading etc, and, finally, its frequency stability. In the nearest future due to a dramatically fast progress in the development of data acquisition and processing hardware we expect that precise measurements of the parameters of the radiated pulse will be a basic method defining radar resolution and instrumentation capabilities. Some promising prospects concerned to this possibility will be discussed later (see Section 4.3.5). Below in this section we will try to analyze requirements to high performance magnetron based radar and discuss some methods to meet them.

4.2 Transmitter.

4.2.1 General consideration

As mentioned above the modern requirements to the radar performance cannot be met otherwise than designing the magnetron environment to ensure as much as possible stability and safety of its operation. Therefore, the transmitter is probably the most valuable part of either magnetron based high performance radar. Before we will proceed to discuss some design approaches used in the transmitters, let us make a simple calculation in order to give an impression about how precisely its circuits should work. Assume that the aforementioned value of pulse-to-pulse frequency stability $\delta f/f$ of 10^{-7} should be provided. The variations of the amplitude of voltage pulse across magnetron should not exceed value given by the following expression:

$$\Delta V \leq \frac{f_{osc}}{F_{volt}} \cdot \left(\frac{\delta f}{f_{osc}} \right) \cdot R_d \quad (4)$$

where f_{osc} is a magnetron oscillation frequency, F_{volt} – a magnetron oscillation frequency pushing factor, R_d – a dynamical resistance of the magnetron in an operational point, i.e. the slope of its volt-ampere characteristic in this point. Let us take into consideration Ka band magnetron and suggest that the magnetron frequency pushing factor is of 500 kHz/A – a very respectable value, inherent to a highly stable coaxial magnetron rather than any other type, and a dynamical resistance of 300 Ohms – a typical value for devices with 10-100 kW peak power. Then the above expression gives an impressive value of about 2 V, or less than 200 ppm typically, for the required value of pulse-to-pulse amplitude instability of magnetron anode voltage! Note, that the indicated value should be ensured during the

interval of data accumulation for Fourier processing. As usual the duration of this interval may vary within the range from tens millisecond up to several portions of second.

Now, when a reference point for the magnetron transmitter design is indicated in some way or other, it is possible to consider solutions enabling its consummation. A simplified block-diagram of a transmitter is depicted in Fig. 6. It includes the following essential units: (i) a high voltage power supply; (ii) a modulator; (iii) a filament power supply; and (iv) a controller. Let us leave the latter unit beyond a more detailed consideration, mention only that it handles other units according the procedures ensuring the most optimal and safe magnetron operational mode as well as provides the

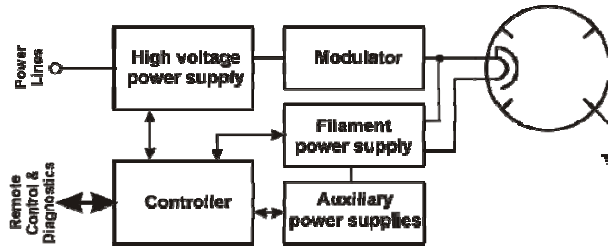


Fig. 6. Block-diagram of magnetron transmitter.

transmitter with remote control and diagnostics abilities. Other above units affect directly the magnetron performance, thus we would like to outline their design in more detail.

4.2.2 High voltage power supply

The high voltage power supply determines essentially the short term magnetron frequency stability, i.e. Doppler performance of whole radar. Thus ensuring its maximal stability is a matter of the highest priority under the development.

A switching mode power supply, based on the utilization of pulse width modulation (PWM) converter, cannot be alternated to produce high voltage in modern systems due to inherent high efficiency, small dimensions, and light weight. However the voltage stability provided by such supply is lower generally than that of linear regulators. On other hand, characteristics of PWM converter may be improved to an extent allowing its standalone utilization. Our experience to develop the high voltage power supplies for the magnetron based radars demonstrates a benefit of the following rules. At first, PWM converter should utilize operation in either peak current or close to it mixed mode rather than in pure voltage mode. Such approach as well as the usage of a frequency compensated high voltage divider assists maximizing both rejection of the input voltage ripples and the overall stability of the voltage regulation loop. Next, it is mandatory to synchronize PWM converter at a frequency multiple to the pulse repetition frequency of the radar, which eliminates practically completely the influence of ripples at PWM operational frequency. And at last, the utilization of a particular pre-regulator is preferably. In this respect, the usage of a power factor corrector for AC powered systems is virtually compulsorily.

For information, the line of Ka band meteorological radar demonstrating a very solid Doppler performance (see Section 0) is equipped with the high voltage power supply developed according strictly to the above recommendations. A flyback topology is used for PWM converter. From our opinion, such topology is the most suitable to the high voltage

applications with the output power up to 1 kW and voltages up to 20 kV for AC powered radar systems or even airborne DC powered radars if an appropriate step-up pre-regulator is used. The essential advance of such scheme is a stable operation with a capacitive load within a wide range of output power as well as the ability to provide the output voltage swing across the primary windings of the high voltage transformer much greater than a supply voltage. The above peculiarities meet perfectly actual operational conditions of the high voltage power supply in a magnetron based transmitters. As can be easily seen from Fig. 3 there is no regular spurious components caused by ripples of the output voltage of high voltage power supply at the harmonics of both AC power line frequency and the operational frequency of PWM converter (folded).

4.2.3 Modulator

In this section we will consider briefly some issues related to the development of up-to date high voltage modulators used in high performance radars. In general the modulator includes circuits to form the pulse with a definite shape across the magnetron terminals. In the most cases a near-rectangle shape of RF pulse is a target under the modulator development. Since the magnetron frequency depends strongly on the applied voltage, any deviation of the pulse shape from the rectangular one results in a drop in the radar sensitivity. Thus, both transients and the distortions of flat part of the pulse should be minimized. Especially it is important for the millimeter wavelengths magnetrons, which are characterized by a rather short width of the output pulse. On other hand the most types of magnetrons requires a well controllable voltage rate during the leading edge of the modulation pulse to facilitate running oscillation (Okress, 1961). In this case faster does not mean better! An opposite situation appears for the trailing edge. As usual a less attention is drawn to ensure its appropriately short duration. However, not only shape of RF envelope should be taken into consideration there. It is due to the magnetrons have a rather considerable threshold current to produce RF oscillation as usual. It means that the current pulse through the magnetron may be much longer than RF pulse as depicted in Fig. 7. Notice that at lower voltages the power of back bombardment of the magnetron cathode is much greater as respect to anode power as indicated in Fig. 7. Evidently, the shorter RF pulse duration and higher pulse repetition rate the stronger the above effect affects the magnetron performance. Thus the above issue should be always taken into consideration while a pulse repetition rate greater than several kilohertz is required.

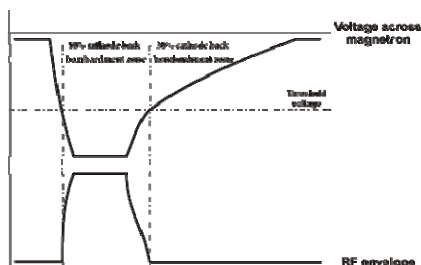


Fig. 7. Waveforms of voltage pulse across magnetron and RF envelope.

Now, when the essential requirements to the modulator circuits have been outlined, some design approaches to meet them can be discussed. Either modulator contains the following parts: (i) energy storage; (ii) a switch or switches, which provides applying voltage across the magnetron within definite time intervals only; (iii) circuits to match the modulator output and the magnetron; and (vi) protection and decoupling circuits. From a variety of modulator types being in use, a line modulator and a modulator with partial discharge are utilized practically exclusively in magnetron transmitters (Sivan, 1994).

A simplified block-diagram of a line modulator is depicted schematically in Fig. 8. A delay line arranged as a piece of cable or assembled from lump inductors and capacitors is used as both to store energy and to form the trailing edge of the pulse across magnetron.

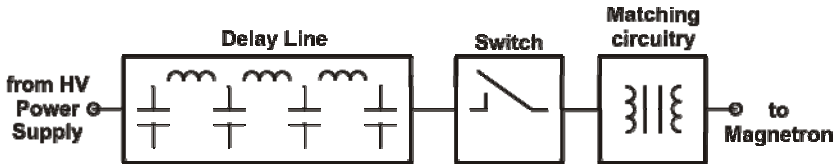


Fig. 8. Block diagram of line modulator.

The utilization of line modulators provides the following advantages: (i) not only fully controlled devices like a hard tubes or MOSFETs may be used in the high voltage switch but also thyristors or thyratrons, which are rated fundamentally to work at much higher currents and voltages (MOSFET *vs.* thyristors comparison); demonstrate a greater efficiency in general; and do not require a precise shape of triggering pulse; (ii) the mandatory utilization of the step-up transformer to match the impedances of delay line and magnetron; (iii) practically complete cancellation of the possible magnetron damage in the case of breakdown due to the total energy stored in the delay line is limited. All above result in the overall complexity and total cost of a transmitter equipped with the line modulator are probably the lowest as compared with other types.

However there are a number of serious disadvantages of such type of modulator. The first is the usage of a lumped element delay line leads us to oscillations appear at flat part of the pulse. Next, it is practically impossible to implement smooth regulating of the output pulse duration. Further, the inherent utilization of the transformer results in the introduction of significant distortions of the modulator output pulse especially due to there is a strong nonlinearity of magnetron volt-ampere characteristic as well as possible appearance of its sensitivity from the voltage rate across the magnetron (Okress, 1961). It makes difficult matching the impedances of the delay line and the magnetron during the leading and trailing edge of the modulation pulse. Both numerical simulation and the experience of utilizing modulators equipped with a transformer prevent us to recommend such approach to be used in the high performance radars. On other hands it should be accepted that almost all mentioned disadvantages of the line modulators are important to achieve the maximum radar performance only and cause no problems in a variety of simple and low cost magnetron based systems.

Another type of high voltage modulator used to drive magnetrons is so called modulator with partial discharge (Sivan, 1994). The essential difference of such type of the modulator from the line modulator is only a small part of energy accumulated in an appropriate

storage is used to form the output pulse. A capacitor is used as the energy storage in the magnetron modulators exclusively. Due to such type of the modulator does not require the utilization of matching circuitry conceptually it provides a much better shape of the output pulse than the line modulator.

A variety of variants can be used to build the modulator with partial discharge. Some of basic configurations are depicted in Fig. 9. Let us consider briefly advantages and disadvantages provided by each of them. The first scheme is traditionally used more frequently than other configurations. It is due to the high voltage switch is grounded, which is a great advantage for whichever hard tube based modulator. In this case a filament and bias power supplies for the modulator tube are grounded also, simplifying considerably the modulator design. This issue is not so important for a solid state switch, arranged usually as a stack of transistors connected in series. Actually, a galvanic decoupling is required anyway to drive each transistor independently on either the high voltage switch is grounded or not.

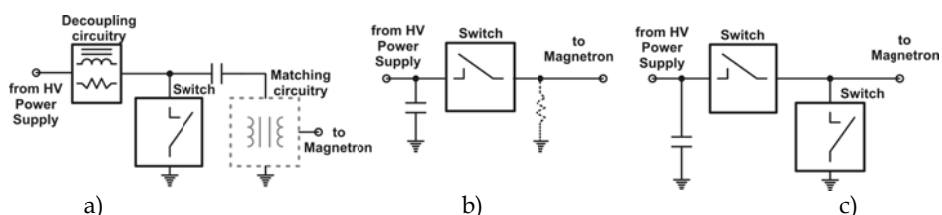


Fig. 9. Schemes of the modulator with partial discharge.

A resistor or choke may be used to decouple the switch from the output of high voltage power supply during interval of pulse formation. In the case of resistor utilization, the distortions of magnetron pulse during its front and flat part are minimal due to no component with frequency dependant impedance is in the pulse formation network. In order to decrease duration of the trailing edge of the output pulse the resistance of the resistor should be chosen small enough, which results in lower modulator efficiency. If a choke is used instead the resistor, the efficiency is better fundamentally. In addition there is a possibility to produce the output pulse with amplitude, which is higher than the value of modulator supply voltage. However due to the pulse formation network includes a reactive component, the output pulse distortions are higher in the case of the choke utilization. Next, generally, there are big constructive difficulties to design a charging choke with required parameters taking into account it is under high pulsed voltage condition. As usual such component is bulky and characterized by a rather large weight as compared with other parts of the modulator. Thus we would not like to recommend the utilization of modulator with inductive decoupling in modern high performance magnetron based radars. Probably only if retrieving of very short pulses at a high repetition rate is required (see (Belikov et al, 2002)), such scheme may appear to be the most optimal choice.

A simplified block-diagram of the modulator with a floating high voltage switch is depicted in Fig 9.b The only capacitor may be used both as the output capacitor of the high voltage power supply and storage capacitor of the modulator. No decoupling circuits are required conceptually in this case. Nevertheless, as mentioned above if a high PRF is suggested, an additional resistor to decrease the duration of the output pulse trailing edge is required as depicted in Fig. 9.b by a dash line. It is difficult evidently to use a hard tube in such circuit

configuration. Instead, from our opinion, it is the most preferable scheme to utilize a solid state high voltage switch.

The push-pull scheme of the modulator is depicted in Fig. 9, c. It provides the tightest control of the output pulse shape as well as the highest energy efficiency among the schemes discussed before. The expense for that is much more complexity in design as compared to previous solutions. It is one of the reasons why the modulators utilizing such approach may be found in a very limited number of radars despite its evident advantages.

Let us now discuss some issues concerned to the selection of an appropriate electronic device to build the high voltage switch. According to modern tendencies solid state devices should be considered as first choice while designing any new electronic system. Two types of solid state devices, namely, MOSFETS, and IGBT may be used in magnetron modulators. Despite IGBT are superior generally to MOSFETS as respect to both maximal rated voltage and current, as well as efficiency provided, they are characterized by a lower switching speed and an attitude to a second-induced breakdown, which confines the overall reliability of the modulator. Thus, MOSFETS remain the only choice among solid state devices to use in the magnetron modulators intended for high performance millimeter wavelength radars featured by rather short operational pulse width.

Hard tubes were historically the first devices used to build high voltage modulators in radars. They remain to be utilized widely until now despite a serious competition from solid state devices. A considerably greater robustness should be indicated as an essential reason. High voltage circuitry have a strong attitude to appearance of various local breakdowns, leakages etc, which are difficult to control and prevent especially for long-term unattended radar operation. Such phenomena stress the modulator parts greatly. Energy to destroy a hard tube is on orders higher than that for any solid state device. Next, the only tube can be used practically always to build any modulator. Instead the limitations for currently available powerful MOSFETS in the maximal rated voltage, makes inevitable utilizing a stack arranged from many transistors connected in series and, possibly, parallel in order to achieve the modulator parameter being enough to drive the most magnetrons. Utilization of pulse transformer allows in principle to minimize number of the transistors used but, as mentioned above, causes considerable pulse distortions. Certainly there is a well-known disadvantage of hard tubes, namely, a limited life time. We dare to claim that it may be considered as almost virtual at the time being. The situation is very similar to that mentioned above for the magnetrons. A current state of cathode manufacturing as well general state of vacuum technique makes expected lifetime of the modulator hard tubes of several ten thousand hours very realistic. These expectations were ascertained completely by our experience of utilization of hard tube based modulators in the line of meteorological radars (see Section 3). The above consideration allows us to make a conclusion that despite of a strong competition from solid state devices, partially MOSFETS, hard tubes are keeping their positions under development of modern magnetron based radars. The only issue may prevent using them in the modulators, namely, their commercial availability and assortment, which decreases actually generally at the time being due to, essentially, a shortage in demand from non-radar application. Certainly we do not mean a fantastic breakthrough in the development of high voltage, high power semiconductor devices, which makes all hard tubes obsolete at one bout!

It should be noticed that the modulator may operates as either voltage or current source. The latter is conceptually better for any cross-field vacuum tube (Sivan, 1994). On other

hand the introduction of the current mode in the modulator makes its design more complex especially in the case if a short pulse length is required. Our experience demonstrates that providing an appropriate stability of the high voltage power supply it is possible to achieve a great magnetron performance even if the much simpler voltage mode is utilized in the modulator. Nevertheless, the development of a modulator, operating in the current mode, remains the greatest challenge a designer faces from our opinion.

4.2.4 Magnetron filament and protection circuits

As mentioned in Section 0, keeping an adequate condition of the cathode surface is the most important issue to prolong the magnetron lifetime. It depends on the following factors: (i) cathode temperature; (ii) vacuum condition inside the magnetron; (iii) electron back bombardment.

The cathode temperature depends both of a filament power applied and the power dissipated on the cathode due to its back bombardment. This temperature should be kept within a rather narrow interval of several tens degrees typically. Thus, the filament power supply should ensure a very tight control of the magnetron filament power as well as provide a dedicated procedure to regulate it depending on the parameters of the magnetron operational mode. In the developed radars (see Section 0) the following proven principle is used. The filament power supply comprises of two parts, low and high side ones correspondingly. The low side part is simply PWM inverter equipped with either analog or digital controller. The high side includes a high voltage decoupling transformer, a rectifier, and a dedicated controller. It should be noticed that we consider that DC filament voltage should be used to supply magnetron filament due to in this case a possible alternating of the magnetron frequency is canceled. The controller is used to measure both filament voltage and current and to transfer the corresponding data to the low side in a digital form. An optical link is used for such communication. The above approach provides accurate and independent measurement and control of the magnetron filament parameters.

The vacuum conditions inside the magnetrons depend not only on quality of manufacturing routine and materials it is made of. Electrical breakdowns affect them strongly. In general, it is considered that the magnetrons demonstrate a rather strong attitude to the development of breakdowns. They may cause in addition direct magnetron damage if no current limiting is provided by the modulator circuitry. It is important for the millimeter wavelengths magnetrons especially due to such magnetrons are characterized by a rather delicate structure of cavities. Hard tubes provide inherently such current limitation, which can be regulated moreover. MOSFETs are featured similarly, but it is difficult to regulate a limit value due to the high voltage switch consists always of several devices connected in series. As a result, this limit is defined by the maximal rated current of the transistors used. Certainly, there is a contradiction between the necessity both to limit the output current and to ensure a minimal settling time of the output voltage of the modulator.

Our experience demonstrates that there is a simple way to prevent possible worsening of the magnetron parameters due to breakdowns without a noticeable degradation in the shape of its output pulse. Namely ferrite beads should be connected in series with the magnetron. This effect may be explained as follows. Breakdown in the magnetron appears usually in two stages. The first stage caused by field emission from a tip located somewhere inside magnetron. This stage runs very fast, typically during several nanoseconds. It cause negligible damages of the magnetron internal parts, but initiates developing the next stage

brought by a local overheating, copper sputtering, and further arcing. This stage requires much longer time to run but can cause significant degradation of the magnetron performance.

The ferrite beads demonstrate rather high impedance under transient conditions. Thus, it leads to fast decrease in the voltage across magnetron during the first stage of the breakdown and prevents developing of the second stage. Moreover the magnetron keeps producing RF oscillations as usual. There are some more benefits from the utilization of ferrite beads. They restrict the change rate of magnetron current resulting in a great reduction of electromagnetic interferences and an increase to overall stability of the transmitter operation. In addition such beads may improve the output pulse shape weakening the influence of stray circuit inductance and capacitance on the pulse front formation. It should be noticed that the usage of ferrite beads is practically mandatory if MOSFET based high voltage switch is used in the modulator. Such devices are characterized by rather low rated dU/dt capability. According to a numerical simulation and experimental investigations, an excess in this value is an essential reason of transistors damage during transients in the magnetron.

At last, it should be noticed that there are evidences that influence of the cathode back bombardment is not limited by thermal effects only as mentioned above. Change in the cathode surface condition has been fixed even after single pulses. Probably it is due to a very high value of instantaneous power of the back bombardment, which is about 10 % of anode power at a nominal anode voltages and much more – up to 30 % - at lower voltages. In order to minimize effect of back bombardment it is necessity to keep the duration of the modulation pulse trailing edge as shorter as possible (see Section 0)

4.3 Receiver

4.3.1 General consideration

The principles to develop receivers for the magnetron based radars are the same as for any other systems. Nevertheless, we would like to discuss below some design approaches, which have proven their efficiency in a number of radars developed in the Institute of Radio Astronomy of National Academy of Sciences of Ukraine.

A simplified block-diagram of a full-featured double channel receiver used in the most modern modifications of Ka band magnetron based meteorological radars (see Section 0) is depicted in Fig. 12. It may be considered as typical and reflecting the essential design approaches. At first, double frequency conversion is used in the receiver. It makes the receiver design more complex apparently, but simplifies greatly the design of local oscillator(s) as well as allows utilizing a simple filtration to reject image frequency. The local oscillator(s) should meet the following requirements: (i) cover wide enough frequency range – typical values of possible frequency variation are 500 MHz for Ka band and 700...1000 MHz for W and G band magnetrons respectively; (ii) provide frequency tuning with a relatively small step; and (iii) ensure a low phase noise with a fast roll-off beyond the band of $\{-PRF/2; PRF/2\}$, which corresponds to the unambiguous frequency range of Doppler processing.

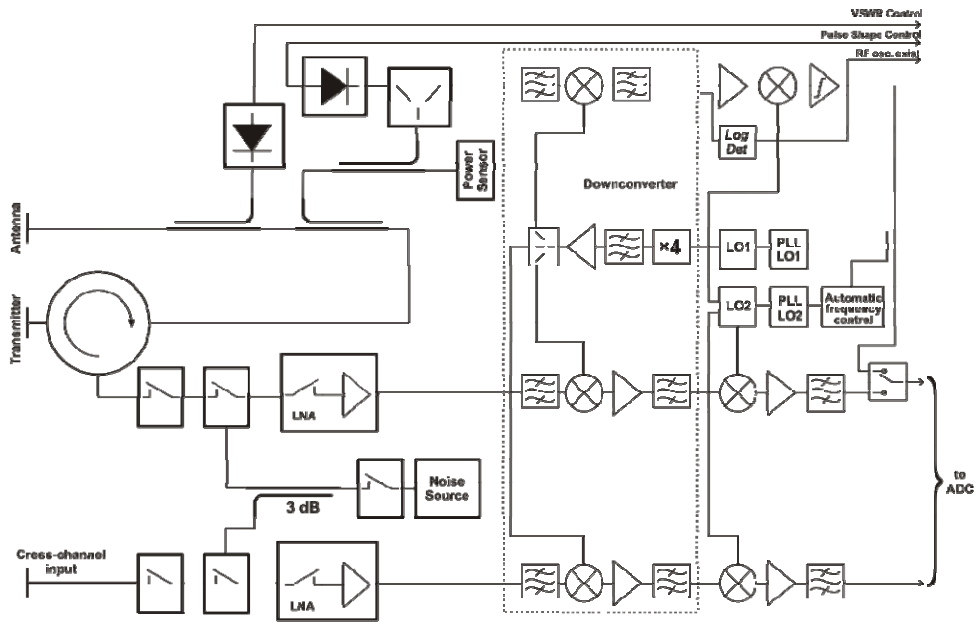


Fig. 10. Block-diagram of receiver for magnetron based Doppler radar.

The latter is required to avoid an increase in the noise floor of coherence-on-receiver processing. In the case of double frequency conversion the first local oscillator operates at a fixed frequency, which makes its design relatively simple. As usual a dielectrically stabilized oscillator with frequency multiplier provides enough performance level for the most cases. If quality of Doppler processing provided by a radar is not an issue, the utilization of single frequency conversion simplifies its design significantly (Volkov et al, 2007)

Next point we would like to discuss is a methods to couple a sample of the transmitted RF pulse to the data acquisition unit to implement coherence-on-receiver processing. An evident way is to use a separate downconverting channel as depicted in Fig. 10. This way provides the highest possible performance but requires additional hardware to be used. Instead a signal, leaked through the receiver protection circuitry, may be used in the way illustrated by Fig. 11. In this case newly introduced circuits operate at the intermediate frequency only. This way is certainly much simpler but characterized by the following disadvantages: (i) an additional phase jitter may be introduced by an antenna environment; (ii) as usual the receiver circuitry operates in a deep saturation, which may cause additional phase instability. Several radars have been developed by utilizing the above approach to pick a sample of the transmitted pulse up. They demonstrated a solid Doppler performance. Nevertheless it was worse on several decibels as compared with the performance of systems, which use a separate downconverting channel. It should be noticed actually that a direct comparison is hardly possible due to the systems in consideration distinguish in much more design details than the method of sampling transmitted pulse.

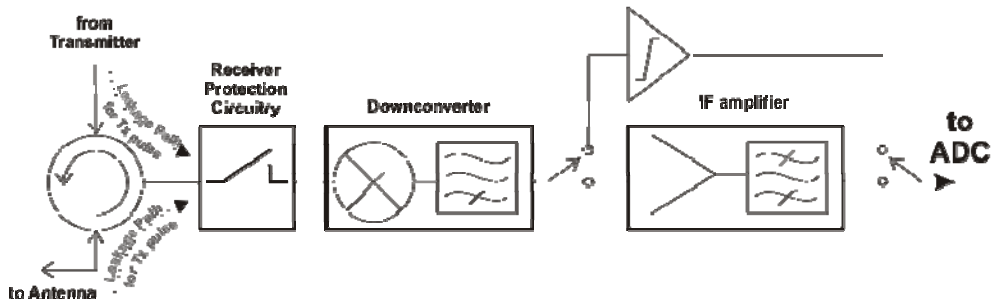


Fig. 11. Utilization of leakage signal to implement coherence-on-receiver technique.

4.3.2 Receiver protection circuitry

As known the magnetron is characterized by a rather high both peak and average power, whereas maximal rated input power of low noise amplifiers (LNA), utilized as the input stage of the radar receiver, is of milliwatt level. Within microwave frequency region a combination of circulator and limiter is the standard de facto solution for providing receiver protection. It may be designed by using only passive circuits. Therefore, no signal is required to control them. It increases reliability considerably. However implementation of similar approach for the radars operating within millimeter wavelength band is complicated due to a lack of suitable limiting diodes accepting kilowatt level peak power. Next, passive limiters allow so-called spikes, which mean that the attenuation provided by such unit may be much less at the front of RF pulse than during its flat part due to a finite forward recovery time of the diode. Evidently the shorter RF pulse front the greater such spikes. Some types of magnetrons, partially the magnetrons with cold secondary emission cathodes is characterized often by a hard self-excitation resulting in a very short RF pulse front duration, which may be of 2-5 nsec only. There are methods to decrease the mentioned spikes in the passive limiters providing, for example, an additional directional coupler and detector in order to bias the limiter diode during RF pulse. However it is hard to find a trade-off between the losses introduced by the biasing circuits and amplitude of the spike. In W band high peak power inherent to the magnetron makes often necessary utilization of two separate antennas for the transmitter and receiver respectively.

The switches based on P-i-N diodes provide better characteristics but nevertheless special approaches should be used to meet above requirements. In order to increase the maximal level of both peak and average power a switch may be build by using multi-diode configuration. It makes its design rather complicated. Another way is to utilize a circulator based switch as it is depicted in Fig. 12, a. A reflective type of P-i-N diodes should be used evidently in the switch. Attenuation in such configuration depends on the isolation of circulator used, whereas insertion losses is determined both by that of circulator and VSWR provided by the diode.

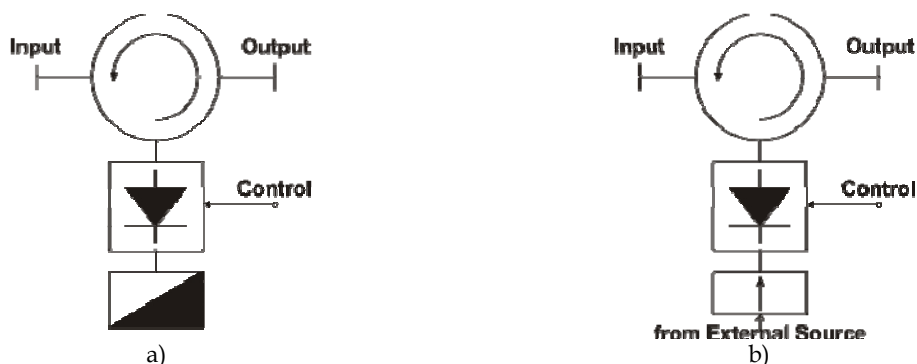


Fig. 12. Design of high power P-i-N switch for receiver protection

Such approach allows us to build an absorptive switch as well as to improve its maximal rated average power due to the incident wave power dissipated on a termination but not on the diode. The parameters of some switches used in Ka band radars (see Section 0) are summarized briefly in Table VII.

The above design of P-i-N switch provides a capability to couple a signal from any external source to its output terminal as depicted in Fig. 12, b. Certainly such configuration of the switch is inferior to that ended by a termination as respect to both an attenuation provided and maximum rated power. However, since the receiver protection circuitry comprises of several switches, a high power rating is not a mandatory requirement for the second and following switches. On other hand there are no additional losses introduced for the external signal. It is important if a noise source is used for the receiver calibration. (see Fig. 10). The output power of such source is low enough requiring a rather high coupling ratio to the receiver input. Evidently, the utilization of passive circuits results in decrease in the radar sensitivity in this case. Certainly there are some disadvantages attending the utilization of above calibration method. Namely, the input circulator and the first protection switch are not inside the calibration loop. Secondly, there is some temperature drift of the calibration introduced by temperature dependency of P-i-N diode characteristics. Nevertheless, the advantages of the above approach are much more meaningful and it can be recommended for wide utilization in the magnetron based radars.

It should be noticed that as follows from Table VII, the most powerful switches, which are capable to handle multi-kilowatt peak power, are characterized by rather low switching speed. It increases the minimal height at which the full receiver sensitivity is achieved. Next, it is rather difficult to provide a tight control of the moment, when the receiver protection switches can be turned on safely. It is due to as mentioned above, in the most modulators there are no circuits to shape the trailing edge of the output pulse in a forced manner, therefore the voltage across magnetron drops rather slowly (see Fig. 7) and duration of this process depends strongly on various parameters. The magnetron is generally characterized by attitude to produce oscillations at rather low anode voltages.

	Switch #1	Switch #2
Bandwidth, MHz	300 MHz	500 MHz
Maximum peak power @ 400 nsek pulse duration, W	> 3500	> 100
Insertion losses, dB	< 0.7	< 0.9
Attenuation, dB	> 25	> 22
VSWR in open state	< 1.2	< 1.3
Switching time @ -3 dB level, nsec	< 1000	< 75
Driving signal	120 mA/-25 V	50 mA/-10 V

Table VII. Parameters of switches of receiver protection circuits operating within Ka band.

These oscillations are weak as usual but may cause LNA damage. A usual way to avoid that is to provide an enough delay before turning the receiver protection switches on. It leads to additional increase in the radar blind zone. The following way is utilized to minimize the response time of the receiver protection system. An additional logarithmic detector is introduced in the channel for sampling the output magnetron pulse (see Fig. 10). Due to its high sensitivity it is possible to detect extremely low level oscillations produced by the magnetron resulting in a tight control of the moment when the switches can be turned on safely. Additionally, by providing two levels detection it is possible to start turning the first – the most powerful and the slowest – switch in advance, at the moment when magnetron is still producing a high but not full power. It allows us to decrease the radar blind zone some more. It should be noticed that there is a very unpleasant effect of the magnetron operation, which affects strongly the receiver safety. Namely, some magnetrons demonstrate the attitude to start producing oscillations not during the front of the modulation pulse but during its trailing edge in opposite. In this case the delay between the triggering pulse and RF pulse may be much longer than usual and it may appear in the moment when the receiver protection circuitry is in a low attenuation state already. Thus such circuitry should process the above condition correctly. In the most of the radars in question if there is no radiation within a definite interval after the transmitter triggering pulse the protection switches remain to be open until next RF pulse.

4.3.3 Receiver dynamical range

A high peak power, which are inherent to magnetron caused not only the above problem while the development of receiver protection circuitry. Another issue is related to maximization of the total receiver dynamical range. Evidently, a high peak power of the transmitter as well as high gain antennas, which can be found in high performance magnetron based radars, lead us to the necessity to introduce rather sophisticated gain regulation circuits in the receiver in order to prevent data loss under either condition. For example, the signal at the receiver input may be as strong as several milliwatts. The total dynamical range for meteorological radars similar to that described in Section 3, should exceed 110 dB. In order to prevent saturation of even the input receiver stage, a regulated attenuator should be used before it. We utilized the following approach. One of the P-i-N diodes of the receiver protection circuitry is driven in the way providing three states, namely, 'off' 'on' '-N dB attenuation' respectively, instead of two states used commonly. It can be achieved by introduction of the corresponding regulation of the current through the diode or the voltage across it. Such way does not require introduction of additional

elements. Despite such approach has proven its usefulness, there were evident disadvantages. At first, the attenuation introduced depends on temperature and frequency rather strongly. Next, every time when the switch is replaced, the corresponding P-i-N diode driver circuits should be re-adjusted in order to keep a standardized attenuation level within allowable margin. An idea to use instead a step attenuator as the third switch (see Fig. 10) looks much more appreciated. However if its implementation seems to cause no serious difficulties in Ka band, for higher frequencies a dedicated development should be done to prove the value of such approach for practical utilization.

4.3.4 Automatic frequency control

Since the transmitter in the radars in question utilizes a free-running magnetron, an automatic frequency control loop (AFC) should be implemented into the receiver in order to tune in it to follow the magnetron frequency. Evidently, AFC should ensure frequency locking over the whole range of possible magnetron operational frequency variation. Next, it should provide a rather good accuracy, especially if an ordinary, non-adaptive matched filtration is used during signal processing.

In early radars AFC design was based on the utilization of analog circuitry including usually some implementation of a frequency discriminator. In this case it is very difficult to meet both above requirements at the same time. Actually in order to achieve a high precision measurement of frequency deviation it is needed to use resonant circuitry with a high figure of merit. On other hand it leads us to decrease in the discriminator operational bandwidth. In addition AFC should operate in a pulsed mode at rather short pulse duration. Moreover, a strong frequency deviation during leading and ending edge of the magnetron output pulse result in additional errors and their dependency on the pulse duration. Nevertheless it was possible to develop AFC on the base of an analog frequency discriminator which demonstrated acceptable performance. The following tricks were used: (i) cropping the input pulse, which reduces the contribution of the frequency modulation during leading and ending edge of the magnetron pulse to the discriminator response; (ii) a periodical throughout calibration of the discriminator circuitry with a dedicated reference signal with the same duration as for the magnetron pulse; (iii) a digital post processing of the rectified output signal of the discriminator including averaging. All above allows us to achieve the long-term AFC accuracy of ± 200 kHz at the central frequency of 280 MHz and frequency locking bandwidth of ± 150 MHz independently on magnetron pulse width varying within the range of 100...400 nsec. The above AFC was used in early Ka band meteorological radars (see Section 0).

Continuous progresses in digital signal processing technique and direct integration of the data acquisition system in the receiver have allowed us developing a fully digital AFC circuitry. It comprises of two loops for a rough and fine frequency locking, correspondingly. The first loop is based on direct measurements of the frequency of a downconverted sampled transmitter signal (see Fig. 10) by using an ordinary digital counter. Pulse cropping is used to improve the accuracy as it was described above. This loop works over the whole range of possible magnetron frequency variations and provides the frequency locking accuracy of about ± 1 MHz at the transmitter pulse duration of 200 ns. The second loop is based on direct measurement of the phase change rate of the downconverted sampled transmitter signal, digitized by an ADC. Due to using a digital quadrature phase detector, the sign of the frequency offset can be measured, and the result of the measurements is

practically independent on the amplitude of the sampled signal. This loop ensures a much better accuracy, which can be as precise as ± 50 kHz at the output pulse duration of 200 ns, but certainly works within Nyquist range of ADC only.

4.3.5 Signal processing- a few remarks

As known (see Section 0) the magnetron produces incoherent oscillations and only the introduction a corresponding signal processing procedure makes possible retrieving Doppler information. Various techniques can be used to implement such processing, see (Li et al, 1994) for example. Their discussion is not subject of matter of this paper. Nevertheless we would like to notice that a potential provided by the introduction of sophisticated signal processing are not confined by the above possibility. Instead it may change radically our mind on the principles of magnetron utilization. Let us cast a very brief look on that below.

As mentioned above achievable resolution, accuracy and measurement capabilities of any magnetron based radar are related tightly to a particular implementation of sampling of the phase of radiated RF pulse. In principle such sampling can be made in one point of time only and it would be enough to implement Doppler processing in principle. But despite an evident simplicity, this method cannot be recommended due to an inappropriate quality of signal processing inherent generally to it. Instead, in our latest radars we are utilizing another approach based on the measurement of so called phase profile – i.e. set of several measurements of phase in equidistant points of time – for each transmitted pulse. Such profile is used to measure the phase shift between transmitted and received pulse by using convolution and filtration procedures. Since the phase profile is used rather than single phase measurement the following advantages are introduced: (i) a reduction of noise due to inherent averaging; (ii) the effect of intrapulse phase variation as well as the appearance of the frequency offset under downconversion are canceled and do not affect the radar sensitivity and Doppler measurement accuracy – i.e. an adaptive matched filtration is implemented in this case.

The above technique can be used to implement intrapulse frequency modulation capability into magnetron based radar. Actually, it is possible to provide frequency chirp by varying the magnetron anode voltage during the modulation pulse. Then a digital technique may be utilized to calculate a correlation function for each radiated pulse and utilize a compression-like processing in order to increase the radar spatial resolution. Namely the millimeter wave magnetrons allow attaining a relatively wide frequency chirp without a significant variation of its output power. For W band magnetrons it is possible to achieve 100 MHz frequency chirp. In the case of successful implementation of the above approach, a considerable improvement both in the radar resolution and sensitivity may be expected.

Next, above we described the successful implementation of precise measurement of the magnetron frequency for every radiated pulse (see Section 0). Fundamentally, the utilization of a similar technique allows us to expect a considerable improvement of Doppler processing quality in radars equipped with non-coaxial magnetrons as well as to reduce requirements for the stability of the voltage pulse across the magnetron. Actually, the usage of a high resolution ADC increases greatly the precision of frequency measurement. Certainly we mean relative measurements. We expect that for 200 ns pulse length the achievable accuracy may be as lower as 1 kHz that corresponds to relative accuracy of $3 \cdot 10^{-8}$ and 10^{-8} for Ka and W band magnetrons respectively. The indicated value is on about order better than the best frequency stability achieved (see Section 0) resulting in the

corresponding improvement of Doppler processing quality. Certainly sophisticated algorithm should be developed to avoid influence of noise, intrapulse frequency modulation etc on the frequency measurements accuracy. This approach is important especially for W band magnetrons, which frequency stability is much less than for Ka band devices and coaxial devices are not produced at all.

5. Conclusion

The above discussion demonstrates clearly that the utilization of recent advances in magnetron manufacturing technology, the introduction of novel approaches in radar design as well as a vast progress in digital signal processing technique result in a solid overall performance of the magnetron based millimeter wavelengths radars. A number of such radars developed and manufactured by our institution, which have been put into operation during last several years as well as the experience of their utilization allow us to claim for a great potential of the magnetrons for the radar development. We dare to affirm that a rather inveterate opinion about futility of such devices to built contemporary radar systems should be considered to be expired.

An evident room for ulterior improvements in both developing high voltage modulators ensuring tighter control of the magnetron operation and introducing sophisticated signal processing algorithms make possible to expect even higher performance level of the magnetron based radars, especially for that operating within short millimeter wavelength bands in the nearest future.

6. Acknowledgments

I am appreciating vastly to Prof. D. M. Vavriv and Dr. V. D. Naumenko for a fruitful discussions and comprehensive assistance.

7. References

- Barker et al. (2005). *Modern Microwave and Millimeter-Wave Power Electronics*. Wiley-IEEE Press.
- Belikov et all. (2002). 95 GHz, 2 kW magnetron transmitter of 20 ns pulses. *Proceedings of German Radar Symposium-2002*, (срр. 571-574). Bonn.
- Brown. (1999). *Technical and Military Imperatives: A Radar History of World War 2*. New York: Taylor & Francis.
- Gritsaenko, S.; Eremka, V.; Kopot, M.; Kulagin, O.; Naumenko, V.; Suvorov, A. (2005). Multi-cavity magnetrons with cold secondary emission cathode: achievements, problems, prospects (in Russian). *Radio Physics & Electronics*, 10 (Secial issue), 499-529.
- Jenett, M.; Kazantsev, V.; Kurekin, A.; Schunemann, K.; Vavriv, D.; Vinogradov, V.; Volkov, V. (1999). Dual 94 and 36 GHz radar system for remote sensing applications. *Proceedings of International Geoscience and Remote Sensing Symposium*, 5, срр. 2596-2598. Hamburg.
- Li, Hua; Illingworth, A. J.; Eastment, J (1994) A simple method of Dopplerizing a pulsed magnetron radar. *Microwave Journal*, 37 (4), 226-235.
- Okress. (1961). *Crossed-field Microwave Devices* (T. 1,2). New York & London: Academic Press.
- Sivan. (1994). *Microwave Tube Transmitters*. London: Chapman&Hill.

- Skolnik, (2008). *Radar Handbook, Third Edition*. New York: McGraw-Hill.
- Tsimring. (2007). *Electron Beams and Microwave Vacuum Electronics*. Hoboken, NJ: John Wiley & Sons, Inc.
- Usikov. (1972). Investigations in Microwave Electronics made in IRE AS Ukraine (in Russian). *Electronic Technics, Ser 1, #12 (12)*, 39-49.
- Vavriv et al. (2002). 95 GHz Doppler polarimetric cloud radar based on a magnetron transmitter. *Proceedings of 32nd Microwave European Conference, 1*, стр. 665 -668. Milan.
- Volkov et al. (2007). A Ka-band, Magnetron based, scanning radar for airborne applications. *Radar Conference, 2007. EuRAD 2007*, (стр. 186-189). Munich.
- Zhu, Di; Dong, Xiaolong; Lin, Wenming (2008). Pulse Compression with Very Low Sidelobes in a Spaceborne Weather Radar, *Proceedings of Geosciences and Remote Sensing Symposium, IGARSS 2008*, Vol. 5, pp. 252-255, ISBN: 978-1-4244-2807-6, Jul. 2008, Boston, USA